Conference Proceedings of the Society for Experimental Mechanics Series

Chad Walber · Patrick Walter
Steve Seidlitz *Editors*

Sensors and Instrumentation, Aircraft/Aerospace, Energy Harvesting & Dynamic Environments Testing, Volume 7

Proceedings of the 37th IMAC, A Conference and Exposition on Structural Dynamics 2019

Springer

Conference Proceedings of the Society for Experimental Mechanics Series

Series Editor

Kristin B. Zimmerman, Ph.D.
Society for Experimental Mechanics, Inc.,
Bethel, CT, USA

More information about this series at http://www.springer.com/series/8922

Chad Walber • Patrick Walter • Steve Seidlitz
Editors

Sensors and Instrumentation, Aircraft/Aerospace, Energy Harvesting & Dynamic Environments Testing, Volume 7

Proceedings of the 37th IMAC, A Conference and Exposition on Structural Dynamics 2019

Springer

Editors
Chad Walber
PCB Piezotronics, Inc
Depew, NY, USA

Steve Seidlitz
Saint Paul, MN, USA

Patrick Walter
Engineering Dept, Tucker Bldg, Rm 200
Texas Christian University
Fort Worth, TX, USA

ISSN 2191-5644 ISSN 2191-5652 (electronic)
Conference Proceedings of the Society for Experimental Mechanics Series
ISBN 978-3-030-12675-9 ISBN 978-3-030-12676-6 (eBook)
https://doi.org/10.1007/978-3-030-12676-6

This Springer imprint is published by the registered company Springer Nature Switzerland AG.
The registered company address is: Gewerbestrasse 11, 6330 Cham, Switzerland

Preface

Sensors and Instrumentation, Aircraft/Aerospace, Energy Harvesting & Dynamic Environments Testing represents one of the eight volumes of technical papers presented at the 37th IMAC, A Conference and Exposition on Structural Dynamics, organized by the Society for Experimental Mechanics and held in Orlando, Florida, on January 28–31, 2019. The full proceedings also include volumes on Nonlinear Structures & Systems; Dynamics of Civil Structures; Model Validation and Uncertainty Quantification; Dynamics of Coupled Structures; Special Topics in Structural Dynamics & Experimental Techniques; Rotating Machinery, Optical Methods & Scanning LDV Methods; and Topics in Modal Analysis & Testing.

Each collection presents early findings from experimental and computational investigations on an important area within sensors and instrumentation and other structural dynamics areas. Topics represent papers on calibration, smart sensors, practical issues improving energy harvesting measurements, shock calibration and shock environment synthesis, and applications for aircraft/aerospace structures.

The organizers would like to thank the authors, presenters, session organizers, and session chairs for their participation in this track.

Depew, NY, USA — Chad Walber
Fort Worth, TX, USA — Patrick Walter
Saint Paul, MN, USA — Steve Seidlitz

Contents

Chapter 1
Historical Review of "Building Block Approach" in Validation for Human Space Flight

Joel W. Sills Jr. and Matthew S. Allen

Abstract The evolution of human spaceflight vehicles including launch vehicles continues to propose a perplexing conundrum in the structural dynamics field. Because of the size and weight of these vehicles, it becomes impossible to perform a ground based modal test that replicates all of the loading events of interest (i.e. liftoff, ascent, staging, etc.). As a result, human spaceflight programs have long relied on "building block approaches" to dynamic model updating and validation. Given the wide interpretation and definition of a "building block" approach to dynamic model validation, this paper reviews the state of art techniques used during the Saturn/Apollo and Space Shuttle dynamic test campaigns and contrasts them with the plans for the Space Launch System (SLS). Some of the lessons learned in each program are presented, in terms of how the building block approach was applied in developing models for stakeholders, using and updating analytical models, and use of other test result outside the dynamic tests.

Keywords Building block approach · Integrated system · Element/component · Scale model · Ground vibration test · Correlation

1.1 Introduction

Accurate prediction of the launch and flight loads is critical to the design and flight readiness verification of both the launch vehicle and its payload. Loads are a function of the structural dynamic properties of the coupled launch/space vehicle system. The structural dynamic properties, however, are a function of the design of the system. This, then, leads to an iterative design and verification process. Initially, estimated design loads size the structure. Analytical models are constructed, and coupled loads are computed. The design iterates, and the loads analyses repeated. The process converges to a design that has positive structural margins against predicted loads. Predicted loads are based on both the expected environment (e.g. forces) and the analytical models (e.g. the modal properties of the vehicle) and, hence, are likely to contain significant errors and uncertainties. Once hardware is built, uncertainties due to the latter can be reduced by performing a mode survey test where the dynamic properties of the vehicle are measured. The measured data are then used to adjust the analytical model.

The process reviewed so far would be adequate if the vehicle as a whole could be tested in every configuration of interest, i.e. mounted on the launch pad, early ascent stage with free boundary conditions and full fuel tanks, partially full tanks during ascent, after separation from stages or boosters, etc.... Clearly the volume of testing that this would require is not feasible. Furthermore, some vehicles, such as the SLS, are too large and heavy to be tested as a whole with free boundary conditions. For these and other reasons, a modal testing and model updating/correlation are performed on subcomponents of these advanced vehicles. Then, testing and model updating must be performed for each subcomponent, and the boundary conditions for each test and the must be selected so the component modes of vibration of each element are connect and the stiffness and damping of the interfaces must also be verified. Hence, the current building block approach may include tests on each subcomponent individually with free or approximately fixed boundary conditions, on assemblies of a few subcomponents, etc. The test-tuned subcomponent models are then used in a final prediction of launch and flight loads across a range of conditions. These loads, once compared with allowable values, establish the launch viability of the structural system for both the launch vehicle and its payload.

J. W. Sills Jr. (✉)
NASA Johnson Space Center, Houston, TX, USA

M. S. Allen
Department of Engineering Physics, University of Wisconsin, Madison, WI, USA

C. Walber et al. (eds.), *Sensors and Instrumentation, Aircraft/Aerospace, Energy Harvesting & Dynamic Environments Testing, Volume 7*, Conference Proceedings of the Society for Experimental Mechanics Series,
https://doi.org/10.1007/978-3-030-12676-6_1

Launch and ascent structural loads are a function of the dynamic properties of the integrated launch vehicle/space vehicle system. Therefore, design changes in one element can result in load changes in all elements, and modeling errors in one element can result in load prediction errors in all elements. Since the dynamic properties of each element will be a function of the structural design of that element, the design process must be iterative. Flight attitude control and pogo analyses are also both dependent on the accuracy of the dynamic model, and failure of either analysis can result in loss of vehicle (LOV) or can severely degrade the ability of the vehicle to meet its flight objectives.

An important item to note is that neither the launch vehicle element organizations (e.g., core section, engines, boosters, second stage) nor the space vehicle organizations (e.g., Multi-Purpose Control Vehicle (MPCV)) control the overall structural dynamic properties of the integrated system since no organization controls the design and, thus, the properties of the other organizations' structure. This, therefore, makes the design of the flight elements (e.g., core section, engines, boosters, second stage) dependent on organizations typically not under the elements' control. This raises an important question. How can the various organizations have sufficient confidence in the quality of the models, and in the analyses performed by the other organizations, to commit to launch, or conversely, invest resources to redesign a system prior to launch?

For the latter, a substructuring approach is a possible alternative. Substructuring is theoretical basis for the building block approach that can provide this confidence. There are two primary ways in which a substructured model of an assembly may be created. One could use the Hurty/Craig-Bampton (HCB) approach, in which case one can be assured that an assembly of HCB models will accurately predict the modes of an assembly (i.e. the dynamics of the vehicle) if the fixed-interface modes of each subcomponent are correct and if each subcomponent has a correct and complete set of constraint modes. The latter describe the stiffness of the interfaces between subcomponents. Hence, using the HCB mindset, testing should focus on assuring that the finite element model (FEM) captures these two types of modes accurately. Alternatively, one could use the Rubin method (or one of the many variants) in which case the free-interface modes of each subcomponent must be accurate as well as the residual attachment modes, which represent the static stiffnesses of the joints between the components. Either case provides a path whereby one can perform tests and correlate subcomponent models and gain assurance that the system level predictions will be correct.

It should be noted, however, that in modern practice we typically couple the full finite element (FE) models of each subcomponent to estimate response of the full vehicle, and so the models contain many modes (or additional degrees of freedom) that aren't fully validated by test. Similarly, each component cannot be tested in every possible configuration (i.e. fuel tank full, aerodynamic shells intact and jettisoned, etc. . . .). However, by checking that the model faithfully reproduces the low frequency dynamics of each subcomponent, the interface stiffnesses, and that it is consistent with engineering drawings or the as built hardware, one can obtain significant assurance that the system level predictions will be accurate.

1.2 Building Blocks and the Integrated System

As NASA embarks on the next evolution in space transportation, it is important to review major NASA program's approaches to low frequency structural testing and model validation and how the current programs within the NASA Human Exploration and Operations Mission Directorate (HEOMD) are approaching integrated dynamic testing. The common thread between the past and present is that each program used a building block testing approach to validate dynamic math models. The building block approach is a common term that defines a strategic test campaign designed to provide confidence and accuracy in modeling of the integrated design. D. B. Spaulding defined an analogous process in fluid dynamics as the "Art of Partial Modeling" [1]. The American Society of Mechanical Engineers (ASME) discuss a bottoms up approach to modeling [2] as an appropriate methodology for performing modeling verification and validation. In this approach a system is decomposed into its constituent subsystems, elements, and components; thus, enabling validation experiments to be conducted at every level and leading ultimately to the system model validation. Figure 1.1 is an example of the ASME approach. The building block approach can manifest itself in many different forms and this paper examines case studies from the Saturn V development, the Space Transportation System (Shuttle), and the current integrated SLS. Each of these programs' processes culminates in a system level ground vibration test.

Size, and hardware and organizational complexities of any complex system preclude validation at the system level except possibly for the lower order "beam bending" modes (i.e., modes with frequencies <10 Hz). Element/component models typically are updated/corrected/adjusted by element organizations making coupled system model correlation potentially complicated. Hence, mode survey tests and model correction/adjustment should be focused and performed at the element/component level. Elements/components should be responsible for delivering test-verified models that satisfy program success criteria. From these element/component models, coupled system loads analysis, pogo stability, and control stability models can then be developed for the appropriate configuration and time of flight.

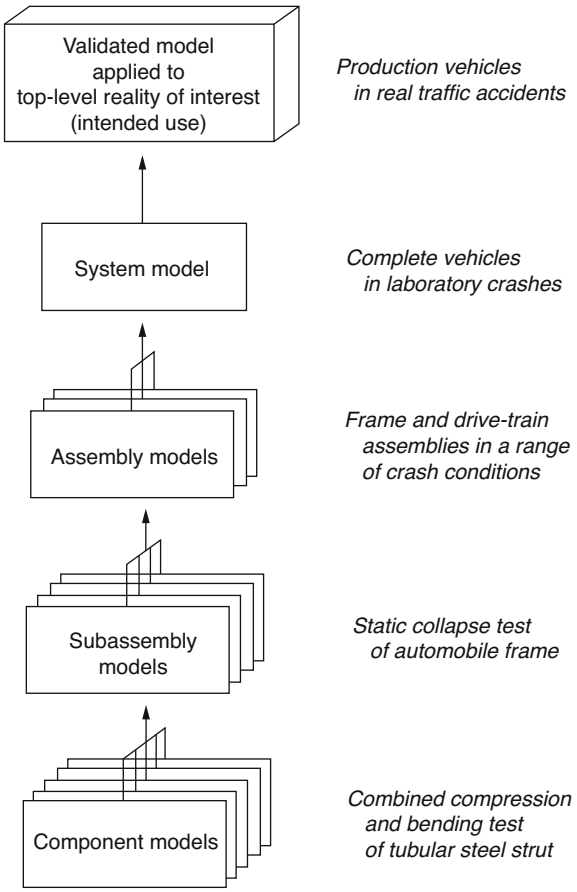

Fig. 1.1 Example of bottom-up approach to V&V [2]

The merits of performing an integrated system test are important enough from a technical perspective, but cannot provide the complete model validation for all phases of flights. In a ground vibration test (GVT) one can only measure the fundamental dynamic characteristics of the launch vehicles, and perhaps only for a few simulated for various phases of flight. However, element/component testing is equally as important because they contain important structural detail that is not exercised in the GVT and/or visible in the modes that can be extracted in that test as the validation of these models provide the basis for ascent integrated vehicle models. Without test-adjusted models, the model uncertainty factor (MUF) is not updated, and this uncertainty can translate into increased mass and vehicle instability due to incorrect modeling and boundary conditions.

Clearly, integrated system testing has considerable merit in that it allows for characterization of the entire system and exercises critical interfaces. This allows analysts to adjust/correct their idealized models and in particular any assumptions regarding the interfaces, which might not be possible in the component level tests. However, an integrated system test is not the final answer since these results must be supplemented with comprehensive flight data. There are specific data that can only be captured during flight that cannot be captured on the ground. These data include system-level responses at flight pressurized levels and free-free vehicle characteristics.

1.3 Saturn V Experience (1960s)

The Saturn V program is the first notable program in human space flight to use a structural dynamic building block approach to validate the integrated vehicle characteristics. The program set forth four principles that were foundational in their approach: (1) Develop dynamic test and analysis program requirements; (2) Perform a scale model test campaign; (3) perform a full scale test campaign; and (4) develop a test validated system math model. These steps are one form of variant of a building block process.

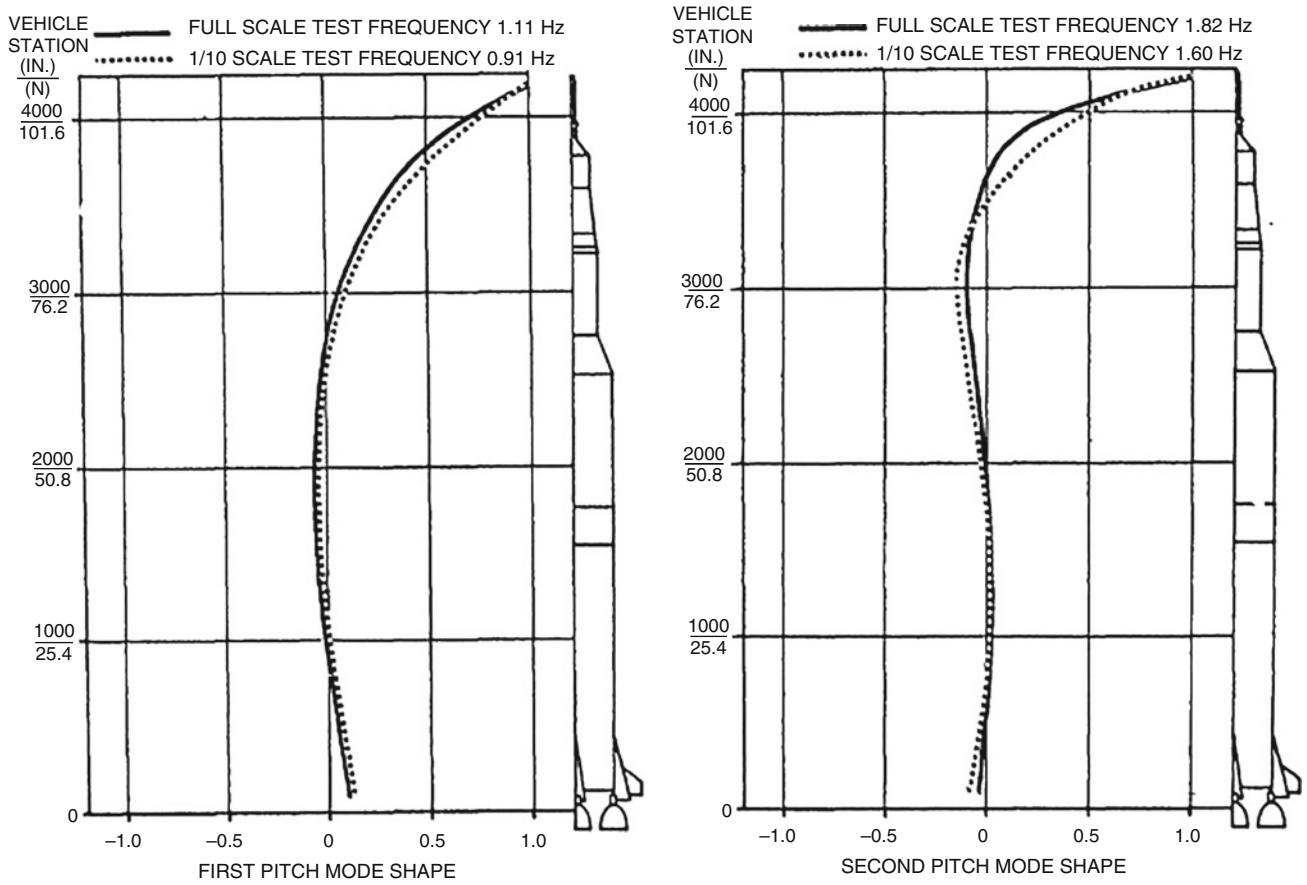

Fig. 1.2 First and second pitch mode shape and frequency comparison between Saturn V 1/10th scale and full scale tests at 100% propellant fill levels [3]

At the beginning of the program, a 1/10th scale model of the Saturn V was created to assess math modeling techniques, validate test methods, and develop procedures for analyzing and testing the full scale article. The scale model simulated the dynamics of three vehicle boost phases. Water was used to simulate the liquid oxygen (LOX) and first stage fuel and the tanks were pressurized to an equivalent flight pressure. Results from the 1/10th scale testing and the full scale testing are shown in Figs. 1.2 and 1.3 for the first two pitch and longitudinal modes respectively. For the pitch modes, mode shape correlation is reasonable, but the frequencies differ by 22 and 14% between the two results. For the longitudinal modes, the mode shape plot agreement shows dramatic differences and the frequencies differ between 23 and 11%. Investigations [3] revealed that differences between the results directly trace to the modeling of joint flexibility that was used to design the scale model, and was not completely understood until the static testing was completed. Had the static test results been incorporated into the design of the scale model, the agreement would have improved. These experiences with the Saturn V program underpin the importance of incorporating component testing, especially the local joint influence coefficient (i.e., force and deflection data), as part of the building block test program. While in this example the model of interest was a physical 1/10 scale model (rather than a FE model in most modern cases), the lessons learned are generally applicable.

The ground test campaign used for the Saturn V program could not simulate the actual flight conditions for several reasons: some flight hardware had been replaced with mass simulators, a suspension system was not available that could adequately simulate the free-free flight conditions, vehicle cryogenic propellants could not be used, and the flight vehicle configuration for each element was different. Given the maturity of analytical tools at the time that the Saturn V program test campaign took place, initial math models were simple beam rod types and served as the pre-test model in determining test requirements. The primary purpose of the beam model was to understand the sensitivities of replacing LOX with water. The modeling evolved when quarter shell models were developed taking advantage of launch vehicle symmetry while still operating within the computer limitations at the time. These quarter shell models were specifically focused on local modeling of sensor locations and the engine/thrust structure area to understand the sensor slopes. The quarter shell model eventually evolved into a full quarter shell representation of the vehicle. This version of the model proved adequate in predicting bending modes to within

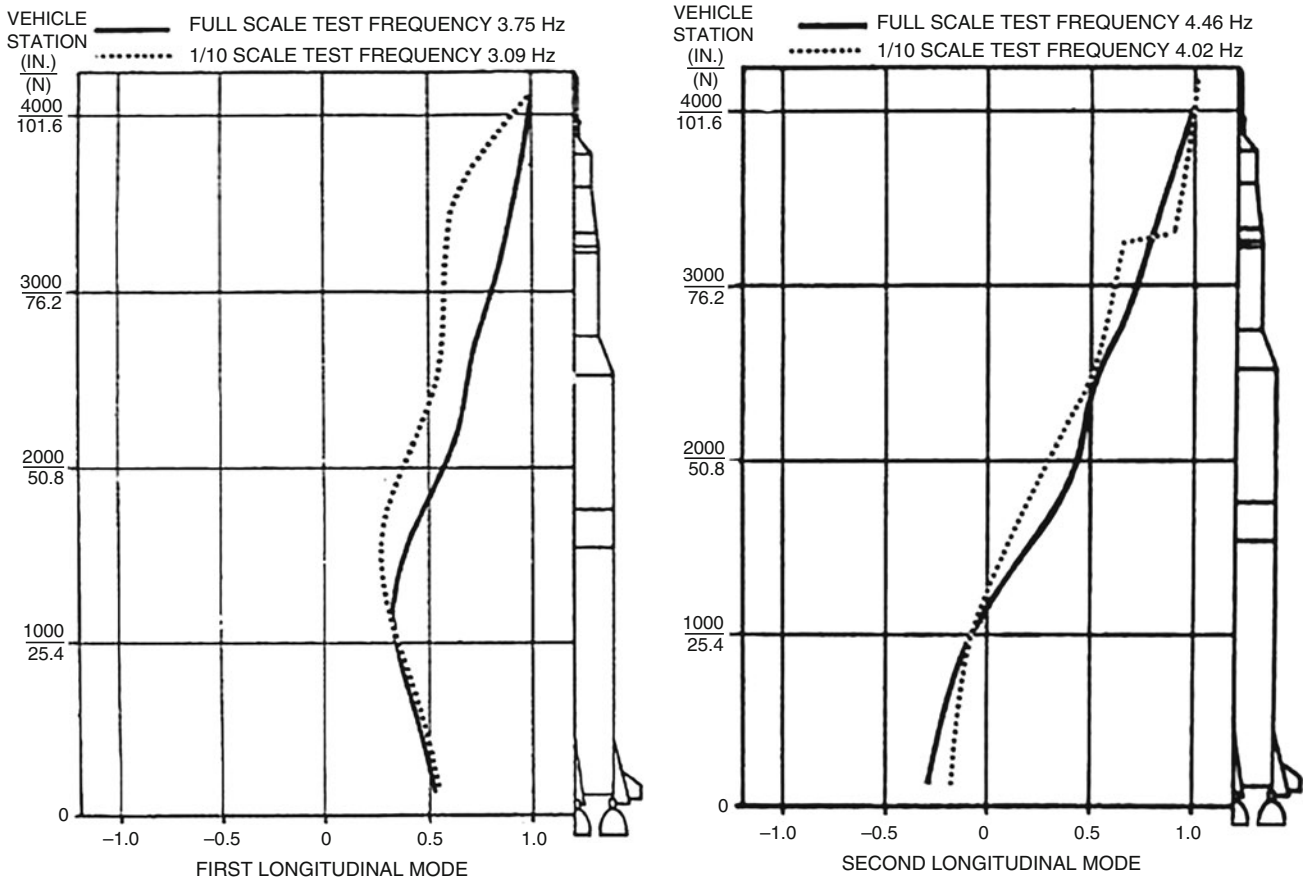

Fig. 1.3 First and second longitudinal mode shape and frequency comparison between Saturn V 1/10th scale and full scale tests at 100% propellant fill levels [3]

4%. The quarter shell model was unable to predict the sensor slopes nor was it able to predict the coupling between the pitch, yaw, and longitudinal planes due to spacecraft eccentricities. Hence, a three dimensional model was developed to capture these missing effects. The three dimensional model was further simplified in insensitive areas and became the model of record for pogo, loads, and flight control predictions. The three dimensional model consisted of 12,000 stiffness DOF that were reduced to 300 dynamic DOF. Figure 1.4 shows the evolution of the Saturn V math models including the number of degrees of freedom for each model.

The Saturn V full scale vehicle testing conducted at the NASA/Marshall Space Flight Center (MSFC) used a 132-channel data acquisition system and a suspension system designed to simulate free-free boundary conditions. The test article was predominantly flight hardware weighing approximately six million pounds. The measured mode shapes are compared with the shapes form the math model in Figs. 1.5 and 1.6 for the two pitch modes and two longitudinal modes respectively. From the figures, one observes that the frequencies are within 4% for the first four vehicle modes and there is relatively good agreement between mode shapes. What is noted in the literature [3, 4] is that local deformations and major element effects could not be captured in this test. Only through element and localized testing and correlation of math models can these effects be captured and incorporated with any accuracy. This is a key component in any building block approach and re-emphasizes the importance of technical due diligence in all element/component testing leading up to an integrated system test.

1.4 STS Experience (1970s)

The Space Shuttle is the second most notable human space flight program to use a structural dynamic building block approach to validate the system characteristics. There are unique challenges with the Space Shuttle that went outside the experience base of the Saturn V effort, as the Shuttle is a reusable spacecraft. However, there are similarities in overall approaches

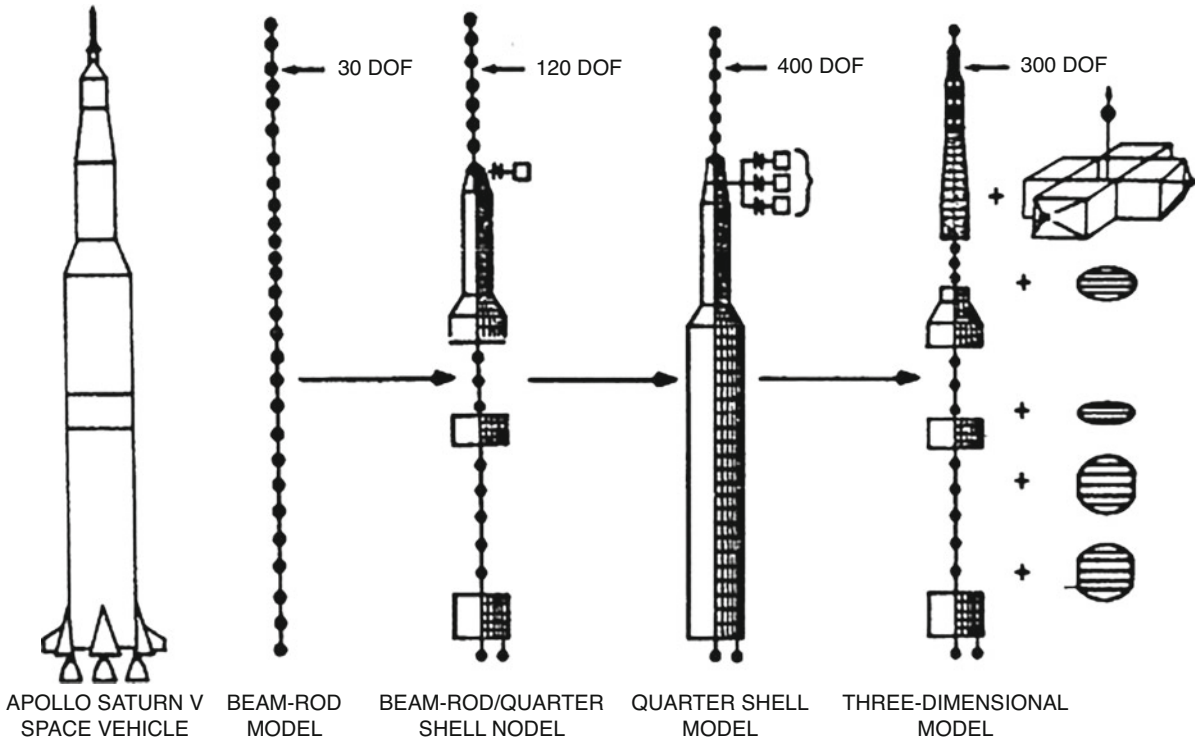

Fig. 1.4 Saturn V system model evolution [3]

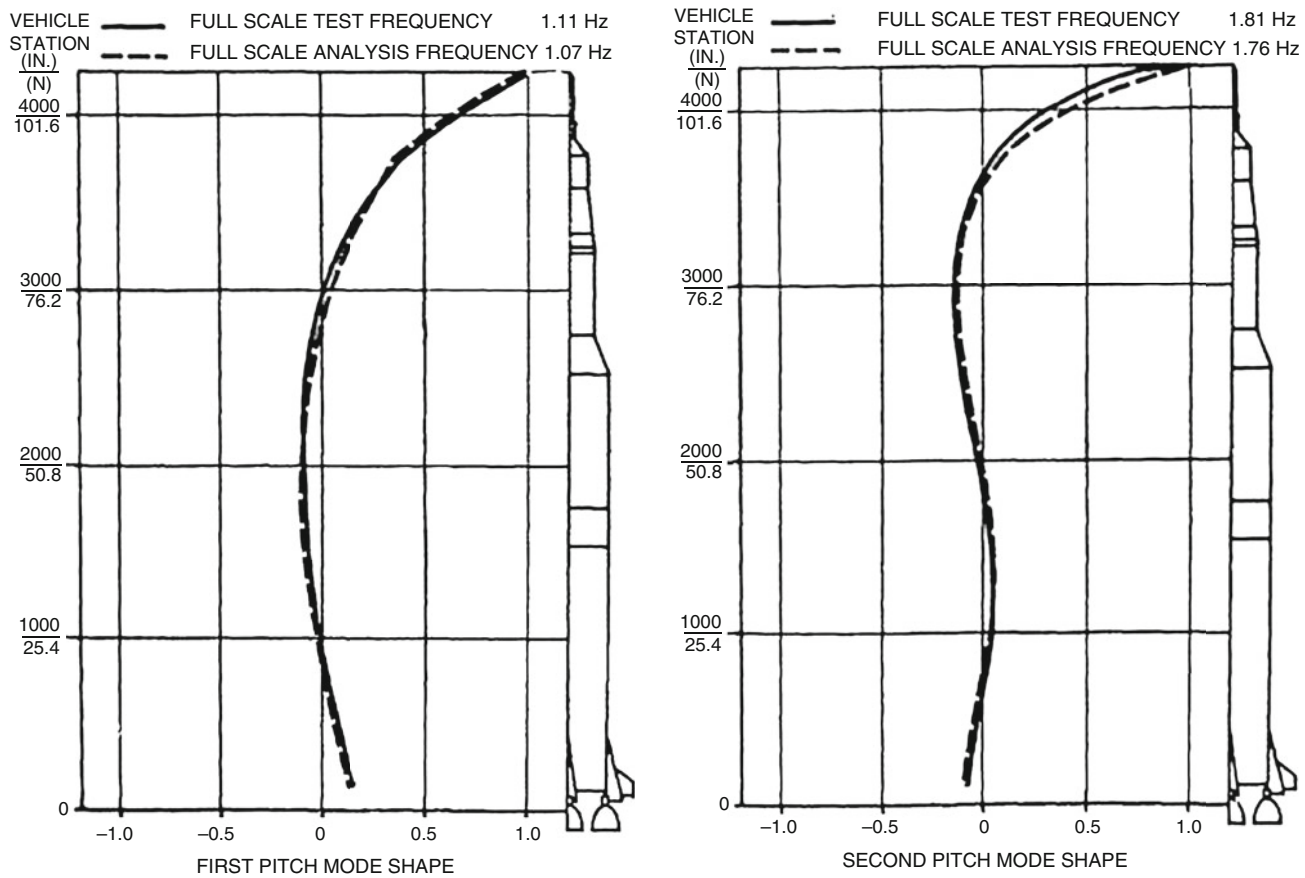

Fig. 1.5 First and second pitch mode shape and frequency comparison between Saturn V system test and analysis at 100% propellant fill levels [3]

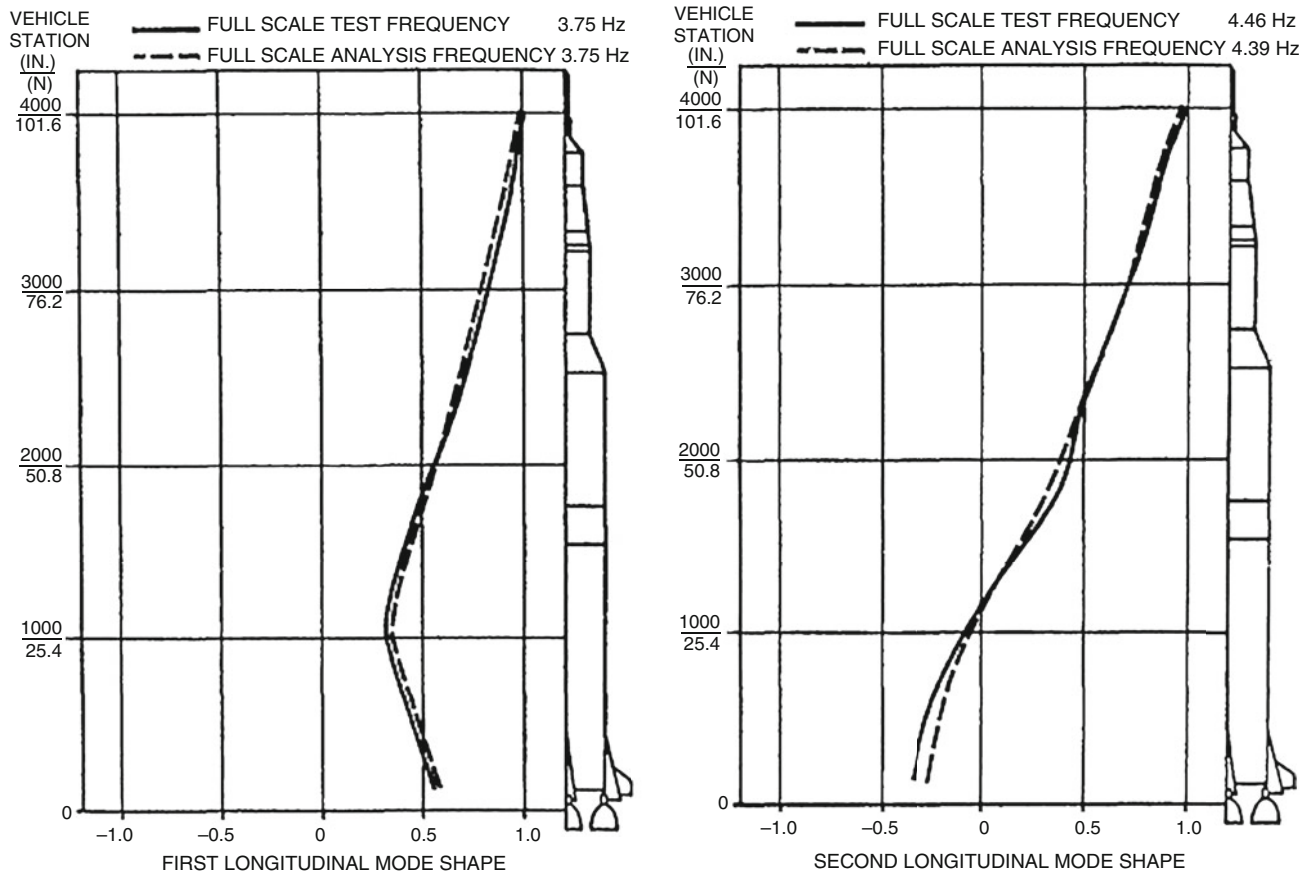

Fig. 1.6 First and second longitudinal mode shape and frequency comparison between Saturn V system test and analysis at 100% propellant fill levels [3]

between the Saturn V and Space Shuttle programs. The shuttle program embarked on a building block approach which sought to test major elements separately and then as a system. There were many discussions on how to approach testing of this new system. In the end it was determined that there was no single test that would answer all stakeholders' requirements. Instead, a systems approach was used to evaluate different stakeholder's requirements and arrive at a set of tests that would provide the necessary validation. These tests comprised the following:

- 1/8th scale model testing—used to understand modeling techniques
- Liquid Oxygen (LOX) tank modal test—used to inform the model of hydrodynamic effects
- Orbiter Horizontal Ground Vibration Test—Used to understand the Orbiter characteristics
- Quarter scale testing—used as early data to inform modeling and to supplement later tests
- Mated Vertical Ground Vibration Test (MVGVT)—used to inform the system model and interface dynamics between elements

There were several other program tests that occurred in the lifetime of the development program that provided opportunities to collect additional experimental data that informed the modeling. These included:

- Main Propulsion Test (MPT)—used to inform the models on engine thrust, frame coupling, and provided pogo transfer functions
- Solid Rocket Motor (SRM) firings—used to inform models about nozzle and actuator dynamics.
- Single Engine Development firings—provided pogo transfer functions and engine gains

Figure 1.7 below provides an overall view of how these tests were used to satisfy technical requirements.

Of equal importance, the program established, within the overarching verification and validation plan, responsibility and accountability for the element contractors to provide correlated/validated structural dynamic models. Within this same framework, the system contractor had responsibility for providing requirements to the element contractors to enable the

REQUIREMENTS	STATIC AND COUPON	HGVT	QUARTER SCALE ELEMENT	QUARTER SCALE COUPLED	SSME MPT	LOX MODAL	MVGVT
HYDROELASTIC			S			P	
VISCOELASTIC	P		S				
DAMPING							P
LOCAL EFFECTS / UNKNOWNS							P
LOAD PATHS (JOINTS AND INTERFACES)	S			S			P
UNSYMMETRICAL DYNAMIC COUPLING				S			P
ACTUATOR/ENGINE/THRUST FRAME/LINE COUPLING					P		
SRB ELEMENT MODEL			P				S
SRB PRESSURE EFFECT	P		S	S			
ET MODEL			S			P	S
ORBITER MODE		P	S				S
EXTRPOLATION TO FLIGHT			S	S			P

NOTE: P = PRIME SOURCE; S = SECONDARY SOURCE

Fig. 1.7 Overall utilization of building block approach for model validation of the shuttle [5]

assembly of the system model for use in system level GVT activities. The specificity of this approach represents an evolution from the Saturn V building block approach, and ensured that lower level testing and model validation would infuse test-based information upwardly to the system level.

The complexity of the Space Shuttle provided new challenges that included higher modal density and lower system frequencies approaching 2 Hz. There were new challenges with modeling as the structural dynamic models derived from stress models had approximately 50,000 DOF for the Space Shuttle structure alone. This represents a two-order of magnitude increase in modeling complexity from the Saturn V models.

To touch upon the validation challenges, early testing was carried out with 1/8th scale models and ¼ scale models followed by component tests, element tests, and systems tests, as outlined in Fig. 1.8. The 1/8th scale model represented a beginning in trying to understand the structural characteristics of the Space Shuttle four body representation (i.e., two boosters, external tank, and Orbiter). This endeavor, while coarse in its representation, confirmed information on low frequency system structural modes (i.e., 200 structural modes below 20 Hz) as well as the coupled interface stiffness that influences these modes.

The 1/8-scale Shuttle Orbiter model program determined the adequacy of analytical modeling technology available at the time (i.e., circa 1974) and was used as in a design of experiments. At the inception, the 1/8-scale mode required that all components (Orbiter, ET and two SRB's) be coupled to determine mated vehicle modes. The technology at the time allowed for a successful calculation of modes for the components, but did not allow for coupling of the structures to form the overall system. The limiting factor was the computing capacity and time available at this period of development. The Orbiter modeling parameters for this effort are show in Table 1.1.

An initial model, Model I, provided the first basis of comparison between analytical and test modes. The results comparison proved to be less than favorable and exacerbated by the computing limitations. This result in itself focused attention to the modeling, design, and fabrication and improvements were made to the modeling to bring the model and test data into better agreement. Further static and dynamic testing led to further model modifications to improve poor joint modeling and incorporate flexibilities for the fin/fuselage support, forward/mid-fuselage splice, cargo door attachments,

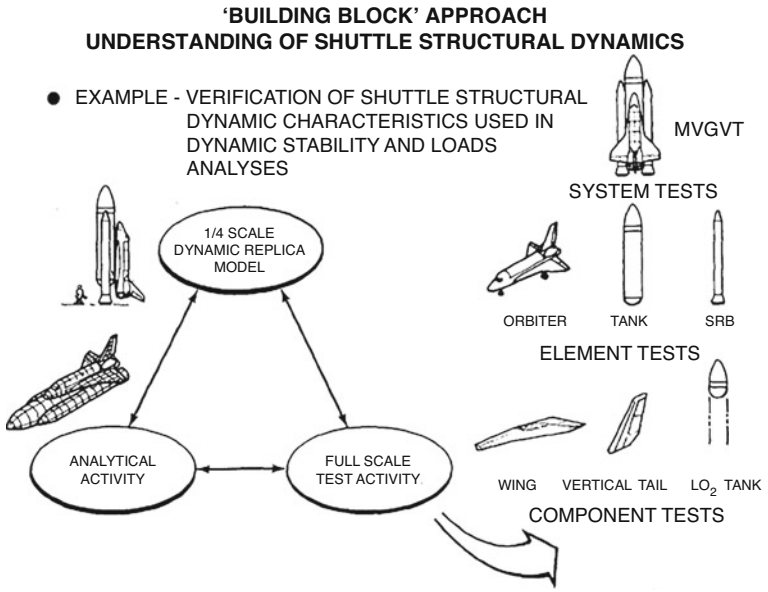

Fig. 1.8 Space shuttle program building block approach to characterizing structural dynamics [5]

Table 1.1 1/8-scale test analysis model sizes [6]

Substructure	No. Grid Points	No. CBAR	No. CQDMEM2	No. CSHEAR	No. CROD	No. CTRMEM	No. CQUAD2	Total No. of Members	SYMM CASE		ANTISYMM CASE	
									DOF After SPC & MPC	DOF After GUYAN	DOF After SPC & MPC	DOF After GUYAN
Payload	12	8	–	–	–	–	–	8	24	24	26	26
Fin	59	–	24	22	65	–	–	111	101	25	99	24
Wing	192	–	149	81	187	8	–	425	531	183	531	183
Doors	134	9	20	64	178	–	16	287	396	26	384	26
Fuselage	537	93	336	172	616	7	–	1224	1417	246	1368	222
Total ½ Orbiter	934	110	529	339	1046	15	16	2055	2469	504	2408	481
Orbiter Analysis ST-3	215	Contains 125 plotel elements							400	339	378	324

wing carry-through structure, payload attachment, and the effective width of the fuselage and wing skins. One of the major takeaways from this effort was that for some joints only static tests could provide the relevant data to model the joint and there was no amount of analytical analysis that could properly characterize these joints. The 1/8th scale model program further uncovered deficiencies in hydroelastic (tank) analysis, which were remedied with details found in NASA Contractor Report-2662 [7]. While these methodologies eliminated fundamental flaws in hydroelastic methodology and modeling, fluid models are not any more reliable than structural models. Therefore, fluid tanks and modeling require the same level of test verification and validation as the structural articles.

Table 1.2 shows a comparison between the Model II (i.e., the updated analytical model with incorporated flexibilities) natural frequencies in Hz and those from scale test data in Hz as well as the March 1973 Shuttle prototype analyses.

With this information, the program baselined three separate ground vibration tests (GVTs): (1) ¼ scale model GVT; (2) the mated vertical ground vibration test (MVGVT); and (3) a horizontal ground vibration test (HGVT).

The ¼ scale test program set forth to demonstrate that scaled math models could be verified as separate elements and as a coupled system building on the lessons learned from the 1/8th scale model testing and mathematical coupling techniques. The testing further set forth to determine transfer functions between the guidance sensors for the Liftoff configuration (i.e., coupled Orbiter, External Tank (ET), and SRB) and boost configuration (i.e., Orbiter and ET). Further notable modeling challenges that surfaced from the ¼ scale GVT campaign included external tank hydroelastic modeling, solid rocket booster propellant viscoelastic modeling, and modeling of joints between the elements, and modeling tank pressures and its effects on structural modes. Reference [7] provides an overarching summary along with detailed references on testing configurations and analyses addressing the modeling issues that surfaced in the ¼ scale GVT campaign. Once these modeling challenges were addressed, with the exception of the SRB propellant viscoelastic modeling, the following frequency comparisons were

Table 1.2 1/8th scale Model II test data comparison to 1/8 scale and 1973 prototype model analysis [6]

1/8 Scale* Model II	1/8 Scale* Test	Prototype**	Normal Mode Description
5.5	5.45	3.56	Fuselage 1st Bending
6.8	6.40	5.26	Wing 1st Bending
–	12.0	5.38	Payload Pitch
–	–	7.23	Payload 1st Bending
15.2	13.4	8.28	Fuselage 2nd Bending
7.9	7.26	11.97	Payload Fore-Aft
–	–	12.32	Aft Crew Comp. Trunion
14.5	13.0	12.59	Wing 1st Torsion
–	–	14.17	Fwd Crew Comp. Trunion
10.0	10.0	14.70	Fin Fore-Aft
–	–	15.40	Wing 2nd Bending
–	–	16.68	Fuselage 1st Longitudinal
–	–	18.00	Fuselage 3rd Bending
–	–	23.05	Fuselage 2nd longitudinal
–	–	24.62	Payload 2nd Longitudinal

*Scale factor on frequencies for replica models if $f_m/f_p = 8/1$
**Results from Grumman analysis of prototype shuttle current in March 1973
ST-7

achieved for the free-free orbiter and the free-free liftoff configurations. Table 1.3 provides an example of the ¼ scale results for the coupled Liftoff configuration. Note that the frequency comparisons vary in percentage difference and that the SRB Roll mode shows considerable variability in the test data and when compared to the analysis representation.

From the ¼ scale testing came the evolution of both the Horizontal and Mated Vertical Ground Vibration Tests. For the purposes of brevity, we will take an overview of the MVGVT only. Within the program at the integration level, a MVGVT requirements board was formed to facilitate coordination between all stakeholder requirements and ensuring verification objectives are met. To this end, the MVGVT focused on the Liftoff and Boost phases of flight. Requirements from the primary stakeholders are shown in Table 1.4. These requirements express the necessary accuracy for capturing key experimental parameters to be used in model validation. The objectives for this test were similar to those identified for the ¼ scale test, with the addition of a requirement to measure the response on the external tank feedline to provide data for validating the feedline math model.

Details of the MVGVT are captured in Reference [8] with a sample Liftoff system mode shape shown in Fig. 1.9 and a summary comparison between test data and analysis results shown in Table 1.5.

From Table 1.5, the frequency difference varies from 1 to 18%. From the testing, several noteworthy items came to light. Most notably, the left and right SRB forward mounted rate gyros exhibited abnormally high transfer functions, which required a structural redesign. Additionally, it was found that the model for the axial mode of the Space Shuttle Main Engine (SSME) did not correlate well with test due to the simplified modeling technique used. As a result, a three-dimensional, asymmetric math model of the Space Shuttle Main Engine (SSME) and thrust structure was constructed. The pre-test analysis used a symmetric half shell technique to model the structure. Finally, local deformations on the Orbiter bulkhead led to unexpected yaw gyro rates leading to re-modeling of that local area.

While volumes of information exist on the topic, this section has attempted to summarize the procedure used for the Space Shuttle program, to provide a sampling of results showing the degree of correlation obtained in test and modeling, and to highlight lessons learned. The exercises revealed a variety of deficiencies in the analysis models, some of which required redesigning the structure to assure its integrity. Modeling deficiencies occur in unexpected places, often due to joints between components or over-simplification of some components in the analysis model; these would not be captured without a test that identifies a mode that is sensitive to the defect.

1.5 Experience to Date and Plans for the Integrated Space Launch System (SLS)

The HEOMD Explorations Systems Development (ESD) enterprise is comprised of three major programs: Exploration Ground System (EGS), the SLS, and the MPCV. All three programs are separate entities with their own internal governance model. Each program represents a complex system comprised of multiple elements and subsystems. The approach to

Table 1.3 ¼-scale liftoff configuration test result comparison to analysis [7]

Mode Sequence No.	Test Mode No.	Frequency (Hz)	Analysis Frequency (Hz)	Test Mode Description (Dominant Motion)	Damping Value (C/Cc)
1	44	6.71	8.04	SRB Roll (0.38) and Pitch (0.18) (Repeat of Test Mode 13 at 226 lb Force)	0.044
2	45	7.00	8.04	SRB Roll (0.33) (Repeat of Test Mode 13 at 143 lb Force)	0.032
3	13	7.29	8.04	SRB Roll (0.33) and Pitch (0.18) 63 lb Force	0.036
4	12	10.46	10.22	SRB Yaw (0.95)	0.008
5	4	11.06	12.54	SRB Pitch (0.51) and Roll (0.13) two Shakers per SRB	0.04
6	43	11.12	12.54	SRB Pitch (0.49) and Roll (0.12) one Shaker Per SRB	0.028
7	6	11.71	12.42	ORB Pitch (0.62), SRB Roll (0.13) and Yaw (0.13)	0.015
8	23	12.70	N/A	First Feed Line Fluid	0.013
9	8	15.77	17.39	SRB Axial (0.45) and Yaw (0.35), and ET Lox (M=2, N=2)	0.008
10	9	20.84	26.41 22.76	ORB Axial (0.24) SRB First Z Bending (0.29) SSMEs Pitch (0.21)	0.018
11	1	22.72	22.76	SRB First Z Bending (0.40), Eng's Oy (0.17) and ET 1 Z (0.15)	0.018
12	2	25.63	27.8	ORB Wing Z Bending (0.90)	0.015
13	14	26.92	30.84	Vert. Tail Pitch (0.40) and Eng. No. 3 Pitch (0.33)	0.017/ 0.027
14	16	27.48	32.36	SRB First Y Bending (0.95) and Wing Z	0.007
15	11	29.68	34.83 35.71	ORB Pitch (0.41), Wind Bending (0.12), and SRB Yaw	0.008
16	10	32.23	31.75	ET Lox (M=1, N=5), (0.77)	0.005
17	21	32.23	32.19	ET LH_2 Shell (0.12), lox Shell (0.10), Dome Axial (0.10), Body Flap (0.18)	0.016
18	26	34.08		Body Flat (0.35), Dome Out-of-Phase w/Lox Line	0.010

Table 1.4 Key MVGVT stakeholder parameters [5, 8]

Items/Users	Control	Pogo	Flutter	Loads
Structure Model	Motion Sensor / Gimbal Force	Propellant Pressure / Thrust Force	Surface Motion / Aero Forces	High Stress Points / All Forces
Frequency Range	0 - 10 Hz	0 - 40 Hz	0 - 40 Hz	0 - 40 Hz
Frequency Accuracy	5% < 4 Hz, 10% > 4 Hz	5% < 3 Hz, 15% > 3 Hz	5%	10%
Damping Range	> 0.005	~ 0.01	~ 0.01	~ 0.01
Damping Accuracy	10% < 4 Hz, 20% > 4 Hz	20%	20%	20%
Slope Accuracy	10% < 4 Hz, 20% > 4 Hz	N/A	15%	20%
Deflection Accuracy	10% < 4 Hz, 20% > 4 Hz	20%	15%	20%
Pressure Accuracy	N/A	30%	Not Tested	Not Tested

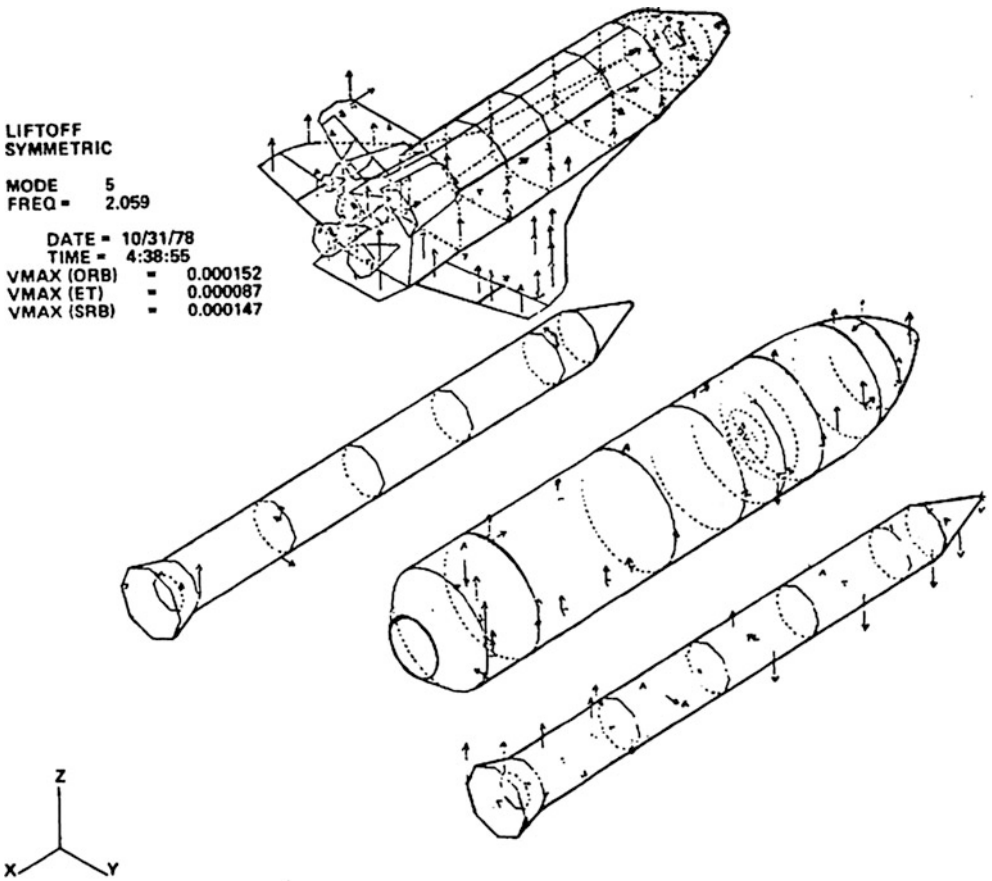

Fig. 1.9 MVGVT liftoff mode shape [5, 8]

Table 1.5 MVGVT liftoff comparison between test data and analytical results [5, 8]

Test Mode				Analysis Mode			
Mode No.	Freq.	Damp	Description	Mode	Freq.	Description	Percent Error
5	2.05	.013	SRB Roll (.34). Pitch (.25). Yaw (.16). Orbiter Pitch (.08). ET-Z (.13)	4	2.11	SRB Roll (.38). Pitch (.45). Yaw (.04). Orbiter Pitch (.04). ET-Z (.07)	3
7	2.64	.014	SRB Yaw (.95). ET Pitch (.02)	6 5	2.93 2.45	SRB Yaw (.84). ET Pitch (.02) SRB Yaw (.83). ET Z (.07)	11 8
9	3.02	.017	SRB Pitch (.38). Roll (.27). ET-Z. Bending (.10). Orbiter-Z (.07)	8	3.18	SRB Pitch (.38). Roll (.34). ET-Z. Bending (.06). Orbiter-Z (.08)	5
11	3.24	.010	ORB Bending (.33). X (.36). SRB Z-Bending (.25)	7	3.14	Orbiter Bending (.44). X (.43). SRB Z-Bending (.06)	-3
12	3.88	.015	SRB-X (.60). Yaw (.13). Fwd ET Shell (.24)	9	3.87	SRB-X (.47). Yaw (.38). Fwd ET Shell (.14)	1
23	4.39	.0013	SRB Z-Bending (.22). Roll (.08). F L Fluid (.17). Orbiter Bending (.17)	11	5.16	SRB Z-Bending (.26). Roll (.06). Orbiter Bending (.54)	18
14	5.26	.016	SRB Z-Bending (.47). ET Bending (.27). Orbiter Bending (.17)	12	5.39	SRB Z-Bending (.15). Y-Bending (.13). ET Bending. Axial (.33). ORB Bend (.15)	2
18	5.65	.005	Orbiter Pitch. Bending. In-Phase Wing Bending (.55). Orbiter X (.18)	11	5.16	Orbiter Z. Bending. In-Phase Wing Bending (.54). Orbiter X (.03)	-9
10	6.43	.037	1st Wing Bending (.68). Out-of-Phase Upper SSME (.13)	15	6.60	1st Wing Bending (.64)	3
21	6.78	.011	SRB Sym Yaw and Y-Bending (.85)	18	7.62	SRB Sym Yaw and Y-Bending (.67). Propellant (.12)	12
15	7.92	.011	Vert Tail Fwd Aft Rocking (.21). Out-of-Phase Wing Bending (.18)	16	6.88	Vert Tail Fwd Aft Rocking (.07). Out-of-Phase Wing Bending (.22)	-2
32	7.45	.031	SSME No. 3 Pitch (.20). Out-of-Phase V.T. Fwd/Aft Rocking (.11)	20	8.08	Lwr SSME Pitch (.50). Out-of-Phase V.T. Fwd/Aft Rocking (.41)	8
27	7.77	.009	1st Lox Tank Bulge. Upr LH_2 (.34). Lox Ogive (.14)	18	7.62	Bulge Mode Overwhelmed by SRB Energy	-2
16	8.42	.016	SRB 2nd Z Bending (.62). Roll (.05)	22	8.36	SRB 2nd Z-Bending (.67). Roll (.08)	-1
13	9.00	.008	Orbiter Pitch and Bending (.76). Out of Phase SRB Pitch (.06)	26	9.40	Orbiter Pitch and Bending (.76). Out-of-Phase SRB (.02)	4

structural model validation parallels the paths of previous NASA manned space programs (i.e., Saturn V and the Space Shuttle program). Each ESD program has employed a building block approach to utilize component, element, and system testing to validate dynamic and structural models. At the overall ESD integrated system, the system models are integrated for different aspects of integrated operations ranging from rollout from the Vertical Assembly Building (VAB) to the pad, to Liftoff, to Ascent, to landing and recovery operations. Each of these operational phases have a very complex set of interactions that must be understood and modeled within the accuracy of today's current computational methods and abilities. Given the complexity of this system of systems, there is not one test nor one model that can address the physics and complex interactions of these systems. For this reason, the building block approach for this undertaking provides a departure from the previous programs. An example of this departure is there is no scale dynamic modal or static testing of the complete integrated system in the liftoff and boost configuration. The other advantage and rationale for not following the previous program testing scripts is that there has been large technology advances in computational mechanics and codes. Computer limitations (i.e., solver time, degree of freedom size limits, etc.) are no longer the constraining factor rather the complexity of these new integrated systems and the ability to physically accommodate and test these systems have become one of the limiting factors. Some of the issues revealed in previous programs, such as hydro-elastic modeling and visco-elastic propellant modeling, have become well understood and characterized. The overall test program does leverage accountability and responsibility for product delivery from the Shuttle Program in that the element providers (i.e., contractors) provide the test validated models and the integrated testing system and modeling is the responsibility of the programs.

Full-scale testing is being largely replaced with focus on testing each element in an attempt to validate these models for multiple phases of flight and to within acceptable test and analysis metrics set forth in program requirements. These validated element models become the "true" building blocks for system level modeling. From the element tests, residual modeling uncertainty is captured and an attempt is made to quantify it at the integrated system level in a cumulative manner. This cumulative residual modeling uncertainty is then to be further quantified in an integrated stacked launch vehicle set of tests that will occur prior to the first flight. These integrated stacked launch vehicle system tests in themselves represent a form of integrated ground vibration tests, but do have some potentially important differences when compared to the Saturn V and Space Shuttle ground vibration test campaigns.

The SLS is a heavy lift system that has a capability above the current United States lift capacity to support an efficient and affordable means to meet multiple launch missions in support of human exploration beyond Low Earth Orbit (LEO),

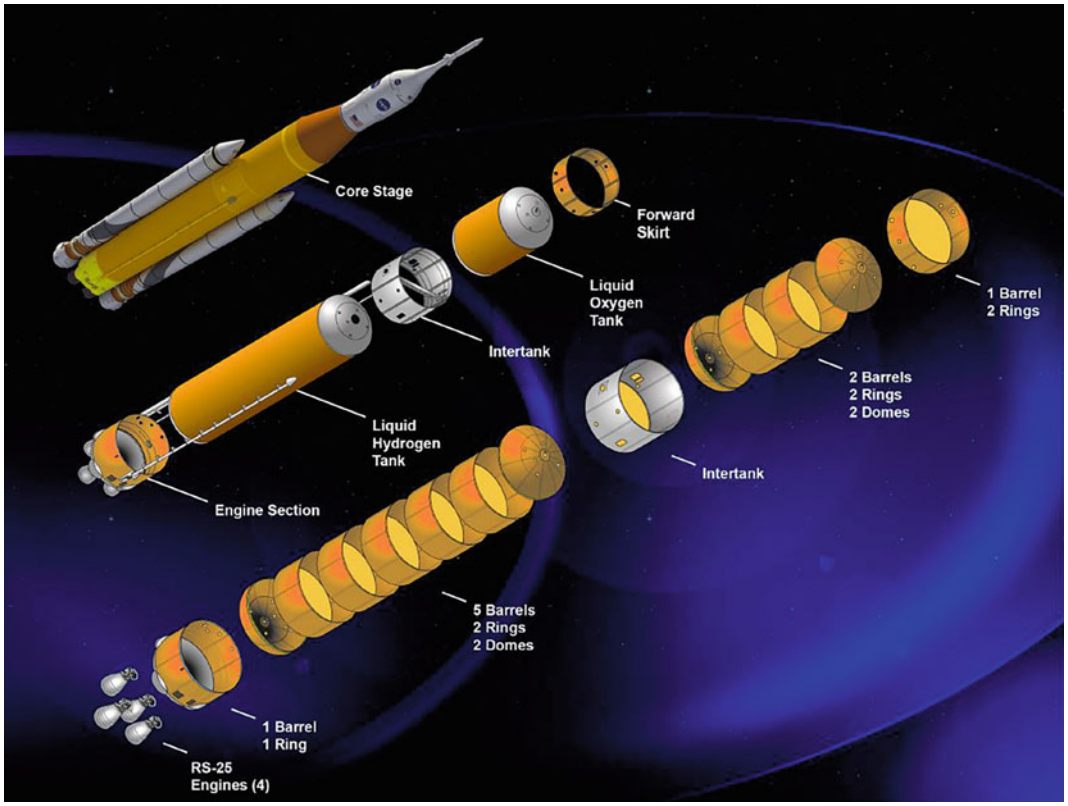

Fig. 1.10 Exploded view of the SLS system

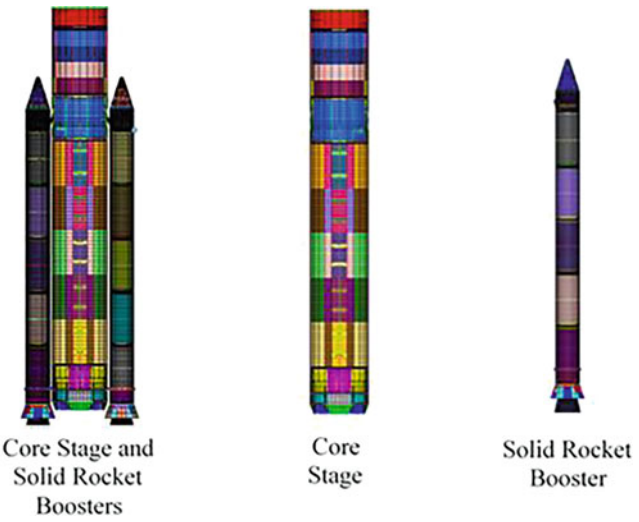

Fig. 1.11 SLS analysis model

and assembly of large and complex structures in space. The SLS includes the following major elements: Stages (Core Stage (includes the LOX, liquid hydrogen (LH2), intertank, forward skirt, and engine section) and Upper Stage), Liquid Engines (Core Stage and Upper Stage), and Boosters (solid). Figure 1.10 shows an exploded view of the SLS system while Fig. 1.11 shows a representation of the SLS analysis model. The model consists of over 165,000 nodes and over 176,000 elements.

The Orion MPCV is designed to accommodate flight crews, cargo, and support equipment during Liftoff from Earth to low Earth orbit (LEO) or lunar orbit and subsequently return the crew to Earth. The Orion MPCV, Fig. 1.12, is comprised of three modules: the Launch abort system (LAS), the crew module (CM), and the European service module (ESM).

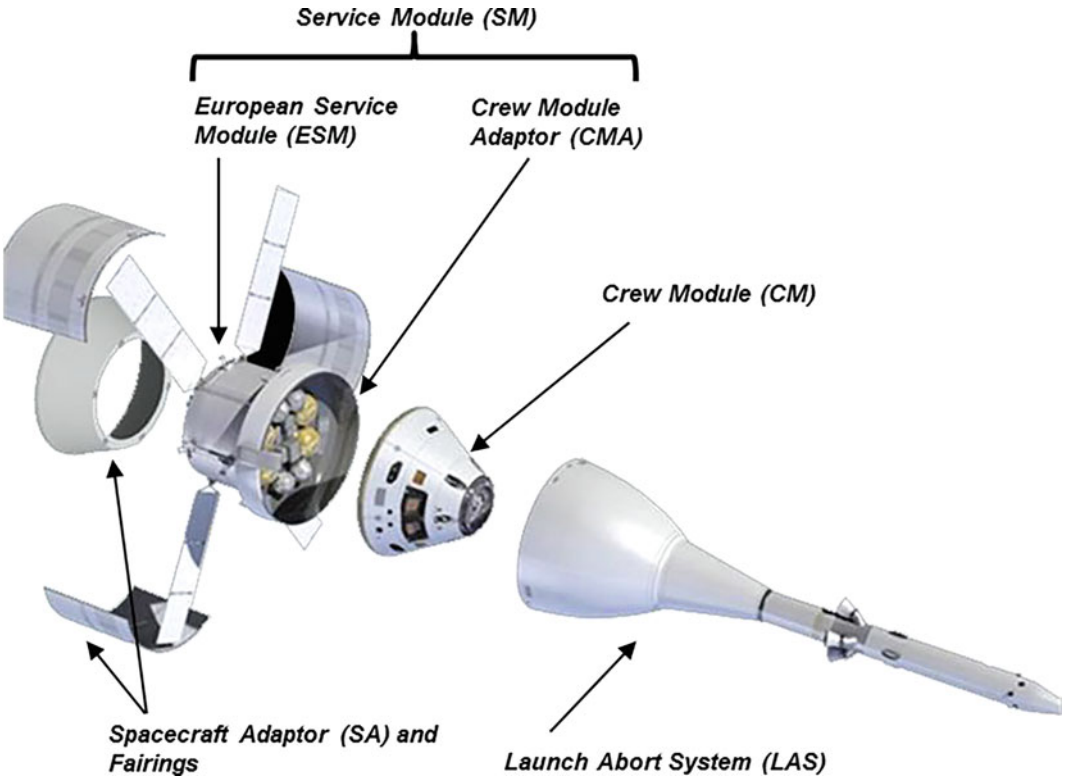

Fig. 1.12 Exploded view of the Orion MPCV system

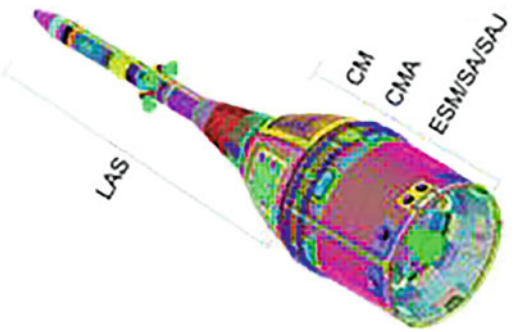

Fig. 1.13 Integrated Orion MPCV analytical model

The LAS tower, positioned atop the crew module, activates within milliseconds to propel the crew module to safety in the event of an emergency during Liftoff or climb to orbit. The system also protects the crew module from dangerous atmospheric loads and heating during the initial mission phase of ascent to orbit and is subsequently jettisoned. The crew module is the transportation capsule that provides a safe habitat for the crew, provides storage for consumables and research instruments, and serves as the docking port for crew transfers. The crew module is the only part of the MPCV that returns to Earth after each mission. The ESM supports the crew module from Liftoff through separation prior to reentry. It provides in-space propulsion capability for orbital transfer, attitude control, and high-altitude ascent aborts. When mated with the crew module, it provides the water, oxygen, and nitrogen needed for a habitable environment, generates and stores electrical power while on-orbit, and maintains the temperature of the vehicle's systems and components. The analysis model representation of the integrated Orion MPCV is shown in Fig. 1.13. The model consists of over 1.3 million nodes and over 1.5 million elements.

The SLS family of vehicles will be stacked, rolled out, and launched from the Mobile Launcher (ML). The ML consists of an Ares I derived tower structure and a Space Shuttle derived base structure. The ML tower, measuring 4152 inches tall, 1329 inches wide, and 718 inches deep at its base, will supply power, propellant, personnel access, and lateral support to the vehicle. The ML base, measuring 291 inches tall, 1596 inches wide, and 1896 inches deep, is the platform on which the vehicle is vertically supported during its assembly, rollout, and prelaunch. There are eight vehicle support posts (VSPs) on

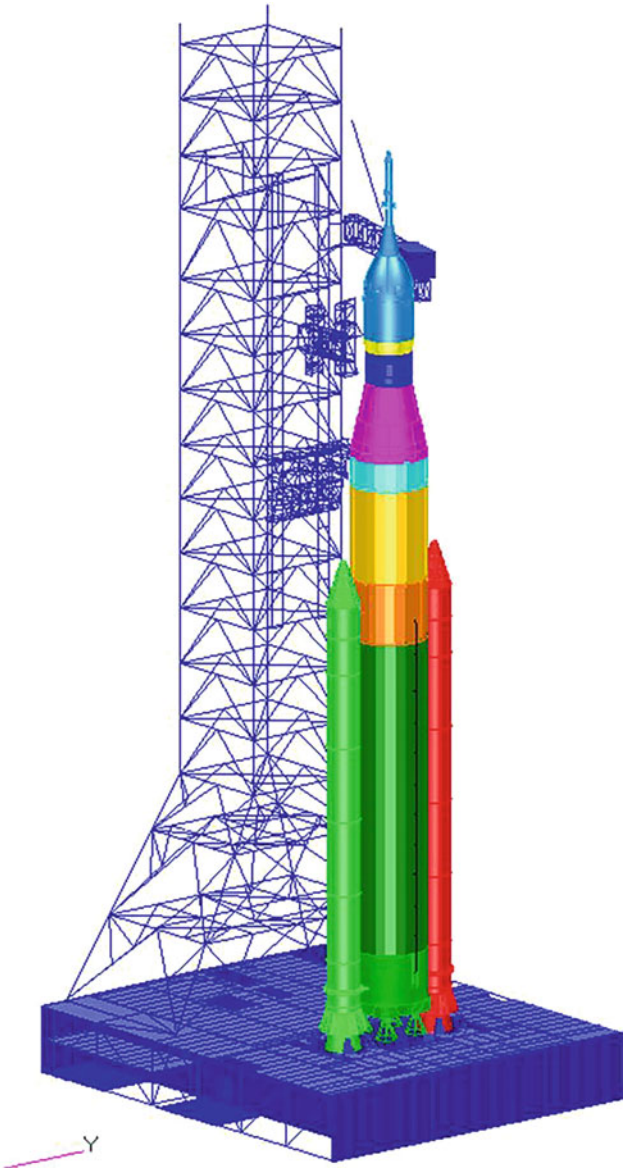

Fig. 1.14 Analytical model representation of the integrated stacked SLS system on the ML

the ML base that constrain the vehicle to the pad; four VSPs constrain the aft skirt of the left-hand booster and four VSPs constrain the aft skirt of the right-hand booster. Figure 1.14 provides an integrated model of the SLS stacked system sitting atop the ML.

Improvements in computational methods provide the ability for a more detailed modeling process compared to what was available in the past for Saturn V and the Space Shuttle program. However, more is not necessarily better. Many of the challenges that existed in the past that still exist today. For instance, the models have lots of detail but still have dramatic simplifications in geometry. This issue manifests itself in two specific areas in particular: (1) in the interfaces where critical joint simplifications are made and where possible non-linear behavior may exist and (2) in the modeling of orthogrid and isogrid structures. As a result, the models may be more predictive than the models used historically, but there are still many places where they could be wrong. Furthermore, while these models are larger it has still been necessary to create reduced order models for certain subcomponents (e.g., Hurty/Craig-Bampton). This is done both for practical reasons (to facilitate sharing of models) and to reduce the computational burden. As a results, Issues may arise in these models due to this reduction process; it is not always possible to retain enough modal information to span the frequency range of interest, and when simplifying the models in this way there is always the potential for errors and model grounding issues.

Table 1.6 Building block tests for the first exploration mission integrated stack vehicle

Test designator	Test description	Test type
Crawler Transporter (CT) /ML/VAB Move Operations to VAB	Rollout without stacked SLS vehicle to VAB	Operational
SRB Modal Survey Test	Full scale modal survey of the five-segment Experimental Solid Rocket Motor 3	Dynamic
FSTA-1, 2	Forward Skirt Static Test Article 1 and 2	Static
LOX Tank SQT	LOX Tank Static Qualification Test (SQT)	Static
LH2 Tank SQT	LH2 Tank Static Qualification Test	Static
LH2 Proof Test	LH2 Proof Test	Static
ES SQT	Engine Section (ES) Tank Static Qualification Test	Static
Intertank SQT	Intertank Tank Static Qualification Test	Static
LOX Forward Dome Tap Test	LOX Forward Dome Tap Test	Dynamic
LOX Aft Dome Tap Test	LOX Aft Dome Tap Test	Dynamic
CS Suspended Modal	Core Stage Cable Suspended Modal Test	Dynamic
LVSA +ICPS+MSA Modal	Launch Vehicle Spacecraft Adapter (LVSA) + ICPS + MPCV Spacecraft Adapter (MSA) Modal Test	Static/Dynamic
E-STA	European Service Module Static Test Article (E-STA)	Static/Dynamic
M-STA	Multi-Purpose Crew Vehicle Static Test Article (M-STA)	Static/Dynamic
Booster Pull Test	Booster Pull Test on ML during stacking operations	Static
PSMT	Partial Stack Modal Test (ML, Boosters, Core Stage)	Dynamic
IMT	Integrated Modal Test (Flight vehicle & ML)	Dynamic
DRT	Dynamic Rollout Test (Flight vehicle & ML on Crawler)	Dynamic

Table 1.6 provides a condensed form of both element and system testing currently in process for the first exploration mission flight. While the information does not include all tests planned and on-going, it provides awareness of the comprehensive program undertaken to address the building blocks of these systems of systems.

The tests listed in Table 1.6 once again re-emphasize that the focus in this building block approach is on the element testing and does include both static and dynamic testing to be used in model validation. As mentioned previously, one of the critical focus areas in the modeling are the joints, especially around major interfaces, in particular the way in which they are simplified. This is recognized by the system analysts and discussion early on with element providers focused on providing requirements to gather interface influence coefficient data (i.e., force deflection data) for modeling purposes.

The structural testing and modeling campaign will culminate with system testing that consists of modal tests to be conducted on the flight hardware at the Kennedy Space Center (KSC) prior to the first exploration mission launch. The tests consist of the ML Only test, the booster pull test, partial stack modal test (PSMT), and the integrated modal test (IMT). Each of these tests will have differing boundary conditions to aid in characterization of ground and Liftoff conditions and to aid in understanding the system modes between the three constituent systems (ML, SLS, and Orion MPCV). These modal tests represent the current program's test strategy in place of a dedicated IVGVT. Figure 1.15 shows how the element tests map to the system level tests and how each system tests builds on the result of the previous test.

Verification and validation (V&V) is a highly challenging undertaking for SLS integrated stack structural dynamics models due to the magnitude and complexity of SLS subassemblies and subassemblies. There are a number of issues that contribute to the overall challenge. Nearly all modal testing will be conducted on non-fueled assemblies and subassemblies in the 0–60 Hz frequency band. Modes that exercise the fueled structure in this frequency band have non-fueled counterparts at natural frequencies well in excess of 60 Hz. Absence of ersatz LOX (water) in the LOX tank is a departure from the STS modal test program, and it represents a challenge in understanding the tank dynamic effects as the lowest frequency full-tank body modes are of different character than empty tank modes. Addition of a series of LOX tank fill level modal tests would reduce the uncertainty, but current plans are to simulate the fluid through the hydrostatic modeling to account for the fuel.

Many SLS and Orion MPCV components are configured as thin, complex construction (waffle, etc. . . .) shell structures with attached, localized structural subassemblies (e.g., ISPE). Overall body, shell breathing, and localized subassembly

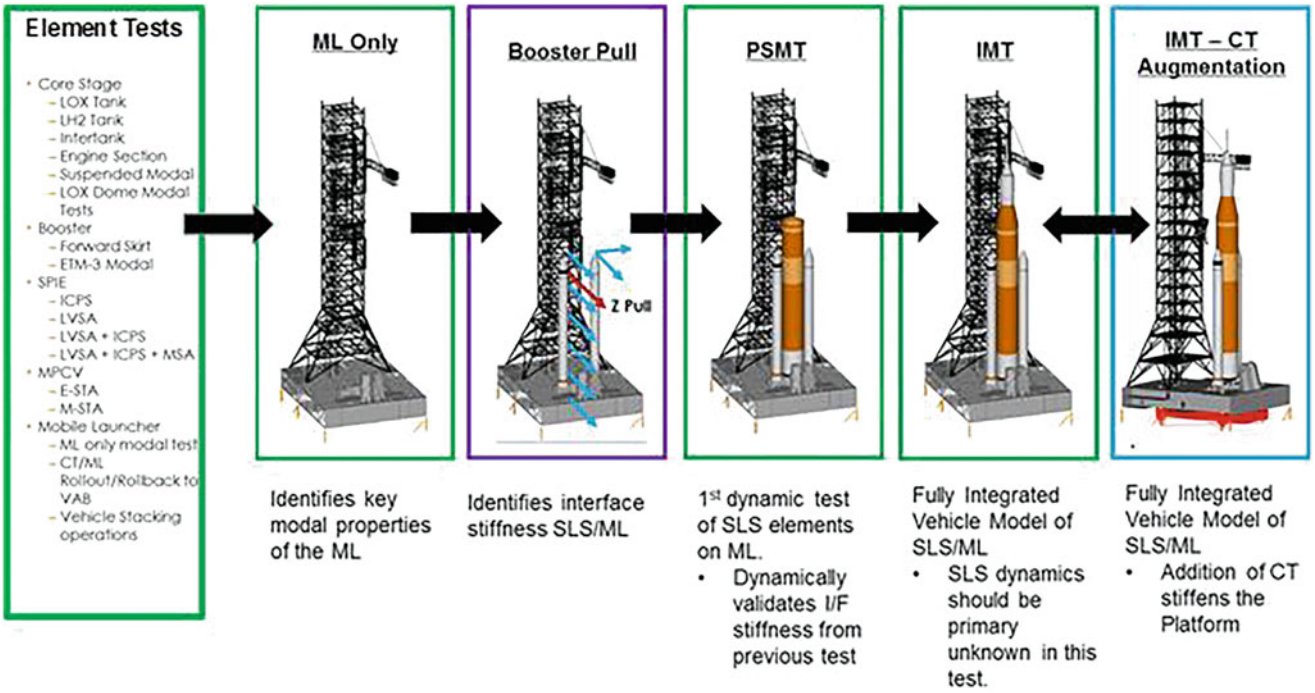

Fig. 1.15 Integrated SLS stacked system level testing

dynamics in the 0–60 Hz frequency band produce a variety of technical challenges including coupling of body, breathing and local kinetic energies in individual modes due to configuration features and imperfections, sensitivity of shell breathing modes to static (pressure) loads, and sensitivity of modes to uncertainties primarily in joint stiffnesses. To address some of these issues, a mode consolidation (MC) strategy is available that can consolidate "split" or "fragmented" modes [9]. This uses selected shape functions, defined in a modified guyan reduction (MGR), to select "body dominant" system modes on the basis of kinetic energy distribution, and consolidate apparently repeated "body dominant" modal fragments into idealized body modes of an apparent "de-featured" dynamic system. By employing MC for the experimental modes combined with MGR for the system mathematical model, test-analysis correlation and reconciliation may be more effective and can deliberately focus on target modes.

There exist a large number of modes (i.e., 1000s for the entire integrated stacked SLS system) in the 0–60 Hz frequency band, resulting in the following technical challenges; (1) Modal test planning and execution requires large instrumentation and excitation resources to appropriately capture the system modes, (2) practically achievable test-analysis correlation and reconciliation must focus on a target mode subset, which is difficult to properly select, and (3) experimental modal analysis of systems with many closely-spaced modes requires objective quality metrics that are independent of mathematical model predictions.

With regard to the integrated system test (e.g., PSMT, IMT, etc.), the primary challenge is the coupling of the SLS vehicle stack with the ML. The SLS is flight hardware and as such there are detailed drawings, traceable plans and fairly well-developed models. In contrast, the ML is a large steel structure akin to a bridge or building, and its construction is not controlled in the same way; efforts to model it are also less mature yet it has many, many modes in the frequency range of interest for the SLS and so its influence cannot be neglected. Hence, it may prove challenging to model the ML with sufficient fidelity that one can use the coupled SLS + ML test to assess the accuracy of the SLS dynamics model. Decoupling of the SLS vehicle stack from the complete "article" should rely on a low-risk strategy. To address this challenge, an ML Only test is planned to obtain dynamic characteristic data to inform the PSMT. The PSMT test will provide the first set of integrated data to understand fully the degree of coupling between the vehicle and ML. To date, all that is available are analytical simulations using uncorrelated models. The simulations to date do suggest that modes above 3 Hz becomes highly coupled and hence potentially problematic. The PSMT test then informs the IMT testing moving forward. One method still under investigation and in process of vetting is using the CT to lift up on the ML base while still connected to another set of mounts. Simulations have shown that this may stiffen the ML base and decrease the coupling between the ML and the integrated stacked vehicle dynamics. Further, alternative data extraction methods are being explored to extract fixed base

modes of the SLS from the IMT test including the fixed base extraction method developed by Napolitano [10, 11] and the dynamic substructuring method developed by Allen and Mayes [12].

Clearly, the integrated stacked SLS testing campaign draws on the history and lessons from the past manned space flight programs. The building block approach focuses on element testing and seeks to exploit advancement in computational mechanics and modeling techniques, seeking to minimize testing and exploit models to the extent possible while using both static and dynamic data to address unknowns in the models and to check for errors or "unknown-unknowns". Many challenges still exist as the testing campaigns continue and technical due diligence is required given the limitations imposed on testing due to schedule, hardware, and programmatic constraints.

1.6 Conclusion

The National Aeronautics and Space Agency (NASA) manned flight programs has an enduring technical history in developing high performance flight systems, and in developing approaches to model, test and validate these complicated vehicles. The approach to understanding these systems is steeped in using a building block approach to understanding the fundamental physics of the integrated structural systems and developing test validated models for use in system analyses. From the Saturn V program to the current integrated stacked SLS system, the general premise of the building block approach was and is employed. The approach has evolved and leveraged lessons learned and observations from the past, while some challenges remain the same (i.e., joints are uncertain, people make mistakes when simplifying the models, etc. . . .).

It is vital to remember that system-level structural dynamic models will be required for computing expected launch and flight loads, and for control and pogo stability analyses. These models will be derived from detailed subsystem FEMs, which will be provided by various elements/organizations. In addition, there is a need for FEMs to predict internal loads and stresses to establish expected structural margins, and for supplementing and supporting strength testing. These models will be required to deal with manufacturing non-conformances. Because of the size and complexity of today's modern integrated systems, significant testing is required to obtain sufficient data to adjust/correct the various subsystem FEMs that will be used to generate the system-level models.

Unique system-level models will be required for numerous times of flight, including liftoff, post-liftoff, various atmospheric flight times, post SRB jettison, exoatmospheric flight, post Launch Abort System (LAS) jettison, post CS separation, and post second stage separation. As such, it is not possible to perform system level testing for all possible flight configurations and propellant loading levels. This leads to the requirement that test adjusted subsystem FEMs, which can be configured analytically to the various flight configurations, be available to generate the required system models. Hence, it is critical to assure that high quality models are created and that the appropriate testing and model tuning activities are performed to catch errors and mitigate uncertainties.

Based on the above considerations, and the complexities involved in mode survey tests of systems with a large number of modes, it is concluded that a system-level GVT by itself cannot provide the data needed to develop accurate subsystem FEMs, which are required to develop models of the coupled system for the various times in flight where analyses are required. The past manned space flight programs and the current integrated SLS stacked system have developed an approach in which subsystem FEMs are tuned to subsystem mode survey and static test data. In this approach each subsystem element organization is responsible for the quality of the tests and final models delivered for integration into the system models. All of the programs, past and present, have instituted some form of GVT that provides additional valuable data as the vehicle elements are being integrated.

Successful implementation of the building block approach requires that uniform criteria are implemented across the elements to gauge the success of the test and model correlation/correction. This includes adherence to standards and implementation of a structural verification plan that specifies consistent test and model correlation requirements for all the elements. These include mode survey test completeness and mode shape orthogonality criteria, model to test frequency and mode shape comparison criteria, and the requirement that all FEM changes made to improve agreement with test data must be consistent with the drawings and the hardware.

References

1. Spaulding, D.B.: The art of partial modeling, Colloqium on modeling principles
2. Performance Test Code 60 Committee, Guide for verification and validation in computational solid mechanics, ASME V&V 10-2006 (2006)

3. Grimes, P.J., McTigue, L.D., Riley, G.F., Tilden, D.L.: Advancements in structural dynamic technology resulting from Saturn V programs, NASA-CR-1539, vol. I, June 1970
4. Grimes, P.J., McTigue, L.D., Riley, G.F., Tilden, D.L.: Advancements in structural dynamic technology resulting from Saturn V programs, NASA-CR-1539, vol. II, June 1970
5. Ryan, R., Jewell, R., Bugg, F., Ivey, W., McComas, R., Kiefling, L., Jones, J.: Dynamic testing of large space systems, NASA-TM-78307, September 1980
6. Mason, P.W., Harris, H.G., Zalesak, J., Bernstein, M.: Analytical and experimental investigation of a 1/8-scale dynamic model of the shuttle orbiter, vol. I – summary report, Grumman Aerospace Corporation, May 1974
7. Coppolino, R.: A numerically efficient finite element hydroelsatic analysis: volume I, theory and results, NASA-CR-2662, April 1976
8. Ivey, E.W.: Mated vertical ground vibration test, NASA-TM-78298, July 1980
9. Coppolino, R.: Methodologies for verification and validation of space launch system (SLS) structural dynamic models, NASA/CR-2018-219800/Volume I and II, January 2018
10. Napolitano, K., Yoder, N.: Fixed base FRF using boundary measurements as references – analytical derivation, Proceedings of the 30th International Modal Analysis Conference (2012)
11. Napolitano, K.L., Winkel, J.P., Akers, J.C., Suarez, V.J., Staab, L.D.: Modal survey of the MPCV orion European service module structural test article using a multi-axis shake table, Proceedings of the 36th International Modal Analysis Conference (2018)
12. Allen, M.S., Mayes, R.L.: Recent advances to estimation of fixed-interface modal models using dynamic substructuring, Proceedings of the 36th International Modal Analysis Conference (2018)

Chapter 2
Analytically Investigating Impedance-Matching Test Fixtures

Thomas M. Hall

Abstract When attempting to recreate an operational environment using a test in the lab there can be many problems to overcome. Of particular importance, particularly when testing components, are the boundary conditions, including both the test fixtures and the excitation methods. This paper is an investigation into "N+1" style test fixtures, and the effect of different lengths of fixture under various excitation and control methods. The investigation uses the Box Assembly and Removable Component (BARC) hardware design from the Boundary Conditions Challenge, and is carried out using Finite Element Analysis.

Keywords Test fixtures · Impedance-matching · Boundary conditions · Excitation methods

2.1 Introduction

When testing a component it is desirable to be able to recreate the operating environment of the component without having to build it into its full assembly. A current common method for this is to take a measurement at the location of the component in the full assembly when the assembly is subjected to the operating environment (or a laboratory simulation of the operating environment) and then use this measurement as an environment to control to. However, little thought is often given to the component boundary conditions in the assembly and the conventional wisdom is to avoid resonances in the range of the test, i.e. a rigid fixture. This type of fixture design makes control easier, however it can also significantly change the response of the component, and can lead to significant over testing, which can lead to expensive design work to unnecessarily ruggedize the component, or under testing, which can lead to failure in service [1]. The reason that rigid fixtures can affect the results so significantly is explained by Edwards [2] as a result of large terms in the non-drive-point FRF responses of real test fixtures meaning that the fixtures cannot be controlled out effectively, and with rigid fixtures this can significantly affect the mode shapes of the item, which causes the eigenvalues to interlace, whereas if the impedance of the fixture is close to the impedance on the item in the field, there is little change in the mode shapes. Investigation into fixture design that takes into account the impedance seen by the component in the field is not new, with examples of similar work dating back to the 1960s [3, 4], and this paper attempts to apply this thinking on the Boundary Conditions Challenge [5] hardware and investigate the effects.

2.1.1 Box Assembly and Removable Component

The Box Assembly and Removable Component (BARC) is a design developed as part of a challenge problem by the Kansas City National Security Campus in conjunction with Sandia National Laboratories [5]. The component is made of two C-channels and a beam bolted together, and this component is bolted to a box section. Figure 2.1 shows the model of the BARC used in in this paper.

T. M. Hall (✉)
AWE Plc, Berkshire, UK
e-mail: tom.hall@awe.co.uk

C. Walber et al. (eds.), *Sensors and Instrumentation, Aircraft/Aerospace, Energy Harvesting & Dynamic Environments Testing, Volume 7*, Conference Proceedings of the Society for Experimental Mechanics Series,
https://doi.org/10.1007/978-3-030-12676-6_2

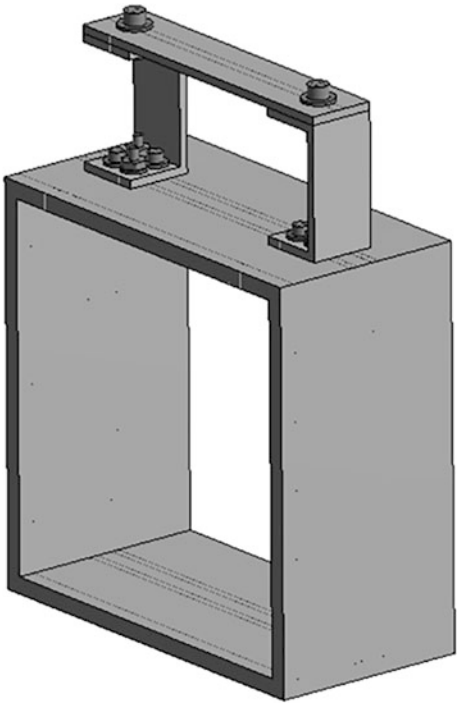

Fig. 2.1 Box assembly and removable component (BARC)

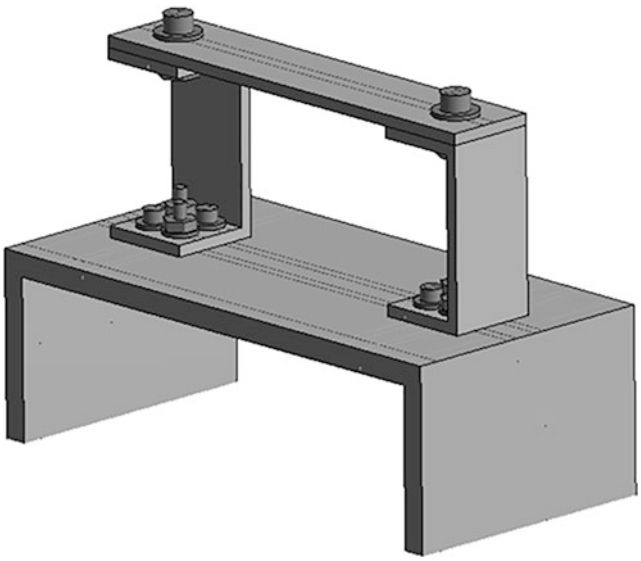

Fig. 2.2 Removable component on an example of an N+1 fixture

2.1.2 N+1 Fixtures

N+1 fixtures are a type of fixture designed by using the assembly that the component is attached into, and using a part of the assembly as the fixture, as shown in Fig. 2.2. N+1 fixtures are a simple way to recreate the impedance at and between any attachment points, and also provide a more representative path for the input of vibration energy to the component assuming the vibration is structure borne.

2.1.3 Excitation Methods

Another significant part of recreating the operating environment is the method used to excite the component. Traditionally, vibration tests use three single axis tests, one in each of the Cartesian directions. The test fixture is typically attached to a nominally rigid shaker table which is vibrated using a single, large electrodynamic shaker.

An alternate method of excitation is a six degree of freedom (6-DoF) shaker table. In this the test fixture is again attached to a nominally rigid shaker table, however in this case the table is vibrated using a collection of shakers allowing simultaneous vibration in six degrees of freedom, the three Cartesian translations and rotations about the axes. This allows for testing that is more representative of the environment it is simulating [6].

The third method used in this paper is the Impedance-Matched Multi-Axis Test (IMMAT) technique [7]. This method uses multiple shakers attached directly to the fixture and can be used to simultaneously excite all six degrees of freedom, potentially exciting the modes in a more representative manner. The component and fixture are suspended in a free-free configuration in order to not add to the impedance of the fixture.

2.1.4 Control Method Used in this Paper

As this investigation was carried out using finite element analysis simulation the input needed to be calculated in order to recreate the environment at the control point or points. The control is carried out in the frequency domain, and involved creating a matrix of the transfer functions between the input(s) and the control point(s), **T**, and using that to calculate the required input using Eq. 2.1.

$$S_{force} = T^{-1} S_{control} \tag{2.1}$$

The $S_{control}$ vector contains the responses at the control points from the "truth" test, and the S_{force} vector is comprised of the force inputs required at the driving points to achieve the control values. However, as the force and control vectors are different lengths depending on the excitation and control methods, and they are rarely the same length as each other, the **T** matrix is often rectangular and therefore the Moore-Penrose pseudoinverse is used in Eq. 2.1, and the responses will not be exact at all control locations.

2.2 "Truth" Data

To attain data to use as control data and as data to compare the results against, the BARC was subjected to a simulated vibration environment. This environment was a series of harmonic inputs with various amplitudes and phases, at a variety of locations on the box assembly, as shown in Fig. 2.3. The responses to this environment are taken at 12 measurement points on the removable component, shown in Fig. 2.3 as yellow dots. These results, or a subset of them, are used as control for the various excitation methods and are also used as a benchmark to compare the results of the various excitation methods and fixture design. In this investigation both the truth data and experimental simulations are carried out in FEA, there is scope to use full body contour plots of variables, such as acceleration or strain, for comparison.

2.3 Single Axis Shaker Excitation

2.3.1 Method

The traditional method of recreating vibration environments is to control at one point and shake in one direction, and repeat this for each of the Cartesian axes. This is simulated by controlling at the point shown in Fig. 2.4 in the direction of excitation to the truth data response at this location. This results in perfect control at this location as there is one control point and one excitation.

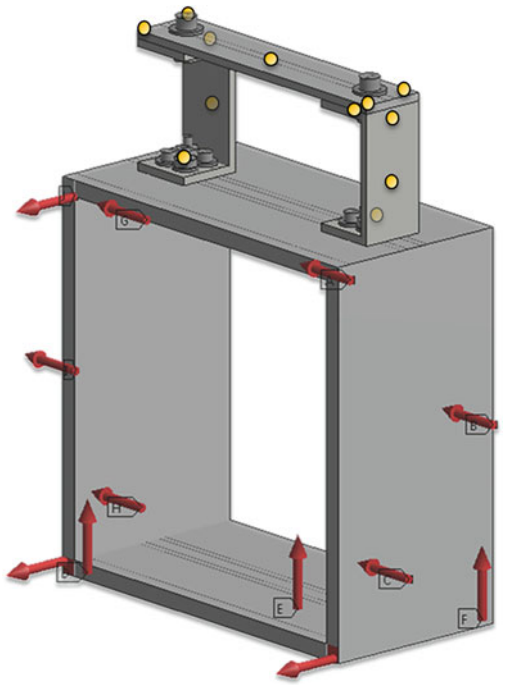

Fig. 2.3 "Truth" environment and control/response measurement points

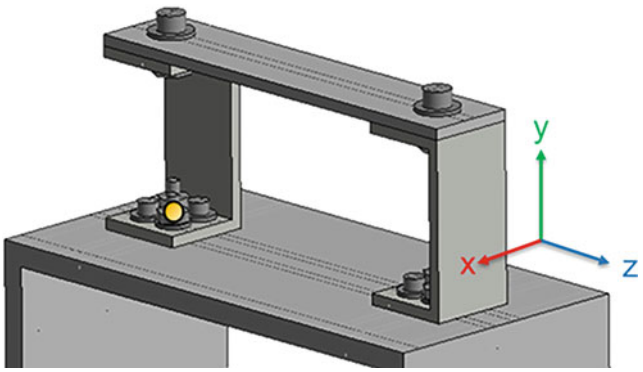

Fig. 2.4 Control point for single axis excitation

For this excitation method the simulation was run with no fixture, i.e. the removable component directly attached to a stiff plate, and with a 3 inch N+1 fixture attached to a stiff plate. A three inch N+1 fixture is used as it is half of the box assembly. Both simulations are run in each of the three Cartesian axes.

2.3.2 Results

The response for the simulations were compared to the responses with the truth data. Figure 2.5 shows the response from in line excitation and cross axis excitation at the centre of the top beam of the removable component.

The response functions at the measurement locations tend to show that the fixture causes a decrease in the accuracy of the replication of the environment with this excitation method. However it is worth noting that with or without the fixture the replication of both amplitude and phase is poor.

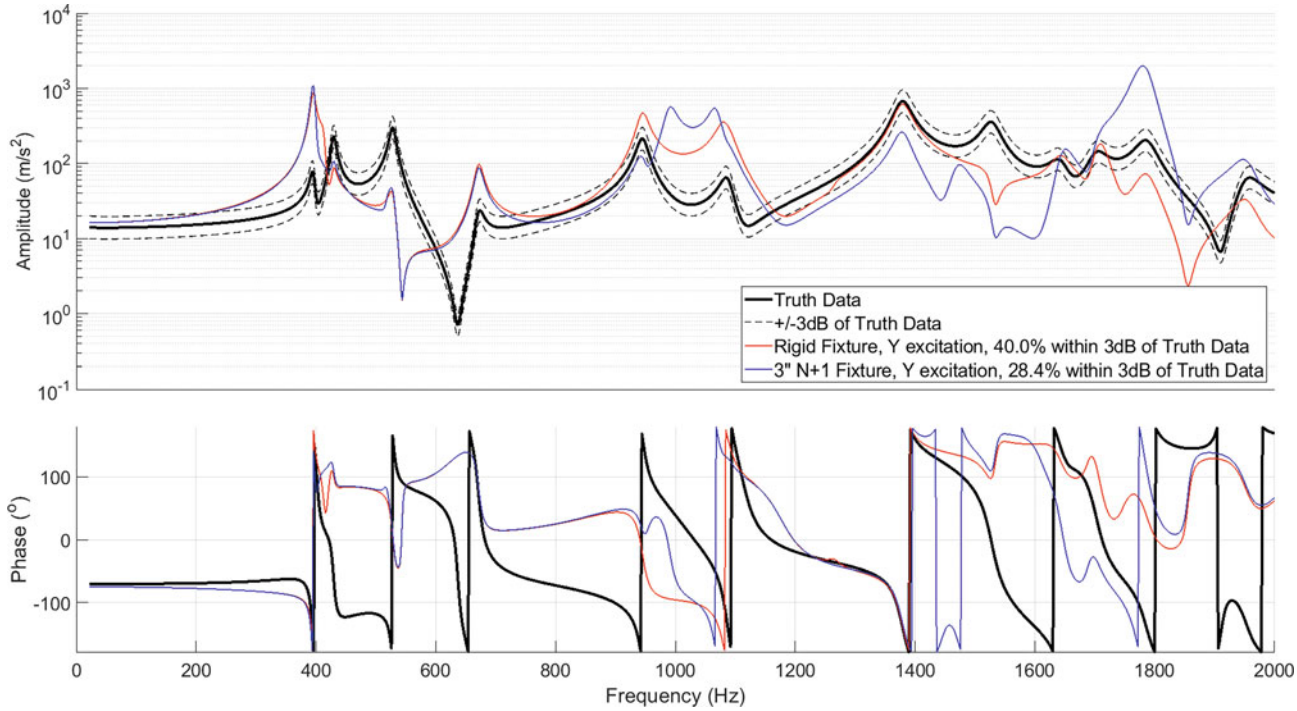

Fig. 2.5 Response from in line excitation at centre of top beam of removable component

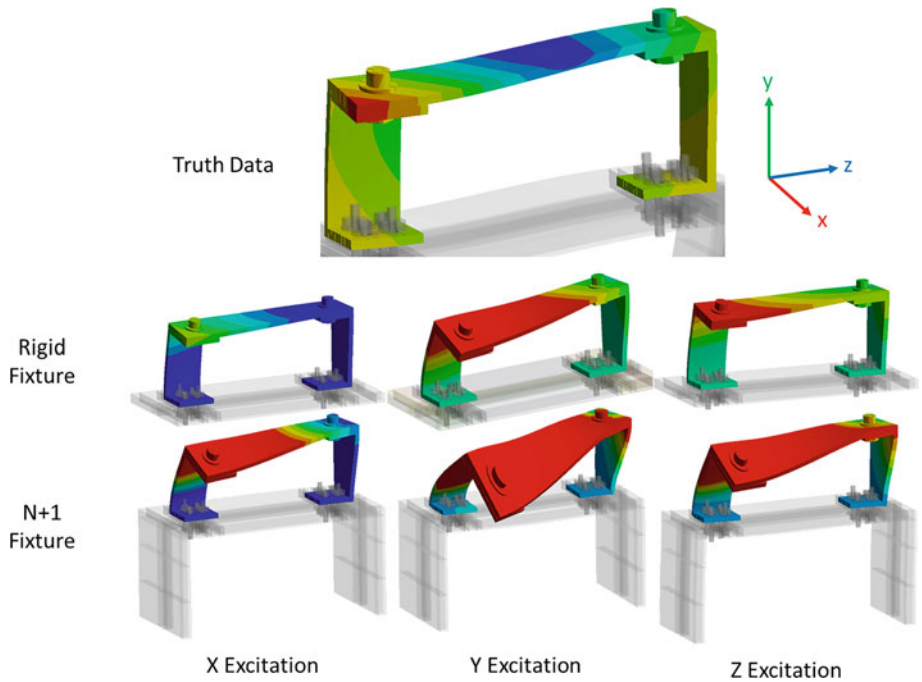

Fig. 2.6 Acceleration magnitude contour plots for vibration at 394 Hz, with truth plot at top

As can be seen in Figs. 2.6 and 2.7, the single axis excitation is poor at recreating the acceleration or strain values from the environment either with or without the fixture. This holds true for frequencies other than those chosen in Figs. 2.6 and 2.7. The highest strain in either test in Fig. 2.7 would still over predict fatigue life for the component by approximately 350 times at the frequency displayed and there are other frequencies where life would be under predicted in either test by approximately 600,000 times.

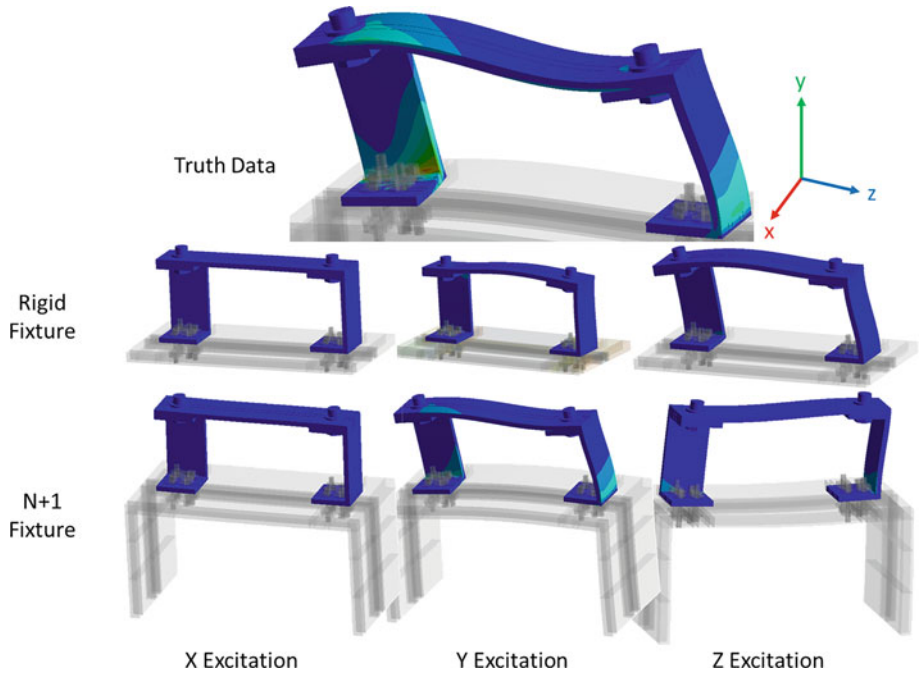

Fig. 2.7 Maximum principal strain contour plots for vibration at 944 Hz, with truth plot at top

2.4 Six DoF Shaker Excitation

2.4.1 Method

The simulation of a 6DoF shaker was carried out by applying inputs at the base of the chosen fixture and controlled at all 12 measurement points shown in Fig. 2.3. This was carried out for N+1 fixtures made of various lengths of the box assembly, from 1″ to 3″, and also for a rigid fixture.

2.4.2 Results

The responses from the simulations of 6DoF shaker excitation were compared to the truth data. Figure 2.8 shows the response at the same location as in Fig. 2.5, and it can be seen that all results are closer to the truth data than with single axis excitation, both in magnitude and phase.

At the centre of the top beam of the removable component, Fig. 2.8 shows that the response improves as the length of the N+1 fixture increases up to 2″, and then plateaus. However, results at other locations show that this trend is not universal, with the similarity of the results to the truth data at some locations improving as the length of the N+1 fixture increases, at some locations decreasing as the length of the fixture is increase, and at other locations similarity to the truth data is highest with a 1″ or 2″ fixture.

The acceleration contour plot at 394 Hz, Fig. 2.9, shows that the main area of difference is near the attachment point to the fixture. At this area it can be seen that the simulation of the environment using a 6DoF shaker is more similar to the

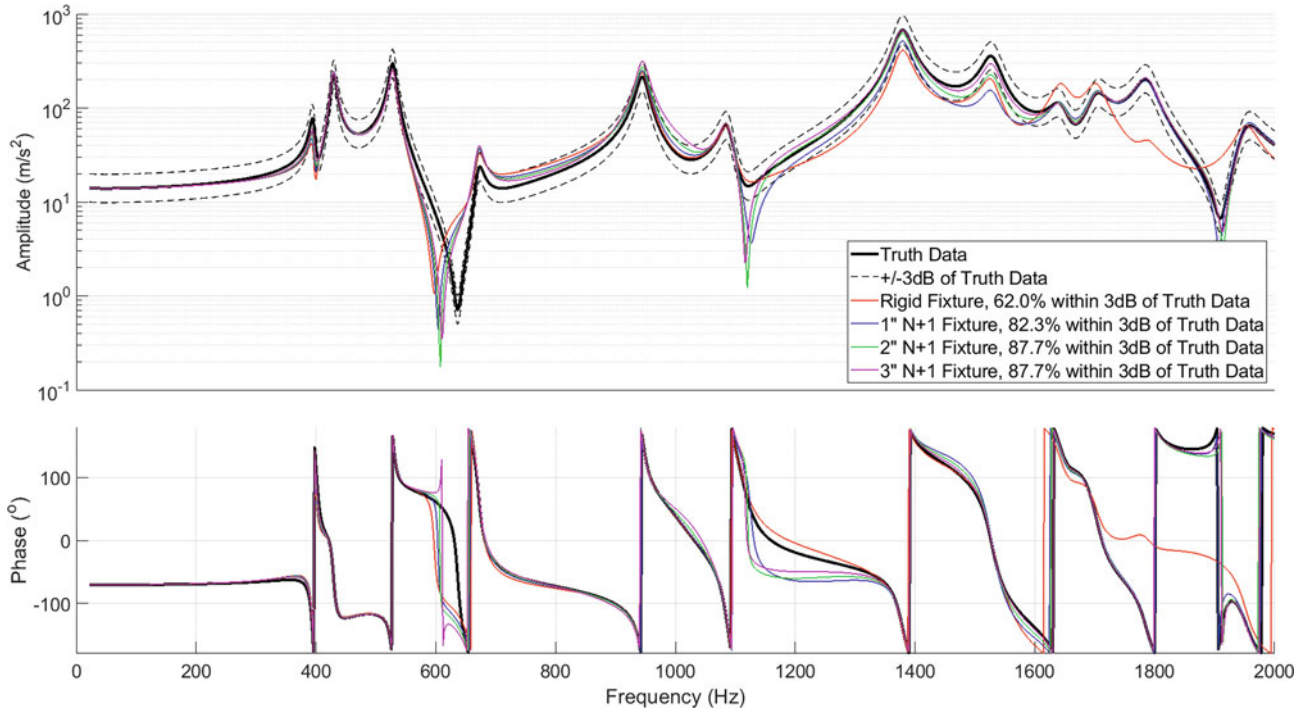

Fig. 2.8 Response at centre of top beam of removable component for various fixtures under 6DoF shaker excitation

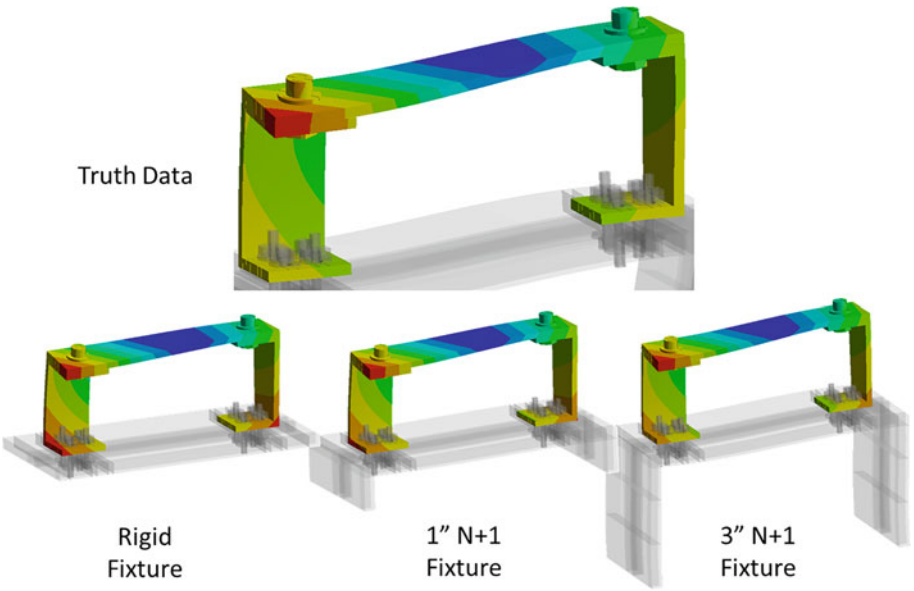

Fig. 2.9 Acceleration magnitude contour plots for vibration at 394 Hz under 6DoF shaker excitation, with truth plot at top

truth data as the fixture length is increased, but other results show this similarity varies depending on frequency, with some frequencies better simulated with a 1″ fixture, and some frequencies better predicted with a 3″ fixture. Likewise, the strain contour plot, Fig. 2.10, shows a significant improvement over the single axis excitation, Fig. 2.7, but there is no consistent relationship between accuracy of environment simulation and fixture length. However, at the frequencies investigated, the 3″ fixture ranges from over predicting fatigue life by 2 times to under predicting marginally, and the 1″ fixture ranges from over predicting life by 4 times to under predicting marginally, which is significantly better than the gross over and under testing that occurs with single axis excitation.

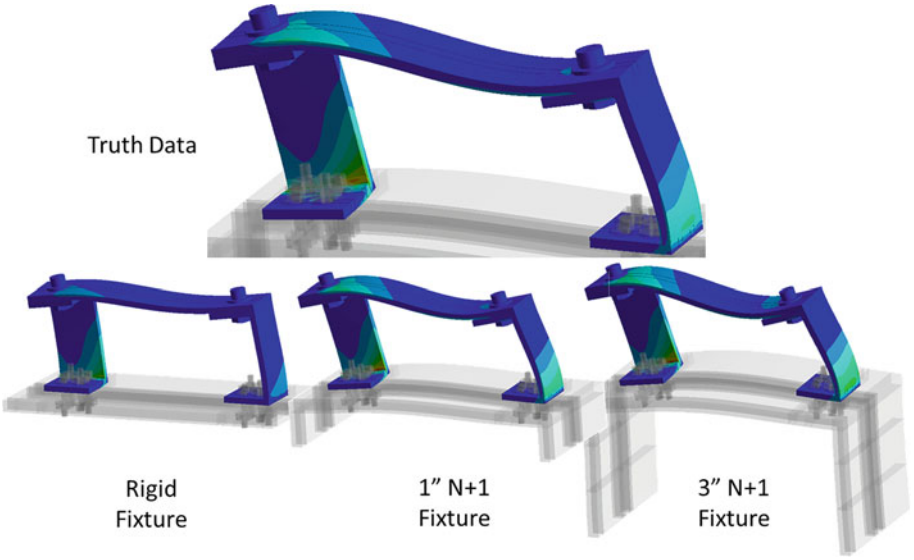

Fig. 2.10 Maximum principal strain contour plots for vibration at 944 Hz under 6DoF shaker excitation, with truth plot at top

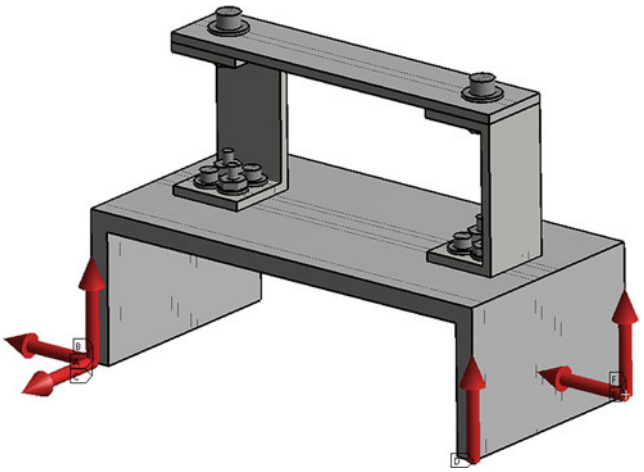

Fig. 2.11 Input locations for multi-shaker excitation

2.5 Multi-Shaker Excitation

2.5.1 Method

The multi-shaker excitation was simulated by applying six force inputs to locations at the base of the fixture, shown in Fig. 2.11. There was no investigation into the optimal location of these inputs so it is possible that they are not ideal, but they were chosen to ensure control of all six degree of freedom of the removable component. As with the 6DoF shaker investigation, the excitation was controlled at all 12 measurement points shown in Fig. 2.3, and the investigation was repeated for various N+1 fixtures, from the top plate of the box assembly to 3″ of the box assembly.

2.5.2 Results

The responses from the simulations of 6DoF shaker excitation were compared to the truth data. Figure 2.12 shows the response at the same location as in Figs. 2.5 and 2.8. As with the 6DoF shaker excitation, at this location there is an increase

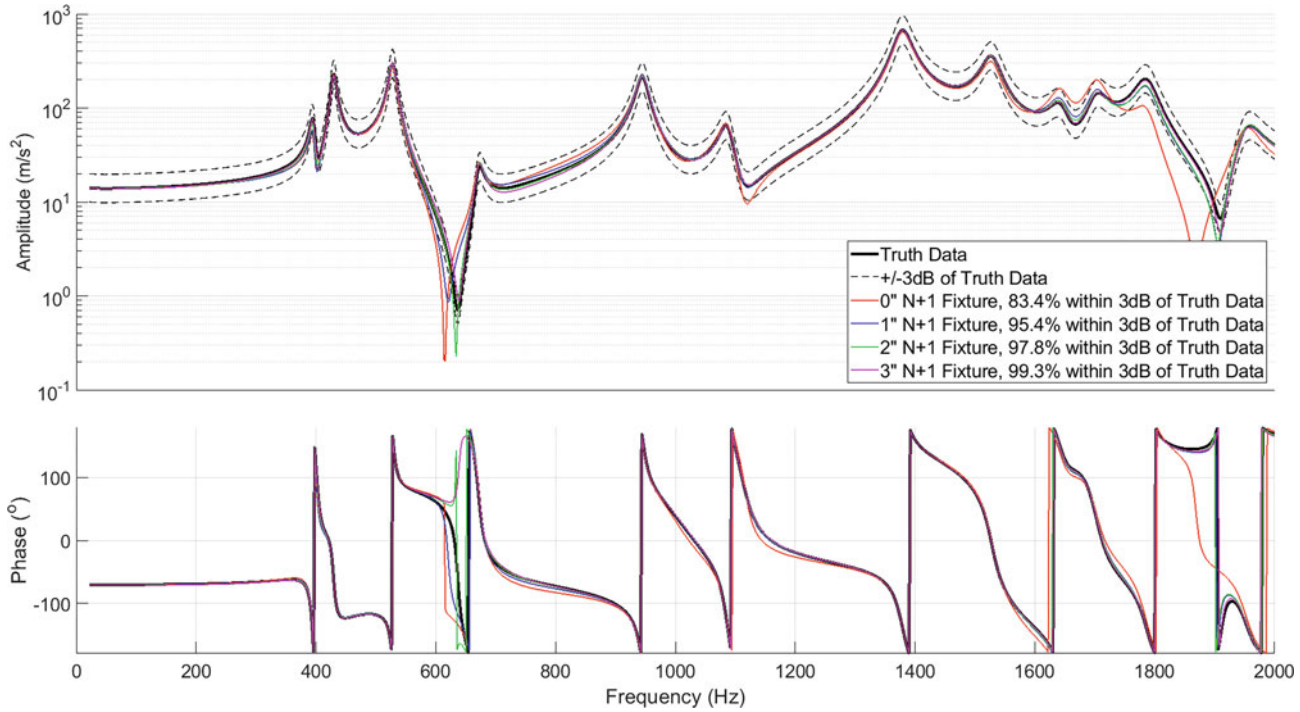

Fig. 2.12 Response at centre of top beam of removable component for various fixtures under multi-shaker excitation

in the similarity of the results to the truth data as the length of the N+1 fixture increases. For the multi-shaker excitation this pattern holds true for the other response locations. This result is reinforced by the acceleration and strain contour plots, which are not shown.

2.6 Conclusions

The results of this investigation show that, while not effective in improving the similarity to the truth data in traditional single axis shaker tests, the N+1 fixture can significantly improve the similarity in 6DoF shaker and multi-shaker tests, and in both cases showing that the larger the N+1 fixture, the better the replication of the environment.

In many cases, depending on the location of interest and the excitation method, there are diminishing returns at a certain size of N+1 fixture. This seems to happen earlier with the multi-shaker excitation then with the 6DoF shaker excitation, but it seems that the ideal fixture design depends on the level of environment replication desired, the excitation method used, and of course the design of the component and the next assembly. This indicates that it would be useful when using an N+1 fixture to carry out a similar investigation to the one carried out in this paper to determine the optimal size of N+1 fixture for the requirements of the test.

It is also possible to make a comparison between the excitation methods, with Fig. 2.13 showing the response at the centre of the top beam of the removable component under the excitation methods investigated with a 3″ fixture, and Fig. 2.14 showing the strain contour plots at 394 Hz. In both comparisons the multi-shaker excitation is the most representative of the truth data, followed by the 6DoF shaker excitation and then the single axis excitation. The improvement between the single axis excitation and the 6DoF excitation is significantly larger than the improvement from the 6DoF shaker excitation to the multi-shaker excitation.

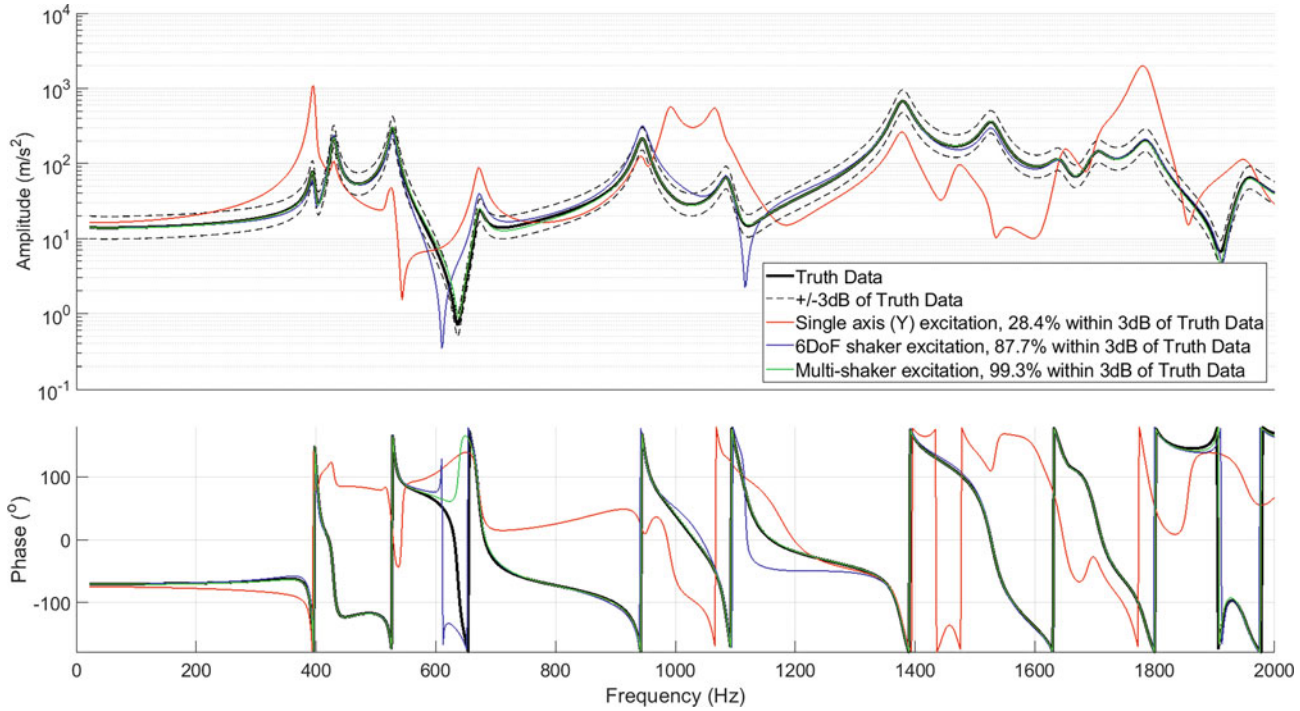

Fig. 2.13 Comparison of excitation techniques—responses at centre of top beam of removable component with 3″ N+1 fixture

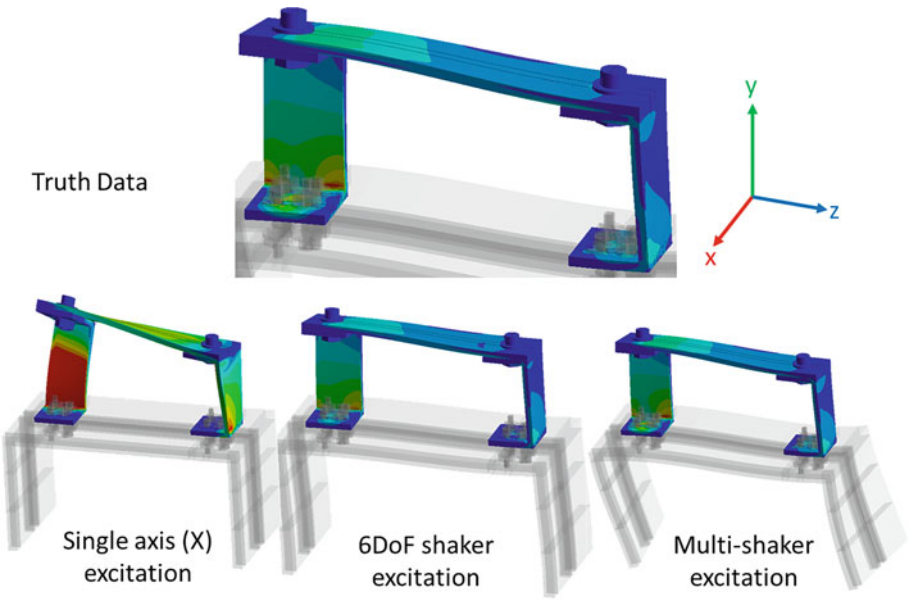

Fig. 2.14 Comparisons of maximum principal strains at 394 Hz between single axis (X) (left), 6DoF shaker (middle), and multi-shaker (right) excitation techniques

References

1. Harvie, J.M.: Using modal substructuring to improve shock and vibration qulaification, Orlando, FL (2018)
2. Edwards, T.S.: Improving bourndary conditions in component-level shock and vibration tests. www.osti.gov/biblio/1146729 (2007). Accessed 2 Oct 2018
3. Salter, J.P.: Taming the general purpose vibration test (1964)
4. Scharton, T.D.: Development of impedance simulation fixtures for spacecraft vibration tests (1969)

5. Soine, D.E., Jones, R.J., Harvie, J.M., Skousen, T.J, Schoenherr, T.F.: Designing hardware for the boundary condition round robin challenge, Orlando, FL (2018)
6. Gregory, D., Bitsie, F., Smallwood, D.O.: Comparison of the response of a simple structure to single axis and multi axis random vibration inputs, San Diego, CA (2009)
7. Daborn, P.M.: Smarter dynamic testing of critical structures. PhD Thesis, University of Bristol, Bristol, UK (2014)

Chapter 3
Harmonic Forcing of Damped Non-homogeneous Elastic Rods

Arnaldo J. Mazzei Jr. and Richard A. Scott

Abstract This work is one of an ongoing series of investigations on the motions of non-homogeneous structures. In the series, natural frequencies, mode shapes and frequency response functions (FRFs) were determined for undamped segmented rods and beams, using analytic and numerical approaches. These structures are composed of stacked cells, which may have distinct geometric and material properties. Here, the steady state response, due to harmonic forcing, of a segmented damped rod is investigated. The objective is the determination of FRFs for the system. Two methods are employed. The first uses the displacement differential equations for each segment, where boundary and interface continuity conditions are used to determine the constants involved in the solutions. Then the response as a function of forcing frequency can be obtained. This procedure is unwieldy and may become unpractical for arbitrary spatial forcing functions. The second approach uses logistic functions to model the segment discontinuities. This leads to a single partial differential equation with variable coefficients, which is solved numerically using MAPLE® software. For free-fixed boundary conditions and spatially constant force good agreement is found between the methods. The continuously varying functions approach is then used to obtain the response for a spatially varying force.

Keywords Segmented rods · Layered structures · Logistic functions · FRFs of non-homogenous structures

Nomenclature

A	Cross-section area (A_i, cross-section area for i-th material)
A_r	Non-dimensional parameter, $A_r = A_2/A_1$
B_i	Constants of integration
C_i	Viscous damping coefficient per unit length
CD_i	Non-dimensional damping coefficient
E	Young's modulus (E_i, Young's modulus for i-th material)
E_r	Non-dimensional parameter, $E_r = E_2/E_1$
G_i	Non-dimensional spatial forcing functions
f_i	Forcing functions (force per unit length)
g_i	Non-dimensional forcing functions
L	Length of rod (L_i, length of i-th cell)
q_j	Non-dimensional logistic functions
R_i	Non-dimensional spatial functions
t	Time
u	Longitudinal displacement of the rod
w	Non-dimensional longitudinal displacement of the rod, $w = u/L$
x	Longitudinal co-ordinate
α	Cell length ratio ($\alpha = L_2/L_1$)
λ	Complex frequency, $\lambda = (a + bI)$
ξ	Non-dimensional spatial co-ordinate, $\xi = x/L$

A. J. Mazzei Jr. (✉)
Department of Mechanical Engineering, C. S. Mott Engineering and Science Center, Kettering University, Flint, MI, USA
e-mail: amazzei@kettering.edu

R. A. Scott
University of Michigan, Ann Arbor, MI, USA

C. Walber et al. (eds.), *Sensors and Instrumentation, Aircraft/Aerospace, Energy Harvesting & Dynamic Environments Testing, Volume 7*, Conference Proceedings of the Society for Experimental Mechanics Series,
https://doi.org/10.1007/978-3-030-12676-6_3

ρ Mass density (ρ_i, density value for i-th material)
ρ_r Non-dimensional parameter, $\rho_r = \rho_2/\rho_1$
τ Non-dimensional time, $\tau = \Omega_0 t$
ω Natural frequency of longitudinal vibrations for the rod
ψ_i Non-dimensional parameter, $\psi_1 = 1$, $\psi_2 = \rho_r/E_r$
Ω_0 Reference frequency

3.1 Introduction

This work is one of an ongoing series (see [1, 2]) on longitudinal vibrations of layered solids. The main interest is the vibration analysis, both theoretical and numerical, of layered rods. The media of interest include solids either with continuous variation of properties, such as Functionally Graded Materials (FGM), or discrete layering. Studies on solids composed by discrete layers are given in [3–6]. Also, a recent article [7] provides a good review of references on this subject. Numerical approaches to waves in non-homogeneous media can be found in [8]. An early study on vibrations of damped rods can be found in [9], where the response to sinusoidal excitation is determined analytically for systems of internally damped rods. In [10] complex eigenvalues and mode shapes of a damped rod were used to analyze the effect of stiffness and damper loss factor on natural frequencies and modal loss factor of the system. Eigen-characteristics of a longitudinally vibrating elastic rod, with locally and non-locally reacting damping, were investigated in [11]. It was shown that there is a direct correlation between the damping ratio and mode shape of the undamped system for the longitudinally vibrating elastic rod, for both locally and non-locally damping cases. Vibrations of rods with concentrated masses and spring-supported at one end were studied in [12]. Damping was considered and the periodic steady state solution was determined.

The current work treats a one-dimensional uniaxial problem composed of two layers of different materials bonded together. The main objective is the determination of frequency response functions (FRFs) when the solid is exposed to different types of forcing functions and boundary conditions. Analytical solutions can be found by developing solutions for each layer and matching these across the layer interfaces. In addition, particular integrals must also be obtained. This approach can be unwieldy and sometimes mathematically untraceable. In order to address this issue, a method is introduced wherein the layers are modeled by continuously varying functions. The resulting differential equations are then solved via direct numerical analysis using MAPLE® software. Maximum amplitudes are monitored and respective numerical FRFs are generated. These numerical solutions are in very good agreement with the ones which can be obtained analytically.

3.2 Basic Structure

Shown in Fig. 3.1 is a two-segmented elastic rod with properties as indicated. Consider this layered structure in which E, ρ, and A vary in a discontinuous manner. The segments are under loads f_1 and f_2 (force per unit length) and viscous damping forces (per unit length, damping coefficients C_1 and C_2).

Approaches for obtaining the steady state response due to harmonic forcing are investigated in the following.

3.3 Analytic Solutions

Consider the two-segmented damped rod shown in Fig. 3.1. The axial displacement $u(x,t)$ of a segment must satisfy the equation:

$$\frac{\partial}{\partial x}\left(A(x)E(x)\frac{\partial u\,(x,t)}{\partial x}\right) + f\,(x,t) - C(x)\frac{\partial u\,(x,t)}{\partial t} - A(x)\rho(x)\frac{\partial^2 u\,(x,t)}{\partial t^2} = 0 \tag{3.1}$$

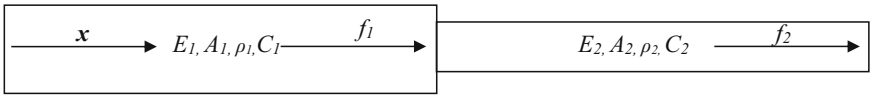

Fig. 3.1 Two-segment rod

where *E(x)*, *A(x)* and *ρ(x)* are functions describing the longitudinal variations of Young's modulus, cross-sectional area and mass density, respectively. *C(x)* represents a varying viscous damping coefficient per unit length.

The longitudinal displacement equation of motion for each segment ("i-th" segment) is:

$$\frac{\partial}{\partial x}\left(A_i E_i \frac{\partial u_i\left(x,t\right)}{\partial x}\right) + f_i\left(x,t\right) - C_i \frac{\partial u\left(x,t\right)}{\partial t} - A_i \rho_i \frac{\partial^2 u_i\left(x,t\right)}{\partial t^2} = 0, i = 1,2 \tag{3.2}$$

where f_i are forces per unit length.

For constant properties in each segment:

$$\frac{\partial^2 u_i\left(x,t\right)}{\partial x^2} - \frac{\rho_i}{E_i}\frac{\partial^2 u_i\left(x,t\right)}{\partial t^2} - \frac{C_i}{E_i A_i}\frac{\partial u\left(x,t\right)}{\partial t} = -\frac{f_i\left(x,t\right)}{E_i A_i}, i = 1,2 \tag{3.3}$$

which, in non-dimensional form, gives:

$$\frac{\partial^2 w_i\left(\xi,\tau\right)}{\partial \xi^2} - \psi_i \frac{\partial^2 w_i\left(\xi,\tau\right)}{\partial \tau^2} - CD_i \frac{\partial w_i\left(\xi,\tau\right)}{\partial \tau} = -g_i\left(\xi,\tau\right), i = 1,2 \tag{3.4}$$

where the following dimensionless variables were introduced: $w = \frac{u}{L}$, $\xi = \frac{x}{L}$, $\tau = \Omega_0 t$, and $\Omega_0^2 = \frac{E_1}{\rho_1 L^2}$, $E_r = \frac{E_2}{E_1}$, $\rho_r = \frac{\rho_2}{\rho_1}$, $A_r = \frac{A_2}{A_1}$, $g_i = \frac{f_i(x,t)L}{E_i A_i}$, $\psi_1 = 1$, $\psi_2 = \frac{\rho_r}{E_r}$, $CD_i = \frac{C_i}{E_i A_i} L^2 \Omega_0$.

For harmonic forcing with frequency λ:

$$g_i\left(\xi,\tau\right) = G_i\left(\xi\right) e^{\lambda\tau} \tag{3.5}$$

one can assume solutions of the following form:

$$w_i\left(\xi,\tau\right) = R_i\left(\xi\right) e^{\lambda\tau} \tag{3.6}$$

Taking $\lambda = (a + bI)$ and separating real and imaginary parts, after some manipulation, leads to:

$$\frac{d^2 R_i\left(\xi\right)}{d\xi} + \left(\psi_i b^2 + \frac{{CD_i}^2}{4\psi_i}\right) R_i\left(\xi\right) = -G_i\left(\xi\right), i = 1,2 \tag{3.7}$$

General solutions to the linear differential Eq. (3.7) involve solutions to the homogeneous equations and "particular integrals". For arbitrary forcing $G_i(\xi)$, finding tractable particular solutions may pose a problem. In the following a constant spatial force is discussed. (Non-constant spatial forcing is treated later numerically.)

3.3.1 Constant Spatial Force

Here constant spatial forcing is considered: $G_1(\xi) = G_{1,0}$, $G_2(\xi) = G_{2,0}$; $G_{1,0}$, $G_{2,0}$ constants.

Then

$$R_1\left(\xi\right) = B_1 \sin\left[\left(\sqrt{\frac{4{\psi_1}^2 b^2 + {CD_1}^2}{4\psi_1}}\right)\xi\right] + B_2 \cos\left[\left(\sqrt{\frac{4{\psi_1}^2 b^2 + {CD_1}^2}{4\psi_1}}\right)\xi\right] - \frac{4G_{1,0}\psi_1}{4{\psi_1}^2 b^2 + {CD_1}^2} \tag{3.8}$$

$$R_2\left(\xi\right) = B_3 \sin\left[\left(\sqrt{\frac{4{\psi_2}^2 b^2 + {CD_2}^2}{4\psi_2}}\right)\xi\right] + B_4 \cos\left[\left(\sqrt{\frac{4{\psi_2}^2 b^2 + {CD_2}^2}{4\psi_2}}\right)\xi\right] - \frac{4G_{2,0}\psi_2}{4{\psi_2}^2 b^2 + {CD_2}^2} \tag{3.9}$$

where B_i are constants to be determined.

The overall analytic solution requires that the boundary conditions be defined. Two sets are considered below.

3.3.1.1 Free-Fixed Boundary Conditions

For these conditions the stress-free end at $\xi = 0$ gives: $\left.\frac{dR_1(\xi)}{d\xi}\right|_{\xi=0} = 0$. The fixed end at $\xi = 1$ gives: $R_2(\xi) = 0$. Next the interface continuity conditions are (assuming the cells have the same length, i.e., $\alpha = 1$, $\alpha = L_2/L_1$): $R_1(\xi) = R_2(\xi)$, $\xi = 0.5$(displacement continuity) and $\frac{dR_1(\xi)}{d\xi} = A_r E_r \frac{dR_2(\xi)}{d\xi}, \xi = 0.5$(force continuity). The constants involved in the solutions, namely, B_1, B_2, B_3 and B_4 can be determined from these conditions. The approach leads to a system of algebraic equations as follows (in matrix form):

$$\begin{bmatrix} \sqrt{\frac{4\psi_1{}^2b^2+CD_1{}^2}{4\psi_1}} & 0 \\ 0 & 0 \\ \sin\left(\sqrt{\frac{4\psi_1{}^2b^2+CD_1{}^2}{16\psi_1}}\right) & \cos\left(\sqrt{\frac{4\psi_1{}^2b^2+CD_1{}^2}{16\psi_1}}\right) \\ \left(\sqrt{\frac{4\psi_1{}^2b^2+CD_1{}^2}{4\psi_1}}\right)\cos\left(\sqrt{\frac{4\psi_1{}^2b^2+CD_1{}^2}{16\psi_1}}\right) & \left(-\sqrt{\frac{4\psi_1{}^2b^2+CD_1{}^2}{4\psi_1}}\right)\sin\left(\sqrt{\frac{4\psi_1{}^2b^2+CD_1{}^2}{16\psi_1}}\right) \\ 0 & 0 \\ \sin\left(\sqrt{\frac{4\psi_2{}^2b^2+CD_2{}^2}{4\psi_2}}\right) & \cos\left(\sqrt{\frac{4\psi_2{}^2b^2+CD_2{}^2}{4\psi_2}}\right) \\ -\sin\left(\sqrt{\frac{4\psi_2{}^2b^2+CD_2{}^2}{16\psi_2}}\right) & -\cos\left(\sqrt{\frac{4\psi_2{}^2b^2+CD_2{}^2}{16\psi_2}}\right) \\ -E_rA_r\left(\left(\sqrt{\frac{4\psi_2{}^2b^2+CD_2{}^2}{4\psi_2}}\right)\cos\left(\sqrt{\frac{4\psi_2{}^2b^2+CD_2{}^2}{16\psi_2}}\right)\right) & E_rA_r\left(\left(\sqrt{\frac{4\psi_2{}^2b^2+CD_2{}^2}{4\psi_2}}\right)\sin\left(\sqrt{\frac{4\psi_2{}^2b^2+CD_2{}^2}{16\psi_2}}\right)\right) \end{bmatrix} \begin{bmatrix} B_1 \\ B_2 \\ B_3 \\ B_4 \end{bmatrix} \tag{3.10}$$
$$= \begin{bmatrix} 0 \\ \frac{4G_{2,0}\psi_2}{4\psi_2{}^2b^2+CD_2{}^2} \\ \frac{4G_{1,0}\psi_1}{4\psi_1{}^2b^2+CD_1{}^2} - \frac{4G_{2,0}\psi_2}{4\psi_2{}^2b^2+CD_2{}^2} \\ 0 \end{bmatrix} \equiv [\mathrm{A}]\{\mathrm{B}\} = \{G\}$$

Note that natural frequencies can found on setting the determinant of [A] to zero.

3.3.1.2 Fixed-Fixed Boundary Conditions

For fixed-fixed conditions, $R_1(\xi) = 0$, $\xi = 0$. In this case the approach gives:

$$\begin{bmatrix} 0 & 1 \\ 0 & 0 \\ \sin\left(\sqrt{\frac{4\psi_1{}^2b^2+CD_1{}^2}{16\psi_1}}\right) & \cos\left(\sqrt{\frac{4\psi_1{}^2b^2+CD_1{}^2}{16\psi_1}}\right) \\ \left(\sqrt{\frac{4\psi_1{}^2b^2+CD_1{}^2}{4\psi_1}}\right)\cos\left(\sqrt{\frac{4\psi_1{}^2b^2+CD_1{}^2}{16\psi_1}}\right) & \left(-\sqrt{\frac{4\psi_1{}^2b^2+CD_1{}^2}{4\psi_1}}\right)\sin\left(\sqrt{\frac{4\psi_1{}^2b^2+CD_1{}^2}{16\psi_1}}\right) \\ 0 & 0 \\ \sin\left(\sqrt{\frac{4\psi_2{}^2b^2+CD_2{}^2}{4\psi_2}}\right) & \cos\left(\sqrt{\frac{4\psi_2{}^2b^2+CD_2{}^2}{4\psi_2}}\right) \\ -\sin\left(\sqrt{\frac{4\psi_2{}^2b^2+CD_2{}^2}{16\psi_2}}\right) & -\cos\left(\sqrt{\frac{4\psi_2{}^2b^2+CD_2{}^2}{16\psi_2}}\right) \\ -E_rA_r\left(\left(\sqrt{\frac{4\psi_2{}^2b^2+CD_2{}^2}{4\psi_2}}\right)\cos\left(\sqrt{\frac{4\psi_2{}^2b^2+CD_2{}^2}{16\psi_2}}\right)\right) & E_rA_r\left(\left(\sqrt{\frac{4\psi_2{}^2b^2+CD_2{}^2}{4\psi_2}}\right)\sin\left(\sqrt{\frac{4\psi_2{}^2b^2+CD_2{}^2}{16\psi_2}}\right)\right) \end{bmatrix} \begin{bmatrix} B_1 \\ B_2 \\ B_3 \\ B_4 \end{bmatrix} \tag{3.11}$$
$$= \begin{bmatrix} \frac{4G_{1,0}\psi_1}{4\psi_1{}^2b^2+CD_1{}^2} \\ \frac{4G_{2,0}\psi_2}{4\psi_2{}^2b^2+CD_2{}^2} \\ \frac{4G_{1,0}\psi_1}{4\psi_1{}^2b^2+CD_1{}^2} - \frac{4G_{2,0}\psi_2}{4\psi_2{}^2b^2+CD_2{}^2} \\ 0 \end{bmatrix} \equiv [\mathrm{A}]\{\mathrm{B}\} = \{G\}$$

3.4 Continuous Variation Model

In the continuous variation model, transitions from one cell to another are modeled via logistic functions. Here these functions, q_j in non-dimensional form, are taken to be:

$$q_j(\xi) = \left(1 + \frac{\delta_2 - \delta_1}{\delta_1}\right)\left(\frac{1}{2} + \frac{1}{2}\tanh\left(500 - \frac{\xi}{2}\right)\right), \; j = 1, 2, 3, 4 \tag{3.12}$$

with δ_j representing a material property, geometric property or damping (E, ρ, A or C).

For these continuously varying functions, Eq. (3.1) can be written as:

$$\frac{\partial}{\partial \xi}\left(q_1(\xi)\, q_3(\xi)\, \frac{\partial w(\xi,\tau)}{\partial \xi}\right) - q_2(\xi)\, q_3(\xi)\, \frac{\partial^2 w(\xi,\tau)}{\partial \tau^2} - CDq_4(\xi)\, \frac{\partial w(\xi,\tau)}{\partial \tau} = -g(\xi,\tau) \tag{3.13}$$

where $E(x) = q_1(\xi)E_1$, $\rho(x) = q_2(\xi)\rho_1$, $A(x) = q_3(\xi)A_1$, $C(x) = q_4(\xi)C_1$, $CD = \frac{C_1}{E_1 A_1}L^2\Omega_0$, $g(\xi,\tau) = \frac{f(x,t)L}{E_1 A_1}$.

As in the analytic approach, for harmonic forcing with frequency λ, one can take:

$$g(\xi,\tau) = G(\xi)\, e^{\lambda\tau} \tag{3.14}$$

with solutions of the form:

$$w(\xi,\tau) = R(\xi)\, e^{\lambda\tau} \tag{3.15}$$

Using $\lambda = (a + bI)$ and separating real and imaginary parts, leads to the following system of equations.

$$\begin{gathered} \frac{d}{d\xi}\left(q_1(\xi)\, q_3(\xi)\, \frac{dR(\xi)}{d\xi}\right) - q_2(\xi)\, q_3(\xi)\left(a^2 - b^2\right) R(\xi) - CDq_4(\xi)(a) R(\xi) = -G(\xi) \\ -q_2(\xi)\, q_3(\xi)(2a) - CDq_4(\xi) = 0 \end{gathered} \tag{3.16}$$

Analytic solutions may not be feasible for Eq. (3.16). Given the material layout and cross section variation, i.e., the corresponding logistic functions, a MAPLE® routine can be used to obtain numerical approximations to the FRF of the system. This is done by monitoring the response for different values of the frequency b. Resonances can also be obtained via a forced-motion approach (see [13]). It consists of using MAPLE®'s two-point boundary value solver to solve a forced motion problem. A constant value for the forcing function G is assumed and the frequency b is varied. By observing the mid-span deflection of the rod, resonant frequencies can be found on noting where changes in sign occur.

Note that Eq. (3.13) could be tackled directly via a numerical approach. This partial differential equation (PDE) can be solved using MAPLE®, but it has proven to be more numerically complex than the approach described.

The procedures are illustrated in the following via numerical examples.

3.5 Numerical Examples

Consider the rod shown in Fig. 3.1 and assume the following materials: Aluminum ($E_1 = 71$ *GPa*, $\rho_1 = 2710$ *Kg/m*^{3}) and Silicon Carbide ($E_2 = 210$ *GPa*, $\rho_2 = 3100$ *Kg/m*^{3}). These values are taken from a paper in the field [14].

3.5.1 Free-Fixed Boundary Conditions

For the free-fixed case, the determinant of [A] in Eq. (3.10) leads to the following values for the first two non-dimensional natural frequencies: $b = 2.2720$ and $b = 5.6336$. (The following parameters apply: $C_1 = C_2$, $E_r = 2.9577$, $\rho_r = 1.1439$, $A_r = 1.0000$, $G_{1,0} = G_{2,0} = 1.0000$, $\psi_1 = 1.0000$, $\psi_2 = 0.3868$, $CD_1 = 0.1000$, $CD_2 = CD_1(C_2/C_1)(1/E_r A_r) = 0.0338$.)

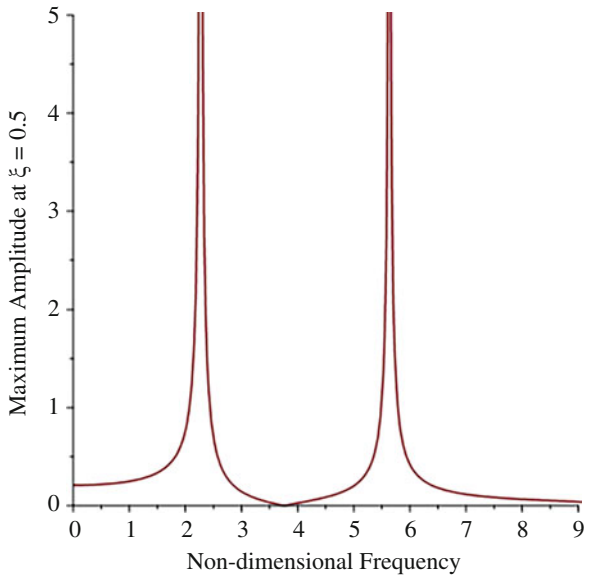

Fig. 3.2 FRF for non-homogeneous rod at mid-point—Free/Fixed

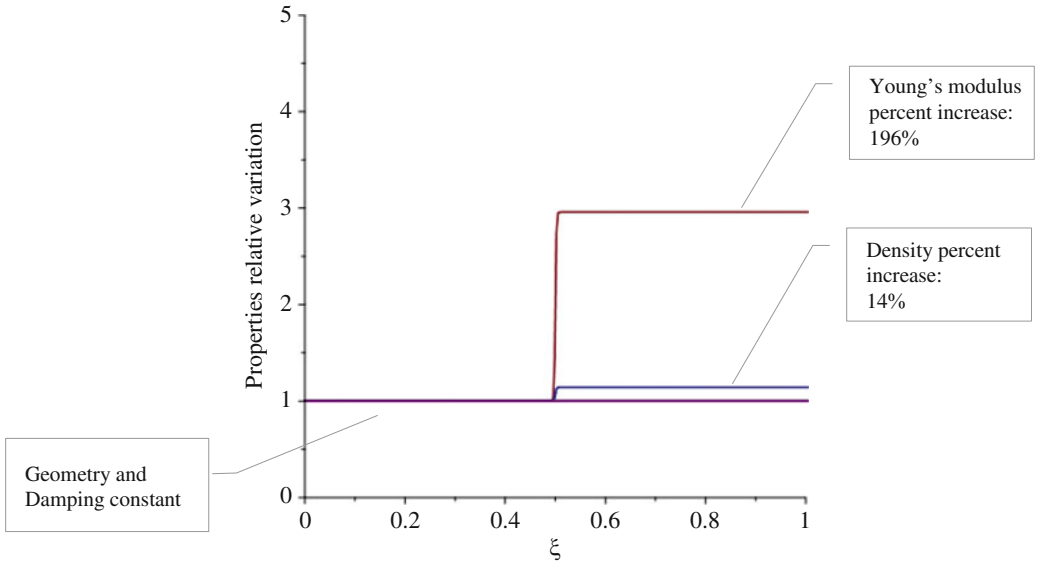

Fig. 3.3 Relative properties variation for two-cell rod

Using Eq. (3.10) to determine the values of the constants B_i and Eq. (3.8), allows for the calculation of the FRF for the system. Setting $\xi = 0.50$(rod mid-span), amplitudes can be calculated for different values of the non-dimensional frequency b.

The frequency response function, spanning the first two natural frequencies, for the mid-point of the rod is shown in Fig. 3.2.

For the continuous variation model and using the numerical values given above, the continuously varying functions are shown in Fig. 3.3.

Assuming a value of *1* for the external forcing $G(\xi)$ and using the forced-motion approach [13], the resultant deflections are plotted bellow for two distinct values of the frequency b.

The resonance frequencies are taken to occur at $b = 2.30$ and $b = 5.65$, as seen in Figs. 3.4 and 3.5 respectively.

Amplitudes for the response at the center of the rod can be monitored from Eq. (3.16) . The approach leads to the numerical FRF shown in Fig. 3.6.

The figure shows an overlap of the numerical results and the results from the analytical approach, Eq. (3.8). It is seen that good agreement is obtained, the first two resonances and amplitude values correspond well.

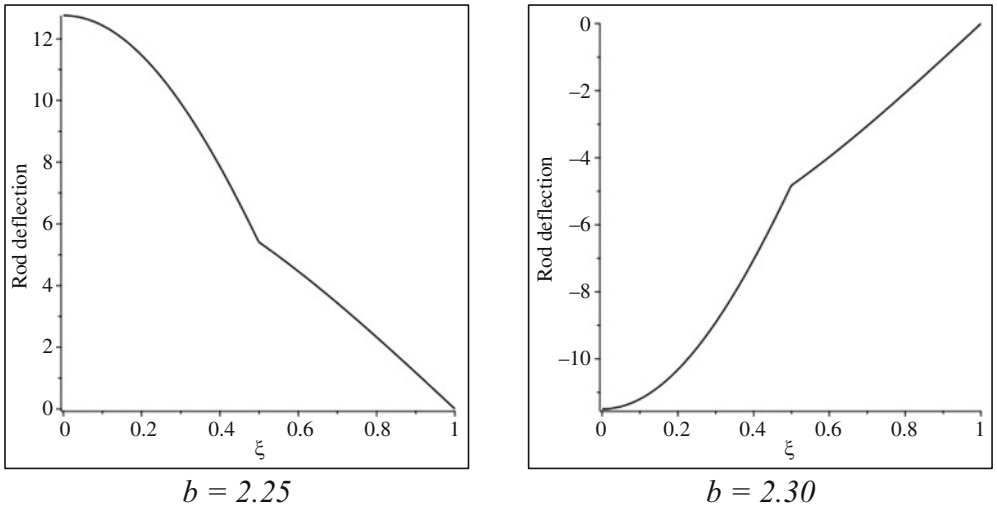

Fig. 3.4 Rod deflections for distinct values of b—Free-Fixed: first resonance

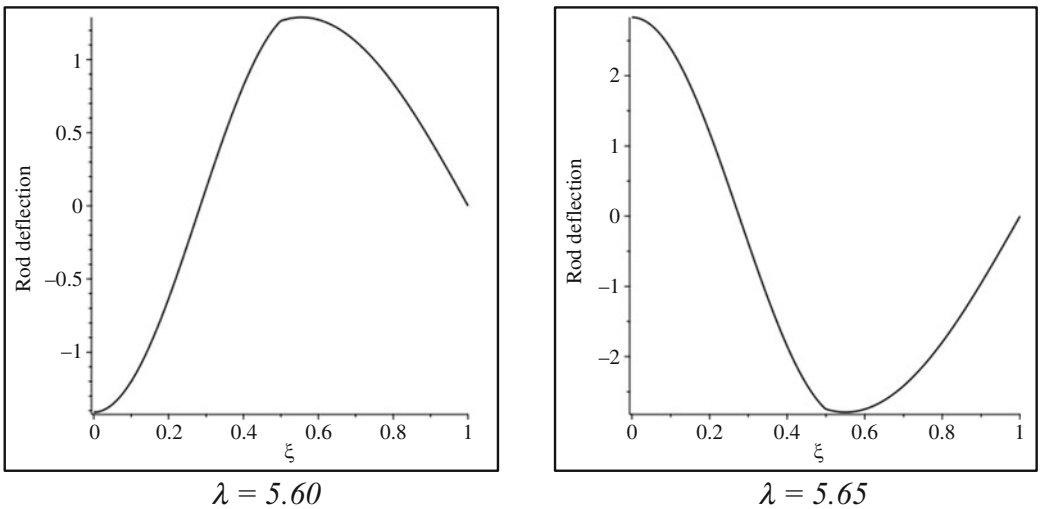

Fig. 3.5 Rod deflections for distinct values of b—Free-Fixed: second resonance

Fig. 3.6 Results comparison—numerical and analytical approaches—Free/Fixed

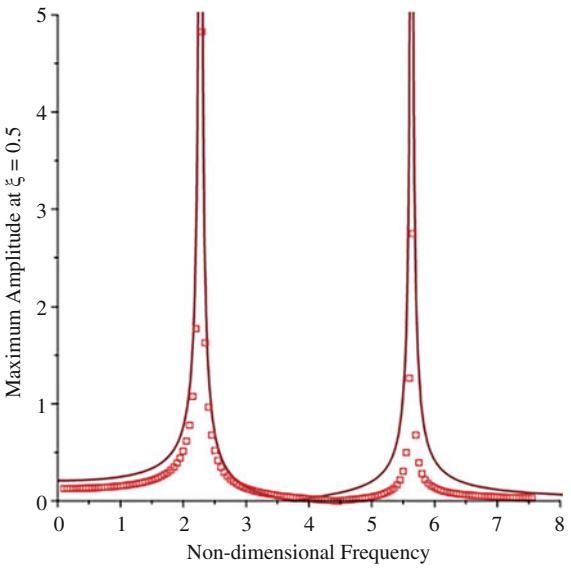

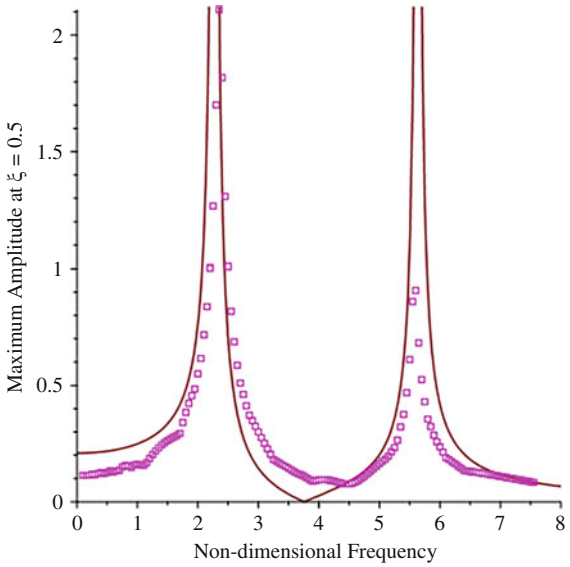

Fig. 3.7 Results comparison—numerical (PDE) and analytical approaches—Free/Fixed

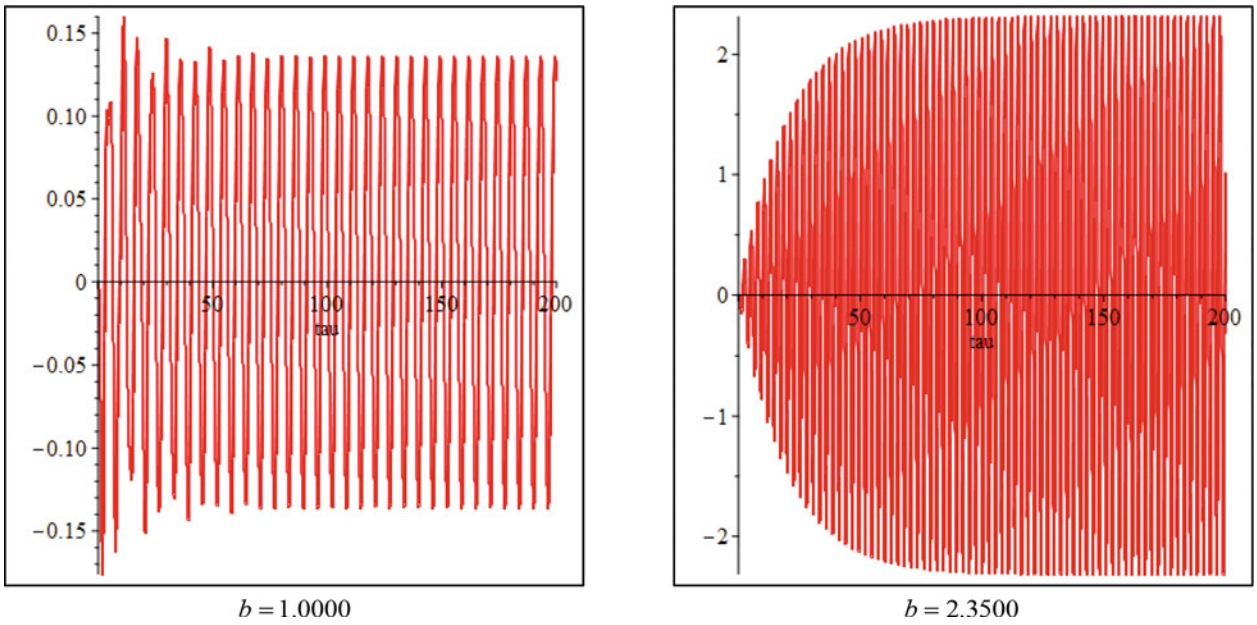

Fig. 3.8 Time response at distinct frequencies (PDE)—Free/Fixed

A direct numerical solution of Eq. (3.13) can also lead to the FRF for this case. To calculate these results the forcing function is taken to be constant in space and sinusoidal in time: $g(\xi, \tau) = \sin(\nu\tau)$. This leads to the FRF given in Fig. 3.7, which is overlapped with the analytic results. Both are in good agreement.

This approach allows for plotting the time response at specific values of frequency. This is shown in Fig. 3.8, where the response is given at a non-resonant frequency and at the first numerical resonance (relatively large amplitudes compared to the non-resonant case). Note that the damping ratio can be estimated for the non-resonant case using a logarithmic decrement approach. Here it is approximately 0.13%.

3.5.2 Fixed-Fixed Boundary Conditions

For the fixed-fixed case, the determinant of [A] in Eq. (3.11) gives the natural frequencies: $b = 4.1323$ and $b = 7.3836$. Equations (3.11) and (3.8) lead to the FRF for the system, which is shown in Fig. 3.9.

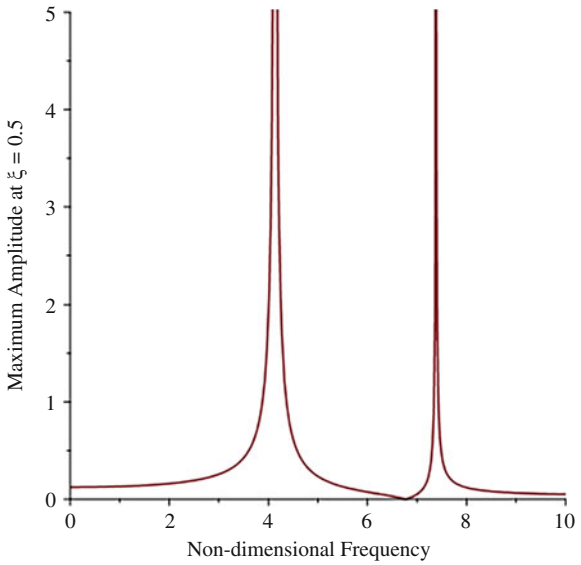

Fig. 3.9 FRF for non-homogeneous rod at mid-point—Fixed/Fixed

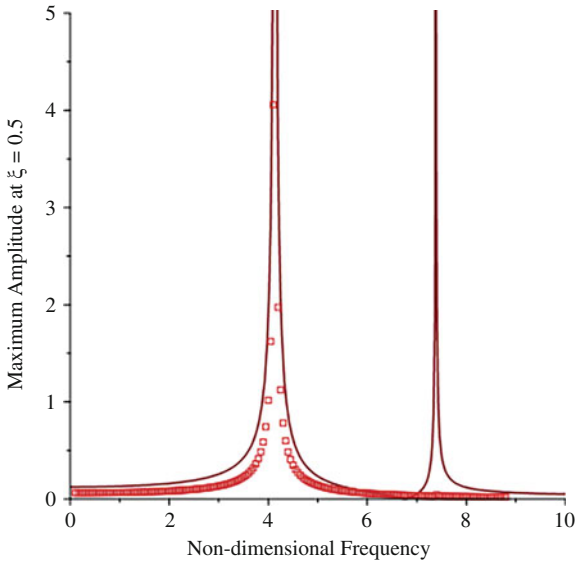

Fig. 3.10 Results comparison—numerical and analytical approaches—Fixed/Fixed

The numerical FRF for this case is seen in Fig. 3.10. The overlap of the numerical results and the results from the analytical approach, Eq. (3.8), show that good agreement is obtained for the first frequency and amplitude values with the second one not quite given the amplitudes seen in the analytical approach (similar results were obtained for the non-damped case, see [1]).

The direct numerical solution for this case leads to the results shown in Fig. 3.11. The overlap of the numerical and analytic results shows, as previously, that the first resonance value and amplitudes are in good agreement.

The time responses at specific values of frequency are shown in Fig. 3.12. Note the relatively large amplitudes at the first resonance (a non-linear model would lead to more accurate peak values). The damping ratio for this case is about 0.13%.

An example is now given in which the spatial force is non-constant. Consider a variable force given by the exponential function: $G(\xi) = e^{-\xi^2}$. For the example the damping properties are also considered to vary from one material to another. The variation is taken as an increase in viscous damping of five times (from the aluminum cell to the silicon-carbide cell). This gives: $q_4(\xi) = (5)(1/2 + 1/2 \tanh(500 - \xi/2))$. Also, the initial value of non-dimensional damping is taken to be $CD_1 = 1.0000$, which is ten times the previous used value.

The results can be found using the continuous variation model. The FRFs for this case are seen in Fig. 3.13.

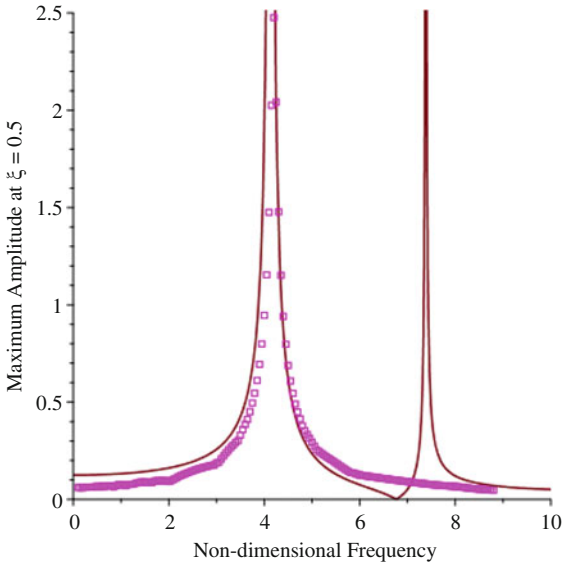

Fig. 3.11 Results comparison—numerical (PDE) and analytical approaches—Fixed/Fixed

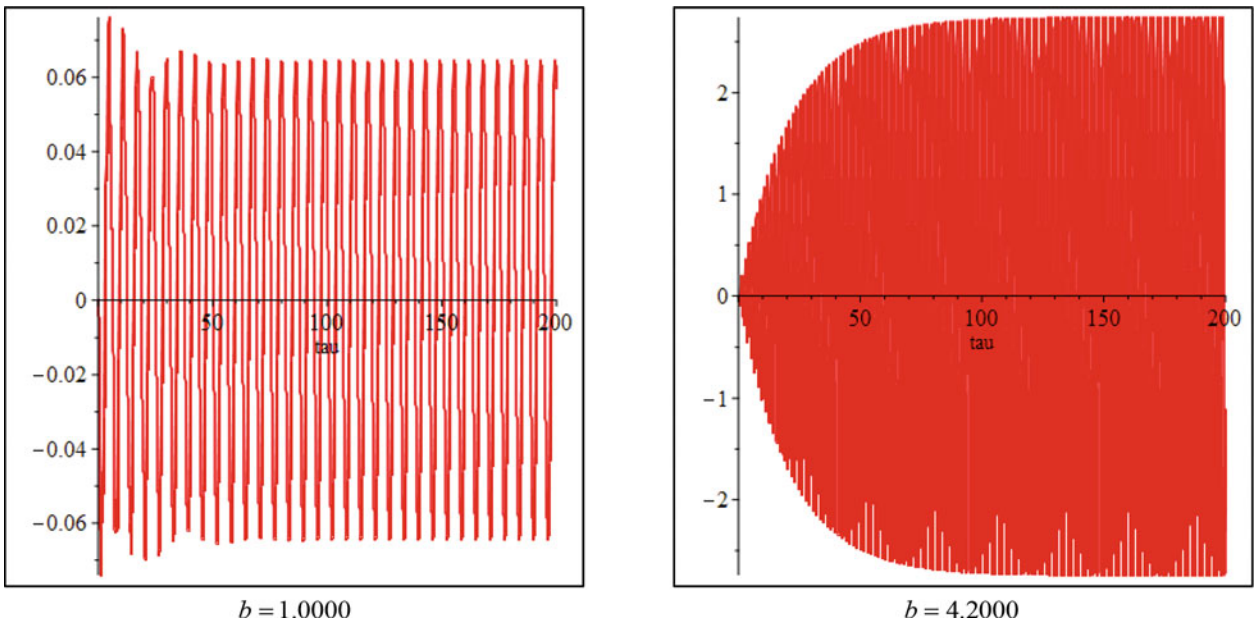

Fig. 3.12 Time response at distinct frequencies (PDE)—Fixed/Fixed

3.6 Conclusions

Harmonic forcing of a two-layer damped elastic rod was examined. Spatial variations of the forcing functions were allowed as well as variations of damping properties from one cell to another. Analytic solutions using rod theory were developed, from which the FRFs at the rod mid-point could be found numerically. These were compared to ones obtained using a continuous variation model and good agreement between the two methods was found.

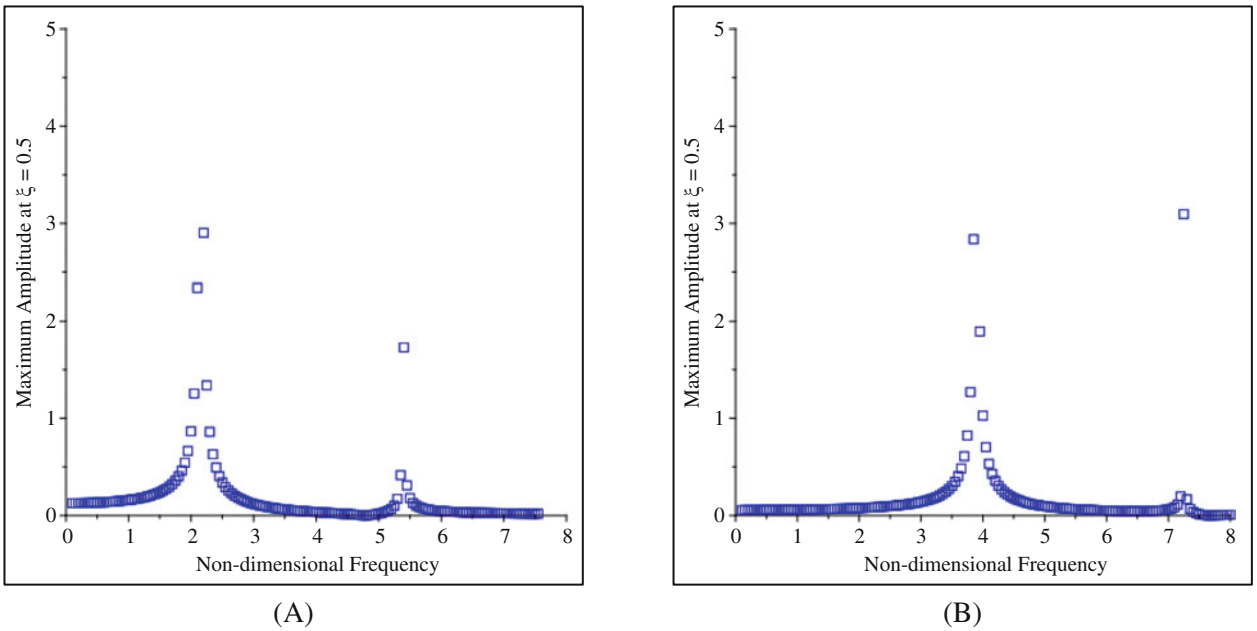

Fig. 3.13 FRFs for exponential force and varying damping—Free/Fixed (**a**), Fixed/Fixed (**b**)

References

1. Mazzei, A.J., Scott, R.A.: Harmonic forcing of a two-segment elastic rod. In: Di Miao, D., Tarazaga, P., Castellini, P. (eds.) Special Topics in Structural Dynamics, Volume 6: proceedings of the 34th IMAC, A Conference and Exposition On Structural Dynamics 2016, pp. 221–231. Springer International Publishing, Cham (2016)
2. Mazzei Jr., A.J., Scott, R.A.: Vibrations of discretely layered structures using a continuous variation model. In: Allemang, R. (ed.) Topics in Modal Analysis II, vol. 8, pp. 385–396. Springer International Publishing, Cham (2014)
3. Lee, E.H., Yang, W.H.: On waves in composite materials with periodic structure. SIAM J. Appl. Math. **25**(3), 492–499 (1973)
4. Hussein, M.I., Hulbert, G.M., Scott, R.A.: Dispersive elastodynamics of 1D banded materials and structures: analysis. J. Sound Vib. **289**(4–5), 779–806 (2006)
5. Hussein, M.I., Hulbert, G.M., Scott, R.A.: Dispersive elastodynamics of 1D banded materials and structures: design. J. Sound Vib. **307**(3–5), 865–893 (2007)
6. Vasseur, J.O., Deymier, P., Sukhovich, A., Merheb, B., Hladky-Hennion, A.C., Hussein, M.I.: Phononic band structures and transmission coefficients: methods and approaches. In: Deymier, P.A. (ed.) Acoustic Metamaterials and Phononic Crystals, pp. 329–372. Springer, Berlin (2013)
7. Hussein, M.I., Leamy, M.J., Ruzzene, M.: Dynamics of phononic materials and structures: historical origins, recent progress, and future outlook. Appl. Mech. Rev. **66**(4), 040802–040802–38 (2014)
8. Berezovski, A., Engelbrecht, J., Maugin, G.A.: Numerical Simulation of Waves and Fronts in Inhomogeneous Solids. World Scientific, Singapore (2008)
9. Snowdon, J.C.: Longitudinal vibration of internally damped rods. J. Acoust. Soc. Am. **36**(3), 502–510 (1964)
10. Cortés, F., Elejabarrieta, M.J.: Longitudinal vibration of a damped rod. Part I: complex natural frequencies and mode shapes. Int. J. Mech. Sci. **48**(9), 969–975 (2006)
11. Yüksel, Ş., Dalli, U.: Longitudinally vibrating elastic rods with locally and non-locally reacting viscous dampers. Shock. Vib. **12**(2), 109–118 (2005)
12. Jia-shi, T., Li, L., Quan-zhong, H.: Vibration analysis of a rod with complex boundary conditions. Appl. Math. Mech. **9**(9), 837–847 (1988)
13. Mazzei, A.J., Scott, R.A.: On the effects of non-homogeneous materials on the vibrations and static stability of tapered shafts. J. Vib. Control. **19**(5), 771–786 (2013)
14. Chiu, T.C., Erdogan, F.: One-dimensional wave propagation in a functionally graded elastic medium. J. Sound Vib. **222**(3), 453–487 (1999)

Chapter 4
Effects of Multi-Axial versus Single-Axial Excitation of Jointed Systems

S. A. Smith and M. R. W. Brake

Abstract In many structural assembly, the main cause of nonlinearities are jointed interfaces. The nonlinearity manifests as a softening response, which is caused by the joint slipping when stick caused by friction forces is overcome. To quantify the friction nonlinearity, the system is typically experimentally tested in each axis independently. This practice assumes that the nonlinearity is directionally uncoupled and can be modeled using the superposition principle. Previous works have shown this is an incorrect assumption. Joints in structural assemblies may not experience excitation from only one direction at a time. This paper experimentally assesses the slip condition of the removable component of the Box Assembly with Removable Component benchmark structure. The slip condition is first studied using single-axis excitation and superposition assumption, and then studies the slip condition under multi-axis excitation. The results show that the slip condition changes when the structure is excited using multi-directional excitation.

Keywords Bolted joints · Nonlinear vibration · BARC · Measurement effects · Multi-axis excitation

4.1 Introduction

There exists many types of nonlinearities in assembled structures, including geometric, material, and jointed interfaces. The jointed interface nonlinearity manifests as a softening response, which arises when the friction force is over come and the joint slips [1]. The quantification of nonlinearities has historically be from unidirectional excitation [2, 5, 6, 8], this practice assumes that nonlinearities are directionally uncoupled, the characterized values are independent, and can be modeled using the superposition principles. This practice may not hold as many structures may not experience unidirectional forces when in practical applications. In recent years, studies have focused on understanding these practical forces using multi-directional excitations (MDEs) [4, 7]. These studies however, do not study the nonlinearities that maybe present in the sample investigated.

This research investigates the effects MDE has on the Box Assembly with Removable Component (BARC) benchmark structure from Sandia National Laboratories [10]. The BARC is first investigated under unidirectional multisine excitations to gain baseline responses for structural mode locations. Once the modes are located the system is tested in individual directions using steady-state responses, and the damping ratio was calculated. Finally the system is excited using MDE; which is expected to highlight whether this type excitation does have an effect on nonlinear parameter estimations.

4.2 Experiment and Results

To study the effects of MDE on the response of the BARC system. The BARC was attached to a three degree of freedom (3DoF) shaker table designed and built at Rice University, shown in Fig. 4.1. The shaker table includes two Modal Shop K2007E01 SmartShakers, a Brüel & Kjær PM Vibration Exciter Type 4808, two PCB 356A03 Triaxial ICP Accelerometers, three PCB 352A24 uniaxial ICP Accelerometers, and a LMS 16 Channel Data Acquisition system. To gain an understanding of the vibration of the BARC structure attached to the fixture, modal analysis using the roving hammer technique [3] was performed., and the first two flexible body modes of the BARC were identified to be at 145.892 and 291.102 Hz. Figure 4.2 gives a comparison of the mode shapes to an uncalibrated finite element (FE) model.

S. A. Smith · M. R. W. Brake (✉)
William Marsh Rice University, Houston, TX, USA
e-mail: brake@rice.edu

C. Walber et al. (eds.), *Sensors and Instrumentation, Aircraft/Aerospace, Energy Harvesting & Dynamic Environments Testing, Volume 7*, Conference Proceedings of the Society for Experimental Mechanics Series,
https://doi.org/10.1007/978-3-030-12676-6_4

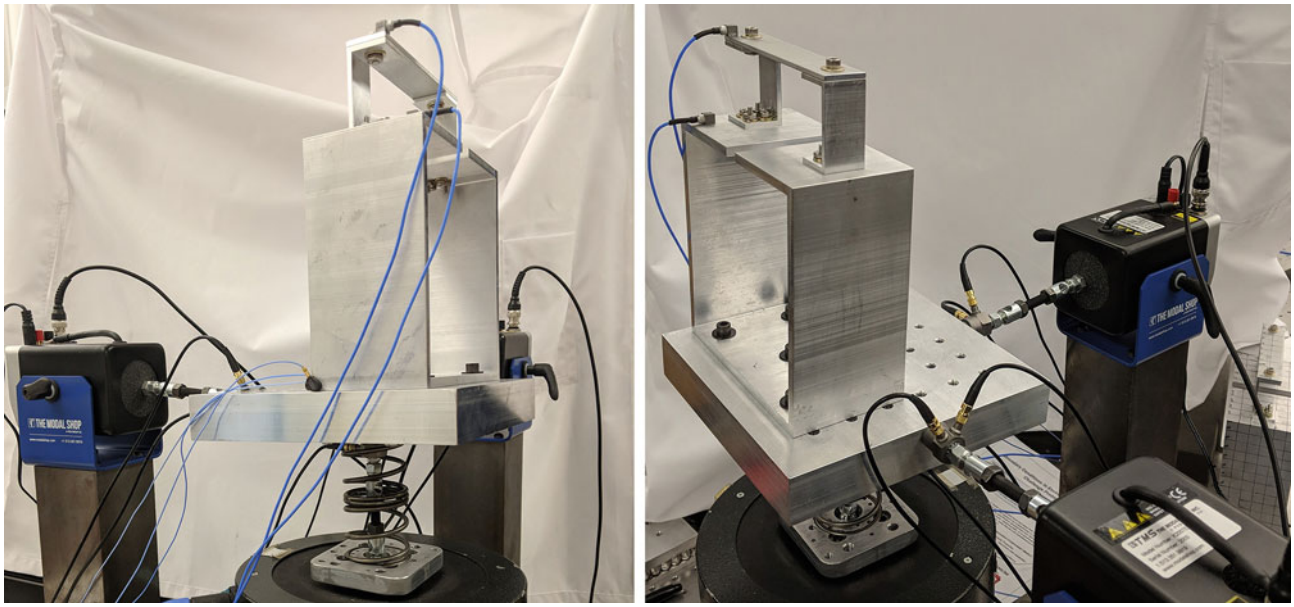

Fig. 4.1 Experimental setup on 3 DoF shaker table

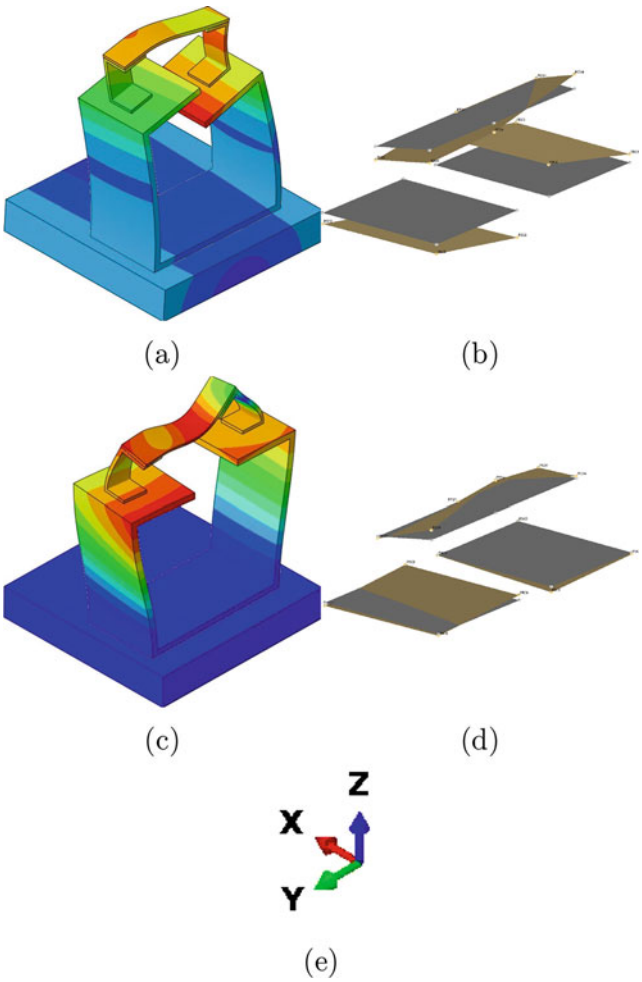

Fig. 4.2 Mode shapes of Mode 1 from (**a**) FE and (**b**) Impact testing, Mode 2 from (**c**) FE and (**d**) Impact testing, and (**e**) coordinates of experiments

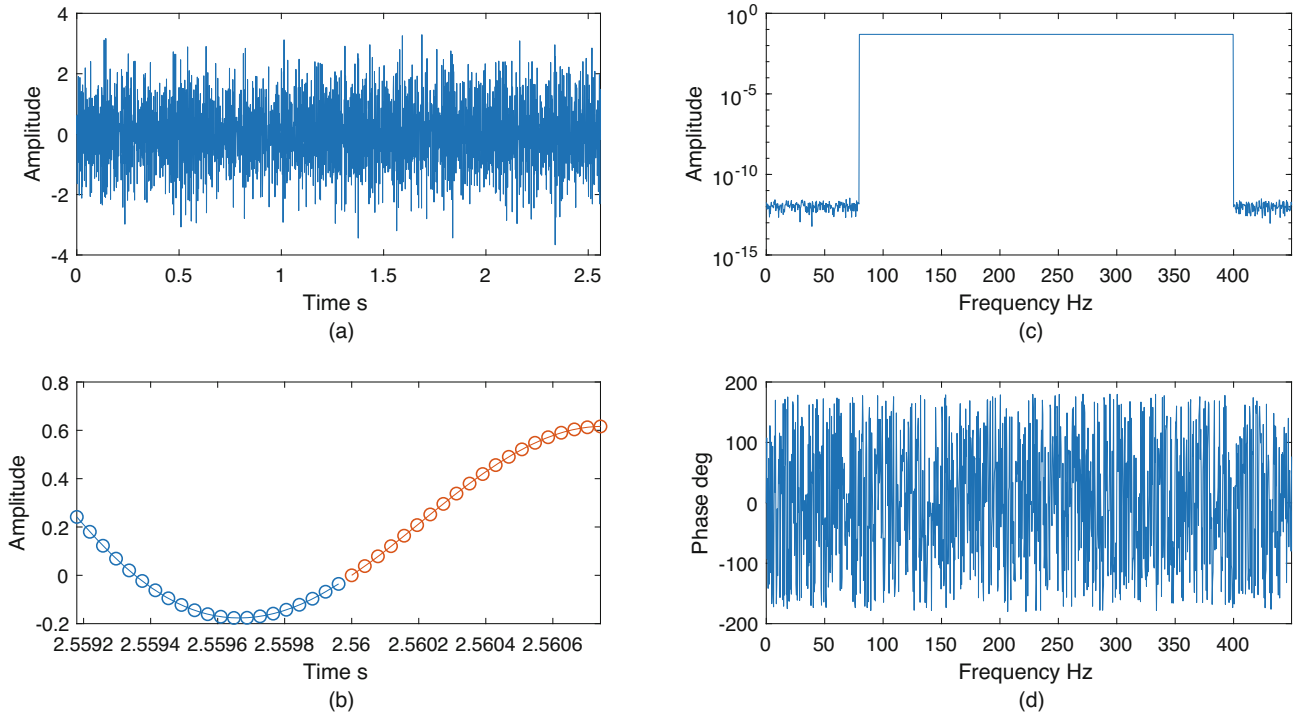

Fig. 4.3 The multisine's (**a**) time signal, (**b**) zoomed section to show repeatability of the signal, (**c**) spectrum, and (**d**) phase

4.2.1 Multisine Test

To find out which modes of the BARC structure can be excited, a multisine signal is utilized. Multisine was selected for its advantages in reducing leakage and ability to focus the excitation energy into a specified frequency band [6, 9]. The multisine and its properties are shown in Fig. 4.3. The spectrum of the multisine shows that all energy is contained in between the desired frequencies (80 and 400 Hz), there is no leakage and the phase is random.

The three DOF shaker table is then excited using the multisine signal such that the acceleration is controlled to 0.06 g RMS. The table is first excited in the x-direction and then the y-direction in two sequential experiments, the response spectrum are shown in Fig. 4.4. The first mode of the BARC structure is excited by y-direction inputs, and the second mode is excited by inputs from either direction. As the first mode is a z-direction mode, this is an indication that the motion from the shaker table is not decoupled for each direction. For the rest of this study it is assumed the coupling is minimal.

4.2.2 Steady State Sine Test

Knowing that the modes can be by excited and measured from the input locations of the shaker table, a steady-state sine test is performed. The system is excited at 146 and 292 Hz, for three different levels (0.04, 0.06, and 0.08 g RMS) in each direction individually then combined with the signals in-phase. The force and drive point acceleration signals are then band-pass filtered to remove any frequency content not of interest. The signals are fit with a sine function, and the acceleration fit is integrated once to get velocity. The velocity, force, amplitude of acceleration, and frequency are then used to calculate the hysteresis damping using [1]:

$$\int_0^{\frac{2\pi}{\omega}} f\,(t)\,\dot{x}\,(t)\,\mathrm{d}t = 2\pi\zeta k X^2 \tag{4.1}$$

where k is the stiffness of the system found from the slope of the ellipse's axis. An example of the hysteresis loop is shown in Fig. 4.5, and the results from the tests are recorded in Table 4.1 and shown in Fig. 4.6. The damping results show that

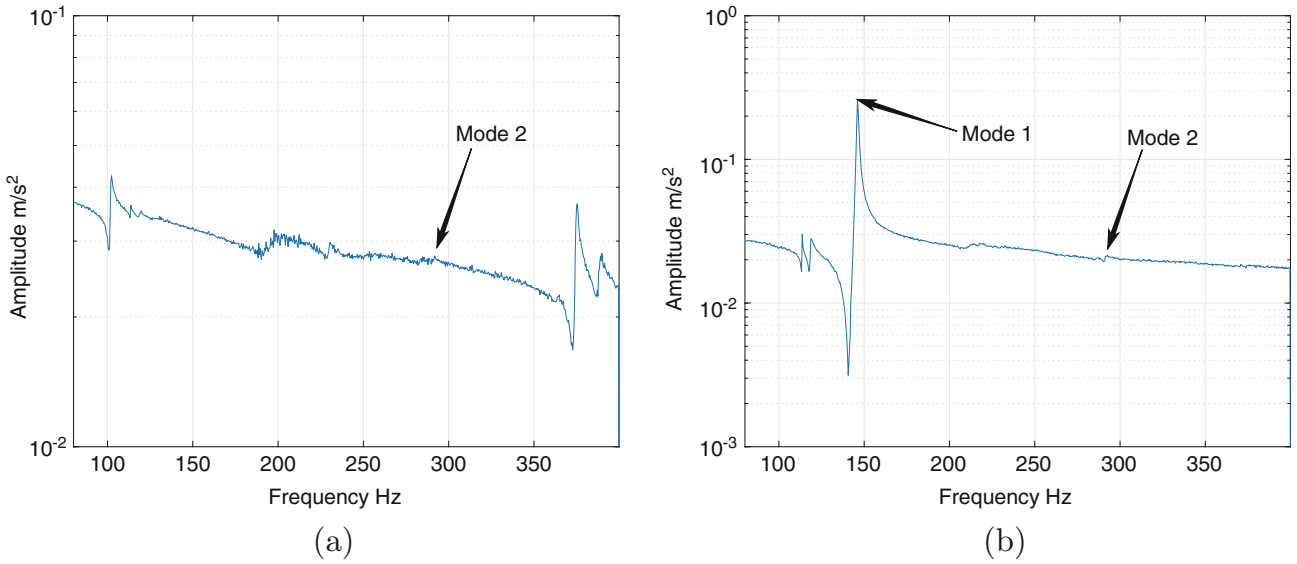

Fig. 4.4 Response of the BARC structure under unidirectional multisine excitation in the (**a**) x-direction and (**b**) y-direction

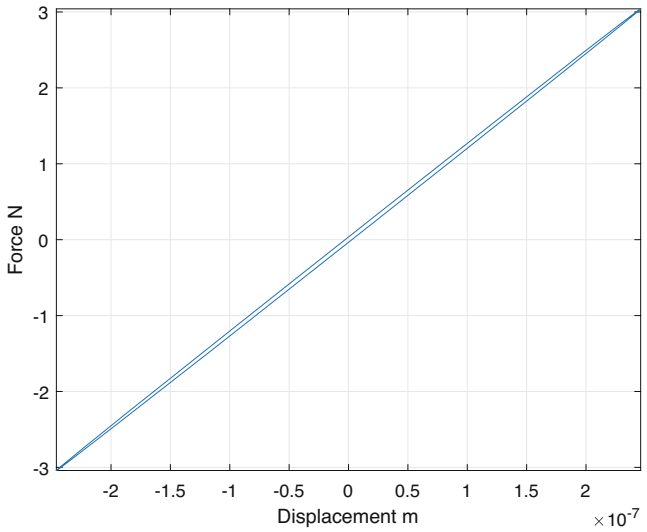

Fig. 4.5 Hysteresis loop for the test in y-direction only at 292 Hz and 0.06 g RMS

as the amplitude of excitation increases the damping decreases, and when both x- and y-directions are active the damping decreases. *This means that the MDE is not a linear combination of the responses from each direction tested individually.*

4.3 Conclusion

With the increased focus of nonlinearities, especially bolted joints, the testing procedure of unidirectional testing is being investigated. This practice introduces superposition back into the nonlinear equations, as it assumes that the multi-directional modes are uncoupled and the responses can be added. The results of this study show:

- There is significant damping nonlinearity in the BARC structure, but not stiffness nonlinearity over the excitations studied;
- MDE changes the damping, specifically decreasing the damping while not changing the trend; and
- The response due to MDE is *not* equivalent to a superposition of single axis excitations.

This work will be expanded by adding the z-direction and then by varying the phase of the input signals.

Table 4.1 Damping ratios of the BARC structure under steady-state excitation

	X-direction	Y-direction	Both	
Exication amplitude (g RMS)	ζ (%)	ζ (%)	ζ_x (%)	ζ_y (%)
146 Hz				
0.04	0.41467	49.637	0.15663	49.740
0.06	0.31902	39.168	0.19977	38.471
0.08	0.31722	42.721	0.19963	41.040
292 Hz				
0.04	0.81707	0.78950	0.049588	0.27764
0.06	0.31474	0.58528	1.1140	0.21534
0.08	0.20292	0.30707	0.041962	0.089934

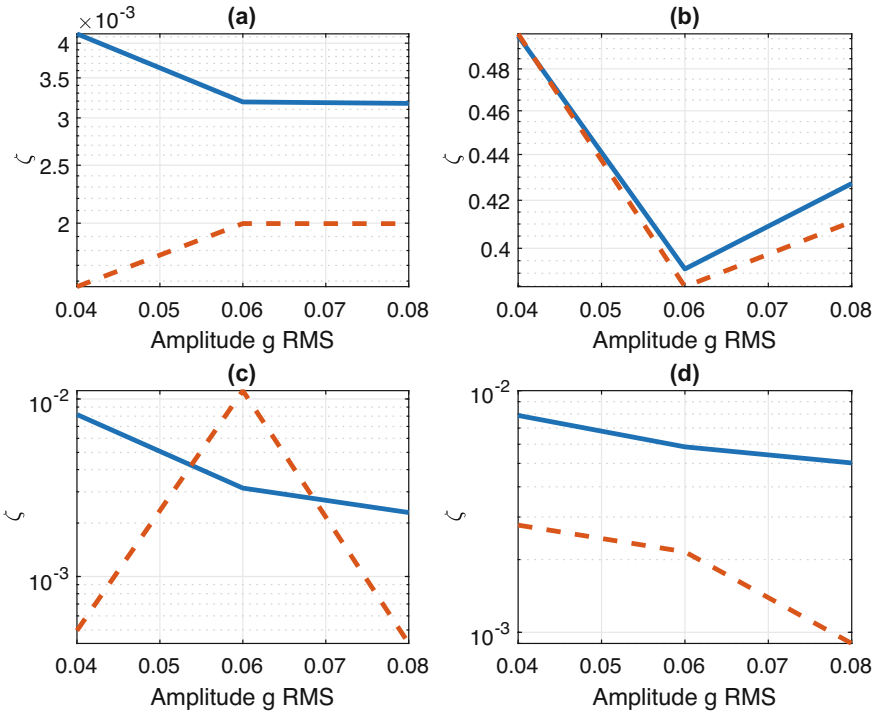

Fig. 4.6 Damping ratio comparison of the unidirectional (solid line, blue) and multi-directional (dashed line, red) excitations for (**a**) x-direction at 146 Hz, (**b**) y-direction at 146 Hz, (**c**) x-direction at 292 Hz, and (**d**) y-direction at 292 Hz

Acknowledgements This work was funded and supported by Sandia National Laboratories. Sandia National Laboratories is a multimission laboratory managed and operated by National Technology and Engineering Solutions of Sandia, LLC., a wholly owned subsidiary of Honeywell International, Inc., for the U.S. Department of Energy's National Nuclear Security Administration under contract DE-NA0003525.

References

1. Brake, M.R.W. (ed.): The Mechanics of Jointed Structures. Springer, New York (2017)
2. Daborn, P.M., Roberts, C., Ewins, D.J., Ind, P.R.: Next-generation random vibration tests. In: 32th International Modal Analysis Conference (IMAC XXXII), Orlando (2014)
3. Herlufsen, H.: Application note: modal analysis using multi-reference and multiple-input multiple-output techniques, Tech. Rep., Brüel & Kjær, Nærum, 2012
4. Jacobs, L.D., Ross, M., Tipton, G., Cross, K., Hunter, N., Harvie, J., Nelson, G.: Experiemntal execution of 6-DOF tests derived from field tests. In: 35th International Modal Analysis Conference (IMAC XXXV), Garden Grove (2017)
5. Kerschen, G., Worden, K., Vakakis, A.F., Golinval, J.C.: Past, present and future of nonlinear system identification in structural dynamics. Mech. Syst. Signal Process. **20**, 505–592 (2006)

6. Noël, J.P., Renson, L., Grappasonni, C., Kerschen, G.: Experimental modal analysis of nonlinear structures using broadband data. In: 33th International Modal Analysis Conference (IMAC XXXIII), Orlando (2015)
7. Ross, M., Jacobs, L.D., Tipton, G., Nelson, G., Cross, K., Hunter, N., Harvie, J.: 6-DOF shaker test input derivation from field test. In: 35th International Modal Analysis Conference (IMAC XXXV), Garden Grove (2017)
8. Scheel, M., Peter, S., Leine, R.I., Krack, M.: A phase resonance approach for modal testing of structures with nonlinear dissipation. J. Sound Vib. **435**, 56–73 (2018)
9. Schoukens, J., Swevers, J., Pintelon, R., Van Der Auweraer, H.: Excitation design for FRF measurements in the presence of non-linear distortions. Mech. Syst. Signal Process. **18**, 727–738 (2004)
10. Soine, D.E., Jones, R.J., Harvie, J.M., Skousen, T.J. and Schoenherr, T.F.: Designing hardware for the boundary condition round robin challenge. In: 36th International Modal Analysis Conference (IMAC XXXVI), Orlando (2018)

Chapter 5
Quantifying the Effect of Component Inertial Properties on System Level Dynamics

Jacquelyn R. Moore, Tyler F. Schoenherr, and Darrius Smith-Stamps

Abstract Structures are subject to many environments in the lifetime of an assembly, and mechanical environments such as vibration are particularly significant when considering structural integrity. In the early development cycle, mechanical environment test specifications are often derived from assemblies with simplified "mass mock" components. The assumptions for these simplified components generally mimic total mass and center of gravity, but do not always capture moments of inertia. Historically, environments for mass mock components are enveloped and used for future iterations of the true component's qualification. This work aims to understand and characterize differences in dynamic response due to changes in inertial properties of a component. The FEM of a test structure for this work includes a system level model with true components that will be compared to a FEM with mass mock components. Both versions of the structure will be evaluated based on dynamic response at the component and system levels. The validity and limitations of using mass mock components with approximate inertial properties for deriving environmental specifications will be explored.

Keywords Inertia · Mass mock · Test specifications · Boundary condition · Component environments

5.1 Introduction

The purpose of this work strives to analytically observe key differences between the use of mass mock components and their true configuration. In this analytical study, mass mock components preserve both mass and center of gravity, while geometric features are simplified, affecting component volume and inertial properties. Center of gravity is maintained through strategic geometric simplification, while component mass is preserved through material density modification. Mass mocks are used to streamline preprocessing and computational time, but are also necessary in early phases of a design cycle, as they allow for flexibility in terms of future detail revisions. As a component develops over time, the primary features such as mass and center of gravity can be held constant while design iterations can improve a characteristic or functionality of a component. Generally, inertia in these mass mocks is not strictly scrutinized, thus understanding how this can impact structural properties and environmental specification development is a goal for this analysis. Modal data, environment responses and specifications derived for component level tests will be the primary sources of comparison. Component specifications are generally derived from field environment tests of a system level structure, where the full assembly can either include true or mock components for this test. Responses at components are then used to develop environmental specifications for the component. Although center of gravity and mass are maintained, inertial properties can affect these specifications.

Understanding changes in inertial properties of isolated components is valuable, but this does not encompass the complexity of coupling dynamics within a system. To emulate a practical application, the moments of inertia of mass mock components will be studied as part of a larger assembly. Understanding this behavior is important because specifications for component level testing are derived from system level tests. Errors due to inaccurate mass mocks can propagate into component specification error. Because of this, the primary goal of this work is characterizing differences in dynamic response due to changes in inertial properties of components.

J. R. Moore (✉) · T. F. Schoenherr · D. Smith-Stamps
Analytical Structural Dynamics, Sandia National Laboratories, Albuquerque, NM, USA
e-mail: jrmoore@sandia.gov; tfschoe@sandia.gov; dsmiths@sandia.gov

C. Walber et al. (eds.), *Sensors and Instrumentation, Aircraft/Aerospace, Energy Harvesting & Dynamic Environments Testing, Volume 7*, Conference Proceedings of the Society for Experimental Mechanics Series,
https://doi.org/10.1007/978-3-030-12676-6_5

5.2 Model Setup & Development

A modular system model was created, allowing for ease of component interchanging, so various fidelities could be utilized. The assembly is a three-tiered plate structure with components attached to the second tier, allowing for non-trivial inputs and coupled dynamics. The full structure and components, modeled as aluminum, has seventeen flexible modes occurring between below 60 Hz. The base is used to excite the structure via a concentrated mass, connected rigidly to the bottom plate, as shown in Fig. 5.1.

The columns that connect the circular plates are symmetric about the translational axes (X and Y) , as shown in Fig. 5.2. Looking at the system from the axial axis, support columns and component connections are equally spaced.

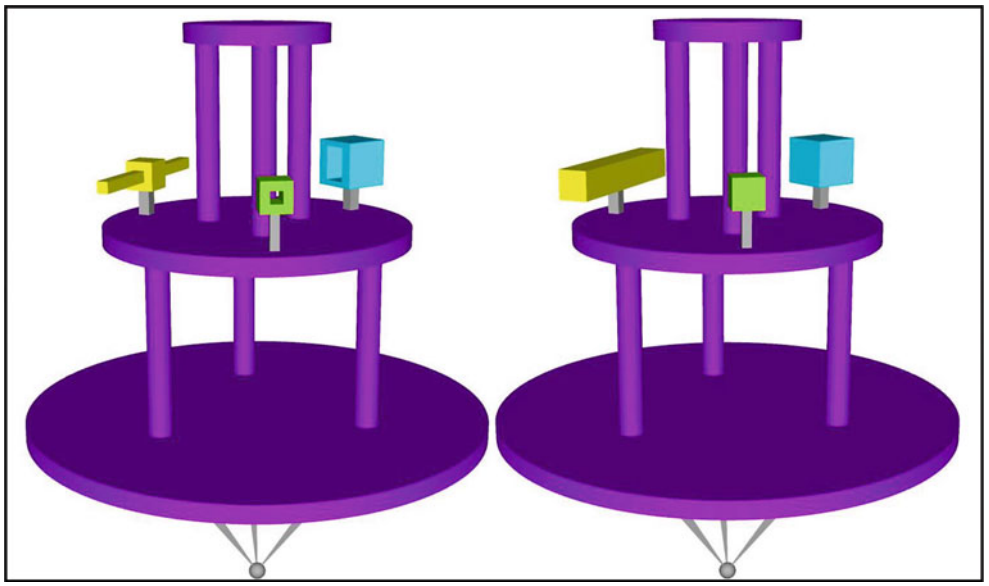

Fig. 5.1 Assembly level configuration of truth (left) and mass mock (right) models

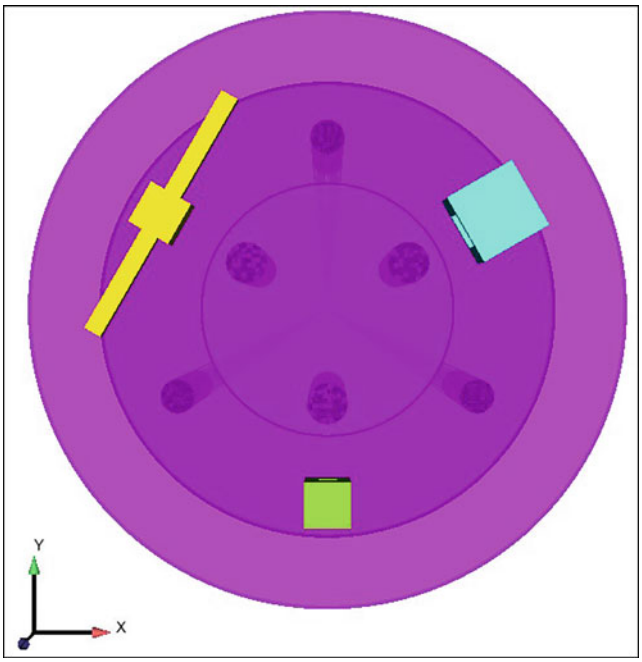

Fig. 5.2 Assembly top view

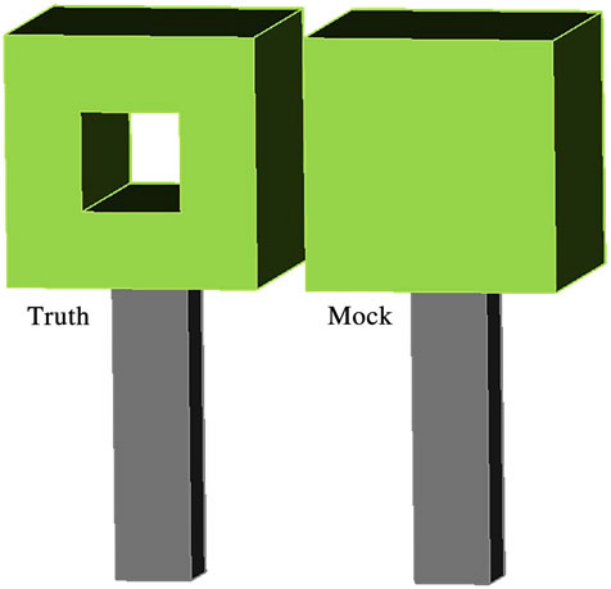

Fig. 5.3 Small box component

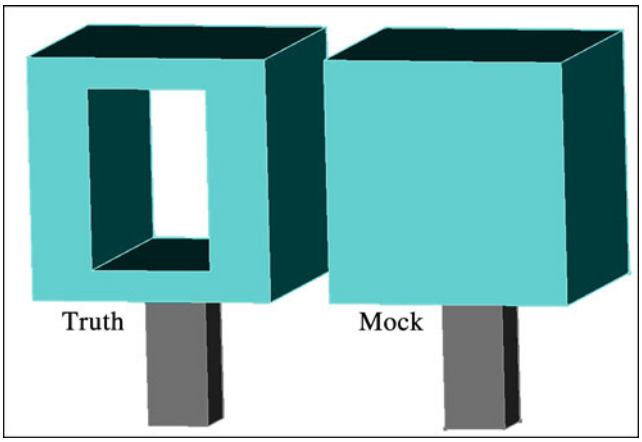

Fig. 5.4 Large box component

A variety of components were designed for being simplified on the system level structure. The mass mock components were designed to replace the truth components and match their center of gravity and mass. Three components were constructed, each with varying degrees of volume and inertia differences. The first two components, illustrated in Figs. 5.3 and 5.4, are cube volumes with translational cuts of material removed from the 'truth' model and solid bodies for the mass mock. These components are identified as small and large box, respectively. Density values for mass mock components were adjusted, so the original mass was preserved.

The third 'beam' component, shown in Fig. 5.5, features a small cube with symmetrical cantilevers suspended from each end. The mass mock block adds significantly more material than the first two components, but still maintains overall mass and center of gravity.

The mass, inertia and volume properties for each component are summarized in Table 5.1. It is evident that the small box has a slight shift in moment of inertia values, while the beam component changes drastically. Mass values are constant between the two iterations of the model and volume inherently changes when each of the components are updated. The table also gives a normalized difference between properties of the mock and truth components with percent difference values. The grey beams are used to connect components to the circular plate assembly, and are not included in Table 5.1s values, but are held constant between model iterations.

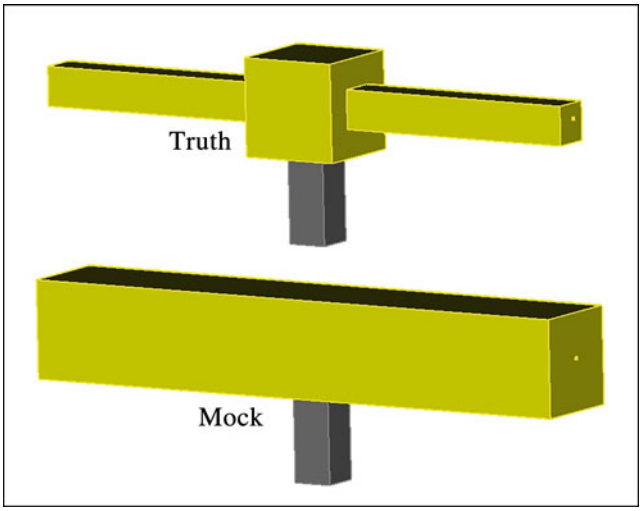

Fig. 5.5 Beam component

Table 5.1 Mass and inertia properties of the truth and mass mock components

	Ix ($kg \times mm^2$)		Iy ($kg \times mm^2$)		Iz ($kg \times mm^2$)		Mass (g)		Volume (cm^3)	
Component	Truth	Mock	Truth	Mock	Truth	Mock	Truth	Mock	Truth	Mock
Small box (Percent difference)	**0.125**	**0.115**	**0.134**	**0.115**	**0.125**	**0.115**	*4.43*	*4.43*	1.64	1.95
	-8.0%		**-14.2%**		**-8.0%**		*0%*		18.9%	
Large box (Percent difference)	**1.17**	**0.9**	**1.07**	**0.9**	**1.1**	**0.9**	*13.5*	*13.5*	5.0	8.0
	-23.1%		**-15.9%**		**-18.2%**		*0%*		60.0%	
Beam (Percent difference)	**1.92**	**3.49**	**0.74**	**1.33**	**2.51**	**4.57**	*9.49*	*9.49*	3.52	11.70
	81.8%		**79.7%**		**82.1%**		*0%*		232.4%	
Assembly (Percent difference)	**4888**	**4889**	**4907**	**4907**	**4000**	**4002**	*1085*	*1085*	401.7	413.2
	0.03%		**0.01%**		**0.05%**		*0%*		2.86%	

5.3 Modal Results

Post processing of the eigen solutions of both the mass mock and truth assemblies were calculated. A Modal Assurance Criteria (MAC) comparison was performed between the two sets of mode shapes, which utilized a sampling of structure and component nodes with consistent locations between model iterations. The plot includes both the modal correlation by color, scaled with a minimum of 0.4 for clarity, as well as the percent difference in frequency of highly correlated modes. Additionally, modal frequencies for the respective system are found along the axes.

From Fig. 5.6, modal correlation for the first five flexible modes, as well as the final four displayed in the MAC table, are predominantly dictated by system response and are not sensitive to component fidelity. The first two mock assembly modes that do not align well are primarily influenced by the motion of the beam component, illustrated in Fig. 5.7.

Differences start arising in modal comparison as dynamic coupling occurs in the structure and component behavior primarily drives mode shapes. Because the discrepancies in moments of inertia of the components and assembly, these differences emerge. Additionally, a large number of modes occur in a relatively small frequency range, such as the mode shapes in Figs. 5.8 and 5.9, so linear combinations can account for other differences.

The modes in the central region of the MAC plot above are primarily driven by component behavior, and tend to be higher in frequency for the mock assembly. Taking a closer look at the mock mode occurring at 38.3 Hz and corresponding truth mode at 37.0 Hz, this can be rationalized with the Eq. (5.1), where ω is modal frequency, K is stiffness and m is mass. This behavior for this mode is driven by the small and large box components, whose moments of inertia are reduced in each direction for the mock model. Because inertia is a mass property and it is decreased, the resulting frequencies are expected to higher for the mock model.

$$\omega = \sqrt{\frac{K}{m}} \tag{5.1}$$

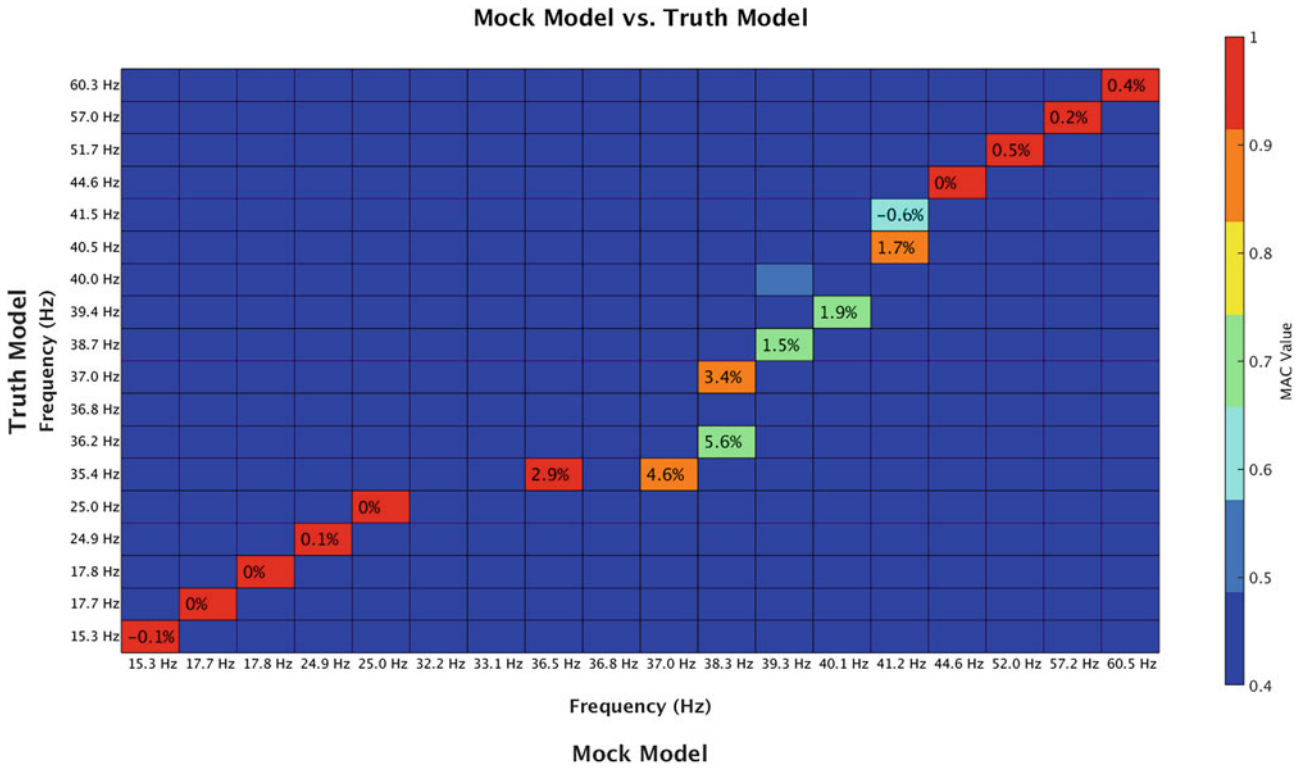

Fig. 5.6 MAC plot mass mock vs. truth assemblies

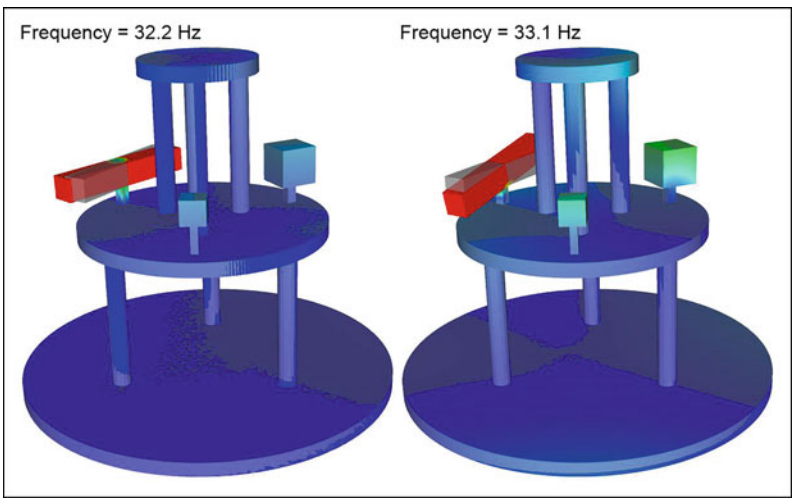

Fig. 5.7 Mock model modes without correlation to truth model modes

Overall, modal correlation is strong in the low and high ends of the frequency range reported in Fig. 5.6. These modes are primarily driven by the assembly's motion, which have little to no contribution from the components. Mid-ranged frequency modes are dictated by component behavior, thus the change in inertia between mock and truth models explains differences shown in Fig. 5.6. These differences could be minimized by developing mass mocks that more accurately match the inertia properties of the truth components along with the mass and center of gravity properties.

Fig. 5.8 Assembly flexible modes—truth

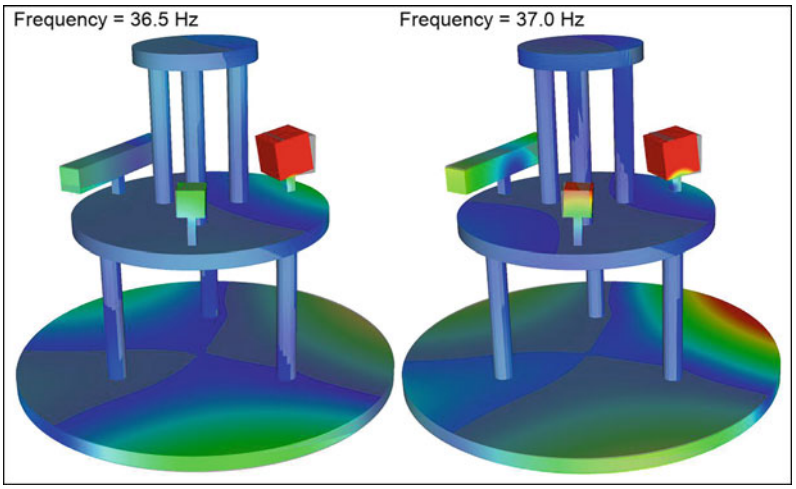

Fig. 5.9 Assembly flexible modes—mock

5.4 Frequency Response Function & Component Test Results

Using a modal based frequency response function (FRF) solution in Sierra Structural Dynamics (Sierra SD) [1], both the mass mock and true component systems were driven with a six degree of freedom base input, to derive the field environment for each of the components. This input force consisted of 10 N in each translational direction and 1 N-m for each rotational direction in the 1–60 Hz frequency regime. The scaling of these loads was chosen to achieve similar response magnitude in the assembly, when isolated. Responses from this excitation, found at the base of each mass mock component were then used as an input into a component-level test, which is shown in Fig. 5.10. Both levels of component fidelity in the system level test were used to derive input specifications for component level tests on the true geometry.

A sample of data was taken from the system and component level tests, as shown in Fig. 5.11 to evaluate differences in plate and component responses. These nodal locations were consistent between both the mock and truth models, even with the differences in component geometry. Variations in response caused by inertial differences are summarized below.

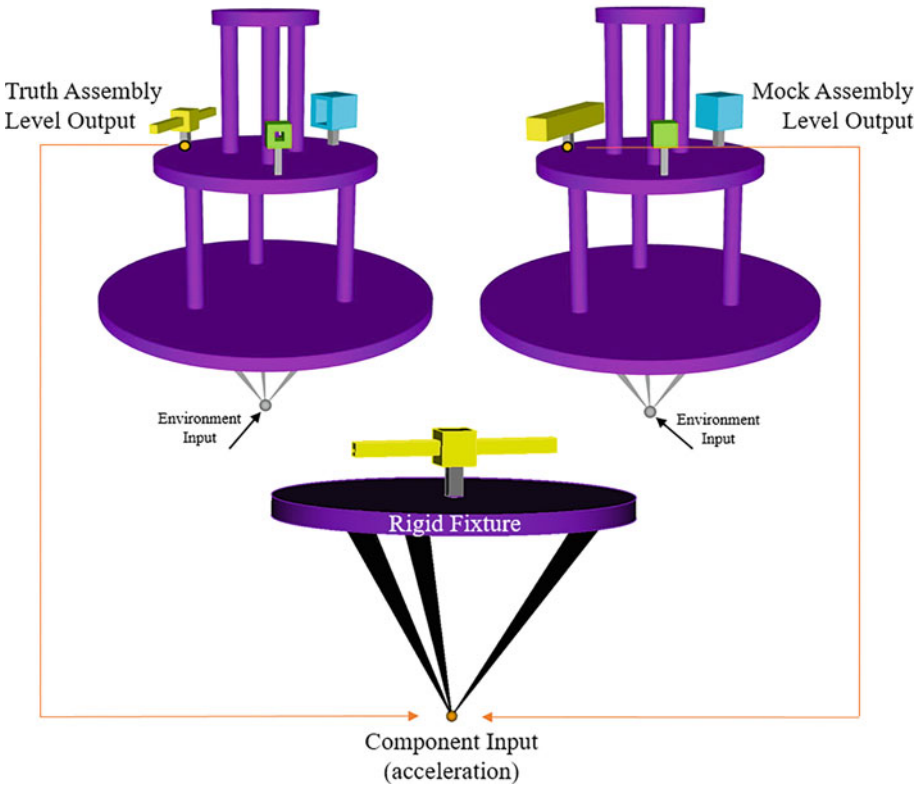

Fig. 5.10 Component level test inputs

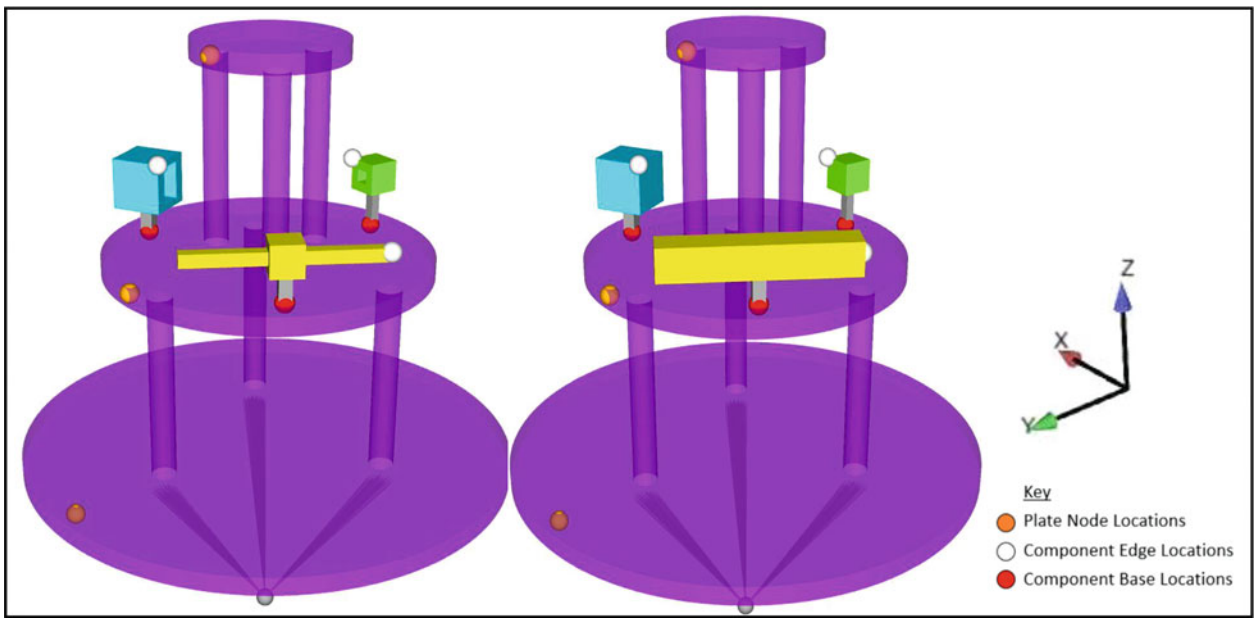

Fig. 5.11 Response node locations

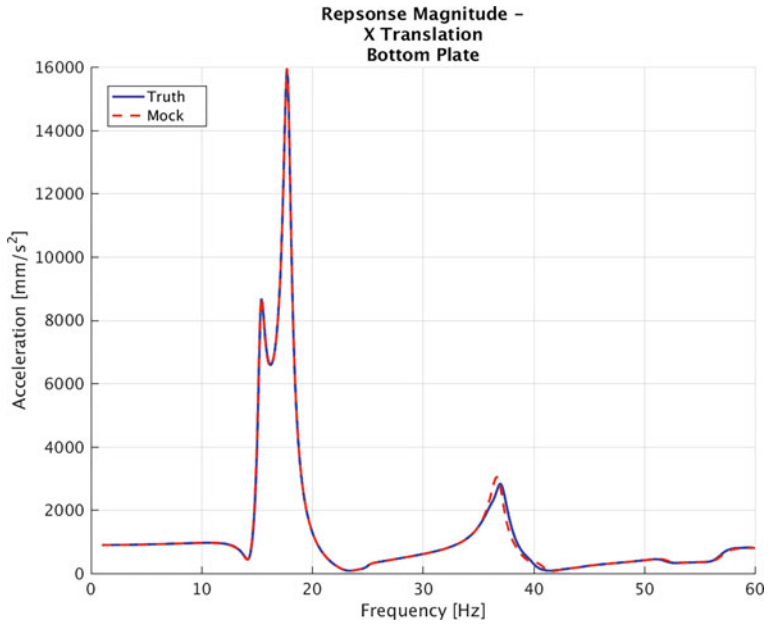

Fig. 5.12 Bottom Plate X translation response

5.4.1 Plates: Assembly Level Responses

With the multi-axis input applied to the concentrated masses of the truth and mock systems, plate responses in the axial direction experience a small propagation of error when comparing the responses of the same points on the truth and mock models. The bottom plate had little variation between the mass mock and truth models, because the components weren't affecting the modes in which this plate was participating. Figure 5.12 illustrates the similarity in translational response of the bottom plate, as they are nearly visually identical. The translational directions, X and Y, revealed fewer differences and were not reported for this reason.

The middle and top plates revealed differences in translational response with the multi-axis input. Both plates follow a general response trend except around 40 Hz, where the driving modes of the system are largely influenced by component behavior. Figures 5.13 and 5.14 show the response FRF for both the middle and top plates, as well as the driving modes in the frequency range of discrepancy

Responses observed in the Y translational direction shared similar differences between the truth and mock configurations as displayed above for X translation. Axial responses for each plate did not reveal significant differences in magnitude or frequency. There is slight variation, but overall the responses of in the plates of the system are not significantly affected by component fidelity.

5.4.2 Small Box Component: Assembly and Component Level Responses

Although the differences both in volume and inertia are small between the true and mass mock small box components, there is a slight variation in response for each direction, based on if the mock or true geometry was utilized in the system level assembly. The axial response at the base of the small box component, responses appear to be visually identical, until about 37 Hz where a small amount of variation arises, shown in Fig. 5.15.

Using the response output from the base of both the true and mock small box component configurations, shown in Fig. 5.15, the specification for the component level test was derived and tested on the truth component. Component test responses are depicted in lighter colors, as seen in Fig. 5.16. There is a slight shift in frequency content as well as response magnitude, even though the inputs only have slight variation. When RMS Von Mises stress was evaluated over the domain, the resulting stress fields on the component are characteristically similar, with roughly a 9% difference in maximum value. RMS stress values were reported in pascals, illustrated in Fig. 5.17. With the amount of conservativism that is generally introduced into environmental specification development for a component, this difference is minimal.

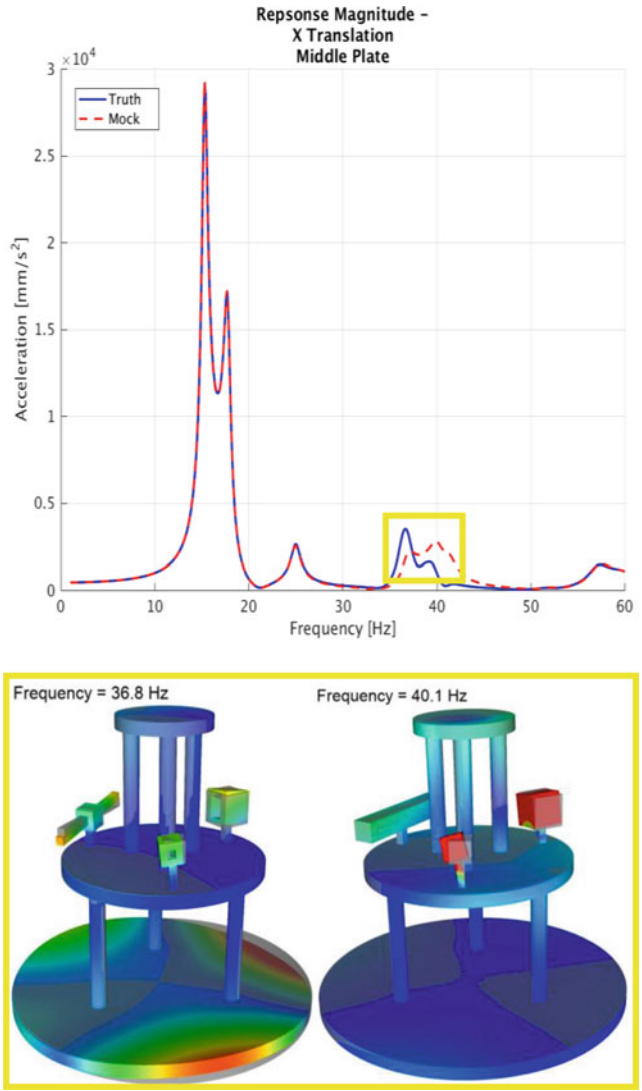

Fig. 5.13 Middle Plate X translation response

5.4.3 Beam Component: Assembly and Component Level Responses

Assembly level responses observed at the base of the beam component are did not have large differences, as shown in Fig. 5.18. In terms of the system, there were no changes to the structure and component support, so it's reasonable that the responses in this part of the model are similar. Observing responses from one of the beam edges revealed significant variation, illustrated in Fig. 5.19. This node on the edge of the beam component, Fig. 5.19, captured the propagation of response error in utilizing mass mocks. Peak differences were apparent in the edge node's FRF below and were further supported by modal and inertial differences of this component in particular.

Similar to the workflow of the small box component, beam base responses were then used as component level inputs, where only the high-fidelity model was utilized. There were similar beam base responses observed at the system level structure, Fig. 5.18, but the component level responses to these inputs experienced some discrepancy, as depicted in Fig. 5.20.

RMS stresses in the component level test revealed differences in maximum values. The overall stress field between the models has slight variation and the environment derived from the truth assembly resulted in stresses roughly 5.4% larger than that of the mass mock derived environment. Figure 5.21 depicts differences in RMS stress between the two inputs and the resulting intensity of stress experienced. This difference in Von Mises RMS stress is relatively small and would likely be

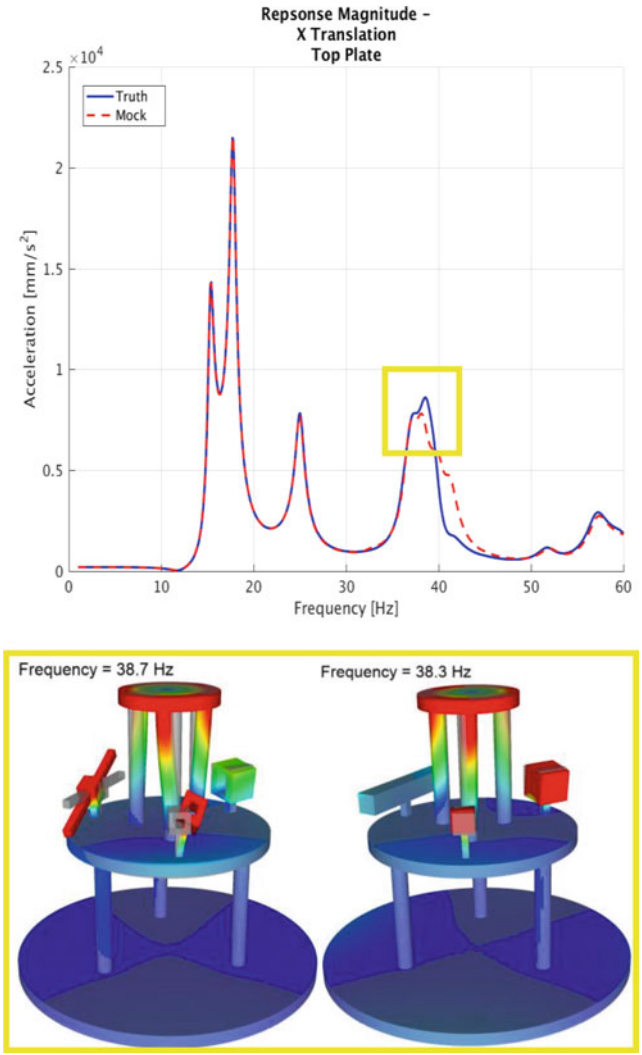

Fig. 5.14 Top Plate X translation response

accounted for through conservativeness commonly built into testing, but it's important to note that portions of the stress field are not fully captured with the mock input. This is seen near the beam edges as well as the component's center block.

For this specific model configuration, it appears that inertia discrepancies less than about 25% assumed a reasonable amount of error in stress and dynamic response, while more significant differences were observed for inertia discrepancies greater than this. Overall model inertia played a key role in resulting component behavior as well. Axial inertia for the assembly was altered the most, 0.05%, and the resulting error in stresses with axial inputs is larger for each respective component compared to both translational directions. This suggests the importance of component inertias on assembly dynamics.

5.5 Conclusion

Mass mock components are useful in streamlining computational simulations and are necessary for environment testing during a component's development, but while mass and center of gravity are generally preserved, inertial properties are often not held constant. As seen in this analysis, component inertias can have relatively small but important effects on system level dynamics and consequent component environment specifications. In normalizing the differences in inertia and RMS stress values, this analysis revealed a general trend of increasing error reported in component level RMS stresses, as the percent difference of a component's inertia increased. It should be emphasized that this trend is specific to the model

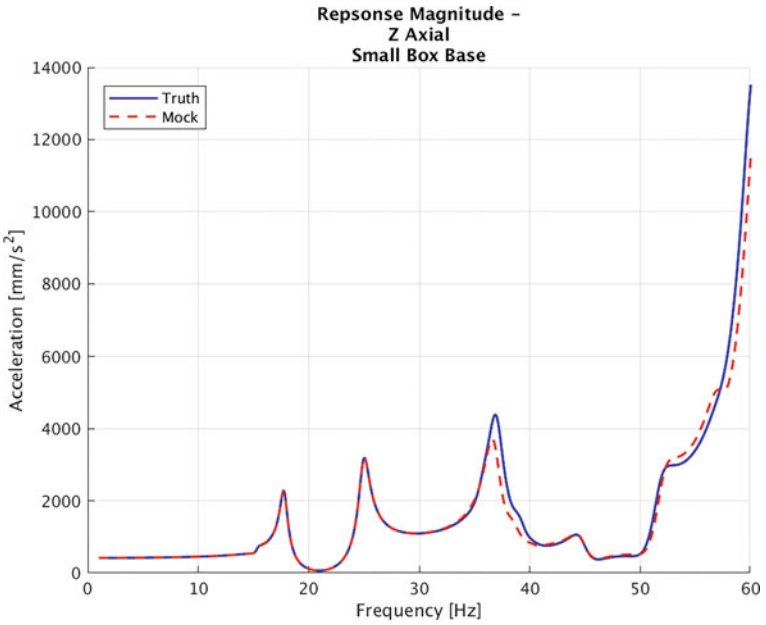

Fig. 5.15 System level axial response—small box

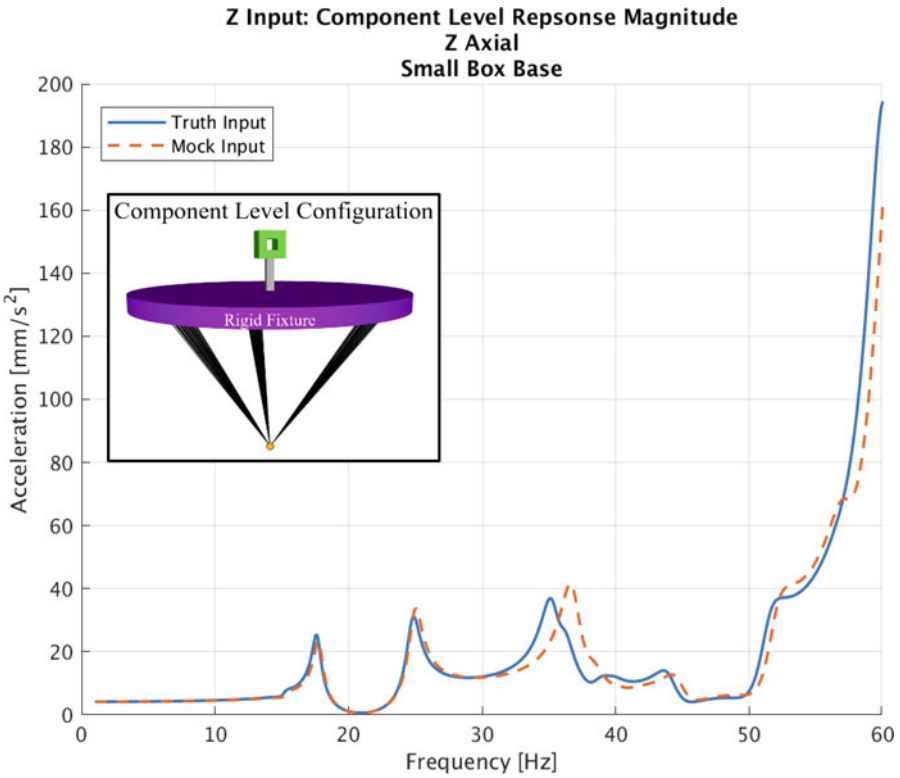

Fig. 5.16 Component level axial response—small box

used in this analysis and future work would be necessary before definitively correlating these properties. These normalized inertia differences, found in Table 5.1, and RMS stress errors were not directly proportional, but the general trend for the model utilized in this work suggests the importance of preserving inertial integrity of mass mock components, particularly for deriving component specifications. Further analysis of studying inertial effects in other model configurations would be needed before conclusively characterizing this behavior, however the presence of these issues demonstrated in a simple model highlights potential problems of inertial approximation.

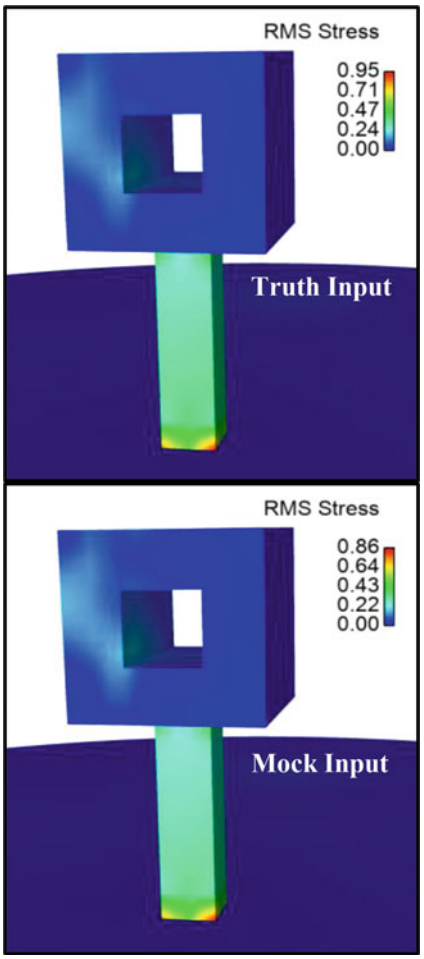

Fig. 5.17 Component level RMS stress—small box

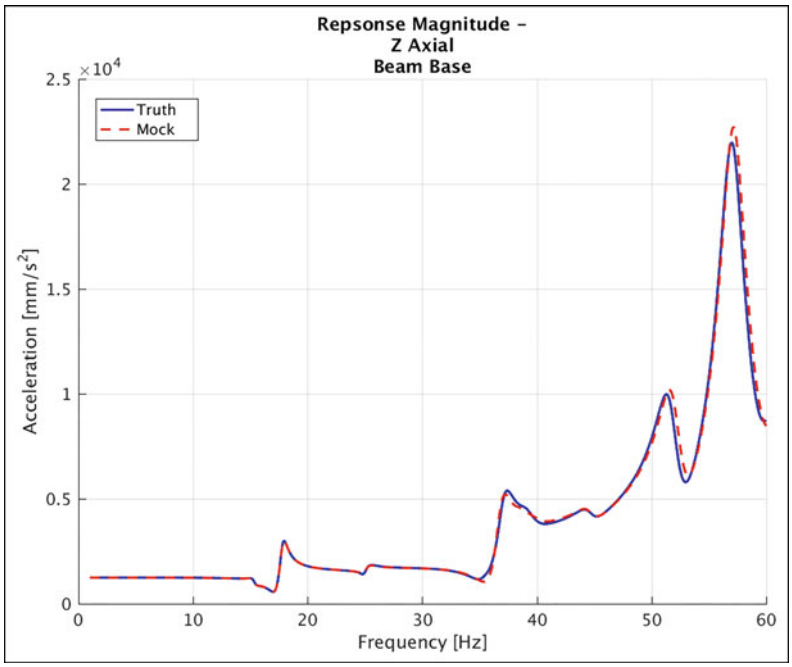

Fig. 5.18 System level Z axial response—beam base

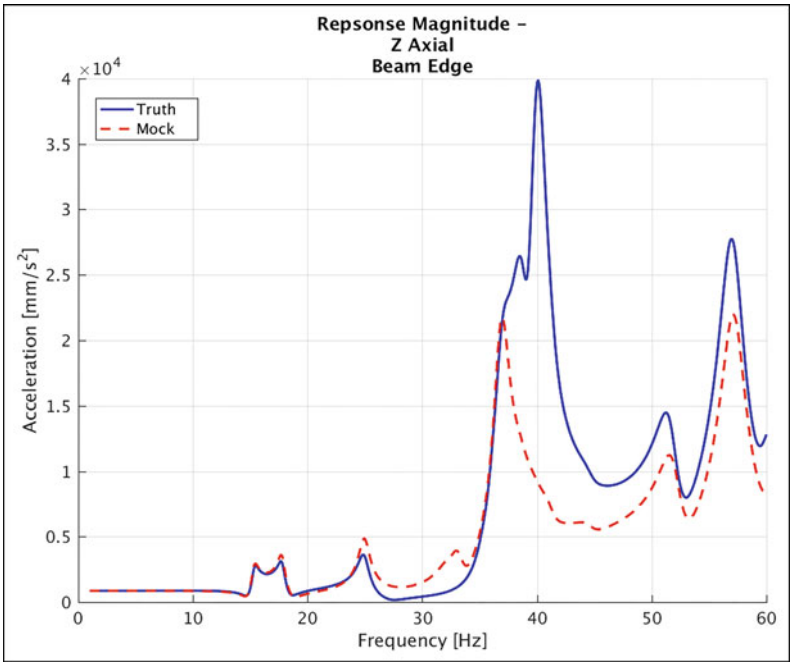

Fig. 5.19 System level Z axial response—beam edge

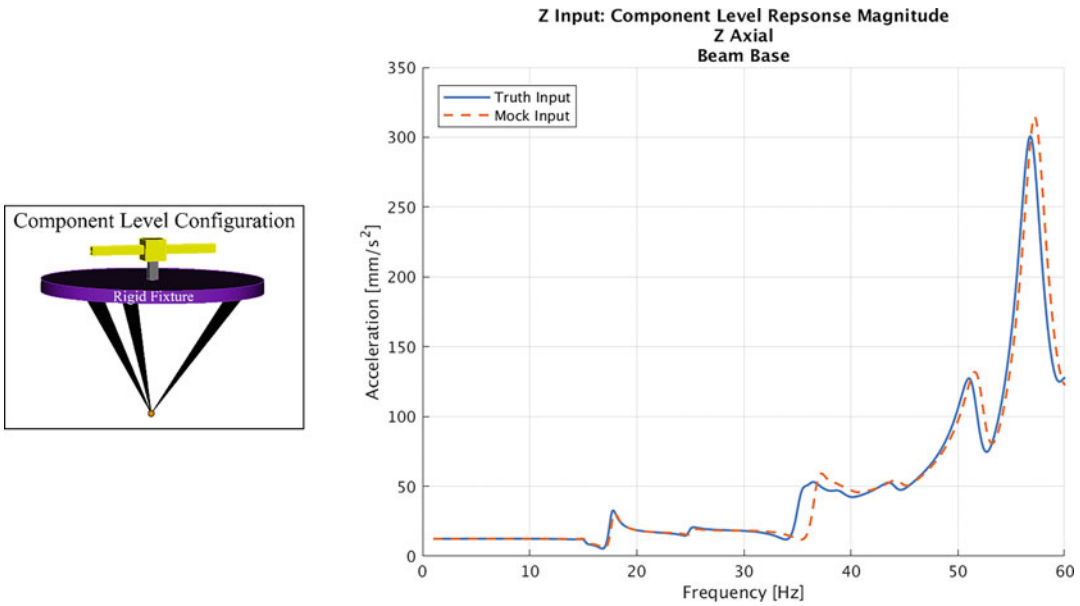

Fig. 5.20 Component level Z axial response—beam base

Although this case study did not reveal significantly large differences in response and RMS stress between mock and truth models, it's important to note that component modes were not excited to high levels. From the modal results and assembly level output FRF's, Figs. 5.12, 5.13, 5.14, 5.15 and 5.18, it's apparent that component modes were not the primary source of motion in the frequency range of interest. Evaluating component inertial approximation in a case study that experiences large response magnitudes in component driven modes would likely result in larger discrepancies in dynamic response and RMS stresses.

Future work should continue to develop the understanding of inertial effects on component response and stresses in a more general sense. This work should aim to better define the relationship between response and inertial properties, possibly through exploring frequency response assurance criterion (FRAC) [2] methods. Additionally, designing a model with inertial variation and better modal correlation would isolate key drivers of output differences.

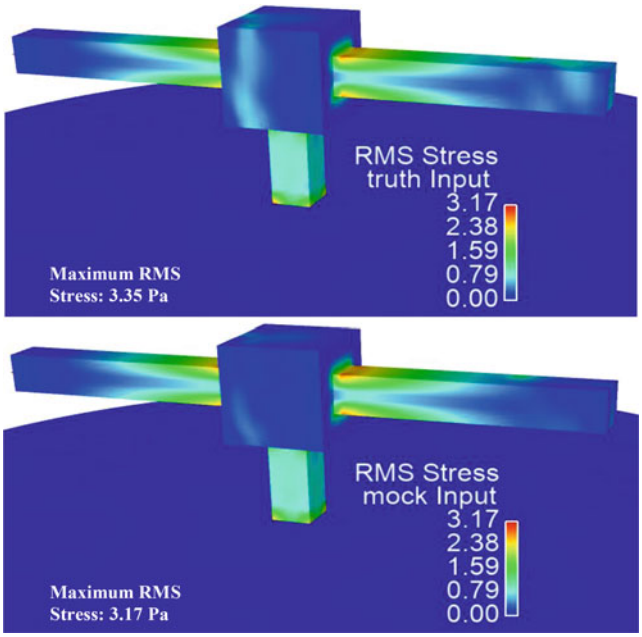

Fig. 5.21 Component level beam RMS stress

All in all, understanding the effect of inertial approximation on environmental specification development is important and this study can serve as general guideline for the impact of inertial approximations and discrepancies on component responses and the resulting specifications.

References

1. Sierra Structural Dynamics Development Team. Sierra structural dynamics – user's notes. Technical Report SAND2017-3553, Sandia National Laboratories, April 2017
2. Marinone, T.: Comparison of FRF Correlation Techniques. Technical Report SAND2014-18820C, Sandia National Laboratories & ATA Engineering Inc., (2014)

Chapter 6
A Method for Determining Impact Force for Single and Tri Axis Resonant Plate Shock Simulations

Brian A. Ferri and Ronald N. Hopkins

Abstract In the past year, resonant plate tests designed to excite all three axes simultaneously have become increasingly popular at Sandia National Labs. Historically, only one axis was tested at a time, but unintended off axis responses were generated. In order to control the off-axis motion so that off-axis responses were created which satisfy appropriate test specifications, the test setup has to be iteratively modified so that the coupling between axes was desired. The iterative modifications were done with modeling and simulation. To model the resonant plate test, an accurate forcing function must be specified. For resonant plate shock experiments, the input force of the projectile impacting the plate is prohibitively difficult to measure in situ. To improve on current simulation results, a method to use contact forces from an explicit simulation as an input load was implemented. This work covers an overview and background of three axes resonant plate shock tests, their design, their value in experiments, and the difficulties faced in simulating them. The work also covers a summary of contact force implementation in an explicit dynamics code and how it is used to evaluate an input force for a three axes resonant plate simulation. The results from the work show 3D finite element projectile and impact block interactions as well as simulation shock response data compared to experimental shock response data.

Keywords Resonant plate · Shock test · Multi-axis test · Shock simulation · Input force

6.1 Introduction

Three axis testing, meaning exciting three degrees of freedom of the system simultaneously, has become an area of research at Sandia National Laboratories for the past few years. It can reduce the number of test needed to qualify a part in a shock environment. Shock environments themselves are often multi-axis environments, so the specifications for components are usually derived as axis specific specifications, and are usually given as a Shock Response Spectrum (SRS). Accelerometers are used to track the time history of the acceleration during a shock test. The time data is transformed to the frequency domain via an SRS calculation and compared to the test specification. The quality of the test is computed as the average decibel (dB) error. For this work, the average dB error was calculated as the mean of the absolute difference between test data and simulation data in dBs. A shock test specification will have a ramp and a knee in the frequency domain. The knee is located at a frequency f_k, and an experiment will be designed such that a resonant fixture will have a peak resonance at f_k.

For structural dynamics work, force inputs to a system can be prohibitively difficult to measure in-situ. For example, the dynamics of a force gauge in the load path of a certain test setup can alter the input load even for low amplitude forces. For shock testing, it can be even more difficult. The test that is described in this work has a 12 lbs. steel projectile that impacts at 59 feet per second (fps). A calibrated strain gage would be the preferred measurement to compute the delivered impulse, however it is not possible to extract the delivered impulse due to the noise issues. Thus, a study into the exact temporal profile of the input load is needed to perform a structural analysis and to predict responses to the loading.

Sandia National Laboratories is a multi-mission laboratory managed and operated by National Technology and Engineering Solutions of Sandia, LLC, a wholly owned subsidiary of Honeywell International, Inc., for the U.S. Department of Energy's National Nuclear Security Administration under contract DE-NA0003525.

B. A. Ferri (✉) · R. N. Hopkins
Analytical Structural Dynamics, Sandia National Laboratories, Albuquerque, NM, USA
e-mail: bferri@sandia.gov

C. Walber et al. (eds.), *Sensors and Instrumentation, Aircraft/Aerospace, Energy Harvesting & Dynamic Environments Testing, Volume 7*, Conference Proceedings of the Society for Experimental Mechanics Series,
https://doi.org/10.1007/978-3-030-12676-6_6

There are inverse methods for input force estimation that are used both at Sandia [1] and in industry [2–3]. These methods, while not applied to shock response typically still follow a similar methodology, which is to measure a dynamic quantity in the lab then rely on the known dynamics of the structure to back out the force via those dynamic relationships. This study follows a similar methodology in which an acceleration is measured, however, the force is found in a separate simulation that only considers the mass and momentum of the loading object. Thus, it is considered a forward problem, meaning that the simulation begins with the inputs in order to calculate unknown results, as opposed to an inverse problem, which is the opposite.

Sierra Solid Mechanics [4] (Sierra SM) is a proprietary code at Sandia National Laboratories and is used in this work to simulate a projectile impacting a resonant fixture using an explicit solver algorithm. This method of analysis uses a frictionless contact surface interaction between the projectile and the resonant fixture. To reproduce this work, a similar finite element code with explicit capability would be sufficient. The contact force in Sierra SM is calculated at each time increment and written to an output file. The resulting contact force is then used as the input to a Sierra Structural Dynamics [5] (Sierra SD) simulation that is performed with Sierra SD's linear transient dynamic capability.

6.2 Background

The primary input parameter to a computational shock simulation is the load function given as a temporal profile. Previous analysis used a load profile as shown in Fig. 6.1.

This load profile is a half sine impulse that was assumed given previous experience modeling lower amplitude dynamic force inputs as the true profile of the high amplitude shock test was unknown.

To determine the contact force exerted by the projectile on the resonant structure, the projectile was modeled with solid hex elements with a linear material model of steel. The projectile was given an initial velocity of 59 fps (which was measured upon exit from the gas gun). This setup is shown as a diagram in Fig. 6.2.

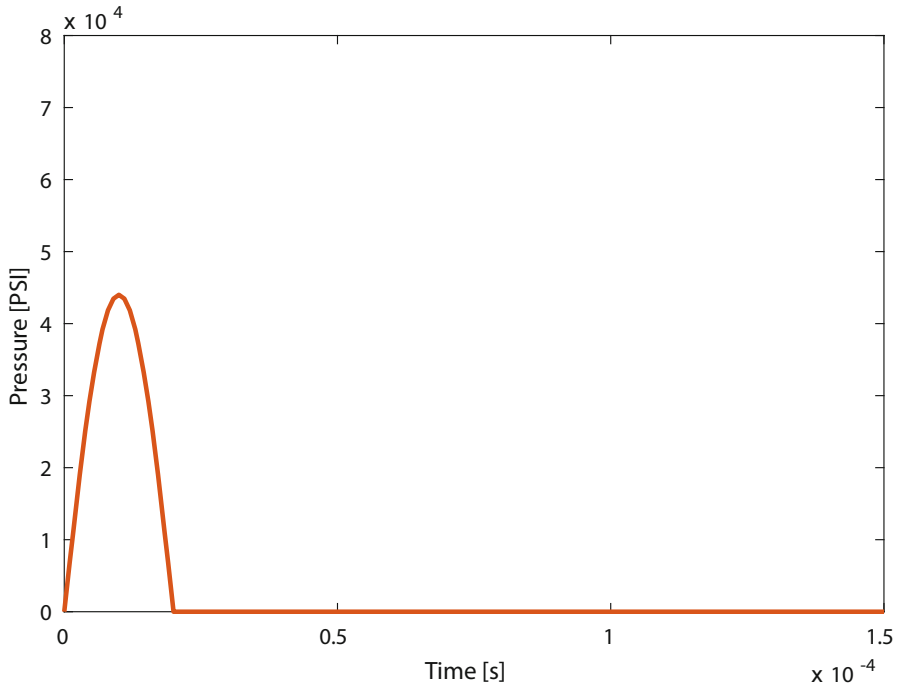

Fig. 6.1 Input that was originally used in previous studies. The load profile has a peak amplitude of 44,000 PSI

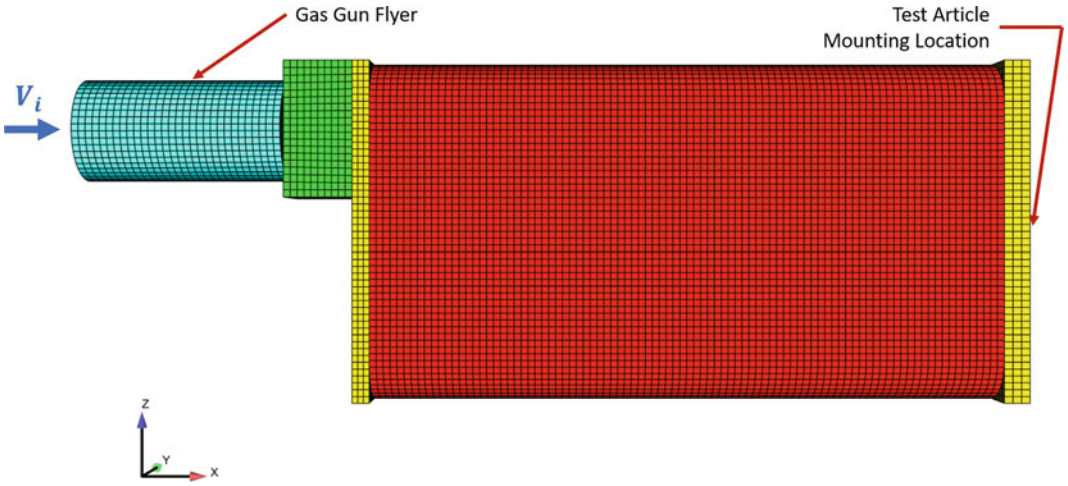

Fig. 6.2 Simulation mesh of projectile and pedestal test configuration

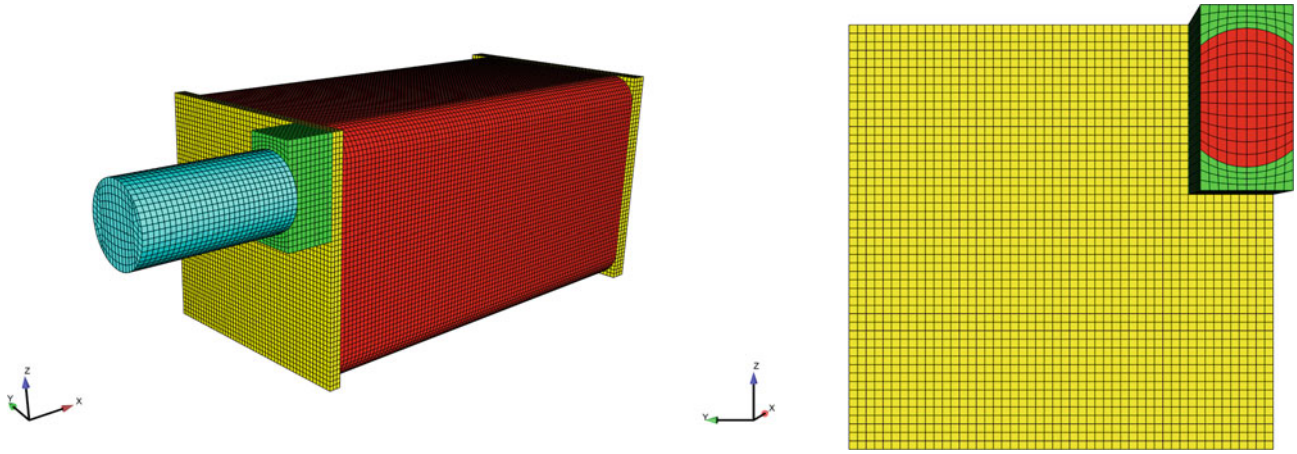

Fig. 6.3 Isometric image of projectile and pedestal setup (left). Front view of impact block with impacting area highlighted (right)

As shown in Fig. 6.2, the Projectile (shown in blue) is a steel cylinder that is 6 in long with a 3 in diameter and travels with a velocity V_i. The Impact Block (shown in green) is an aluminum block that is 4in by 2in by 2in. The Pedestal (shown in red) with plates (shown in yellow) on either end is constructed from steel. The test article is center mounted on the side opposite the impact block (shown on the right in this diagram). The projectile interfaces with an impacting block that is firmly attached to the resonant fixture. The interface between the projectile and the block is modelled as a frictionless contact interaction. This eliminates forces in the 'Y' and 'Z' directions, which would not be useful in prescribing a load in the 'X' direction. Fig. 6.3 shows the isometric and front view of the resonant structure and impacting block.

Since the load is not applied through the center of gravity, the force from the projectile, while not containing 'Y' or 'Z' components, will impart a moment about 'Y' and 'Z', which is the basis for the three axis excitation.

6.3 Analysis

The results from the Sierra SM contact force extraction produce a load profile as shown in Fig. 6.4.

When comparing the Sierra SM contact force results in Fig. 6.4 to the original profile in Fig. 6.1, the two largest discrepancies are the pulse length and pulse amplitude. Additionally, the rise time for the Sierra SM results is much steeper. This shortening of the loading time vastly increases the amount of high frequency response that will be in the system.

The SRS for the 'X' axis response for the original profile and the profile found from Sierra SM are shown for four separate locations shown in Fig. 6.5.

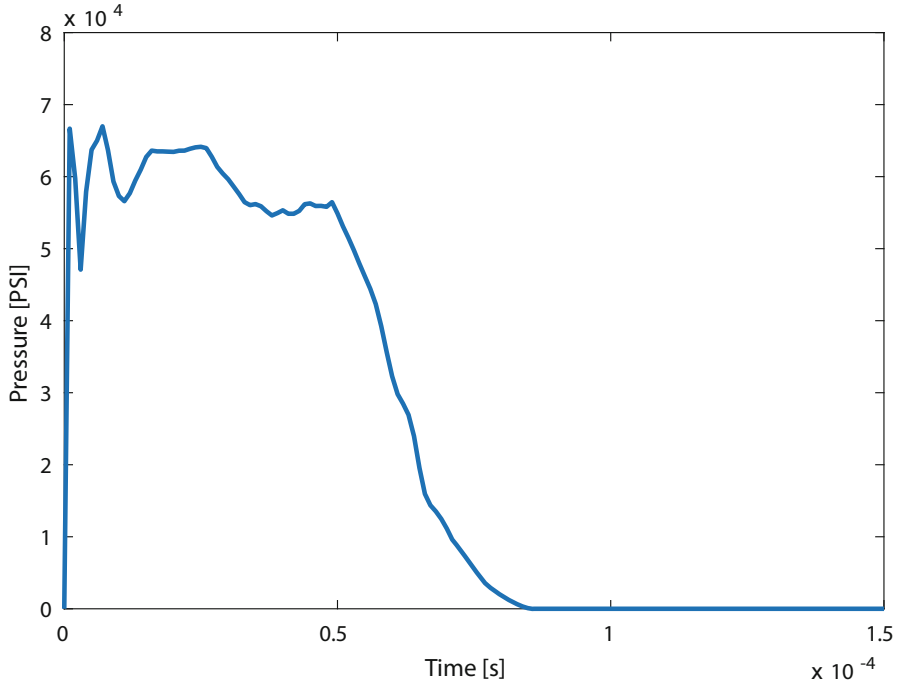

Fig. 6.4 Input that found using Sierra SM frictionless contact. The load profile has a peak amplitude of 67,000 PSI

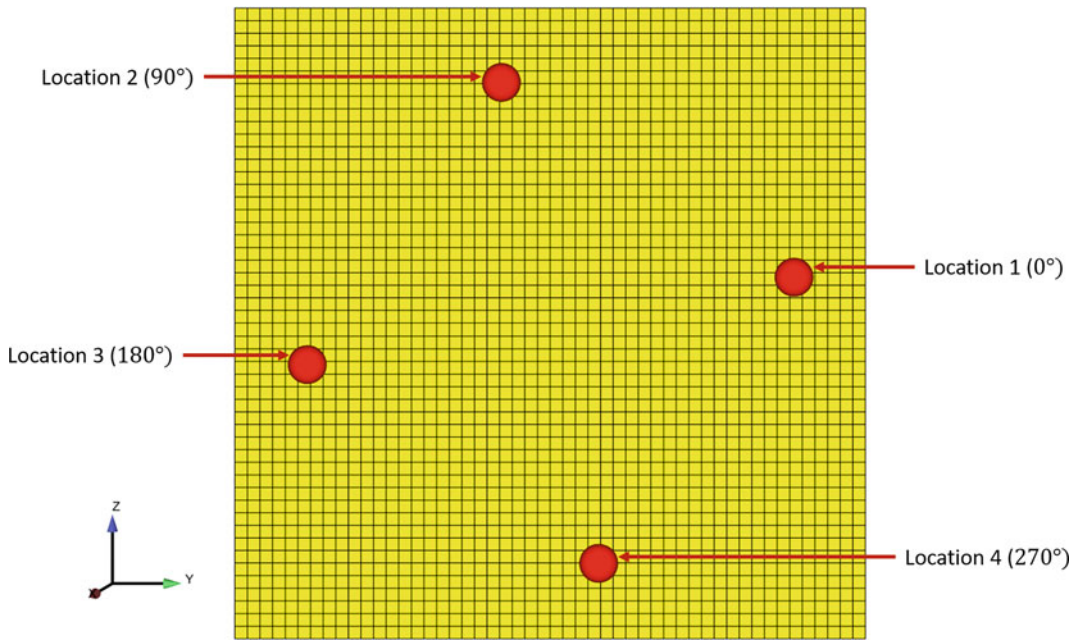

Fig. 6.5 Diagram of four locations along with relative orientation angle in the 'Y-Z' plane

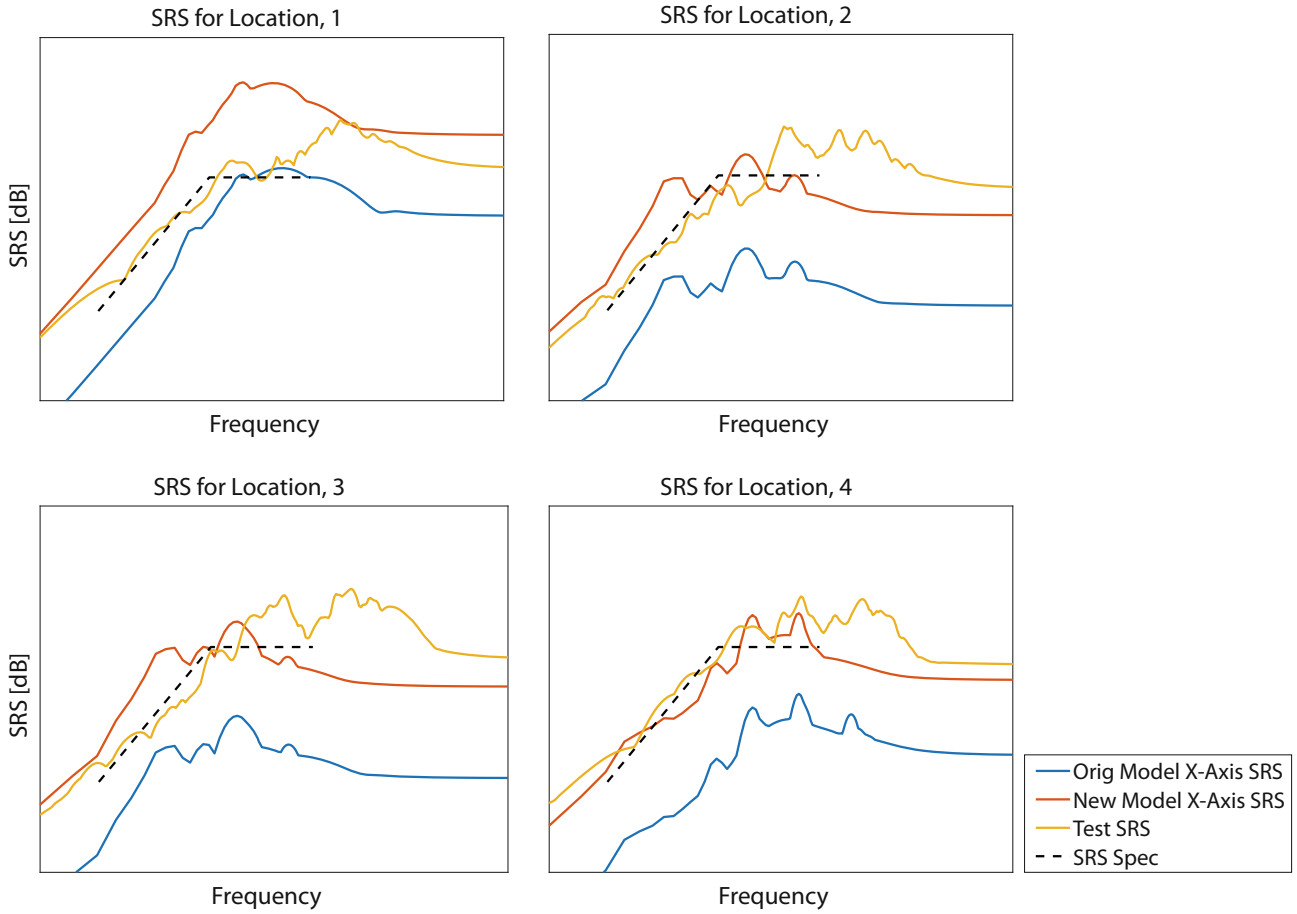

Fig. 6.6 'X' axis SRS response at four separate locations for the original model load profile and the new model load profile along with the SRS Spec for the 'X' direction

Because of the orientation of the locations about the 'Y-Z' plane, there are different expected responses at each location. The model and test results corresponding to the given 'X' axis specification is shown in Fig. 6.6.

As seen in Fig. 6.6, the new model load profile has better agreement with the test data. The average dB error from the model to the test data goes from 14.19 dB with the original model load profile to 7.07 dB with the new model load profile over the frequency range of the SRS specification. This is a 475% improvement in the error.

Since this is a three axis test, the off-axes acceleration at the same four locations was captured simultaneously via a tri-axis accelerometer. The 'Y' and 'Z' response data is shown in Figs. 6.7 and 6.8 respectively.

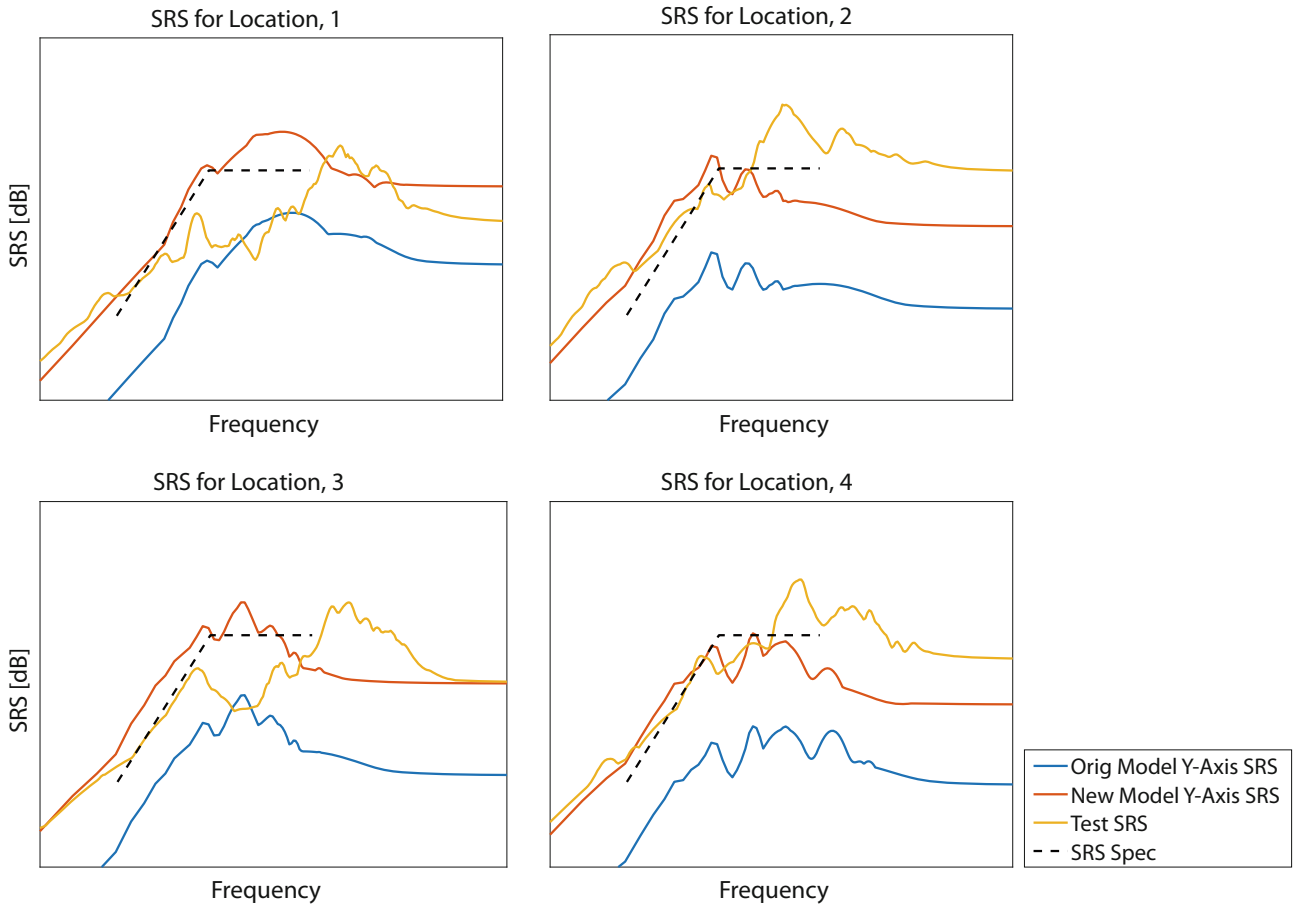

Fig. 6.7 'Y' axis SRS response at four separate locations for the original model load profile and the new model load profile along with the SRS Spec for the 'Y' direction

As seen in Figs. 6.7 and 6.8, there is also noticeable improvement in the SRS from the original model load profile to the new model load profile including an average dB decrease in error of 14.23 dB to 7.76 dB for the 'Y' direction and 15.36 dB to 4.58 dB for the 'Z' direction. This is a 440% and 720% decrease in error respectively.

6.4 Conclusion

Assuming a linear model, the SRS results can be scaled for the original model load profile using a scale factor, and the results would have a closer match the test. The major drawback to this, however, is that the system must be assumed to be linear and that the SRS output must be known to determine the scale factor. For modelling performed prior to a test, there is no known response for the system to match the model via scaling or to find the force via traditional inverse methods. However, the load profile found using this method can be applied to new test articles given the same projectile and resonant structure configuration, making it possible to perform in a repeatable fashion. Further discrepancies of the model's response to the calculated load input can be attributed to uncertainties in other areas of the model.

Going forward, this method has proved useful in determining loading conditions for single and three axis testing. In the current work, there are efforts to add a 'programmer material' to the Sierra SM simulation to further enhance the fidelity of computing a delivered impulse for different test setups. Additionally, there are current efforts to introduce non-linear materials to the simulation environment, which show stiffening or softening given higher amplitude inputs. These types of non-linearities would remove the ability to effectively scale the output given previous approaches.

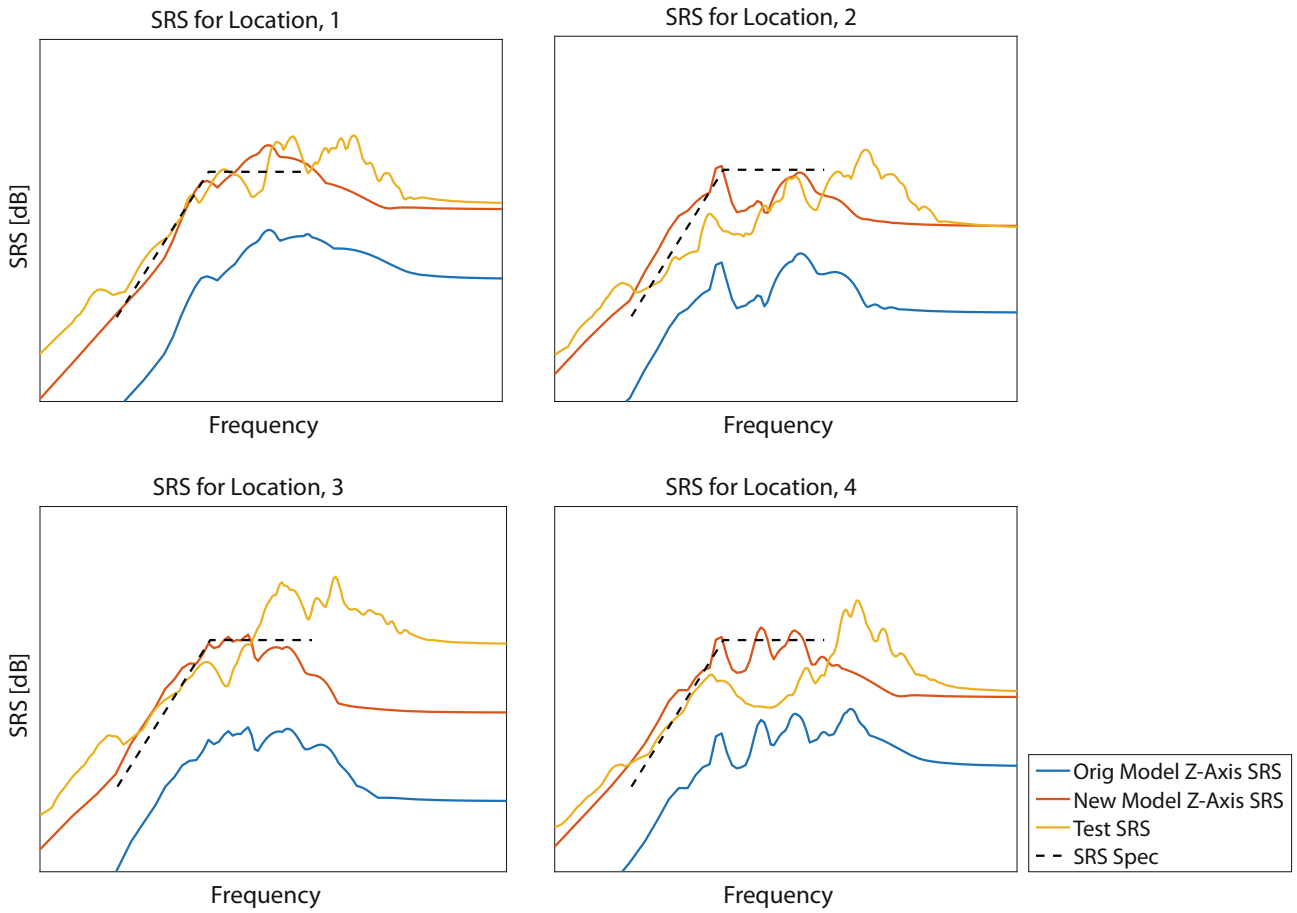

Fig. 6.8 'Z' axis SRS response at four separate locations for the original model load profile and the new model load profile along with the SRS Spec for the 'Z' direction

Acknowledgements David Weigand—Project Leader and Technical Direction; Bill Bonahoom—Hardware Development and Test Engineer; Mikhail Mesh—Technical Consultant; Matt Spletzer—Resonant Fixture Test Engineer

References

1. Schoenherr, T. F.: Calculating the impact force of supersonic hail stones using SWAT-TEEM. In: Conference Proceedings of The Society for Experimental Mechanics Series, Shock & Vibration, Aircraft/Aerospace, and Energy Harvesting, vol. 9, pp. 67–79. Springer, Cham (2015)
2. Risaliti, E., Cornelis, B., Tamarozzi, T., Desmet, W.: A state-input estimation approach for force identification on an automotive suspension component. In: Conference Proceedings of the Society for Experimental Mechanics Series, Model Validation and Uncertainty Quantification, vol. 3, pp. 359–369. Springer, Cham (2016)
3. Klinkov, M., Fritzen, C.P.: An updated comparison of the force reconstruction methods. Key Eng. Mater. **347**, 461–466 (2007)
4. Sierra Solid Mechanics Development Team. Sierra solid mechanics – user's notes. Technical Report SAND2018-2961, Sandia National Laboratories, April 2018
5. Sierra Structural Dynamics Development Team. Sierra structural dynamics – user's notes. Technical Report SAND2018-2449, Sandia National Laboratories, March 2018

Chapter 7
Non-stationarity and non-Gaussianity in Vibration Fatigue

Janko Slavič, Martin Česnik, Lorenzo Capponi, Massimiliano Palmieri, Filippo Cianetti, and Miha Boltežar

Abstract In vibration fatigue the frequency contents of dynamic loading and structure's dynamic response overlap, resulting in amplified stress loads of the structure. Time domain fatigue approach does not give a good insight into the underlying mechanics of failure and therefore recently vibration fatigue in frequency domain is getting a lot of scientific attention. Gaussianity and stationarity assumptions are applied in frequency-domain methods for obtaining dynamic structure's response and frequency-domain methods for calculating damage accumulation rate. However, in application, the structures are excited with non-Gaussian and non-stationary loads and this study addresses the effects of such dynamic excitation to experimental time-to-failure of a structure.

The influence of non-Gaussian, but stationary excitation, is experimentally studied via excitation signals with equal power density spectrum and different values of kurtosis. The non-Gaussianity was found not to significantly change the structure's time-to-failure and therefore, the study focuses on the non-stationary excitation signals that are also inherently non-Gaussian. The non-stationarity of excitation was achieved by amplitude modulation and significantly shorter times-to-failure were observed when compared to experiments with stationary non-Gaussian excitation.

Additionally, the structure's time-to-failure varied with the rate of the amplitude modulation. To oversee this phenomenon the presented study proposes a non-stationarity index which can be obtained from the excitation time history. The non-stationarity index was experimentally confirmed as a reliable estimator for severity of non-stationary excitation. The non-stationarity index is used to determine if the frequency-domain methods can safely be applied for time-to-failure calculation.

Keywords Vibration fatigue · Non-stationarity · Non-Gaussianity · Structural dynamics · Run-test evaluation

7.1 Introduction

When discussing product's resistance to vibrations an automotive, aerospace and other testing standards specify vibration loads that should be applied to a product in a controlled laboratory conditions via electro-magnetic shaker. In such cases of fatigue failure, the damage accumulation is not exclusively vibration load dependent, but is coupled with structure's dynamic properties in frequency domain. Thus, when dealing with vibration fatigue the frequency counting methods that are based on power spectral density (PSD) of stress response [1] [2] are easily applicable, computationally effective and fast [3] also for longer time histories. Frequency counting methods assume signal's stationarity [4]. Furthermore, due to reasons of analytical deduction, an additional assumption of Gaussian nature of stress signal should also be sufficed. When both assumptions are respected, the frequency methods give reliable fatigue life estimations [3]. However, when dealing with real service loads or environment conditions, the non-Gaussian and non-stationary signals are commonly observed. An influence of non-Gaussian excitation to response signal and fatigue life was numerically investigated by Rizzi et al. [5] and Kihm et al. [6], who used kurtosis and skewness as estimators of non-Gaussianity.

This manuscript presents an experimental and numerical analysis of non-Gaussianity and non-stationarity on vibration fatigue. Firstly, a number of specimens was excited with different sets of random signals, obtained by combining different kurtosis values and non-stationarities. As the non-stationary non-Gaussian excitation was experimentally shown to be significantly more damaging the research later focused on experimental and numerical evaluation of non-stationarity rate of

J. Slavič (✉) · M. Česnik · M. Boltežar
Faculty of Mechanical Engineering, University of Ljubljana, Ljubljana, Slovenia
e-mail: janko.slavic@fs.uni-lj.si

L. Capponi · M. Palmieri · F. Cianetti
Department of Engineering, University of Perugia, Perugia, Italy

C. Walber et al. (eds.), *Sensors and Instrumentation, Aircraft/Aerospace, Energy Harvesting & Dynamic Environments Testing, Volume 7*, Conference Proceedings of the Society for Experimental Mechanics Series,
https://doi.org/10.1007/978-3-030-12676-6_7

excitation signal. In this manuscript a run-test method [7] is proposed to obtain a non-stationarity index γ [8]. Its applicability will be tested on a large number of fatigue tests and the relation between the amplitude-modulated non-stationarity and time-to-failure will be researched.

7.2 Background

This chapter presents only a condensed review of fundamental theory regarding non-stationarity. Background on structural dynamics and damage accumulation, that is later applied to actual experimental data, can be found in [3] and [8].

Run-test [7] is a non-parametric method that divides a signal in time windows and calculates a variation of a chosen statistical variable over the whole signal. For each time window a chosen variable is met with a criterion related to whole signal; in presented study a condition is defined as:

$$V(n) = \begin{cases} 1; & |R_W(n) - R_T| > \sigma_R \\ 0; & |R_W(n) - R_T| \leq \sigma_R \end{cases}, \tag{7.1}$$

where $R_W(n)$ is a RMS value of a n-th window, R_T a RMS value of the whole signal and σ_R is a standard deviation of all window RMSs, as illustrated on signal time history on Fig. 7.1a). A *run* is a sequence of identical observations V, followed and preceeded by different observation. Too many or too little runs in a whole signal is a proof of signal's non-stationarity. Any difference of actual number of runs r from expected mean σ_r indicates a non-stationarity in signal. If a number of runs lays outside $\mu_r \pm \sigma_r$, a signal is considered non-stationary. Additionally, a non-stationarity index γ is defined as $\gamma = r/\mu_r$.

7.2.1 Non-Gaussianity vs. Non-stationarity

The first part of the study focuses on both, non-Gaussianity and non-stationarity of random excitation signal and its influence on vibration fatigue life. For this purpose, an aluminium alloy A-S8U3 Y-shaped specimen is used, Fig. 7.1b). The specimen was excited with flat-shaped force PSD profile with frequency range 600–850 Hz so that it's 4th natural frequency of 775 Hz lied within excited frequency band.

Random signals with similar PSD profiles but different kurtosis k_u [6] and non-stationarities γ are generated and applied to the Y-specimens, as indicated in Table 7.1. Influence of non-Gaussianity and non-stationarity is then studied for fatigue lives at given excitation signal type.

The initial fatigue lives of specimens excited with random stationary Gaussian signal were used to obtain material fatigue parameters using a numeric model that was built and validated. Using the identified fatigue parameters, the Basquin's equation can be written as $\sigma = 987.5 \cdot N^{-0.169}$.

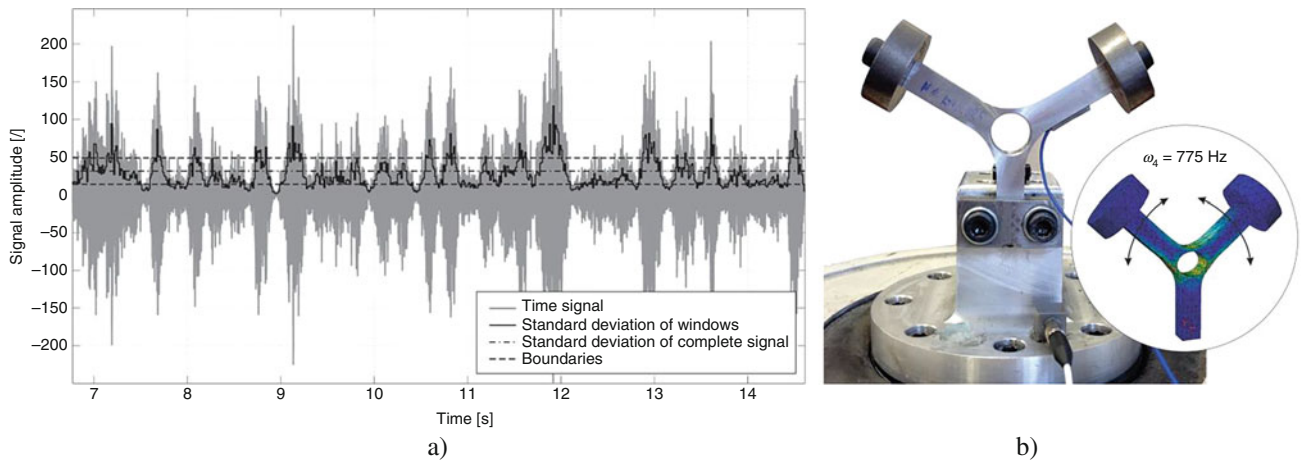

Fig. 7.1 (**a**) Run-test evaluation of a non-stationary time signal and (**b**) test specimen with excited modeshape

Table 7.1 Excitation signal types

Nr.	Signal type	k_u
1.	Gaussian stationary	2.96
2.	Non-Gaussian stationary	7.36
3.	Non-Gaussian stationary	5.43
4.	Non-Gaussian non-stationary	7.08

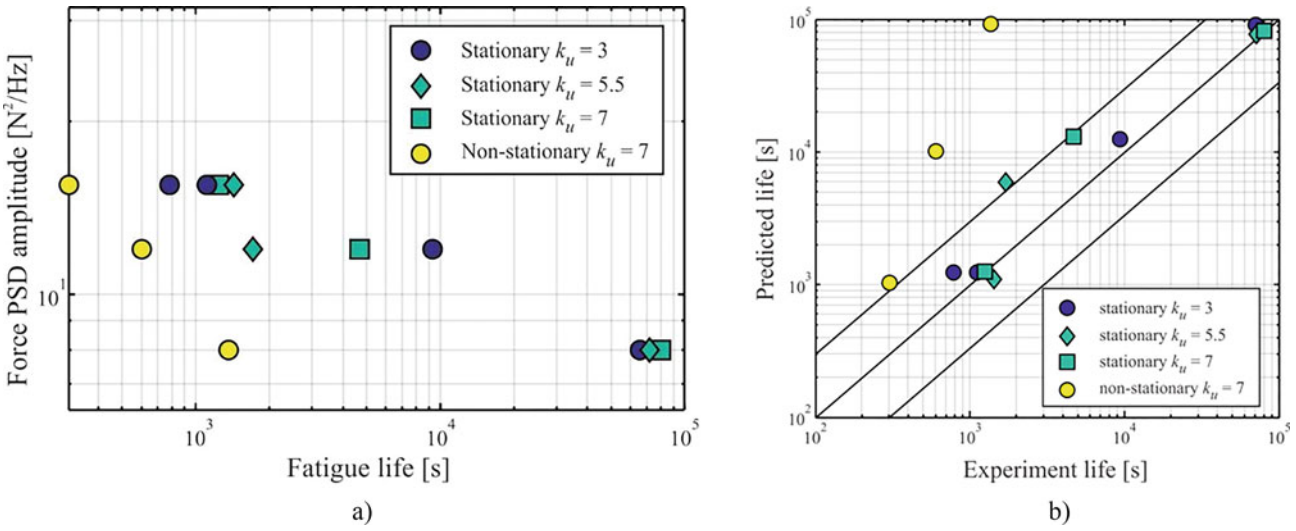

Fig. 7.2 Experimental and calculated fatigue lives: (**a**) Fatigue life vs force PSD amplitude, (**b**) Experimental life vs predicted life

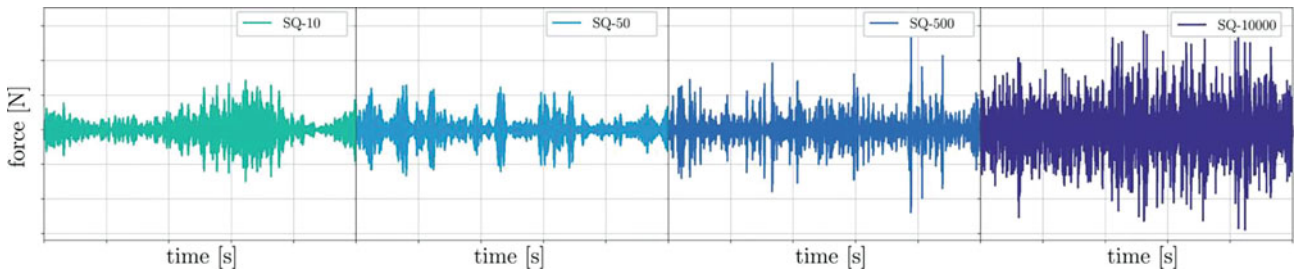

Fig. 7.3 Non-stationary signals SQ-10, SQ-50, SQ-500 and SQ-10000

A total of nine Y-shaped specimens were tested under non-Gaussian excitation, three for each signal type 2–4. The results of conducted test are presented in Fig. 7.2. Fatigue lives for Gaussian and non-Gaussian excitation differ only slightly. In contrast, for the case of non-stationary non-Gaussian excitation, the comparison shows significant difference between the calculated and the actual fatigue lives. The latter difference arises due to the non-Gaussianity of the stress response. If the input signal is quasi-stationary, the output kurtosis always tends to the Gaussianity; however, if the input signal is non-stationary, the stress response remains strongly non-Gaussian and leads to shorter fatigue lives than expected.

7.3 Non-stationarity Index

This section focuses on quantification of non-stationarities in excitation signal and on identification of non-stationary signals that result in reduced vibration fatigue life. A non-stationary time signal was obtained with beta-distribution amplitude modulation of stationary signal; different rates of non-stationarity were achieved by squeezing (compressing) an original signal. A signal was denoted as SQ-500 for compression of an original signal from 500 time units to 1 time unit, as illustrated in Fig. 7.3. All time signals had the same PSD and kurtosis, but different levels of non-stationarity.

A number of experiments were conducted on Y-specimens to obtain fatigue lives under different rates of non-stationarity. The results are shown in Fig. 7.4a) and the influence of non-stationarity rate is evident. The excitation signals were evaluated

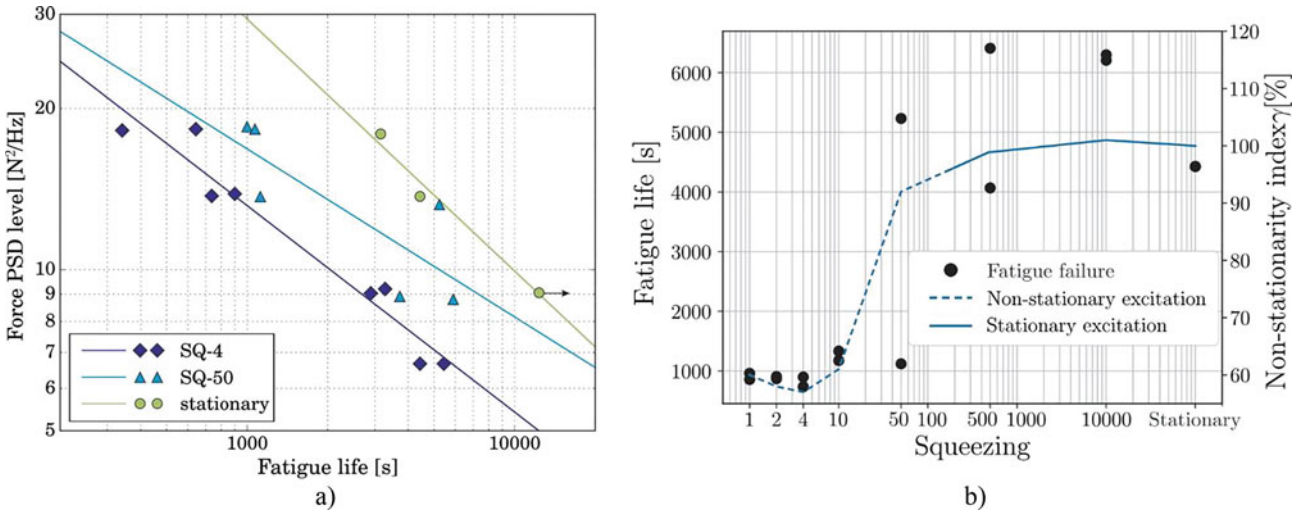

Fig. 7.4 (**a**) Influence of non-stationarity rate on fatigue life and (**b**) correlation between fatigue life and non-stationarity index

with proposed run test method. Interestingly, the non-stationarity index γ reliably identifies those excitation signals, that will, when applied, result in significantly lower fatigue life of tested structure, as shown in Fig. 7.4b).

7.4 Conclusions

The fatigue life of Y-shaped specimens was investigated in order to determine how a change in the excitation kurtosis and stationarity affects the fatigue life of a real structure. It was found that if the non-Gaussian excitation is stationary, the calculated fatigue lives with classical frequency-counting methods are comparable to the fatigue lives under Gaussian excitation. In contrast, for the case of non-Gaussian excitation, the obtained fatigue life exhibits a significantly higher damage accumulation For this reason, considering a non-stationary non-Gaussian excitation as Gaussian and consequently adopting the classic frequency-counting methods may result in a wrong fatigue-life estimation.

To this end, a study later focused on identifying critical non-stationary amplitude-modulated signals in terms of actual fatigue life and on answering the question: what rate of non-stationarity can still be considered as stationary and how does the rate of non-stationarity effect the fatigue life? To answer this, additional tests were performed using squeezed signals with the same PSD and kurtosis, but different rates of non-stationarity. The signals that were identified as non-stationary with run-test method resulted in a significantly shorter fatigue life than the ones that were identified as stationary. If the non-stationarity of excitation is identified, the resulting fatigue life was shown to significantly decrease (in this research to 1/5th).

References

1. Benasciutti, D., Tovo, R.: Spectral methods for lifetime prediction under wide-band stationary random process. Int. J. Fatigue. **27**(8), 867–877 (2005)
2. Mršnik, M., Slavič, J., Boltežar, M.: Multiaxial vibration fatigue - a theoretical and experimental comparison. Mech. Sys. Signal Proc. **76–77**, 409–423 (2016)
3. Mršnik, M., Slavič, J., Boltežar, M.: Frequency-domain methods for a vibration-fatigue-life estimation – application to real data. Int. J. Fatigue. **47**, 8–17 (2013)
4. Bendat, S., Piersol, G.: Random Data: Analysis and Measurement Procedures, 4th edn. Wiley, New York, NY (2010)
5. Rizzi, S. A., Prezekop, A., Turner, T.: On the response of a non-linear structure to high-kurtosis non-Gaussian random loadings. In: 8th Eurodyn, Leuven (2011)
6. Kihm, F., Rizzi, S. A., Fergusson, N. S., Halfpenny, A.: Understanding how kurtosis is transferred from input acceleration to stress response and its influence on fatigue life. In: 11th RASD, Pisa (2013)
7. Rouillard, V.: Quantifying the non-stationarity of vehicle vibrations with the run test. Packag. Technol. Sci. **27**(3), 203–219 (2014)
8. Capponi, L., Česnik, M., Slavič, J., Cianetti, F., Boltežar, M.: Non-stationarity index in vibration fatigue: Theoretical and experimental research. Int. J. Fatigue. **104**, 221–230 (2017)

Chapter 8
Use of Topology Optimization to Design Shock and Vibration Test Fixtures

Tyler F. Schoenherr, Pete Coffin, and Brett Clark

Abstract Engineering designers are responsible for designing parts, components, and systems that perform required functions in their intended field environment. To determine if their design will meet its requirements, the engineer must run a qualification test. For shock and vibration environments, the component or unit under test is connected to a shaker table or shock apparatus and is imparted with a load to simulate the mechanical stress from vibration. A difficulty in this approach is when the stresses in the unit under test cannot be generated by a fixed base boundary condition. A fixed base boundary condition is the approximate boundary condition when the unit under test is affixed to a stiff test fixture and shaker table. To aid in correcting for this error, a flexible fixture needs to be designed to account for the stresses that the unit under test will experience in the field. This paper will use topology optimization to design a test fixture that will minimize the difference between the mechanical impedance of the next level of assembly and the test fixture. The optimized fixture will be compared to the rigid fixture with respect to the test's ability to produce the field stresses.

Keywords Topology optimization · Dynamic test fixture · Vibration test · Frequency response function · Qualification

Nomenclature

Field Configuration	The hardware assembly in its designed assembled state
Field Environment	The setting where external force(s) are imparted on the field configuration while in its normal designed operating environment and the corresponding response of the field configuration in that environment
Component	The hardware or subsystem of interest within the field configuration that needs to be tested prior to release into its field environment
Laboratory Configuration	The hardware assembly of the component, test fixture, and the excitation apparatus
Laboratory Environment	The setting where the component is subjected by a controlled, prescribed force to cause a desired response of the component
Next Level of Assembly	The structure to which the component is connected in its field configuration
Test Fixture	The piece of hardware to which the component is connected in its laboratory configuration

Sandia National Laboratories is a multi-mission laboratory managed and operated by National Technology and Engineering Solutions of Sandia, LLC., a wholly owned subsidiary of Honeywell International, Inc., for the U.S. Department of Energy's National Nuclear Security Administration under contract DE- NA-0003525.

T. F. Schoenherr (✉) · P. Coffin · B. Clark
Sandia National Laboratories, Albuquerque, NM, USA
e-mail: tfschoe@sandia.gov

C. Walber et al. (eds.), *Sensors and Instrumentation, Aircraft/Aerospace, Energy Harvesting & Dynamic Environments Testing, Volume 7*, Conference Proceedings of the Society for Experimental Mechanics Series,
https://doi.org/10.1007/978-3-030-12676-6_8

8.1 Introduction

For many industries, the only experimental method for predicting if the system or component that they design will mechanically fail in its field environment is to design and execute a vibration or shock test in a laboratory. The objective of the laboratory test is to replicate the component's mechanical stress from the field environment in the laboratory environment. By replicating the component's mechanical stresses, insight is gained on the possible failure modes and component limitations. This information informs the designers if the component will survive the field environment and how to redesign the component if it doesn't survive. This is all done prior to deployment.

One must know what causes stress to design a vibration or shock laboratory test to replicate the stresses in the field. Responses including displacement, acceleration, and stress over the entire system or component is the product of the input forcing function and the transfer functions or frequency response functions (FRF). These transfer functions dictate the responses to a given input and are functions of the mass, stiffness, and damping of the system. Figure 8.1 illustrates the product between the input and FRFs of the field and laboratory configurations and the objective of the shock or vibration test.

The laboratory configuration's FRFs are the focus for this paper. The laboratory configuration consists of the component, the test fixture, and the connection of the two structures. Because the component performance is of interest, only the test fixture can be modified to ensure the component's response in the laboratory test matches to the field configuration's response.

For the past 60 years, test fixtures were designed to have their first natural frequency outside the frequency bandwidth of the test. This makes the test fixture "rigid" compared to the component. One reason for this guidance is because the "rigid" fixture has a constant transfer function between the input force or enforced motion and the base motion of the component. Another reason for the guidance of a "rigid" fixture is that the "rigid" fixture does not introduce any new resonances to the component that the component did not experience in the field configuration.

Although rigid fixtures have advantages over flexible fixtures, rigid fixtures only excite a component's fixed base mode shapes and the stresses that result from those shapes. If the component is attached to a relatively flexible next level of assembly and the relative motion of the connection degrees of freedom cause significant stress, the rigid fixture will not be adequate as it does not allow for relative motion between the connection degrees of freedom. This short-comming of a rigid fixture was identified by NASA engineers On and Sharton as they identified the need to examine the impedance of the field configuration's next level of assembly and proposed theories on how to design a flexible test fixture [3, 4].

Recent proposals by Daborn et al. [1] and Edwards [2] focus on the laboratory configuration and the desire the replicate the impedance of the next level of assembly. The proposed methods involve taking a section of the next level of assembly and integrating it into the laboratory configuration. It was postulated that this would limit the impedance mismatch between the field and laboratory configurations.

The focus of this paper is on the connection between the component and the test apparatus through the test fixture in the laboratory configuration. The connection can be defined by the impedance of the test fixture in the laboratory environment. It is desired to design the test fixture to match the impedance of the component's next level of assembly in the field

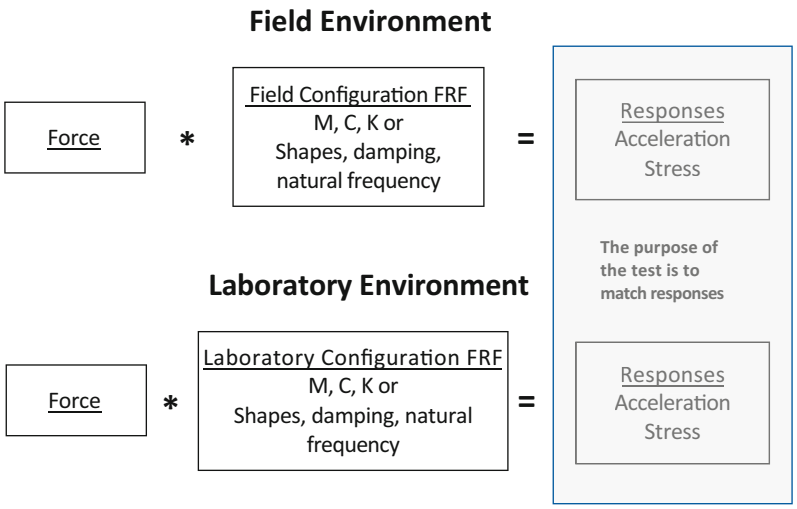

Fig. 8.1 Flowchart demonstrating the desired relationship between the field and laboratory environments for a component of interest

configuration. Matching this impedance ensures the existence of a forcing function or a series of forces to recreate the field environment in the laboratory. Topology optimization was the tool explored in the design of a test fixture to meet the requirement of matching the next level of assembly's impedance.

This paper discusses the background on the requirements and design of a laboratory test. It presents a proposal for designing a dynamic test fixture that allows the component in the laboratory to match the stress in the field. The paper presents a case study for which topology optimization was used to determine the applicability and practicality of using a topology optimized test fixture. The objective function used for the topology optimization was frequency response function matching. This objective function was found to have a non-convex solution space, which made converging to a single global minimum difficult. However, some results were found where the optimized test fixture provided an improvement over a rigid test fixture.

8.2 Theory

A successful laboratory test needs to be defined to develop a metric to quantify the test fixture's ability to replicate the field environment. The majority of structural dynamic testing that is executed in the laboratory has the purpose of determining if the component will mechanically fail in the field environment. The goal of replicating the correct stresses in the correct locations to reproduce failure modes in the laboratory environment is the basis for the success of the test.

Although the test fixture design plays a critical role in the response, the response of the component is the product of the input forcing function and the system transfer functions or frequency response matrix shown as

$$\bar{F} \cdot \mathbf{H} = \bar{x}, \tag{8.1}$$

where $\bar{F}$ is the external forcing function vector acting on the system, $\mathbf{H}$ is the system's frequency response matrix and $\bar{x}$ is the vector of responses. The frequency response matrix is symmetric and a function of the mass, stiffness, and damping of the structure. If the frequency response functions are examined in the modal domain, they are functions of the mode shapes, natural frequencies, and modal damping.

For the purpose of this paper, there are two systems of equations derived from Eq. (8.1),

$$\bar{F}_F \cdot \mathbf{H}_F = \bar{x}_F, \tag{8.2}$$

and

$$\bar{F}_L \cdot \mathbf{H}_L = \bar{x}_L, \tag{8.3}$$

where the subscript F designates the field configuration and the subscript L designates the laboratory configuration.

A successful laboratory test is defined to have matching responses to the field environment

$$\bar{x}_F = \bar{x}_L. \tag{8.4}$$

Substituting Eqs. (8.2) and (8.3) into (8.4), the expression

$$\bar{F}_L \cdot \mathbf{H}_L = \bar{F}_F \cdot \mathbf{H}_F \tag{8.5}$$

shows that in order to have a successful test, the product of the forcing function and the FRF matrix must be the same in both the field and laboratory configurations. Stated previously, the FRF matrix is a function of the mass, damping and stiffness matrices of the respective hardware configuration and the laboratory's FRF matrix is a function of the test fixture. If the test fixture can be designed in a way that the laboratory configuration's FRF matrix is equal to the field configuration's FRF matrix, then there will exist a forcing function for the laboratory test that will produce identical responses as was observed in the field environment.

8.3 Topology Optimization

This paper examines the possibility of using topology optimization to design a test fixture. In order to use topology optimization, one must define an objective function to optimize to a minimum or a maximum. The objective function chosen for this study was developed with the intent of matching the frequency response matrix of the laboratory configuration to the frequency response matrix of the field configuration. The purpose for choosing the frequency response matrix for the objective function is detailed in Sect. 8.2. The objective function used in this paper is written as

$$J_{FRF}(\bar{u}, \bar{\tilde{u}}, \bar{p}) = \sum_{k=1}^{N_{freq}} \left\{ \sum_{m=1}^{N_{loads}} \left(\sum_{i=1}^{N_{dof}} \left[\frac{\left(\bar{u}^I_{kmi} - \bar{\tilde{u}}^I_{kmi}\right)^2}{A_{kmi}} + \frac{\left(\bar{u}^R_{kmi} - \bar{\tilde{u}}^R_{kmi}\right)^2}{A_{kmi}} \right] \right) \right\} \tag{8.6}$$

with $\bar{p}$ the vector of design variables, $\bar{u}$ the vector of response variables in the optimization model, and $\bar{\tilde{u}}$ the vector of reference or target response variables. With respect to any optimization parameters in this paper, the response variables are FRFs. The $\bar{u}$ are the FRFs of the laboratory configuration and the $\bar{\tilde{u}}$ are the FRFs of the field configuration. Since the FRF is complex, the differences in the FRFs are calculated for the real part, designated by the R superscript, and the imaginary part, designated by the I superscript. Each difference was scaled by the variable A which was calculated as the absolute value of the maximum of $\bar{\tilde{u}}_{mi}$ and $\bar{u}_{mi}$ at each frequency i.

To gain insight on the behavior of the FRF matching objective function in Eq. (8.6), a single design parameter case study was developed. This case study involved a cantilever beam with a fixed width and length and a thickness of 0.2 in. as shown in Fig. 8.2. The design parameter was the thickness of the beam varied between 0.05 and 0.5 in. For reference, the FRFs of the minimum and maximum thickness beams were plotted against the reference beam. Figure 8.3 shows the FRF of the minimum thickness, 0.05 in., and the reference FRF. Figure 8.4 shows the FRF of the maximum thickness, 0.5 in., and the reference FRF.

The error with respect to the single thickness parameter was calculated over the range allowed and plotted in Fig. 8.5. Figure 8.5 shows the error for the baseline objective function defined by Eq. (8.6) along with several methods for taking the difference between two FRFs. These methods included taking only the differences between the real or imaginary parts of the FRFs, the difference between the magnitude of the FRFs, and determining the log magnitude of the shortest distance between the two FRFs. The shortest distance objective function takes each frequency line of the varying FRF to the nearest point of the reference FRF on a log normalized scale.

Optimization algorithms use the derivatives of the objective function per the design parameter space that it is given to determine how the parameters should change to minimize the objective function in this case. These derivatives examine the slope of the objective functions to determine how to change the design parameters in order to find the extrema of the objective function. Figure 8.5 shows that the proposed objective functions for matching FRFs were not convex, meaning there were multiple minima to which the objective function could converge. These local minima increase in number as the number of design parameters increase. Since the design parameters are the finite elements or surfaces of finite elements, it is expected that the optimization would converge to a local minima. This was verified empirically.

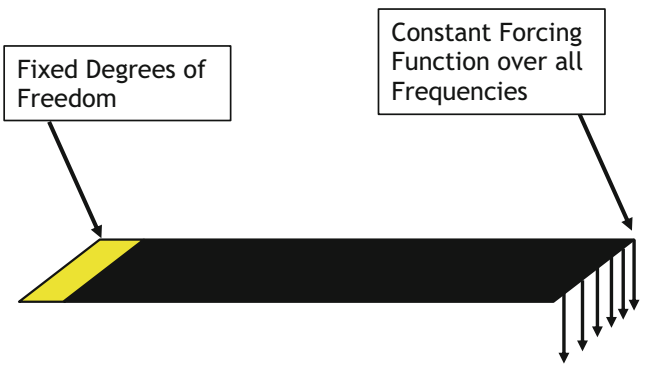

Fig. 8.2 Cantilever beam of which the thickness was varied to minimize the difference between a reference FRF and a varying FRF

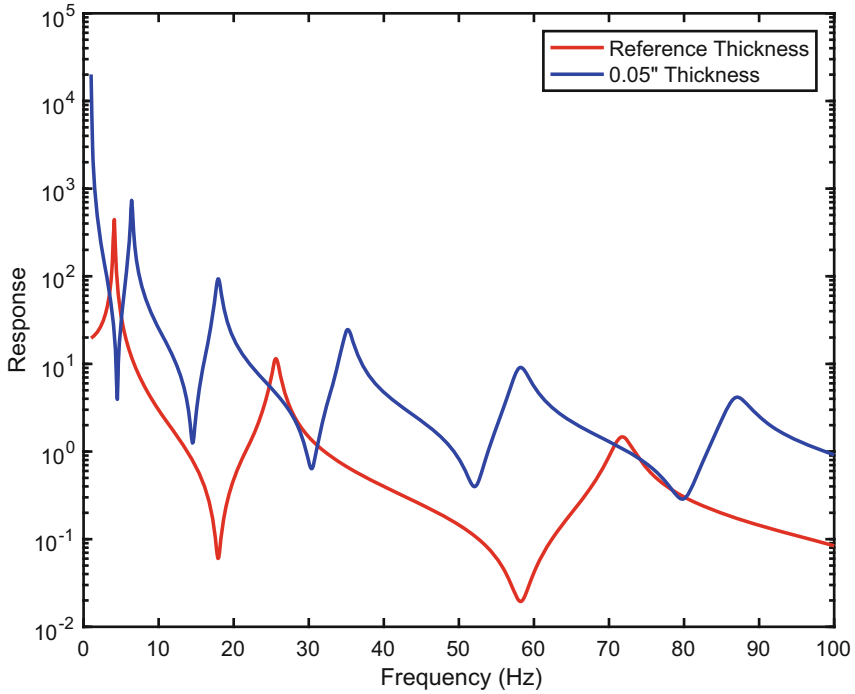

Fig. 8.3 Plot showing the FRF of the reference thickness of the cantilever beam and the minimum thickness of the cantilever beam

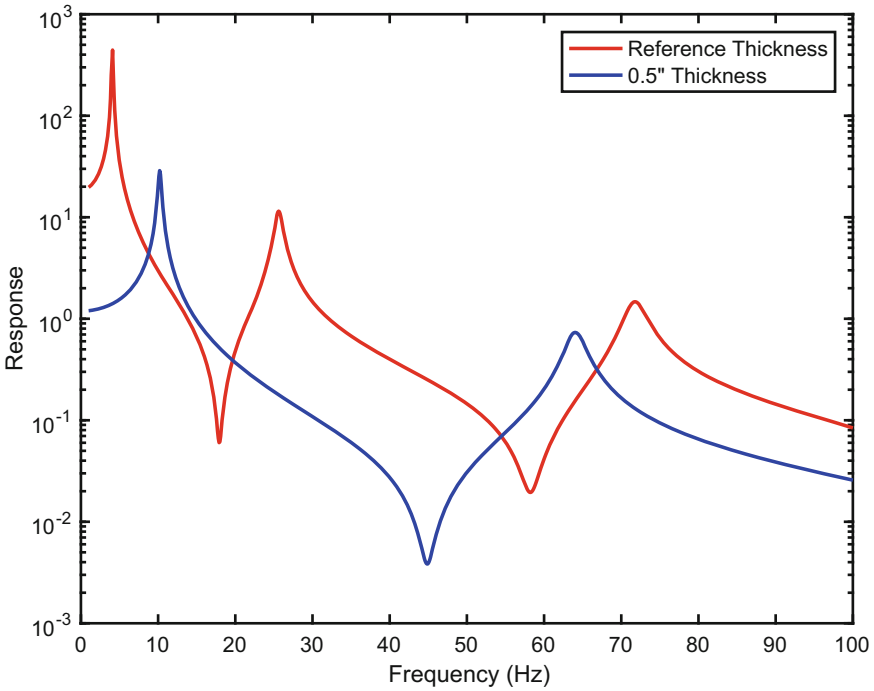

Fig. 8.4 Plot showing the FRF of the reference thickness of the cantilever beam and the maximum thickness of the cantilever beam

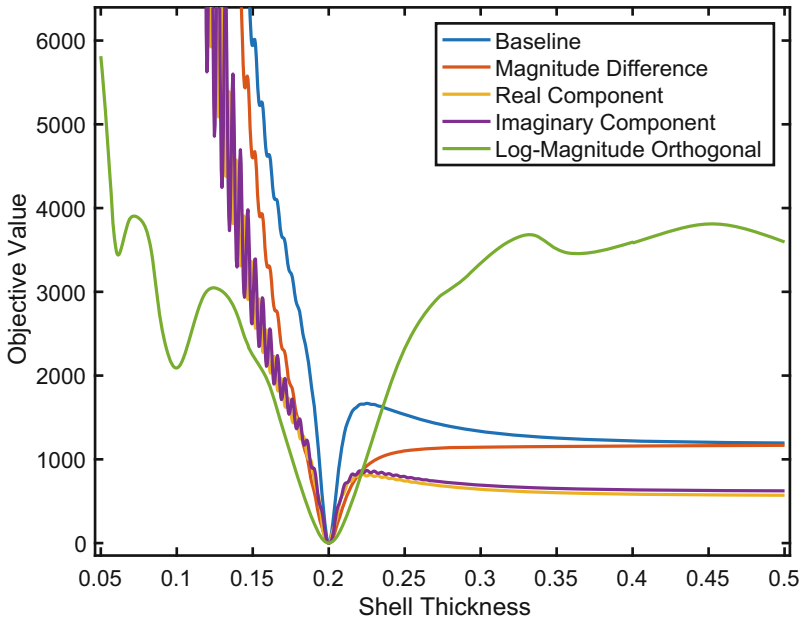

Fig. 8.5 The FRF matching objective value for a variety of objective functions for the cantilever beam of varying thickness

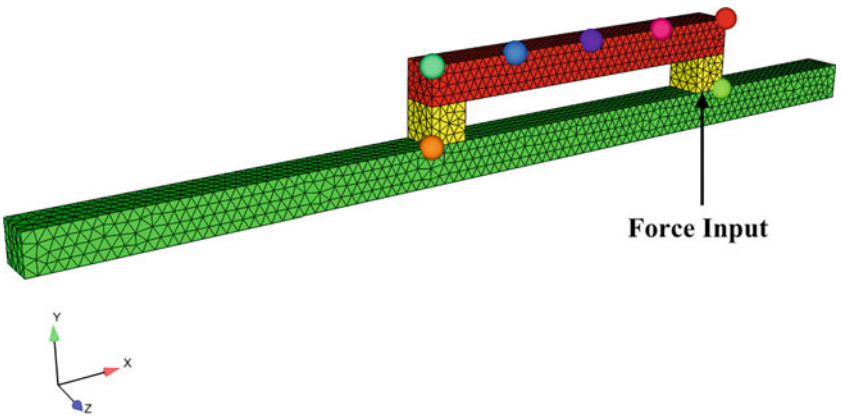

Fig. 8.6 Field configuration and nodes used for the FRF matching optimization analysis. The red and yellow sections were the component and the green section was the next level of assembly

8.4 Case Study

8.4.1 Creating an Optimized Test Fixture

A case study was developed to provide an example of a topology optimized test fixture and its effectiveness with respect to replicating a field environment. This study compared the optimized test fixture to a rigid fixture. A rigid test fixture was defined to be a structure having no elastic modes in the frequency band of the test. A rigid fixture was chosen because it is the common method of designing a test fixture for current laboratory tests.

The field configuration for the case study is shown in Fig. 8.6 and the laboratory configuration with the rigid fixture in Fig. 8.7. A field environment was created by applying a force at the location designated in Fig. 8.6 with an amplitude of 1000 lbs for all frequencies. The rigid fixture was modeled by using the next level of assembly and tying all of the degrees of freedom on its bottom face to a concentrated mass with rigid bar elements. This forced all of the degrees of freedom on that face to move with zero displacement relative to each other and forced the fixture to be rigid.

An optimized test fixture was designed using topology optimization. The optimization problem was given the initial geometry shown in Fig. 8.8 with the cyan sections as the design space for the optimization problem. The initial geometry

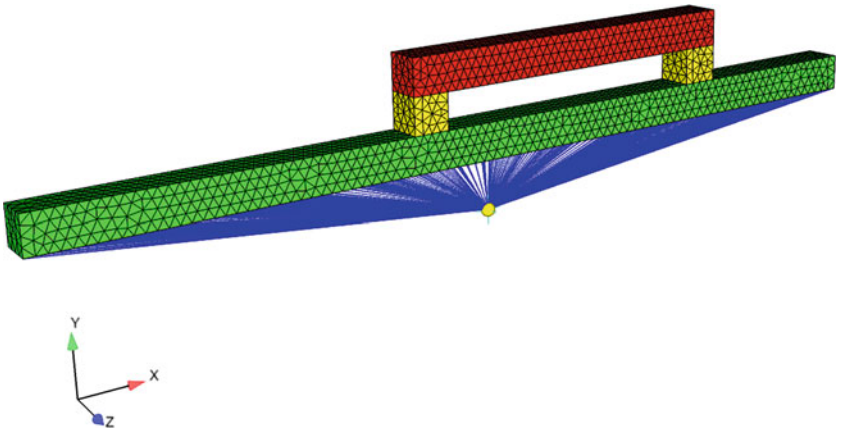

Fig. 8.7 The component mounted to a "rigid" fixture. The rigid of the fixture was accomplished by tying the next level of assembly to a concentrated mass via rigid bar elements

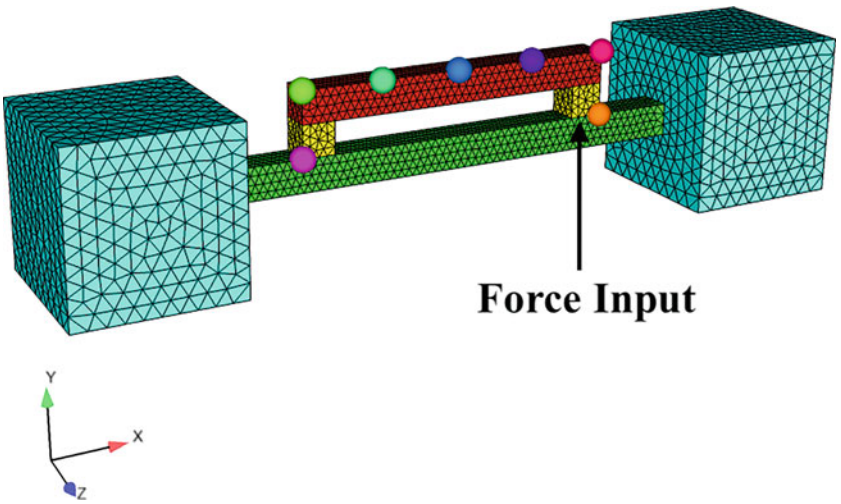

Fig. 8.8 Initial model for the topology optimization. The cyan blocks were the design space

included parts of the next level of assembly from the field configuration, shown in green in Fig. 8.8. This was done because it is acceptable to assume that an engineer would be able to replicate parts of the next level of assembly in the test fixture design.

The PLATO optimization software developed by Sandia National Laboratories was used for this analysis. The optimization was executed using the FRF matching objective function from Eq. (8.6). The degrees of freedom chosen were the translation degrees of freedom of the nodes highlighted in Figs. 8.6 and 8.8. The input was defined as a traction force on the entire surface between the yellow and green sections as shown in Fig. 8.8 and was the same input for both the field configuration and the optimization problem.

The optimization was executed using a continuation approach to help guide the analysis to a better local minimum. The continuation approach runs consecutive optimization problems that uses result of the previous optimization as the initial condition for the current optimization. The first iteration for the optimization problem computed the minimum of the objective function over the frequency range of 60–160 Hz. These frequencies were chosen because they consisted only of rigid body motion for the field configuration. It was postulated that matching mass properties would be easier for the optimizer.

After the optimization problem converged for rigid body motion, the result of the optimization was used as the initial configuration of the next optimization with the frequency range extended to 300 Hz. This included the first elastic mode of the field configuration. The value of the objective function was tracked per iteration and is shown in Figs. 8.9 and 8.10. The FRFs for the field environment or 'reference' was compared to the current iteration for a single degree of freedom. The degree of freedom that was used in Figs. 8.9 and 8.10 was in the center of the component in the Y-direction, identified in Fig. 8.11.

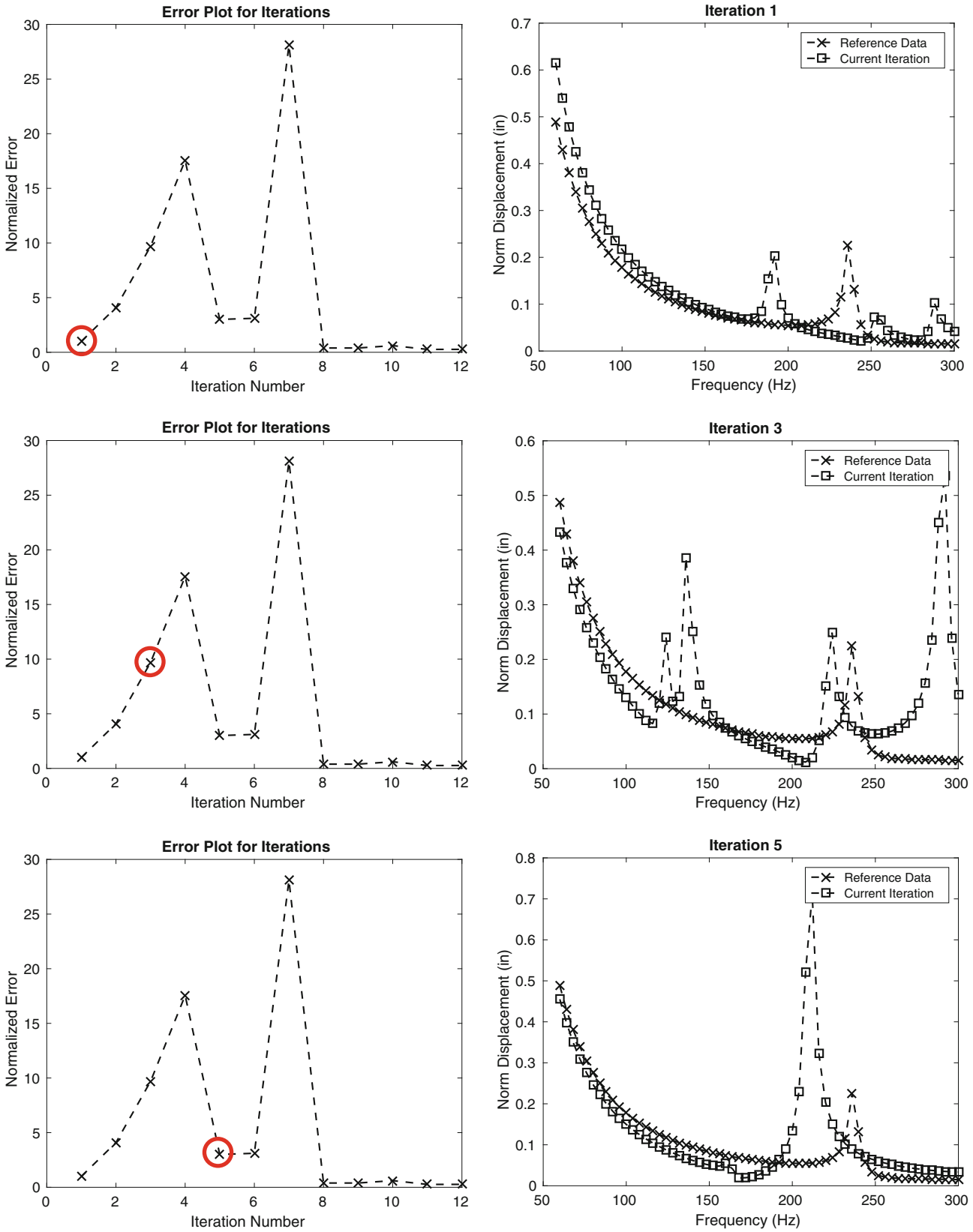

Fig. 8.9 Error and FRF plots for iterations 1, 3, and 5 of optimizing over the 60–300 Hz range

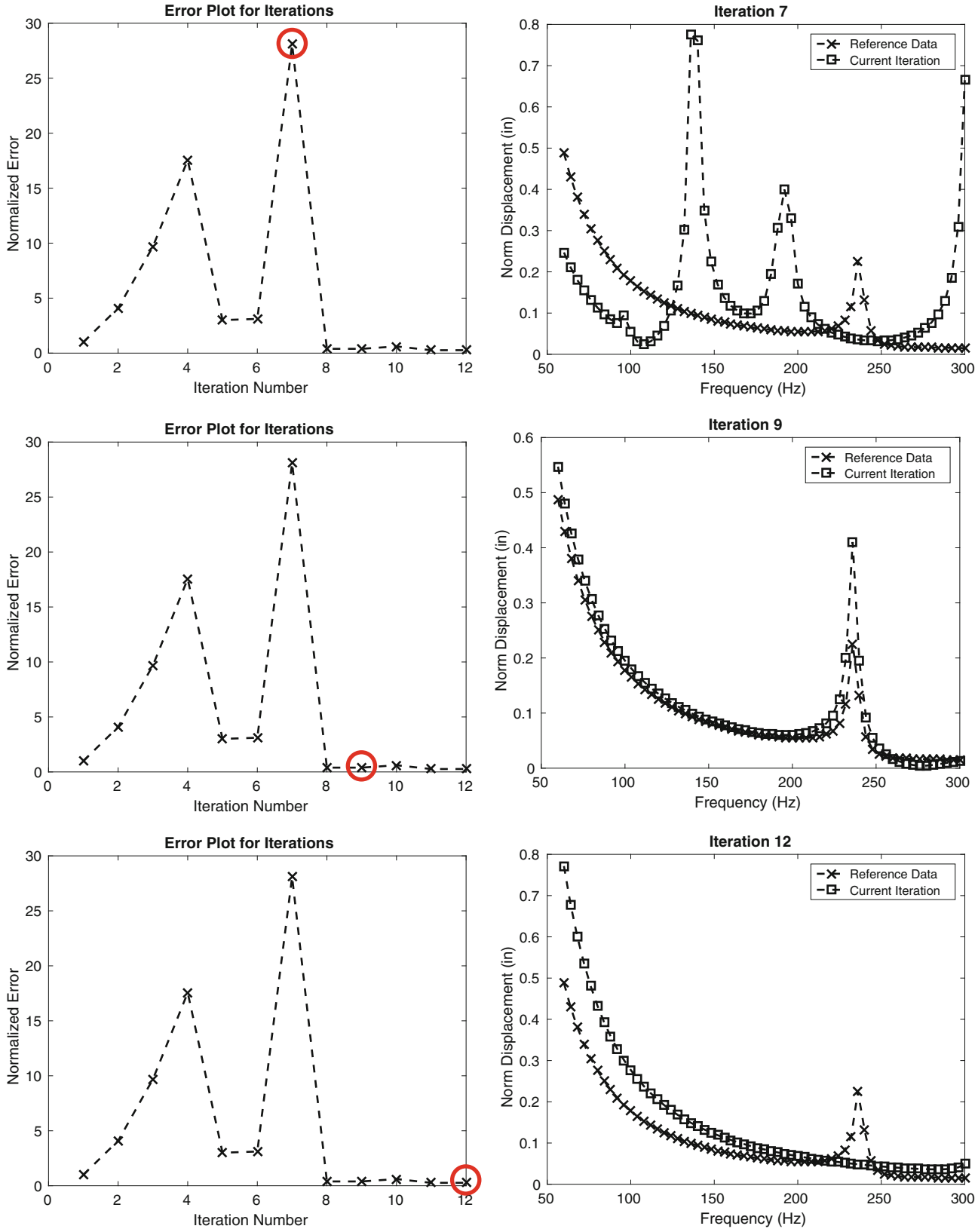

Fig. 8.10 Error and FRF plots for iterations 7, 9, and 12 of optimizing over the 60–300 Hz range

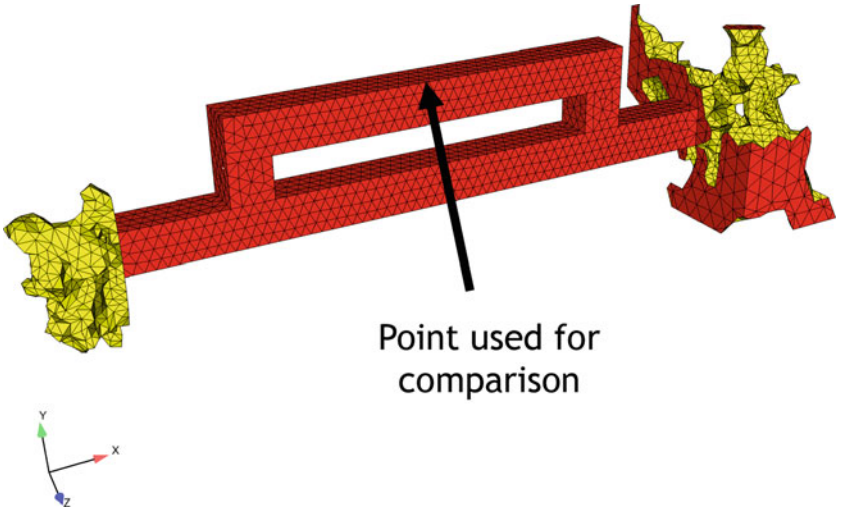

Fig. 8.11 Topology optimized test fixture derived from iteration 9 optimized over the frequency range 60–300 Hz

Several observations are made from the examination of Figs. 8.9 and 8.10:

- Iteration 1 showed generally good agreement in the lower frequencies. This was due to the first optimization run between 60 Hz and 160 Hz.
- The error plot did not show smooth convergence to a minima. Instead, the error increased and decreased multiple times into different local minima. This was due to the aggressive parameters chosen for the optimization algorithm. The points chosen per iteration were few and they reached far from the initial location and sometimes increased in error.
- The FRFs did not have a smooth transition from one iteration to the next. Modes were introduced or eliminated depending on the iteration.
- The 9th iteration had a natural frequency at the correct frequency, however, the optimization stiffened that natural frequency to lower the error in iteration 12. The error for iteration 9 was 0.39 and 0.26 for iteration 12.

When selecting which iteration would provide the best test fixture, iteration 9 was selected over iteration 12 because 12 had no natural frequency in the frequency range of interest. This meant that for iteration 12, the fixture was rigid in the frequency range of interest and would provide the same results as the rigid fixture in Fig. 8.7. The finite element model of the optimized fixture for iteration 9 is shown in Fig. 8.11 with the compared point in the FRF figures identified.

The note above that iteration 12 had lower error than iteration 9 deserves additional discussion. For iteration 9, the lower frequencies matched and the natural frequency was correct. The only deviation between the two FRFs was the amplitude at the natural frequency. From modal analysis theory, the amplitude of each degree of freedom at the natural frequency is the mode shape. If the mode shape matches between the field and laboratory configurations, the amplitude at the natural frequency will be at worst different by a scalar factor and the stress distribution for the mode shape will be the same.

To determine the differences in the shapes, a modal analysis was computed on the field configuration and the optimized configuration. Snapshots of the mode shapes at approximately 230 Hz are illustrated in Fig. 8.12. At first glance, it appeared that the two shapes were very different as the majority of the motion in the field configuration was in the Y-direction and the majority of the motion in the optimization configuration was in the Z-direction. After closer examination, the nodes of each mode had similar locations and there was some deflection in the Y-direction in the optimization configuration's mode.

8.4.2 Comparing the Optimized and Rigid Test Fixtures

The rigid fixture was compared to the optimized fixture by simulating three environments. The first environment was the field environment. The responses from the field environment were the targets for the laboratory environments. The second environment was a laboratory environment that used the rigid fixture shown in Fig. 8.7. The third environment was a laboratory environment that used the optimized fixture shown in Fig. 8.11.

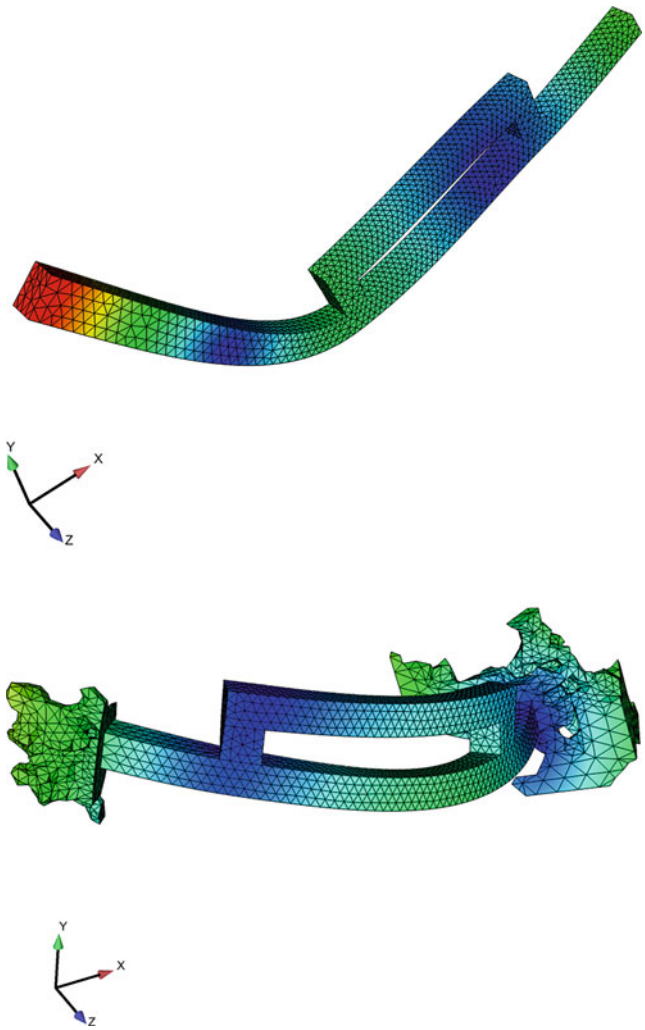

Fig. 8.12 First elastic mode shape of the field configuration (top) and the optimization configuration (bottom)

The input for the laboratory environment that used the rigid fixture was derived using enforced motion because it is a common method for obtaining shaker inputs. The enforced motion method is illustrated in Fig. 8.13 where the motion of the base in the field environment is measured and the laboratory fixture is forced to match that measured motion.

The laboratory configuration with the optimized test fixture was tested by deriving and imparting a single forcing function applied at the location shown in Fig. 8.14. In reality, this forcing function could be imparted by a modal shaker with attached stinger or equivalent. The forcing function was computed by multiplying the pseudo inverse of the FRFs of the laboratory configuration with the optimized test fixture multiplied by the target motion of the component,

$$\mathbf{H}^{+}\bar{x} = F. \tag{8.7}$$

With both laboratory environments defined and simulated, the stresses were calculated. The Von Mises stress was calculated per frequency line and the total stress was calculated as a root mean squared (RMS) value per

$$x_{rms} = \frac{1}{n}\sqrt{\sum_{m=1}^{n} x_m^2} \tag{8.8}$$

where x is the variable of interest, and n is the total number of discrete points in the signal. The plots of the Von Mises stresses for the field, optimization fixture laboratory, and rigid fixture laboratory configurations are shown in Figs. 8.15, 8.16, and 8.17 respectively.

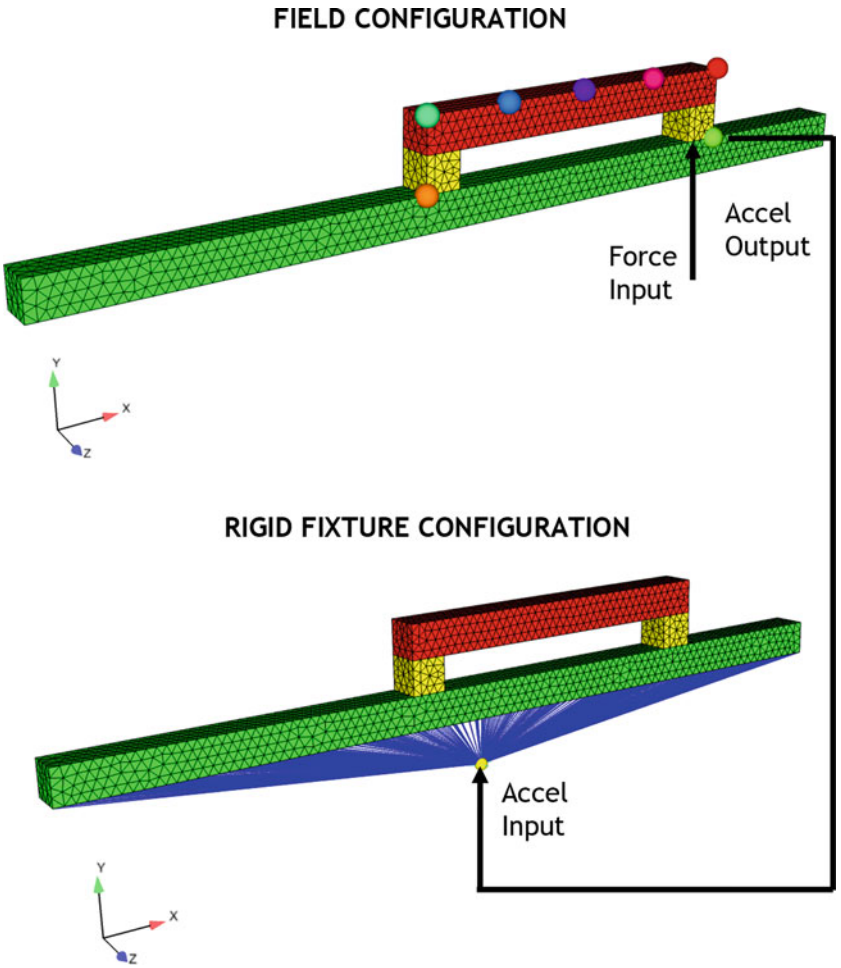

Fig. 8.13 Laboratory setup for the rigid test fixture and enforced motion

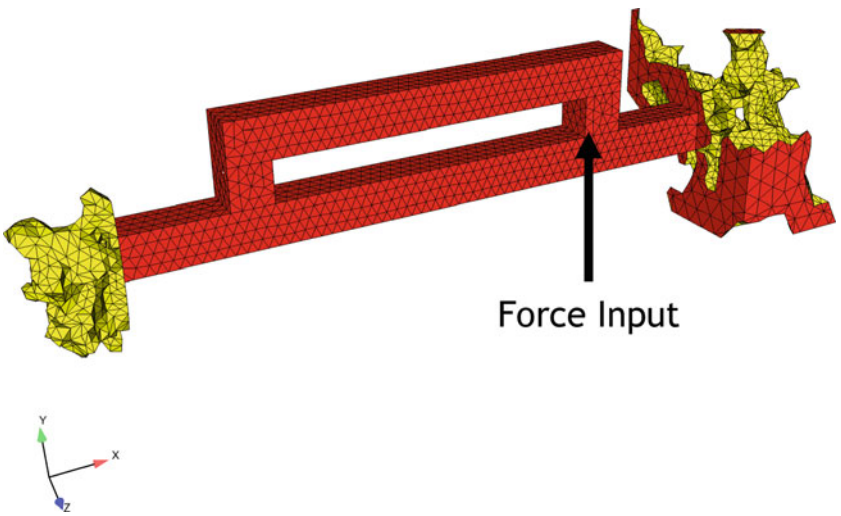

Fig. 8.14 Laboratory setup for the optimization configuration

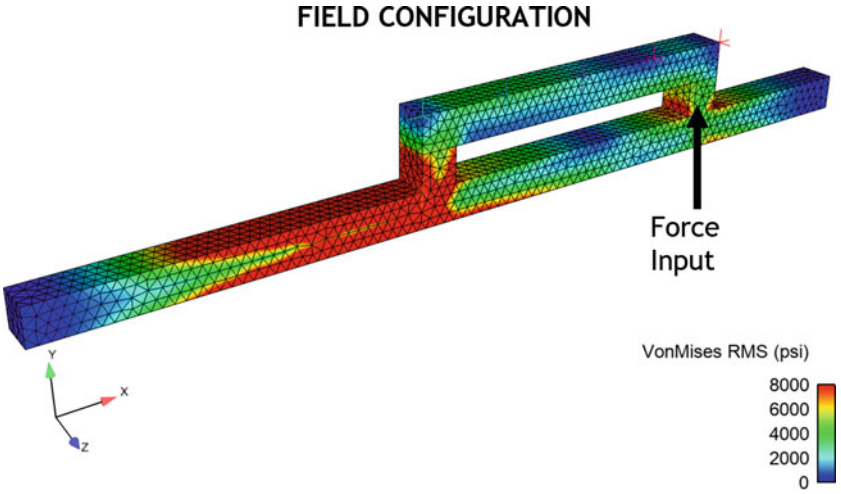

Fig. 8.15 RMS response of Von Mises stress for the field configuration and environment

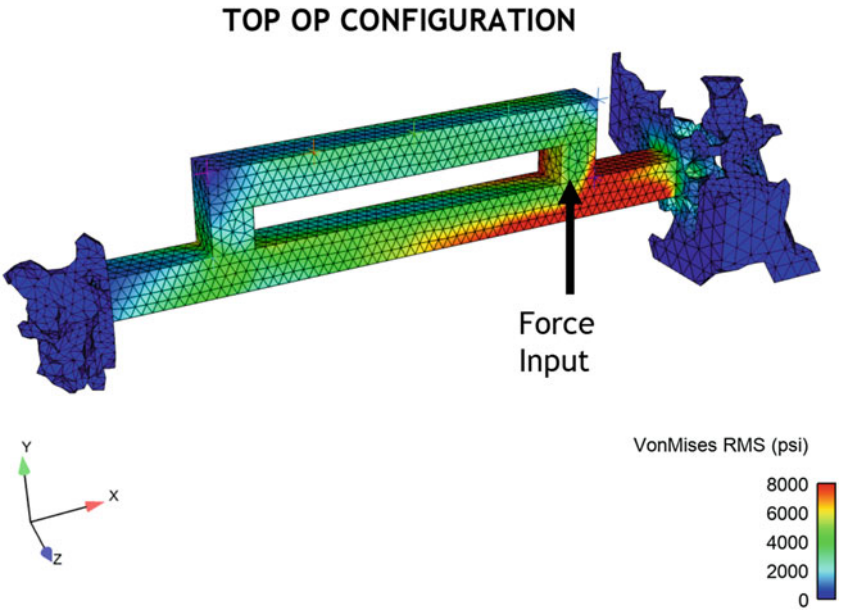

Fig. 8.16 RMS response of Von Mises stress for the optimization configuration and laboratory environment

The comparison between Figs. 8.15, 8.16, 8.17 show that although the optimized fixture did not perfectly replicate the stresses in the field environment, there was a relative increase in fidelity over the rigid test fixture. The stresses in the laboratory environment with the rigid fixture had an error of a factor of eight and the high stress concentrations were all in incorrect locations compared to the field environment.

One could argue that if the stress field for the laboratory configuration with the rigid fixture was known a priori, the input specification for the laboratory configuration with the rigid fixture could be amplified by a factor of approximately 16 in order to make the stress in the laboratory at least as much as in the field. However, due to the boundary conditions and the stress field of the rigid laboratory configuration, the stress at the middle of the component would be an over test by approximately a factor of 8 and could cause a failure that would not occur in the field.

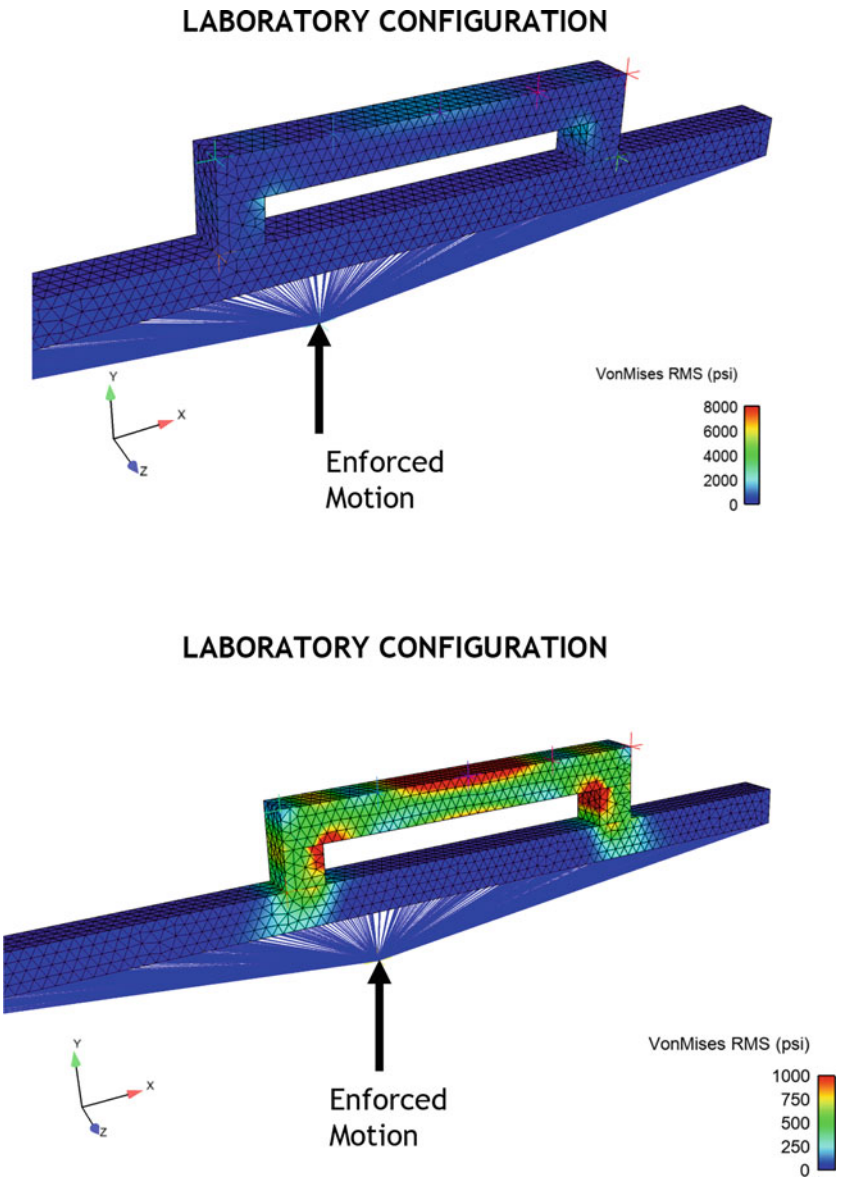

Fig. 8.17 RMS response of Von Mises stress for the rigid configuration and laboratory environment. Common colormap to other configurations (top) and rescaled colormap (bottom)

As previously stated, the stresses in the laboratory environment was the product of the forcing function and the configuration's FRFs. Because the forcing functions for the two laboratory environments were derived using different methods, it was difficult to determine how much the derivation of the forcing function effected the stress results.

In an effort to remove the forcing function's effect on the comparison between the rigid fixture and the optimized fixture, the method of deriving an input force used for the optimized fixture was applied to the rigid fixture. Two changes were made to the laboratory configuration with the rigid fixture in order be able to apply a forcing function. First, the rigid elements connecting the next level of assembly to the concentrated mass and the concentrated mass itself were removed. Next, the elastic modulus of the next level of assembly beam was increased by a factor of 100. These steps created a "rigid" fixture that had free boundary conditions that matched the configuration of the optimized laboratory configuration.

With the new laboratory configuration containing a rigid fixture, the process of applying a force derived using Eq. (8.7) was performed. This forcing function was applied at the same location as referenced in Fig. 8.6 and was derived using exactly the same method as was done to the optimized test fixture. The two forcing functions are compared in Fig. 8.18.

Figure 8.18 shows that the forcing function calculated for the rigid fixture was approximately a factor of six higher than the forcing function for the optimization forcing function. The reason for this difference in force magnitude lies in the

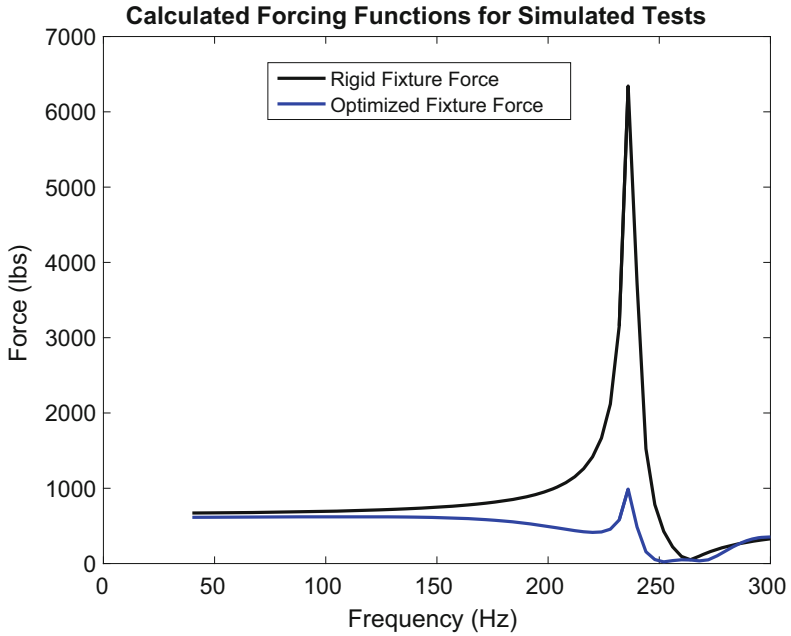

Fig. 8.18 Calculated input forces for the optimized laboratory configuration and the free rigid laboratory configuration

aforementioned force inversion process. The force inversion process calculates a forcing function that gives a least squared error fit to the response data. Because the mode shape of the rigid fixture configuration differed from the field configuration more than the optimized configuration, the derived forcing function produced a relatively higher force.

Stresses were calculated using the forcing function for the rigid fixture shown in Fig. 8.18 into its respective laboratory configuration. The resultant stresses are shown in Fig. 8.19. They qualitatively show similar results to the rigid fixture with the enforced motion input. This shows that the forcing function cannot change the response field as long as the response is linear. This is due to the fact that the only elastic mode shape being excited in this frequency range is not modified by the forcing function. The mode shape is only modified by the test fixture to which the component is attached.

8.5 Conclusion

This paper introduced and demonstrated a method for optimizing a structural dynamic test fixture to match the field configuration's FRFs in order to provide a higher fidelity test. Through the process of optimization, it was discovered that optimizing on matching FRFs was intractable due to the objective function's amount of local minima and the difficulties of finding the global minima. This difficulty was shown through an example of a single design parameter optimization problem and all of the local minima that existed in the objective function space.

One proposal for future work would be to determine if a smaller amount of design parameters could be used. An example of this would be to use shape optimization instead of topology optimization where a handful of dimensions were subject to change which would reduce the parameter space. Another proposal would be to explore other objective functions that still define the dynamics of the system. Redefining the objective function has the possibility of making the objective function space convex and eliminating some, many, or all of the local minima.

Lastly, this paper demonstrated that even an optimization solution that only solved to a local minima has the potential to have large improvements in the resulting stresses relative to a rigid fixture. These improvements are dependent on the field configuration and how well the stresses on the component can be replicated by fixed base modes. If the components stresses are a linear combination of the fixed base mode shapes of the component, then a rigid test fixture is the best fixture for the laboratory test.

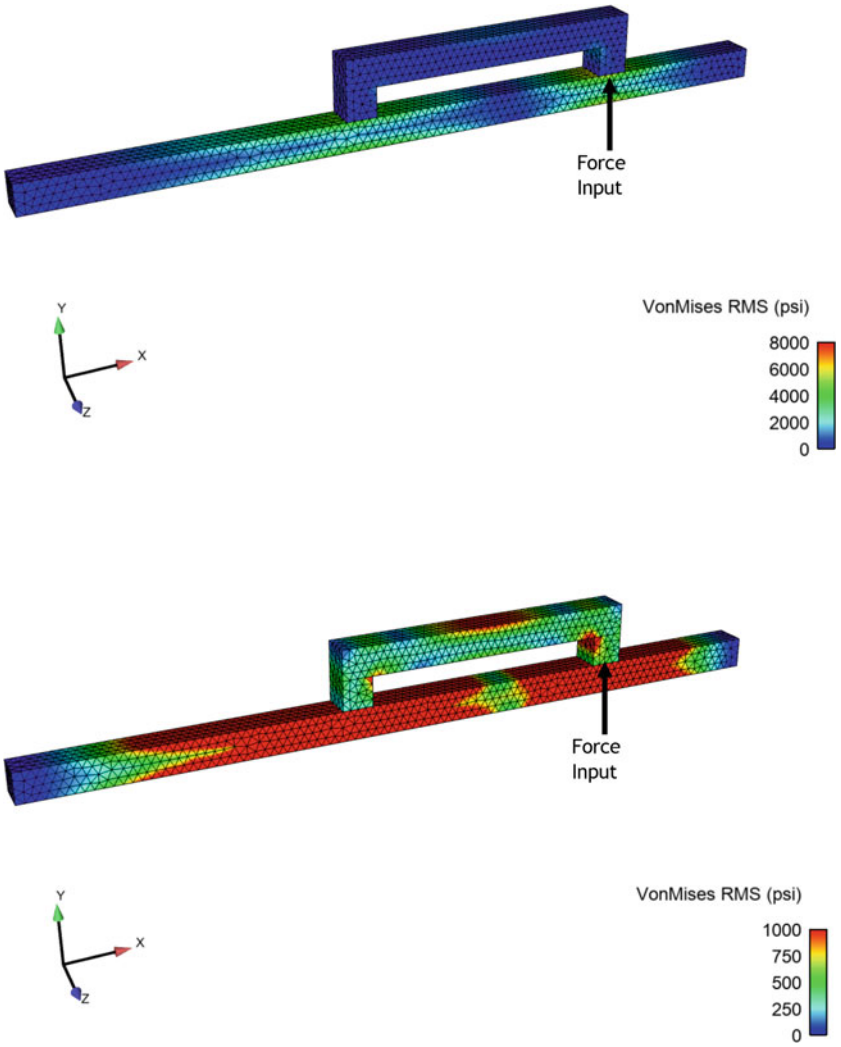

Fig. 8.19 Resultant stresses of the laboratory environment with a rigid fixture and a calculated input force. Top figure's stress is scaled identically to the optimized laboratory configuration and field configuration. Bottom figure's stress is scaled for qualitative evaluation

References

1. Daborn, P.M., Roberts, C., Ewins, D.J., Ind, P.R.: Next-Generation Random Vibration Tests, pp. 397–410. Springer, Cham (2014)
2. Edwards, T.: The effects of boundary conditions in component-level shock and vibration testing. In: Proceedings of the 79th Symposium on Shock and Vibration. Sandia National Laboratories, Albuquerque (2008)
3. On, F.J.: Mechanical impedance analysis for lumped parameter multi-degree of freedom/multi-dimensional systems. Technical report, NASA Goddard Space Flight Center, 1967
4. Sharton, T.D.: Development of impedance simulation fixtures. Shock Vib. Bull. **40**(Pt. 3), 230–256 (1969)

Chapter 9
Electromechanical Impedance Method for Applications in Boundary Condition Replication

Timothy A. Devine, V. V. N. Sriram Malladi, and Pablo A. Tarazaga

Abstract One of the most challenging parts of modeling structural dynamics is realistically replicating boundary conditions from either a theoretical or experimental perspective. In a finite element model, the mechanical impedance of bolted joints in an assembly can be modeled, as a first step, as an equivalent spring-damper connection. For relatively simple systems, the parameters of such an approximation are updated such that the dynamic characteristics of the model match with the jointed structure. When the assembled structure is in an operational environment, joints are one of the first components of the assembly to change their dynamic characteristics. As a result, identifying a change in their dynamics and further keeping track of the changes is burdensome. Additionally, if a change is detected, it is equally difficult to modify the structure to its previous state without exhaustive testing.

To address some of these issues, the present work leverages coupled electro-mechanical impedance-based techniques to monitor the jointed boundary conditions. In this technique, the mechanical impedance of the assembly is indirectly tracked by measuring the electrical impedance of the attached piezoelectric (PZT) system. In the present study, a PZT patch is bonded to the Box Assembly with a Removable Component (BARC) test structure with ten dry bolt connections. First, a baseline electro-mechanical measurement of the ideal assembly is determined and then the torque of the connecting bolts is then slightly altered. As a result, the dynamic properties of the BARC structure along with electrical impedance response of the PZT changes. The feasibility of tracking these changes and determining the modifications necessary to bring the system to its previous dynamic state is the focus of this work.

Keywords Boundary conditions · BARC · Piezoelectric actuator · Electromechanical impedance method

9.1 Introduction

The most accurate way to ensure similar testing of systems is to match mechanical impedance of the boundaries. Matched boundaries will ensure the structures response to an input will be repeatable. As assemblies become more and more complex, these boundaries become more complex to model in simulations or analytically.

Additionally, accessing the boundary becomes a difficult task as well. Placing any sensor at the boundary (or inline with the boundary) will cause an inherent change in the mechanical impedance of the structure. A system used to monitor and detect changes in the boundary conditions must be able to carry out this detection without modifying the connections. One potential method for doing this is the electromechanical impedance method [1]. This method allows for a non-invasive measurement method to characterize a specific configuration of a system. If a change occurs in the dynamic properties of the system, a corresponding change will occur in the impedance signature of the system. It has been used prior in literature to detect loosened bolts in assemblies [2] and detect mechanical damages in structures [3, 4].

Over the past few years, IMAC: A Conference and Exposition on Structural Dynamics has introduced a common test specimen, the Box Assembly with Removable Component (BARC). This piece was designed with the purpose of having a multi-pronged approach to study the boundary condition problem in a common test article. With the assembly having specified torques at the boundaries, it creates an ideal scenario to study the ability to detect changes in boundary conditions, specifically alterations to the specified torques.

T. A. Devine (✉) · V. V. N. S. Malladi · P. A. Tarazaga
Vibrations, Adaptive Structures, and Testing Lab, Department of Mechanical Engineering, Virginia Tech, Blacksburg, VA, USA
e-mail: timd@vt.edu

C. Walber et al. (eds.), *Sensors and Instrumentation, Aircraft/Aerospace, Energy Harvesting & Dynamic Environments Testing, Volume 7*, Conference Proceedings of the Society for Experimental Mechanics Series,
https://doi.org/10.1007/978-3-030-12676-6_9

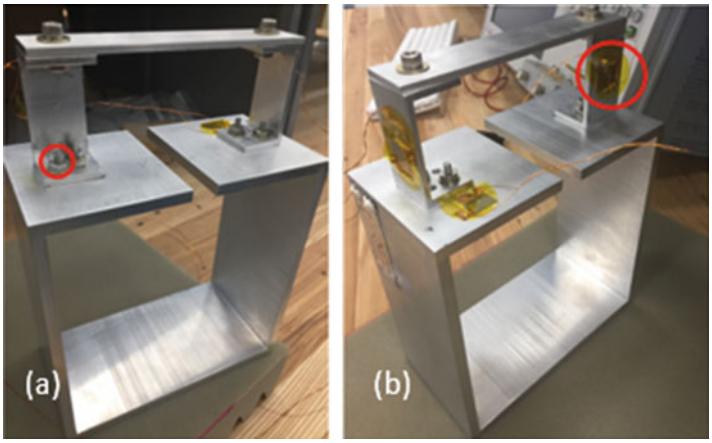

Fig. 9.1 Modified BARC with PZT actuators. The red circled bolt in (**a**) was the bolt modified during testing. The red circled PZT in (**b**) was the actuator used for testing

9.2 Background

This work aims to detect changes in a specified boundary configuration by using a collocated piezoelectric (PZT) sensor/actuator. The PZT was attached to the sub component of the BARC on the body of the C-shaped piece. Impedance was monitored using a Keysight impedance analyzer over 3 frequency ranges: 29–34 kHz, 57–62 kHz, and 99–106 kHz. These regions were chosen because they exhibited large peaks in the electromechanical impedance signature when the structure was excited over a range of frequencies from 10–150 kHz. Testing occurred first with each bolt tightened to the specification of 20 in-lb on the lower bolts and 50 in-lb on the upper bolts using an AC Delco digital torque wrench. There were four bolts removed, as can be seen in Fig. 9.1, due to the inability to maneuver the torque wrench into the space to tighten the bolts to specification. The impedance signature was then recorded for each of the frequency ranges and later used as a baseline measurement, which can be seen in Fig. 9.2. Once all frequency ranges were completed, one bolt, identified in Fig. 9.1a, was completely loosened off of the structure and then replaced, again to specification. The same testing procedure followed by removal was repeated to establish a baseline of the specified torque scenarios. All tests were carried out on a base of acoustic foam, as it is the common testing condition (free-free) for the BARC. The mean of all baseline torque tests was calculated and subtracted from each torque test to find the error from the mean in each test. This error was summed over all frequencies in the range of interest for each trial to create a total error for the range. The mean and standard deviation of the trials was then calculated.

After several baseline measurements, the torque of the bolt was lowered to 13.5 in-lb and again tested at the same frequency ranges. The mean of the baseline torque responses was subtracted from this trial and then was summed over the range of interest to once again create a sum of errors in the range. To determine if there was a significant difference, the summed error of the below specification torque was compared with the mean and standard deviation of the specified trials to determine how many standard deviations the below specification torque was away from the mean. Any value greater than 2 standard deviations (95%) was considered a significant difference.

9.3 Analysis

Figure 9.3 shows the errors of the specified torque cases from their mean as well as the below specification case's error with respect to the baseline mean for all frequency ranges. The lowest frequency band of 29–34 kHz showed the greatest difference between the baseline specification and the below specification cases, with the below specification case falling 12.98 standard deviations away from the mean. This showed a significant difference between the two conditions. The next

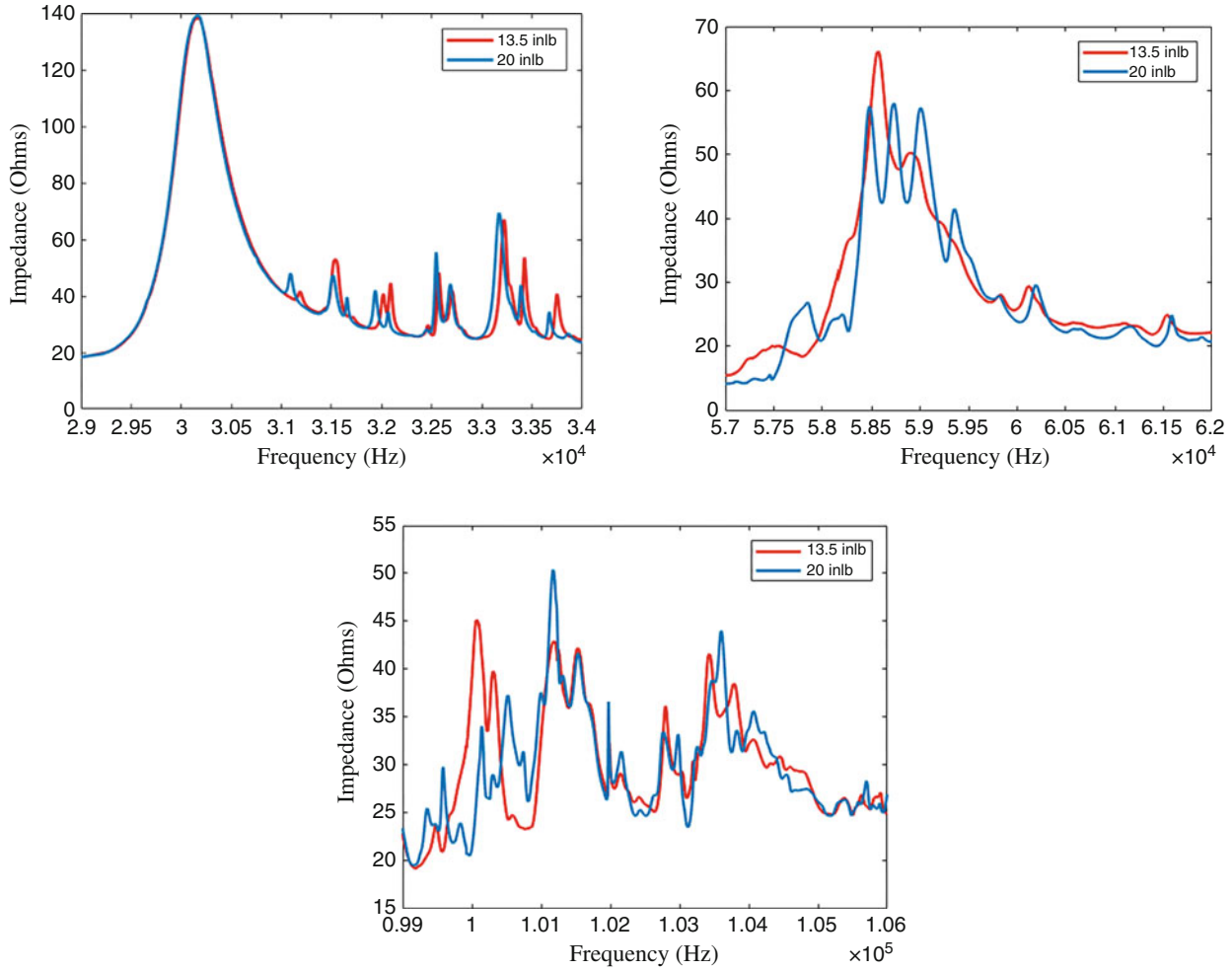

Fig. 9.2 Real component of the impedances of each frequency band of interest for the baseline mean and below specification torque cases

frequency band showed a difference between the baseline and below specification cases, with the below specification case being 4.87 standard deviations from the mean baseline. The final band of 99–106 kHz showed a significant difference, with the below specification case 5.10 standard deviations from the mean baseline. All ranges showed some significant differences, however the first range seems to be the most repeatable as it had the lowest mean error between the baselines with the smallest standard deviation of the bands. This can be seen in Table 9.1.

9.4 Conclusion

This study was capable of distinguishing a below specification torque in the structure using PZT actuators in the impedance method. The first frequency band showed the most promise in determining a difference, with the below specification error being over 12 standard deviations away from the error of the baseline tests.

Future studies conducted will test other bolts being loosened with more PZT actuators being used on the structure. If a baseline impedance can be well enough established that any bolt on the assembly can be loosened then the impedance method will be able detect this bolt. A machine learning algorithm will be developed in future works to attempt to determine if the assembly is off from specification, which bolt is off specification and potentially by how much torque is it off specification. Future studies will also include larger sample populations as well as over specification torques.

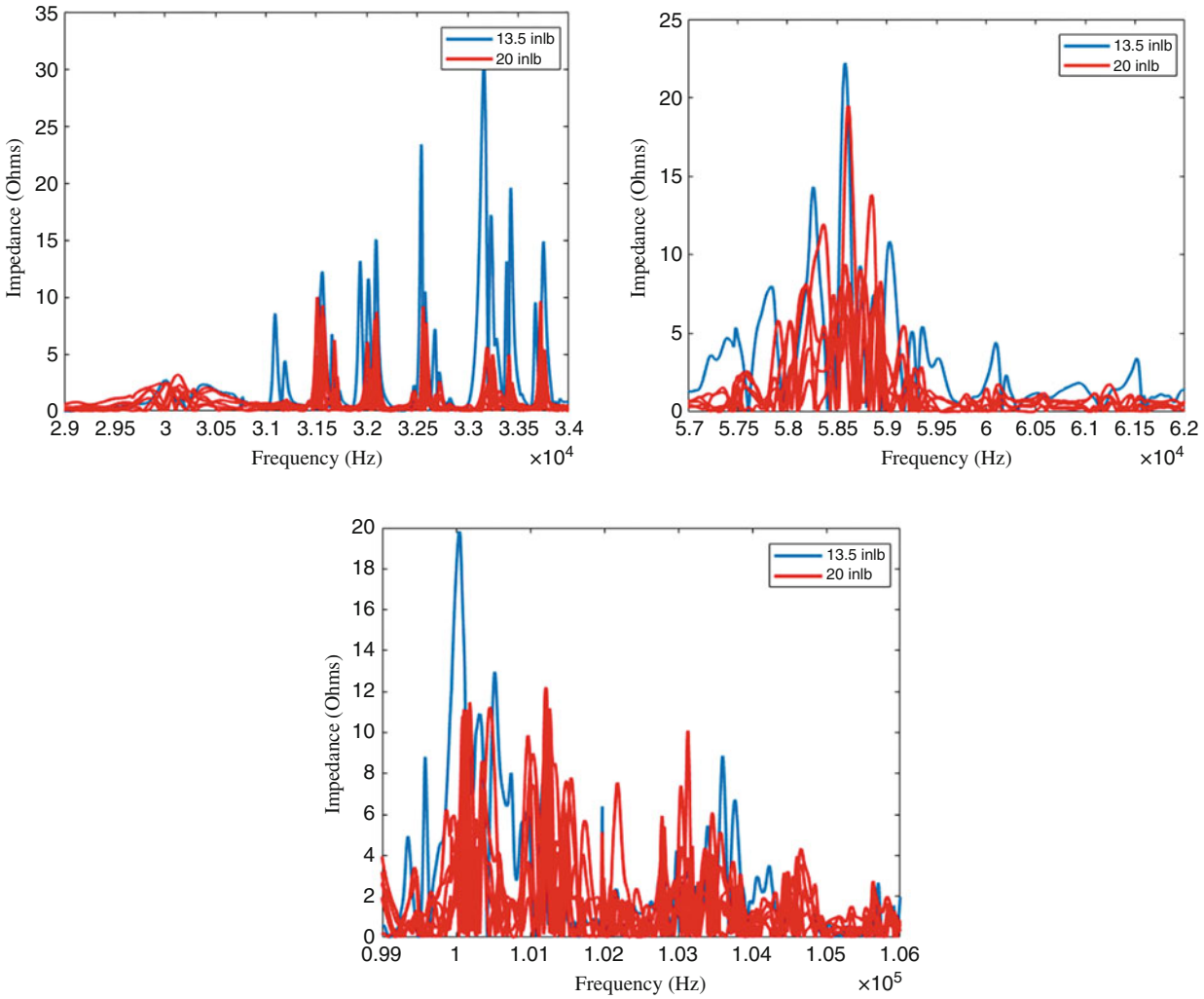

Fig. 9.3 Errors between the baseline tests and the mean of the baseline compared to the below specification error for the 3 frequency bands of interest

Table 9.1 Means and standard deviation of the baseline cases for the frequency bands of interest

Frequency range (kHz)	Mean error (Ohms)	Standard deviation (Ohms)
29–34	1192	226
57–62	2294	560
99–106	2649	342

Acknowledgements Dr. Tarazaga would like to acknowledge the support provided by the John R. Jones III Faculty Fellowship.

References

1. Liang, C., Sun, F., Rogers, C.: An impedance method for dynamic analysis of active material systems. J. Vib. Acoust. **116**, 120–128 (1994)
2. Priya, C., Reddy, A., Rao, G., Gopalakrishnan, N., Rao, A.: Low frequency and boundary condition effects on impedance based damage identification. Case Stud. Non Destr. Test. Eval. **2**, 9–13 (2014)
3. Peairs, D., Tarazaga, P., Inman, D.: Frequency range selection for impedance-based structural health monitoring. J. Vib. Acoust. **129**, 701–709 (2007)
4. Park, G., Sohn, H., Farrar, C., Inman, D.: Overview of piezoelectric impedance-based health monitoring and path forward. Shock Vib. Digest. **35**(6), 451–463 (2003)

Chapter 10
Latest Design Trends in Modal Accelerometers for Aircraft Ground Vibration Testing

Yves Govers, Julian Sinske, and Thomas Petzsche

Abstract Accelerometers are widely encountered in structural analysis applications such as modal analysis with vibrational or impact input excitation and operational modal analysis. This paper aims to outline design trends and requirements for acceleration sensors in order to insure optimal structural analysis measurement results. Key parameters for a performing modal sensor are: sensitivity, mass, noise level, amplitude and phase frequency response, as well as thermal transient response, thermal sensitivity response, transverse sensitivity (cross axis), base strain and survivability which will be taken into detailed consideration in this paper.

Nowadays three IEPE (Integrated Electronic Piezo Electric) sensor designs can be considered: piezo-ceramic shear, piezo-bending beam and piezo-crystal shear mode sensing elements. Unfortunately, none of the sensor technologies available on the market today will allow for the best of all parameters mentioned earlier. Advantages and disadvantages have to be considered in order to make the optimal choice. Even though Variable Capacitive (VC) MEMS sensors can be used in cases of operational modal analysis at ultra-low frequencies, such as Bridge Structural Testing or Monitoring, only IEPE technology will be in this study.

Besides the technical properties of an accelerometer, the handling qualities during installation and removal are extremely important for high channel count systems. Installation time, error rate and reliability for more than 10 years during several tests a year are of special interest for the user. Among the considerations made here, easy monitoring and sensitive axis alignment compared to the overall coordinate system will be examined.

The German Aerospace Center (DLR) will illustrate the applicability of accelerometers in context of industrial testing such as Ground Vibration Testing (GVT) of aircraft structures or structural and modal testing of wind turbine blades where innovative methods such as allowing one free adjustable degree of freedom around one rotational axis in order to freely orient the sensitive axis.

Keywords Accelerometers · IEPE · MEMS · Modal analysis · Aircraft ground vibration testing (GVT)

10.1 Introduction

To measure mechanical properties like force, pressure or acceleration, piezoelectric sensors have a long tradition in the industry. Since the beginning, Kistler Instruments is one of the leading companies in this technology and helped drive the development forwards. Piezoelectric sensors are based on the principle that a mechanical deformation to a non-centrosymmetric crystal lattice system, like quartz or some ceramic materials results in a proportional electric charge on the electrodes. This charge signal can be converted with a charge converter into an analog voltage signal. If the sensor is used for a fixed measurement range, low impedance IEPE sensors with integrated charge to voltage converters are commonly used.

Acceleration sensors have a diverse application use for noise and vibrations measurements and also in experimental modal analysis. For best results, the sensor should strive to be invisible to the structural unit under test having high sensitivity, low mass, high signal to noise ratio and very little cross talk effects to other influences. Other aspects that should be minimized are cross axis sensitivity, base strain sensitivity, sensitivity against case deformations, thermal transient response for sudden

Y. Govers · J. Sinske
DLR – German Aerospace Center, Institute of Aeroelasticity, Göttingen, Germany

T. Petzsche (✉)
Kistler Instrumente GmbH, Sindelfingen, Germany
e-mail: thomas.petzsche@kistler.com

C. Walber et al. (eds.), *Sensors and Instrumentation, Aircraft/Aerospace, Energy Harvesting & Dynamic Environments Testing, Volume 7*, Conference Proceedings of the Society for Experimental Mechanics Series,
https://doi.org/10.1007/978-3-030-12676-6_10

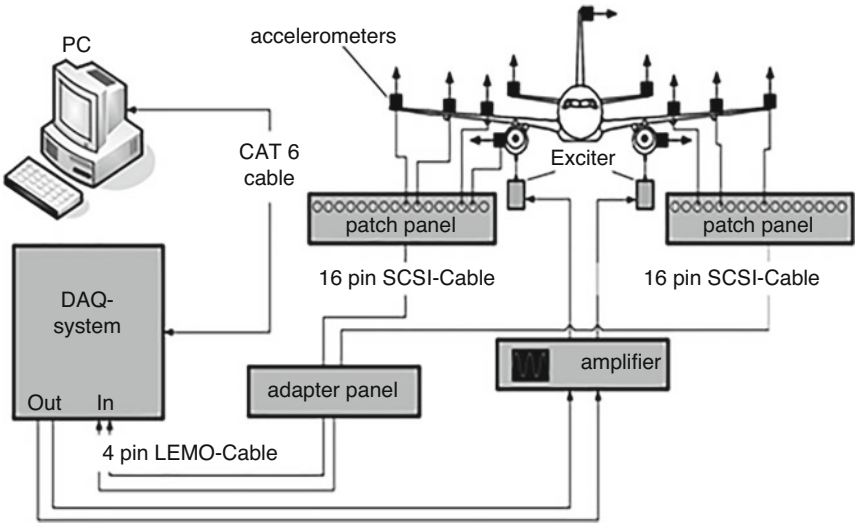

Fig. 10.1 Scheme of data acquisition for ground vibration testing at DLR

(a) **(b)**

Fig. 10.2 Recent ground vibration tests performed by the German Aerospace Center from Göttingen Germany. (**a**) Beluga XL ground vibration test in June 2018 [11]. (**b**) Wind turbine blade modal testing in Feb. 2018

temperature changes, low thermal sensitivity shifts and others. For a guideline of common practices of these test procedures where the above sensor properties are in most cases standardized refer to international standards like the older series of ISO 5743 [1], which is transferred to the new standard series part by part ISO16063 [2] or national standards like the RP37.2 of the Instrumentations Society of America [3]. These standards provide in most cases a guideline for traceable and uniform specifications of vibration and shock sensors. In some cases, specifications are not standardized, such as resolution, threshold and signal to noise related data.

This paper describes the requirements of accelerometers for modal investigations of large mechanical structures like Ground Vibrations Tests (GVT) on complete airframe structures or wind mill blades as they are used more and more frequently for renewable power generation. This kind of modal testing is mainly a MIMO test configuration (multiple input—multiple output) where several electrodynamic modal shakers excite a structure in swept sine or white noise modes to its natural frequencies or Eigen modes. A network of up to several hundred accelerometers measure the signals at the test structure is necessary to resolve the mode shapes from such complex structures. A general scheme of test setup and data acquisition during ground vibration testing is given in Fig. 10.1.

In most of structural analysis applications, easy monitoring and sensitive axis alignment compared to the overall coordinate system are required. Sensor mounting methods such as stud, clip, wax or magnet mounting will be considered. In addition, innovative methods such as allowing one free adjustable degree of freedom around one rotational axis in order to freely orient the sensitive axis can be used. Such a solution using a cylindrical sensor shape that can freely rotate in a specifically designed housing will be presented here.

For selected optimal designs, two examples of modal testing applications of large structure using MIMO methods will be in focus: (a) Ground Vibration Testing of Aircraft and (b) Structural and Modal Testing of Wind turbine blades shown in Fig. 10.2.

10.2 Requirements of Accelerometers for Large Structure Modal Testing

Large test structures described here are mainly characterized by low frequencies of their structural modes (Eigen frequencies) and a wider scale of amplitudes. This is a result of the measurement points being different distances away from the driving points. Special requirements are related to the numerous numbers of input channels and the possibilities to arrange mounting and demounting of the sensors to the test structure for easy, quick and reliable test arrangements.

For the assembly of the numerous sensors to the test structure, it should be easily possible to adjust the measurement direction in one degree of freedom (DOF) as shown in Fig. 10.3. For this purpose the sensing element has to be designed in a compact, small cylindrical housing which allows one rotational degree of freedom within a cubic polymer adapter by a small special adjustment wrench, where the sensitive direction of the accelerometer can be fixed by a clamping mechanism. This one axis sensor can now be arranged in a planar way in three axes (Fig. 10.4) to measure concurrent acceleration components in an orthogonal coordinate belonging to a unified coordinate system of the test structure. The acceleration vectors measured are positioned to the sensitive axis intersecting with the center of gravity (COG) of sensor seismic mass.

In addition to the housing and adapter, certain specifications have been required which are summarized in Table 10.1.

In order to answer the application requirements, the full scale range has been set to $\pm 50\ g_n$. The frequency response should cover 0.5 Hz to 1 kHz with the sensor mounted in the adapter for a sensitivity deviation of $\leq \pm 5\%$ referenced at 10 Hz. Phase shift response should not deviate more than 15° at 0.5 Hz and phase shift congruence between sensors should be within 3°. Last but not least, noise should be at the lowest feasible range. This will allow the threshold to resolve a measurement signal as low as possible. Details are listed in Table 10.2.

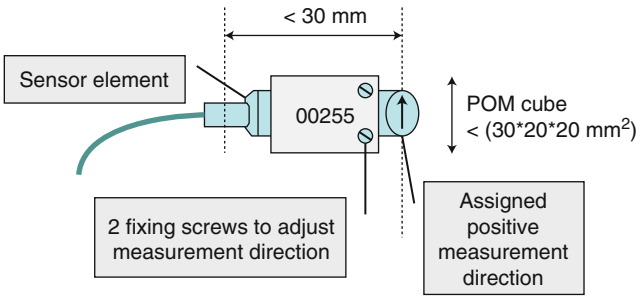

Fig. 10.3 Sensor and adapter requirements for adjusting sensitive direction

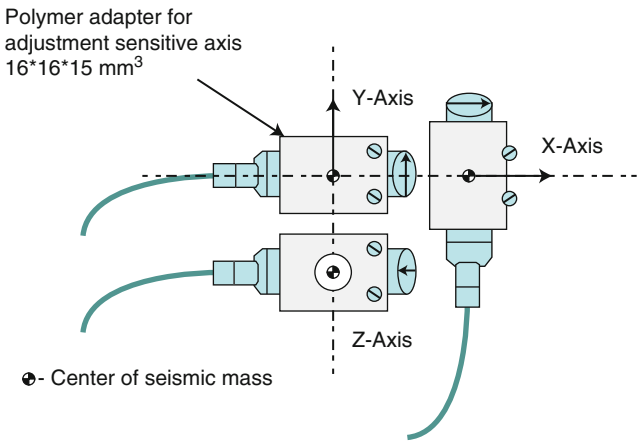

Fig. 10.4 Instance for triaxial planar arrangement of the accelerometer with COG marked

Table 10.1 Comprehensive comparison of specifications for ceramic shear, crystal shear, bending bimorph and variable capacitance accelerometers for typical sensors

	Piezoceramic shear	Piezocrystalline shear, PiezoStar	Piezoelectric bending bimorph, PiezoBeam	Variable Capacitance (MEMS)
Electronic interface	IEPE	IEPE	IEPE	Differential or single ended, bipolar
Power supply	Constant current 2 . . . 18 mA	Constant current 2 . . . 18 mA	Constant current 2 . . . 20 mA	Excitation voltage 6 . . . 50 V DC
Full Scale range	$\pm 50\ g_n$	$\pm 50\ g_n$	$\pm 50\ g_n$	$\pm 50\ g_n$
Amplitude non-linearity	±1%	±1%	±1%	±0.3%
Sensitivity	100 mV/g_n	100 mV/g_n	100 mV/g_n	80 or 160 mV/g_n
HP-Corner frequency (−5%)	0.5 Hz	0.5 Hz	0.5 Hz	0 Hz DC
Max. Frequency for sensitivity deviation for (+5%) to reference	10 kHz	10 kHz	5 kHz	1.5 kHz
Mounted resonance frequency	>50 kHz	>40 kHz	>25 kHz	>5.8 kHz
Damping ratio of seismic system, nom.	Very weak	Very weak	Very weak	0.7
Phase shift (max.) @ 0.5 Hz	15°	15°	15°	0°
@ 10 Hz	1°	1°	1°	2°
@ 100 Hz	1°	1°	1°	10°
Wideband threshold 1 Hz to 10 kHz	400 μg_n	1200 μg_n	360 μg_n	2450 μg_n
Thermal sensitivity shift	−54 . . . 23 °C: 0.07%/K 23 . . . 100 °C: −0.01%/K	0.004%/K	0.16%/K	0.01%/K
Thermal transient response	Low	Very low	High, constant thermal ambient conditions are required	Very low
Operating temperature range	−54 . . . 100 °C	−55 . . . 165 °C	−40 . . . 65 °C	−55 . . . 125 °C
Cross axis sensitivity shift, typ.	2%	3%	1.5%	1%
Base strain sensitivity @250μStrain	0.002	0.015	0.004	
Shock survivability 1 ms haversine	5000 g_n	2000 g_n	5000 g_n	6000 g_n
Mass, sensor	2.9 g	7.6 g	3.5 g	15 g
Ground isolation	With accessory	Yes	With accessory	Yes
Reference type	8774B050S	8703A50	8640A50	8316A050..

10.3 Accelerometer Technologies for Modal Applications

For the realization of the most common technologies available today in sensor design, consider these following principles:

- the piezoelectric ceramic shear technology
- the piezoelectric crystal shear technology, based on present advanced crystal technologies like Kistler PiezoStar® KI-85
- the piezoelectric bimorph bending beam technology, called PiezoBeam® within Kistler and a
- K-Beam® MEMS sensor design in silicon based on a variable capacitive (VC) sensing element.

Designs such as traditional piezoresistive accelerometer technology were not consider as it is believed that the highly sensitive sensor elements made in the past in the bonded strain gage technology are costly and less robust against environmental influences, like shock or misuse. Piezoresistive accelerometers have also been replaced more and more by variable capacitive MEMS sensor technologies in ranges below 200 g.

Table 10.2 DLR Application requirements vs. type 8000M095/800M166 specifications

	Requirements	Sensor Solution Type 8000M095 with Adapter 800M166
Sensitive axis	Uniaxial, 360° rotatable (within polymer adapter)	Uniaxial, 360° rotatable (within POM™ Adapter 800M166)
Electronic interface	IEPE	IEPE
Power supply	Constant current 2 . . . 18 mA	Constant current 2 . . . 18 mA
Full Scale range	$\pm 50\ g_n$	$\pm 50\ g_n$
Amplitude non-linearity (3 Hz . . . 1 kHz)	±2%	±1%
Sensitivity, ref.	100 mV/g_n ± 2%	100 mV/g_n ± 2%
HP-Corner frequency (−5%)	0.5 Hz	0.5 Hz
Max. Frequency for sensitivity deviation for (+5%) to reference	1 kHz	1 kHz
Mounted resonance frequency (without adapter)	>10 kHz-	>62 kHz without adapter
Damping ratio of seismic system, nom.	Very weak	Very weak
Phase shift (max.)		
0.5 Hz to 3 Hz	15°	15°
3 Hz to 1 kHz	1°	1°
Phase deviation between sensors 0.5 Hz . . . 1 kHz	<±3°	<±3°
Wideband threshold 1 Hz to 10 kHz	–	400 μg_n
Thermal sensitivity shift	–	−54 . . . 23 °C: 0.07%/K 23 . . . 100 °C:-0.01%/K
Thermal transient response	Low	Low
Operating temperature range	−15 . . . 60 °C	−54 . . . 100 °C
Cross axis sensitivity shift, typ.	2%	2%
Base strain sensitivity @250μStrain	–	0.002 (8774B)
Shock survivability 1 ms haversine	5000 g_n	5000 g_n
Mass, sensor	<25 g	10 g
Ground isolation	With accessory	With accessory
Size	<20*20*30 mm^3	

The MEMS VC technology, like Kistler K-Beam® sensors [4], would open the frequency response down to static accelerations and is mainly very shock resistant against misuse, such as dropping the sensor to the floor. On the opposite side with this latest technology, sufficient low noise characteristics are not available in comparison to the IEPE technology. A main problem here would become the shape of the sensor and the damping characteristics of the seismic element. The damping coefficient of approx. 0.7 offers a steady changing phase shift between electrical output and mechanical input signal from DC to the upper frequency limit, which makes them unsuitable for this kind of application. In addition, it has not been possible to accommodate a MEMS sensing element in a compact, small cylindrical housing to allow one rotational degree of freedom to adjust the sensitive direction of the accelerometer. Consequently this principle has not been considered for use.

All the piezoelectric sensor technologies for applications here are capable of 120 °C operation and in some cases up to 165 °C, with today's IEPE technology and its integrated charge converter already in the sensor housing. This low impedance output signal opens the door for long cables with sufficiently low EMI problems and is today's most technical standard. In addition, the lower frequency response can be accommodated down to 0.5 Hz with reasonable phase response as required by the application. The IEPE combination with TEDS (Transducer Electronic Data Sheets) belonging to IEEE 1451.4 allow sensor identification and read out of sensor data by the data acquisition system. This arrangement enables channel range scaling as Class I type sensors with digital and analog signal path in the same coaxial wiring.

Since its introduction over 30 years ago, the PiezoBEAM® [5] has become a successful line of small and low mass accelerometers specifically designed for modal and seismic applications. The PiezoBEAM combines the requirements of a lightweight and precise sensor for measurement of linear accelerations, with sufficient wide frequency range. It is the first choice of sensors for modal and seismic applications where a high signal to noise ratio for high resolution data and lowest mass loading are required. These accelerometers are basically the lowest weight sensor with the highest resolution on the

market and therefore ideal for the application of interest. For example, since the mid-1990's and until the end of the program in 2011, the NASA Space Shuttle program (GVT) has been performed at various locations using these types of sensors for monitoring the conditions of the shuttle and its payloads [6]. Manufacturing these sensors with very low rates of cross axis sensitivity can be easily achieved in the order of 1.5%.

It should also be noted that a disadvantage of such technology can be the limited use under transient thermal conditions. The thermal transient response of the bending bimorph has been greatly lowered by design changes, but is still in a magnitude where sudden temperature changes can sometimes saturate the output signal.

Using a shear design is the preferred method to keep thermal transient response as low as possible during quick thermal cycling. Two technologies are considered; ceramic shear or crystalline shear based on Kistler PiezoStar® crystal KI-85 [7]. In addition, especially in applications with steady thermal cycling PiezoStar® sensors have advantages, as their thermal sensitivity shift between −55 and 165 °C is very low (in the range of 3% deviation overall). The very stiff KI-85 piezoelectric crystal material provides a very flat sensitivity response with almost no frequency dependency, in comparison to ceramic shear which always exhibits a slope in the frequency response of the sensitivity. On the other end, their dynamic range is, unfortunately limited compared to a ceramic shear design; the noise level is higher, consequently leading to a higher threshold.

Table 10.1 is offering an exhaustive comparison of all four different principles based on specific existing sensors.

10.4 The Near-Perfect Sensor Solution

Ultimately, a ceramic shear element has been selected. A specific design has been derived from Kistler's new sensor family type 8774B050 and 8776B050 elements. This design provides ruggedness, low mass and low threshold for a high dynamic range of 102 dB. In addition, the thermal sensitivity shift and the thermal transient response are sufficiently low for the application (within ambient temperature ranges from 0 to 40 °C). The element frequency response for sensitivity and phase falls within the tight specified limits. On the other end, the cross axis sensitivity of less than 2% requires a selection process during production. The technical specifications are summarized in Table 10.2.

Based on this technology, the sensor element type 8000M095 has been designed in a cylindrical shape with one hexagonal end for adjustment of the sensitive direction (see Fig. 10.5). On the connector side is a cone-shape form in order to securely fix the sensor element in the cubic adapter type 800M166, see Fig. 10.6. After adjustment, two small metric M3 Nylon headless screws are securing the sensor element within the adapter. An 8 mm hex wrench can be used to adjust the sensitive direction during installation. The sensor-in-adapter assembly is then glued to the structure under test and provides ground isolation to prevent ground loops. The sensitive direction can easily be identified by an arrow at the hex face side and is more visible by a red dot at the arrow top. Figure 10.7 shows the whole sensor assembly with cable for illustration.

10.5 Installation Procedure for the Accelerometers

The sensors are affixed to the structure using double-adhesive tape. The tape is already applied to the bottom of the sensor housing before starting the test campaign. Therefore they can be very quickly installed on the cleaned surface of the test structure, see Fig. 10.8a. A tri-axial arrangement of three uni-axial accelerometers is presented in Fig. 10.8b. This installation requires the rotation of two accelerometers within its housing to account for both horizontal axes of the local coordinate system.

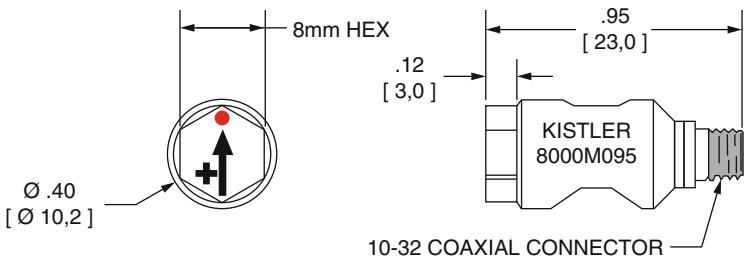

Fig. 10.5 Design of the sensor type 8000M095

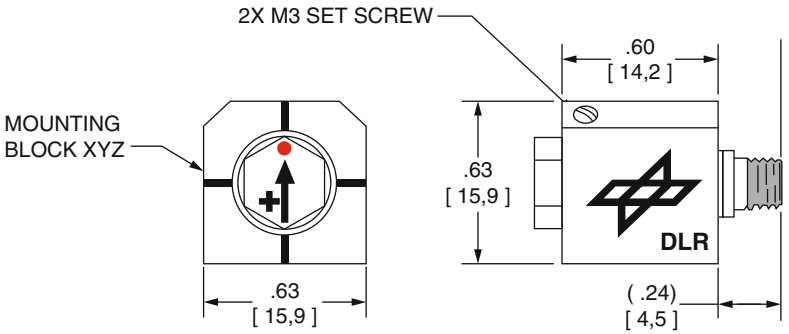

Fig. 10.6 Design of the insulating adapter type 800M166 accommodating the sensor element type 8000M095

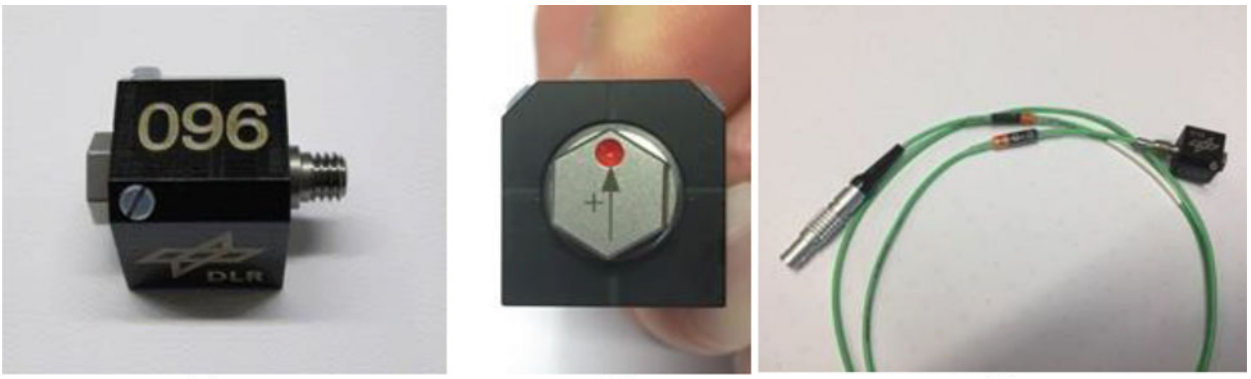

Fig. 10.7 Sensor type 8000M095 with adapter 800M166 and cable assembly. (**a**) Side View. (**b**) Front View. (**c**) With Cable Assembly

Fig. 10.8 Sensor installation. (**a**) uni-axial application. (**b**) tri-axial application

A reliable sensor installation needs to be done within a very short time duration. Especially in the final phase of an aircraft development, added pressure forces the provider of a GVT to install up 600 sensors within three days. For DLR as GVT supplier, with several hundred accelerometers, it is therefore important to have clear documentation of the entire sensor installation. For this reason the sensor housing is engraved with a unique DLR internal sensor number for photo documentation. This number also reflects the channel on the acquisition system which guarantees fail-safe cabling to the measurement system.

10.6 Typical Test Setup and Results

A typical application of the described acceleration sensor is shown in Fig. 10.9 for the modal test on a wind turbine blade [8]. The experimental modal analysis of this wind turbine blade was performed within the German research project SmartBlades2. Within the scope of this project passive load alleviation techniques are analyzed. The analyzed wind turbine blade has been designed with a passive bend-twist coupling mechanism to reduce the root bending moment for gust encounters. Therefore a detailed analysis of the structural behavior was of high interest.

This test was conducted with a high resolution sensor setup of ∼300 acceleration sensors. The sensor setup is described in Fig. 10.10. Each arrow in Fig. 10.10 represents a uni-axial acceleration sensor.

Typically time data is acquired from all acceleration and also force sensors. Time histories of all accelerometers from a swept-sine excitation ranging from 5 to 35 Hz are visualized in Fig. 10.11. Swept-sine excitation yields good signal to noise ratio and also provides the possibility to identify non-linearities of all kinds of structures in cases using different force levels from the same excitation location.

The conversion to frequency domain is accomplished using the Welch method with overlapping Hanning windows while referencing the introduced forcing signal. The frequency response functions shown in Fig. 10.12 are calculated from the time histories presented in Fig. 10.11.

Finally a modal identification algorithm needs to be applied to the frequency response functions which yield the modes for the experimental modal model. Some modes from this modal test campaign are shown in Fig. 10.13. The identified modes are used for finite element model validation and updating.

Fig. 10.9 Setup of measurement campaign on wind turbine blade

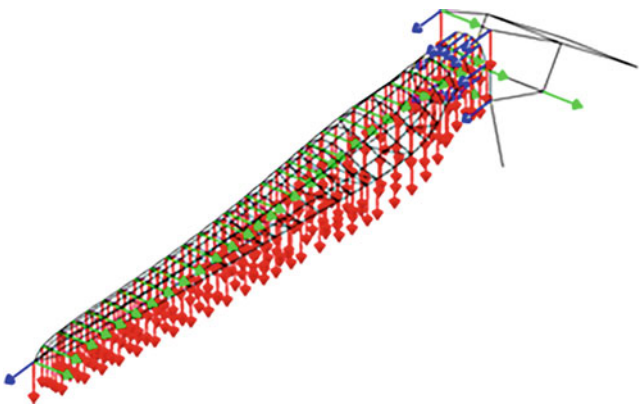

Fig. 10.10 Sensor setup for high resolution modal testing

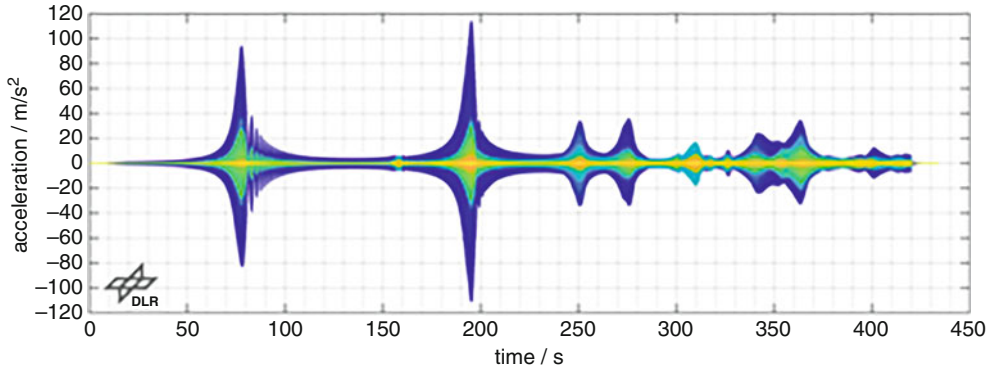

Fig. 10.11 Time data from swept-sine excitation of ∼300 accelerometers

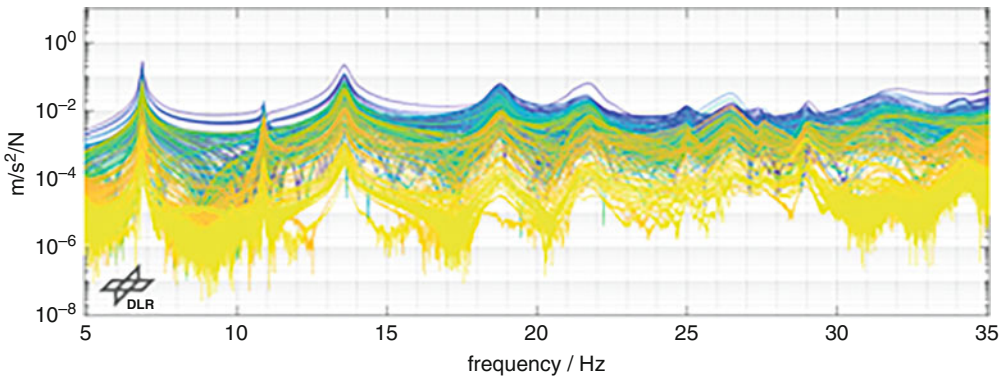

Fig. 10.12 Frequency response functions from time data of Fig. 10.11

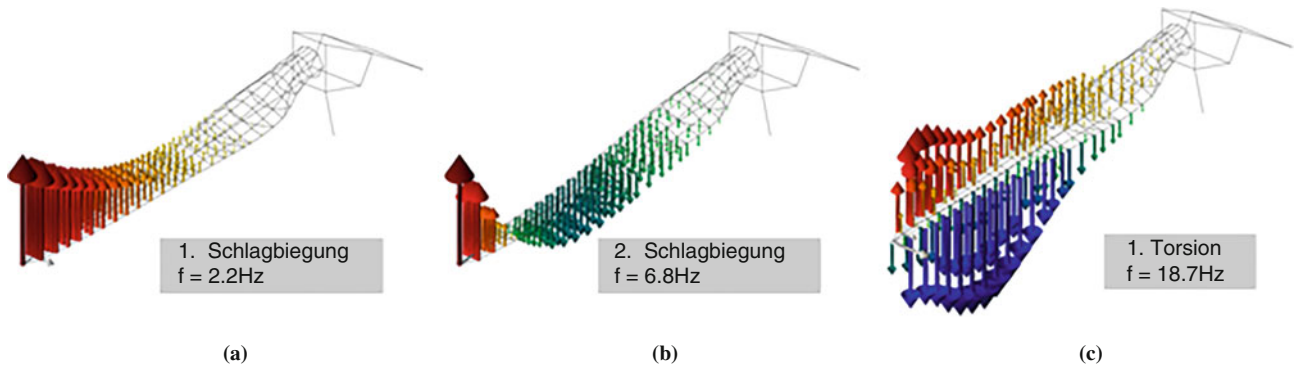

Fig. 10.13 Some identified mode shapes. (**a**) 1st bending mode. (**b**) 2nd bending mode. (**c**) 1st torsion mode

10.7 Summary and Conclusions

Today, the properties of an appropriate accelerometer from different technologies, mounting adapter and mounting procedure have been described and incorporated into the test procedure necessary to accomplish large scale modal tests such as the GVT of airframe structures or similar. The techniques have been developed over many years following strict precautions and guidelines and have proven to yield excellent results under very tight time constraints. Even a very sensitive test structure can be thoroughly and efficiently tested if a well-trained, disciplined group follows well defined and proven procedures. This involves a good working relationship between hardware installers, data collectors and structural analysts. Every aspect of the test is equally important and all are interrelated [9, 10].

References

1. ISO 5347-xx series: “Methods for the calibration of vibration and shock transducers”, here in detail: ISO 5347-13:1993, Part 13: Testing of base strain sensitivity; ISO 5347-14:1993, Part 14: Resonance frequency testing of undamped accelerometers on a steel block, replaced by ISO16063-32; ISO 5347-15:1993, Part 15: Testing of acoustic sensitivity; ISO 5347-16:1993, Part 16: Testing of torque sensitivity; ISO 5347-17:1993, Part 17: Testing of fixed temperature sensitivity; ISO 5347-18:1993, Part 18: Testing of transient temperature sensitivity; ISO 5347-19:1993, Part 19: Testing of magnetic field sensitivity; ISO 5347-22:1997, Part 22: Accelerometer Resonance Testing-General Methods
2. ISO 16063-xx:1998 “Methods for the calibration of vibration and shock transducers” here in detail: ISO 16063-1: 1998: “Part 1: Basic concepts”; ISO 16063-21:2003 + Cor. 1:2009 + Amd. 1:2016: Vibration calibration by comparison to a reference transducer; ISO 16063-31: Part 31: Testing of transverse vibration sensitivity; ISO 16063-32: Part 32: Resonance testing-Testing the frequency and the phase response of accelerometers by shock excitation; ISO 16063-43: 2016: Part 43: Calibration of accelerometers by model-based parameter identification
3. Instrumentation Society of America; Recommended Practices: ISA-RP37.2-1982 (1995): Guide for Specifications and Tests for Piezoelectric Acceleration Transducers for Aerospace Testing
4. Kistler K-Beam® Capacitive Accelerometers – Micromachined for Static Response; Sound & -Vibration 06.1996 (Kistler Special Print 20.179e-0696), present data sheet type 8316A_003-324a-08.17
5. Kubler, J.M., Bill, B.: PiezoBeam® accelerometers: a proven and reliable design for modal analysis, Kistler Special Print 20.148e-08.93
6. Insalaco, M.D., Henning, T.B.: An efficient shuttle modal inspection system test, Kistler Special Print 920-243e-04.04
7. Zwolinski, B., Petzsche, T., Schnellinger, J., Kinsley, N.: Precision vibration measurement in dynamic temperature environments with PiezoStar® IEPE accelerometers, Kistler Special Print 920-360a-08.07
8. Gundlach, J., Govers, Y.: Experimentelle Modalanalyse an einem aeroelastisch optimierten Rotorblatt mit Biege-Torsions-Kopplung im Projekt SmartBlades2. In: 9. VDI Fachtagung Schwingungen von Windenergieanlagen. Bremen, Germany (2018)
9. Govers, Y., Boeswald, M., Lubrina, P., et al.: AIRBUS A350XWB Ground Vibration Testing: Efficient techniques for customer oriented on-site modal identification. In: International Conference on Noise and Vibration Engineering. KU Leuven, Belgium (2014)
10. Boeswald, M., Vollan, A., Govers, Y., et al.: Solar impulse – ground vibration testing and finite element model validation of a lightweight aircraft. In: International Forum on Aeroelasticity and Structural Dynamics. Paris, France (2011)
11. Airbus Industries: https://www.airbus.com/newsroom/press-releases/en/2018/06/airbus-belugaxl-passes-ground-vibration-test.html#media-list-image-image-all_ml_0-2

Chapter 11
Test-Based Uncertainty Quantification and Propagation Using Hurty/Craig-Bampton Substructure Representations

Daniel C. Kammer, Paul Blelloch, and Joel W. Sills Jr.

Abstract This work presents a method for uncertainty propagation that is consistent with the "building-block approach" in which components of a system are tested and validated individually instead of an integrated vehicle test and validation being performed. The approach gives a unified methodology for representing and quantifying uncertainty in a Hurty/Craig-Bampton component based on component test results and propagating the uncertainty in component models into system-level predictions. Uncertainty in the Hurty/Craig-Bampton representations is quantified using a new hybrid parametric variation approach based on Soize's maximum entropy method. The proposed approach combines parametric and nonparametric uncertainty by treating the Hurty/Craig-Bampton fixed-interface eigenvalues as random variables and treating the corresponding mass and stiffness as random matrices. The proposed method offers several advantages over traditional approaches to uncertainty quantification in structural dynamics: the number of parametric random variables is relatively small compared to the usually large number of potential random finite element model parameters; therefore, time-consuming parametric sensitivity studies do not have to be performed. In addition, nonparametric model-form uncertainty is easily included using random matrix theory. The method requires the selection of dispersion values for the Hurty/Craig-Bampton fixed-interface eigenvalues and the corresponding mass and stiffness matrices. Test/analysis frequency error is used to identify the fixed-interface eigenvalue dispersions, and test/analysis cross-orthogonality is used to identify the Hurty/Craig-Bampton stiffness matrix dispersion value. Currently, the mass matrix dispersion is based on engineering judgment, past experience, and historical results. The proposed uncertainty quantification methodology is applied to the Space Launch System liftoff configuration. Robustness of the attitude control system is studied by propagating derived component uncertainty models into gain uncertainty in specific transfer functions relating engine inputs to rate sensors on the core stage, and frequency uncertainty for the fundamental bending and roll modes.

Keywords Uncertainty quantification · Hurty/Craig-Bampton · Random matrix · Maximum entropy · Model-form

Acronyms

aftRGA	Aft rate gyro assembly
COV	Coefficient of variation
CS	Core stage
DCGM	Diagonal cross-generalized mass metric
DOF	Degree of freedom
FEM	Finite element model
GNC	Guidance, navigation, and control
HCB	Hurty/Craig-Bampton
HPV	Hybrid parametric variation
ICPS	Interim cryogenic propulsion stage
ISPE	Integrated spacecraft payload element
itRGA	Intertank rate gyro assembly
LSRB	Left solid rocket booster

D. C. Kammer (✉) · P. Blelloch
ATA Engineering, Inc., San Diego, CA, USA
e-mail: daniel.kammer@wisc.edu

J. W. Sills Jr.
NASA Johnson Space Center, Houston, TX, USA

C. Walber et al. (eds.), *Sensors and Instrumentation, Aircraft/Aerospace, Energy Harvesting & Dynamic Environments Testing, Volume 7*, Conference Proceedings of the Society for Experimental Mechanics Series,
https://doi.org/10.1007/978-3-030-12676-6_11

LVSA	Launch vehicle stage adapter
MC	Monte Carlo
ME	Maximum entropy
MEM	Modal effective mass
MPC	Multipoint constraint
MPCV	Multi-purpose crew vehicle
MSA	MPCV stage adapter
ODM	Off-diagonal generalized mass metric
PDF	Probability distribution function
RINU	Replaceable inertial navigation unit
RMS	Root mean square
RMT	Random matrix theory
RSRB	Right solid rocket booster
RSS	Root sum square
SE	Strain energy
SLS	Space launch system
TAM	Test analysis model
UQ	Uncertainty quantification
XO	Cross-orthogonality

11.1 Introduction

In many cases involving large aerospace systems, it is difficult, uneconomical, or impossible to perform an integrated system modal test. However, it is still vital to obtain test results that can be compared with analytical predictions to validate models, so the "building-block approach" is used, in which system components are tested individually, and component models are correlated and updated to agree with test results as closely as possible. The Space Launch System (SLS) consists of a number of components that are assembled into a launch vehicle. In order to predict system performance, finite element models (FEMs) of the components are developed, reduced to Hurty/Craig-Bampton (HCB) models, and assembled to represent different phases of flight. There is always uncertainty in every model, which flows into uncertainty in predicted system results. Uncertainty quantification (UQ) is used to determine statistical bounds on prediction accuracy based on model uncertainty. For the SLS, model uncertainty is at the component HCB level. The HCB component displacement vector is given by $u_{CB} = \left\{u_t^T \;\; q^T\right\}^T$, where u_t is the vector of physical displacements at the component interface and q is the vector of generalized coordinates associated with the component fixed-interface modes. Assuming that the fixed-interface modes are mass normalized, the corresponding HCB mass and stiffness matrices have the form

$$M_{CB} = \begin{bmatrix} M_S & M_{tq} \\ M_{tq}^T & I \end{bmatrix} \qquad K_{CB} = \begin{bmatrix} K_S & 0 \\ 0 & \lambda \end{bmatrix}$$

in which M_S and K_S are the component physical mass and stiffness matrices statically reduced to the interface, M_{tq} is the mass coupling between the interface and the fixed-interface modes, I is an identity matrix, and λ is a diagonal matrix of the fixed-interface mode eigenvalues. Details of the HCB component derivation can be found in Craig and Bampton [1].

In this work, uncertainty in the component HCB representations is quantified using a new hybrid parametric variation (HPV) approach that combines parametric and nonparametric uncertainty. In the structural dynamics community, a parametric approach is probably the most common for modeling uncertainty. This type of uncertainty is also referred to as irreducible or aleatoric uncertainty. In this approach, component parameters that are inputs to the FEM (and thus the HCB representations), such as Young's modulus, mass density, geometric properties, and so on, are modeled as random variables, and the parameter uncertainty can be propagated into the system response using a method such as stochastic finite element analysis [2]. Alternatively, an ensemble of random components, including mass, damping, and stiffness matrices, can easily be generated using a matrix perturbation approach in which the random components are assembled into an ensemble of random systems and then a Monte Carlo (MC) analysis is performed to calculate the desired system response statistics. The advantage of the parametric approach is that each of the random sets of model parameters represents a corresponding random FEM. However, there are several disadvantages associated with the parametric method; it can be very time consuming to determine a reduced set of parameters that have a significant impact on the system response, and the selected parameter probability distributions are usually not available. The most significant drawback is that the

uncertainty that can be represented is limited to the form of the nominal FEM, but it is known that most errors in a FEM are associated with modeling assumptions and not parameter errors. Because of this, in practice, the parameter changes are typically surrogates for the actual model errors.

It turns out that uncertainty in model form is one of the biggest contributors to uncertainty in complex built-up structures. This type of uncertainty cannot be directly represented by FEM input parameters and thus cannot be included in a parametric approach. Examples of model form uncertainty include unmodeled nonlinearities and errors in component joint models. Model-form uncertainty is a type of epistemic or reducible uncertainty that can be modeled using random matrix theory (RMT), where a probability distribution is developed for the matrix ensemble of interest. Random matrix theory was introduced and developed in mathematical statistics by Wishart [3]. Wigner [4] applied RMT in atomic physics by postulating that spectrum line spacing in heavy atomic nuclei should resemble the spacings between eigenvalues of a random matrix. More recently, Soize [5, 6] pioneered a nonparametric approach for representing model-form uncertainty in structural dynamics applications. Adhikari [7, 8] expanded upon Soize's approach by using Wishart distributions to model random structural mass, damping, and stiffness matrices. The nonparametric matrix-based approach for representing structural uncertainty has been used extensively in aeronautics and aerospace engineering applications [9–11].

11.2 Theory

Soize [5] used the maximum entropy (ME) principle to derive the positive and positive-semidefinite ensembles SE^{+} and SE^{+0} that follow the matrix variate gamma distribution and are capable of representing random structural matrices. This means that the matrices in the ensembles are real and symmetric and possess the appropriate sign definiteness to represent structural mass, stiffness, or damping matrices. Ensemble members have diagonal terms that are positive-valued gamma random variables, and off-diagonal terms that are zero-mean Gaussian. As the dimension of the random matrix n increases, the matrix variate gamma distribution converges to a matrix variate Wishart distribution. In applications involving structural dynamics, the matrix dimensions are usually sufficient to give a negligible difference between the two distributions. Letting ensemble member random matrix G be any of the random mass, stiffness, or damping matrices, it is therefore assumed in the remainder of this work that G follows a matrix variate Wishart distribution, $G \sim W_n(p, \Sigma)$. The diagonal terms are now chi-square random variables. In general, a Wishart distribution with parameters p and Σ can be thought of as the sum of the outer product of p independent random vectors X_i all having a multivariate normal distribution with zero mean and covariance matrix Σ. Parameter p is sometimes called the shape parameter. If $p = \Sigma = 1$, the Wishart distribution reduces to the chi-square distribution. The random matrix G can be written as

$$G = \sum_{i=1}^{p} X_i X_i^T \qquad X_i \sim N_n(0, \Sigma) \tag{11.1}$$

where the expected value is given by

$$E(G) = \overline{G} = p\Sigma \tag{11.2}$$

The dispersion or normalized standard deviation of the random matrix G is defined by the relation

$$\delta_G^2 = \frac{E\left(\left\|G - \overline{G}\right\|_F^2\right)}{E\left(\left\|\overline{G}\right\|_F^2\right)} \tag{11.3}$$

in which $\|*\|_F^2$ is the Frobenius norm squared, or trace$({}_*{}^T{}_*)$. Soize [6] showed that in order to obtain consistent convergence properties for the response of the stochastic system as the dimension n approaches infinity, the inverse moments of the random system matrix ensembles must exit, meaning that

$$E\left(\left\|G^{-1}\right\|_F^{\upsilon}\right) < \infty$$

The shape parameter can then be defined as $p = \theta + n + 1$, where $\theta = 2\upsilon$ is twice the order of the inverse moments of G that are being constrained to exist within the ensemble.

It can be shown that Eq. (11.3) reduces to the expression

$$\delta_G^2 = \frac{1}{p}\left[1 + \frac{\left(tr\left(\overline{G}\right)\right)^2}{tr\left(\overline{G}^T\overline{G}\right)}\right] = \frac{1}{p}\left[1 + \gamma_G\right] \tag{11.4}$$

where $\gamma_G = \frac{\left(tr(\overline{G})\right)^2}{tr\left(\overline{G}^T\overline{G}\right)}$. The uncertainty in the random matrix G is dictated by the shape parameter p, the number of inner products in Eq. (11.1). The larger the value of p, the smaller the dispersion δ_G. Suppose G_1 and G_2 represent structural matrices—for example stiffness—from two different system components. There may be instances when it is desired to have the same amount of uncertainty in each of the substructures. This means that the shape parameter p must be the same for both ensembles. However, Eq. (11.4) shows that even if $p_1 = p_2 = p$, the dispersion values are not the same in general, $\delta_{G_1}^2 \neq \delta_{G_2}^2$, unless $\gamma_1 = \gamma_2$. To have the matrix uncertainties be the same in terms of dispersion values, Eq. (11.4) must be applied to both G_1 and G_2, p_1 must be set equal to p_2 and eliminated between the two relations, yielding

$$\delta_{G_2} = \delta_{G_1}\sqrt{\frac{1+\gamma_2}{1+\gamma_1}} \tag{11.5}$$

This expression leads to the definition of a normalized dispersion

$$\delta_{G_n} = \frac{\delta_{G_1}}{\sqrt{1+\gamma_1}} = \frac{\delta_{G_2}}{\sqrt{1+\gamma_2}} = \frac{1}{\sqrt{p}} \tag{11.6}$$

which is constant between the two component matrix ensembles. However, just because two components have the same normalized dispersion does not mean that they will have the same modal parameter uncertainty, such as mean root mean square (RMS) frequency uncertainty. Where the normalized dispersion is small, the modal statistics of the two components tend to be close, but as the normalized dispersion increases, the modal statistics for the two components become more disparate. If the dispersion of a component has been set using test data and it is desired to have the same level of uncertainty for another untested component, Eq. (11.5) can be used to scale the required dispersion, but ultimately the dispersion has to be adjusted to be consistent with the test data. This can be accomplished by stepping through a series of dispersion levels about the level designated by Eq. (11.5), computing modal uncertainty statistics using MC analysis, and comparing them with the test data. It has been found that mean RMS frequency uncertainties and mean diagonal RMS cross-orthogonality both vary smoothly with respect to the normalized matrix dispersion value.

The random matrix method developed by Soize [5, 6] is referred to as method 1 by Adhikari [7]. The Wishart parameters are selected as p and $\Sigma = G_o/p$ where G_o is the nominal value of G. The mean of the distribution is given by Eq. (11.2) as $\overline{G} = p\Sigma = p\left(G_o/p\right) = G_o$. Therefore, method 1 preserves the nominal matrix as the mean of the ensemble. In general, the nominal matrix can be decomposed as

$$G_o = LL^T \tag{11.7}$$

In the case of a positive definite matrix, this would just be the Cholesky decomposition. When the nominal matrix is positive semidefinite, an alternative decomposition can be used, which is discussed later. Let $(n \times p)$ matrix X be given by

$$X = \left[x_1\ x_2\ \cdots x_p\right] \tag{11.8}$$

in which x_i is an $(n \times 1)$ column vector containing standard random normal variables such that $x_i \sim N_n(0, I_n)$. Note that $p \geq n$ must be satisfied in order for G to be full rank. An ensemble member $G \sim W_n(p, G_o/p)$ can then be easily generated for MC analysis using the expression

$$G = \frac{1}{p}LXX^TL^T \tag{11.9}$$

It has been found that ensembles of random component mass matrices are best represented using method 1. It was noted by Adhikari [7] that method 1 does not maintain the inverse of the mean matrix as the mean of the inverse; that is,

$$E\left(G^{-1}\right) \neq [E(G)]^{-1} = \overline{G}^{-1} \tag{11.10}$$

In some cases, the two can be vastly different, which is clearly not physically realistic. Instead, Adhikari [7] proposed method 3, in which the Wishart parameters are selected as p and $\Sigma = G_o/\theta$ where

$$\theta = \frac{1}{\delta_G^2}[1 + \gamma_G] - (n+1) \tag{11.11}$$

An ensemble member $G \sim W_n(p, G_o/\theta)$ can then be generated using the relation

$$G = \frac{1}{\theta} L X X^T L^T \tag{11.12}$$

In this case, the inverse of the mean matrix is preserved as the mean of the ensemble inverses, where the mean matrix is now given by

$$\overline{G} = p\Sigma = p\,(G_o/\theta) = \frac{p}{\theta} G_o \tag{11.13}$$

Note that in method 3, the dispersion defined in Eq. (11.3) is now calculated with respect to the method 3 mean given in Eq. (11.13), and Eqs. (11.5) and (11.6) also hold for method 3. It has been determined that ensembles of random component stiffness matrices are best represented using method 3. Therefore, the nonparametric portion of the HPV method is based on a method 1 randomization of a component mass matrix and a method 3 randomization of the component stiffness matrix. In this application, the random component mass and stiffness matrices are assumed to be totally independent.

Note that the Wishart matrix uncertainty model results in uncertainty in both mode shapes and frequencies. However, an extensive amount of MC simulation and analysis has shown that component mode shapes tend to be sensitive to the nonparametric matrix randomization provided by methods 1 and 3, but the corresponding modal frequencies tend to be relatively insensitive. Therefore, a parametric component of uncertainty was added to the HPV approach in which the eigenvalues of the fixed-interface modes in the component HCB representation are also assumed to be random variables. Arbitrarily assuming a probability distribution for the random fixed-interface eigenvalues would in general give an incorrect result. For example, making the common assumption of a normal distribution would yield a finite probability that a fixed-interface eigenvalue could be negative, which is clearly not possible. In contrast, this work also uses ME to derive the probability distribution function (PDF) for the HCB fixed-interface eigenvalues. The ME principle produces a PDF based solely on the available information and nothing more. The resulting PDF is the one that corresponds to the largest uncertainty on the set of all PDFs that satisfy the constraints defined by the available information. In this case, there are two pieces of information available. First, the ith random eigenvalue must be strictly positive, $\lambda_{ri} \in R^+$, meaning that the support of the corresponding PDF is also R^+. The second piece of information is the expected value of the random eigenvalue, given by the nominal value, $E(\lambda_{ri}) = \lambda_i$. Applying ME yields a gamma distribution, $\lambda_{ri} \sim G(k_i, \theta_i)$, where the shape parameter k_i and the scale parameter θ_i are given by $k_i = \delta_i^{-2}$ and $\theta_i = \lambda_i \delta_i^2$, in which δ_i is the corresponding coefficient of variation (COV), or dispersion.

The fixed-interface eigenvalues are then random parameters within the HCB component stiffness matrix. During each iteration in an MC analysis, a random draw of HCB fixed-interface eigenvalues is selected to generate a random HCB component stiffness matrix. Note that the mean of this ensemble would just be the nominal HCB stiffness matrix. However, for the current iteration, the parametrically randomized HCB stiffness is treated as the nominal matrix, and method 3 is applied to provide model-form uncertainty on top of the fixed-interface eigenvalue parametric uncertainty. This is analogous to the approach proposed by Capiez-Lernout et al. [9] for separating parametric and nonparametric uncertainty. In contrast to the nonparametric model-form uncertainty, the mode shapes are relatively insensitive to the parametric fixed-interface eigenvalue uncertainty. Therefore, the HPV approach provides the capability to almost independently adjust the uncertainty in the component frequencies and mode shapes. Component frequency uncertainty can be based on component test/analysis frequency correlation, and the nonparametric mass and stiffness dispersion can be based on the corresponding orthogonality and cross-orthogonality results.

11.2.1 Special Treatment for Component Mass Matrices

The component slosh modes are likely to have much less uncertainty associated with them. In addition, there may be times when the component mass must be randomized while the rigid body mass is preserved. A special methodology has been developed to preserve the component slosh modes and rigid body mass when desired. This same methodology can be applied to any subset of the component modes.

It is assumed that the component modes are ordered as

$$\Phi = \left[\phi_r \ \phi_s \ \phi_e \right]$$

where ϕ_r are the n_r rigid body modes, ϕ_s are the n_s slosh modes, and ϕ_e are the n_e elastic (non-slosh) modes. Assuming that the component modes are orthogonal and normalized with respect to the mass matrix, oblique projectors [12] onto the rigid body, slosh, and elastic modal spaces can be generated as

$$P_r = \phi_r \phi_r^T M_{CB} \tag{11.14}$$

$$P_s = \phi_s \phi_s^T M_{CB} \tag{11.15}$$

$$P_e = \phi_e \phi_e^T M_{CB} \tag{11.16}$$

respectively. The nominal component HCB mass matrix can be written as the direct sum

$$M_{CB} = M_r \bigoplus M_s \bigoplus M_e$$

where the rigid body, slosh, and elastic mass components are given by

$$M_r = P_r^T M_{CB} P_r = P_r^T M_{CB} = M_{CB} P_r \tag{11.17}$$

$$M_s = P_s^T M_{CB} P_s = P_s^T M_{CB} = M_{CB} P_s \tag{11.18}$$

$$M_e = P_e^T M_{CB} P_e = P_e^T M_{CB} = M_{CB} P_e \tag{11.19}$$

11.2.1.1 Rigid Body Mass Not Preserved

Define $\Phi_{re} = \left[\phi_r \ \phi_e \right]$ and $M_{re} = M_r \bigoplus M_e$, which is the combined rigid body and elastic mode component mass. Using Eqs. (11.17) and (11.18), the combined mass can be decomposed as

$$M_{re} = M_{CB} \Phi_{re} \Phi_{re}^T M_{CB} = L_{mre} L_{mre}^T \tag{11.20}$$

in which $L_{mre} = M_{CB} \Phi_{re}$ is an $(n \times n_{re})$ matrix, $n_{re} = n_r + n_e$. Using method 1 to randomize the component mass matrix, following the discussion from the previous section, the shape parameter p_m can be expressed as

$$p_m = round \left\{ \frac{1 + \gamma_{mre}}{\delta_m^2} \right\} \tag{11.21}$$

where

$$\gamma_{mre} = \frac{(tr\,(M_{re}))^2}{tr\left(M_{re}^T M_{re}\right)} \tag{11.22}$$

round( ) assigns the nearest integer, and the mass matrix dispersion δ_m is set by the user. Using Eq. (11.9), the randomized version of M_{re} is given by

$$M_{rer} = \frac{1}{p_m} L_{mre} X X^T L_{mre}^T \tag{11.23}$$

in which X is an $(n_{re} \times p_m)$ matrix of standard random normal variables described in Eq. (11.8). Note that n_{re} must be greater than p_m. Adding back the unperturbed slosh mass, the randomized HCB mass matrix is given by

$$M_{CBr} = M_s + M_{rer} \tag{11.24}$$

Method 1 preserves the nominal mass matrix as the mean of the ensemble; therefore, $E(M_{CBr}) = M_{CB}$.

11.2.1.2 Rigid Body Mass Preserved

In this situation, only the elastic component of the mass matrix M_e is randomized. Following the approach outlined in the previous section, Eq. (11.19) can be used to decompose M_e as

$$M_e = M_{CB} \phi_e \phi_e^T M_{CB} = L_{me} L_{me}^T \tag{11.25}$$

The shape parameter p_m is now given by

$$p_m = round \left\{ \frac{1 + \gamma_{me}}{\delta_m^2} \right\} \tag{11.26}$$

where

$$\gamma_{me} = \frac{(tr\,(M_e))^2}{tr\left(M_e^T M_e\right)} \tag{11.27}$$

The randomized version of M_e is given by

$$M_{er} = \frac{1}{p_m} L_{me} X X^T L_{me}^T \tag{11.28}$$

in which X is now $(n_e \times p_m)$. Note that n_e must be greater than p_m. Adding back the unperturbed rigid body and slosh mass, the randomized HCB mass matrix is given by

$$M_{CBr} = M_R + M_s + M_{er} \tag{11.29}$$

As before, the nominal mass matrix is preserved as the mean of the ensemble; therefore, $E(M_{CBr}) = M_{CB}$.

11.2.2 Special Treatment for Component Stiffness Matrices

In the case of an SLS flight component that has rigid body modes and a positive semidefinite stiffness matrix, special steps must be taken to decompose the nominal HCB stiffness matrix (Eq. 11.7) for subsequent randomization using method 3 and Eq. (11.12). As in the case of component mass randomization, the slosh mode stiffness K_s must be preserved. In addition, the rigid body stiffness must be preserved as the null matrix. The procedure follows that of the mass matrix decomposition but is somewhat different. The nominal component HCB stiffness matrix can be written as the direct sum

$$K_{CB} = K_s \bigoplus K_e \tag{11.30}$$

The slosh and elastic mode stiffness matrix components are given by

$$K_s = P_s^T K_{CB} P_s \tag{11.31}$$

$$K_e = P_e^T K_{CB} P_e \tag{11.32}$$

Substituting Eq. (11.16) into Eq. (11.32) yields

$$K_e = M_{CB}\phi_e\phi_e^T K_{CB}\phi_e\phi_e^T M_{CB} = M_{CB}\phi_e\lambda_e\phi_e^T M_{CB} \tag{11.33}$$

where λ_e is the diagonal matrix containing the component elastic mode eigenvalues. The elastic stiffness can then be decomposed into the form of Eq. (11.7) as $K_e = L_{ke}L_{ke}^T$ where

$$L_{ke} = M_{CB}\phi_e\lambda_e^{1/2} \tag{11.34}$$

The shape parameter p_k is now given by

$$p_k = round\left\{\frac{1+\gamma_{ke}}{\delta_k^2}\right\} \tag{11.35}$$

where

$$\gamma_{ke} = \frac{(tr\,(K_e))^2}{tr\left(K_e^T K_e\right)} \tag{11.36}$$

which produces parameter $\theta_k = p_k - (n_e + 1)$. The randomized version of K_e is then given by

$$K_{er} = \frac{1}{\theta_k} L_{ke} X X^T L_{ke}^T \tag{11.37}$$

Note that random matrix X is now $(n_e \times p_k)$, and n_e must be greater than p_k. Adding back the unperturbed slosh stiffness produces the randomized HCB stiffness matrix

$$K_{CBr} = K_s + K_{er} \tag{11.38}$$

In contrast with the random mass matrix ensemble, the stiffness matrix ensemble preserves the inverse of the nominal stiffness as the mean of the random stiffness matrix inverses, $E\left(K_{CBr}^{-1}\right) = K_{CB}^{-1}$. Method 3 gives the mean of the random stiffness matrix ensemble as

$$E\,(K_{CBr}) = \frac{p_k}{\theta_k} K_{CB} \tag{11.39}$$

In the case when parametric uncertainty is included by randomizing the HCB component fixed-interface eigenvalues, a slightly different approach must be taken. During each iteration within the MC analysis, the HCB fixed-interface eigenvalues are first randomized; the resulting stiffness matrix $K_{\lambda r}$ maintains the model form associated with the original FEM and HCB representation. Method 3 is then applied to the random matrix as though it were the nominal HCB stiffness. In this manner, the ME-based nonparametric model-form uncertainty is layered on top of the parametric uncertainty associated with the random HCB eigenvalues. In this case, the elastic partition of the random HCB stiffness matrix $K_{\lambda r}$ can be written as

$$K_e = \phi_{ke}\lambda_{ke}\phi_{ke}^T \tag{11.40}$$

where ϕ_{ke} are the elastic orthonormal modes and λ_{ke} are the associated elastic eigenvalues of $K_{\lambda r}$. The decomposition in Eq. (11.34) is then replaced by

$$L_{ke} = \phi_{ke} \lambda_{ke}^{1/2} \tag{11.41}$$

The remaining procedure laid out in Eqs. (11.35)–(11.39) remains the same. Note that this alternative decomposition of the stiffness can also be used instead of Eq. (11.34) in the case where the HCB fixed-interface eigenvalues are not randomized.

11.3 Selection of Component Eigenvalue and Matrix Dispersion Values

The HPV approach for modeling component uncertainty requires the selection of dispersion values for the HCB component fixed-interface eigenvalues, mass matrix, and stiffness matrix. Ideally, these dispersion values are selected based on component test results. In this work, test/analysis modal correlation metrics are used to determine the dispersions. Test/analysis frequency error is used to identify the HCB fixed-interface eigenvalue uncertainties. Details of the procedure are discussed in the following section. Assuming that the test modes are correct, error or uncertainty in the test mode orthogonality should only be a function of the error or uncertainty in the corresponding FEM or static test analysis model (TAM) mass matrix. If the component FEM mass matrix is certain and there is no error in the TAM reduction, then there is no uncertainty in the test mode orthogonality matrix. The test mode orthogonality matrix could therefore theoretically be used to determine the mass dispersion value. One possibility would be to use the RMS off-diagonal value for the component test mode self-orthogonality matrix as a metric (ODM). For this, a series of MC analyses is performed in which the HCB mass matrix dispersion value is swept over a range and the most probable value of ODM is computed for each MC analysis. The goal is to select the mass dispersion value that gives the most probable ODM value that is equal to the test value. Note that the diagonal values of the test and random self-orthogonality matrices are always unity and there is no constraint between the diagonal values and the off-diagonal values. Therefore, the ODM metric is not sensitive to mode truncation and can be directly compared between test and random self-orthogonality matrices (where there are usually vastly differing numbers of modes involved). However, when the accelerometer sensor configuration used during the component test is sufficient, it is often possible to obtain a test mode self-orthogonality matrix that is very close to an identity matrix regardless of the error in the FEM mass matrix. Therefore, it has been found that the test self-orthogonality ODM metric is not sufficiently sensitive to mass error to give a reliable estimate of mass matrix dispersion. Future work will focus on deriving an alternative approach to identify the dispersion of the mass matrix based on component test results. At present, rather than using a systematic approach based on the test results, the mass matrix dispersion is based on engineering judgment, past experience, and historical results.

Once the eigenvalue and mass dispersions have been identified, test/analysis cross-orthogonality can be used to identify the dispersion of the component stiffness matrix. In this case, the RMS diagonal value of the component test/analysis cross-orthogonality matrix is used as the metric (DCGM). The same MC-based approach is used to identify the HCB stiffness matrix dispersion value that produces the most probable DCGM value equal to the test result. In contrast with the self-orthogonality matrix, the diagonal and off-diagonal values in a cross-orthogonality matrix are directly related due to mass normalization of the test and analysis modes. In the case of a cross-orthogonality matrix, the DCGM and the ODM metrics are directly related by the expression

$$DCGM^2 + (n-1)\, ODM^2 = C \tag{11.42}$$

where n is the number of modes and the C is the mean square length of the matrix columns. The metrics are statistically correlated in the MC analyses. If all of the modes are present, $C = 1.0$. Due to the constraint in Eq. (11.42), the metric ODM is now sensitive to modal truncation and cannot be directly compared between test results and MC-based results due to the difference in number of modes. In contrast, the DCGM is not sensitive to modal truncation and can be directly compared. Therefore, the DCGM metric alone is used to identify the HCB stiffness dispersion value. Details of the identification procedure are discussed below.

In some cases, there may be no component tests and no test/analysis correlation results available for dispersion identification. For example, this is the situation for the SLS boosters. However, the booster models have been test validated in the past, and the models have been used with success in past programs. Therefore, it is proposed that booster dispersion values can be based on those derived for a current test-validated SLS component.

11.3.1 Nominal ICPS/LVSA Based on ISPE Configuration 3

Dispersion values for the nominal interim cryogenic propulsion stage (ICPS)/ launch vehicle stage adapter (LVSA) HCB components are based on the integrated spacecraft payload element (ISPE) configuration 3 modal test/analysis correlation results. The FEM representation of ISPE configuration 3 is shown in Fig. 11.1. There are eleven FEM target modes matched to eleven of the nineteen test modes. Only these target modes are considered in this analysis, because the other eight modes are dominated by the MPCV stage adapter (MSA)/Multi-Purpose Crew Vehicle (MPCV) simulator, which is not part of the ICPS/LVSA component. The test/analysis frequency correlation results are listed in Table 11.1. The nominal model accurately predicts the first bending test mode frequencies. This is consistent with the static test results, which showed good agreement between the nominal model and the test results for overall bending and axial stiffness. Only one second-order bending test mode was identified in the test data, and no axial modes were identified. The nominal model does a poor job of predicting the second-order bending test mode frequency, and the LVSA shell test mode frequencies are even less accurately predicted. Note that the frequency error is calculated relative to the nominal FEM frequency rather than the test; this is done because the uncertainty analysis is performed relative to the FEM HCB representation. In general, the SLS test components and the corresponding HCB component models are not a structural match. In the case of the ICPS/LVSA HCB component, there is no MSA or MPCV simulator. In addition, the SLS components are not tested in the flight configuration. In general, there is rarely a one-to-one comparison between the tested component and the corresponding HCB flight component. However, it is assumed that the component test correlation results can be used as an indicator of what level of uncertainty can be expected in the corresponding HCB component model.

The first level of uncertainty to be specified is the dispersion of the 33 non-slosh fixed-interface modal frequencies for the HCB component. These modes have the base of the LVSA and the top of the ICPS at the MSA interface constrained, whereas during the test, the base of the LVSA is attached to the core simulator, and the top of the ICPS is attached to the MSA/MPCV simulator. Therefore, there will not be a one-to-one comparison between HCB fixed-interface modes and component FEM

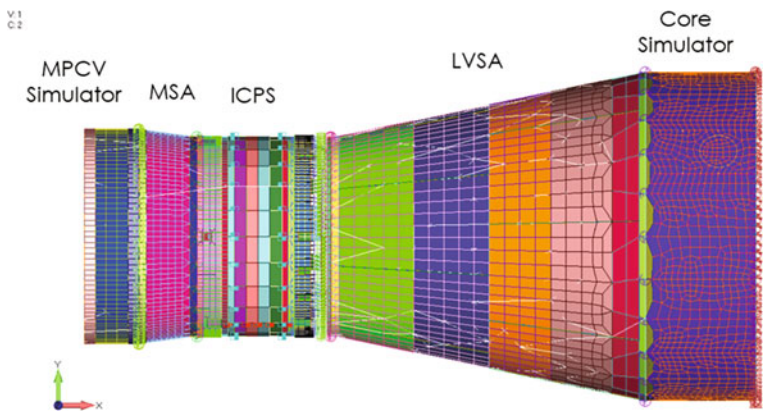

Fig. 11.1 ISPE configuration 3 FEM representation

Table 11.1 Test/analysis frequency error for configuration 3 nominal model

Test mode	Pretest mode	%Err	Posttest mode	%Err	Description
1	6	−0.16	6	−0.89	First bending
2	5	−1.94	5	−2.70	First bending
3	9	10.13	7	1.43	LVSA shell ND 5
4	10	9.95	8	1.23	LVSA shell ND 5
5	11	7.21	9	3.96	LVSA shell ND 4
6	12	6.97	10	3.50	LVSA shell ND 4
9	14	12.90	14	−0.23	LVSA shell ND 6
10	13	12.60	13	−0.57	LVSA shell ND 6
14	24	15.29	20	−0.01	LVSA shell ND 7
15	23	14.98	19	−0.33	LVSA shell ND 7
19	22	−8.63	24	−4.72	Second bending

Table 11.2 Nominal ICPS/LVSA HCB fixed-interface MEM

Mode	Tx	Ty	Tz	Rx	Ry	Rz
5	0.00	0.04	0.01	0.17	0.01	0.04
6	0.00	2.74	0.01	0.00	0.01	2.93
7	0.00	0.02	**5.36**	0.00	**5.65**	0.03
8	0.00	0.40	**56.65**	0.00	**57.91**	0.41
9	0.00	**61.44**	0.35	0.00	0.36	**62.76**
10	0.02	0.00	2.04	0.00	1.99	0.00
11	0.02	0.00	0.03	0.00	0.03	0.00
12	2.57	0.00	0.57	0.00	0.53	0.00
13	**67.26**	0.00	0.01	0.00	0.01	0.00
14	1.01	0.00	0.21	0.00	0.18	0.00
15	0.00	0.22	0.00	0.00	0.00	0.20
16	0.00	0.00	0.00	0.00	0.00	0.00
17	0.00	0.00	0.00	0.00	0.00	0.00
18	0.00	0.00	0.03	0.00	0.02	0.00
19	0.00	0.00	0.00	0.00	0.00	0.00
20	0.01	0.00	0.00	0.00	0.00	0.00
21	0.00	0.00	0.00	0.00	0.00	0.00
22	0.00	0.91	0.00	0.01	0.00	0.78
23	0.00	0.00	0.00	0.00	0.00	0.00
24	0.00	0.04	0.00	0.02	0.00	0.04
25	0.00	0.00	0.00	0.00	0.00	0.00
26	0.00	0.00	0.00	0.00	0.00	0.00
27	0.00	0.00	0.08	0.00	0.07	0.00
28	0.00	0.00	0.01	0.00	0.01	0.00
29	0.02	0.02	0.08	0.00	0.07	0.02
30	0.12	0.10	0.08	0.03	0.07	0.09
31	0.00	0.04	0.35	0.05	0.30	0.04
32	**5.66**	0.00	**6.82**	0.94	**5.92**	0.00
33	2.40	2.80	**5.40**	**6.41**	**4.71**	2.55
34	1.46	3.64	0.21	**14.33**	0.18	3.21
35	2.50	**11.16**	2.47	1.15	2.17	**9.87**
36	0.03	0.07	3.83	0.02	**4.31**	0.07
37	0.07	1.01	0.22	0.22	0.21	1.46
Sum	83.16	94.87	95.02	23.35	94.89	94.66

test-configuration modes. In addition, the ICPS/LVSA HCB component includes the mass of the fuel, so it is difficult to compare the two sets of modes even on a frequency-band basis. Instead of using frequency, test/analysis frequency error is mapped to the fixed-interface modes using a combination of modal effective mass (MEM), cross-orthogonality (XO), and modal strain energy (SE). However, only the ICPS/LVSA interface is common to both the ISPE configuration 3 FEM and the HCB model, so XO and SE results are difficult to interpret.

The nominal FEM ISPE configuration 3 MEM is dominated by the fundamental bending and axial modes and to a lesser extent the second-order bending modes. The LVSA shell modes have little or no MEM. The MEM values for the nominal ICPS/LVSA HCB component fixed-interface modes are listed in Table 11.2. Values over 4% are shown in bold emphasis. The first four modes are slosh modes, which are excluded from the analysis. Based on MEM, XO, and SE, the fixed-interface modes are placed in three different bins of uncertainty. Fixed-interface modes 8, 9, and 32–35 are placed in bin 1, corresponding to the FEM configuration 3 first bending pair. Modes 32–35 are residual modes that have large overall motion with significant MEM. Bin 1 is assigned a frequency dispersion of 1.37%, corresponding to the RMS error in the prediction of the first bending configuration 3 test mode pair frequencies. The modal frequencies are assumed to follow the gamma distribution described previously. Fixed-interface mode 13 is the fundamental axial mode, and based on the accuracy of the nominal configuration 3 model in predicting the static test results, this mode is also assigned to bin 1. Fixed-interface modes 6, 7, 10–12, 36, and 37 are assigned to bin 2 with a frequency dispersion of 8.63%, corresponding to the test/analysis

frequency error of the second-order bending test mode. The remaining fixed-interface modes have little or no effective mass content, analogous to the LVSA shell test modes. Therefore, these modes are assigned to bin 3 with a frequency dispersion of 11.65%, corresponding to the RMS frequency error in the configuration 3 LVSA shell modes. Figure 11.2 illustrates the percent COV by nominal frequency assigned to the non-slosh fixed-interface modes. The three bins or uncertainty levels are apparent.

Once the fixed-interface eigenvalue uncertainty is set, dispersions for the HCB mass and stiffness matrices are identified. Currently, it is assumed that the HCB mass matrix has little error, so no mass dispersion is imposed. The fixed-interface eigenvalue uncertainty is applied, and then dispersion of the stiffness matrix is determined by computing the DCGM metric based on cross-orthogonality, which is the RMS value of the diagonal after modes are matched and resorted accordingly. The nominal ISPE configuration 3 cross-orthogonality matrix is listed in Table 11.3. Analysis mode pairs were rotated by NASA to better align with the corresponding test mode pairs. Based on the nominal ISPE configuration 3 cross-orthogonality matrix for the eleven target modes, the dispersion metric has the value DCGM = 90.44.

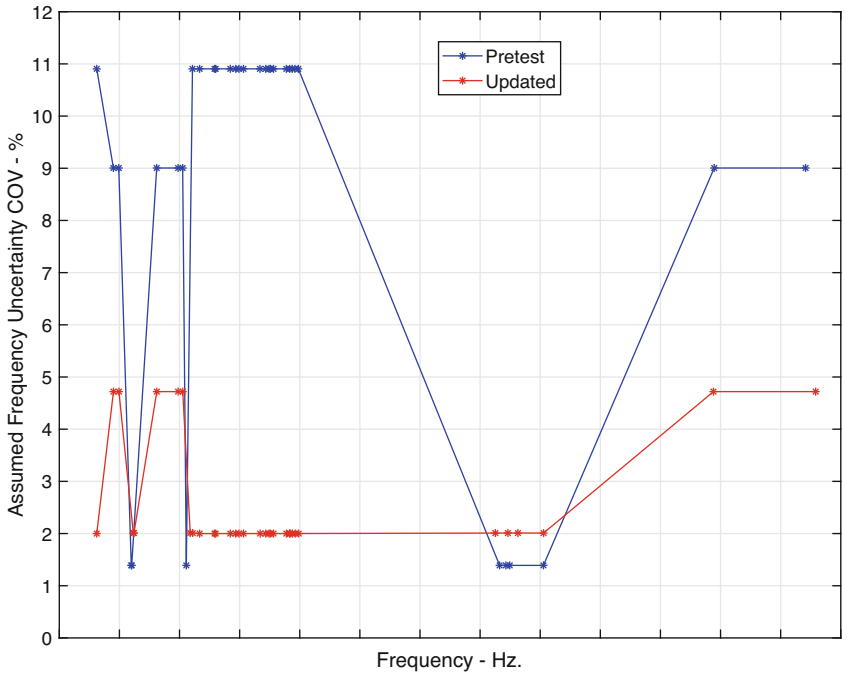

Fig. 11.2 Percent COV for nominal ICPS/LVSA HCB fixed-interface mode frequencies

Table 11.3 Nominal ISPE configuration 3 cross-orthogonality for rotated modes

Analysis modes	Test modes										
Mode	2	1	3	4	5	6	10	9	19	15	14
5	−0.94	0.03	−0.09	−0.06	−0.04	−0.04	−0.02	0.01	−0.07	−0.01	0.01
6	0.04	−0.95	−0.02	0.03	−0.01	0.00	−0.01	0.01	0.09	0.01	0.01
9	−0.04	−0.01	0.94	0.00	0.04	0.04	−0.01	−0.01	0.01	−0.03	−0.01
10	−0.03	0.07	0.00	0.95	−0.04	0.01	−0.01	0.02	−0.00	−0.07	−0.00
11	0.02	0.02	0.10	0.08	−0.98	0.01	−0.00	−0.00	0.00	−0.02	0.03
12	−0.01	0.01	0.04	−0.02	0.01	−0.96	0.05	0.06	−0.01	−0.04	−0.00
13	0.02	0.00	0.03	0.00	0.02	−0.01	−0.97	−0.03	0.00	−0.00	−0.00
14	−0.01	−0.02	0.03	0.03	0.01	−0.03	0.04	0.97	0.01	0.02	0.02
22	0.03	−0.03	−0.01	0.02	−0.02	−0.01	0.01	−0.00	0.73	−0.00	−0.60
23	−0.06	−0.01	−0.01	0.02	−0.01	−0.03	−0.00	0.00	0.02	−0.75	0.00
24	−0.02	0.01	−0.02	−0.01	−0.03	−0.02	0.01	0.02	−0.60	0.01	−0.75

The goal is to select a stiffness dispersion value for the MC analysis such that the test-based metric value is the most probable. The MC analysis is based on the first 37 nominal HCB elastic non-slosh modes and 3000 ensemble members. The selected fixed-interface eigenvalue uncertainties are applied, and then a series of MC analyses are performed with stiffness dispersion swept over a range of values from 3.0% to 9.0%. During the MC analysis, cross-orthogonality of modes within 1% frequency of the unique-best-fit mode were combined using a root-sum-square (RSS) approach [13] to yield results comparable to the mode pair rotation in Table 11.3. The DCGM metric is computed for each ensemble member cross-orthogonality matrix within each MC analysis, and the metric that has the largest probability for each stiffness dispersion is identified. Figure 11.3 illustrates the DCGM most probable value versus the stiffness matrix dispersion, and the test value.

It can be seen in Fig. 11.3 that the relation is almost linear. The intersection of the two blue lines is approximately at a dispersion value of 7.0%. Figure 11.4 illustrates the RMS cross-orthogonality for the first 37 ICPS/LVSA non-slosh elastic modes when the selected fixed-interface frequency uncertainty and the 7.0% stiffness matrix dispersion are applied in an MC analysis. There is little mode-shape uncertainty for the first six modes. Figure 11.5 shows the corresponding RMS frequency uncertainty. Note that the mean RMS frequency uncertainty with the stiffness dispersion alone is only 0.78%, showing that the matrix dispersion produces more shape uncertainty than frequency uncertainty.

As mentioned, static test results for ISPE configuration 3 showed very good agreement (between 1.0% and 2.0%) with predictions using both the pretest and updated FEMs, indicating that both models accurately predict the overall bending stiffness. This is also reflected in accurate pretest model prediction of the first bending mode, as listed in Table 11.1. Therefore, there was a concern that the combination of the fixed-interface frequency dispersion with the 7.0% stiffness matrix dispersion dictated by the ISPE test/analysis modal correlation results would adversely affect the accuracy of the ICPS/LVSA static stiffness.

To study the effects of the imposed uncertainty on the static stiffness of the ICPS/LVSA HCB component, a static analysis was performed with the LVSA interface fixed. A new node was added at the center of the ICPS/MSA interface, with deflections based on the average of the displacements of the 24 nodes around the MSA interface. Six static loads were applied individually to the center node for 3000 stiffness matrices randomized using the identified fixed-interface frequency uncertainties, and a 1.9% stiffness matrix dispersion based on Adhikari's ME approach, which maintains the mean ensemble flexibility matrix as the nominal component flexibility. Note that a 1.9% stiffness matrix dispersion for the constrained ICPS/LVSA with the added load application node is equivalent to a 7.0% dispersion of the free-free ICPS/LVSA HCB component based on Eq. (11.5). The applied load levels are listed along with the results in Table 11.4. In each of the six load cases, the COV of the displacement of the load application point along the direction of the applied load is between 1.21% and

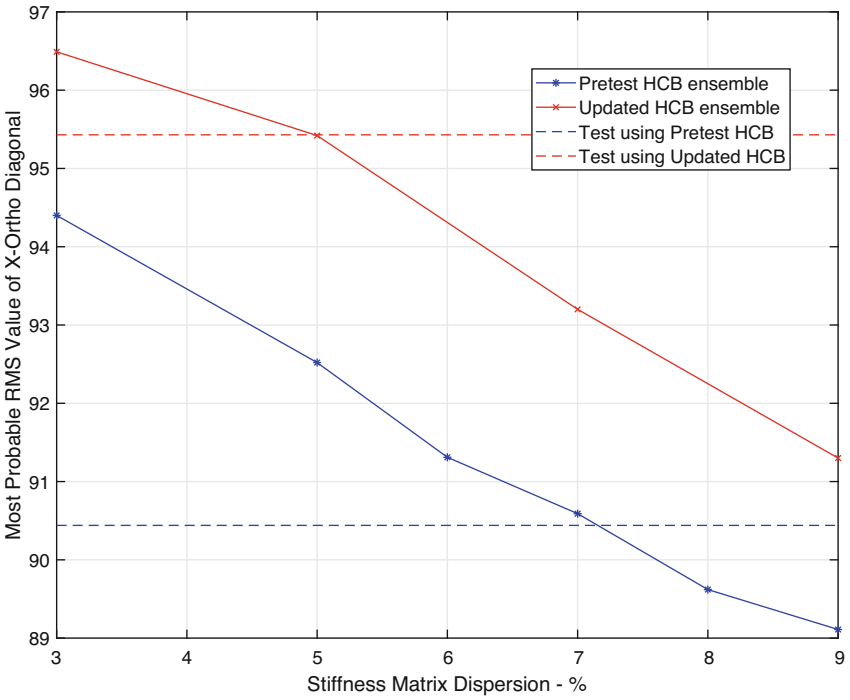

Fig. 11.3 Cross-orthogonality metric vs. stiffness dispersion

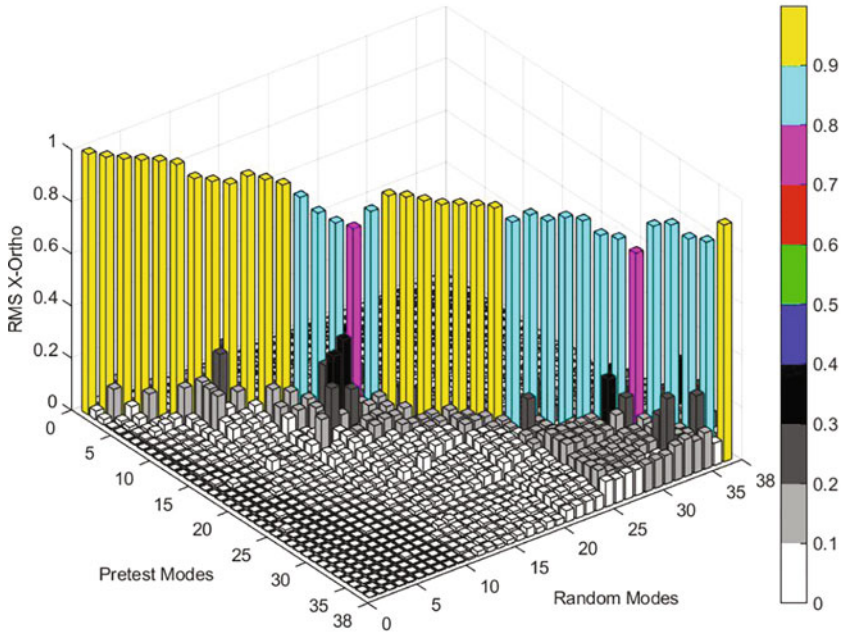

Fig. 11.4 RMS cross-orthogonality for first 37 pretest ICPS/LVSA non-slosh elastic modes

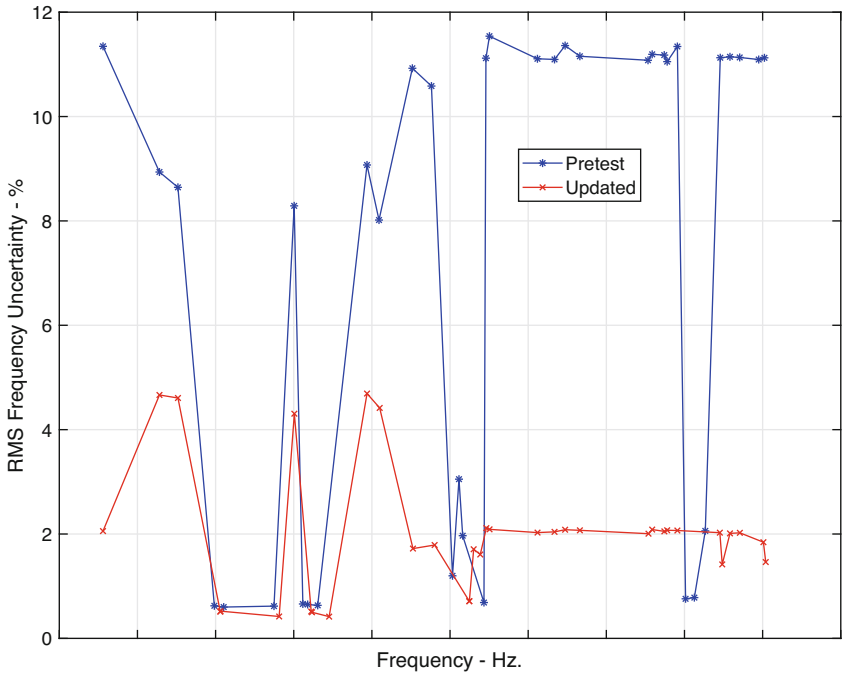

Fig. 11.5 RMS frequency uncertainty for first 37 (pretest)/35 (updated) ICPS/LVSA non-slosh elastic modes

1.23%, meaning that the uncertainty in the static stiffness due to the imposed fixed-interface frequency and stiffness matrix dispersion is in good agreement with the static ISPE configuration 3 test results. This gives further evidence that the ME approach is capable of modeling structural uncertainty in a physically realistic manner. Also, the mean displacements are essentially equal to the nominal displacements, indicating that the ensemble mean flexibility matrix is equal to the nominal flexibility, as expected.

Table 11.4 Static load results for constrained ICPS/LVSA MC analysis

Load	Direction	Nominal displacement	Mean displacement	% COV
310 kips	X	0.131	0.131	1.21
80 kips	Y	0.337	0.337	1.23
80 kips	Z	0.337	0.337	1.22
630 in-kips	RX	0.047	0.047	1.23
27,900 in-kips	RY	1.993	1.994	1.22
27,900 in-kips	RZ	2.013	2.013	1.22

Table 11.5 Updated ISPE configuration 3 cross-orthogonality for rotated modes

Analysis modes	Test modes										
Mode	2	1	3	4	5	6	10	9	15	14	19
5	−0.94	0.03	−0.09	−0.06	−0.04	−0.04	−0.02	0.00	−0.01	0.01	−0.08
6	−0.04	0.95	0.02	−0.04	0.00	−0.01	0.01	−0.01	−0.01	−0.01	−0.10
7	0.04	0.01	−0.95	0.00	−0.06	−0.04	0.02	0.02	0.03	0.01	−0.01
8	0.03	−0.08	0.00	−0.95	−0.01	−0.01	0.01	−0.02	0.06	0.00	0.00
9	−0.02	−0.02	−0.12	−0.13	0.97	−0.01	0.00	−0.00	0.03	−0.03	−0.00
10	0.01	−0.01	−0.04	0.01	−0.01	0.96	−0.05	−0.06	0.04	0.00	0.01
13	0.02	0.01	0.03	0.00	0.02	−0.01	−0.97	−0.03	−0.00	−0.00	−0.00
14	0.01	0.02	−0.03	−0.04	−0.01	0.03	−0.04	−0.97	−0.02	−0.02	−0.00
19	−0.04	−0.01	−0.01	0.02	−0.03	−0.04	0.01	0.00	−0.95	−0.00	−0.01
20	−0.01	0.02	0.02	−0.01	0.03	0.01	−0.02	−0.01	0.01	0.94	−0.05
24	−0.03	0.01	−0.01	−0.02	−0.01	−0.00	0.00	0.01	0.00	−0.06	−0.94

11.3.2 Updated ICPS/LVSA Based on ISPE Configuration 3

A posttest correlation was performed to update the ISPE configuration 3 FEM. Dispersion values for the updated ICPS/LVSA HCB component are based on the updated ISPE configuration 3 FEM. As in the nominal model analysis, there are eleven FEM target modes matched to eleven of the nineteen test modes. The test/analysis frequency correlation results are listed in Table 11.1. Note that the frequency error for the LVSA shell modes and the second-order bending modes have been dramatically reduced. There are now 39 HCB fixed-interface modes in the updated ICPS/LVSA HCB component. The first four are still slosh modes. The fixed-interface MEM was calculated with little change with respect to the nominal model values. Based on MEM, XO, and SE, the same three-bin uncertainty assignment strategy was applied. Fixed-interface modes 8, 9, and 34–37 are matched to the FEM configuration 3 first bending pair; modes 34–37 are residual modes that again have large overall motion with significant MEM. These six fixed-interface modes are assigned a frequency dispersion of 2.00%, corresponding to the RMS error in the prediction of the first bending test mode pair. The modal frequencies are again assumed to follow a gamma distribution deduced by ME. Fixed-interface modes 13 and 14 are axial modes. Based on the accuracy of the nominal configuration 3 model in predicting the static test results, these modes are also assigned a frequency dispersion of 2.00%. Fixed-interface modes 6, 7, 10–12, 38, and 39 are assigned a frequency dispersion of 4.72%, corresponding to the test/analysis frequency error of the second-order bending test mode. As in the nominal model analysis, the remaining fixed-interface modes have little or no effective mass content, analogous to the LVSA shell test modes. Therefore, these modes are assigned a frequency dispersion of 2.01%, corresponding to the RMS frequency error in the configuration 3 LVSA shell modes. Figure 11.2 illustrates the assigned percent COV by nominal frequency for the non-slosh fixed-interface modes.

Once again, it is assumed that the HCB mass matrix has little error, so there is no mass dispersion imposed. The fixed-interface eigenvalue uncertainty is applied, and then the dispersion of the stiffness matrix is determined by computing the RMS cross-orthogonality diagonal metric, DCGM. The updated ISPE configuration 3 cross-orthogonality matrix is listed in Table 11.5. As before, analysis mode pairs were rotated to better align with the corresponding test mode pairs. Based on the updated ISPE configuration 3 cross-orthogonality matrix for the eleven target modes, the dispersion metric has the test value DCGM = 95.43.

The selected fixed-interface eigenvalue uncertainties were applied, and then a series of MC analyses were performed with stiffness dispersion swept over a range of values from 3.0% to 9.0%. The MC analysis was based on the first 35 nominal HCB elastic non-slosh modes and 3000 ensemble members. An RSS value of 1% was applied to the MC cross-orthogonality to yield results comparable to the mode pair rotation in Table 11.5. The DCGM metric was computed for each

ensemble member cross-orthogonality matrix. The stiffness dispersion that produced the most probable DCGM metric that was in greatest agreement with the test value was 5.0%, as shown in Fig. 11.3. Figure 11.5 illustrates the RMS frequency uncertainty for the 35 ICPS/LVSA non-slosh elastic modes when the selected fixed-interface frequency uncertainty and the 5.0% stiffness matrix dispersion are applied in an MC analysis. There is now little mode shape uncertainty.

11.4 Propagation of Uncertainty into Control System Transfer Function Metrics

The guidance, navigation, and control (GNC) team uses a specific set of transfer functions for the assessment of attitude control system stability and performance. The control system must be robust in the presence of uncertainty in the analytical model. Uncertainty in modal frequencies and transfer function gain are of interest. For the fundamental bending modes, 4 dB uncertainty in gain and 10% uncertainty in frequency are absolute maximums. In this work, uncertainty analysis is performed using the approach outlined in the previous sections for the SLS liftoff configuration. The liftoff configuration consists of seven different components: MPCV + MSA, ICPS + LVSA, core stage (CS), left solid rocket booster (LSRB), right solid rocket booster (RSRB), LSRB_CBAR, and RSRB_CBAR. All the components are HCB models except for LSRB_CBAR and RSRB_CBAR, which are simple bar representations of the connections between the boosters and the CS. The component models are assembled and reduced, producing a system model that contains 779 degrees of freedom (DOFs), which is then used in the uncertainty propagation. There are three sensor locations on the CS—the replaceable inertial navigation unit (RINU), the intertank rate gyro assembly (itRGA), and the aft rate gyro assembly (aftRGA)—as illustrated in Fig. 11.6, and a total of six engine gimbals (two on the SRBs and four on the CS). All DOFs used for the transfer functions are in coordinate systems that are aligned with the vehicle basic system. An allocator matrix was provided by GNC that allocates lateral forces at each engine gimbal to provide 1 rad/s^2 rotational acceleration about the roll, pitch, and yaw axes for that phase of flight, based on the mass properties in the GNC trajectory files.

In the uncertainty analysis, a set of eleven transfer functions, or GNC metrics, are calculated using flexible modes only. Nine of these are the rotational velocity of the three sensors for corresponding unit rotational acceleration commands, and the last two are the translational acceleration of the RINU in the pitch and yaw plane for the corresponding unit rotational acceleration commands. In all cases, the transfer functions are calculated from 0.1 to 10 Hz, based on system modes to 20 Hz and 0.5% critical modal damping applied at the system level. Uncertainty in the GNC metrics, modal correlation metrics, and modal coefficients are computed using MC analyses with 10,015 ensemble members, and the uncertainty in the GNC metrics is given by the ratio of the random over the nominal transfer function expressed in decibels.

An initial liftoff configuration uncertainty analysis is presented in this paper in which the system uncertainty model is based on the component uncertainty models derived for the pretest and updated ICPS/LVSA. These component uncertainty models were generated based on the ISPE configuration 3 test/analysis correlation results presented in the previous section. In the pretest ICPS/LVSA component uncertainty model, uncertainties are assigned to individual component fixed-interface eigenvalues. The corresponding frequency uncertainties are shown in Fig. 11.2. The HCB stiffness matrix dispersion is assigned to be 7.0%, and there is no component mass dispersion. The test value of the XO metric DCGM (RMS value of the XO diagonal) is 90.44. In the updated ICPS/LVSA component uncertainty model, uncertainties are assigned to individual component fixed-interface eigenvalues consistent with the frequency uncertainties also shown in Fig. 11.2. Stiffness matrix dispersion is set to 5.0%, and there is also no mass dispersion. The test value of the XO metric DCGM is 95.43.

In this system uncertainty analysis, the pretest uncertainty model is used for the ICPS/LVSA HCB component. However, at this time there is no test/analysis correlation data available for any of the other six components. Therefore, the uncertainty models for these components are based on the models derived for the ICPS/LVSA using two levels of uncertainty. The pretest

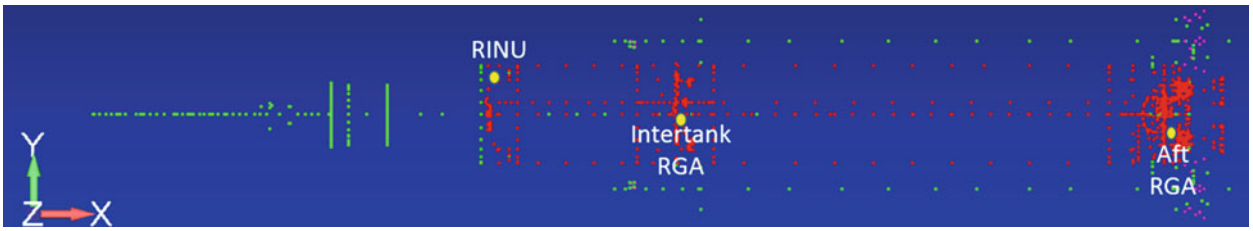

Fig. 11.6 Sensor locations for GNC transfer functions

level is based on the ICPS/LVSA pretest uncertainty model and corresponds to a 10% RMS uncertainty of all HCB fixed-interface eigenvalues, no mass dispersion, and an HCB stiffness dispersion that provides a DCGM value that corresponds to the test value of 90.44. The stiffness dispersion is derived using a series of component MC modal cross-orthogonality analyses for all component modes <20.0 Hz as discussed in the previous sections. The 10% eigenvalue uncertainty is the average of the RMS uncertainty level assigned to the first bending pair and the uncertainty assigned to the second bending mode in the pretest ICPS/LVSA model. The uncertainty level associated with the shell modes is excluded due to its exceptionally high value. This uncertainty model is applied to components that have no heritage and no available modal test/analysis correlation data, such as the MPCV/MSA.

The updated uncertainty level is based on the updated ICPS/LVSA component uncertainty model. It corresponds to a 5% RMS uncertainty of all HCB fixed-interface eigenvalues, no mass dispersion, and an HCB stiffness dispersion that provides a DCGM value that corresponds to the updated test value of 95.43. The 5% eigenvalue uncertainty is the average of the uncertainty levels assigned to all the HCB fixed-interface modes in the updated ICPS/LVSA component model. This uncertainty model is applied to components that have a heritage of previous use, testing, and model validation, such as the boosters. Table 11.6 summarizes the resulting uncertainty models for all seven components based on the two uncertainty levels. The entries in the fixed-interface eigenvalue dispersion column are the dispersion values assigned to all of the eigenvalues of the associated HCB component. The mean HCB eigenvalue dispersion values are the mean RMS uncertainties of the corresponding component free-free eigenvalues computed in the component stiffness dispersion MC analyses. The actual stiffness matrix dispersion values are the corresponding component HCB stiffness matrix dispersions computed relative to the nominal component stiffness matrix using Eq. (11.3). The matrix dispersions are slightly different from the assigned dispersions because Adhikari's method 3 is used to randomize the component stiffness matrices, and method 3 maintains the inverse of the nominal stiffness as the mean of the ensemble inverses so the mean of the ensemble stiffness matrices is no longer the nominal.

Also, note that the CS is highlighted in bold in Table 11.6 because the CS mode shape uncertainty is very sensitive to both the assigned fixed-interface eigenvalue uncertainty and the stiffness matrix dispersion. In fact, for the assigned level of 10% fixed-interface eigenvalue dispersion, the MC-based DCGM XO metric has a value of 89.02, which is already below the test value without any stiffness matrix dispersion. Rather than assigning zero stiffness dispersion, it was decided that a value of 3% would be assigned using Eq. (11.5), which is consistent with having the same normalized stiffness dispersion for the CS as was assigned to the pretest ICPS/LVSA component. The left and right boosters are assigned the same updated level uncertainty model, even though the HCB representations are slightly different, and the impact of the boosters being statistically correlated was found to be small, so the boosters are assumed to be uncorrelated in this system uncertainty analysis. The two booster CBAR components are assumed to be relatively simple components; therefore, they are assigned the updated level of uncertainty, although in this case a slightly different approach must be taken to assign an uncertainty model. These two components are essentially triaxial springs with twelve rigid body modes and three elastic modes. They are not HCB component representations; therefore, fixed-interface eigenvalue uncertainty cannot be assigned. The three elastic modes are always very close to being orthogonal, no matter what the value of the stiffness dispersion; therefore, DCGM was not used to assign the stiffness matrix uncertainty. Instead, the stiffness dispersion was assigned such that the mean RMS uncertainty of the three elastic eigenvalues had a value of 5%, corresponding to the assumed level of fixed-interface eigenvalue uncertainty in the updated model.

Once the component uncertainty models are assigned, a system-level MC analysis is performed to propagate the component uncertainties into the system results. Figure 11.7 shows the system RMS frequency uncertainty for the first 92 non-slosh elastic modes below 10.0 Hz. The average RMS uncertainty is 3.92%, with a maximum value of 10.93% for system mode 43. The corresponding system-level RMS XO is presented in Fig. 11.8. The mean diagonal value is 85.38. As mentioned, eleven GNC transfer function metrics are computed for each of the 10,015 random system ensemble members.

Table 11.6 Assumed uncertainty models for SLS liftoff components

Component	Uncertainty level	Assigned HCB fixed-interface eigenvalue dispersion (%)	Mean HCB eigenvalue dispersion (%)	Assigned stiffness dispersion (%)	Actual stiffness dispersion (%)
MPCV/MSA	Pretest	10.0	13.38	5.0	5.20
ICPS/LVSA	Pretest	Identified from test	14.54	7.0	7.54
CS	**Pretest**	**10.0**	**9.98**	**3.0**	**4.33**
LSRB	Updated	5.0	4.47	1.5	1.53
RSRB	Updated	5.0	4.47	1.5	1.53
LSRB-CBAR	Updated	0.0	4.86	7.0	7.02
RSRB-CBAR	Updated	0.0	4.86	7.0	7.07

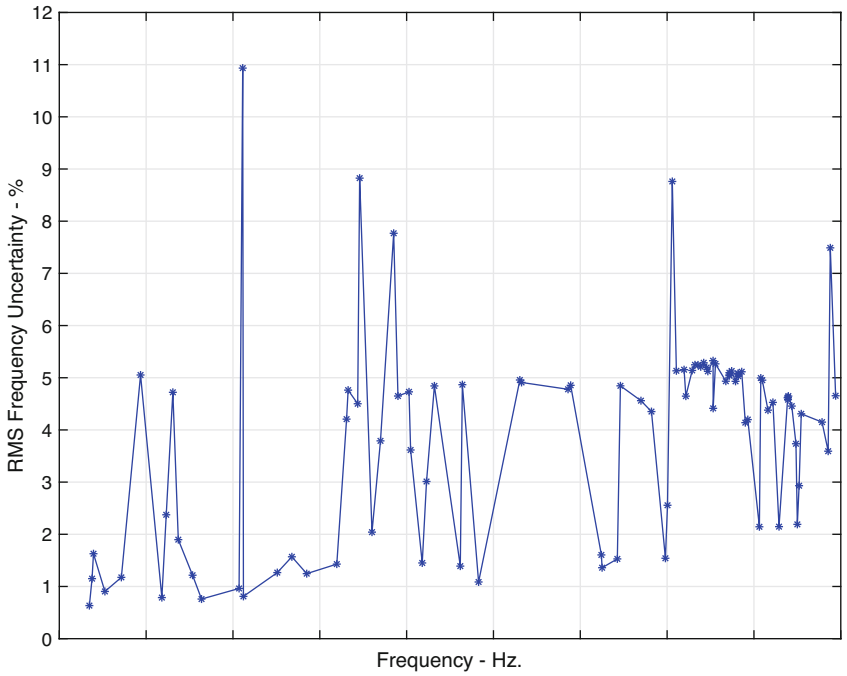

Fig. 11.7 RMS system frequency uncertainty

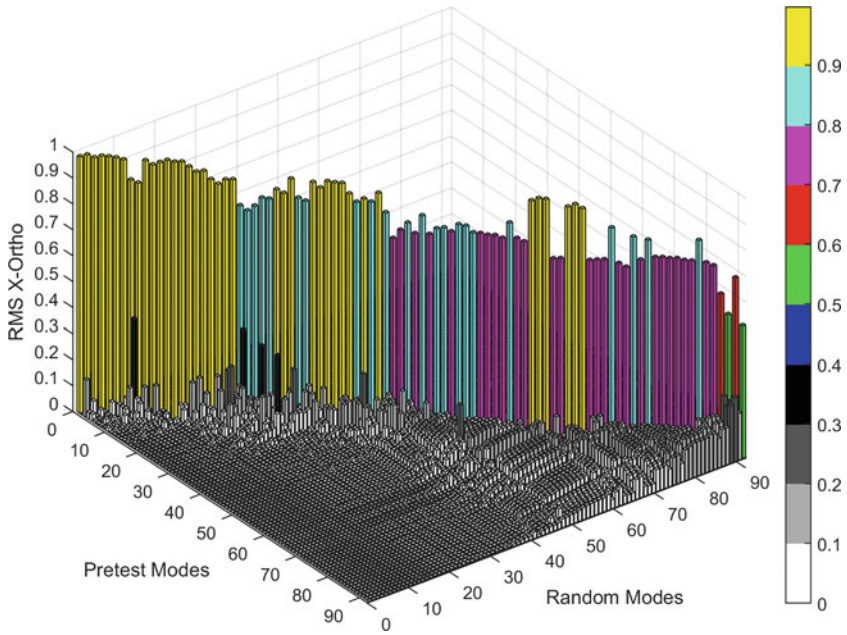

Fig. 11.8 RMS system XO

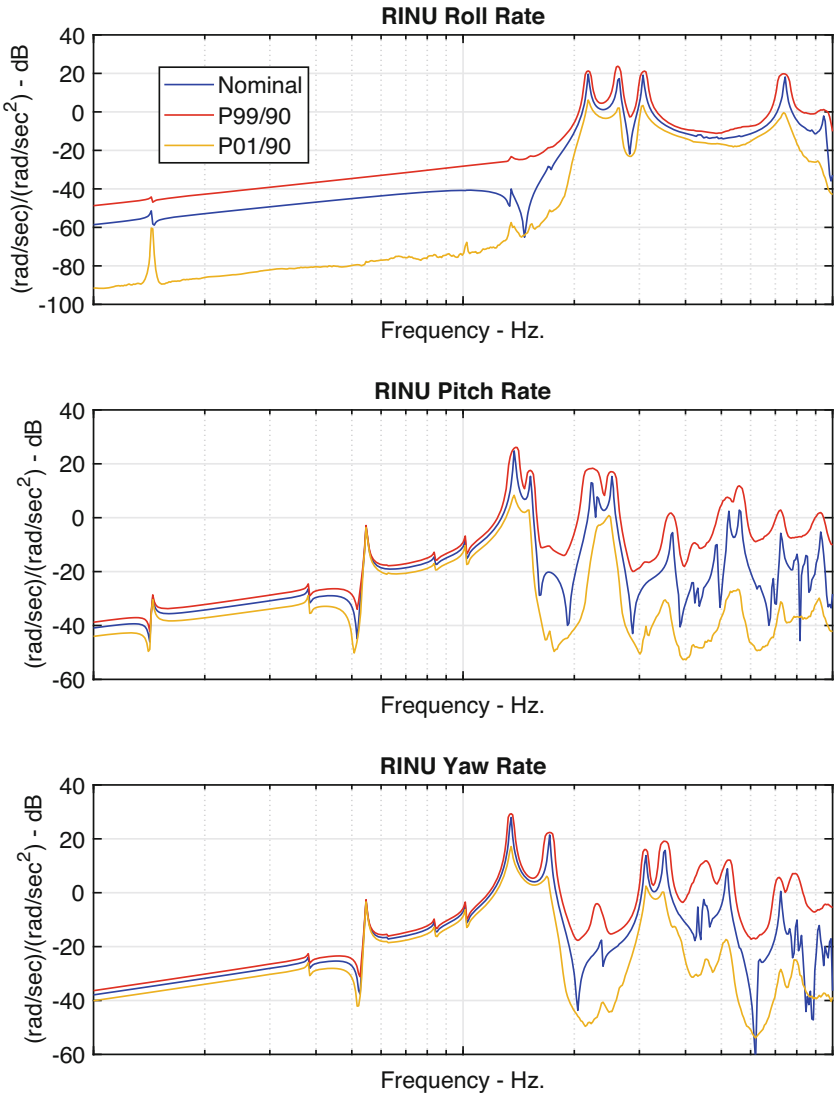

Fig. 11.9 RINU rotational rate transfer functions and P99/90 extremes

Figure 11.9 illustrates the roll axis (Rx), pitch axis (Ry), and yaw axis (Rz) response rates (flex modes only) at the RINU due to unit rotational acceleration commands specified about roll, pitch, and yaw for the nominal liftoff configuration. To conserve space, the corresponding response rates for the itRGA and aftRGA are not presented. Figure 11.10 presents the last two transfer functions corresponding to the translational acceleration of the RINU in the pitch (XZ) and yaw (XY) plane for corresponding unit rotational acceleration commands. In all cases, the transfer functions were calculated from 0.1 to 10 Hz, based on modes to 20 Hz. and 0.5% critical damping. The plots also include the P99/90 (99th percentile at 90% confidence) response extremes calculated at each frequency by sorting all 10,015 gain values from high to low and keeping the 88th largest value (P99/90) and also keeping the 88th smallest value (P01/90).

The adequacy of the robustness built into the control system can be determined by predicting the uncertainty in the GNC metric gains and the uncertainty in the modal frequencies. Two-dimensional scatter plots of GNC gain uncertainty vs. uncertainty in the corresponding modal frequency can be used to quickly determine whether allowables are violated. Figure 11.11 shows scatter plots for the GNC rate metric gain uncertainty at the RINU for roll, pitch, and yaw due to roll, pitch, and yaw commands vs. the percentage uncertainty in frequency for the fundamental roll, first bending in pitch, and first bending in yaw modes, respectively. The gain value of each random system ensemble member is computed by matching the random modes to the nominal system first roll, first bending in pitch, and first bending in yaw modes using the unique best-fit XO

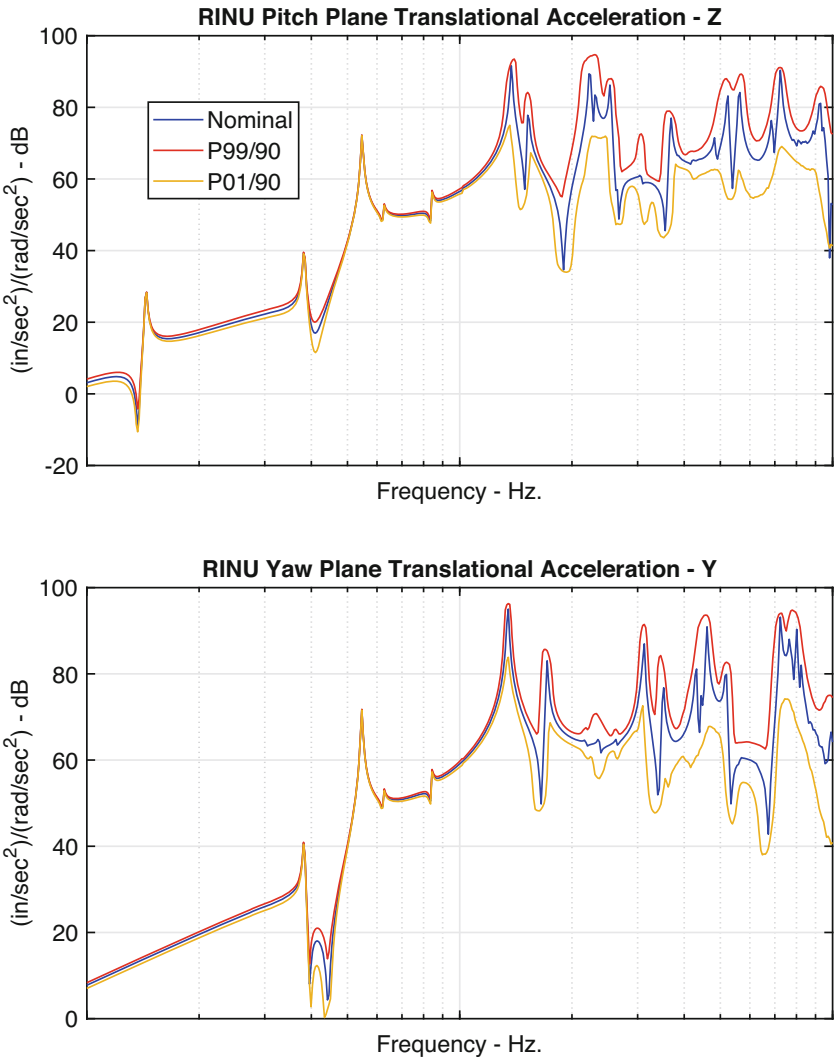

Fig. 11.10 RINU translational acceleration transfer functions and P99/90 extremes

and then computing the GNC metric at the corresponding random mode resonant frequencies. In contrast with the P99/90 extremes presented in Figs. 11.9 and 11.10, all 10,015 data points are used in the scatter plots (Figs. 11.11 and 11.12). In the case of the fundamental bending modes, the gain uncertainty must be <4 dB and the frequency uncertainty should be greater than −10%. As illustrated in Fig. 11.11, these constraints are satisfied for both pitch and yaw at the RINU. The constraints are also satisfied for roll at the RINU except for two points in 10,015 that are slightly above 4 dB. The results for the itRGA and aftRGA sensors are similar. In both cases, the gain and frequency uncertainty constraints are met for pitch, yaw, and roll. Figure 11.12 illustrates the gain uncertainty for the transverse GNC acceleration metric at the RINU due to pitch and yaw commands vs. the uncertainty in the fundamental pitch and yaw bending mode frequencies. The uncertainty constraints are also satisfied in these scatter plots.

11.5 Conclusion

A method has been presented for uncertainty quantification and propagation that is consistent with the building-block approach in which components of a system are tested and validated individually instead of an integrated vehicle test and validation being performed. A unified methodology has been presented for representing and quantifying uncertainty in an HCB component based on component test results and then propagating the uncertainty in the component models into system-

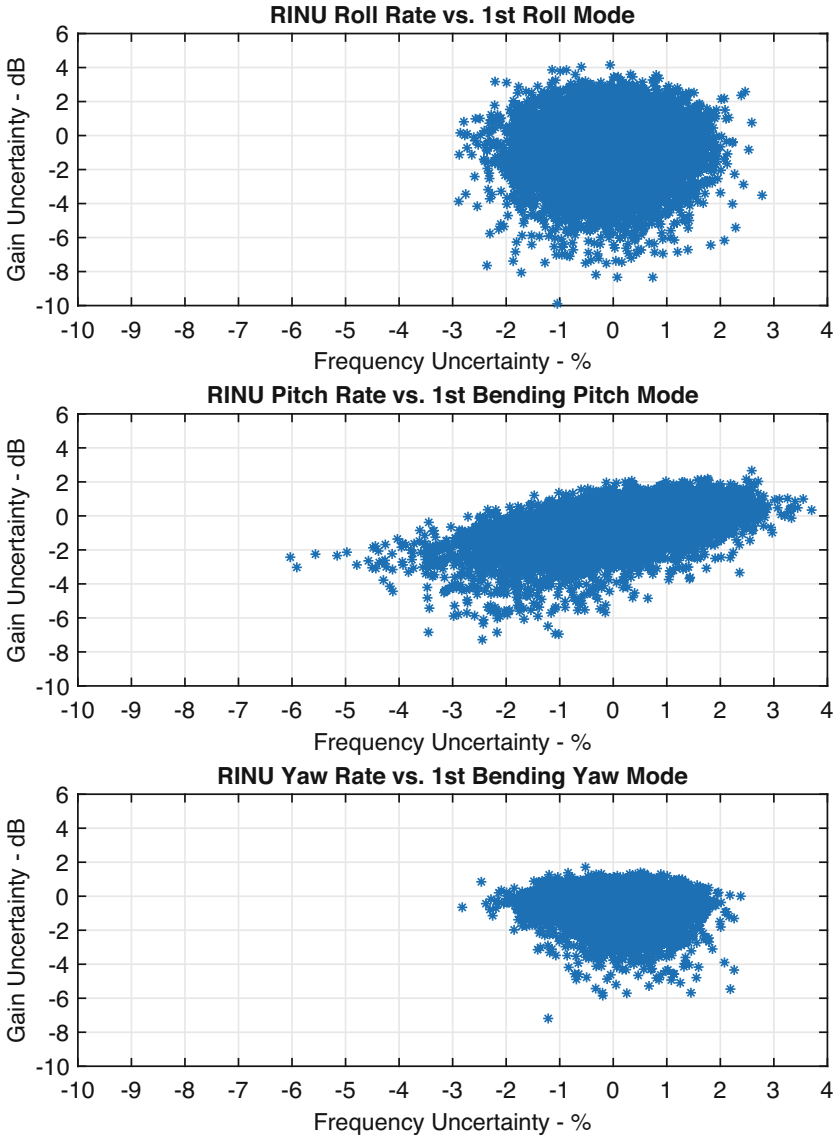

Fig. 11.11 Uncertainty in GNC rate metric vs. uncertainty in modal frequency at RINU

level predictions. Uncertainty in the HCB representations is quantified using an HPV approach based on Soize's ME method. The approach combines parametric and nonparametric uncertainty by treating the HCB fixed-interface eigenvalues as parametric random variables, and treating the component mass and stiffness as random matrices. If desired, component slosh modes and rigid body mass properties can be preserved during the uncertainty analysis. The proposed method offers several advantages over traditional approaches to UQ in structural dynamics: the number of random variables is relatively small compared with the usually large number of potential random FEM parameters, so time-consuming parametric sensitivity studies do not have to be performed. In addition, nonparametric model-form uncertainty is easily included using RMT. The method requires the selection of dispersion values for the HCB fixed-interface eigenvalues and the corresponding mass and stiffness matrices. Component test/analysis frequency error is used to identify the fixed-interface eigenvalue dispersions, and test/analysis cross-orthogonality is used to identify HCB stiffness dispersion values. Currently, the mass matrix dispersion is based on engineering judgment, past experience, and historical results, but future work will focus on developing a systematic approach for selecting the mass matrix dispersion based on component test results.

The proposed UQ methodology was applied to the SLS liftoff configuration. Uncertainty models were derived for the seven components in the liftoff configuration based on the ISPE configuration 3 test/analysis correlation. Robustness of the attitude control system was studied by propagating derived component uncertainty models into gain uncertainty in specific transfer functions relating engine inputs to rate sensors on the CS, and frequency uncertainty for the fundamental bending

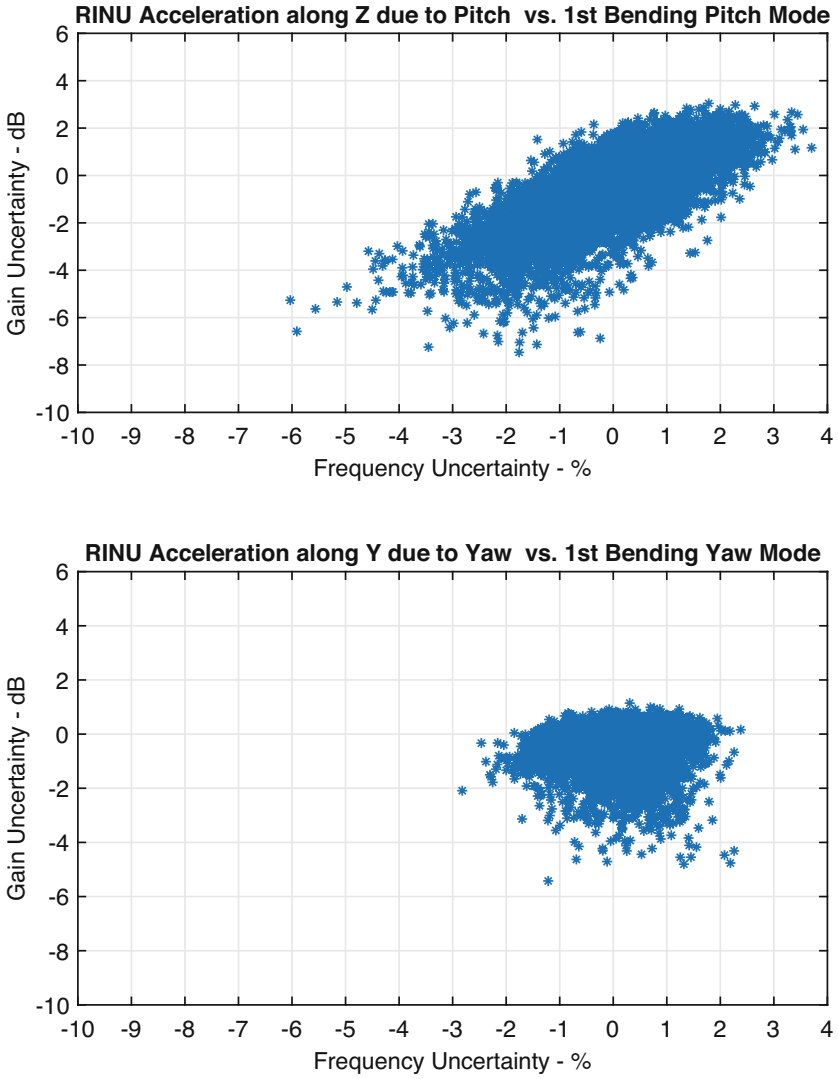

Fig. 11.12 Uncertainty in GNC acceleration metric vs. uncertainty in frequency at RINU

and roll modes. For the preliminary uncertainty model selected, the transfer function gain uncertainty and the corresponding fundamental bending mode frequency uncertainty constraints for attitude control system stability were met.

References

1. Craig, R.R., Bampton, M.C.C.: Coupling of substructures for dynamic analysis. AIAA J. **6**, 1313–1319 (1968)
2. Ghanem, R., Spanos, P.: Stochastic Finite Elements: A Spectral Approach. Springer, New York (1991)
3. Wishart, J.: Generalized product moment distribution in samples. Biometrika. **20A**(1–2), 32–52 (1928)
4. Wigner, E.: Characteristic vectors of bordered matrices with infinite dimensions. Ann. Math. **62**(3), 548–564 (1955)
5. Soize, C.: A nonparametric model of random uncertainties for reduced matrix models in structural dynamics. Probab. Eng. Mech. **15**(3), 277–294 (2000)
6. Soize, C.: Maximum entropy approach for modeling random uncertainties in transient elastodynamics. J. Acoust. Soc. Am. **109**(5), 1979–1996 (2001)
7. Adhikari, S.: Wishart random matrices in probabilistic structural mechanics. J. Eng. Mech. **134**(12), 1029–1044 (2008)
8. Adhikari, S.: Generalized wishart distribution for probabilistic structural dynamics. Comput. Mech. **45**, 495–511 (2010)
9. Capiez-Lernout, E., Pellissetti, M., Pradlwarter, H., Schueller, G.I., Soize, C.: Data and model uncertainties in complex aerospace engineering systems. J. Sound Vib. **295**(3–5), 923–938 (2006)

10. Pellissetti, M., Capiez-Lernout, E., Pradlwarte, H., Soize, C., Schueller, G.: Reliability analysis of a satellite structure with a parametric and a non-parametric probabilistic model. Comput. Methods Appl. Mech. Eng. **198**(2), 344–357 (2008)
11. Mignolet, M., Soize, C., Avalos, J.: Nonparametric stochastic modeling of structures with uncertain boundary conditions/coupling between substructures. AIAA J. **51**(6), 1296–1308 (2013)
12. Ben-Israel, A., Greville, T.: Generalized Inverses: Theory and Applications, 2nd edn. Springer, New York (2003)
13. Blelloch, P.: Cross-orthogonality of closely spaced modes. In: IMAC, St. Louis (2006)

Chapter 12
Accumulated Lifetimes in Single-Axis Vibration Testing

Adam Bouma, Abigail Campbell, Thomas Roberts, Stuart Taylor, Colin Haynes, and Dustin Harvey

Abstract Vibration qualification testing verifies and quantifies a system's longevity in its proposed service environments. Service environments a system could encounter can impart many ranges of excitation in all directions; however, multi-axis excitation testing capabilities for simulating realistic environments are rare and costly. Therefore, multiple, single-axis vibration tests are commonly used to qualify a system and its components to a lifetime of service environments. Quantifying the equivalent amount of time a component has been tested can be difficult when limited to single-axis tests. Further complications arise due to the fact that real-world service conditions are often measured at a system level without instrumentation on each component. In addition, many mechanical systems include joints and contact surfaces that, if altered, can significantly change the component's vibration characteristics. This makes replicating the boundary conditions of each component difficult. Therefore, another crucial part of single-axis vibration testing is determining boundary conditions to replicate best the real-world environment onto each component. This paper aims to analyze the effects on lifetime estimates using single-axis vibration testing of components under variations in boundary conditions, testing strategies, control locations, and other configuration options. Methods such as power spectral density (PSD), fatigue damage spectrum (FDS), and Miner's Rule, with quantities such as fatigue cycles, peak response, and RMS response are used to evaluate boundary conditions, study the response of the components, and determine the severity of various test strategies as it pertains to the overall lifetime of the system.

Keywords Vibration · Fatigue · Lifetime · Boundary conditions · Single-axis

12.1 Introduction

Vibration testing using shaker excitation is a common method for qualifying systems and their components when placed in certain service environments. However, it is difficult to replicate the multi-axis test environment in a lab setting. This shortcoming is commonly addressed by sequentially vibrating the system and/or its components on a linear shaker in each primary direction [1]. This single-axis vibration method is easy to perform, widely used, and typically assumed to be equivalent to the multi-axial service environment [2]. However, because of the cross-axis responses that occur when a structure is excited in a single direction, it can be difficult to quantitatively evaluate the service life imposed by multiple, single-axis tests. The lifetime of vibration environments can be calculated in several ways, including power spectral densities (PSD) [3], extreme response spectrums (ERS) [4], fatigue damage spectrums (FDS) [5], as well as taking the peak and root mean square (RMS) [6] of the acceleration time histories. The peak and RMS of the acceleration are scalar values, while the PSD, ERS, and FDS are spectral measures that are each quantified with a specific scalar, as discussed later in the paper in Sects. 12.3.3, 12.3.4, and 12.3.5. Using a scalar such as a peak provides insight into instantaneous brittle failure, while

A. Bouma
Department of Mechanical Engineering, New Mexico State University, Las Cruces, NM, USA

A. Campbell
Department of Mechanical Engineering, University of Utah, Salt Lake City, UT, USA

T. Roberts
Department of Mechanical Engineering, Rose-Hulman Institute of Technology, Terre Haute, IN, USA

S. Taylor · C. Haynes · D. Harvey (✉)
Los Alamos National Laboratory, Los Alamos, NM, USA
e-mail: harveydy@lanl.gov

C. Walber et al. (eds.), *Sensors and Instrumentation, Aircraft/Aerospace, Energy Harvesting & Dynamic Environments Testing, Volume 7*, Conference Proceedings of the Society for Experimental Mechanics Series,
https://doi.org/10.1007/978-3-030-12676-6_12

scalars such as the RMS help to quantify ductile failure. Each of these lifetime definitions can vary from the others and cause further uncertainty when estimating the lifetime imposed on the system.

Additionally, because the boundary conditions in the laboratory usually differ from those in the service environment, it can be difficult to replicate a system's service environment response. In any given system, boundary conditions can include contact surfaces and joints, which can significantly affect responses when altered. Such discrepancies may result in inaccurate stress states and missed failure modes [2], which will ultimately lead to an undesirable amount of life imposed on the system, especially at locations away from the control location. In addition, the boundary conditions tend to change when testing a component of a system on its own [7], which creates more opportunity for inaccuracy when applying system-level measurements to a single-component test.

Finally, it is not always possible to obtain the data from the service environment that is pertinent to the component of interest. It can be difficult to instrument every component within the system due to limited instrumentation, space, or data acquisition capabilities. Thus, it becomes necessary to estimate the response of the component through data that is not specific to the component of interest. This adds another layer of unreliability to the lifetime imposed on the component.

12.2 Experimental Setup

12.2.1 Structure

The structure that was used for this experiment was the Box Assembly with Removable Component (BARC) (Fig. 12.1) developed at Sandia National Laboratories and Kansas City National Security Campus for the Boundary Condition Round Robin Challenge [8]. This structure was specifically developed to provide a common test bed for researchers to use when designing environmental shock and vibration tests and addressing the challenges in determining the "appropriate boundary conditions and input stimulus required to qualify a product" [8]. The structure consists of a partial aluminum box channel subassembly and removable component bolted to the top of the box.

12.2.2 Instrumentation

Acceleration measurements were used for control and data analysis. The entire system included six tri-axial accelerometers. Figure 12.1 shows the placement of the different sensors on the component and the box respectively. Accelerometers 1, 2, and 6 were placed on the box, while accelerometers 3, 4, and 5 were placed on the removable component. Accelerometers 5 and 6 were used at different times for closed-loop test control, while accelerometers 1–4 were used primarily for response characterization. In Fig. 12.1, accelerometers 1 and 4 are out of view on the opposite side of the structure. Initially, three

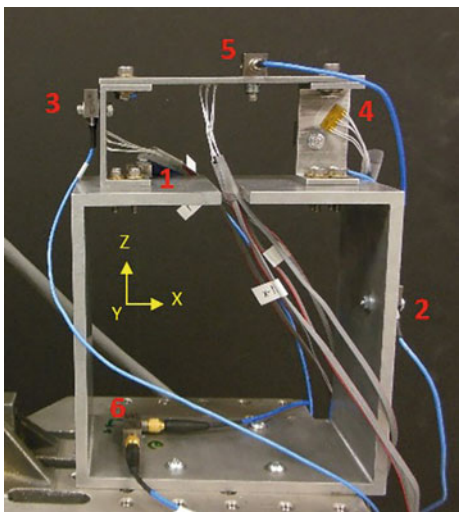

Fig. 12.1 Box and Removable Component (BARC) fixture used in this paper and placement of sensors on the component (3, 4, 5) and the box (1, 2, 6)

rosette strain gages were placed at locations 3, 4, and 5; however, the service environment strain data did not exhibit a sufficient signal to noise ratio, so all strain information was neglected in this paper.

12.2.3 Boundary Condition Variations

One limitation of single-axis vibration testing is the difficulty of recreating service boundary conditions in the lab environment. Component-level tests in a lab are often performed with rigid attachment to a shaker table, which contrasts with more flexible boundary conditions likely to be seen when the component is assembled in the system. For this experiment, two types of boundary conditions are used to study the effects varying boundary conditions can have on the severity of the single-axis tests. The first boundary condition has the component attached to the box portion of the BARC; this boundary condition will be referred to as flexible and can be seen in the left-hand portion of Fig. 12.2. The flexible boundary condition provides a flexible base when compared to the second, more rigid boundary condition studied in this experiment. The latter will be referred to as the rigid boundary condition and can be seen in the right-hand portion of Fig. 12.2. The rigid boundary condition is a rigid aluminum base that is used to attach the component directly to the shaker table.

12.2.4 Service Environment

A service environment is any real environment a system is expected to withstand during the system's service life. For this experiment, the service environment was generated with random input to the system in three axes. The responses of the fully instrumented system were recorded to be used as control and comparison data for future tests and analyses. Figure 12.3 depicts the configuration of the system and three single-axis inputs to generate the service environment.

One important aspect of the service environment set up is the boundary condition for the box portion of the system. By fixing the system to a stiff plate, the system is isolated from any unwanted forces from the suspension cords. In addition,

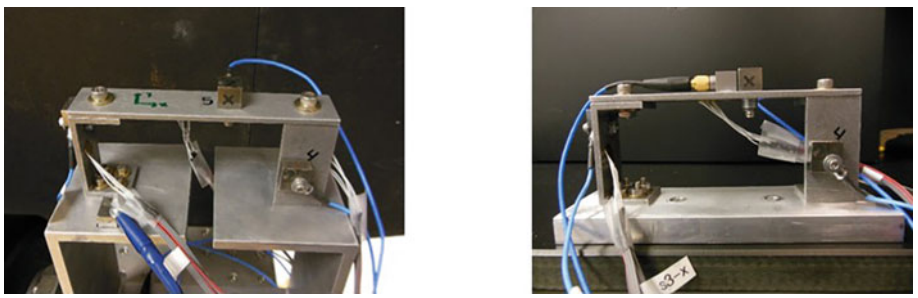

Fig. 12.2 Flexible boundary condition (left) and rigid boundary condition (right)

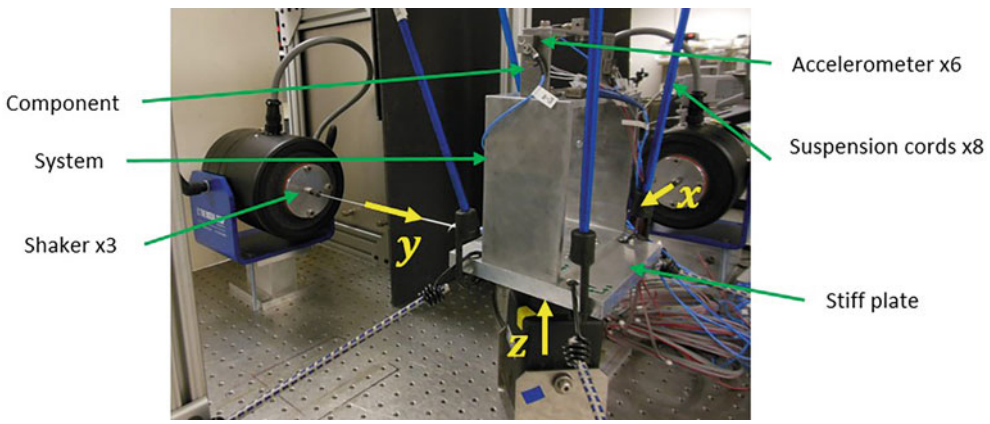

Fig. 12.3 Service environment equipment set up consisting of the fully instrumented system, support structure, and three single-axis shakers

this boundary condition is similar to when the system is fixed to the shaker table; using this boundary condition removes one more level of inconsistency from the testing strategies.

12.2.5 Service Environment Data Limitations

Often when performing field tests to obtain data on the service environment of a system, data is not obtained from every component of interest. Absence of component data could be due to lack of sufficient data acquisition capability or the inability to physically instrument a component to measure its response. In order to test the effects of this data limitation, two control accelerometers at locations 5 and 6 were utilized. Accelerometer 5 was placed at the top of the component and measured the component's response to the service environment. Accelerometer 6 was placed at the base of the subassembly and measured the ground response to the service environment. These two data sources were then used as control input locations for different single-axis tests.

If instrumentation is lacking on a component of interest, it may be necessary to perform an intermediate test to obtain a derived version of the service environment; this process is outlined in Fig. 12.4. This intermediate system-level test is controlled by the data obtained in the original service environment at a measured location not on the component, and then measures the response of the component. Once the component data is obtained, it is then used to control the subsequent component-level tests. In this experiment, service environment data from location 6 was used to control three single-axis intermediate tests at the system level. The component's response at location 5 was recorded in the excited directions to serve as the derived service environment for use in future tests, thus the system-level data can be transferred from the base location at accelerometer 6 up to the component at accelerometer 5.

12.2.6 Controlled Single-Axis Tests

All single-axis tests were controlled by power spectral density data taken from the service environment or the derived service environment. Four groups of single-axis tests were conducted with each group consisting of three tests, one test in each axis. Table 12.1 summarizes the four groups of tests and their distinguishing characteristics. Note that component responses from test group 2 serve as the derived service environment used to control test group 4.

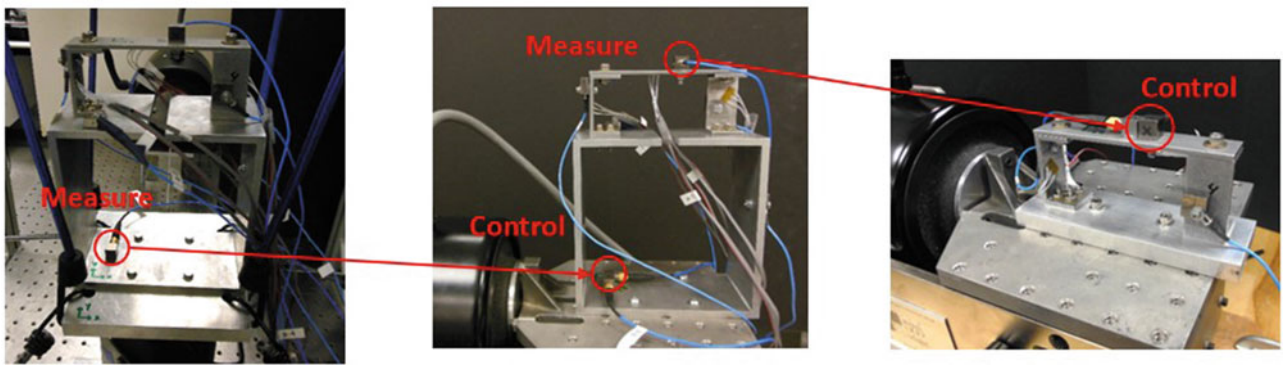

Fig. 12.4 Flow of data through the intermediate test to obtain the derived service environment. The response is measured at accelerometer location 6 and is used to control the intermediate test. The response to that test is measured at accelerometer location 5 and then used to control the component test

Table 12.1 Details of the four different single-axis test groups

Test group	Boundary condition	Control location	Control data
1	Flexible	Component (a5)	Service Env. (a5)
2	Flexible	Box (a6)	Service Env. (a6)
3	Rigid	Component (a5)	Service Env. (a5)
4	Rigid	Component (a5)	Derived Service Env. (a5)

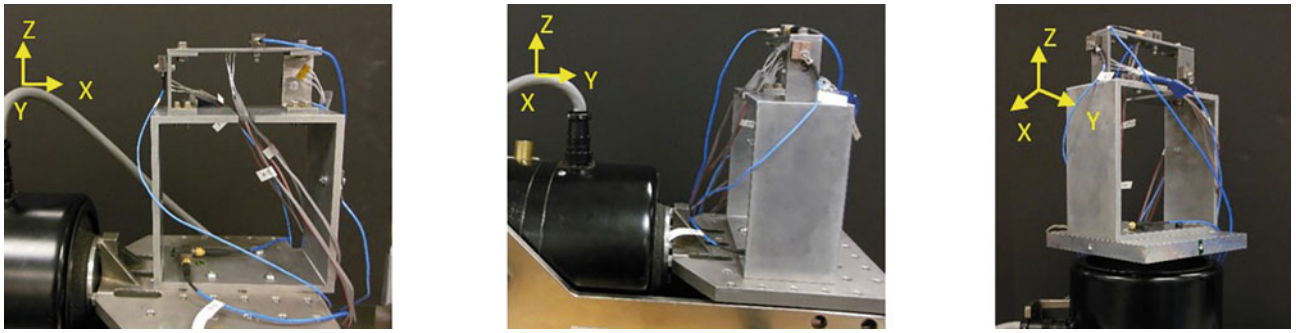

Fig. 12.5 Experimental setup for three single-axis flexible boundary condition tests (test groups 1 and 2) for the x (left), y (center), and z (right) excitation axes

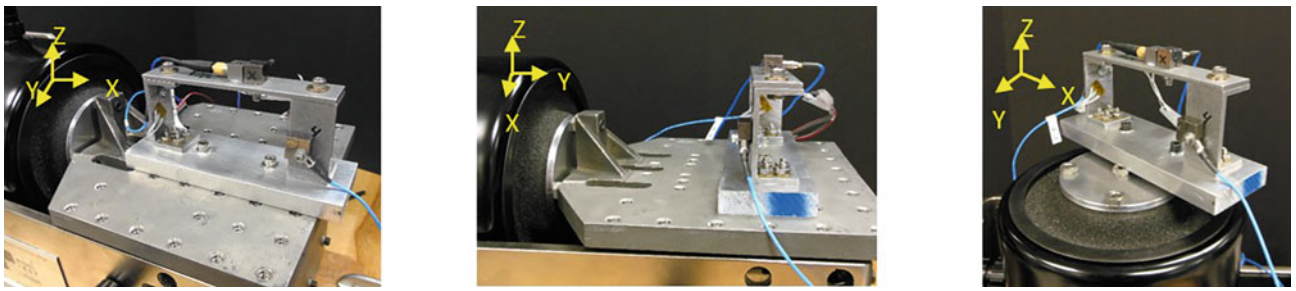

Fig. 12.6 Experimental setup for three single-axis rigid boundary condition tests (test groups 3 and 4) for the x (left), y (center), and z (right) excitation axes

Each group of tests provides a specific change in the testing strategy that allows conclusions to be drawn about which aspects of single-axis vibration testing are most significant. Test groups 1 and 2 utilize the box subassembly of the BARC to look at the effects of flexible boundary conditions. Group 1 is controlled using data directly from the component at control location 5. Group 2 is controlled using data from the base of the system at control location 6. Figure 12.5 shows the experimental setup for system level tests in groups 1 and 2.

Test groups 3 and 4 are performed using the rigid boundary conditions. Test group 3 is controlled using service environment data at control location 5 while test group 4 is controlled using the derived system data that was described in Sect. 12.2.5. Figure 12.6 shows the experimental setup for component level tests in groups 3 and 4.

Through this test strategy, it is possible to look at the effects of changing boundary conditions by comparing test groups 1 and 3 and the effects of changing the data source by comparing test groups 3 and 4. Comparison between groups 1 and 2 also illustrates the effects of changing data source, however this paper will focus on test groups 3 and 4, while test group 2 will be used solely for generating the derived service environment. The next section discusses how using different lifetime definitions allows comparison of strategies for estimating lifetime.

12.3 Methods

Cross-axial responses are present during a single-axis vibration test, and they must be considered in a rigorous estimation of the imposed lifetime. To compare the lifetime of a test to the service environment, the test cases must be combined to account for cross-axial responses of the system/component. This can be done by using Palmgren-Miner Rule (Miner's Rule) which is expressed by an inverse power rule as

$$\frac{t_{test}}{t_{serivce}} = \left(\frac{S_{service}}{S_{test}}\right)^{m}. \tag{12.1}$$

Here, t is the duration of a test, S is the severity of a test, and m is the exponent relating to the material and damage measure [8]. This inverse power rule determines the severity ratio between the service environment and the test environment.

In this paper, Miner's Rule was used to combine multiple tests when the severity measure involves power spectral density. All tests were the same length in this experiment, so severity ratios based on PSDs were used as the scalars to combine multiple tests. In the following sections, different measures of test severity are discussed.

12.3.1 Peak of Time History

The peak of a time history can be quickly calculated from an acceleration time history. The peak response of a signal can be acquired by finding the maximum of the absolute value of a signal. This measure can be compared between the service environment and the various test cases to obtain a severity ratio.

12.3.2 RMS of Time History

The RMS of a time history can be calculated quickly from an acceleration time history as well. The RMS values of the service environment and test cases can be compared to obtain a severity ratio. In order to combine multiple tests of different severity, Miner's Rule can be implemented with the severity ratios calculated with each individual RMS value.

12.3.3 Power Spectral Density (PSD)

The power spectral density is the average power of a signal as a function of frequency. This measure is often used to control vibration tests. The PSD can be calculated in order to determine the severity of each test. Miner's Rule can be applied to combine the like-direction responses to each axis of single-axis testing. An "equivalent" PSD can be calculated and compared to the service environment PSD. To create an equivalent PSD from multiple signals, the severity ratio PSD value of the tests and the service environment at every frequency can be recorded. Miner's Rule is then implemented to combine the values of the test PSDs at each frequency. Furthermore, the RMS values from the combined PSD and the service environment can be used to calculate a severity ratio. These severity ratios will show which test set is the most severe compared to the service environment as well as clarify any over and under testing.

12.3.4 Fatigue Damage Spectrum (FDS)

The fatigue damage spectrum (FDS) is the cumulative damage as a function of frequency. One method to calculate an FDS is by using the time history response and applying the method proposed by McNeill [5]. In this method, the pseudo-velocity response is calculated followed by a rainflow cycle count. Rainflow counting is a common way to count the number of fatigue cycles a system experiences. This cycle-counting method uses a time domain signal from a vibration test to count full and half cycles and the respective amplitudes of those cycles [9]. The cumulative damage can be computed using Miner's rule and the S-N law. Plotting the cumulative damage vs. the frequency band will yield an FDS. It is important to note that for an FDS it assumes a linear SDOF system and relies on a linear damage accumulation assumption from Miner's Rule. The damping factor and fatigue exponent are also assumed constants [10].

Once the FDS is computed for the service environment and all test cases, the FDS for each test can be summed according to direction. Since the FDS is a measure of accumulated damage as a function of frequency, multiple FDS's can be summed together as long as the frequency indices remain consistent. To compare these damage measures, the FDS is transformed into a PSD from a method used by McNeill [5]. The RMS values from the FDS generated PSD and the service environment can then be compared via a severity ratio.

12.3.5 Extreme Response Spectrum (ERS)

The extreme response spectrum (ERS) is defined as the highest peak of the response of a linear SDOF system to the vibration input, according to its frequency for an assumed damping ratio [11]. The response is described by the relative movement of the mass in relation to its support and is closely related to the shock response spectrum (SRS). SRS utilizes a system's highest response during or after a shock, where ERS utilizes the system's maximum response during a longer duration vibration input [12]. The ERS can be calculated either from a time history or from a PSD.

Since the ERS is closely related to the SRS, the method used by Smallwood [13] for calculating the SRS can be applied to calculating the ERS. This method uses a digital recursive filter to simulate a single-degree-of-freedom system. The output of the filter using sampled input is assumed to be a measure of the response of the SDOF system. The response is then searched for the maximum value. This process is repeated for each natural frequency of interest [13].

For this project, the ERS of the service environment and each test were computed from the time history responses. In order to compare severity, the ERSs for all tests were enveloped from like-direction responses. This envelope can then be compared to the service environment ERS. Peaks from the ERS can be observed to obtain the scalar value to produce a severity ratio between the tests and service environment, similar to the RMS values calculated from the PSD.

12.4 Results and Discussion

The results presented in the following sections are comparisons between the service environment and the single-axis test groups described in Sect. 12.2.2.6 that were intended to reproduce the service environment responses. A severity ratio was computed for each test case, direction, and accelerometer depending on the lifetime measures of interest as described in Sect. 12.3. All severity ratios are presented in dB scale. A full table of all numeric severity ratios can be found in in Table 12.9 and Fig. 12.17 in Appendix.

12.4.1 General Results

As a whole, under-testing was uncommon in most testing strategies due to the cross-axis responses to single-axis inputs. The combination of these off-axis responses caused the overall equivalent test to be more severe than the service environment. Figure 12.7 shows the severity ratios for all test groups at accelerometer locations a3, a4, and a5 using the lifetime measure of RMS of the time history. Each severity ratio in Fig. 12.7 represents the combination of each specific direction's response in all three tests for every test group. The combination of responses is discussed in further detail in Sect. 12.3. This format is consistent for all following severity ratio figures.

The severity ratios for most metrics and groups were greater than one, or 0 dB, which represents a large trend of over-testing. Evidence for this observation can be seen through the power spectral densities from accelerometer location a3 during the three single-axis tests in test group 1, as seen in Fig. 12.8. The off-axis responses for all three input directions were close to or even orders of magnitude larger than the controlled direction responses, which are shown in the Group 1 a5 plots of Fig. 12.8. This was particularly evident in the y and z input directions within a frequency range of 400–800 Hz. When all three responses were combined, the overall test severity was often larger than the service environment severity.

Of the four test groups, test group 4 was the only one to show consistent trends of under testing. Test group 4 was controlled with derived service environment data, thus the severity ratios between the test group 4 tests and the service environment were much more susceptible to showing under testing. This can be seen in Fig. 12.9 which shows the power spectral density data for the service and derived service environments at accelerometer location a5.

The derived service environment signal for the x-direction contained significantly less power than the service environment signal. As the x-direction test for test group 4 was controlled to the derived service environment data, we expect to see a fair amount of under testing when comparing to the service environment. Figure 12.10 shows the severity ratios for all lifetime measures in the x, y, and z-directions for test group 4 at accelerometer location a5. As expected, the x-direction was consistently under tested when compared to the service environment. This trend was consistent in accelerometers locations a3 and a4, and this information can be found in Fig. 12.17 and Table 12.9 in Appendix.

It is also clear form Fig. 12.9 that there is significant over testing in the y direction. Analyzing the results from all tests shows this trend of over testing in the y-direction is consistent across all groups and all accelerometers. One instance of this can be seen in the z-input portion of Fig. 12.8, where the y-response to the z-input is nearly two orders of magnitude higher

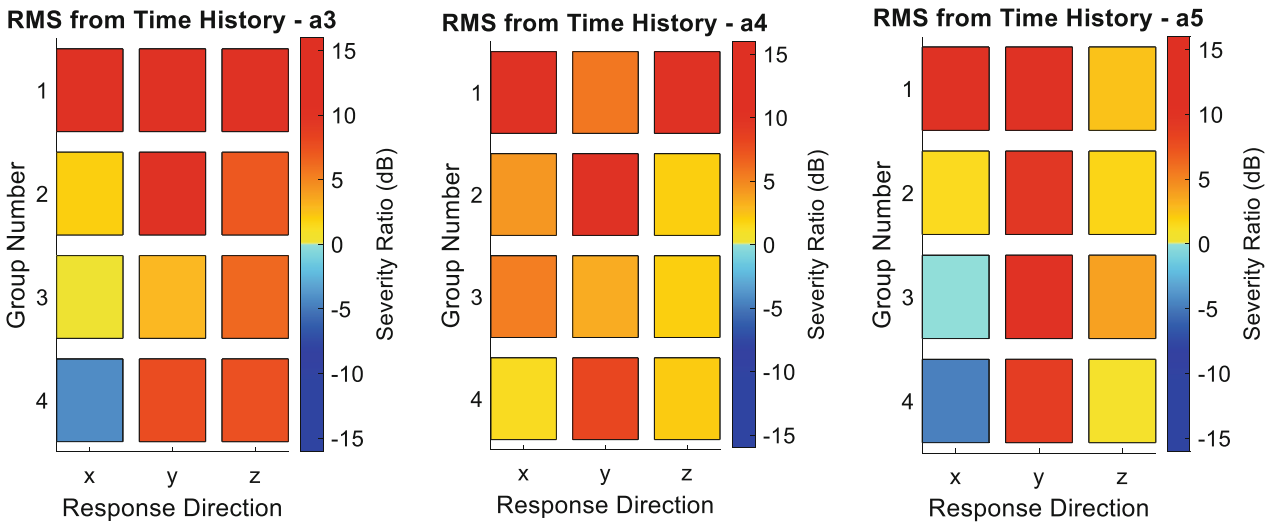

Fig. 12.7 Severity ratios based on RMS of the time history for all groups at accelerometer locations a3, a4, and a5. Reference Table 12.2 in Appendix for numeric severity ratio values

than that of the y-direction service environment. A similar trend can be seen in Fig. 12.11 where the y-direction severity ratios are shown for all groups and all lifetime measures at accelerometer location a3. All groups exhibited significant over testing regardless of the lifetime measure used to assess test severity. The consistency of this result between all groups and lifetime measures suggests that the source of this over testing is not within a testing strategy, but rather due to some feature of the BARC structure in the y-direction. The large difference between the y-direction test severities and the x and z-directions suggests that there is a possibility for large variation in results depending on the response direction of interest.

Another area of interest in this experiment is the effect on lifetime estimation depending on where the structure is measured. As previously described, each test was controlled at only one location and in one direction. All other measurement locations were likely to exhibit some degree of undesirable behavior, as their responses were not being controlled. As an example, to study these effects the severity ratios for test group 4 at accelerometer locations a3, a4, and a5 are shown in Fig. 12.12. Because test group 4 was controlled with derived service environment data, the severity ratios shown in Fig. 12.12 may not be exactly 1, or 0 dB, in the excited directions. The severity ratios across all three measurement locations appear to be rather consistent especially in the x and z response directions. The mean values of severity ratio between the three measurement locations differ by a maximum of 28%. Future results in this section will show that a 28% difference in the mean value of severity ratio is rather insignificant compared to other sources of variation within the testing strategies. With other sources of variability largely outweighing variations due to measurement location, single-axis component test could be controlled at any convenient location and measured elsewhere without much concern of the effects of instrumentation location.

Other topics of interest in estimating lifetimes are changing the lifetime estimation measure, changing boundary conditions, and changing control data. The following three subsections target each one of these sources of variability in order to assess their effects on the estimate lifetimes imposed on the component.

12.4.2 Changing the Lifetime Estimation Measure

Another notable feature of Fig. 12.10 is the consistency in severity ratios between each different lifetime measure. The rows of Fig. 12.10 show very little variation in their severity ratios, which suggests that all of the lifetime measures considered here provide consistent results. This result holds for nearly all groups, locations, and directions. Figure 12.13 shows the severity ratios for all lifetime measures for test group 4 at accelerometer locations a3 and a4—Fig. 12.10 is the last of the set of 3 figures for test group 4. The standard deviations (SD) of the severity ratios for each direction quantitatively show the consistency between the lifetime measures across all measurement locations. This consistency removes the possibility of variability in the results from different lifetime measures. Thus, the majority of the following results will focus on a single lifetime measure.

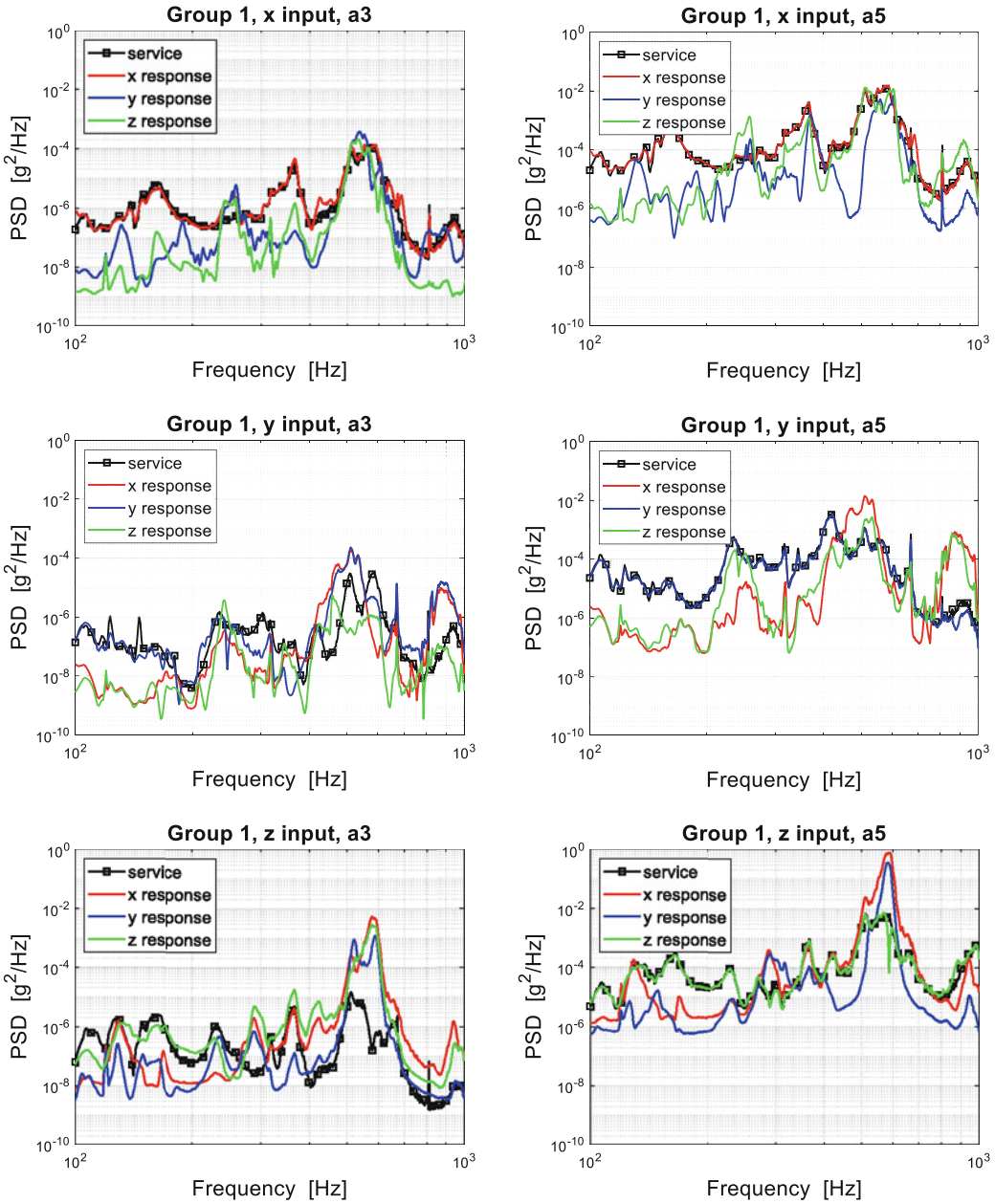

Fig. 12.8 PSD of responses to three single-axis inputs for test group 1 at accelerometer locations a3 and a5. Test group 1 was controlled at accelerometer location a5

12.4.3 Changing Boundary Conditions

Test groups 1 and 3 were used to study the effects of changing boundary conditions on test severity. As mentioned in Table 12.1, test group 1 utilizes the flexible boundary conditions while controlling the test at accelerometer location a5. Test group 3 utilizes the rigid boundary conditions while still controlling at accelerometer location a5. Of these two groups, test group 3 over-tested less than test group 1. The difference between the groups' severity ratios is significant, as can be seen in Fig. 12.14.

With the exception of the results at accelerometer location a5 in the z-direction, test group 1 always experienced higher severity than test group 3. The mean severity ratios between groups 1 and 3 differ by nearly 70%. In this case, the rigid boundary conditions in test group 3 allow for better test control than the flexible boundary conditions in test group 1. This result implies that rigid boundary conditions restrict the amount of off-axis response in each single-axis test. Figure 12.15

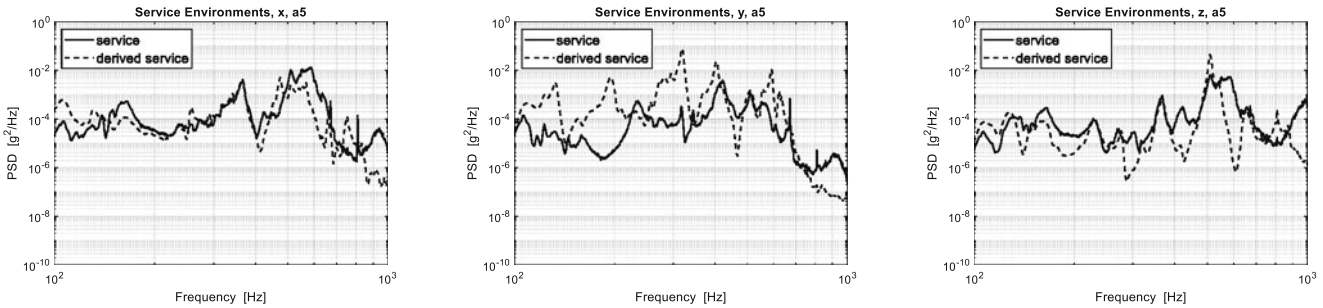

Service RMS = 1.00 g
Der. Service RMS = 0.583 g

Service RMS = 0.411 g
Der. Service RMS = 1.23 g

Service RMS = 0.714 g
Der. Service RMS = 0.812 g

Fig. 12.9 PSD of service and derived service environments in all directions at accelerometer location a5

Fig. 12.10 Severity ratios for all directions and lifetime measures for test group 4 for at accelerometer location a5. Reference Table 12.3 in Appendix for numeric severity ratio values

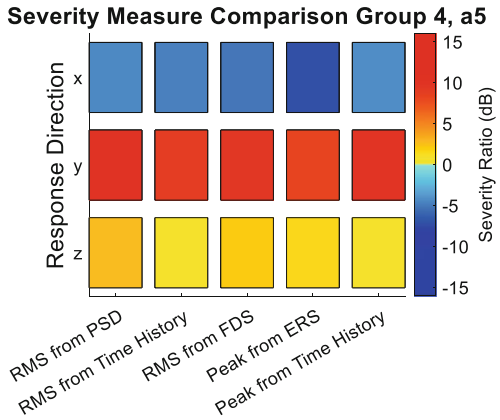

Fig. 12.11 Severity ratios in the y-direction for all test groups and lifetime measures at accelerometer location a3. Reference Table 12.4 in Appendix for numeric severity ratio values

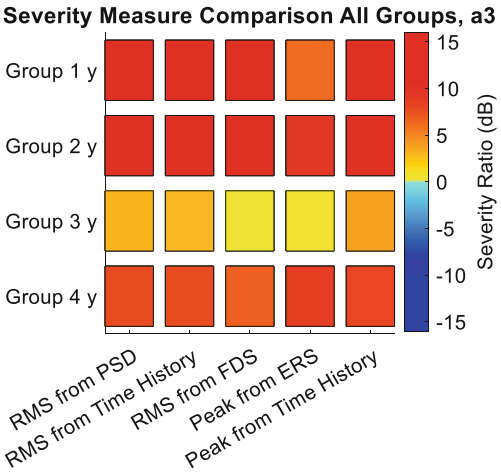

shows the power spectral densities from test groups 1 and 3 at accelerometer location a4 when the system was excited in the z-direction. Test group 1 experienced significant off-axis response in the 400–800 Hz frequency range, while test group 3 experiences much less off-axis response. The x-direction response to the z-direction input decreased by nearly four orders of magnitude when the boundary conditions were changed from flexible to rigid. The y-direction response to the z-direction input decreased less than the x-direction, but still justifies the claim that the rigid boundary conditions limit the off-axis response in the structure.

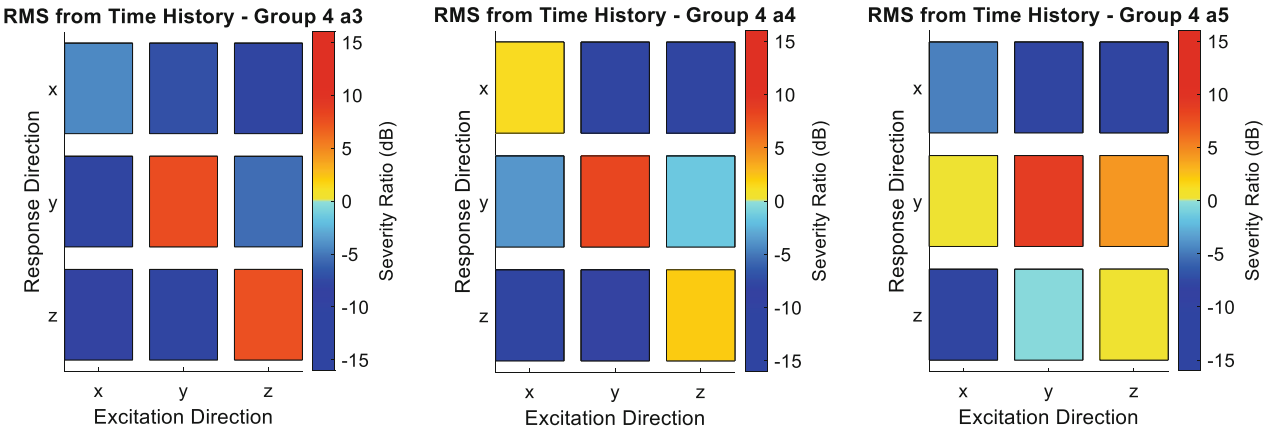

Fig. 12.12 Severity ratios based on RMS of the time history for test group 4 at accelerometer locations a3, a4, and a5. Reference Table 12.5 in Appendix for numeric severity ratio values

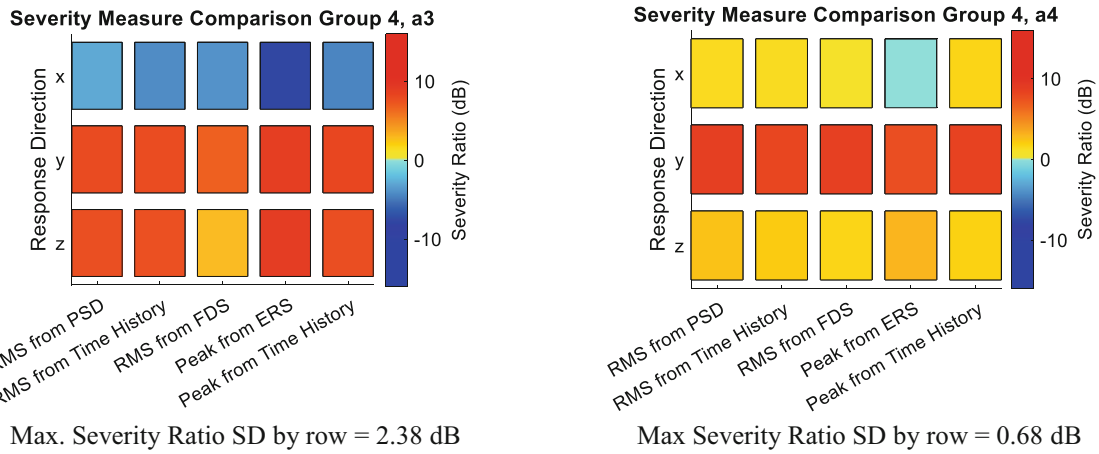

Fig. 12.13 Severity ratios for all lifetime measures for group 4 at accelerometer locations a3 and a4. The maximum values for standard deviation (SD) of the severity ratios (by row) are shown below the severity ratio figures. Reference Table 12.6 in Appendix for numeric severity ratio values

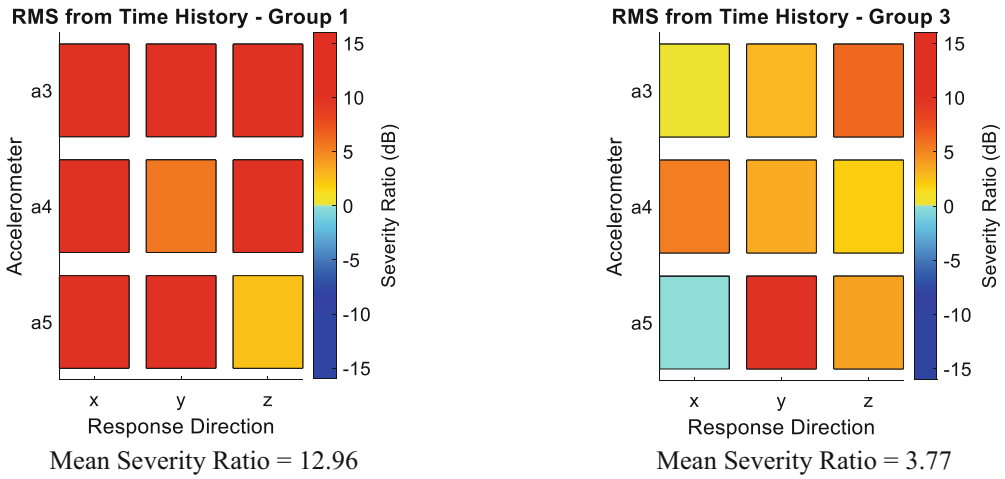

Fig. 12.14 Severity ratios based on RMS of the time history for test groups 1 and 3 in all directions and at all accelerometer locations. Reference Table 12.7 in Appendix for numeric severity ratio values

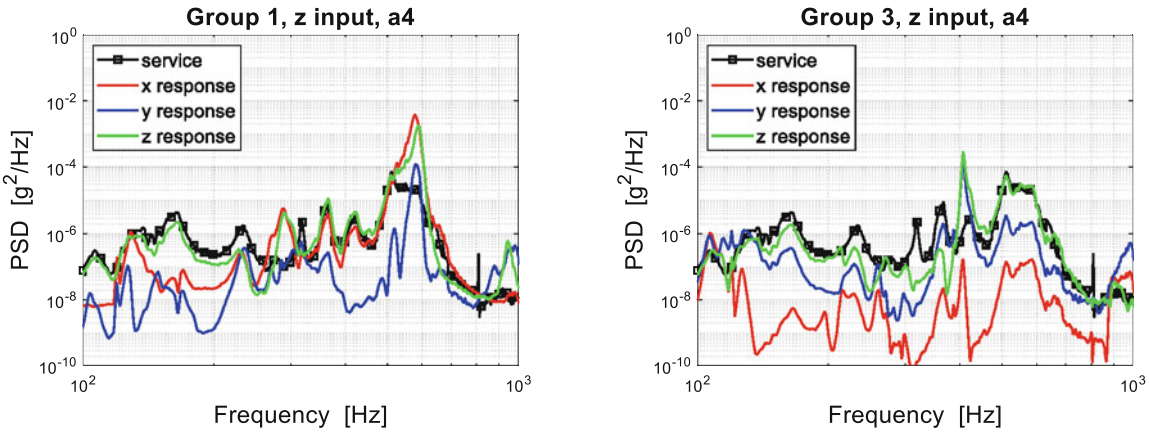

Fig. 12.15 PSD of responses to z-axis inputs from test groups 1 and 3 at accelerometer location a4

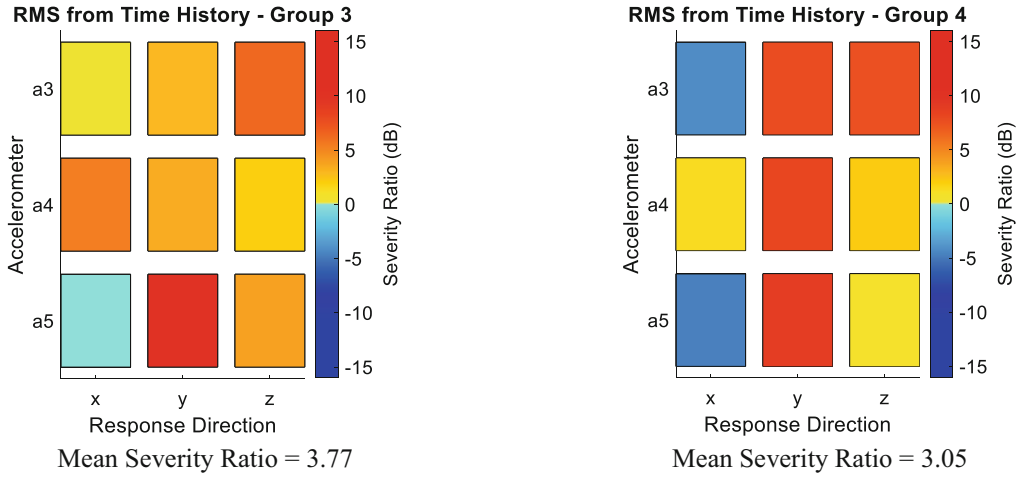

Fig. 12.16 Severity ratios based on RMS of the time history for groups 3 and 4 in all directions and at all accelerometer locations. Reference Table 12.8 in Appendix for numeric severity ratio values

12.4.4 Changing Control Data

Test groups 3 and 4 were used to study on the effects of changing control data on test severity. As mentioned in Table 12.1, test group 3 utilizes the rigid boundary conditions while controlling at accelerometer location a5 with service environment data. Test group 4 also uses the rigid boundary conditions but instead controls at accelerometer location a5 with derived service environment data. Comparison of the severity ratios from test groups 3 and 4, as shown in Fig. 12.16, yields a 19% difference between the mean severity ratios, suggesting that changing control data has a relatively minimal effect on test severity when compared to the effect of changing boundary conditions. Even though the service environment (used for control in test group 3) is not identical to the derived service environment (used for control in test group 4), the effect on test severity is less significant. Thus, the minimal effect of changing control data is likely due to the role of the rigid boundary conditions reducing the off-axis responses.

12.5 Conclusions

Different vibration testing strategies were studied through a series of single-axis vibration tests on a structure consisting of a box and a component. The experiments focused on replicating a service environment on the component through previously mentioned test strategies in order to determine their effect on the estimation of the imposed lifetime. Three major

changes were made between all of the test groups: changing the lifetime measure, boundary conditions, and control data. Over-testing is common when taking into account the off-axis responses in severity estimations, especially when flexible boundary conditions are used. The y-direction on the BARC structure experienced the most severe tests, which suggests that the estimated lifetime imposed on the system may vary significantly by response direction. Overall, changing the lifetime estimation method had a significantly smaller effect than changing boundary conditions, control data, or measurement location. Of the three main changes to the testing strategies, changing boundary conditions from rigid to flexible had the largest effect on test severity. Changing control data and varying measurement location still had measurable effects on test severity, but their effects were significantly less than changing boundary conditions. For this particular system (BARC), it could be suggested that component level vibration tests be controlled with derived service environment data with little repercussion from the lack of service environment information. Practitioners of other structures could employ this methodology to determine if this BARC-specific conclusion applies to more structures. In addition, component level tests could be fixtured using simple rigid boundary conditions for better test control. Lastly, the tests could be controlled from any easy access point on the component, and the measurements from the non-controlled locations should still be just as valid as the control location.

The next step for this experiment would be to design new tests to drive all severity ratios to unity. Depending on which test group is of interest, different excitations could be scaled in order to make the accumulated lifetime from the test environment match the service environment. Depending on the frequency range of interest, some tests resulted in severity ratios very close to unity. However, in the frequency range of 400–800 Hz, this structure would require a significant amount of changes to the control data to reduce the test severity. In addition, the collection of strain data would be an improvement for further characterization the response of any system of interest as well as allowing more methods for estimating the imposed lifetime.

A.1 Appendix

This appendix contains numeric values pertaining to the severity ration figures presented throughout Sect. 12.4. All severity ratios are presented in dB scale.

Table 12.2 Severity ratios based on RMS of the time history for all groups at accelerometer locations a3, a4, and a5

		RMS from time history—a3			RMS from time history—a4			RMS from time history—a5		
Group number	1	12.858	13.698	21.358	18.508	5.665	11.157	14.128	16.874	2.398
	2	1.907	11.357	7.082	4.190	11.445	1.935	1.364	9.533	1.629
	3	0.045	2.862	6.298	5.311	3.311	1.895	−0.069	10.497	3.785
	4	−4.281	7.799	7.533	1.296	8.107	2.078	−4.789	8.882	0.803
		x	y	z	x	y	z	x	y	z
		Response direction			Response direction			Response direction		

Table 12.3 Severity ratios for all directions and lifetime measures for test group 4 for at accelerometer location a5

		Severity measure comparison group 4, a5				
Resp. Dir.	x	−4.401	−4.789	−5.164	−7.162	−4.224
	y	10.063	8.882	9.552	8.245	9.909
	z	2.670	0.803	2.058	1.524	0.778
		RMS from PSD	RMS from time history	RMS from FDS	Peak from ERS	Peak from time history

Table 12.4 Severity ratios in the y-direction for all test groups and lifetime measures at accelerometer location a3

	Severity measure comparison all groups, a3				
Group 1 y	14.414	13.698	11.838	6.055	12.980
Group 2 y	12.760	11.357	11.186	9.499	11.543
Group 3 y	2.992	2.862	0.042	0.408	3.736
Group 4 y	7.853	7.799	6.652	8.708	8.111
	RMS from PSD	RMS from time history	RMS from FDS	Peak from ERS	Peak from time history

Table 12.5 Severity ratios based on RMS of the time history for test group 4 at accelerometer locations a3, a4, and a5

		RMS from time history—group 4, a3			RMS from time history—group 4, a4			RMS from time history—group 4, a5		
Resp. Dir.	x	−4.433	−7.264	−16.719	1.296	−15.059	−15.495	−4.791	−13.195	−21.751
	y	−15.463	7.799	−5.158	−3.821	8.106	−1.584	0.043	8.841	4.134
	z	−9.633	−12.466	7.533	−16.725	−9.573	2.078	−13.543	−0.455	0.1424
		x	y	z	x	y	z	x	y	z
		Excitation direction			Excitation direction			Excitation direction		

Table 12.6 Severity ratios for all lifetime measures for group 4 at accelerometer locations a3 and a4

		Severity Measure Comparison Group 4, a3					Severity Measure Comparison Group 4, a4				
Resp. Dir.	x	−2.994	−4.281	3.991	−7.881	4.519	1.317	1.296	0.868	−0.079	1.676
	y	7.853	7.799	6.652	8.708	8.111	8.613	8.107	8.589	7.591	8.355
	z	7.5776	7.533	2.729	8.856	7.608	2.328	2.078	1.627	2.931	1.829
		RMS from PSD	RMS from time history	RMS from FDS	Peak from ERS	Peak from time history	RMS from PSD	RMS from time history	RMS from FDS	Peak from ERS	Peak from time history

Table 12.7 Severity ratios based on RMS of the time history for test groups 1 and 3 in all directions and at all accelerometer locations

		RMS from time history—group 1			RMS from time history—group 3		
Accel.	a3	12.858	13.698	21.358	0.040	2.862	6.298
	a4	18.508	5.666	11.157	5.311	3.311	1.895
	a5	14.128	16.874	2.398	−0.069	10.497	3.785
		x	y	z	x	y	z
		Response direction			Response direction		

Table 12.8 Severity ratios based on RMS of the time history for groups 3 and 4 in all directions and at all accelerometer locations

		RMS from time history—group 3			RMS from time history—group 4		
Accel.	a3	0.040	2.862	6.298	−4.281	7.799	7.533
	a4	5.311	3.311	1.895	1.296	8.107	2.078
	a5	−0.069	10.497	3.785	−4.789	8.815	0.803
		x	y	z	x	y	z
		Response direction			Response direction		

Table 12.9 Severity ratios for all test groups, accelerometers, directions and lifetime measures

a3x	12.968	12.858	10.368	3.342	9.448	3.005	1.907	2.195	−7.287	0.671	0.593	0.040	−0.497	−0.941	−0.291	−2.994	−4.281	−3.991	−7.881	−4.519
a3y	14.414	13.698	11.838	6.055	12.980	12.760	11.357	11.186	9.500	11.543	2.992	2.862	0.042	0.408	3.736	7.853	7.799	6.652	8.708	8.111
a3z	21.436	21.358	14.390	22.563	19.429	8.300	7.081	2.050	13.742	7.100	6.372	6.298	1.525	5.302	6.750	7.578	7.533	2.729	8.856	7.608
a4x	18.579	18.508	16.977	12.616	16.955	5.751	4.190	4.998	3.583	4.722	5.342	5.311	4.330	6.300	5.200	1.317	1.296	0.868	−0.079	1.676
a4y	6.775	5.666	3.342	4.586	2.406	11.784	11.445	11.962	13.126	11.109	5.397	3.310	5.009	0.991	3.013	8.613	8.107	8.589	7.591	8.355
a4z	12.053	11.157	8.124	14.305	8.226	4.021	1.935	2.364	−1.167	0.730	2.011	1.895	1.800	0.373	1.946	2.328	2.078	1.627	2.931	1.829
a5x	14.181	14.128	11.440	−0.091	11.073	2.431	1.364	1.659	−6.543	0.843	0.262	−0.069	−0.779	−1.177	0.265	−4.401	−4.789	−5.164	−7.162	−4.224
a5y	16.961	16.874	13.931	5.051	14.301	9.853	9.533	9.458	8.434	9.286	10.757	10.497	11.580	9.045	10.935	10.063	8.881	9.552	8.245	9.910
a5z	3.161	2.398	2.243	15.767	2.950	3.574	1.630	2.684	5.074	0.501	4.910	3.785	2.809	8.167	3.437	2.670	0.803	2.058	1.524	0.778
	RMS from PSD	RMS from Time History	RMS from FDS	Peak from ERS	Peak from Time History	RMS from PSD	RMS from Time History	RMS from FDS	Peak from ERS	Peak from Time History	RMS from PSD	RMS from Time History	RMS from FDS	Peak from ERS	Peak from Time History	RMS from PSD	RMS from Time History	RMS from FDS	Peak from ERS	Peak from Time History
	Group 1					Group 2					Group 3					Group 4				

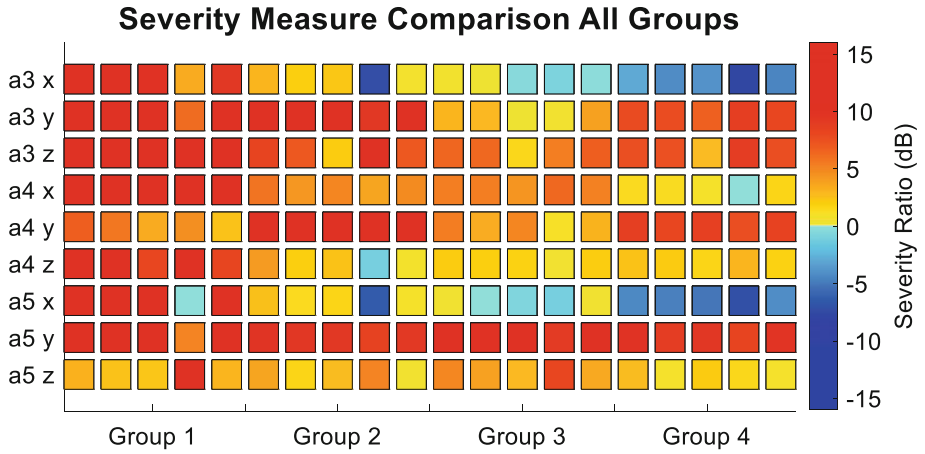

Fig 12. 17 Severity ratios for all groups, accelerometers, directions, and lifetime measures. Reference Table 12.9 for numeric severity ratio value

References

1. Harman, C., Pckel, M.B.: Multi-axis vibration reduces test time. Eval. Eng. **45**(6), 44–48 (2006)
2. Smallwood, D.O.: The challenges of multiple input vibration testing analysis, Sandia National Laboratory (2013)
3. Brandt, A.: Noise and Vibration Analysis: Signal Analysis and Experimental Procedures. John Wiley & Sons, Chichester (2011)
4. Henderson, G.R.: Evaluating vibration environments using the shock response spectrum. Sound Vib. **262**, 18–20 (2003)
5. McNeill, S.I.: Implementing the fatigue damage spectrum and fatigue damage equivalent vibration testing. In: Proceedings of the 79th Shock and Vibration Symposium, Orlando, FL (2008)
6. McConnel, K.: Vibration Testing: Theory and Practice. John Wiley & Sons, New York (1995)
7. Avitable, P.: Can test setup have an effect on the measure of modal data? Modal space. In: Our Little World, December 2011
8. Sione, D.E., Jones, R.J., Harvey, J.M., Skousen, T.J., Schoenherr, T.: Deisgning hardware for the boundary condition round Robin Challenge, Kansas City National Security Campus, Sandia National Laboratories (2017)
9. Murakami, Y.: The Rainflow Counting Method in Fatigue, The Fatsuo Endo Memorial Volume. Butterworth-Heinemann (2013)
10. Lalanne, C.: Fatigue Damage, Mechanical Vibration and Shock Analysis, vol. 4, 3rd edn. John Wiley & Sons, Hoboken, NJ (2014)
11. Lalanne, C.: Specification Development, Mechanical Vibration and Shock Analysis, vol. 5, 3rd edn. John Wiley & Sons, Hoboken, NJ (2014)
12. Lalanne, C.: Mechanical Shock, Mechanical Vibration and Shock Analysis, vol. 2, 2nd edn. John Wiley & Sons, Hoboken, NJ (2009)
13. Smallwood, D.O.: An improved recursive formula for calculating shock response spectra. Shock Vib. Bull. **51**, 4–10 (1981)

Chapter 13
Instrumentation and Data Acquisition Mistakes in a Structural Dynamics Facility and How to Learn from Them

Matthew S. Stefanski

Abstract Many common mistakes are made as a new engineer or technician using dynamics instrumentation such as accelerometers, pressure transducers, and strain gages. A lot of these are well known or documented and published. Working in a combined-environment testing facility such as AFRL's Structural Dynamics Lab provides an additional layer of complexity by pushing instrumentation and data acquisition hardware to the limits of their operation parameters. This paper will discuss some of those lessons learned the hard way so that others can learn to not repeat them.

Keywords Sensors · Instrumentation · AFRL · Mistakes · Lessons

13.1 Introduction

When conducting structural dynamics tests the sensors and instrumentation are often the last consideration or an afterthought, a necessary evil, in order to extract the information, the data, for analysis or validate the model. Working in a laboratory with combined forces such as thermal-acoustic and thermal-vibration forces there's a greater emphasis on planning, choosing, installing, and signal processing because often tests are expensive and short lived. Often with only one test article there's little to no room for error during a test. Often times the test cannot be repeated so data has to be collected and stored correctly the first time. Mistakes are made because of the unique testing environment, unknown materials and coatings on test articles, and trying to use instrumentation in ways not traditionally intended.

13.2 Background

The Air Force Research Laboratory's (AFRL) Combined Environment Acoustic Chamber (CEAC) is a progressive wave tube (PWT) research facility that can simultaneously impose acoustic, thermal, and mechanical loads on aerospace test articles and is shown in Fig. 13.1. The CEAC is able to impose up to 170 db overall sound pressure levels from 12 acoustic modulators. The radiant quartz lamp bank is able to impinge a maximum of 72 BTU/ft^{2}s, enough to heat test articles well over 2000 °F. High volume air fills the acoustic modulators where the modulator valve will "chop" the air based upon the drive signal sent from control amplifiers. The acoustic waves are combined in a horn and create "grazing" waves that pass down the duct of the PWT and excite the surface of the test article. This unique environment creates a challenge in selecting, using, acquiring data and getting instrumentation to survive a test run.

M. S. Stefanski (✉)
U.S. Air Force Research Laboratory, Aerospace Systems Directorate, Aerospace Vehicles Division, Structural Validation Branch (AFRL/RQVV), Wright-Patterson AFB, OH, USA
e-mail: matthew.stefanski@us.af.mil

C. Walber et al. (eds.), *Sensors and Instrumentation, Aircraft/Aerospace, Energy Harvesting & Dynamic Environments Testing, Volume 7*, Conference Proceedings of the Society for Experimental Mechanics Series,
https://doi.org/10.1007/978-3-030-12676-6_13

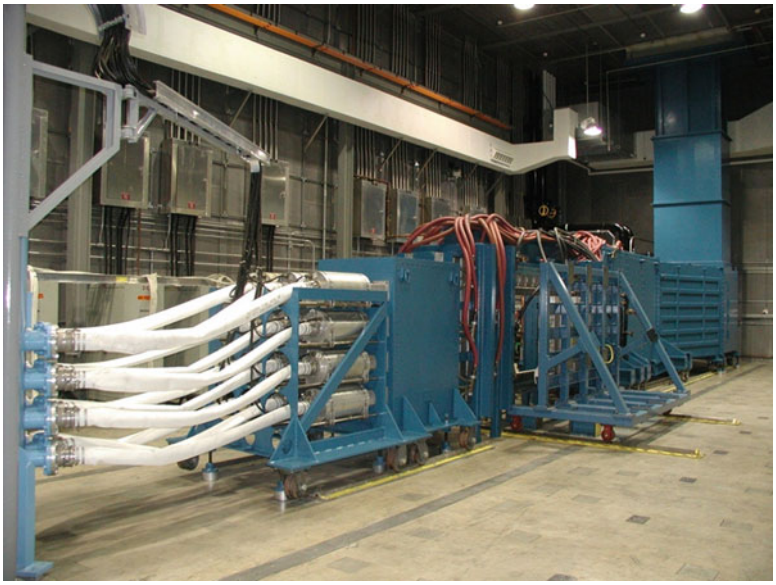

Fig. 13.1 AFRL's combined environment acoustic chamber (CEAC) ref. 88ABW-2018-3807

13.3 Lessons Learned

13.3.1 Accelerometers

Many mistakes are made using accelerometers in an elevated temperature environment. First is survivability. Choosing accelerometers that can withstand the temperature environment limit is critical. Often accelerometers are only able to be used for room temperature or low elevated temperature test runs. The lesson to learn is to make sure in test plans to note the removal of accelerometers before thermal testing begins. Many accelerometers have been "cooked" by not properly documenting the test procedures that should occur between test runs.

Installation of accelerometers is also a challenge. The goal is to have intimate contact between the test article and accelerometer sensing head. This can be accomplished with either a hard mount stud or the use of an adhesive or wax. The nature of test articles in the CEAC either results in thin-skinned metallic or a composite type structure that negates the possibility of using a hard mount. Adhesives present an additional layer of things that can go wrong. Mistakes that have been made include: adhesives not able to withstand temperature limits of the test article, adhesives unable to withstand the dynamic environment, adhesives incompatible with the test article material, and adhesives requiring an elevated temperature cure with no possibility to cure in place on the test article. The lessons learned here are planning and preparation. Know the limits of where and how accelerometers can be installed and what adhesives will give the best chance for success. Another lesson learned is risk reduction by trying out different adhesives on a sample of the test article material. Test and down-select adhesives by thermally cycling samples in an oven, and if possible mechanically exciting the coupon with an electrodynamic shaker. This activity should give confidence for choosing the best adhesive for a particular test where prior results are unknown.

Mistakes in cabling and in-line amplification are easily overlooked and can be avoided. One mistake made is using an accelerometer cable not rated for the temperature environment in which it is located. The lesson to learn is to make sure the cable has the same temperature rating as the accelerometer and the preference is to buy both together as a matched system with an in-line charge amplifier. Another mistake often made is improper strain relief and incorrect bonding of the accelerometer cable to the test article. Sufficient cable strain relief is needed at the connection to the accelerometer so that the weight of the cable doesn't pull the cable out of the connector or fatigue the connection during testing. Cables need to be bonded continuously to the test article with either tape or adhesive until transitioned off the test article to avoid unwanted cable vibration and cable fatigue.

Finally, signal processing mistakes to avoid. Keep track of calibration sheets and ensure accelerometers are on a regular calibration cycle. Regular calibrations will ensure the most accurate sensitivity and provide linearity across frequency ranges. When using charge type accelerometers with inline amplifiers install the amplifier as close as possible to the accelerometer by limiting the length of cable between the two. The capacity of the cable between the accelerometer and the amplifier can

affect the sensitivity. If possible perform an end to end calibration with the accelerometer and inline amplifier and adjust the sensitivity.

13.3.2 Strain Gages

Strain gages are a thin film (traditional) or thin free-filament (high temperature) strain measurement instrument that is bonded in intimate contact with the test article. Thin adhesives, such as cyanoacrylate, are traditionally used to bond strain gages to test articles. Bonding is when a majority of mistakes happen due to various reasons. Bonding mistakes increase more when operating in a combined test environment. Incorrectly performing or ignoring surface prep area by not removing paint, coatings, and following a surface preparation guide, for example Vishay Precision Group technote B-129, prevents the gage from being correctly bonded to the test article surface and either failing during testing, or worse, giving bad data that is assumed to be true. In an elevated temperature environment, surface prep becomes more important. An example would be applying a strain gage to titanium where the manufacturing oils haven't been baked out and wiped clean. When heated, manufacturing oils will rise to the surface of titanium, create bubbles under the strain gage and effectively ruin the bond of the strain gage.

When using strain gages in elevated temperatures it's important to match the coefficient of thermal expansion (CTE) of the material and the strain gage as closely as possible. If ignored, when the temperature of the test article material increases there will be a mismatch of thermal expansion between the test article and the strain gage. This will give false static strain data and can prematurely fail the gage when thermal and/or dynamic forces are cycled.

Strain gages, unlike piezo accelerometers, are a bridge-type constant voltage device that are not as immune to electrical noise as constant current powered accelerometers. Radiant thermal sources, such as those from quartz bulbs can introduce electrical (AC) noise, thus increasing the uncertainty of the measurements. This is a larger problem when using free-filament strain gages that are more susceptible to electrical noise. For signal processing, the lesson learned is to use a signal processing amplifier that can use constant current sourcing in a non-Wheatstone bridge configuration. This provides the most immunity against electrical noise and reduces the uncertainty of the measurement.

13.3.3 Pressure Transducers

Few microphones or dynamic pressure transducers that operate in the audible range can operate in the elevated temperature of the CEAC. For survivability purposes water cooling jackets are used to create a cold boundary condition and thermal sink to keep the temperature of the device in its operating range. A lesson learned is to have a flow switch or flow meter on the water supply to ensure there is enough water flow or there is no blockage in the tubing. Cabling for pressure transducers, both bridge and piezo type, need to be addressed in similar ways as accelerometers. Any cabling in airflow should be adhered to the surface of the test article as much as possible to reduce the risk of fatigue due to acoustic and air induced vibrations.

13.4 Conclusion

Instrumentation used in a combined environment lab adds an extra level of complexity where mistakes more frequently occur. Documentation, risk reduction activities, and collaboration with OEM experts can minimize the possibility of mistakes and at the very least ensure the mistake isn't repeated. Documenting, collaborating, and experimenting with creative ideas are ways to increase the level of success when operating at the edge of instrumentation working environments to ensure quality data is being delivered.

Distribution A. Cleared by 88ABW-2018-5179.

Chapter 14
Adaptive Multi-modal Tuned Mass Dampers Based on Shape Memory Alloys: Design and Validation

M. Berardengo, G. E. P. Della Porta, S. Manzoni, and M. Vanali

Abstract The use of shape memory alloys (SMA) is really promising in the field of vibration mitigation. Indeed, several works are already available in the literature, describing how to exploit the special features of SMAs in order to design and build dampers and tuned mass dampers (TMD).

Regarding TMDs, the features of SMA materials allow to design adaptive TMDs able to change their eigenfrequencies in order to keep the TMD tuned on the primary system to be damped in case of changes of the dynamic features of the primary system (e.g. changes of the eigenfrequency due to thermal shifts). The possibility to ensure the tuning between the TMD and the primary system allows to achieve an optimal damping action.

The adaptive TMDs based on SMAs described in the literature are usually able to work on a single eigenfrequency of the primary system. Conversely, this paper proposes a new adaptive TMD able to change more than one eigenfrequency at the same time with a given level of independence. This allows to work on at least two eigenfrequencies of the primary system, thus realizing a multi-modal adaptive TMD.

The paper explains that this multi-modal adaptive TMD is based on a special configuration made from a system of masses and SMA wires. Particularly, each mass is connected to the adjacent masses by SMA wires. The possibility to tune more than one eigenfrequency is achieved by heating/cooling the different SMA wires independently. Indeed, this allows to change the geometry of the adaptive TMD and, at the same time, the tensile load into the SMA wires. This double effect is suitable for building multi-modal adaptive TMDs.

The paper first describes the working principle of the adaptive TMD. Then, simulations are presented in order to show the effectiveness of the proposed device.

Keywords Adaptive tuned mass damper · Damping · Shape memory alloys · Vibration · Vibration control

14.1 Introduction

The use of smart materials for vibration reduction has been proved to be very promising thanks to their advantageous features. Indeed, piezoelectric materials (e.g. [1, 2]), shape memory alloys (SMA) (e.g. [3–9]), magnetic memory alloys (e.g. [10]), and magnetorheological materials (e.g. [11, 12]) have been fruitfully employed in damping applications.

In particular, these materials showed to be effective for the design of tuned mass dampers (TMD). TMDs are in general really effective in reducing vibrations but suffer of two main drawbacks:

- Their performances decrease significantly when mistuning occurs;
- They are usually effective on a single mode.

As for the first point, smart materials can give significant contributions because their properties are particularly suitable to the design of adaptive tuned mass dampers (ATMD) (e.g. [13]). ATMDs able to adapt their own eigenfrequencies can follow the changes of one resonance frequency of the primary system (PS) to be damped, enabling a constant tuning between the ATMD and the PS, thus having an optimal damping action. Changes of the dynamical features of the PS are a critical issue since they often occur because of a number of possible reasons (thermal shifts, as an example).

M. Berardengo · M. Vanali
Department of Engineering and Architecture, Università degli Studi di Parma, Parma, Italy

G. E. P. Della Porta · S. Manzoni (✉)
Department of Mechanical Engineering, Politecnico di Milano, Milan, Italy
e-mail: stefano.manzoni@polimi.it

C. Walber et al. (eds.), *Sensors and Instrumentation, Aircraft/Aerospace, Energy Harvesting & Dynamic Environments Testing, Volume 7*, Conference Proceedings of the Society for Experimental Mechanics Series,
https://doi.org/10.1007/978-3-030-12676-6_14

Among the various smart materials, this article has its focus on SMAs. Indeed, SMAs have been successfully employed to damp vibrations in light structures, and especially to design and construct ATMDs capable of changing their eigenfrequency, thanks to the unique physical properties of these materials.

Moreover, they are cheap if compared to other materials and can be manufactured with shapes (wires, as an example) which allow to have low weights. This is an important characteristic since it enables to design and build adaptive devices avoiding high load effects in light structures.

Several works on adaptive devices based on SMAs are available in the literature to prove the possibility to apply SMA-based devices in real engineering applications. As examples, Mani and Senthilkumar developed an application where an absorber composed by SMA springs damps the vibration of a centrifugal pump with time-varying excitation frequency [14], whereas Zuo and Li showed that SMA dampers are suitable to damp the vibrations of cables [15]. The various works proposed by the scientific community on ATMDs based on SMAs differ in the physical principle employed to adapt the TMD eigenfrequency and for the used control strategy. As an example, Rustighi et al. showed the effectiveness of cantilever beams made from SMA material to implement reliable ATMDs [16]. The principle by which the eigenfrequency of the ATMD is changed is a change of the SMA material temperature, which in turn causes a change of its Young's Modulus. Various approaches for controlling this type of ATMDs are discussed in Ref. [17]. Williams et al. developed an ATMD based on a series of cantilever beams made from SMA in Ref. [18], using the same physical principle presented in Ref. [16]. Furthermore, Williams et al. discussed a non-linear control approach for the same device [19]. A different concept is presented by Savi et al., who studied the behavior of a spring of SMA to be employed for controlling vibrations [20], highlighting its capability to change damping and stiffness properties by changing temperature and using the so-called pseudoelastic effect. A similar device was studied experimentally by Aguiar et al. [21]. Instead, Tiseo et al. showed by means of experiments that an ATMD can be built with a SMA wire with constrained ends and a mass placed at its centre: the eigenfrequency of the system can be thus changed by varying the wire temperature [22]. Even if the effectiveness of this working principle was demonstrated in the paper, no models of the structure, and quantification of the performance in terms of adaptation capability were discussed in this work.

Recently, Berardengo et al. [23, 24] proposed a new ATMD based on SMA, which is able to change its eigenfrequency of more than 100% of its initial value, by coupling a SMA wire, a central mass and elastic elements. Moreover, this ATMD configuration showed to have two further advantages if compared to the other SMA-based ATMDs:

- It works properly with any kind of SMA material, therefore without requiring high-performance SMAs (i.e. SMAs with special features like high change of the Young's modulus with temperature);
- It allows to easily add devices able to change the damping level of the ATMD as well. This was achieved in the referenced papers by using an eddy current damper but other systems/principles could be used (magnetic or mechanical devices, as examples).

Although the effectiveness of SMAs in the development of ATMDs is mainly proved by most of the referenced works, the other main drawback of these ATMDs (i.e. they usually act on a single mode, see above) is still an open issue. There is a lack of works in the literature proposing ATMDs based on smart materials able to work at the same time on more than one mode of the PS independently. Hence, the aim of this article is to investigate the possibility to design multi-mode (MM) ATMDs based on SMAs which are able to change more than one eigenfrequency in specific frequency ranges independently (or, actually, with a given level of independency) and at the same time. This would allow to have an ATMD able to recover any possible change of the PS eigenfrequencies, thus assuring a satisfactory damping of the PS vibrations. The design approach and the working principle are the same described in Ref. [23] because the device proposed there guarantees an extended frequency range, and high flexibility of the layout if compared to other ATMDs based on SMAs.

The next section recalls the SMA features, while Sect. 3 recalls the SMA-based ATMD presented in Ref. [23], for understanding the newly proposed MM ATMD. Then, the same section discusses the physical principle of the MM ATMD. Finally, Section 4 presents some simulations in order to show the effectiveness of the proposed layout.

14.2 Shape Memory Alloys

This section summarizes the main properties of SMA materials [25] which are useful to comprehend the working principle of the proposed adaptive device. SMAs are characterized by transformations among three different solid phases, which occur when the material faces a change of either the applied stress or the temperature value. The solid phase transition leads to a change of mechanical properties (the Young's modulus, as an example) and can lead to a change of the shape of the

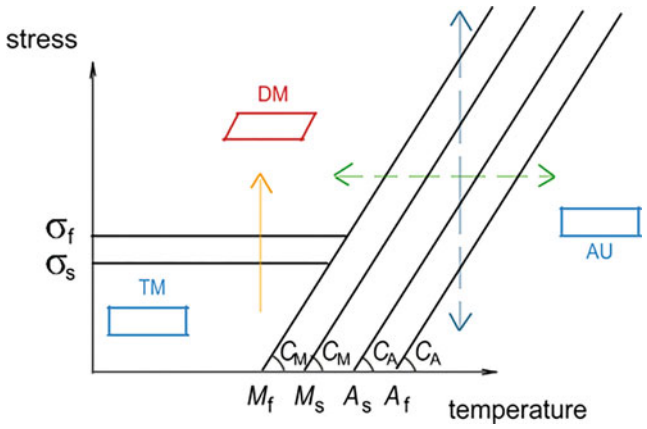

Fig. 14.1 Temperature-stress diagram of SMA materials

Table 14.1 Data for the SMA material used in this work (identified with experiments)

A_s	A_f	M_s	M_f	C_A	C_M	H^{cur}	$E_{w,DM}$	$E_{w,AU}$	α
68.6 °C	78.9 °C	55.2 °C	42.7 °C	9.90 MPa/°C	6.83 MPa/°C	4.39%	32.1 GPa	39.5 GPa	10^{-6} °C^{-1}

SMA device. The three phases involved in these transformations are: austenite (AU), twinned martensite (TM), detwinned martensite (DM).

Figure 14.1 shows the temperature-stress diagram of SMAs, where σ_s is the stress value at which the transformation from TM to DM starts at environmental temperature, while σ_f is the stress value at which the transformation is completed. Moreover, M_s is the temperature value at which the transformation from AU to TM starts at null stress, and M_f is the value at which the transformation is completed, A_s is the temperature value at which the transformation from TM to AU starts at null stress, A_f is the value at which the transformation is completed. C_M and C_A are the angular coefficients of the transformation lines. Table 14.1 shows the values of the parameters shown in Fig. 14.1 for the SMA materials employed in this paper (identified through experimental tests), which is Nitinol (made from nickel and titanium). In Table 14.1, α is the thermal expansion coefficient, H_{cur} is the strain due to the change of shape during the change of phase between TM and DM (see the vertical solid arrow in Fig. 14.1), named the current maximum transformation strain. Moreover, $E_{w,AU}$ and $E_{w,DM}$ are the Young's moduli of the AU and DM phases, respectively.

Figure 14.1 evidences that the shape of an SMA device can be changed when either transformations from TM to DM occur or the SMA changes phase from DM to AU and vice versa. The shape in the TM and AU phases is almost the same (which is the unstrained shape). Thus, a change of the shape can be achieved applying a stress value higher than σ_s (transformation from TM to DM, see the vertical solid arrow in Fig. 14.1) and the original shape can be recovered by increasing the temperature (transformation from DM to AU). When the SMA is in AU, the shape can be changed using the AU-DM transformation (and vice versa) and therefore changing the applied stress (pseudoelastic effect, see the vertical dashed double arrow in Fig. 14.1) and/or the temperature (temperature-induced phase transformation, see the horizontal dashed double arrow in Fig. 14.1).

As for the strain of the SMA wires ε_w, it can be expressed by the following general relation, according to Ref. [25]:

$$\varepsilon_w = \varepsilon_w^e + \varepsilon_w^t + \varepsilon_w^{th} \tag{14.1}$$

Here, ε_w^e is the elastic strain component, ε_w^{th} is the strain component due to the thermal expansion, and, finally, ε_w^t is the strain component due to the thermo-elastic martensitic transformation (which is the strain caused by the change of shape from TM to DM; see Fig. 14.1).

14.3 Adaptive Tuned Mass Damper

The MM ATMD presented in this work takes advantage from the ATMD proposed by Berardengo et al. [23]. Therefore, it is worth recalling in brief its working principle.

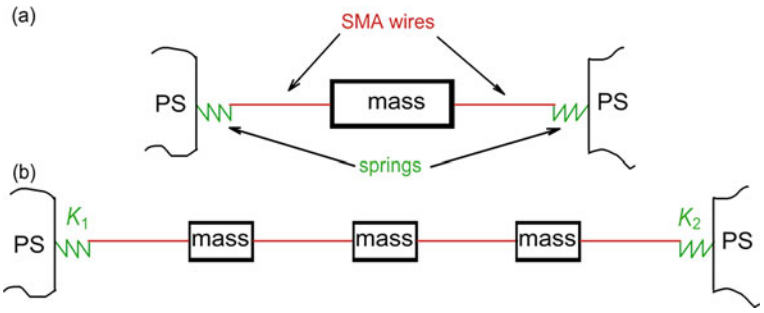

Fig. 14.2 Layout of the original ATMD (**a**), and of the MM ATMD (here, an example with three masses is shown) (**b**)

The ATMD presented in Ref. [23] relies on the use of two (or more) SMA wires, a central mass and some elastic elements (see Fig. 14.2a). The elastic elements link this ATMD to the PS to be damped and allow to apply a pre-stress (and thus a pre-strain) to the wires. The value of this pre-stress is set above σ_f (refer to Fig. 14.1) to have the SMA wires in the condition of DM. Hence, a further change of the shape (i.e. the length mainly) of the wires can be obtained through a temperature variation, thanks to the transformation between DM and AU. Being the wires connected to the PS by the elastic elements, this change of shape allows to change the axial tensile load F in the wires, which in turn enables to have a change of the eigenfrequency of the ATMD [26–28]. The basic working principle of the ATMD can be thus summarized as: a temperature change causes a shape change and thus even a change of stress in the SMA wires occurs. More in detail, when the wires are heated, they change their phase from DM to AU, and this implies that they recover their initial shape (refer to Fig. 14.1) and therefore their length decreases. This causes a stretch of the spring and an increase of the axial load. On the other hand, when the wires are cooled form AU to DM, their length increases and thus the springs shorten and the axial load decreases. As said, the axial load changes cause changes of the ATMD eigenfrequency (if the axial load increases, the eigenfrequency increases; while if the axial load decreases, the eigenfrequency value decreases). Such a configuration, that is mostly based on changes of the axial load of the wires rather than the change of their Young's moduli, enables changes of the ATMD eigenfrequency of more than 100% of the starting value, does not require high current values to heat the wires with Joule's effect, can be easily coupled to devices for adapting also the ATMD damping, and does not require any special feature of the SMA material employed [23]. All these features make such a layout very attractive, and, for this reason, this paper further develops the concepts presented in Ref. [23] to the aim of developing an MM ATMD.

The idea presented in this paper is to design the ATMD with more than one mass (a number of masses higher than/equal to the number of the ATMD eigenfrequencies to be adapted; see, as an example, Fig. 14.2b) connected each other by an SMA wire. Then, each wire is heated/cooled independently from the others. Indeed, the eigenfrequency of the first q modes of an adaptive TMD with q masses (that are the modes with significant eigenvector components at the degrees of freedom of the masses [29]) can be changed in two ways: changing the axial load, as already discussed (see previously), and changing the ATMD geometry. Both these effects are obtained through a change of the temperatures of the SMA wires.

The decrease/increase in the axial load changes all the ATMD eigenfrequencies at the same time, while heating the different wires independently can result in changes of the ATMD geometry and therefore of its eigenfrequencies. With this combined effect, the value of one eigenfrequency is not expected to be completely linked to the value of the others.

14.4 Numerical Simulations

The MM ATMD has been tested numerically. This was possible by using the model describing its behavior. This model is composed by three different models which run in sequence: a thermal model which allows to calculate the temperatures of the wires, given the currents flowing in the wires (which are set by either a user or a controller), the model of the material which links the wire temperatures to the length of the wires and the stress acting along them, and, finally, a dynamic model which finds the eigenfrequencies and the mode shapes of the ATMD starting from the outputs of the model of the material.

The whole model is not described here. It comes from the model presented in Ref. [23] and its is completely developed in Ref. [30].

A simulation of an ATMD with two masses (one equal to 100 g and the other to 200 g) and three wires is presented here. The global length of the ATMD is 40 cm and all the wires have at environmental temperature the same length.

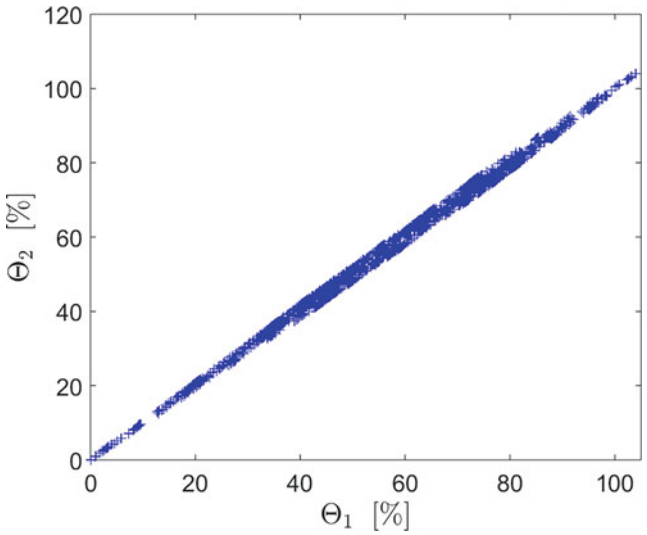

Fig. 14.3 Adaptation plot: percentage change of the second eigenfrequency (Θ_2) as function of the percentage change of the first eigenfrequency (Θ_1). The blank spaces are due to the step used for the simulations (i.e. 2 °C). A narrower step would fill the spaces

In order to test the behavior of the ATMD, the temperatures of the three wires were initially set at the environmental temperature and the stress into the wires was 50 MPa. The model discussed previously was used to calculate the eigenfrequencies of the ATMD at environmental temperature. The temperature of the first wire was then increased of 2 °C and the eigenfrequencies were calculated again. The temperature of the first wire was then changed step by step of 2 °C up to 120 °C, which is a temperature higher than that at which the wires complete the transformation in AU at a stress value of 200 MPa (which is the maximum target stress in these simulations). The temperature of the wire was then decreased again to the environmental temperature in steps of 2 °C. At each step, the eigenfrequencies of the ATMD were calculated.

After this cycle, the temperature of the second wire was increased of 2 °C and the cycle for the temperature of the first wire was then repeated. When also the second wire had completed the temperature cycle (i.e. the second wire was finally cooled again to ambient temperature), the temperature of the third wire was changed by 2 °C and the previous procedure was then repeated. The simulations ended when also the third wire had completed a temperature cycle.

This simulation allows to build a diagram with all the possible pairs of values of the first two eigenfrequencies of the ATMD. The plot obtained is shown in Fig. 14.3 and it presents the resulting percentage plot for the ATMD. The symbol Θ indicates the percentage change of the eigenfrequencies. The reference values for calculating the percentage values are the eigenfrequency values with all the wires at environmental temperature in DM.

The plot of Fig. 14.3 confirms that it possible to obtain two different values for the second eigenfrequency, when the first eigenfrequency is at a given value, and vice versa. This is made possible by the working principle presented in the previous section (i.e. the combined effect of the change of the axial load and of the change of the geometry of the ATMD).

14.5 Conclusion

This paper has discussed an MM ATMD based on SMAs. The simulations carried out confirm that it possible to achieve two different values for one eigenfrequency, when another eigenfrequency is at a given value. This is made possible by the working principle presented (i.e. the combined effect of the change of the axial load and of the change of the geometry of the ATMD).

Therefore, the simulations confirm that it is possible to change the eigenfrequencies of the proposed ATMD with a given level of independence. This enables to recover the changes of two (or more) eigenfrequencies of the PS with the ATMD. This is made possible by the special features of the SMA materials, and setting independently the temperatures of the different wires of the ATMD.

References

1. Berardengo, M., Manzoni, S., Vanali, M.: The behaviour of mistuned piezoelectric shunt systems and its estimation. Shock. Vib. **2016**, 9739217 (2016)
2. Berardengo, M., Manzoni, S., Thomas, O., Giraud-Audine, C.: A new electrical circuit with negative capacitances to enhance resistive shunt damping. In: Proceedings of the ASME 2015 Conference on Smart Materials, Adaptive Structures and Intelligent Systems—SMASIS 2015, 21–23 September 2015. ISBN: 9780791857298, ID 8836
3. Ozbulut, O.E., Mir, C., Moroni, M.O., Sarrazin, M., Roschke, P.N.: A fuzzy model of superelastic shape memory alloys for vibration control in civil engineering applications. Smart Mater. Struct. **16**, 818–829 (2007)
4. Mavroidis, C.: Development of advanced actuators using shape memory alloys and electrorheological fluids. Res. Nondestruct. Eval. **14**, 1–32 (2002)
5. Senthilkumar, P., Umapathy, M.: Use of load generated by a shape memory alloy for its position control with a neural network estimator. J. Vib. Control. **20**, 1707–1717 (2014)
6. dos Santos, F.A., Nunes, J.: Toward an adaptive vibration absorber using shape-memory alloys, for civil engineering applications. J. Intell. Mater. Syst. Struct. **29**, 729–740 (2018)
7. Piccirillo, V., Balthazar, J.M., Tusset, A.M., Bernardini, D., Rega, G.: Application of a shape memory absorber in vibration suppression. Appl. Mech. Mater. **849**, 27–35 (2016)
8. Torra, V., Carreras, G., Casciati, S., Terriault, P.: On the NiTi wires in dampers for stayed cables. Smart Struct. Syst. **13**, 353–374 (2014)
9. Dieng, L., Helbert, G., Chirani, S.A., Lecompte, T., Pilvin, P.: Use of shape memory alloys damper device to mitigate vibration amplitudes of bridge cables. Eng. Struct. **56**, 1547–1556 (2013)
10. Majewska, K., Żak, A., Ostachowicz, W.: Magnetic shape memory alloys for forced vibration control of beam-like structures. Smart Mater. Struct. **16**, 2388–2397 (2007)
11. Weber, F., Maślanka, M.: Frequency and damping adaptation of a TMD with controlled MR damper. Smart Mater. Struct. **21**, 055011 (2012)
12. Caterino, N., Spizzuoco, M., Occhiuzzi, A.: Understanding and modelling the physical behaviour of magnetorheological dampers for seismic structural control. Smart Mater. Struct. **20**, 065013 (2011)
13. Heuss, O., Salloum, R., Mayer, D., Melz, T.: Tuning of a vibration absorber with shunted piezoelectric transducers. Arch. Appl. Mech. **86**, 1715–1732 (2016)
14. Mani, Y., Senthilkumar, M.: Shape memory alloy based adaptive-passive dynamic vibration absorber for vibration control in piping applications. J. Vib. Control. (2013). https://doi.org/10.1177/1077546313492183
15. Zuo, X., Li, A.: Numerical and experimental investigation on cable vibration mitigation using shape memory alloy damper. Struct. Control Health Monit. **18**, 20–39 (2011)
16. Rustighi, E., Brennan, M.J., Mace, B.R.: A shape memory alloy adaptive tuned vibration absorber: design and implementation. Smart Mater. Struct. **14**, 19–28 (2005)
17. Rustighi, E., Brennan, M.J., Mace, B.R.: Real-time control of a shape memory alloy adaptive tuned vibration absorber. Smart Mater. Struct. **14**, 1184–1195 (2005)
18. Williams, K., Chiu, G., Bernhard, R.: Adaptive-passive absorbers using shape-memory alloys. J. Sound Vib. **249**, 835–848 (2002)
19. Williams, K.A., Chiu, G.T.-C., Bernhard, R.J.: Nonlinear control of a shape memory alloy adaptive tuned vibration absorber. J. Sound Vib. **288**, 1131–1155 (2005)
20. Savi, M.A., De Paula, A.S., Lagoudas, D.C.: Numerical investigation of an adaptive vibration absorber using shape memory alloys. J. Intell. Mater. Syst. Struct. **22**, 67–80 (2010)
21. Aguiar, R.A., Savi, M.A., Pacheco, P.M.: Experimental investigation of vibration reduction using shape memory alloys. J. Intell. Mater. Syst. Struct. **24**, 247–261 (2012)
22. Tiseo, B., Concilio, A., Ameduri, S., Gianvito, A.: A shape memory allous based tunable dynamic vibration absorber for vibration tonal control. J. Theor. Appl. Mech. **48**, 135–153 (2010)
23. Berardengo, M., Cigada, A., Guanziroli, F., Manzoni, S.: Modelling and control of an adaptive tuned mass damper based on shape memory alloys and eddy currents. J. Sound Vib. **349**, 18–38 (2015)
24. Berardengo, M., Cigada, A., Guanziroli, F., Manzoni, S.: An adaptive tuned mass damper based on shape memory alloys with an extended range of frequency. In: Proceedings of EESMS 2014–2014 IEEE Workshop on Environmental, Energy and Structural Monitoring Systems, Naples, Italy, pp. 90–95, 17–18 September 2014
25. Lagoudas, D.C.: Shape Memory Alloys: Modeling and Engineering Applications. Springer, New York (2008)
26. Meirovitch, L.: Fundamentals of Vibrations. McGraw-Hill, New York (2001)
27. Acar, M.A., Yilmaz, C.: Design of an adaptive–passive dynamic vibration absorber composed of a string–mass system equipped with negative stiffness tension adjusting mechanism. J. Sound Vib. **332**, 231–245 (2013)
28. Rainieri, C., Fabbrocino, G.: Development and validation of an automated operational modal analysis algorithm for vibration-based monitoring and tensile load estimation. Mech. Syst. Signal Process. **60**, 512–534 (2015)
29. Gómez, B.J., Repetto, C.E., Stia, C.R., Welti, R.: Oscillations of a string with concentrated masses. Eur. J. Phys. **28**, 961–975 (2007)
30. Berardengo, M., Della Porta, G.E.P., Manzoni, S., Vanali, M.: A multi-modal adaptive tuned mass damper based on shape memory alloys. J. Intell. Mater. Syst. Struct. **30**(4), 536–555 (2019). https://doi.org/10.1177/1045389X18818388

Chapter 15
Application of Transfer Path Analysis Techniques to the Boundary Condition Challenge Problem

Julie M. Harvie and Maarten van der Seijs

Abstract A Boundary Condition Challenge Problem was released in May 2017 by Sandia National Laboratories and Kansas City's National Security Campus (KCNSC). The challenge problem is intended to facilitate collaborative research on methods used for laboratory shock and vibration testing of aerospace components. Specifically, the challenge problem presents a test bed structure consisting of two sub-systems and an applied shock loading. The goal is to replicate the environment observed on one of the sub-systems when it is attached to a different sub-system in a laboratory testing environment.

Meanwhile, transfer path analysis (TPA) tools have been available for several decades. TPA techniques are used extensively for noise, vibration and harshness (NVH) engineering in the automotive industry. The techniques provide insight into the vibration transmission of a source excitation to a receiving structure. By re-framing the boundary condition problem into the TPA framework, it becomes clear that TPA tools are directly applicable to the boundary condition challenge problem.

Keywords Shock and vibration · Transfer path analysis · Boundary conditions

Nomenclature

DoF	Degree of freedom
FRF	Frequency response function
u	Dynamic displacements/rotations
f	Applied forces/moments
g	Interface forces/moments
Y	Admittance FRF matrix
$\star^{AB}$	Pertaining to the assembled system
$\star^{A};\star^{B}$	Pertaining to the active/passive component
$\star_1$	Source excitation DoF
$\star_2$	Interface DoF
$\star\star_3$	Receiver DoF
$\star_4$	Indicator DoF
$\star_{ps}$	Pseudo-force DoF

15.1 Introduction

15.1.1 Shock and Vibration Qualification Testing

The Box Assembly with Removable Component (BARC) is an academic structure designed by Sandia and KCNSC [1] and is shown in Fig. 15.1. The structure is intended to represent a more complex system that undergoes some operational exposure to shock and vibration environments. The BARC consists of two sub-components: the Box Assembly (BA) and the

J. M. Harvie (✉) · M. van der Seijs
VIBES.technology, Delft, The Netherlands
e-mail: jharvie@vibestechnology.com

C. Walber et al. (eds.), *Sensors and Instrumentation, Aircraft/Aerospace, Energy Harvesting & Dynamic Environments Testing, Volume 7*, Conference Proceedings of the Society for Experimental Mechanics Series,
https://doi.org/10.1007/978-3-030-12676-6_15

Fig. 15.1 Box assembly with removable component (BARC) hardware

Removable Component (RC). The intent of the challenge problem is to design a laboratory test to qualify the Removable Component to a specified system shock loading.

Laboratory qualification testing is performed to ensure that aerospace systems will survive their operational environments with margin [2]. The laboratory tests are often cheaper than testing the entire system in the operational scenario and the inputs can be applied in a more controlled manner. Typically, laboratory qualification testing involves attaching the component of interest to a large electrodynamic shaker or shock machine using a rigid fixture as an adapter plate. The inputs to the laboratory test are determined using acceleration measured near the component attachment points in the system test. Practical limitations must be considered in the development of these tests, for example testing the components in three perpendicular axes in series rather than simultaneously due to the prominence of single-axis shaker equipment.

However, in recent years there has been an increase in the desire to improve the quality and realism of these laboratory tests. Over the past decade, there has been significant research toward the use of 6-DoF shaker tables [3–5]. The inputs for these tests rely on the assumption that the component's interface is rigid across the bandwidth of interest. This may be an appropriate assumption for certain families of components, but for many components with multiple attachment points, the assumption will not hold for a significant frequency range.

Another field of multi-axis testing, Impedance-Matched Multi-Axis Testing (IMMAT) [6], has also evolved recently. As the name suggests, this type of testing employs multi-axis testing along with fixtures that more accurately represent the impedance of the next level of assembly. One unique aspect of IMMAT testing is that several smaller modal shakers are used to excite the structure, although the optimal location and quantity of these shakers is still being investigated [7]. Additionally, the accelerometer locations used for target setting in IMMAT have been chosen somewhat arbitrarily in the previous research.

There has also been recent interest in using modal substructuring techniques to specify and analyze these types of tests [8, 9]. While this solution is promising, modal techniques are generally not ideal for systems with closely spaced modes and high damping, as is the case with many aerospace structures. So while the modal techniques may perform well on academic structures like the BARC, their applicability to real structures may not hold.

Naturally, the majority of qualification testing relies on acceleration-based specifications, as it is much easier to measure accelerations than forces in the field. However, matching a prescribed acceleration does not guarantee that the forces going into the component are correct. For the past several decades, NASA has been a proponent of force-limited vibration testing [10] to ensure that components are not exposed to unrealistic environments in the laboratory test. However most force-based techniques are difficult to implement and are not widely practiced today.

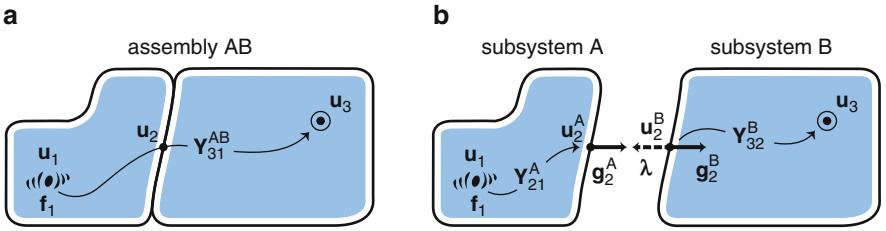

Fig. 15.2 The transfer path problem: (**a**) based on the admittance of assembly AB and (**b**) based on the admittances of subsystems A and B [11]

15.1.2 Transfer Path Analysis

Transfer Path Analysis is used to analyze the vibration transmission paths between an active source and a receiving structure. An in-depth overview of transfer path analysis techniques is provided in Ref. [11], and an overview is shown schematically in Fig. 15.2. The assembly AB consists of an active vibrating subsystem A and a passive receiving subsystem B. The system is excited by some force $\mathbf{f_1}$ that cannot easily be directly measured. It is desired to understand the response at locations of interest $\mathbf{u_3}$ on the passive structure through an interface $\mathbf{u_2}$ due to this excitation.

The response at the locations of interest on the passive component can therefore be described by[1]

$$\mathbf{u_3} = \mathbf{Y_{31}^{AB}} \mathbf{f_1} \tag{15.1}$$

However, as mentioned above, the excitations $\mathbf{f_1}$ and corresponding FRFs $\mathbf{Y_{31}^{AB}}$ are usually unmeasurable in practice. There are several methods available to analyze this problem, and they can be divided into three families: classical TPA, component-based TPA, and transmissibility-based TPA. The two former types are investigated here, and all methods are described in more detail in Ref. [11].

Classical TPA involves determining interface forces between the active and passive components and is typically used in existing products because the determined forces will reflect the dynamics of both components. Component-based TPA involves determining a set of equivalent forces that are a property of the source alone and can therefore be applied to an assembly AB with any receiving side B. When applied to system AB, the equivalent forces $\mathbf{f^{eq}}$ will yield the same responses $\mathbf{u_3}$ as the original source $\mathbf{f_1}$. Equivalent forces at the interface can be calculated using an in-situ approach [12, 13] with

$$\mathbf{f_2^{eq}} = \left(\mathbf{Y_{42}^{AB}}\right)^{+} \mathbf{u_4} \tag{15.2}$$

where $\mathbf{u_4}$ indicator sensors near the interface are used to improve the conditioning of the FRF matrix $\mathbf{Y_{42}^{AB}}$. To obtain this FRF matrix with references exactly at the interfaces, the virtual point transformation [14] is used. This provides a full six degree of freedom description of the forces acting exactly at the interface. This type of equivalent force is often referred to as a blocked force in the literature, as the forces acquired will ideally be equal to the forces that would be measured if subsystem A was rigidly fixed or blocked at the interface.

The equivalent forces can be validated by applying them to the assembly AB with

$$\mathbf{u_3} = \mathbf{Y_{32}^{AB}} \mathbf{f_2^{eq}} \tag{15.3}$$

and comparing the synthesized responses $\mathbf{u_3}$ to validation measurements. As seen in this equation, the equivalent forces must be applied to the complete assembly. This can easily be done using finite element or experimental models, and again is particularly useful to evaluate cases where the dynamics of the passive component B are changing.

However, with laboratory qualification testing, it is usually desired to test the passive component B without the rest of the system. For cases such as these, interface forces can be calculated using

$$\mathbf{g_2} = \left(\mathbf{Y_{42}^{B}}\right)^{+} \mathbf{u_4} \tag{15.4}$$

[1] The responses can also be written in terms of subsystem admittances with $\mathbf{u_3} = \left[\mathbf{Y_{32}^{B}}\left(\mathbf{Y_{22}^{A}} + \mathbf{Y_{22}^{B}}\right)^{-1}\mathbf{Y_{21}^{A}}\right]\mathbf{f_1}$.

where again $\mathbf{u_4}$ indicator sensors can be used to improve matrix conditioning. In this calculation, the FRFs $\mathbf{Y^B_{42}}$ are obtained on the passive component B by itself. These interface forces can be validated similarly by applying them to component B with

$$\mathbf{u_3} = \mathbf{Y^B_{32}} \mathbf{g_2} \tag{15.5}$$

and comparing the synthesized responses $\mathbf{u_3}$ to validation measurements. However, as detailed in Ref. [11], these interface forces are a characteristic of the coupled system AB and will therefore change if the dynamics of component B are altered. But if equivalent forces have already been determined, they can be transformed to interface forces using[2]

$$\mathbf{g_2} = \left(\mathbf{Y^B_{42}}\right)^{+} \mathbf{Y^{AB}_{42}} \mathbf{f^{eq}_2} \tag{15.6}$$

and again validated using Eq. (15.5). The application of this scenario and corresponding benefits are discussed in the following section.

Equivalent forces can also be calculated on the active structure at locations away from the interfaces. These so-called "pseudo forces" are calculated using

$$\mathbf{f_{ps}} = \left(\mathbf{Y^{AB}_{4ps}}\right)^{+} \mathbf{u_4} \tag{15.7}$$

where once again the rank and conditioning of the FRF matrix being inverted must be considered. Pseudo forces are useful when FRFs near the interfaces cannot be obtained. These pseudo forces are again a property of the active component A only and will not be influenced by the dynamics of component B. As with the equivalent forces at the interfaces, pseudo forces can be validated by applying them to the assembly AB and comparing synthesized responses to validation measurements.

15.1.3 Application of Transfer Path Analysis to Shock and Vibration Qualification Testing

As mentioned above, shock and vibration qualification testing is often performed in the laboratory on components and subassemblies of complex systems that undergo complex environmental loadings. Rather than attempting to model these complex loading scenarios using multi-physics simulation codes, transfer path analysis concepts can be employed. The complex system is divided into subcomponents such that subsystem A includes the locations where the vibrations are entering the system, and subsystem B is the component or subassembly of interest that will be tested in the laboratory.

Equivalent forces can be particularly useful in the definition of a component's environment specifications during the development phase. During development, while the components are still being designed, mock components are often employed in the system tests. The mock components are typically designed to have accurate mass properties to meet system requirements, but often the dynamic properties are not considered and will be different from the dynamics of the real components. Even as preliminary component design hardware is implemented in the system tests, the component dynamics will typically evolve until the design is finalized. However, the component's environment specifications must be defined prior to this design finalization. Thus, the usefulness of equivalent forces to describe the active source independently from the passive component dynamics becomes apparent. The equivalent forces can be extracted from system tests with mock or preliminary design components and applied to the final design. These equivalent forces can easily be applied to system models to evaluate component performance.

If pseudo forces are used to capture the system environments, these pseudo forces can then be used for laboratory testing of the complete system, another critical element of the qualification process. Like component testing, the inputs to these system tests are often derived using limited acceleration measurements and do not fully capture the complex forces being applied. Using the pseudo force technique, inputs to the system tests can be derived such that the inputs to the component(s) of interest will match those of the operational tests. This type of testing is seemingly quite similar to the IMMAT technique, but with acceleration targets specifically chosen to optimize the inputs to the component(s) of interest.

While these equivalent forces can be extremely useful for many qualification activities, they are limited in the fact that they must be applied to the full system. Often the components and subassemblies will also be tested and analyzed independently.

[2]The interface forces can also be written in terms of subsystem admittances with $\mathbf{g_2} = \left(\mathbf{Y^A_{22}} + \mathbf{Y^B_{22}}\right)^{-1} \mathbf{Y^A_{22}} \mathbf{f^{eq}_2}$.

This is where interface forces must be considered. If interface forces are calculated directly, they will reflect the dynamics of both the active component A and the passive component B. This may be undesirable if the dynamics of component B are variable. However, if equivalent forces are used to capture the system environments, they can later be transformed to interface forces using Eq. (15.6) once the design is finalized.

15.2 Analysis

15.2.1 Overview of Models and Operational Environments

Analytical modal models of the BARC were provided by Sandia. An operational environment was simulated using the recommended forcing function from the challenge problem [1], a modal hammer input approximated with a half-sine signal to excite modes up to at least 2000 Hz. The forcing function shown in Fig. 15.3b was applied at the red arrow shown in Fig. 15.3a. Within 2000 Hz, the box component has twelve flexible modes while the removable component has seven flexible modes. Additional details about the structure can be found in Refs. [15, 16]. All models were simulated using 5% modal damping. Since the external loading is applied to the box, the box is considered the active A component and the removable component is considered the passive B component within the TPA framework defined above.

The accelerometers in Fig. 15.3a represent the locations where responses were simulated. As seen, three tri-axial indicator accelerometers were placed on the removable component near each of the two attachment points, designated VP 1 and VP 2. A supplementary accelerometer was added at an arbitrary location on top of the removable component. This supplementary accelerometer is the location of interest $\mathbf{u_3}$ used to validate the process. The following studies concentrate on the Y-direction measurement at this location, although similar results were observed in other axes and at other locations.

Aside from operational measurements, FRFs are also needed to perform the TPA. Following an experimental approach, FRFs were simulated for the accelerometer locations in Fig. 15.3a and several impact locations around the interfaces. The virtual point transformation was used to transform these FRF references to 6-DoF references exactly at the interfaces in the center of each foot. These FRFs were calculated for the complete BARC assembly for use with equivalent forces, and also for the Removable Component independently for use with interface forces.

Additionally, a modified version of the Removable Component was generated to illustrate some of the characteristics of the techniques used. The modified RC has natural frequencies that are ten percent higher than the original model, but the mode shapes are unchanged. This modification is illustrated with a sample FRF on the RCs in Fig. 15.4.

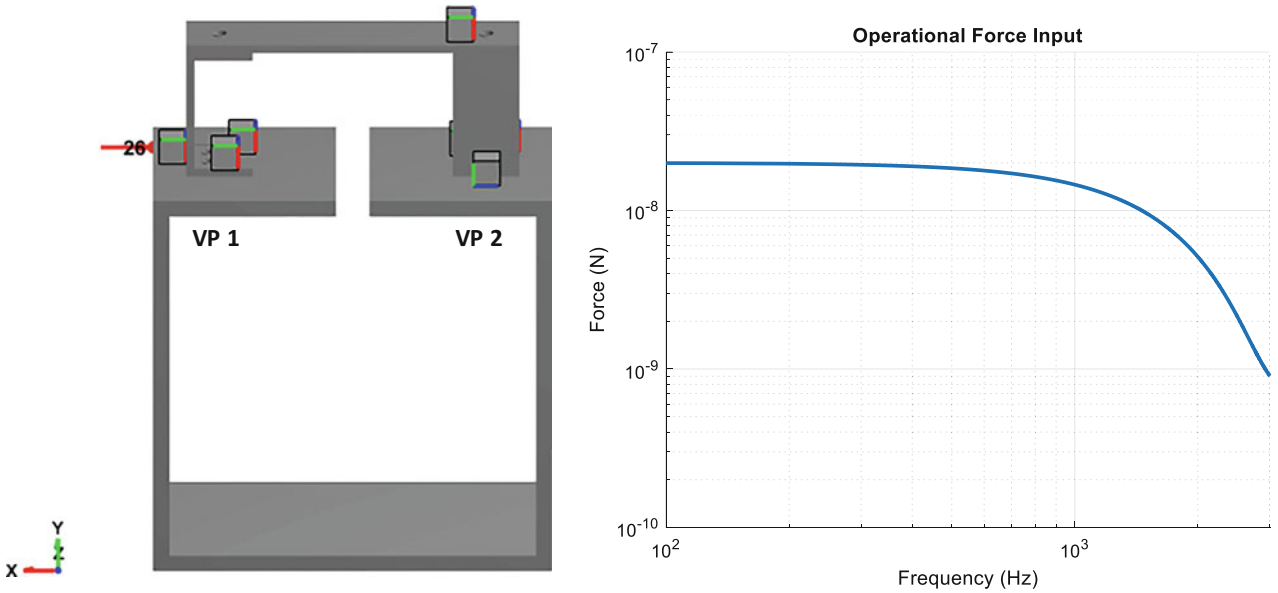

Fig. 15.3 BARC operational environment: (**a**) simulated test setup and (**b**) forcing function

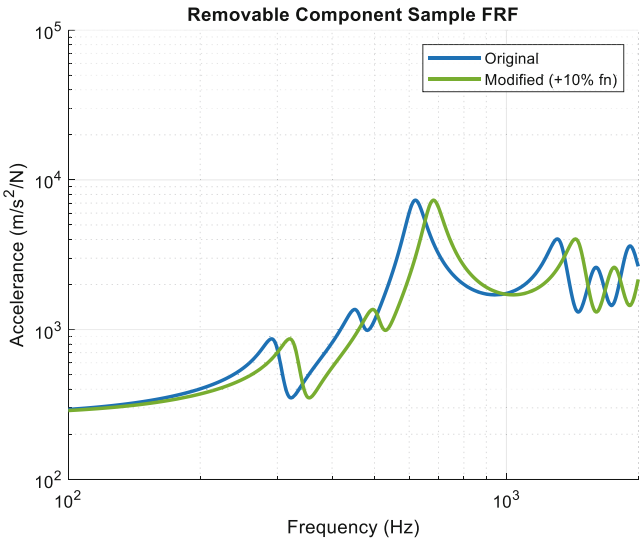

Fig. 15.4 Sample FRF of the Removable Component, original and +10% frequency modifications

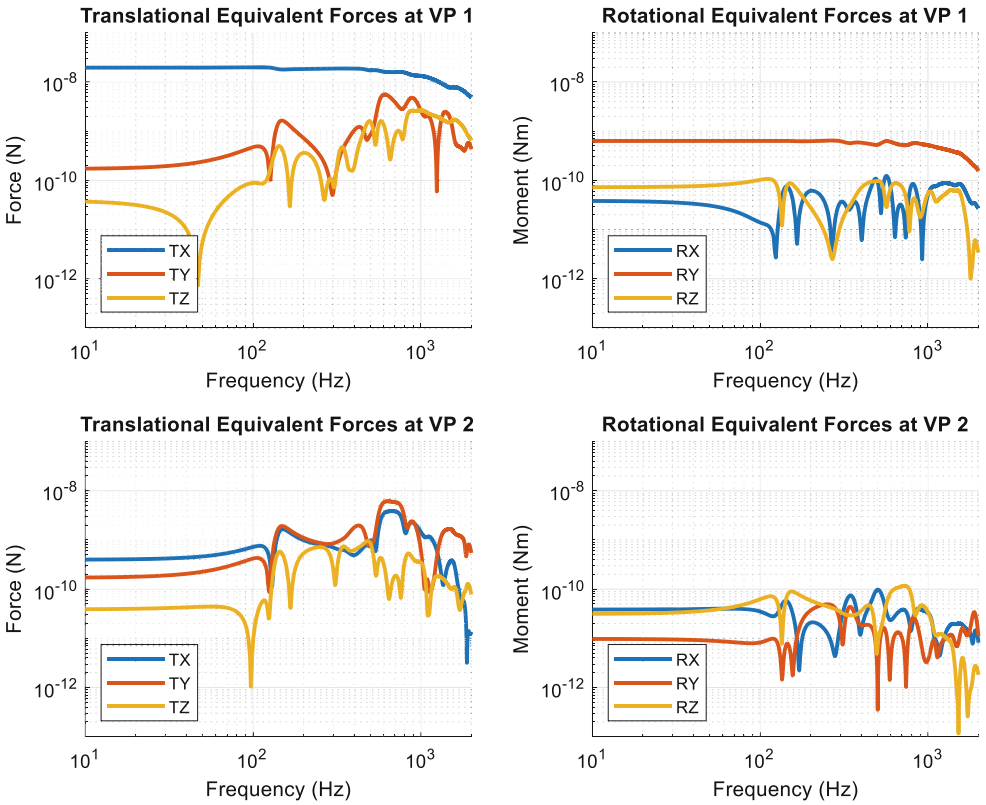

Fig. 15.5 Equivalent forces and moments at the two interfaces between the box assembly and the removable component

15.2.2 Equivalent Forces

Equivalent forces in the operational environment were calculated for six DoF at each of the two interfaces. The equivalent forces are shown in Fig. 15.5. These forces can then be validated by applying them to the BARC and comparing the response to that in the true operational environment. This validation was done for both the system with the original RC and that with the modified RC, as seen respectively in Fig. 15.6a, b. The TPA synthesis in blue matches the validation in black very accurately for both systems, confirming that the equivalent forces are not influenced by the dynamics of the Removable

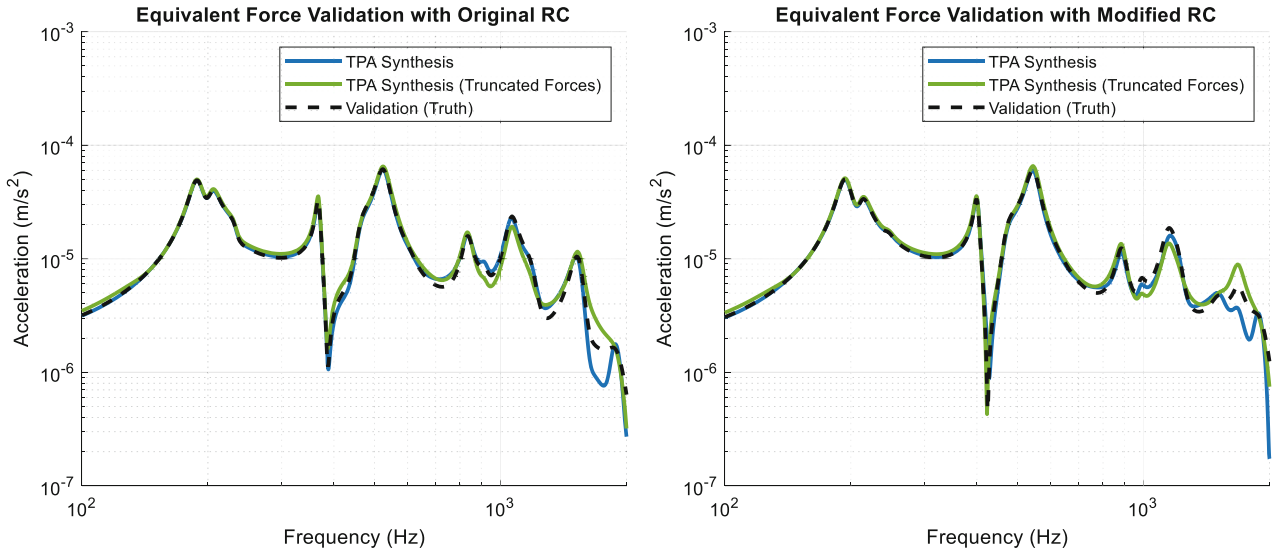

Fig. 15.6 Validation of the equivalent forces applied at the interfaces of the BARC with (**a**) the original Removable Component and (**b**) the modified Removable Component

Component. Some minor differences can be observed in the synthesis at higher frequencies; these differences are a result of the interface not being perfectly rigid in those frequency ranges.

Realistically, applying six forces and six moments to this structure may be challenging in practice. As seen in Fig. 15.5, the TX and RY signals at VP 1 stand out as being higher magnitude than the remaining signals. Thus the set of equivalent forces was also reduced from twelve DoF to these two DoF and the validation was repeated. As seen in the green curves of Fig. 15.6, this reduced set of equivalent forces still provides a very accurate representation of the operational environment.

15.2.3 Interface Forces

As mentioned above, interface forces can be used to test and analyze a passive component without the remaining assembly. Interface forces in this operational environment were calculated for six DoF at each of the two interfaces. The resulting forces are shown in Fig. 15.7. These forces can then be validated by applying them to the Removable Component and comparing the response to that in the true operational environment. This validation was done for both the system with the original RC and that with the modified RC, as seen respectively in Fig. 15.8a, b. As seen in Fig. 15.8a, the interface force approach produces accurate results if the same Removable Component is used in the force calculation and the validation. However, the blue curve in Fig. 15.8b reveals that those interface forces calculated from the original BARC can not be applied to the modified BARC accurately. This is because the interface forces are a property of both the BA and the RC.

To remedy this, interface forces were also calculated using equivalent forces from the original BARC and dynamics of the modified BARC, as in Eq. (15.6). The green curve in Fig. 15.8b reveals that this is a more appropriate way to determine component interface forces for cases where the dynamics of the component are changing. Thus, the interface forces can still be used to test and analyze the component if they are derived appropriately.

15.2.4 Pseudo Forces

Pseudo forces were also calculated on the BARC using the same indicator accelerometers as above. The locations of the pseudo forces were chosen arbitrarily on the box. Twelve inputs were used because there are a total of twelve degrees of freedom at the interfaces. The physical locations of the pseudo forces that were calculated are shown in Fig. 15.9a. The resulting pseudo forces are shown in Fig. 15.9b.

The pseudo forces are validated by applying them to the full system and reviewing the response at the validation sensor. This validation is shown in Fig. 15.10. As seen, the pseudo force synthesis compares very well with the validation

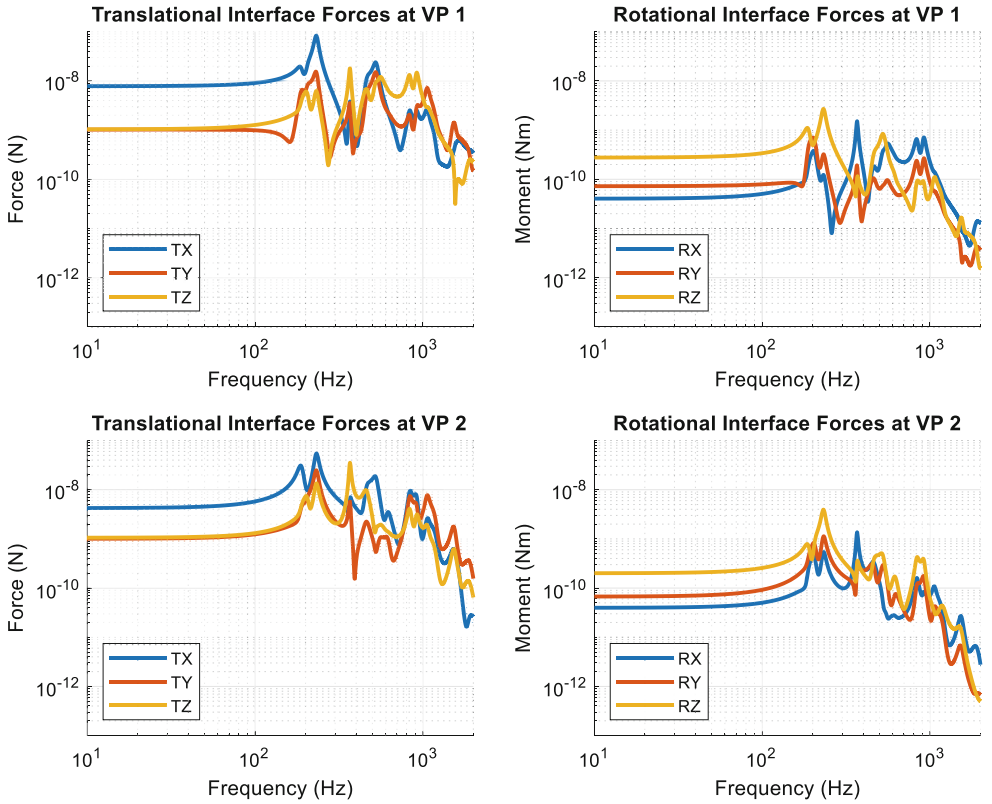

Fig. 15.7 Interface forces and moments at the two interfaces between the box assembly and the removable component

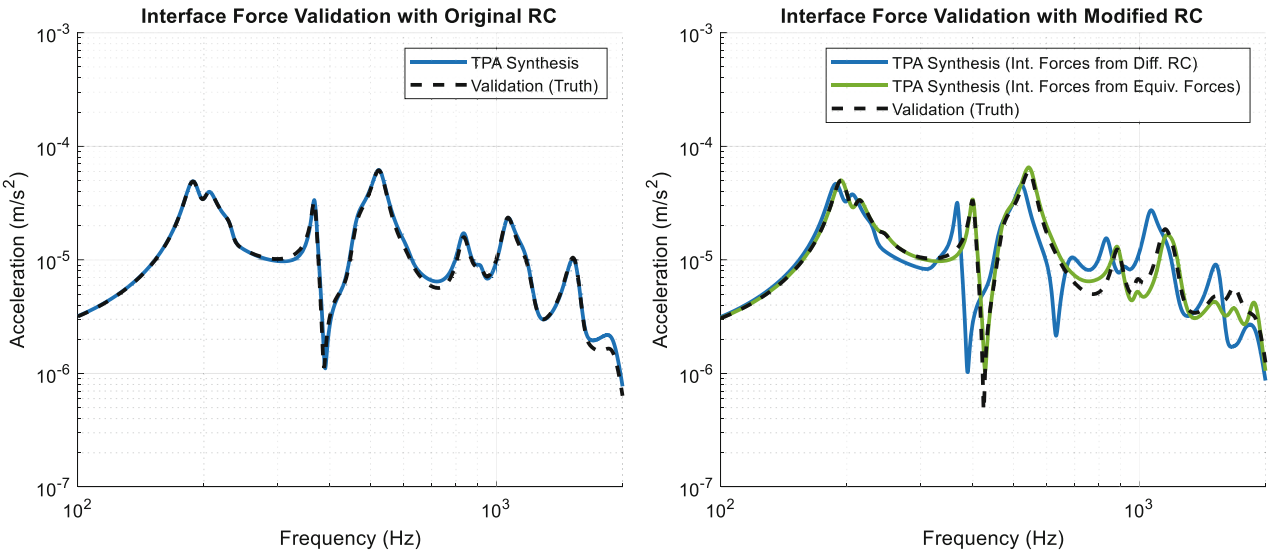

Fig. 15.8 Validation of the interface forces applied at the interfaces of the BARC with (**a**) the original Removable Component and (**b**) the modified Removable Component

measurement. The pseudo forces can be applied to either the BARC with the original RC or the modified RC and both cases produce very accurate results because the pseudo forces are not a function of the dynamics of the RC. These pseudo forces were placed arbitrarily on the structure, but it is expected that the pseudo force locations and quantity could be more methodically optimized to produce an accurate response on the passive component. There is currently research being performed by Sandia and the Atomic Weapons Establishment to optimize shaker locations for IMMAT testing [7] which may also be applicable for determination of optimized pseudo force locations.

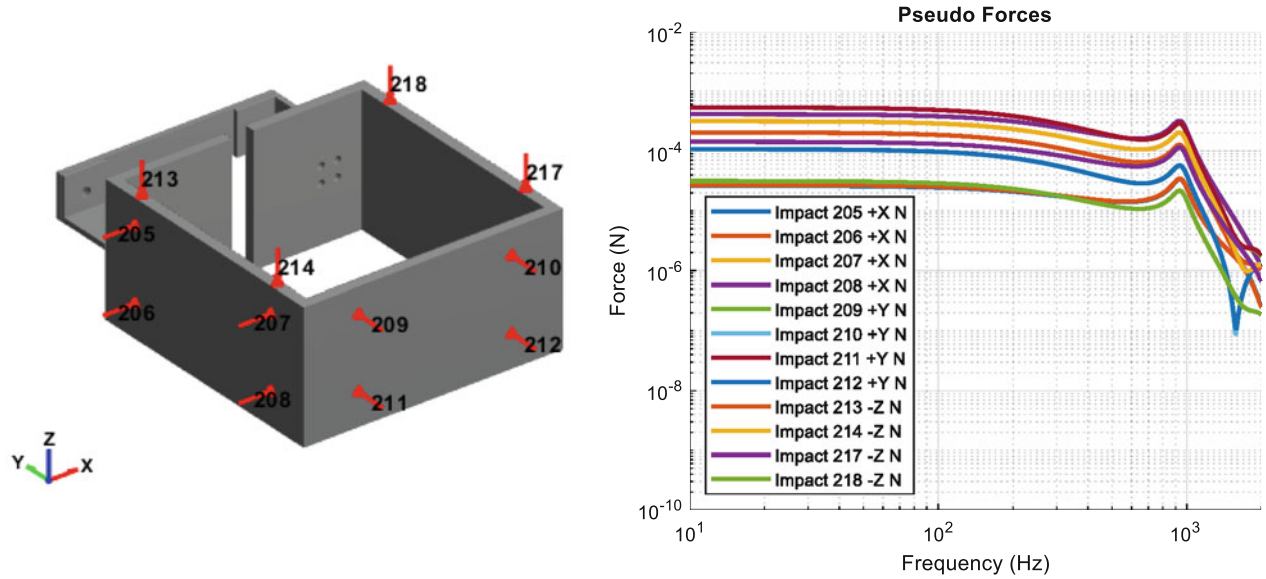

Fig. 15.9 Pseudo forces: (**a**) physical locations and (**b**) calculated forces

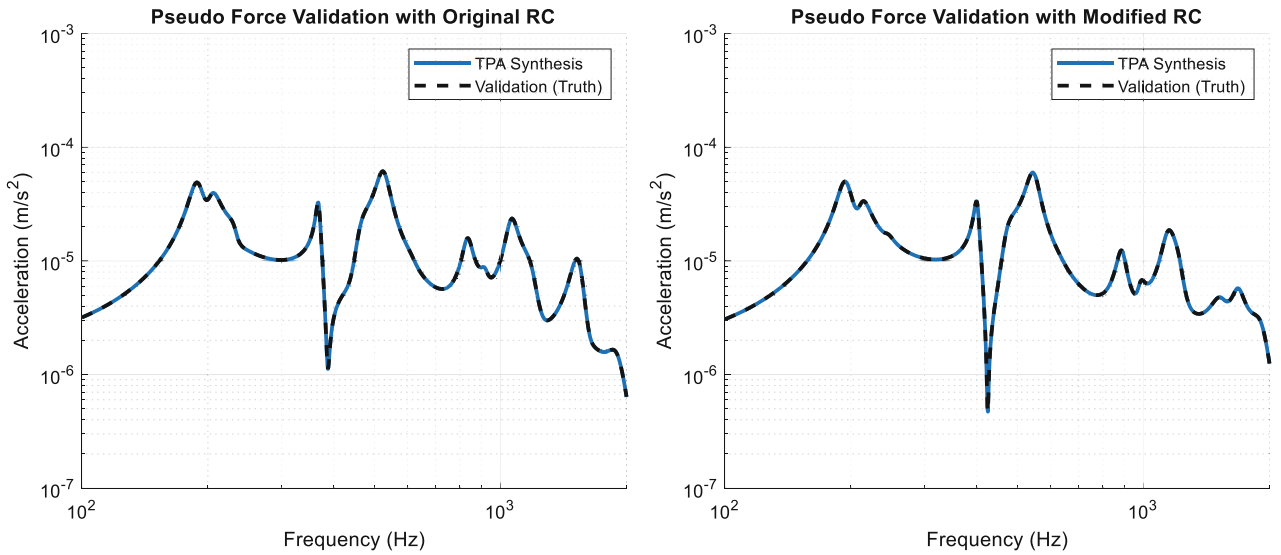

Fig. 15.10 Validation of the pseudo forces applied at the interfaces of the BARC with (**a**) the original Removable Component and (**b**) the modified Removable Component

15.3 Summary

Although traditionally used in the automotive industry, this paper has demonstrated how transfer path analysis techniques can be used in shock and vibration aerospace qualification testing. The equivalent force concept, in particular, is useful for describing the forces acting on passive components within a structure. If equivalent forces are used to capture environments, the equivalent forces can be applied to systems with different passive components. This is useful if mock or early design hardware is used in an operational test and the data will subsequently be used to test and analyze newer hardware with different dynamics.

Equivalent forces can be applied to either a finite element model or experimental model of the system to better understand the dynamics and performance of the component(s) of interest. If the equivalent forces are determined as pseudo forces across the active structure, the pseudo forces can also be easily implemented in a laboratory test of the complete system.

However, when the component must be tested or analyzed independent from the rest of the system, interface forces must be considered. If the system design is already finalized and the dynamics are unchanging, interface forces can provide an

accurate description of the forces entering the component(s) of interest. However, interface forces reflect the dynamics of both the active and passive components, and therefore cannot simply be calculated for one system configuration and applied to a passive component with different dynamics. Thus if interface forces will be used during the product development phase, equivalent forces should first be calculated and then transformed to interface forces for the specific design iteration.

The TPA concepts were applied to Sandia's academic BARC structure in this work. However, these FRF-based techniques generally perform quite well for complex systems with closely spaced modes and high damping and should therefore easily extend to more realistic aerospace structures. In fact, with the Removable Component's small size and low weight, it is expected that these techniques would be quite challenging to implement experimentally on the BARC. The tools would likely perform better on a larger more realistic structure.

References

1. Schoenherr, T.: Boundary conditions in environmental testing challenge problem, Sandia National Laboratories. https://connect.sandia.gov/sites/TestBoundaryConditions
2. Qualification testing – Space vehicle design criteria, Technical Report, NASA Langley Research Center; Hampton, VA, United States, May 1970
3. Gregory, D.L., Bitsie, F., Smallwood, D.O.: Comparison of the response of a simple structure to single axis and multiple axis random vibration inputs. In: 80th Shock and Vibration Symposium, San Diego, CA, October 2009
4. Owens, B., Tipton, D.G., McDowell, M.: 6 Degree of Freedom shock and vibration: testing and analysis, 86th Shock and Vibration Symposium, Orlando, FL, October 2015
5. Ross, M., et al.: 6-DOF shaker test input derivation from field test. In: 35th International Modal Analysis Conference, Orlando, FL, February 2017
6. Daborn, P.M.: Scaling up of the impedance-matched multi-axis test (IMMAT) technique. In: 35th International Modal Analysis Conference, Orlando, FL, February 2017
7. Mayes, R., et al.: Optimization of shaker locations for multiple shaker environmental testing. Paper accepted for the 37th international modal analysis conference, Orlando FL, January 2019
8. Mayes, R.L.: A Modal Craig-Bampton substructure for experiments, analysis, control and specifications. In: 33rd International Modal Analysis Conference, Orlando, FL, February 2015
9. Harvie, J.M.: Using modal substructuring to improve shock & vibration qualification. In: 36th International Modal Analysis Conference, Orlando, FL, February 2018
10. Scharton, T.D.: Force limited vibration testing monograph, NASA Reference Publication RP-1403, Jet Propulsion Laboratory, California Institute of Technology, Pasadena, CA, May 1997
11. van der Seijs, M., de Klerk, D., Rixen, D.J.: General framework for transfer path analysis: history, theory and classification of techniques. Mech. Syst. Signal Process. **68–69**, 217–244, August 2015
12. Elliott, A.S., Moorhouse, A.T.: Characterisation of structure borne sound sources from measurement in-situ. J. Acoust. Soc. Am. **123**(5), 3176 (2008). https://doi.org/10.1121/1.2933261
13. Moorhouse, A.T., Elliott, A.S., Evans, T.A.: In situ measurement of the blocked force of structure-borne sound sources. J. Sound Vib. **325**(4–5), 679–685 (2009). https://doi.org/10.1016/j.jsv.2009.04.035
14. van der Seijs, M., et al.: An improved methodology for the virtual point transformation of measured frequency response functions in dynamic substructuring, COMPDYN 2013, Kos Island, Greece, pp. 12–14, June 2013
15. Soine, D., et al.: Designing hardware for the boundary condition Round Robin challenge. In: 36th International Modal Analysis Conference, Orlando, FL, February 2018
16. Rohe, D., et al.: Testing Summary for the Box and Removable Component Structure. Paper accepted for the 37th international modal analysis conference, Orlando FL, January 2019

Chapter 16
Testing Summary for the Box Assembly with Removable Component Structure

Daniel P. Rohe, Scott Smith, Matthew R. W. Brake, James DeClerck, Mariano Alvarez Blanco, Tyler F. Schoenherr, and Troy J. Skousen

Abstract The boundary conditions of a test will have an effect on the dynamic response of a test unit. The industry standard of designing the most rigid fixture possible may not be the correct approach to replicate responses to service environment loads. The Box Assembly with Removable Component (BARC) structure was developed as a challenge problem for those investigating boundary conditions and their effect on these tests. Several BARC structures have been manufactured and sent to collaborators who have performed a variety of structural tests on the hardware. This paper serves as a collection and comparison of the dynamic testing that has been performed to date by several organizations taking part in this research challenge problem. Of particular interest is the variability in modal parameters between different test articles, as well as any nonlinearities that can be identified.

Keywords BARC · Modal · Comparison · Nonlinear · Expansion

16.1 Introduction

For a traditional environmental vibration test, the component of interest is typically attached to the shaker used to excite the structure via some kind of fixture. The traditional approach is to make such a fixture as rigid as possible to ensure the dynamics of the component under test are not influenced by the dynamics of the fixture; however, such a fixture often provides incorrect boundary conditions to the part. The testing community has recognized the shortcomings of such an approach, and a boundary condition challenge problem has been developed to provide a collaborative environment in which alternative approaches can be investigated [1]. The structure of interest is the Box Assembly with Removable Component (BARC) structure, which consists of an assembly of two subcomponents: a removable component composed of two C-channels and a beam connecting them, and a cut section of a box beam that represents the system on which the removable component rides during its environment.

Sandia National Laboratories is a multimission laboratory managed and operated by National Technology & Engineering Solutions of Sandia, LLC, a wholly owned subsidiary of Honeywell International Inc., for the U.S. Department of Energy's National Nuclear Security Administration under contract DE-NA0003525.

This paper describes objective technical results and analysis. Any subjective views or opinions that might be expressed in the paper do not necessarily represent the views of the U.S. Department of Energy or the United States Government.

D. P. Rohe (✉) · T. F. Schoenherr · T. J. Skousen
Sandia National Laboratories, Albuquerque, NM, USA
e-mail: dprohe@sandia.gov

S. Smith · M. R. W. Brake
William Marsh Rice University, Houston, TX, USA

J. DeClerck
Practice, Mechanical Engineering—Engineering Mechanics, Michigan Technological University, Houghton, MI, USA

M. Alvarez Blanco
Siemens Industry Software NV, Leuven, Belgium

C. Walber et al. (eds.), *Sensors and Instrumentation, Aircraft/Aerospace, Energy Harvesting & Dynamic Environments Testing, Volume 7*, Conference Proceedings of the Society for Experimental Mechanics Series,
https://doi.org/10.1007/978-3-030-12676-6_16

This work summarizes the dynamic testing that has been performed to date on the BARC structure. It compares five modal tests performed by collaborators on the challenge problem. The natural frequencies and damping ratios for the extracted modes are reported, and comparisons are made between the shapes. Finite element expansion was used to produce a consistent set of measurement points between the four data sets so the shapes could be compared.

16.2 Summary of Testing Performed

Many dynamic tests have been performed to date on the BARC hardware. Modal testing has been performed at a number of institutions, a comparison of which will be the focus of this paper. In addition to these modal tests, a number of other tests have been performed. Sandia National Laboratories has performed modal testing on an additional BARC configuration that does not have the cut in the box beam portion of the assembly. Sandia has also performed studies of the removable component attached to various fixtures, both to investigate the ability to measure or compute strain during a test [2] as well as to evaluate fixture designs [3]. Michigan Technological University performed a sensitivity study of the BARC assembly [4].

16.3 Modal Test Comparisons

Five institutions provided modal test data on the BARC structure for this paper. The test geometries for each test are shown in Fig. 16.1. The tests targeted different frequency bandwidths using various test methods. Modal Test 1 extracted 55 modes below 10,000 Hz using a small modal hammer to excite the structure and a 3D Scanning Laser Doppler Vibrometer to measure responses. Modal Test 2 extracted 22 modes below 4000 Hz. Modal Test 3 extracted 11 modes below 1500 Hz using a roving hammer technique. Modal Test 4 extracted 14 modes below 1200 Hz using a roving accelerometer technique with four triaxial accelerometers, though it was noted that this caused mode splitting due to the changing mass-loading, and the test was repeated using only a single set of four triaxial accelerometers to identify modal parameters. Finally, Modal Test 5 extracted 16 modes below 2100 Hz also using a roving accelerometer technique. For the purposes of this paper, only the modes below 4000 Hz will be compared. Modal assurance criterion (MAC) matrices with natural frequencies and damping ratios are shown for each test in Fig. 16.2.

In order to compare modal parameters between tests, a mapping between the modes extracted in each test must first be established. This is traditionally done by comparing mode shapes, e.g. for a simple beam one might compare the modal parameters of the first bending mode between tests. One confounding factor for this work is that the differing geometry between each test makes comparing shapes directly difficult. To get around this issue, each set of mode shapes was expanded using a finite element model, from which a consistent set of measurement degrees of freedom could be chosen (Fig. 16.3).

A finite element model had been created at Sandia National Laboratories for other BARC work, and that model is re-used here. The System Equivalent Reduction Expansion Process [5] was used to perform the expansion. All finite element modes within the bandwidth of each test (including rigid body modes) were used in the expansion procedure. The Modal Test 5 dataset did not contain sufficient instrumentation for the finite element expansion to succeed and therefore was not included in this analysis. Figure 16.4 shows the first mode from each test expanded to the full finite element model. For the Modal Test 2 and Modal Test 4 datasets, which had measurement points primarily on the corners of the box beam portion of the BARC, over-fitting occurred during the expansion process; this can be seen in Fig. 16.4b and to a lesser extent in Fig. 16.4d. Without many measurement points in the middle of the box beam spans to constrain the motion of the finite element model modes at those points, the expansion procedure is free to add higher order modes into the expanded shape to better match the corner motion. A comparison then between, for example, Fig. 16.4a and b would result in a poor shape due primarily to the improper expansion rather than true differences in the data. In order to make a reasonable shape comparisons, the expanded finite element shapes were reduced down to the Modal Test 2 geometry. The downside of reducing the geometry is that modes begin to look like one another, as can be seen in the relatively high off-diagonals in the MAC matrix of Fig. 16.2b. This reduction, however, is necessary to accurately map mode shapes between tests.

Figure 16.5 shows a comparison of all shapes from the study. It is clear that the reduction down to the sparser set of degrees of freedom produces more severe off-diagonal entries in the MAC (compare for example Fig. 16.2a to the columns and rows in Fig. 16.5 corresponding to Modal Test 1), but there are still strong enough diagonals to be able to map modes between tests. Due to the mode splitting in Modal Test 4, the columns and rows corresponding to the test show a less clear correspondence to the other tests, but by more closely examining the shapes, a mapping can still be derived. Table 16.1

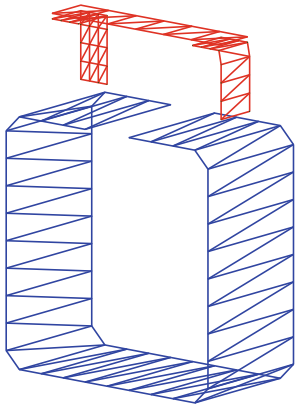

(a)

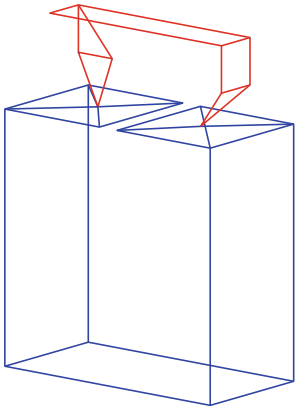

(b)

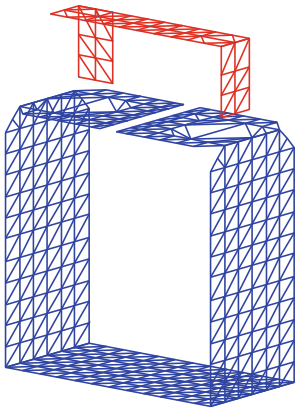

(c)

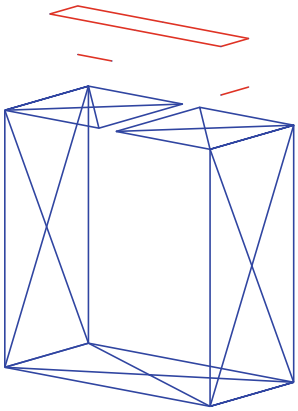

(d)

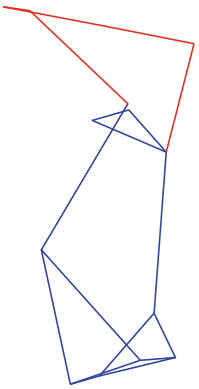

(e)

Fig. 16.1 Geometry used for each dataset during modal testing of the BARC. **(a)** Modal Test 1 geometry. **(b)** Modal Test 2 geometry. **(c)** Modal Test 3 geometry. **(d)** Modal Test 4 geometry. **(e)** Modal Test 5 geometry

presents the modes grouped by similar shapes. Although the shape comparison could not be performed for the Modal Test 5 dataset, it was found to have natural frequencies that correlated well the other data sets, so it is included in Table 16.1.

16.4 Nonlinearity

Three institutions also contributed time histories to this study, on which qualitative nonlinear analysis was performed. The Zeroed Early-Time Fast Fourier Transform (ZEFFT) [6] was used to try to identify any nonlinear behaviors in the part. Of the three time histories provided, one excited the structure to much higher levels than the other two, so that is the time history that will be considered for this section of the paper. The time history analyzed is shown in Fig. 16.6, and the ZEFFT of that time signal is shown in Fig. 16.7. The majority of the modes of the structure appeared linear to the levels that they were

Mode Number			1	2	3	4	5	6	7	8	9	10	11	12	13	14	15	16	17	18	19	20	21	22	23
	Frequency (Hz)		188	208	263	441	476	565	586	666	1112	1205	1509	1629	1730	1765	1964	2065	2271	2367	2643	2685	2980	3060	3477
		Damp	0.55%	0.32%	0.23%	0.18%	0.16%	0.21%	0.17%	0.19%	0.28%	0.10%	0.10%	0.35%	0.10%	0.13%	0.08%	0.20%	0.11%	0.11%	0.05%	0.07%	0.11%	0.15%	0.09%
1	188	0.55%	100	0	5	1	4	15	0	2	2	1	0	0	0	4	0	2	0	0	0	0	0	0	0
2	208	0.32%	0	100	0	4	4	1	1	0	0	2	1	0	8	1	3	1	1	2	0	2	0	0	0
3	263	0.23%	5	0	100	2	0	14	0	0	9	2	1	0	0	0	2	0	1	0	0	0	0	0	0
4	441	0.18%	1	4	2	100	18	0	2	2	0	0	0	0	0	1	1	0	1	1	0	1	0	0	0
5	476	0.16%	4	4	0	18	100	2	0	1	0	0	0	0	0	1	0	2	0	4	0	1	0	0	0
6	565	0.21%	15	1	14	0	2	100	0	3	5	1	2	0	0	2	6	1	3	0	1	0	0	0	0
7	586	0.17%	0	1	0	2	0	0	100	2	0	0	1	0	2	2	0	0	0	2	0	0	0	0	0
8	666	0.19%	2	0	0	2	1	3	2	100	0	6	0	0	2	0	0	0	1	0	0	0	1	0	0
9	1112	0.28%	2	0	9	0	0	5	0	0	100	13	5	0	1	0	4	1	1	0	0	0	2	1	0
10	1205	0.10%	1	2	2	0	0	1	0	6	13	100	2	2	2	0	0	0	0	0	0	0	3	2	1
11	1509	0.10%	0	1	1	0	0	2	1	0	5	2	100	0	5	1	6	0	0	1	0	0	1	0	0
12	1629	0.35%	0	0	0	0	0	0	0	0	0	2	0	100	0	0	0	0	0	0	0	0	0	0	0
13	1730	0.10%	0	8	0	0	0	0	2	2	1	2	5	0	100	4	2	2	2	0	3	0	4	2	1
14	1765	0.13%	4	1	0	1	1	2	2	0	0	0	1	0	4	100	4	2	0	7	0	4	0	0	0
15	1964	0.08%	0	3	2	1	0	6	0	0	4	0	6	0	2	4	100	1	0	3	0	1	0	0	0
16	2065	0.20%	2	1	0	0	2	1	0	0	1	0	0	0	2	2	1	100	0	3	0	2	0	0	0
17	2271	0.11%	0	1	1	1	0	3	0	1	1	0	0	0	2	0	0	0	100	0	1	1	0	0	1
18	2367	0.11%	0	2	0	1	4	0	2	0	0	0	1	0	0	7	3	3	0	100	0	4	0	0	0
19	2643	0.05%	0	0	0	0	0	1	0	0	0	0	0	0	3	0	0	0	1	0	100	0	0	0	0
20	2685	0.07%	0	2	0	1	1	0	0	0	0	0	0	0	0	4	1	2	1	4	0	100	0	0	0
21	2980	0.11%	0	0	0	0	0	0	0	1	2	3	1	0	4	0	0	0	0	0	0	0	100	36	3
22	3060	0.15%	0	0	0	0	0	0	0	0	1	2	0	0	2	0	0	0	0	0	0	0	36	100	2
23	3477	0.09%	0	0	0	0	0	0	0	0	0	1	0	0	1	0	0	0	1	0	0	0	3	2	100

(a)

Mode Number			1	2	3	4	5	6	7	8	9	10	11	12	13	14	15	16	17	18	19	20	21	22
	Frequency (Hz)		187	206	446	477	569	584	666	1112	1244	1513	1629	1693	1782	2010	2075	2300	2376	2689	2719	3014	3105	3489
		Damp	0.17%	0.12%	0.13%	0.21%	0.09%	0.12%	0.06%	0.06%	0.12%	0.06%	0.15%	0.28%	0.16%	0.10%	0.10%	0.07%	0.10%	0.07%	0.11%	0.13%	0.11%	0.09%
1	187	0.17%	100	1	0	1	9	0	21	0	1	7	0	0	0	0	0	2	1	0	0	0	0	0
2	206	0.12%	1	100	2	2	0	3	4	0	1	0	1	3	7	0	1	2	15	1	0	0	0	0
3	446	0.13%	0	2	100	4	1	0	0	0	0	0	0	0	0	1	4	2	8	0	0	0	0	0
4	477	0.21%	1	2	4	100	0	1	0	0	0	1	1	0	20	1	0	2	0	0	0	0	0	1
5	569	0.09%	9	0	1	0	100	0	0	23	1	2	0	1	1	1	0	0	0	0	0	0	1	6
6	584	0.12%	0	3	0	1	0	100	1	6	0	1	3	1	2	14	1	0	0	0	0	0	0	1
7	666	0.06%	21	4	0	0	0	1	100	14	2	38	5	0	0	0	0	0	0	0	0	4	0	0
8	1112	0.06%	0	0	0	0	23	6	14	100	12	0	32	0	0	0	0	0	0	0	0	7	9	37
9	1244	0.12%	1	1	0	0	1	0	2	12	100	8	12	0	1	0	3	2	0	1	0	40	45	0
10	1513	0.06%	7	0	0	1	2	1	38	0	8	100	0	3	0	0	0	0	0	1	0	1	3	1
11	1629	0.15%	0	1	0	1	0	3	5	32	12	0	100	5	1	4	5	10	1	3	0	3	2	41
12	1693	0.28%	0	3	0	0	1	1	0	0	0	3	5	100	0	0	2	0	0	0	0	17	18	0
13	1782	0.16%	0	7	0	20	1	2	0	0	1	0	1	0	100	0	48	3	9	7	1	0	0	6
14	2010	0.10%	0	0	1	1	1	14	0	0	0	0	4	0	0	100	2	17	29	5	8	0	0	2
15	2075	0.10%	0	1	4	0	0	1	0	0	3	0	5	2	48	2	100	21	10	1	1	0	0	4
16	2300	0.07%	2	2	2	2	0	0	0	0	2	0	10	0	3	17	21	100	1	42	0	0	1	1
17	2376	0.10%	1	15	8	0	0	0	0	0	0	0	1	0	9	29	10	1	100	13	9	0	1	0
18	2689	0.07%	0	1	0	0	0	0	0	0	1	1	3	0	7	5	1	42	13	100	0	0	0	0
19	2719	0.11%	0	0	0	0	0	0	0	0	0	0	0	0	1	8	1	0	9	0	100	0	0	0
20	3014	0.13%	0	0	0	0	0	0	4	7	40	1	3	17	0	0	0	0	0	0	0	100	89	5
21	3105	0.11%	0	0	0	0	1	0	0	9	45	3	2	18	0	0	0	1	1	0	0	89	100	4
22	3489	0.09%	0	0	0	1	6	1	0	37	0	1	41	0	6	2	4	1	0	0	0	5	4	100

(b)

Fig. 16.2 MAC matrices including natural frequency and damping ratio for each dataset. **(a)** Modal Test 1 MAC and modal parameters. **(b)** Modal Test 2 MAC and modal parameters. **(c)** Modal Test 3 MAC and modal parameters. **(d)** Modal Test 4 MAC and modal parameters. **(e)** Modal Test 5 MAC and modal parameters

Mode Number			1	2	3	4	5	6	7	8	9	10	11
	Frequency (Hz)		183	204	256	421	461	548	575	649	1079	1141	1481
		Damp	0.21%	0.09%	0.15%	1.15%	1.14%	0.16%	0.46%	0.24%	0.19%	0.15%	0.17%
1	183	0.21%	100	1	0	0	0	3	0	11	2	0	1
2	204	0.09%	1	100	0	0	0	0	0	3	1	0	0
3	256	0.15%	0	0	100	0	0	7	2	4	4	2	0
4	421	1.15%	0	0	0	100	1	0	1	0	1	0	0
5	461	1.14%	0	0	0	1	100	0	0	0	0	0	0
6	548	0.16%	3	0	7	0	0	100	3	2	0	0	2
7	575	0.46%	0	0	2	1	0	3	100	2	0	0	0
8	649	0.24%	11	3	4	0	0	2	2	100	3	0	1
9	1079	0.19%	2	1	4	1	0	0	0	3	100	13	0
10	1141	0.15%	0	0	2	0	0	0	0	0	13	100	1
11	1481	0.17%	1	0	0	0	0	2	0	1	0	1	100

(c)

Mode Number			1	2	3	4	5	6	7	8	9	10	11	12	13	14
	Frequency (Hz)		183	204	257	410	431	469	549	575	645	655	1036	1085	1115	1151
		Damp	0.48%	0.30%	0.11%	0.79%	0.36%	0.07%	0.22%	0.50%	0.34%	0.08%	1.00%	0.16%	0.30%	0.12%
1	183	0.48%	100	0	3	1	3	2	3	0	11	2	2	1	2	0
2	204	0.30%	0	100	0	6	4	2	0	2	1	0	1	0	0	1
3	257	0.11%	3	0	100	2	0	0	10	0	0	0	4	0	2	1
4	410	0.79%	1	6	2	100	0	5	0	4	0	7	0	0	0	0
5	431	0.36%	3	4	0	0	100	3	0	1	0	1	0	1	0	1
6	469	0.07%	2	2	0	5	3	100	3	1	0	0	1	0	2	0
7	549	0.22%	3	0	10	0	0	3	100	0	14	3	0	13	6	1
8	575	0.50%	0	2	0	4	1	1	0	100	4	2	0	2	0	0
9	645	0.34%	11	1	0	0	0	0	14	4	100	1	1	11	0	5
10	655	0.08%	2	0	0	7	1	0	3	2	1	100	3	17	2	7
11	1036	1.00%	2	1	4	0	0	1	0	0	1	3	100	0	73	0
12	1085	0.16%	1	0	0	0	1	0	13	2	11	17	0	100	0	9
13	1115	0.30%	2	0	2	0	0	2	6	0	0	2	73	0	100	0
14	1151	0.12%	0	1	1	0	1	0	1	0	5	7	0	9	0	100

(d)

Mode Number			1	2	3	4	5	6	7	8	9	10	11	12	13	14	15	16
	Frequency		185	207	259	440	475	556	580	660	1094	1172	1504	1622	1686	1752	1945	2024
		Damp	0.23%	0.16%	0.65%	0.19%	0.05%	0.36%	0.15%	0.11%	0.12%	0.14%	0.07%	0.21%	0.22%	0.11%	0.28%	0.10%
1	185	0.23%	100	24	66	10	23	75	37	66	43	75	65	35	35	34	55	7
2	207	0.16%	24	100	29	48	75	16	69	15	10	19	13	9	31	26	19	3
3	259	0.65%	66	29	100	28	47	55	52	49	30	41	46	31	31	32	41	9
4	440	0.19%	10	48	28	100	68	9	63	14	6	10	10	6	17	25	9	1
5	475	0.05%	23	75	47	68	100	18	77	20	13	19	15	14	39	38	20	7
6	556	0.36%	75	16	55	9	18	100	23	48	38	54	53	30	35	33	64	12
7	580	0.15%	37	69	52	63	77	23	100	34	23	29	31	24	31	27	27	7
8	660	0.11%	66	15	49	14	20	48	34	100	69	64	69	55	41	47	40	22
9	1094	0.12%	43	10	30	6	13	38	23	69	100	51	59	86	45	51	36	51
10	1172	0.14%	75	19	41	10	19	54	29	64	51	100	62	46	44	46	53	12
11	1504	0.07%	65	13	46	10	15	53	31	69	59	62	100	60	43	40	58	18
12	1622	0.21%	35	9	31	6	14	30	24	55	86	46	60	100	49	50	38	60
13	1686	0.22%	35	31	31	17	39	35	31	41	45	44	43	49	100	70	54	32
14	1752	0.11%	34	26	32	25	38	33	27	47	51	46	40	50	70	100	43	46
15	1945	0.28%	55	19	41	9	20	64	27	40	36	53	58	38	54	43	100	20
16	2024	0.10%	7	3	9	1	7	12	7	22	51	12	18	60	32	46	20	100

(e)

Fig. 16.2 (continued)

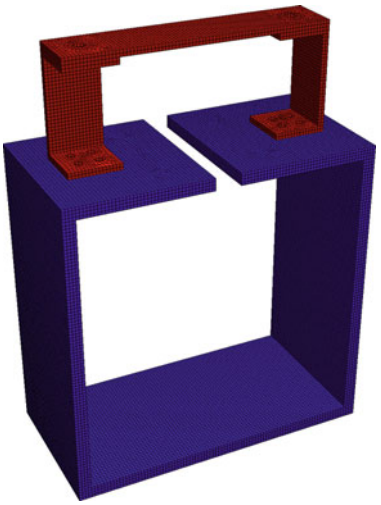

Fig. 16.3 BARC finite element model used for shape expansion

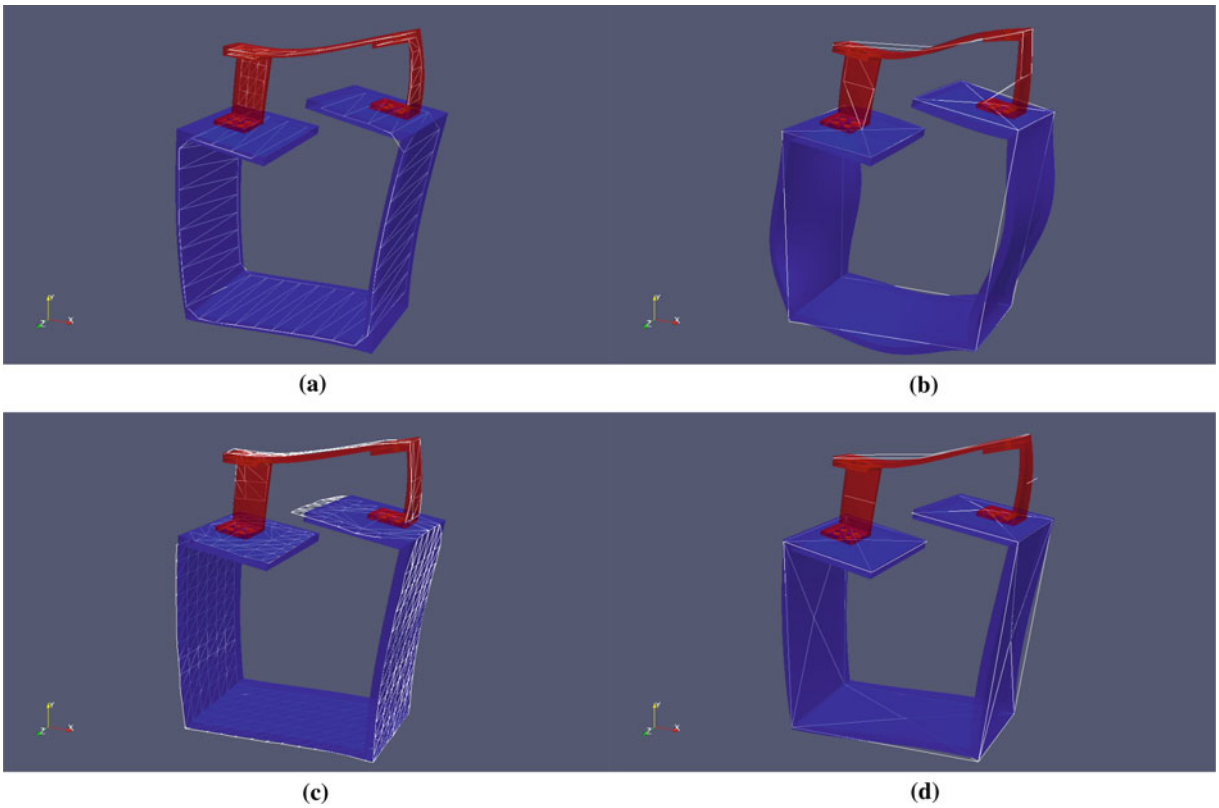

Fig. 16.4 Finite element expansion from the test geometry for the first elastic mode. The test geometry is shown in white trace lines beneath the semi-transparent finite element expansion. Note that Modal Test 3 data set used a roving hammer technique, so the only experimental degrees of freedom are those perpendicular to the surface; for this reason, it may look like there are significant differences between the test data and the expansion when there really are not. **(a)** Modal Test 1 expansion. **(b)** Modal Test 2 expansion. **(c)** Modal Test 3 expansion. **(d)** Modal Test 4 expansion

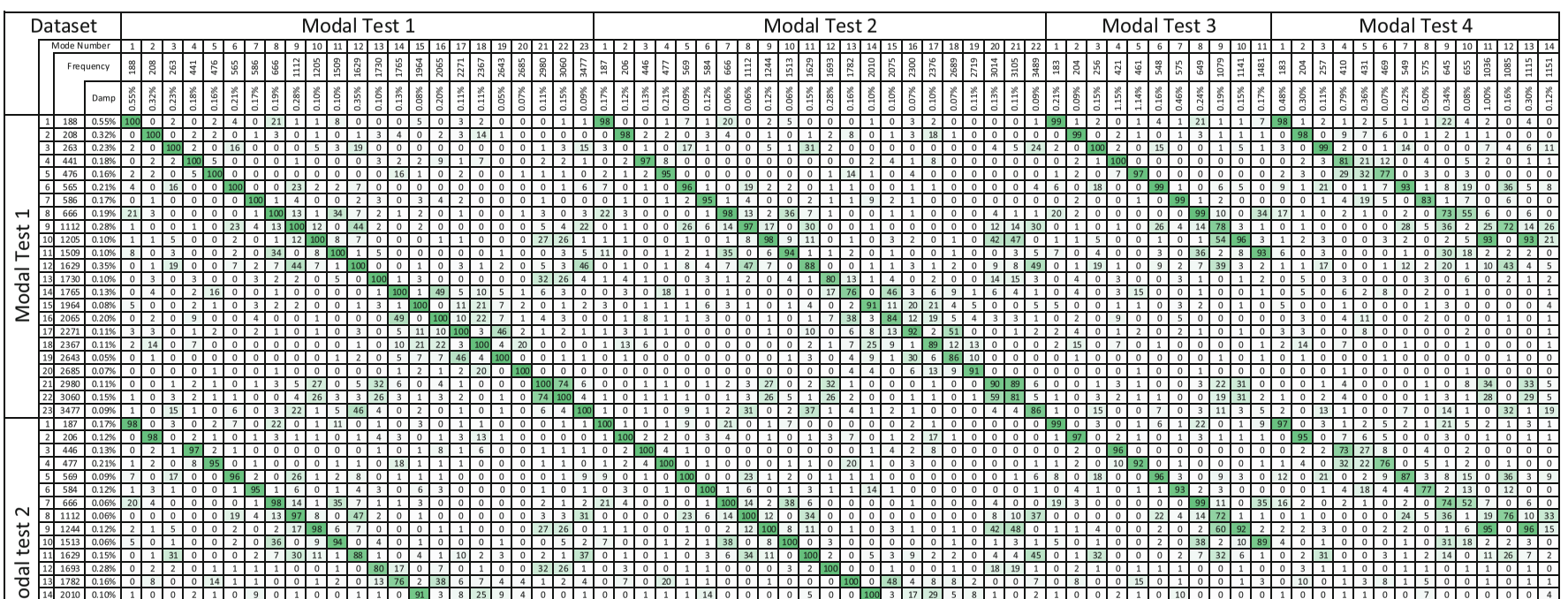

Fig. 16.5 Comparison of all shapes reduced down to the geometry of Modal Test 2

Table 16.1 Summary of modes extracted from the four tests grouped by similar modes

Modal Test 1			Modal Test 2			Modal Test 3			Modal Test 4			Modal Test 4 No Roving			Modal Test 5		
Mode	Frequency	Damping	Mode	Frequency	Damping	Mode	Frequency	Damping	Mode	Frequency	Damping	Mode	Frequency	Damping	Mode	Frequency	Damping
1	188	0.55%	1	187	0.17%	1	183	0.21%	1	183	0.48%	1	182.842	0.52%	1	185	0.23%
2	208	0.32%	2	206	0.12%	2	204	0.09%	2	204	0.30%	2	201.221	0.42%	2	207	0.16%
3	263	0.23%	–	–	–	3	256	0.15%	3	257	0.11%	3	256.399	0.21%	3	259	0.65%
4	441	0.18%	3	446	0.13%	4	421	1.15%	4[a] 5[a]	410 431	0.79% 0.36%	4	417.72	0.89%	4	440	0.19%
5	476	0.16%	4	477	0.21%	5	461	1.14%	6	469	0.07%	5	460.1	0.45%	5	475	0.05%
6	565	0.21%	5	569	0.09%	6	548	0.16%	7	549	0.22%	6	545.442	0.42%	6	556	0.36%
7	586	0.17%	6	584	0.12%	7	575	0.46%	8	575	0.50%	7	572.074	0.46%	7	580	0.15%
8	666	0.19%	7	666	0.06%	8	649	0.24%	9[a] 10[a]	645 655	0.34% 0.08%	8	648.57	0.29%	8	660	0.11%
9	1112	0.28%	8	1112	0.06%	9	1079	0.19%	11[a] 12[a]	1036 1085	1.00% 0.16%	9	1069.98	0.35%	9	1094	0.12%
10	1205	0.10%	9	1244	0.12%	10	1141	0.15%	13[a] 14[a]	1115 1151	0.30% 0.12%	10	1125.11	0.37%	10	1172	0.14%
11	1509	0.10%	10	1513	0.06%	11	1481	0.17%							11	1504	0.07%
12	1629	0.35%	11	1629	0.15%										12	1622	0.21%
13	1730	0.10%	12	1693	0.28%										13	1686	0.22%
14	1765	0.13%	13	1782	0.16%										14	1752	0.11%
15	1964	0.08%	14	2010	0.10%										15	1945	0.28%
16	2065	0.20%	15	2075	0.10%										16	2024	0.10%
17	2271	0.11%	16	2300	0.07%												
18	2367	0.11%	17	2376	0.10%												
19	2643	0.05%	18	2689	0.07%												
20	2685	0.07%	19	2719	0.11%												
21	2980	0.11%	20	3014	0.13%												
22	3060	0.15%	21	3105	0.11%												
23	3477	0.09%	22	3489	0.09%												

[a]Denotes a split mode due to changing accelerometer locations mid-test

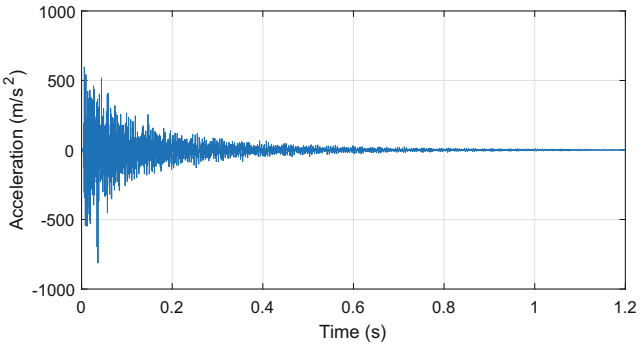

Fig. 16.6 Time history used to examine nonlinearities in the structure

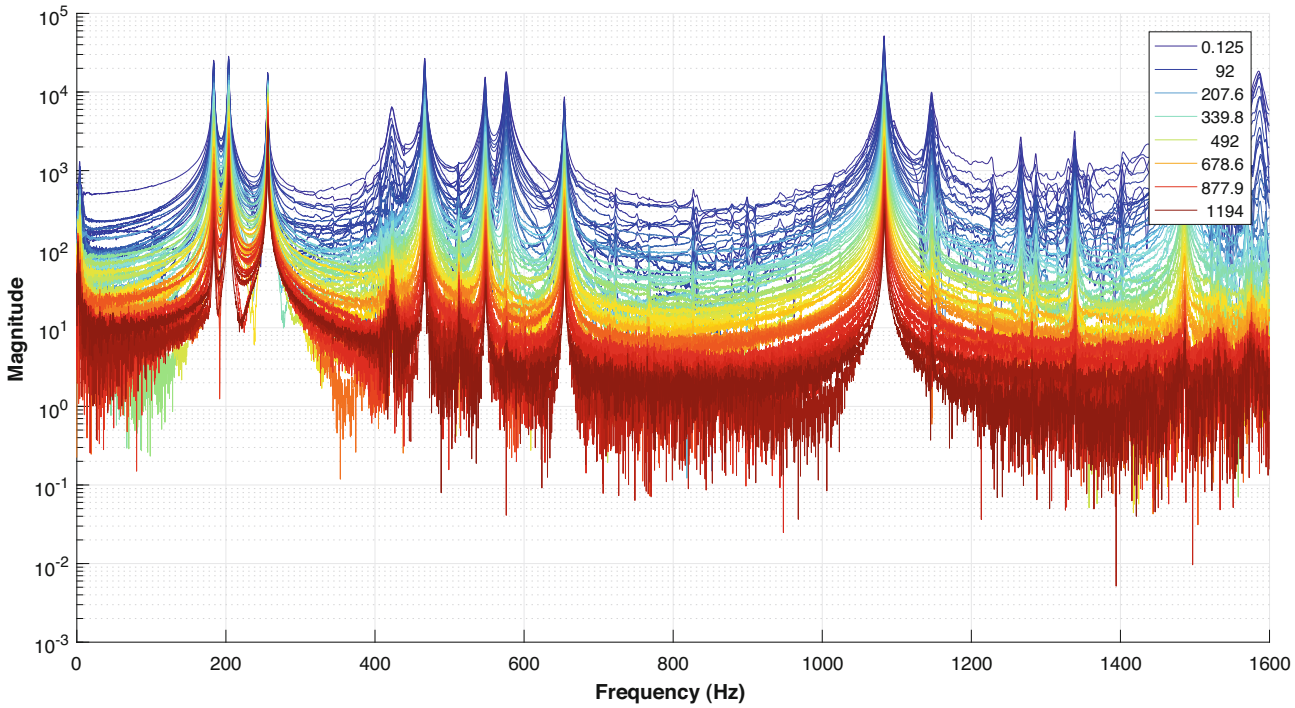

Fig. 16.7 ZEFFT of the data showing all frequencies up to 1600 Hz. Legend entries show time up to which the signal has been zeroed (in milliseconds)

excited (see e.g. Fig. 16.8a); however, one mode was found below 1600 Hz that was nonlinear with significant frequency shifts. Figure 16.8b shows this mode, which was the third mode extracted in the Modal Test 1, Modal Test 3, Modal Test 4, and Modal Test 5 data sets. The Modal Test 2 dataset did not have this mode extracted. Figure 16.9 shows the expanded mode 3 shape overlaid with the test geometry for all datasets where it was extracted. Significant deformation is seen in the shape in the removable component, especially near the joints which are the likely cause for the nonlinearity.

16.5 Discussion

There is good agreement between the tests as to the number of modes in the bandwidth; however, different measurement techniques produced different values for the natural frequencies and damping ratios. Modal Test 3 and Modal Test 4 tended to have lower natural frequencies for a given mode than Modal Test 1 or Modal Test 2, with Modal Test 5 typically in the middle. Due to the relatively low mass and stiffness of the structure, the application of different instrumentation sets and boundary conditions can have a significant effect on the extracted modal parameters. Modes in the Modal Test 4 dataset show spreads

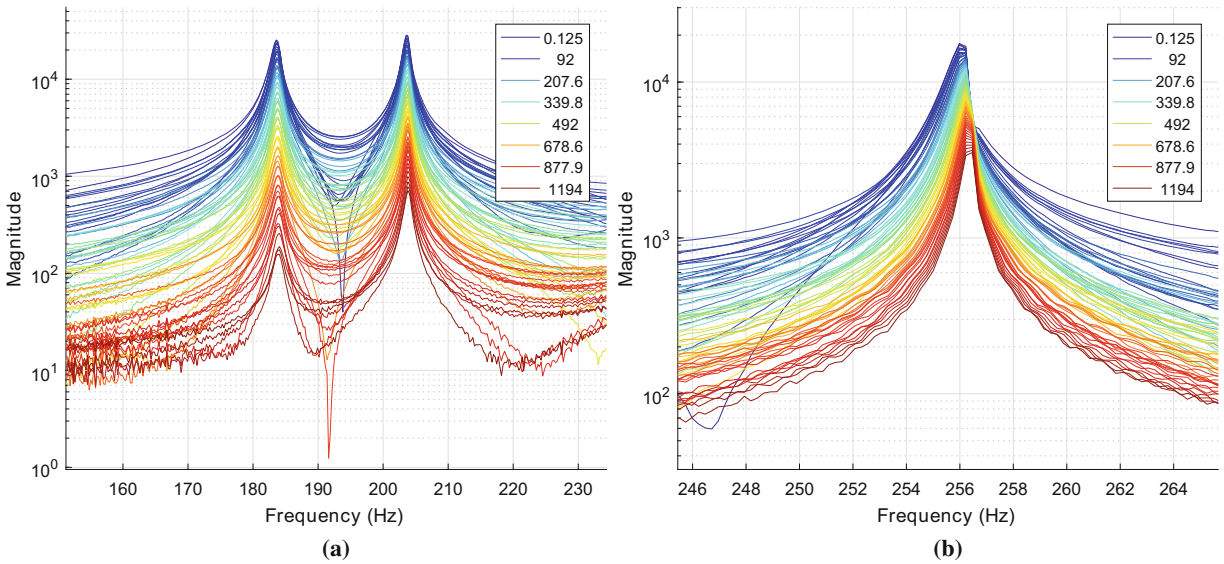

Fig. 16.8 Zoom of modes of the ZEFFT. **(a)** Zoom of the ZEFFT results showing the first two modes; the majority of modes appeared linear to the levels tested. **(b)** Zoom of the ZEFFT results showing the third mode; this mode was the most nonlinear mode seen in the ZEFFT, with significant frequency shifting at high levels

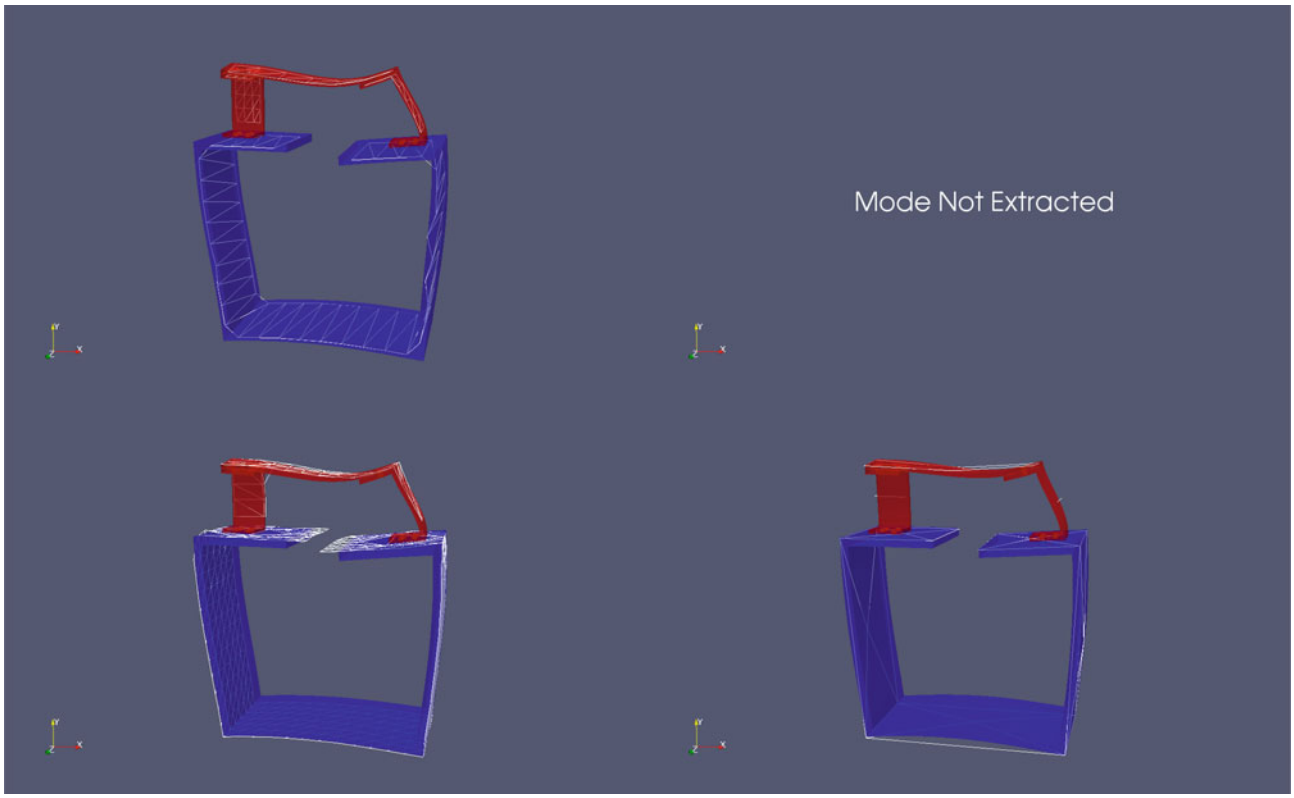

Fig. 16.9 Mode identified as the most nonlinear by the ZEFFT analysis. Significant deformation in the removable component near the joints can be seen in this shape

of up to 5% in natural frequency for some modes due to the varying locations of only four accelerometers. The Modal Test 1 dataset, which used a scanning laser vibrometer and impact hammer excitation, meaning it had no instrumentation adhered to the surface, typically had the highest natural frequencies (likely due to minimal mass loading); however, the damping ratios are also higher than the other datasets likely due to the relatively stiff boundary conditions (foam) required to eliminate large rigid body motion of the part due to the impact, which would preclude a good laser vibrometer measurement. Due to the sensitivity of the part to the test conditions, it is difficult to distinguish between unit-to-unit variability and variability due to the test setup, especially with only five datasets to compare.

16.6 Summary

This paper presented a comparison between the results of five modal tests on the BARC hardware, and a rudimentary nonlinear analysis of one time history. It was difficult to draw any conclusions about the unit-to-unit variability of the BARC structure due to differences in the test setups and the sensitivity of the BARC structure to mass loading due to instrumentation or test boundary conditions. The finite element expansion worked reasonably well as a vehicle for comparing modal tests with different instrumentation sets, though trouble was had where the instrumentation set was not sufficient to prevent overfitting using higher order modes. The reduced instrumentation set was sufficient to map modes between the tests, so the modal parameters could be compared between modes. Even if shapes could not be compared, the natural frequencies were consistent enough to be able to map similar modes between tests.

Acknowledgements The authors would like to acknowledge Atomic Weapons Establishment (AWE) for contributing a dataset to this work in addition to those provided by the coauthors listed above.

References

1. Soine, D.E., Jones, Jr. R.J., Harvie, J.M., Skousen, T.J., Schoenherr, T.F.: Designing hardware for the boundary condition round robin challenge. In: Mains, M., Dilworth, B. (eds.) Topics in Modal Analysis & Testing. Conference Proceedings of the Society for Experimental Mechanics Series, vol. 9, pp. 119–126. Springer, Cham (2019)
2. Witt, B.L., Rohe, D.P., Schoenherr, T.F.: Full field strain shape estimations from 3D SLDV. In: Proceedings of the 37th International Modal Analysis Conference, Orlando, FL, January (2019)
3. Rohe, D.P., Schultz, R.A., Schoenherr, T.F., Skousen, T.J.: Comparison of multi-axis testing of the barc structure with varying boundary conditions. In: Proceedings of the 37th International Modal Analysis Conference, Orlando, FL, January (2019)
4. DeClerck, J., Blough, J., Larsen, W., VanKarsen, C., Soine, D., Jones, R.: Sensitivity study of BARC assembly. In: Proceedings of the 37th International Modal Analysis Conference, Orlando, FL, January (2019)
5. O'Callahan, J.C., Avitable, P., Riemer, R.: System equivalent reduction expansion process. In: Proceedings of the Seventh International Modal Analysis Conference, Las Vegas, NV, Febraury (1989)
6. Allen, M.S., Mayes, R.L.: Estimating the degree of nonlinearity in transient responses with zeroed early-time fast fourier transforms. Mech. Syst. Signal Process. **24**(7), 2049–2064 (2010)

Chapter 17
Comparison of Multi-Axis Testing of the BARC Structure with Varying Boundary Conditions

Daniel P. Rohe, Ryan A. Schultz, Tyler F. Schoenherr, Troy J. Skousen, and Richard J. Jones

Abstract The Box Assembly with Removable Component (BARC) structure was developed as a challenge problem for those investigating boundary conditions and their effect on structural dynamic tests. To investigate the effects of boundary conditions on the dynamic response of the Removable Component, it was tested in three configurations, each with a different fixture and thus a different boundary condition. A "truth" configuration test with the component attached to its next-level assembly (the Box) was first performed to provide data that multi-axis tests of the component would aim to replicate. The following two tests aimed to reproduce the component responses of the first test through multi-axis testing. The first of these tests is a more "traditional" vibration test with the removable component attached to a "rigid" plate fixture. A second set of these tests replaces the fixture plate with flexible fixtures designed using topology optimization and created using additive manufacturing. These two test approaches are compared back to the truth test to determine how much improvement can be obtained in a laboratory test by using a fixture that is more representative of the compliance of the component's assembly.

Keywords BARC · MIMO · Boundary conditions · Multi-axis · Expansion

17.1 Introduction

For a typical vibration test, the component of interest is attached to the shaker used to excite the structure via some kind of fixture. The traditional approach is to make such a fixture as rigid as possible to ensure the dynamics of the component under test are not influenced by the dynamics of the fixture; however, such a fixture often provides incorrect boundary conditions to the part. The testing community has recognized the shortcomings of such an approach, and a boundary condition challenge problem has been developed to provide a collaborative environment in which alternative approaches can be investigated [1].

In this work, the Box Assembly with Removable Component (BARC) structure from the boundary condition challenge problem was excited in a multi-axial "truth" or "environment" test, providing data to which a "laboratory" test could attempt to replicate. A three degree-of-freedom (DoF) shaker was constructed from modal shakers and a vibration cube fixture to perform the trial vibration tests. Four fixtures were investigated, one of which being a traditional "rigid" plate fixture. The goal of this work was to determine if specially designed fixtures could more closely replicate the dynamics of the component in its original assembled configuration compared to traditional rigid fixtures.

Sandia National Laboratories is a multimission laboratory managed and operated by National Technology & Engineering Solutions of Sandia, LLC, a wholly owned subsidiary of Honeywell International Inc., for the U.S. Department of Energy's National Nuclear Security Administration under contract DE-NA0003525.
The Department of Energy's Kansas City National Security Campus is operated and managed by Honeywell Federal Manufacturing & Technologies, LLC under contract number DE-NA0002839.
This paper describes objective technical results and analysis. Any subjective views or opinions that might be expressed in the paper do not necessarily represent the views of the U.S. Department of Energy or the United States Government.

D. P. Rohe (✉) · R. A. Schultz · T. F. Schoenherr · T. J. Skousen
Sandia National Laboratories, Albuquerque, NM, USA
e-mail: dprohe@sandia.gov

R. J. Jones
Kansas City National Security Campus, Kansas City, MO, USA

C. Walber et al. (eds.), *Sensors and Instrumentation, Aircraft/Aerospace, Energy Harvesting & Dynamic Environments Testing, Volume 7*, Conference Proceedings of the Society for Experimental Mechanics Series,
https://doi.org/10.1007/978-3-030-12676-6_17

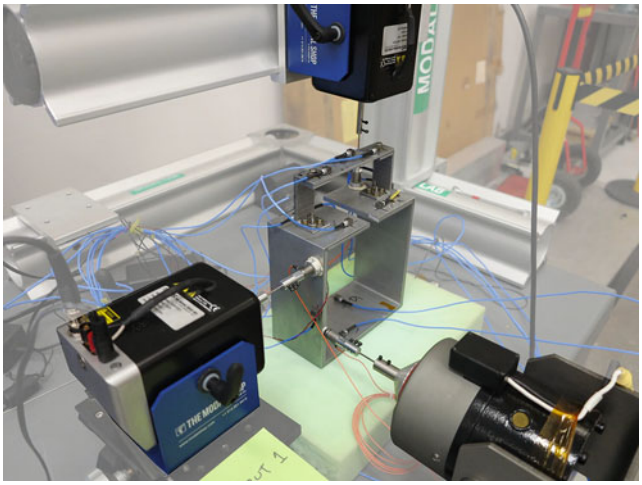

Fig. 17.1 The BARC structure shown in the "truth" test configuration

17.2 Hardware Description

The BARC is a relatively simple structure composed of a "component", consisting of the assembly of two C-channels connected by a beam, and a "system", consisting of a cut box-beam, on which the component rides. Figure 17.1 shows the BARC structure in the truth test configuration. The BARC structure has been characterized by a number of groups from academia and industry [2], and well-correlated finite element models exist for the structure.

For all tests described in this report, the BARC structure was instrumented with 9 triaxial accelerometers on the removable component portion. For the truth test, several locations on the box-beam were also instrumented to aid in distinguishing modes of the system.

For the laboratory tests described in this paper, the BARC was mounted to the vibration cube via a number of fixtures. The first fixture examined in this work is a plate fixture, shown in Fig. 17.2a with the removable component attached. This represents the traditional fixture design where the component would be attached to a fixture that was as rigid as possible.

Subsequent fixtures were designed using topology optimization. The fixtures were designed with the assumption of a fixed-based input. The truth data was generated by applying a fixed boundary condition to the bottom of the BARC and gravity loads in the coordinate directions. The displacement at the Box and Bench interface for the various loads conditions was used to estimate the stiffness of the structure. The estimated stiffness was then used as target objectives in the topology optimization. The two leg fixture had three DoF (X,Y,Z) static objectives with the Y direction weighted a factor of 2. The three leg fixture had three degree of freedom (X,Y,Z) static objectives. Design 12 had 6 degree of freedom (X,Y,Z,RX,RY,RZ) static objectives. Modal analysis of these fixtures can be found in [3].

17.3 Testing Strategy

For all tests performed in this work, B+K Lan-XI data acquisition systems were used to drive the shakers and record the responses to those excitations. The arbitrary source capabilities of the Lan-XI hardware was used to play signals that were generated off-line, so no closed loop control was performed. Cross-power spectral density (CPSD) matrices for the control were either specified (e.g. for the truth test described in Sect. 17.3.1) or derived from the control equation described in Sect. 17.3.2

To generate time histories from the target CPSD matrix, the matrix is first converted to a linear spectrum magnitude matrix with a matrix square root. Then, realizations of the linear spectrum are obtained by multiplying the linear spectrum magnitudes by a random process (i.e. a random phase). This results in complex linear spectra for each signal which maintain the correlation relationship from the CPSD matrix. Next, those linear spectra can be turned into time signals with an inverse Fourier transform. Typically, frequency resolution in the spectrum would result in a short time signal. To generate long time histories, multiple realizations are used to generate many signal segments which are then combined into a composite, long duration signal using an overlap and add process [4, 5].

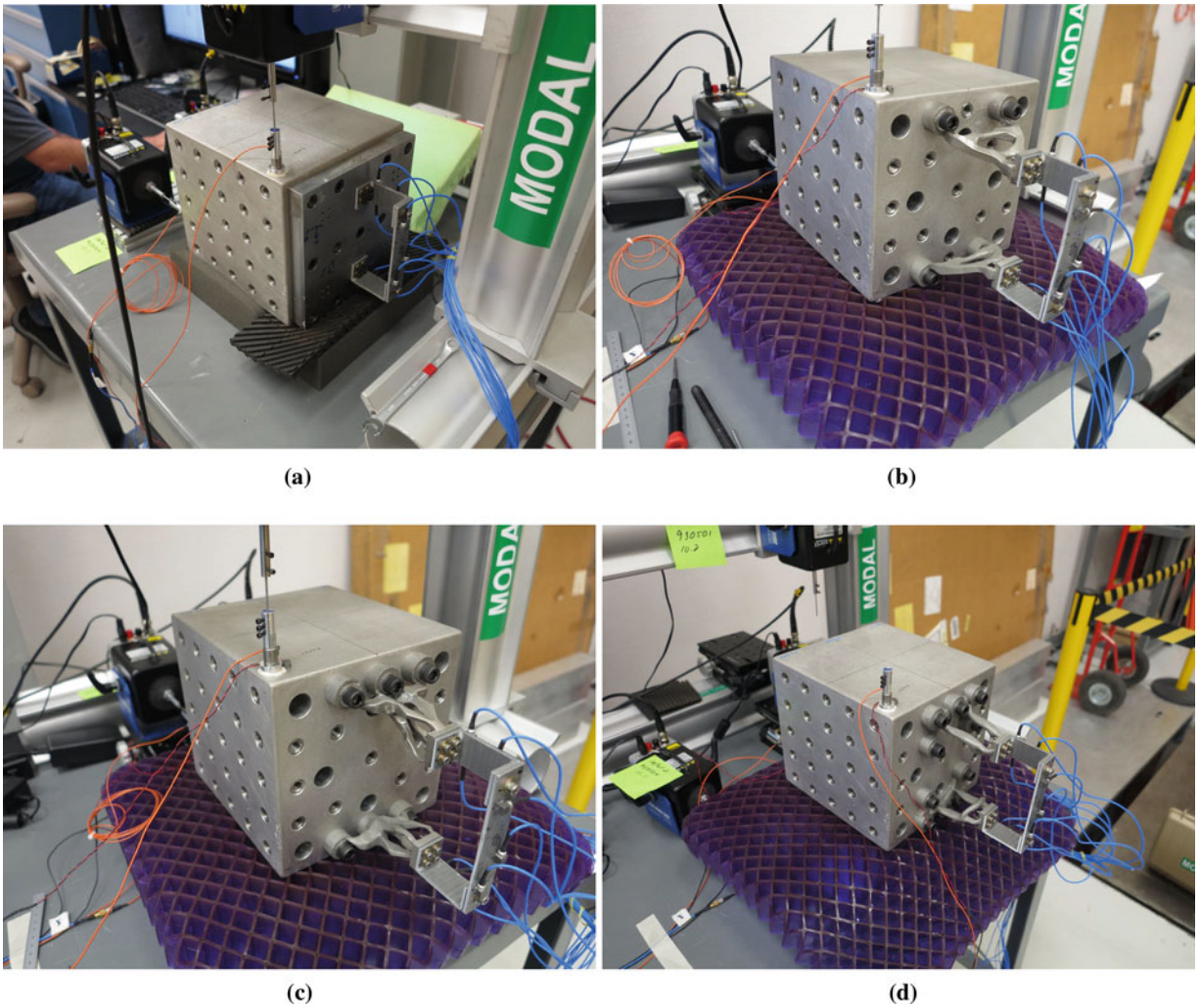

Fig. 17.2 Fixtures examined for this test series. (**a**) Removable component attached to the vibration cube using a traditional plate structure. (**b**) 2-leg Fixture. (**c**) 3-leg Fixture. (**d**) Design 12

17.3.1 Truth Test

The first step in understanding the fixture effects during a laboratory test was to generate environment data that the laboratory tests could attempt to match. In order to better represent a real field environment, was desirable to create a multi-axis environment, so three shakers were attached to the structure in the three principal directions (see Fig. 17.1). Three uncorrelated voltage inputs, shown in Fig. 17.3, were developed to be played into the shakers. The truth test resulted in acceleration on the removable component between 2 and 14 G root-mean-square (RMS).

17.3.2 Control Strategy

Control for the laboratory tests was performed in an open loop sense using the arbitrary source capabilities of the Lan-XI data acquisition systems. For each configuration, an initial white noise (buzz) test was performed to develop transfer functions between the shaker amplifier input voltages and the response channels on the component. Once transfer functions are derived, the input CPSD matrix can be calculated using the standard pseudo-inverse computations

$$\mathbf{G}_{\ddot{x}\ddot{x}} = \mathbf{H}_{\ddot{x}v}\mathbf{G}_{vv}\mathbf{H}^{*}_{\ddot{x}v} \tag{17.1}$$

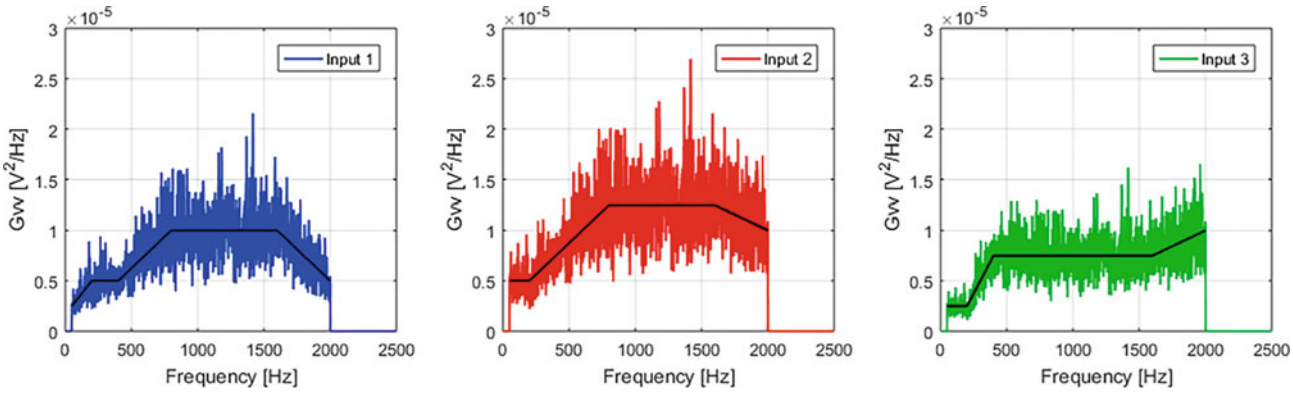

Fig. 17.3 Voltage PSDs played into the shaker. The black curve is the target PSD and the colored curves are one realization of the PSD

$$\tilde{\mathbf{G}}_{vv} = \mathbf{H}^{+}_{\ddot{x}v}\mathbf{G}_{\ddot{x}\ddot{x}}(\mathbf{H}^{*}_{\ddot{x}v})^{+} \tag{17.2}$$

where $\mathbf{G}_{\ddot{x}\ddot{x}}$ is the desired acceleration CPSD matrix, $\mathbf{H}_{\ddot{x}v}$ is the transfer function matrix between the voltage inputs and acceleration outputs, and $\mathbf{G}_{vv}$ is the input voltage CPSD matrix with the tilde ($\tilde{}$) representing an estimated quantity. The * superscript denotes the matrix conjugate transpose operation.

The computation is performed for all 1951 frequency lines between 50 and 2000 Hz, inclusive. Time histories are then computed from the voltage CPSD matrix $\tilde{\mathbf{G}}_{vv}$ and played to the shaker amplifiers using the arbitrary source capabilities of the Lan-XI data acquisition system.

To evaluate a given test, it was desirable to be able to reduce the results down to a single figure or metric; this way tests can be easily compared against one another. The metric of choice for this test was RMS decibel (dB) error in the autospectral density (ASD) functions (real-valued diagonals of the CPSD matrix).

$$e_{\mathrm{ASD}}(f_j) = \sqrt{\frac{1}{n_{gauge}}\sum_{i=1}^{n_{gauge}}\left(\mathrm{dB}\left(G^{t}_{\ddot{x}\ddot{x}(i,i)}\left(f_j\right)\right) - \mathrm{dB}\left(G^{e}_{\ddot{x}\ddot{x}(i,i)}\left(f_j\right)\right)\right)^2} \tag{17.3}$$

where $G^{t}_{\ddot{x}\ddot{x}(i,i)}\left(f_j\right)$ and $G^{e}_{\ddot{x}\ddot{x}(i,i)}\left(f_j\right)$ denote the jth frequency line of the autospectrum of the ith control channel for the test and environment data, respectively, and n_{gauge} is the number of control channels. This can be rolled up into a single value by computing the RMS over all frequency lines, where n_{freq} is the total number of frequency lines.

$$e_{\mathrm{ASD}} = \sqrt{\frac{1}{n_{freq}}\sum_{j=1}^{n_{freq}} e_{\mathrm{ASD}}(f_j)^2} \tag{17.4}$$

A second metric that has also been used historically is a "sum of ASD" metric, e.g. in [6].

$$e_{\Sigma\mathrm{ASD}}(f_j) = \mathrm{dB}\left(\sum_{i=1}^{n_{gauge}}\left(G^{t}_{\ddot{x}\ddot{x}(i,i)}\left(f_j\right)\right)\right) - \mathrm{dB}\left(\sum_{i=1}^{n_{gauge}}\left(G^{e}_{\ddot{x}\ddot{x}(i,i)}\left(f_j\right)\right)\right) \tag{17.5}$$

This can also be reduced to a single value by taking the RMS value of $e_{\Sigma\mathrm{ASD}}(f_j)$ over all frequency lines:

$$e_{\Sigma\mathrm{ASD}} = \sqrt{\frac{1}{n_{freq}}\sum_{j=1}^{n_{freq}} e_{\Sigma\mathrm{ASD}}(f_j)^2} \tag{17.6}$$

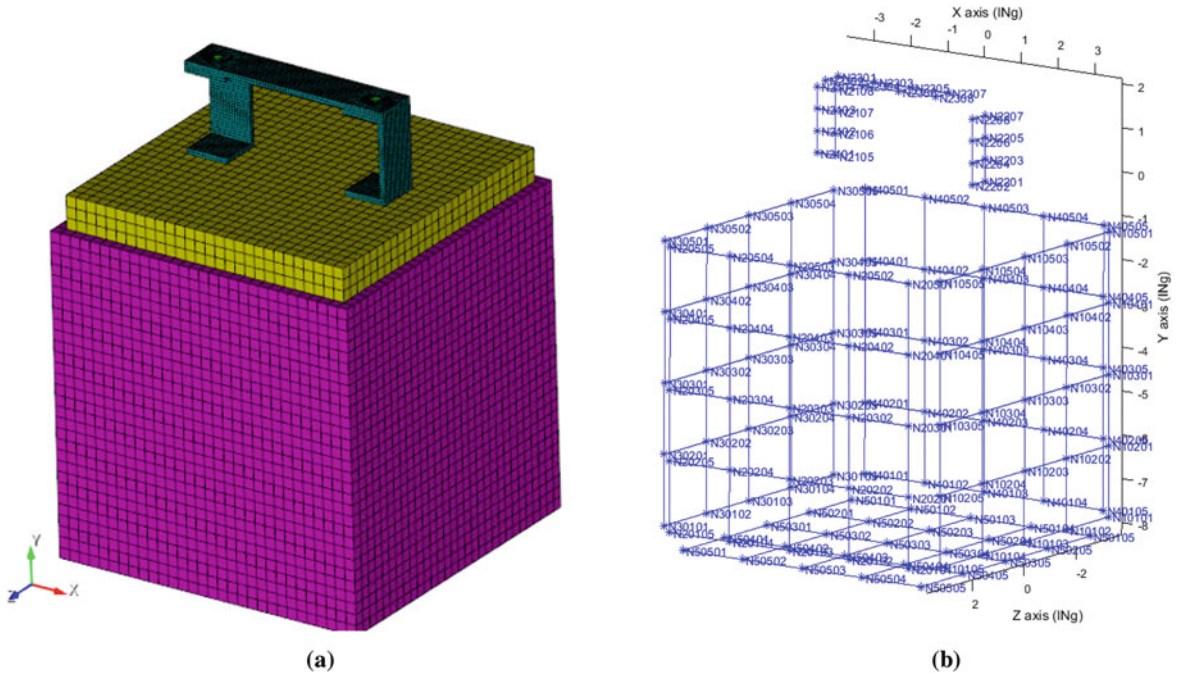

Fig. 17.4 Shaker placement analysis. (**a**) Finite Element Model used to develop transfer functions between force and acceleration response. (**b**) Candidate shaker placement locations in a 5 × 5 grid on each face of the cube

17.3.3 Shaker Placement

The laboratory tests, it was decided to directly force the vibration cube, to which the removable component was attached via a fixture, using three shakers. To determine where on the vibration cube the shakers should be placed, analysis was performed using a finite element model of the removable component mounted to the plate fixture, shown in Fig. 17.4a. The finite element model could be used to create transfer functions between force inputs on the cube and responses at the instrumentation locations in the truth test.

To make a brute-force computation of the control problem for all combinations of three shaker input locations on the cube tractable, the candidate shaker set was reduced to a 5 × 5 grid on each face of the cube, shown in Fig. 17.4b. To further reduce the problem, the cube was assumed rigid, so only input locations on three of the faces were considered. This reduced the 317,750 potential shaker combinations down to 67,525. Even for this reduced number, solving the control problem at all 1951 frequency lines would take a large amount of time, so the control problem was instead only solved at 88 frequency lines in unique parts of the spectrum (peaks, valleys, etc.).

With each solution of the control problem, the ability of the shakers to match the truth test responses could be evaluated. In addition, the estimated amount of force required to achieve that control could also be estimated. Since both are key factors for a successful test, the shaker setup that minimized both the force required and the RMS dB error was devised.

Results from all of the control simulations were ranked from 1 (best) to 67,525 (worst) for both dB error on the control gauges (Fig. 17.5a) and RMS force required (Fig. 17.5b), noting that the best set for dB error was not the best set for the smallest force. Summing the two rankings gave a new metric that considered both force and control error. Shaker configurations were then re-ranked by this new metric (Fig. 17.5c).

The shaker set that was selected consisted of two shakers on the face opposite the removable component and one shaker on a face perpendicular to the removable component, as shown in Fig. 17.6. This configuration was used for all fixtures tested on the vibration cube.

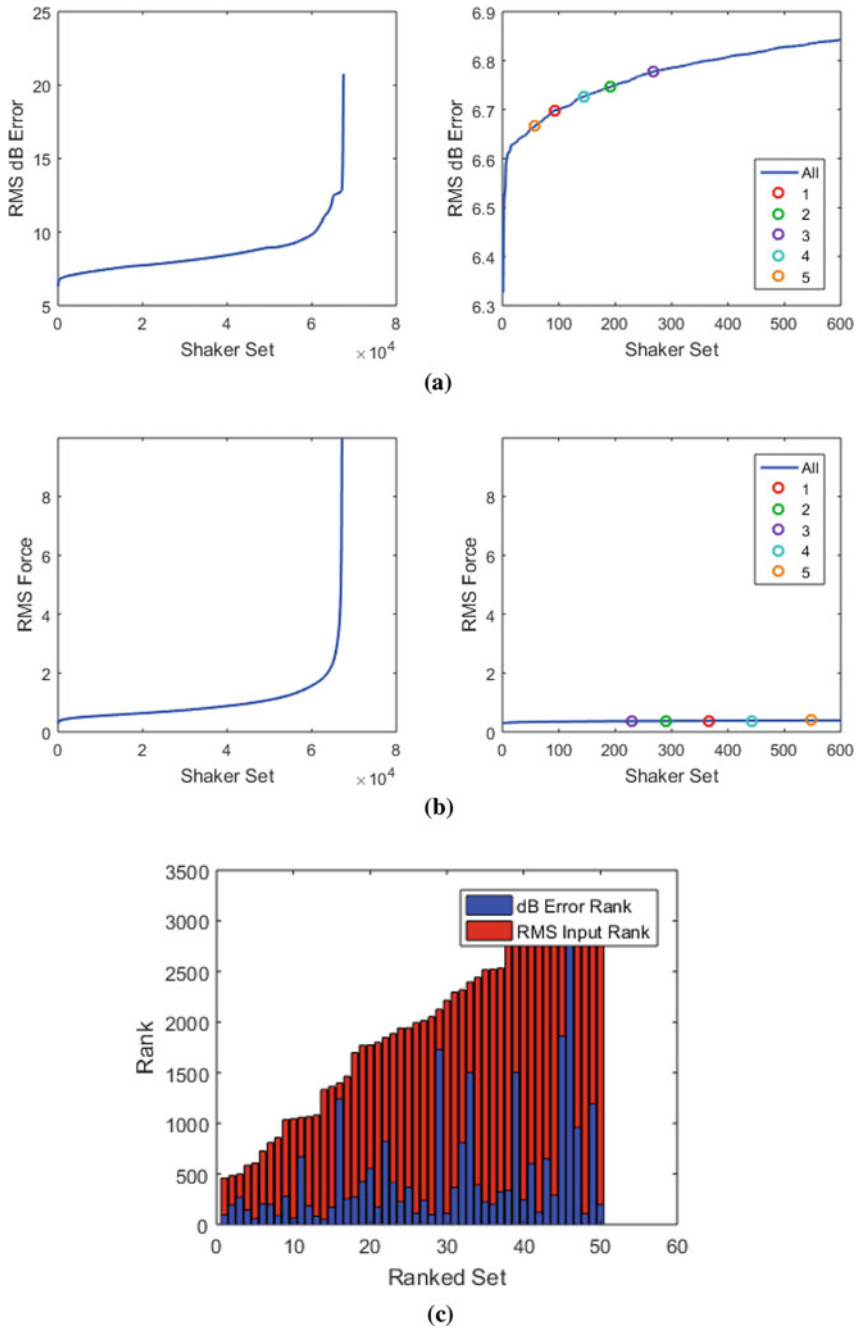

Fig. 17.5 Shaker configuration selection metrics, with the top five shaker configurations from the summed-ranking metric shown. (**a**) Ranking of dB error, all configurations (left) and zoomed in on the best configurations (right). (**b**) Ranking of RMS force required, all configurations (left) and zoomed in on the best configurations (right). (**c**) Stacked bar plot showing the top 50 shaker configurations sorted by sum of force and error rankings

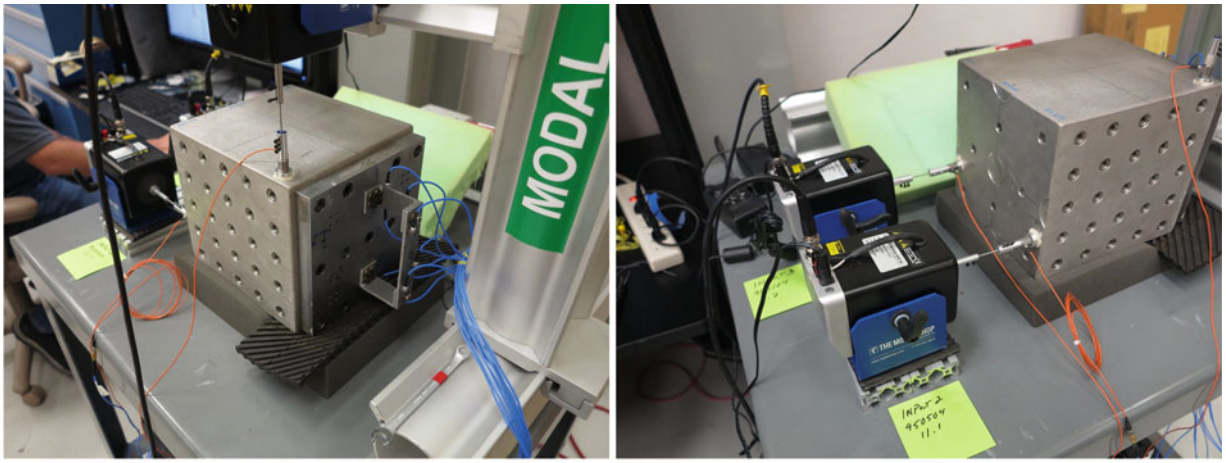

(a) (b)

Fig. 17.6 Shaker setup for tests using the vibration cube. (**a**) One shaker mounted on the face orthogonal to the removable component. (**b**) Two shakers mounted on the face opposite the removable component

17.4 Test Results

The control problem was run for five cases. The first case was a replica of the truth test, which was used as a benchmark to compare all the other tests against. The test was set up identically to the truth test, except rather than specifying the voltage inputs like was done in the truth test, the voltage inputs were instead derived using the desired responses and the control Eq. (17.2). This would represent the "best-case" impedance-matched multi-axis testing scenario: performing a test that captures all of the forces in the actual environment, with the component attached to identical boundary conditions. The other cases consist of the removable component mounted to the fixtures shown in Fig. 17.2.

Note that due to the large mass of the vibration cube compared to BARC, the shakers could not achieve the required levels to match the environment, and larger shakers could not be used due to the limited space on the vibration cube; instead the targets were scaled down by a factor of 20 for the plate fixture and 10 for the additively manufactured fixtures, which assumes the structure is linear. The results have been rescaled up to full levels for all comparisons made in this paper.

Figure 17.7 shows the acceleration ASDs for each of the control gauges on the removable component as well as the two error metrics described in Sect. 17.3.2. Figure 17.8 shows the forces required to achieve that control.

Looking at the error metrics in Fig. 17.7, large errors can be seen in "peaks" in specific frequency ranges. These peaks correspond to modes of the test article mounted to the fixture that cannot be controlled out by the test. Figure 17.9 shows that large errors in the plate test for each of the two metrics correspond directly to modes of the test article mounted to the fixture.

17.5 Computing Strain in the Component

While acceleration CPSD matrices have been historically compared to judge whether or not a test is sufficiently accurate in reproducing an environment, strain may be a more appropriate measure due to its more direct link to failure in materials. One issue with strain is the difficulty in measuring it dynamically. Strain gauges are a relatively mature technology, but they are limited to surface measurements and will tend to average strain over the area of a gauge. They may also be difficult to get into locations with strain concentrations. Digital Image Correlation and 3D Scanning Laser Doppler Vibrometry have also shown strain measurement capabilities [7], but it may be difficult to field either of these techniques on an environment test.

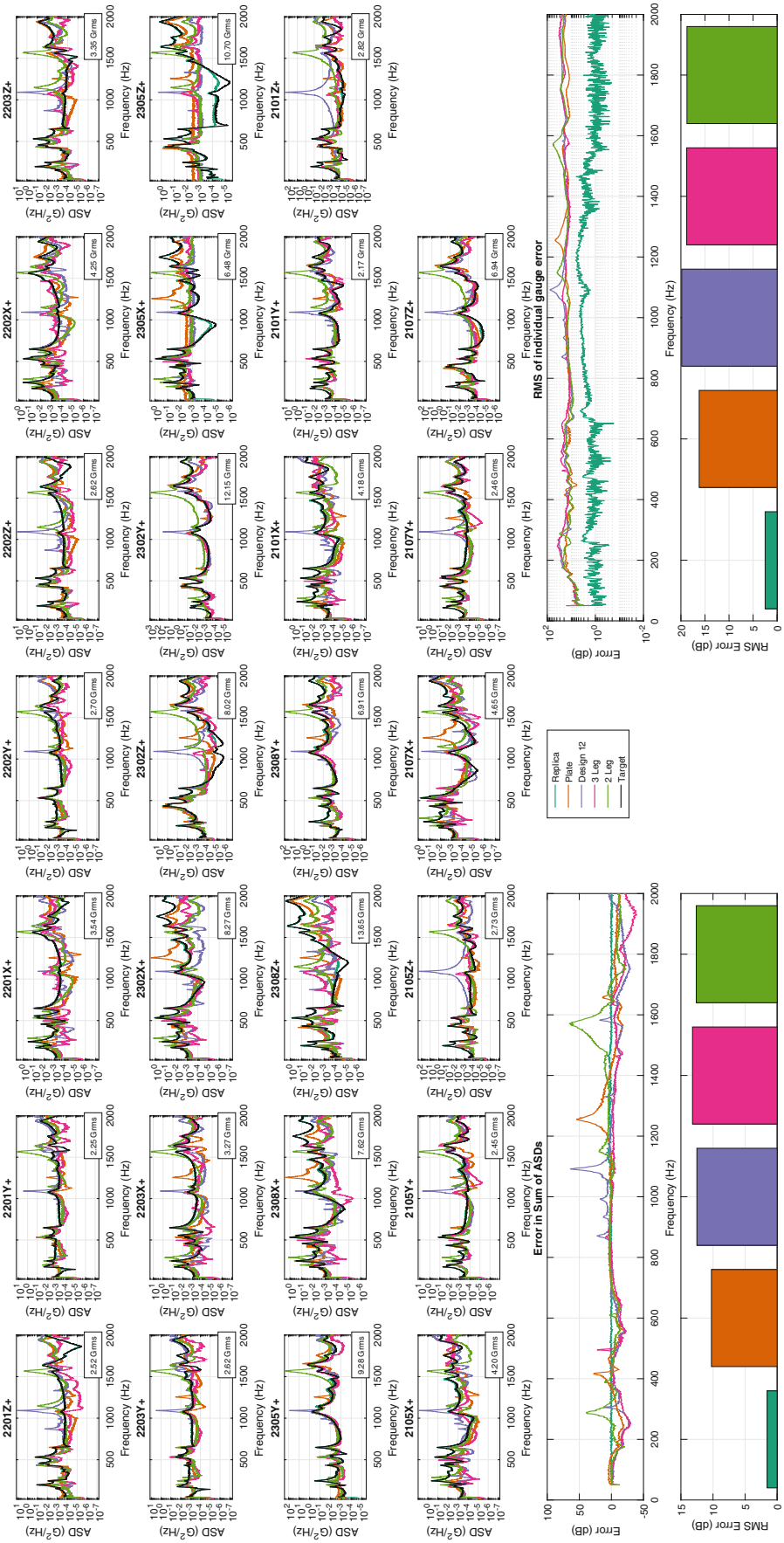

Fig. 17.7 Comparison of control for various fixtures. The top four rows of plots show the autospectral density functions for each control gauge and how well the individual control gauges matched. The plots in the fifth row show the dB error in the sum of the autospectral density functions ($e_{\Sigma \mathrm{ASD}}$ from Eq. (17.5)) and the dB error in the autospectral density (e_{ASD} from Eq. (17.3)) at each frequency line. The bottom two plot RMS of the same error metrics over all frequency lines

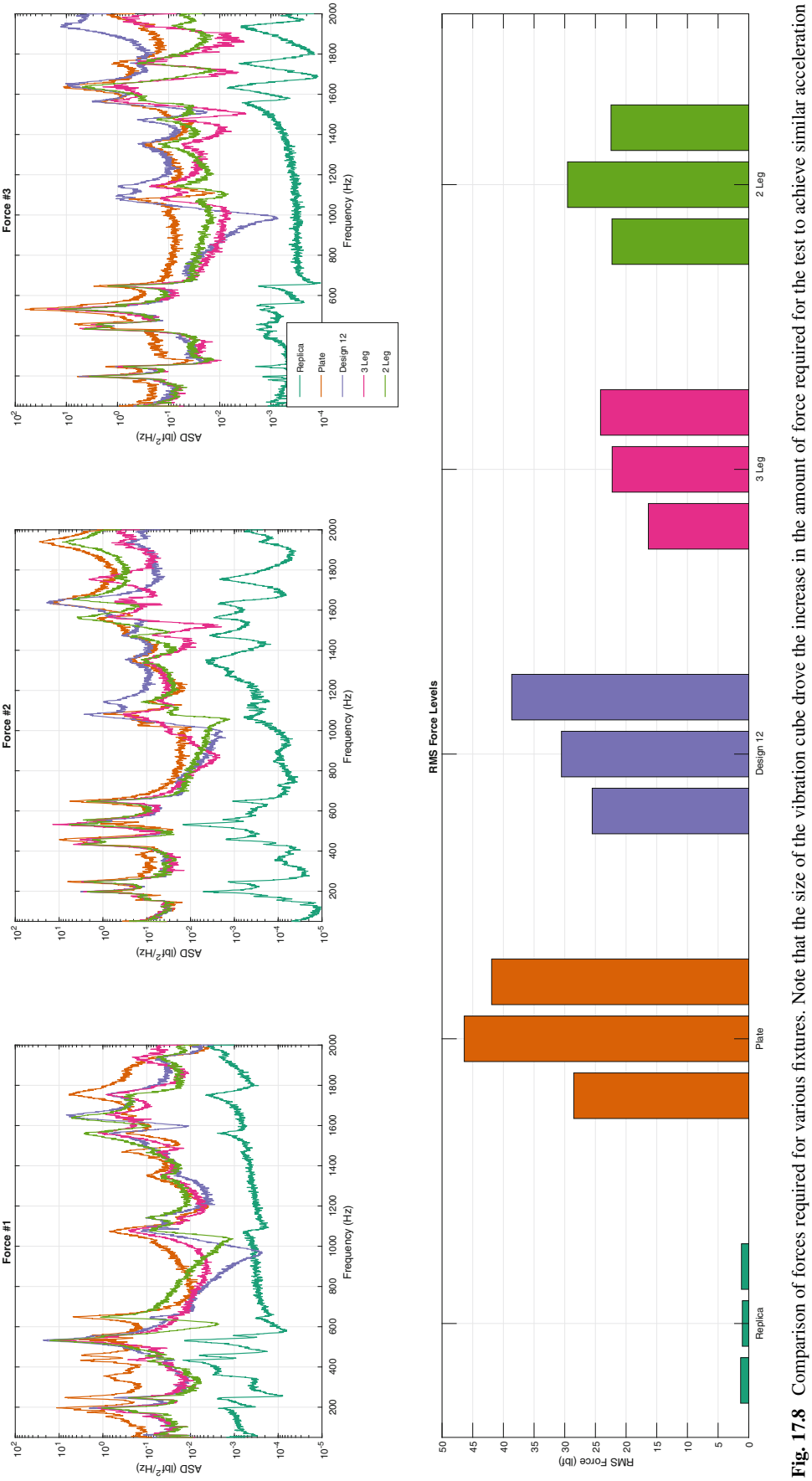

Fig. 17.8 Comparison of forces required for various fixtures. Note that the size of the vibration cube drove the increase in the amount of force required for the test to achieve similar acceleration levels

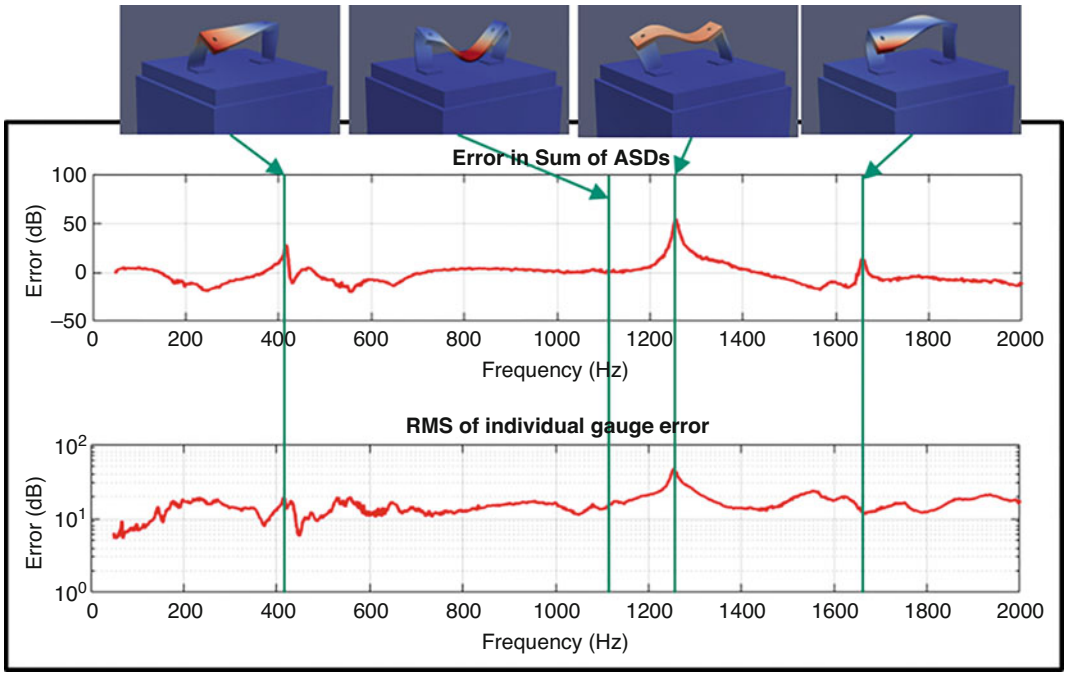

Fig. 17.9 Plate test errors and corresponding mode shapes and natural frequencies

17.5.1 SEREP Expansion

An alternative method to directly measuring strain is to compute it using finite element model expansion. Recent work [8, 9] has shown the capability to expand modal or operating data to a full finite element space, allowing the extraction of strain if that information exists in the finite element model. The System Equivalent Reduction-Expansion Process (SEREP) [10] is used to expand the measured accelerations to finite element space:

$$\begin{bmatrix} \mathbf{X}_{fem} \\ \boldsymbol{\varepsilon}_{fem} \end{bmatrix} = \begin{bmatrix} \Phi_{fem} \\ \mathbf{E}_{fem} \end{bmatrix} \Phi_{exp}^{+} \mathbf{X}_{exp} \tag{17.7}$$

where $\mathbf{X}$ represents the displacement in the experiment, $\boldsymbol{\varepsilon}$ represents the strain in the experiment, and Φ and $\mathbf{E}$ represent the displacement and strain mode shapes in the finite element model, respectively. The subscripts fem and exp denote the degree of freedom set corresponding to those in the finite element model and those in the experiment, respectively. Equation (17.7) shows that the displacements and the strains at all of the finite element model degrees of freedom can be recovered from the experimental data.

For a CPSD matrix $\mathbf{G}_{xx,exp} = \mathbf{X}_{exp}\mathbf{X}_{exp}^{*}$, we can expand to the full finite element space $\mathbf{G}_{xx,fem} = \mathbf{X}_{fem}\mathbf{X}_{fem}^{*}$ by simply substituting the upper partition of Eq. (17.7):

$$\mathbf{G}_{xx,fem} = \Phi_{fem}\Phi_{exp}^{+}\mathbf{G}_{xx,exp}(\Phi_{exp}^{+})^{*}\Phi_{fem}^{*} \tag{17.8}$$

The measured quantities, however, are not displacements $\mathbf{X}_{exp}$ but are instead accelerations $\ddot{\mathbf{X}}_{exp}$. The two can be related via frequency domain integration at each frequency line, $\mathbf{X}_{exp}(\omega) = \ddot{\mathbf{X}}_{exp}(\omega)/-\omega^2$, so the final expansions equation relating measured acceleration CPSD matrices to full finite element displacement and strain CPSD matrices are

$$\mathbf{G}_{xx,fem}(\omega) = \Phi_{fem}\Phi_{exp}^{+}\frac{\mathbf{G}_{\ddot{x}\ddot{x},exp}(\omega)}{\omega^4}(\Phi_{exp}^{+})^{*}\Phi_{fem}^{*} \tag{17.9}$$

$$\mathbf{G}_{\varepsilon\varepsilon,fem}(\omega) = \mathbf{E}_{fem}\Phi_{exp}^{+}\frac{\mathbf{G}_{\ddot{x}\ddot{x},exp}(\omega)}{\omega^4}(\Phi_{exp}^{+})^{*}\mathbf{E}_{fem}^{*} \tag{17.10}$$

For the SEREP expansion of the CPSD matrix, the resulting matrix is a complex $n_{fem} \times n_{fem}$ matrix, where n_{fem} is the number of finite element degrees of freedom. Even for a relatively small model such as BARC, the approximately $90,000 \times 90,000$ entry complex matrix will take up approximately 140 GB of memory and therefore cannot be processed in-core. Since in the end we will only be looking at the ASDs, we can examine the linear algebra to reduce the size of the problem to only the diagonal entries.

Starting with Eq. (17.9), we can make the substitutions $\mathbf{A} = \Phi_{fem}$, $\mathbf{Q} = \Phi^{+}_{exp} \frac{\mathbf{G}_{\ddot{x}\ddot{x},exp}(\omega)}{\omega^4} (\Phi^{+}_{exp})^*$, and $\mathbf{B} = \mathbf{G}_{xx,fem}(\omega)$ (Note that $\Phi^*_{fem} = \mathbf{A}^T$ due to Φ_{fem} being a real-valued matrix.)

$$\mathbf{B} = \mathbf{A}\mathbf{Q}\mathbf{A}^T \tag{17.11}$$

Converting to summation notation where n_{modes} is the number of modes used in the SEREP expansion, and focusing on diagonal values of $\mathbf{B}$ the equation

$$B_{ii} = \sum_{l=1}^{n_{modes}} \left(\sum_{k=1}^{n_{modes}} A_{ik} Q_{kl} \right) A_{il} \tag{17.12}$$

is obtained, which can be expressed in efficient, vectorized MATLAB code as `sum((A*Q).*A,2)`, where no matrix bigger than $n_{fem} \times n_{modes}$ is ever needed. Since $n_{fem} \gg n_{modes}$, this is a large savings in memory. A similar strategy was used for the strain shapes, setting $\mathbf{A} = \mathbf{E}_{fem}$ instead of $\mathbf{A} = \Phi_{fem}$.

17.5.2 Selecting the Proper Expansion Shape Set

Previous experience using SEREP has revealed that the set of modes Φ used in the expansion can have a significant impact on the results. If too few modes are used, real portions of the response can be filtered out. However, if too many modes are used, the expansion can also be erroneous and portions of the model away from the points being fit can behave unrealistically. To investigate the proper basis for the SEREP expansion, the expansion was first performed on the modes of the test articles within the bandwidth of interest. This was done because mode shapes tend to have intuitive, smooth shapes, so it is more obvious when overfitting is occurring. Additionally, the modes in the bandwidth should form a relatively good basis for the responses in the multi-input multi-output (MIMO) controlled test, so a good set of FEM modes to expand the experimental modes in the bandwidth of interest should also form a good basis for expanding the results of the MIMO controlled test.

To fit modes to the data, the voltage-acceleration transfer functions measured during the buzz tests needed to be recomputed as force-acceleration transfer functions expected by curve fitting software. Modes were then fit to the data using the Synthesize Modes and Correlate [11] algorithm. A modal assurance criterion (MAC) matrix was formed between the experimental shapes and the FEM mode shapes reduced to the experimental degrees of freedom to determine which modes were important in the expansion. To validate the expansion, the experimental shapes were overlaid with the expanded shapes to ensure the expansion was not distorting the results, and a few of these are shown in Fig. 17.10. Note that there was no finite element model for the 2-leg or 3-leg fixture designs, so the Design 12 finite element shapes were used for a basis to expand the 2-leg and 3-leg experimental data.

Minor over-fitting was found to be occurring in the box of the Truth structure and the fixtures and vibration cube in the 2-leg, 3-leg, and Design 12 fixture models; this was due to the fact that there was insufficient instrumentation located on the box and fixtures. However, this was not thought to be an issue due to the fact that the removable component portion of each model seemed to be accurately described by the expansion, so strains in the removable component should be reasonably accurate as well.

17.5.3 Strain Comparisons

Using the mode sets that provided the best expansions for the mode shapes, strains were computed for the diagonal values in the CPSD matrix for each strain component (ε_{xx}, ε_{yy}, ε_{xy}, etc.) using the vectorized (Eq. (17.12)) form of Eqs. (17.9) and (17.10). The RMS values of each strain component were computed from these diagonal entries and plotted on the finite element model of the removable component to identify "hot spots" where strain would be largest. Figures 17.11 and 17.12 show such locations for two strain components. The CPSD functions could then be investigated at each of these locations to provide more information, with Fig. 17.13 showing an example. It is clear that strain is overestimated for all fixtured tests,

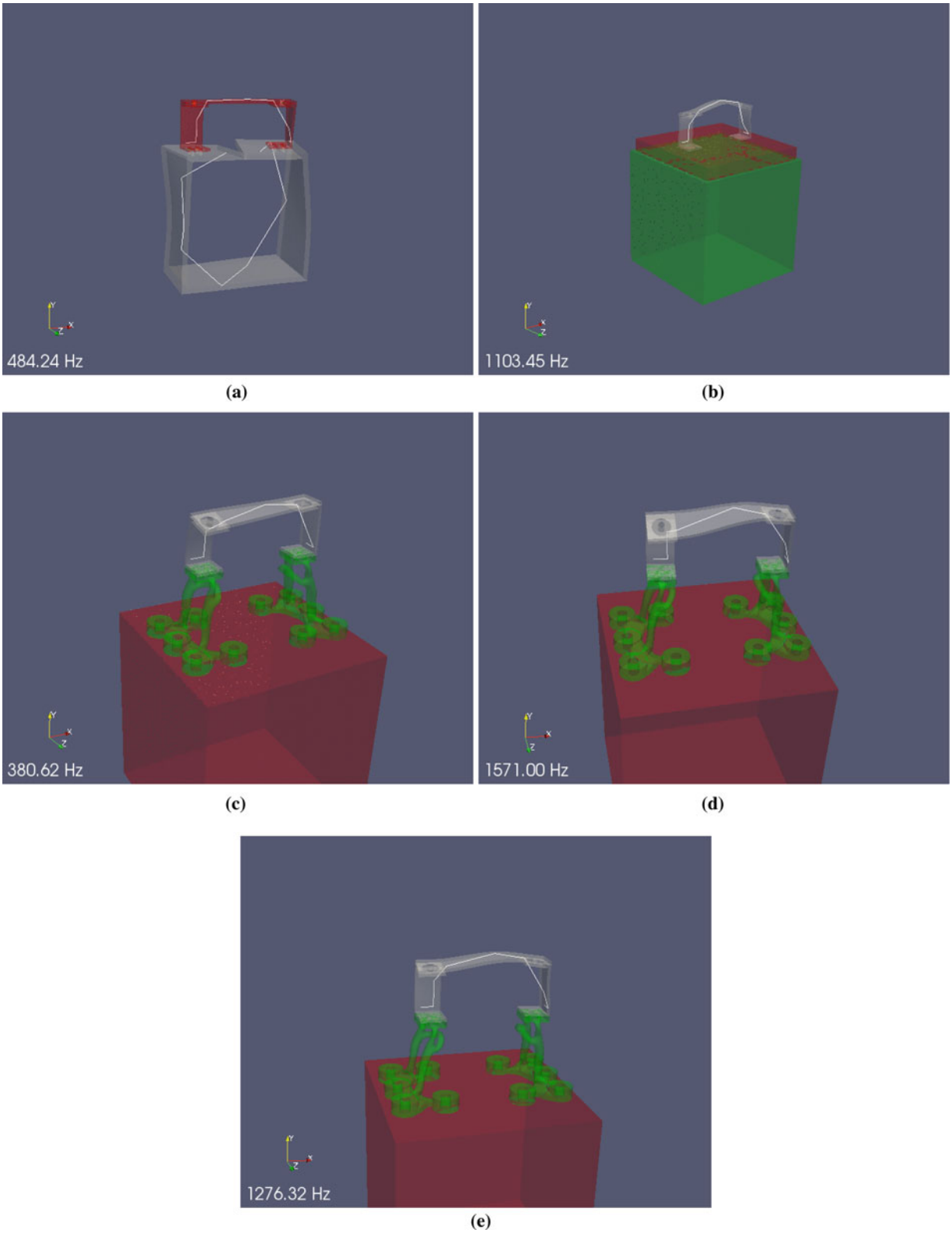

Fig. 17.10 Examples of experimentally derived and expanded mode shapes. The white lines represent the experimental degrees of freedom, and the transparent solid shapes represent the expanded finite element models. (**a**) Mode 5 of the BARC structure. (**b**) Mode 2 of the removable component on the plate fixture. (**c**) Mode 4 of the removable component on the Design 12 fixture. (**d**) Mode 8 of the removable component on the 2-leg fixture. (**e**) Mode 7 of the removable component on the 3-leg fixture

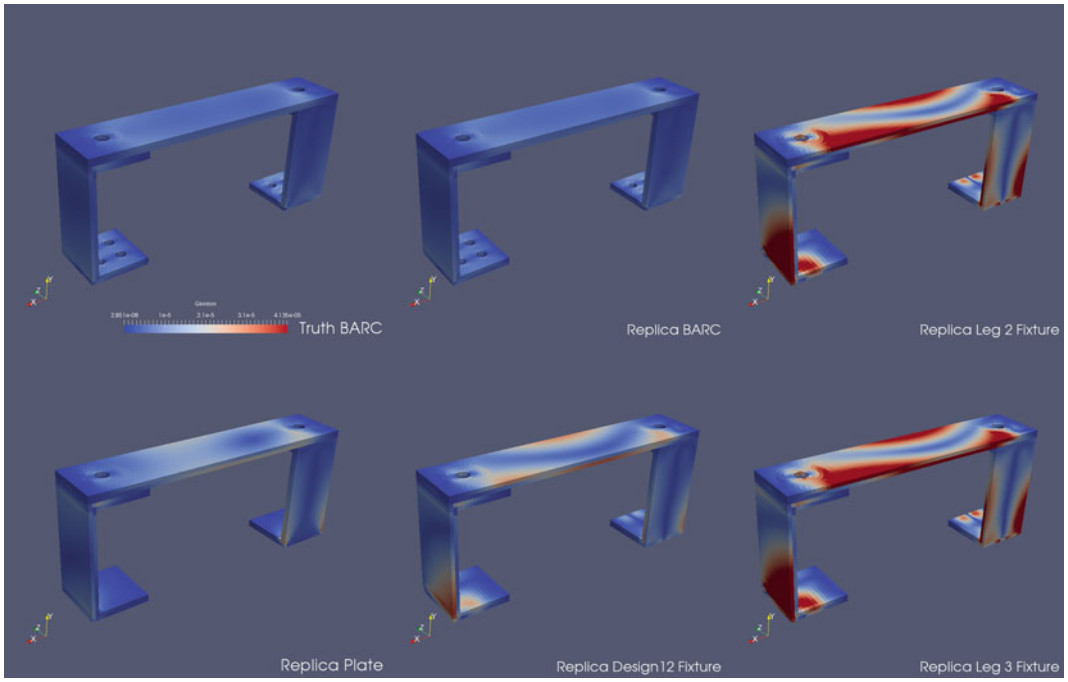

Fig. 17.11 RMS ε_{xx} strain

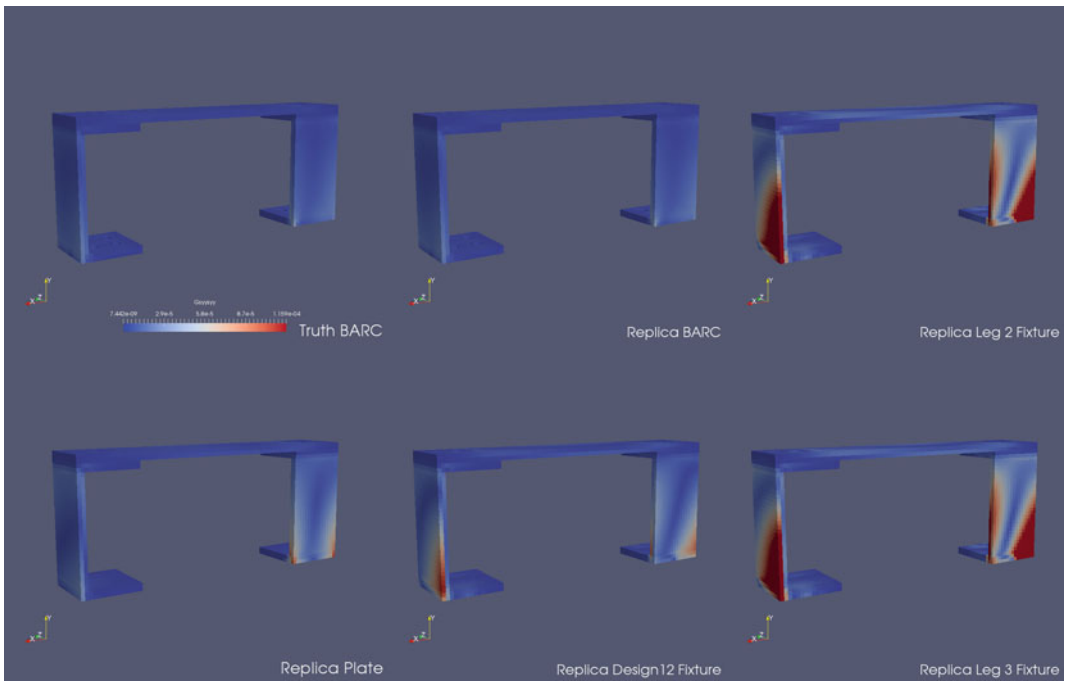

Fig. 17.12 RMS ε_{yy} strain

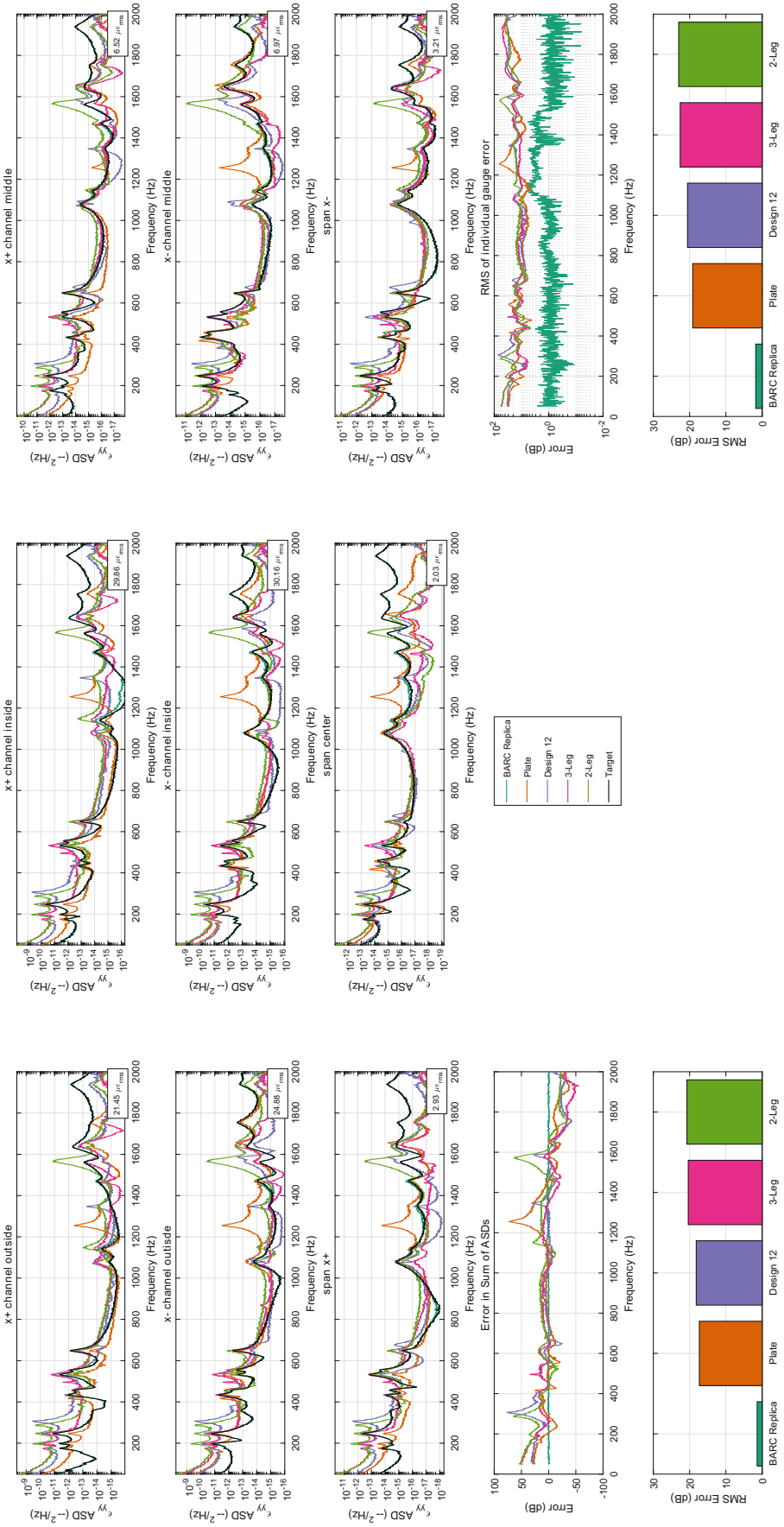

Fig. 17.13 Strain auto-spectral density functions for the ε_{yy} strain component

but is the worst for the 2-leg and 3-leg fixtures. Like in the acceleration domain, largest errors in the strain occur at resonant frequencies of the part. One interesting point is that by the metrics used in this paper, the Design 12 fixture appeared to be a better fixture than the 2- or 3-leg fixtures in terms of strain error, but was a worse fixture in terms of acceleration error. This suggests that the definition of what makes a "good" test should somehow involve the failure mechanism being investigated. All three topology-optimized fixtures ended up providing a worse strain estimate than the simple plate fixture. This result is taken to suggest not that topology optimized fixturing is not suitable for this application, but rather that increased research into the selection of the correct optimization method is required.

17.6 Conclusions

The removable component of the BARC structure was tested in a variety of configurations that are representative of the current state of multi-axis vibration testing, including an IMMAT-like test as well as a fixed-base "3-DOF" test. The goal of this work was to determine if an additively manufactured fixture could be designed to replicate the dynamics of the Box component of the BARC structure.

Three fixtures were designed and printed and were compared against a more traditional plate fixture as well as a best-case IMMAT test. Finite element expansion was used to predict strain results, which could be compared between the tests in addition to the more traditional acceleration comparisons. It was found for all fixtures that the control schemes used in this test struggled to deal with modes of the assembly, and large errors were found both in the acceleration and strain CPSDs at the frequencies corresponding to these modes. The plate was found to perform slightly better than the fixtures, likely due to it having fewer modes in the bandwidth. The control scheme used in this paper was rudimentary open loop control. It would be interesting to see whether or not these modes could be better controlled using a more advanced closed loop control scheme.

The primary lesson learned from this test is that the fixture that is used with the test article should be optimized as much as possible for the dynamic response of the structure it aims to emulate. Optimizing for other parameters such as static deformation or stiffness does not improve the test, but likely reduces its accuracy due to the introduction of additional spurious modes that the control system will struggle to control. Future work will focus on developing topology optimization algorithms and objective functions for matching the dynamic response of the component.

References

1. Soine, D.E., Jones, Jr., R.J., Harvie, J.M., Skousen, T.J., Schoenherr, T.F.: Designing hardware for the boundary condition round robin challenge. In: Mains, M., Dilworth, B. (eds.) Topics in Modal Analysis & Testing, vol. 9, Conference Proceedings of the Society for Experimental Mechanics Series, pp. 119–126. Springer, Cham (2019)
2. Smith, D.P.R.S.A., Brake, M.R.W., DeClerck, J., Blanco, M.A., Schoenherr, T.F., Skousen, T.: Testing summary for the box and removable component structure. In: Proceedings of the 37th International Modal Analysis Conference, Orlando, FL (2019)
3. DeClerck, J., Blough, J., Larsen, W., VanKarsen, C., Soine, D., Jones, R.: Modal analysis of BARC equivalent geometry optimized fixtures. In: Proceedings of the 37th International Modal Analysis Conference, Orlando, FL (2019)
4. Smallwood, D.O., Paez, T.L.: A frequency domain method for the generation of partially coherent normal stationary time domain signals. Shock. Vib. **1**(1), 45–53 (1991)
5. Smith III, J.O.: Spectral audio signal processing. https://ccrma.stanford.edu/~jos/sasp/ (2018). Accessed April 2018
6. Mayes, R.L., Rohe, D.P.: Physical vibration simulation of an acoustic environment with six shakers on an industrial structure. In: Brandt, A., Singhal, R. (eds.) Shock & Vibration, Aircraft/Aerospace, Energy Harvesting, Acoustics & Optics, vol. 9, Conference Proceedings of the Society for Experimental Mechanics Series, pp. 29–41. Springer, Cham (2016)
7. Reu, P.L., Rohe, D.P., Jacobs, L.D.: Comparison of DIC and LDV for practical vibration and modal measurements. Mech. Syst. Sig. Process. **86**, 2–16 (2016)
8. Carr, J., Baqersad, J., Niezrecki, C., Avitable, P., Slattery, M.: Predicting dynamic strain on wind turbine blade using digital image correlation techniques in conjunction with analytical expansion methodologies. In: Allemang, R., De Clerck, J., Niezrecki, C., Wicks, A. (eds.) Special Topics in Structural Dynamics, vol. 6, Conference Proceedings of the Society for Experimental Mechanics Series, pp. 295–302. Springer, New York (2013)
9. Witt, B.L., Rohe, D.P., Schoenherr, T.F.: Full field strain shape estimations from 3D SLDV. In: Proceedings of the 37th International Modal Analysis Conference, Orlando, FL (2019)
10. O'Callahan, J.C., Avitable, P., Riemer, R.: System equivalent reduction expansion process. In: Proceedings of the Seventh International Modal Analysis Conference, Las Vegas, NV (1989)
11. Hensley, D.P., Mayes, R.L.: Extending SMAC to multiple reference FRFs. In: Proceedings of the 24th International Modal Analysis Conference, St. Louis, MO, pp. 220–230 (2006)

Chapter 18
Strategies for Shaker Placement for Impedance-Matched Multi-Axis Testing

Daniel P. Rohe, Garrett D. Nelson, and Ryan A. Schultz

Abstract Multi-axis testing is growing in popularity in the testing community due to its ability to better match a complex three-dimensional excitation than a single-axis shaker test. However, with the ability to put a large number of shakers anywhere on the structure, the design space of such a test is enormous. This paper aims to investigate strategies for placement of shakers for a given test using a complex aerospace structure controlled to real environment data. Initially shakers are placed using engineering judgement, and this was found to perform reasonably well. To find shaker setups that improved upon engineering judgement, impact testing was performed at a large number of candidate excitation locations to generate frequency response functions that could be used to perform virtual control studies. In this way, a large number of shaker positions could be evaluated without needing to reposition the shakers each time. A brute force computation of all possible shaker setups was performed to find the set with the lowest error, but the computational cost of this approach is prohibitive for very large candidate shaker sets. Instead, an iterative approach was derived that found a suboptimal set that was nearly as good as the brute force calculation. Finally, an investigation into the number of shakers used for control was performed, which could help determine how many shakers might be necessary to perform a given test.

Keywords MIMO · IMMAT · Aerospace · Shaker · Excitation

18.1 Introduction

When a test article is operating in its service environment, it often experiences complex three-dimensional loading. However, when ground tests are performed, this complex environment is often reduced to a series of three uniaxial vibration tests. These uniaxial tests often do not accurately replicate the environment, especially considering that the test article must be bolted or otherwise attached to the shaker table, which can significantly alter the part's dynamics.

Impedance-Matched Multi-Axis Testing (IMMAT) is a technique that aims to improve the deficiencies in uniaxial vibration testing [1, 2]. IMMAT uses multiple smaller shakers to excite the structure, rather than a single large shaker. These smaller shakers allow spatially varying excitation in multiple directions simultaneously and additionally do not disrupt the boundary conditions of the test article as severely as when it is constrained in a vibration fixture on a large shaker. The IMMAT technique also attempts to match the boundary conditions of the test article in its service environment in order to allow the structure's dynamics to aid in meeting the environment (i.e. let the structure vibrate how it wants to vibrate). The key assumption is that if the responses of some set of control accelerometers are matched to the environment, the rest of the structure should also match the environment.

Often the data that can be obtained in a field environment test is limited. There are typically channel count limitations due to the necessity of an on-board data recorder. Due to the expense of performing environment tests in the field, the number

Sandia National Laboratories is a multimission laboratory managed and operated by National Technology & Engineering Solutions of Sandia, LLC, a wholly owned subsidiary of Honeywell International Inc., for the U.S. Department of Energy's National Nuclear Security Administration under contract DE-NA0003525.

This paper describes objective technical results and analysis. Any subjective views or opinions that might be expressed in the paper do not necessarily represent the views of the U.S. Department of Energy or the United States Government.

D. P. Rohe (✉) · G. D. Nelson · R. A. Schultz
Sandia National Laboratories, Albuquerque, NM, USA
e-mail: dprohe@sandia.gov

C. Walber et al. (eds.), *Sensors and Instrumentation, Aircraft/Aerospace, Energy Harvesting & Dynamic Environments Testing, Volume 7*, Conference Proceedings of the Society for Experimental Mechanics Series,
https://doi.org/10.1007/978-3-030-12676-6_18

of iterations that can be performed to achieve good data is limited as well. For a ground test in the laboratory, many of these constraints are relaxed. A ground test can easily contain hundreds of channels; high-quality commercial data acquisition systems can be used, and instrumentation can be optimized for the specific portion of the environment that the ground test is examining. If a technique such as IMMAT can accurately reproduce an environment test on the ground, then many of the limitations of environment testing can be overcome.

One of the open questions regarding IMMAT is how to optimize shaker locations on the test article of interest. Often times for aerospace structures, the loading in service is provided by distributed aeroacoustic loads in addition to mechanical loads, which can make it difficult to intuitively reduce the service loading down to a handful of discrete force locations. With the goal of the IMMAT technique being to match the responses of control gauges in the laboratory test to those in the environment test, one important consideration is how well a given set of input locations can achieve the desired response. A second important consideration is how much force or power is required to achieve those responses, as larger shakers will take up more room around the test article and will require more infrastructure in terms of electrical power, voltage, and current as well as rigging and hoisting materials to support them. This paper aims to investigate shaker placement strategies for IMMAT on a realistic aerospace structure controlled to real environment data.

18.2 Test Hardware and Instrumentation

The structure of interest in this work is the bomb shown in Fig. 18.1. The structure was attached to a supporting rack. Soft bungee cords were used to support the rack. A frame was built up around the structure to create a flexible way to position shakers. During the environmental test, 21 channels of instrumentation were recorded, so for the ground test these instrumentation locations were reproduced. Nineteen of these channels were used for control, and two were used for validation. A number of additional channels of instrumentation were also placed on the exterior of the structure for extra diagnostics and potential drive point locations; however because there was no environment data for these locations, they could not be used for control during the laboratory test.

B+K Lan-XI data acquisition systems were used to record all channels of the laboratory test. These data acquisition systems can provide arbitrary source capabilities which were used in this test for open loop control. In addition, the control channels were teed off to a Spectral Dynamics Jaguar control system which provided closed loop control. The channels that were split were powered using external Kistler Piezotron Coupler signal conditioners.

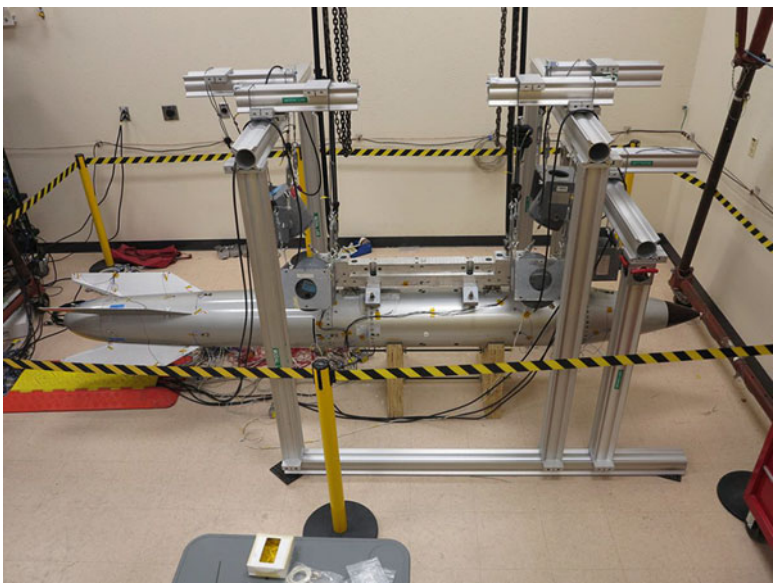

Fig. 18.1 Test Article with frame built for supporting shakers

18.3 What is a "Good" Test?

Prior to being able to make any kind of meaningful comparison between different shaker setups or control strategies, a suitable metric is needed that describes how well a test performed. For a single axis vibration test with one control accelerometer, such metrics can be derived easily; the power spectral density (PSD) function of the control accelerometer can be plotted against the target PSD, and a decibel (dB) error can be computed at each frequency line. The number of lines out of some tolerance can be counted, or an RMS dB error could be computed. For IMMAT this is more complicated. The single PSD curve in the single axis case becomes a complex-valued, square cross-power spectral density matrix, containing not only auto-power spectral density functions, but coherences and phases between the various control gages. This results in potentially hundreds of functions that could be compared between target and achieved responses. Clearly, some amount of data reduction is needed to be able to reduce this massive amount of data down to a more digestible metric.

In previous work on a similar structure, Mayes and Rohe used a "sum of autospectral densities" (ΣASD) metric to reduce the massive amount of data down to a single meaningful plot [3]. The metric used was the error in the sum of diagonal (trace) of the PSD matrix. Only the diagonals are considered, noting that the off-diagonal terms are strongly dependent on the dynamics of the individual test article and may vary between environment and ground tests. To compute the error metric, the dB error is computed between the target sum of ASDs and the actual response sum of ASDs. dB error was chosen due to the desire to compare relative magnitudes between control and achieved responses, rather than a linear error which would be biased towards the higher responding frequency lines.

This metric is shown in (18.1), where $G^t_{xx(i,i)}\left(f_j\right)$ and $G^e_{xx(i,i)}\left(f_j\right)$ denote the jth frequency line of the ith autospectrum (diagonal entry) for the test and environment data, respectively, and n_{gauge} is the number of control channels.

$$e_{\Sigma\mathrm{ASD}}(f_j) = \mathrm{dB}\left(\sum_{i=1}^{n_{gauge}}\left(G^t_{xx(i,i)}\left(f_j\right)\right)\right) - \mathrm{dB}\left(\sum_{i=1}^{n_{gauge}}\left(G^e_{xx(i,i)}\left(f_j\right)\right)\right) \tag{18.1}$$

This can also be reduced to a single value by taking the RMS value of $e_{\Sigma\mathrm{ASD}}(f_j)$ over all frequency lines, where n_{freq} is the number of frequency lines:

$$e_{\Sigma\mathrm{ASD}} = \sqrt{\frac{1}{n_{freq}}\sum_{j=1}^{n_{freq}} e_{\Sigma\mathrm{ASD}}(f_j)^2} \tag{18.2}$$

The error in the sum of the PSDs can give an estimate of the total energy in the system, but does not give a good estimate of the spatial distribution of that energy. The error in the sum of the PSDs may still be small even if the control is poor, because some gauge that is responding to a higher level than it should might make up for a gauge that is responding at a lower level than it should. A second metric considered in this work is an "RMS dB error" which calculates the dB error in the ASD for each gauge, and then calculates the RMS value over all gauges.

$$e_{\mathrm{ASD}}(f_j) = \sqrt{\frac{1}{n_{gauge}}\sum_{i=1}^{n_{gauge}}\left(\mathrm{dB}\left(G^t_{xx(i,i)}\left(f_j\right)\right) - \mathrm{dB}\left(G^e_{xx(i,i)}\left(f_j\right)\right)\right)^2} \tag{18.3}$$

Like the previous metric, this can be rolled up into a single value by computing the RMS over all frequency lines:

$$e_{\mathrm{ASD}} = \sqrt{\frac{1}{n_{freq}}\sum_{j=1}^{n_{freq}} e_{\mathrm{ASD}}(f_j)^2} \tag{18.4}$$

This second e_{ASD} metric will be the primary metric used in this paper to determine whether or not a test is better or worse than another test. The $e_{\Sigma\mathrm{ASD}}$ metric will also be presented for completeness and consistency with previous testing.

18.4 Control Strategies

While the focus of this paper is shaker placement optimization, it is helpful to understand the control schemes used for the testing described subsequently. Three different control schemes were utilized to control the response channels to the target responses; these are Uncorrelated Open Loop control, Closed Loop control, and Closed Loop Blended control, as described in the following sections. For all control strategies investigated, control channels 6 and 7 (shown on subsequent plots) were used for validation rather than control, allowing the authors to gain an understanding of what was going on at locations other than the control locations.

18.4.1 Uncorrelated Open Loop Control

An open loop uncorrelated (OL) control scheme was used successfully in [3], so it is used here as a starting point to compare against other more complex control schemes. The open loop scheme used in [3] computed shaker inputs using the pseudo-inverse of the transfer function matrix assuming uncorrelated inputs.

One issue with the approach in [3] is that there is no numerical constraint that the voltage autospectra remain positive, though this is a physical constraint. In the cases where the desired voltage autospectra were found to be negative, they were instead set to zero. This additional energy resulted in the responses of the control gauges being larger than the control specifications. Though the Tikhonov regularization reduced the incidences of negative energy being desired by the open loop control scheme, it could not completely eliminate them.

A non-negative least squares solver is available in MATLAB via the `lsqnonneg` function, which uses the algorithm from [4]. This algorithm solves the least squares problem with the constraint that the solution cannot be negative, effectively ensuring that physical voltage signals could be reproduced from the response. Using the non-negative least square solver produced better matches to the control accelerometers than the Tikhonov solution, so it was used for all open loop uncorrelated control.

In order to perform an open loop test, first a baseline "buzz" test was performed to establish the transfer functions. A pseudo-random signal was generated consisting of the summation of unit-amplitude sine waves at frequencies corresponding to the frequency bins of the Discrete Fourier Transform (DFT) with randomized phases for each frequency line for each frame. The signals were then scaled so they were 1/3 V RMS (approximately 1 V peaks) for each shaker. This signal was then fed through the shaker amplifiers by the arbitrary source capabilities of the B+K Lan-XI data acquisition systems, and the amplifier gains were adjusted to produce approximately 10 lbf RMS.

The MIMO transfer functions between the input voltage and output responses were computed from the baseline "buzz" test data. These transfer functions were then passed into the control equation and new voltage autospectra were computed via the non-negative least squares solution. The amplitudes of the baseline sinusoids were then scaled by the square root of the ratio between the new voltage autospectra and the old voltage autospectra, again with randomized phases to produce the updated input signal. This signal was then played by the arbitrary source capabilities of the B+K Lan-XI data acquisition systems and the responses to the control inputs were recorded.

18.4.2 Closed Loop Control

As a step up in complexity from the uncorrelated open loop control, a closed loop (CL) control scheme was attempted using the Spectral Dynamics Jaguar MIMO control system as described in Sect. 18.2. The Jaguar system attempts to solve the control equation directly without making assumptions on the inputs. This includes attempting to control to the off-diagonal entries of the PSD matrix, rather than discarding them to only match autospectra as was done in the Open Loop Uncorrelated control scheme. It does this by not only specifying the amplitudes of the voltage signals output to the shaker amplifiers, but also the phasing and coherence between the voltage signals.

18.4.3 Closed Loop Blended Control

While the nominal closed loop control described previously used both autospectra and crossspectra from the environment data, previous work [2] has suggested that better control can often be achieved by computing the cross-power spectral density

terms using the dynamics of the ground test structure rather than the environment test data. This so-called closed loop blended (CLB) approach uses as its control targets the diagonal of the PSD matrix from the environment test data but populates the off-diagonal terms of the target PSD matrix using the coherence and phase of the off-diagonals from a test performed at similar excitation level (typically from the closed loop control test). Attempting to control the off-diagonal terms to the environment data can be counter-productive due to differences in the dynamics between the environment test article and the ground test article; better control to the diagonal terms of the PSD matrix can be achieved if the ground test unit is allowed to vibrate in its preferred way.

To compute the coherence and phase, the response PSD matrix is taken from the closed loop control test. The coherence $\gamma^2_{(i,j)}$ and phase $\phi_{(i,j)}$ are computed for each (i, j) off-diagonal term in the PSD matrix as follows:

$$\gamma^2_{(i,j)} = \frac{\left|G_{xx(i,j)}\right|^2}{G_{xx(i,i)}G_{xx(j,j)}} \tag{18.5}$$

$$\phi_{(i,j)} = \arctan \frac{\text{imag}\left(G_{xx(i,j)}\right)}{\text{real}\left(G_{xx(i,j)}\right)} \tag{18.6}$$

Then the off-diagonal terms of the target environment PSD matrix are recomputed using the phase and coherence from the ground test and the diagonal terms of the target environment PSD matrix.

$$G_{xx(i,j)} = \sqrt{\gamma^2_{(i,j)}G_{xx(i,i)}G_{xx(j,j)}}e^{\hat{i}\phi_{(i,j)}} \tag{18.7}$$

With the blended PSDs created, they could be loaded into the Jaguar system as the control targets. The test would then proceed as described in Sect. 18.4.2.

18.5 Shaker Placement Strategies

Excitation locations have proven to be an important consideration for the IMMAT technique. This work aimed to investigate different shaker setups to see how shaker setup could be optimized in future tests. Initially shaker placement proceded using engineering judgement, which has been shown to provide reasonable shaker locations [3]; however recent works have attempted to provide a more algorithmic or automatic approach. In [2] the authors developed modal approaches to positioning shakers while limiting the force required. For large, complicated aerospace structures such as the one in this test which may have hundreds of modes in the bandwidth of interest, a mode-based approach may not be feasible; there may be insufficient instrumentation available to fit all the modes in the bandwidth, and a finite element model from which modes could be extracted may not be accurate due to the complexity of the structure.

18.5.1 Engineering Judgement

The initial positions of the shakers in the test were decided upon using the previous test in [3] as a starting point and then modifying the shaker set based on engineering judgment. The shakers started in a configuration that closely matched the rack configuration from [3] with one shaker located on the tail. This configuration, shown schematically in Fig. 18.2, is called the Rack-Tail configuration in this report.

The second shaker configuration was created by moving the shakers from the rack to the bomb, which was also done in [3]. The tail shaker location from the Rack-Tail configuration was noted to improve control significantly, so a second shaker was added at this location perpendicular to the first tail shaker. The remaining three shakers were spaced along the length of the bomb. This configuration is shown in Fig. 18.3 and is hereafter called the Bomb shaker configuration.

After testing the Bomb shaker configuration, it was noted that the axial control locations weren't responding accurately, likely because there is no significant axial shaker excitation. The Bomb configuration was modified such that the shaker at the middle of the bomb was rotated 45° to provide half axial/half radial excitation. This configuration is called Bomb2 and is

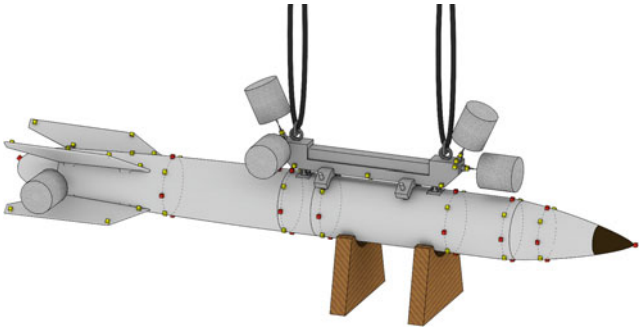

Fig. 18.2 Rack-Tail shaker configuration

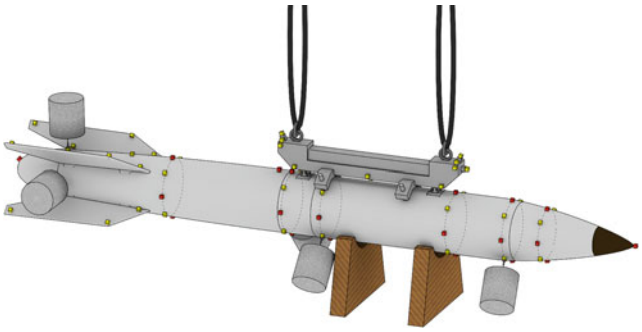

Fig. 18.3 Bomb shaker configuration

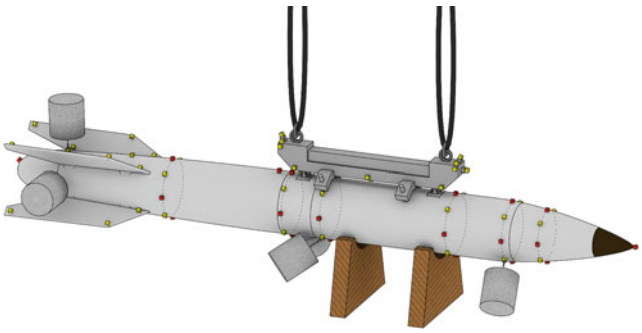

Fig. 18.4 Bomb2 shaker configuration

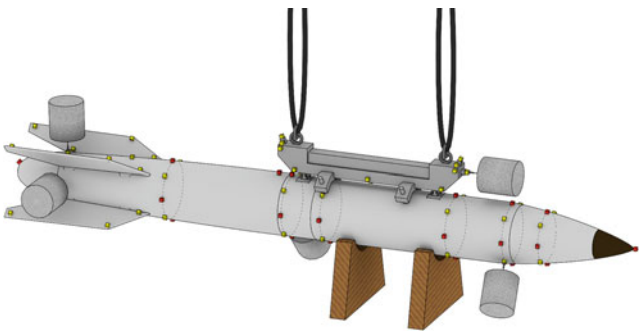

Fig. 18.5 Rack-Bomb shaker configuration

shown in Fig. 18.4. Noting that the additional axial input improved the result, that shaker was moved to the axial location on the bomb rack to provide even better axial control. This configuration is called Rack-Bomb and is shown in Fig. 18.5. This configuration was considered the "best" configuration achieved using engineering judgment.

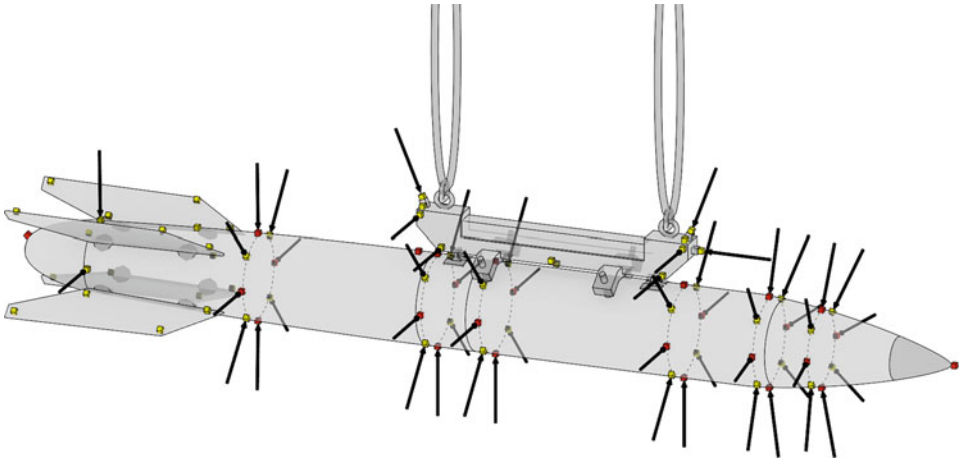

Fig. 18.6 Hammer impact locations to populate shaker candidate location transfer functions

18.5.2 Impact Testing to Populate the Transfer Function Matrix for Candidate Shaker Locations

The four shaker location sets described above were chosen based on engineering judgment and provided seemingly reasonable results. However, they are likely not the optimal set of shaker locations to provide the best results. Ideally, the test engineer would have some way of selecting a shaker setup that was optimal in some sense, rather than simply reacting to the results that are being achieved. For the investigation into optimal shaker setups, control was simulated analytically to try to find the best set of shaker locations. This allowed many shaker setups to be evaluated without spending the time repositioning the shakers between each evaluation.

Predictions of the response PSD matrices from a set of inputs can be computed via the control equation if a transfer function matrix is available for the candidate input locations. If a large number of columns (i.e. candidate input locations) are available, the test engineer can simply pick one of those columns for each shaker, run them through the control law analytically, and get estimates of the response to inputs at the locations corresponding to those five columns. The optimal input locations can then be selected as the five columns of the transfer function matrix that produced the best matches to the environment data. Setting up a large number of shakers to populate a large number of columns in the transfer function matrix can be time consuming due to the need to provide support for the shaker, align the stinger, and adhere the shaker hardware to the test article. An alternative to shaker excitation is hammer or impact excitation where an instrumented hammer can be used to excite the structure in more locations more quickly.

Impact hammer data was acquired at all external gauges on the body of the bomb where the bomb rack did not interfere with the impact testing (i.e. not on the fins or between the bomb rack and the bomb), as well as at six locations on the bomb rack for a total of 54 different input locations to populate candidate shaker locations. These impact locations are shown in Fig. 18.6. This set of locations contained all of the shaker locations used previously as described in Sect. 18.5.1, so the comparison between the responses predicted from Hammer transfer functions and actual shaker control responses could be performed.

18.5.3 Brute Force Computation of Minimum Error

It is straightforward to compute the estimated responses and compare them to the environment data for a set of shaker locations, so an attractive path forward might be to simply compute the responses for every combination of five shakers from the candidate set. With 54 candidate shaker locations, there are 3,162,510 unique combinations of five shakers, and the number grows quickly as more candidate locations are added. However, it was desired to simulate the control problem at each of these 3 million shaker setups to get an idea of the distribution of the error metrics and determine a true best shaker configuration against which other methods of shaker selection could be compared. The Closed Loop control scheme was chosen for this analysis over the Closed Loop Blended due to it being less computationally intensive; the Closed Loop Blended scheme requires two solutions of the control problem, the first to generate coherence and phase to update the off-

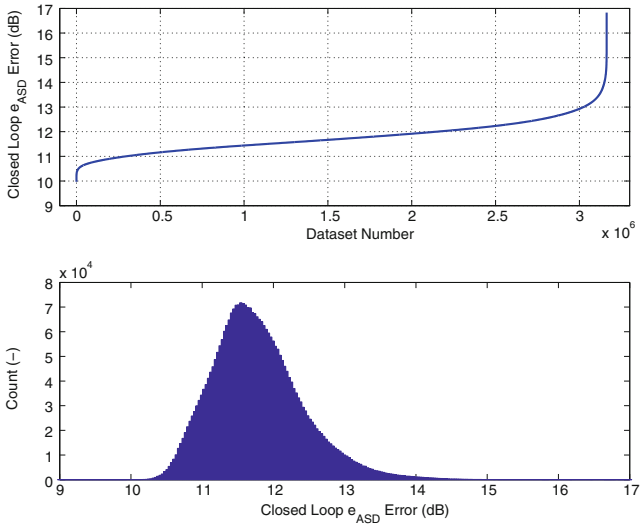

Fig. 18.7 Distribution of Error e_{ASD} for all 3,162,510 combinations of five shakers from 54 candidate locations

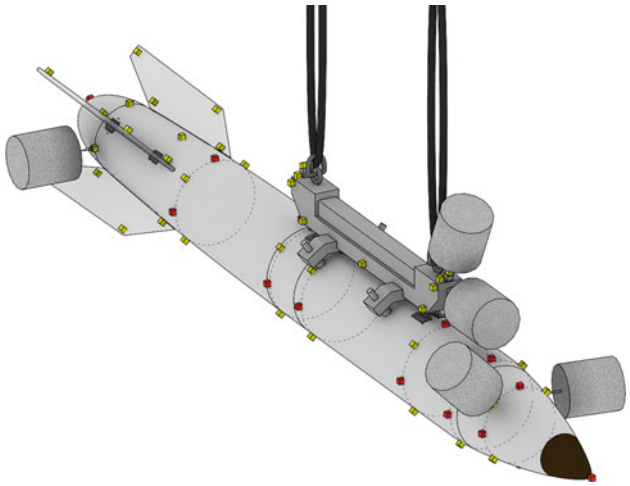

Fig. 18.8 Optimal Closed Loop shaker configuration showing two shakers on the rack and three on the bomb computed by brute force solution of all of the combinations of five shakers from 54 candidate shaker locations

diagonal terms of the target PSD matrix, and the second to compute the control to those updated targets. The Closed Loop control scheme only requires one solution of the control problem.

The Closed Loop computation of the full set of shaker input combinations was able to be performed on a laptop computer over approximately 36 h. The resulting error distribution is shown in Fig. 18.7. The distribution is skewed towards higher errors; there are many bad shaker locations, a large body of reasonable shaker locations, and a few good shaker locations. The shaker setup corresponding to the best Closed Loop prediction is shown schematically in Fig. 18.8 and will be referred to as the "Best Brute Force" shaker configuration. Unfortunately this configuration was unable to be set up in the laboratory due to the shaker trunnions, which are not shown in Fig. 18.8, interfering with adjacent shakers at the front of the rack; however, it is still useful as a comparison benchmark.

Note that there is a near-infinite number of candidate shaker locations on the bomb that could have been used so even this exhaustive search of the 54 candidate shaker locations may not select the *true* optimal shaker set as the locations that would provide such a set may not be included in the 54 candidate shaker locations.

The computational complexity of the brute force approach would grow exponentially if more candidate shaker locations were to be added, and would therefore not be feasible if, for example, a finite element model consisting of thousands of candidate locations were to be used to populate the full space of excitation locations. Therefore, a more computationally efficient method was desired to select a set of shakers from a potentially enormous candidate set.

18.5.4 Shaker Positioning by Iterative Addition of the Shaker that Minimizes Error

To provide an alternative to the brute force approach to compute a nearly optimal shaker set, a technique was derived that iteratively adds shakers that produce the minimum e_{ASD} error. Starting with zero shakers, the technique solves the Closed Loop Blended control problem with all candidate shaker locations individually, resulting in 54 response sets and 54 error metrics each derived using only a single shaker to excite the structure. The shaker that provides the lowest error is kept and the problem begins again except on the second iteration the shaker that was picked in the first iteration is combined with all remaining candidate shaker locations individually, resulting in 53 response sets and 53 error metrics each derived using two shaker locations. Again, the combination of two shakers that produces the lowest error metric is kept. The process continues until five shakers are selected. In total, only 260 solutions of the control problem are needed to perform this algorithm, rather than 3 million to exhaustively search the input space.

The shaker selection algorithm chose the configuration shown in Fig. 18.9. Note that this is not the same configuration selected by the best brute force calculation and is therefore suboptimal, though much more computationally efficient. The best single shaker was placed at the middle of the bomb in the lateral direction. This configuration also maintained the two tail shakers from the previous Bomb, Bomb2, and Rack-Bomb configurations. The final two shakers were placed on the nose, which provides the majority of the axial input for this configuration, and near where the aft bomb rack contacts the bomb. This configuration will be referred to as the "Bomb Suboptimal" shaker configuration. Because the shakers were reasonably spread out along the bomb, the configuration could be set up in the laboratory, and this is shown in Fig. 18.9b.

Control results for the four shaker configurations from Sect. 18.5.1 as well as the Bomb Suboptimal configuration are shown in Fig. 18.10, both for hammer predictions as well as laboratory results. It shows the control results from the laboratory test are predicted quite well by the impact hammer transfer functions, which validates the predictive ability of the hammer transfer functions.

18.5.5 Comparison of Shaker Selection Techniques

The shaker sets selected by the Closed Loop Brute Force and Iterative Shaker Addition algorithms were compared analytically against the Rack-Bomb setup, which was thought to be the best setup using engineering judgment, for the Open Loop, Closed Loop, and Closed Loop Blended control schemes, shown in Fig. 18.11. One interesting point that can be seen in Fig. 18.11 is that the best shaker setup for one control scheme is not necessarily the best for other control schemes. For example, the Bomb Suboptimal shaker set performed better than the Best Brute Force shaker set for the Open Loop control, significantly worse for the Closed Loop control, and only slightly worse for the Closed Loop Blended.

This is an interesting point because the brute force calculation showed the Bomb Suboptimal shaker setup selected by the Iterative Shaker Addition algorithm was only in the top 1.5% of shaker setups, with over 45,000 of the 3 million candidate shaker setups performing better; however this brute force computation was performed using the Closed Loop control scheme rather than the Closed Loop Blended control scheme. It appears that the Bomb Suboptimal shaker setup would have performed much closer to the Best Brute Force setup had the Closed Loop Blended control scheme been used in the brute force computation.

To further investigate this phenomenon, the responses from the Open Loop, Closed Loop, and Closed Loop Blended control problems were predicted using hammer impact data for 15,000 random shaker sets of five shakers from the 54 candidate locations shown in Fig. 18.6 and compared against those shaker sets that have been described previously. Figure 18.12 shows histograms of the errors from the 15,000 samples for the three shaker control schemes, with the positions of the Rack-Tail, Bomb, Bomb2, Rack-Bomb, Bomb Suboptimal, and Best Brute Force shaker configurations labeled. The distribution of each control scheme's errors was again skewed towards larger errors. Another way to look at the distributions is shown in Fig. 18.13, which sorts the datasets by increasing error.

To get an idea of how well error in one control scheme correlated to error in another control scheme, the predicted errors were compared between control schemes for individual shaker sets. Figure 18.14 shows these results. The Rack-Tail, Bomb, Bomb2, Rack-Bomb, Bomb Suboptimal, and Best Brute Force shaker setups are also marked on the plots so one can see how well they performed compared to other shaker sets. It is obvious from these plots that there is a difference between performance of a given shaker configuration between control schemes. For example, the Rack-Tail configuration, which performed rather poorly compared to other shaker setups in the Open Loop case actually performed quite well in the Closed Loop and Closed Loop Blended cases. And while there were many shaker configurations found to be better than the Bomb Suboptimal setup in the Closed Loop case (over 45,000 different combinations or 1.5% per the brute force analysis), in the

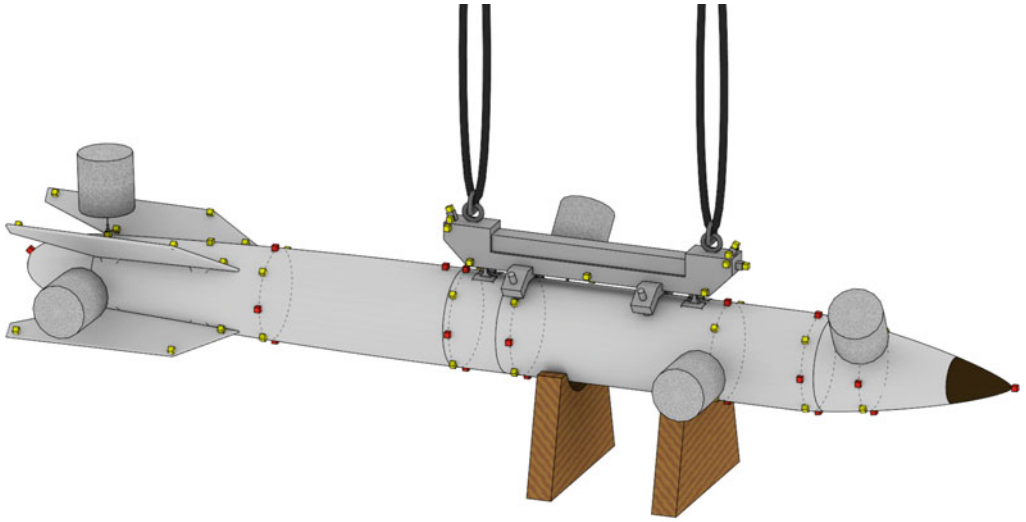

(a)

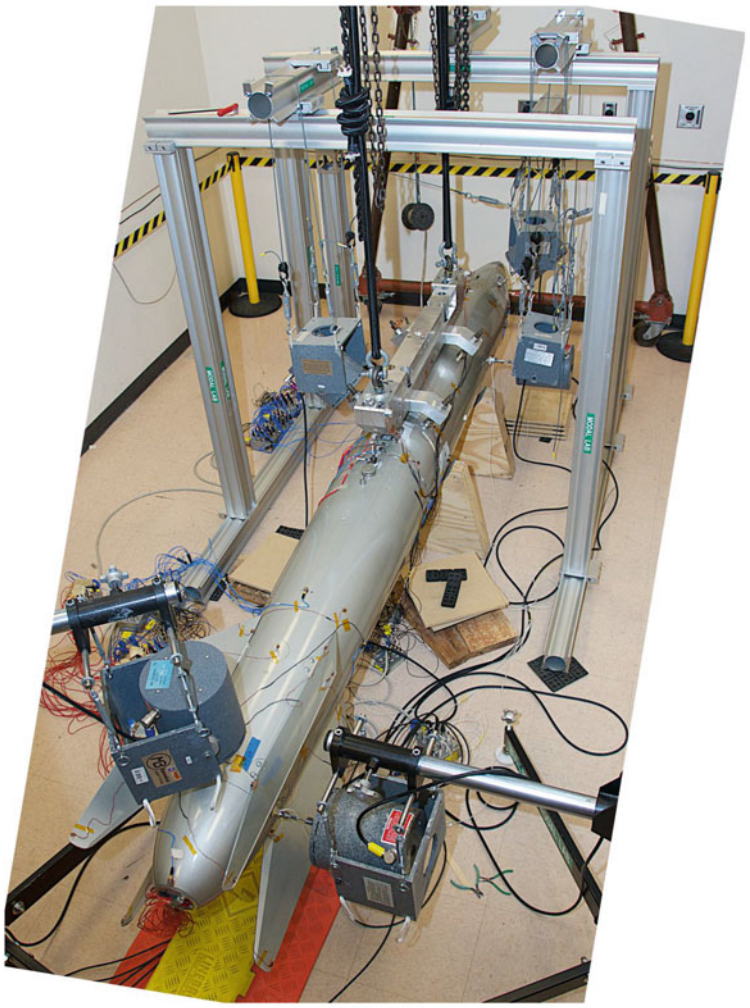

(b)

Fig. 18.9 Suboptimal shaker configuration showing all five shakers located on the bomb. (**a**) Schematic view. (**b**) Test article with shakers attached

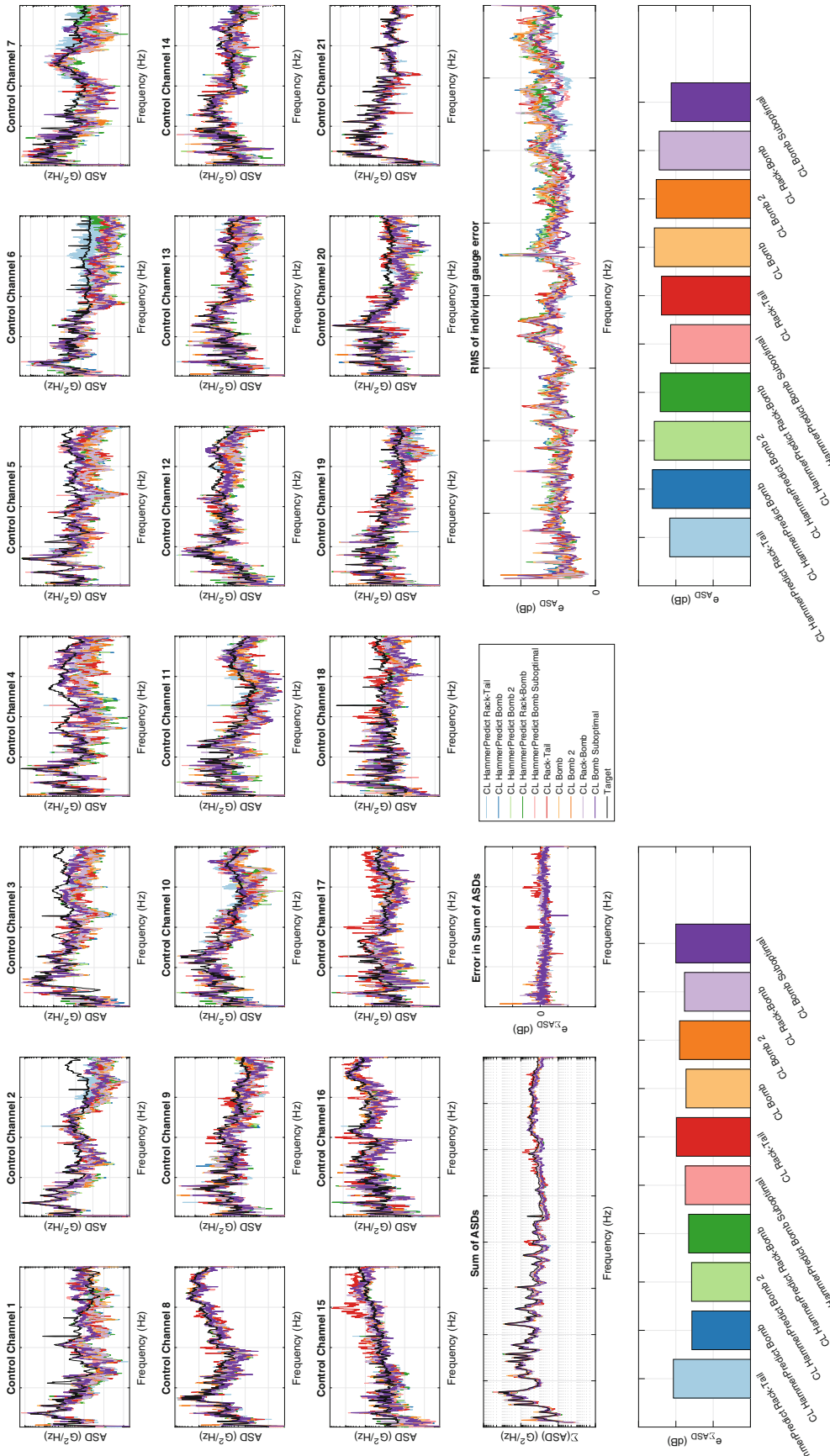

Fig. 18.10 Validation of hammer predictions showing that the predicted Bomb Suboptimal error was actually achieved in the laboratory

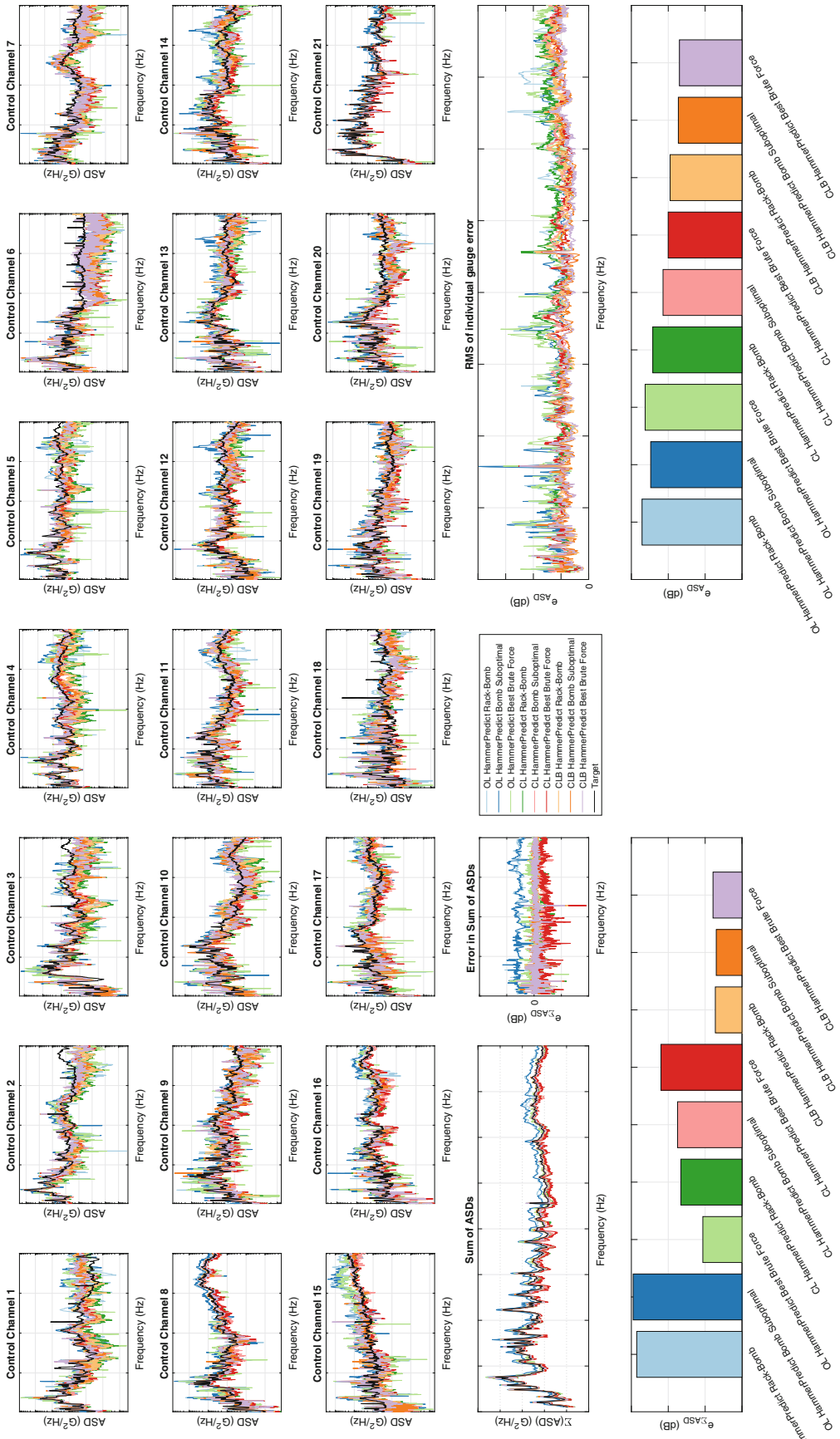

Fig. 18.11 Predicted control for the Rack-Bomb, Bomb Suboptimal, and Best Brute Force configurations for Open Loop, Closed Loop, and Closed Loop Blended shaker control strategies

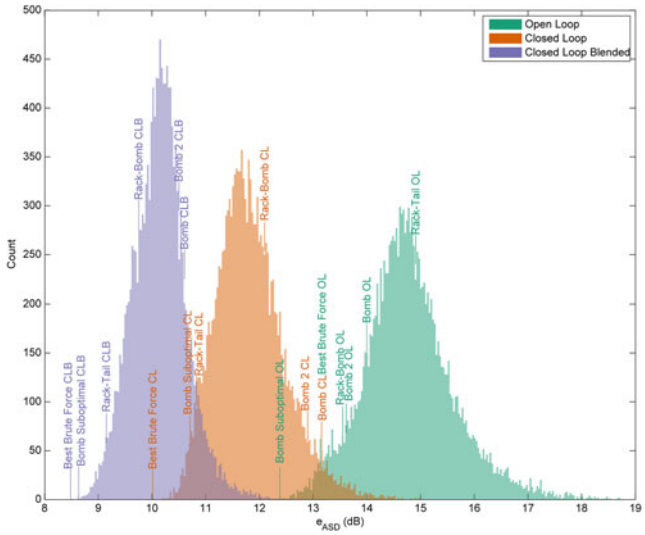

Fig. 18.12 Histogram of e_{ASD} errors for 15,000 random shaker sets for Open Loop, Closed Loop, and Closed Loop Blended control schemes. Specific shaker setups discussed previously are marked on each histogram

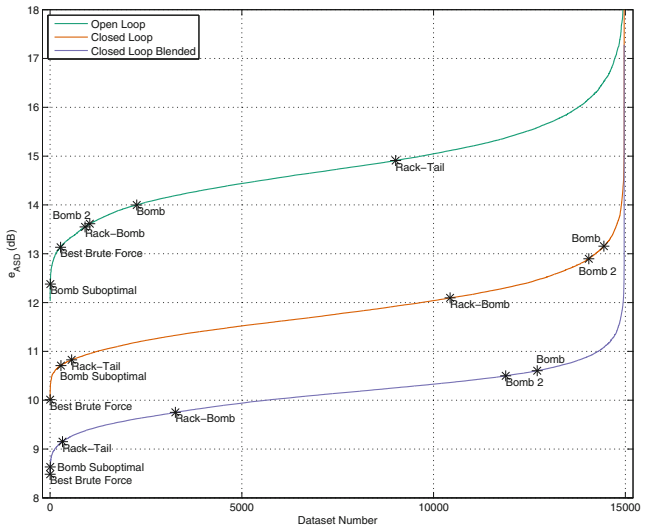

Fig. 18.13 Shaker setups sorted by increasing error for Open Loop, Closed Loop, and Closed Loop Blended control schemes for 15,000 shaker setups. Specific shaker setups discussed previously are marked on each curve

Closed Loop Blended case it was very nearly the best shaker setup found (only the Best Brute Force shaker setup was found to be better). The Open Loop control scheme generally performed worse than the Closed Loop control scheme; however one shaker setup was found that performed better in the Open Loop control than in the Closed Loop control. This can be seen in Fig. 18.14a where a single point is above the diagonal green line that designates equal errors between the two control schemes.

The comparison between the Closed Loop and Closed Loop Blended control schemes in Fig. 18.14c showed the best correlation with the least amount of spread from the line of best fit. This suggests that it might be allowable to perform the computationally simpler Closed Loop control scheme to predict the best shaker setup, whereas performing the shaker optimization using an Open Loop control scheme might be less likely to produce a good Closed Loop Blended shaker setup. This is consistent with the Best Brute Force shaker setup computed from Closed Loop predictions also having the best Closed Loop Blended response out of all the shaker configurations checked, though it is possible that there is a better setup that simply has not been found as only 0.5% of the configurations were checked.

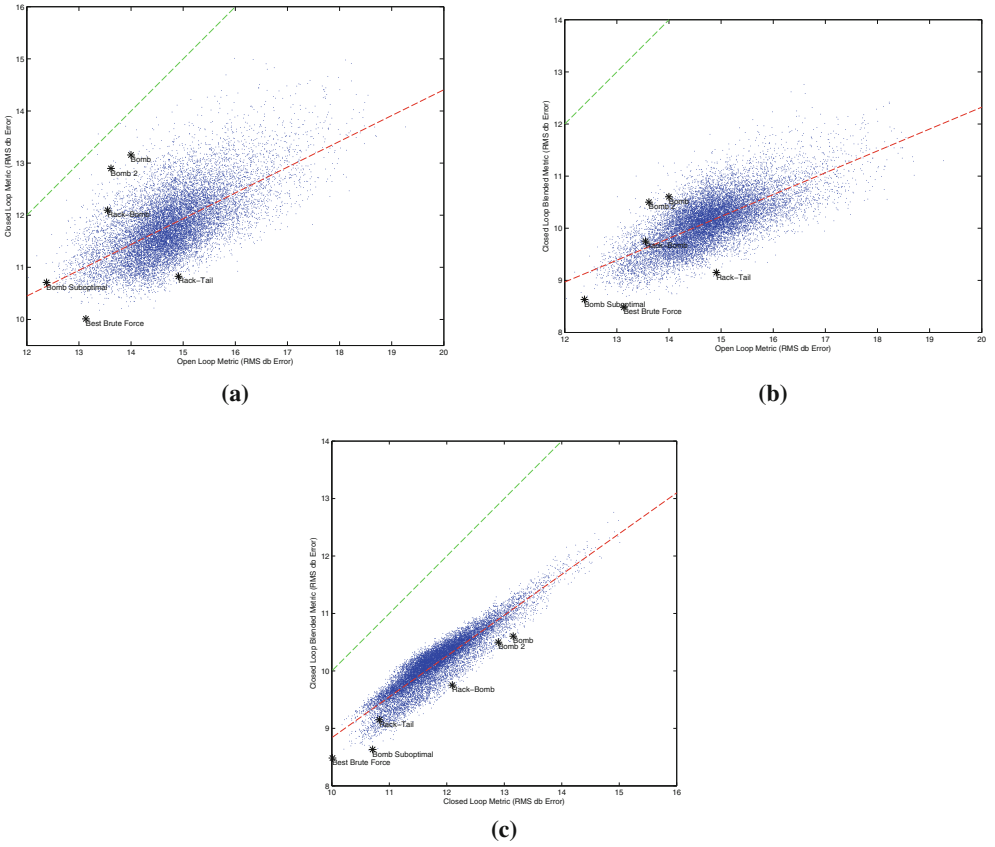

Fig. 18.14 Comparisons of Errors Between Control Schemes for 15,000 shaker setups. (**a**) Comparison between Open Loop and Closed Loop error. (**b**) Comparison between Open Loop and Closed Loop Blended error. (**c**) Comparison between Closed Loop and Closed Loop Blended error

18.5.6 Discussion of Number of Shakers Used for Control

In addition to the positions of the shakers, the number of shakers is also a parameter that the test engineer can control. Of particular interest is how the control and forces required change as shakers are added or removed. The Iterative Shaker Addition algorithm was again solved on the 54 candidate shaker locations; however instead of stopping after five shakers, the algorithm was allowed to run until 30 shakers were added. Recalling that there were 21 internal instrumentation channels, of which only 19 were used for control, the addition of the 19th shaker created a square control problem that is theoretically exactly solvable, and additional shakers past the 19th turn the rectangular "least-squares" solution where there is no exact solution (only a "best fit" solution) into a "underdetermined" or "minimum norm" solution where there are infinitely many solutions but only one that produces a minimum norm of the input. Note that because the Iterative Shaker Addition algorithm adds shakers based on the one that produces the minimum error, and the error is theoretically zero (though practically is some small number), it isn't clear that additional shakers added after the problem becomes square are in any way optimal or if they are based on small floating point errors. They could potentially be optimal in the sense that there may be larger floating point errors in the case where the matrix is more ill-conditioned, and thus the algorithm should pick the shaker that produces the best conditioned transfer function matrix, but further investigation is necessary prior to making that claim.

Figure 18.15 shows the effect of continually adding shakers on the control gauges and validation gauges (channels 6 and 7). The errors in the control gauges trend towards zero and are approximately zero when the control problem becomes square at 19 shakers. As more shakers are added, the approximately zero error slightly decreases likely due to an improving condition number on the transfer function matrix resulting in smaller numerical errors. If one examines only the response gauges used in the control process, it would appear that performing square control would be optimal; nearly perfect control is achieved using the minimum number of shakers. However there are a number of problems when the control problem becomes square.

Figure 18.16 plots the condition number of the transfer function matrix against the number of shakers in the control problem. The condition number is at its worst for a square problem and decreases as columns are added or removed.

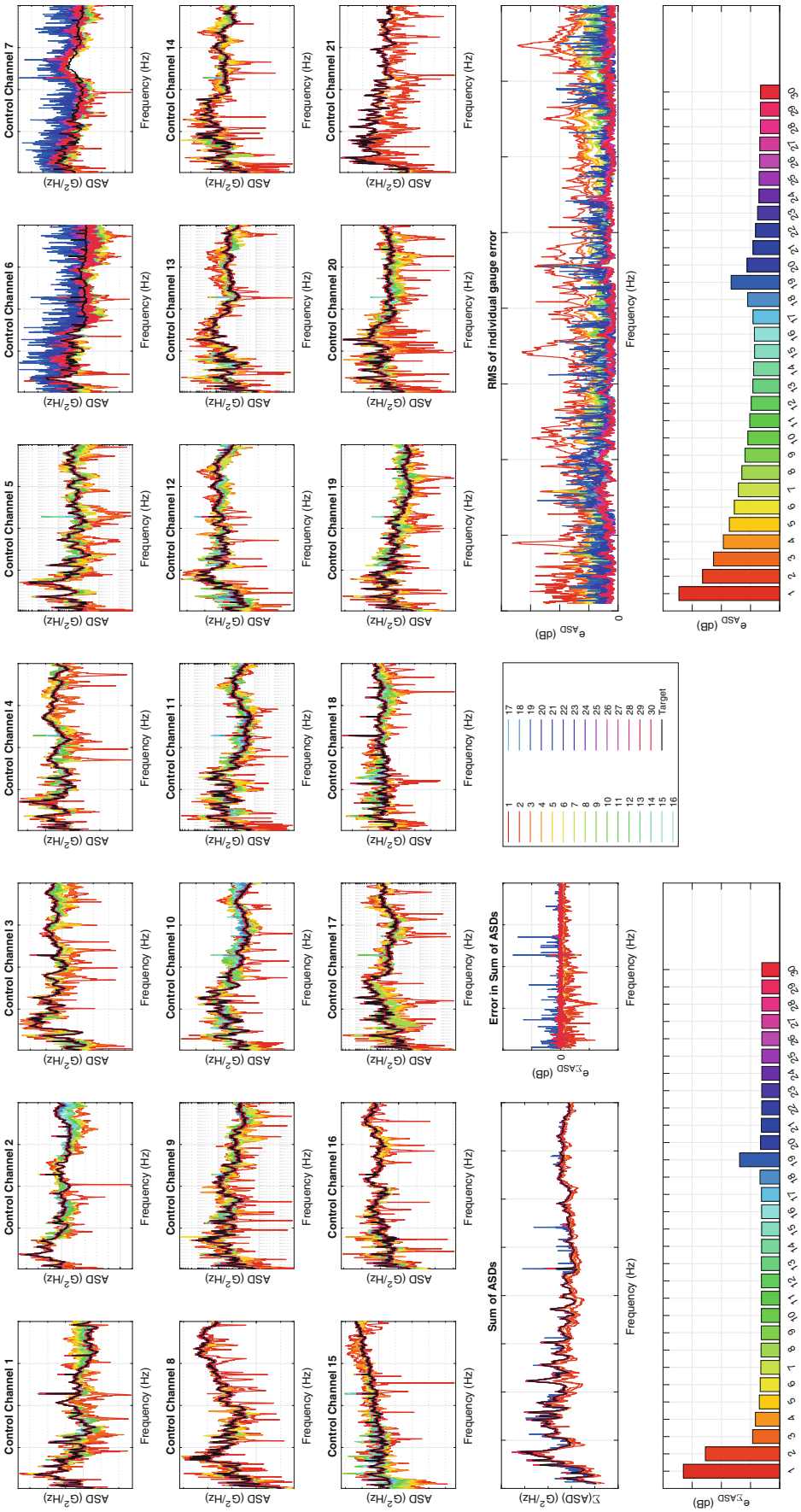

Fig. 18.15 Comparison of control for varying number of shakers. The top three rows of plots show the autospectral density functions for each control gauge, and how well the individual control strategies matched. The two plots in the fourth row show the dB error in the sum of the autospectral density functions ($e_{\Sigma \mathrm{ASD}}$ from Eq. (18.1)) and the dB error in the autospectral density (e_{ASD} from Eq. (18.3)) at each frequency line. The bottom two plots show the same error metrics over all frequency lines

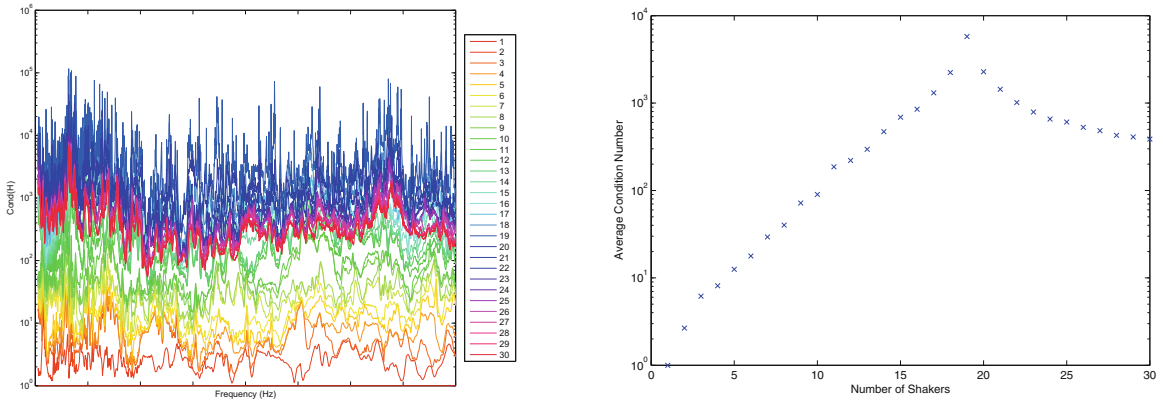

(a) (b)

Fig. 18.16 Condition number of the transfer function matrix as the number of shakers is varied. (**a**) Condition number of the transfer function matrix for each frequency as the number as shakers is increased. (**b**) Average condition number of the transfer function matrix as the number as shakers is increased

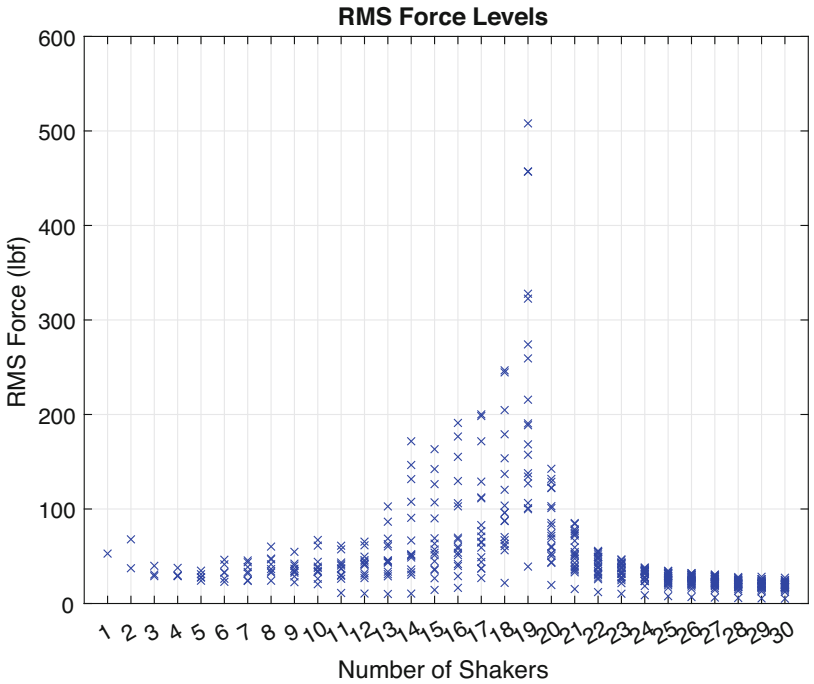

Fig. 18.17 RMS forces predicted to achieve control with an increasing number of shakers

Physically, a large condition number means that in order to achieve a small change in the responses, a large change in the input forces is required. This can be seen clearly in Fig. 18.17, which plots the RMS forces required to achieve the control. There is a clear maximum in the forces required at square control. One might expect that the force required should decrease with the number of shakers because the shakers can work together, and indeed this would be the case if the same number of control channels were used (i.e. split one control voltage to multiple shakers). However, the addition of extra control degrees of freedom gives the shakers more opportunity to fight against each other to achieve better control. Once past the point of square control, the solution to the control problem becomes a minimum norm solution that quickly reduces the maximum force required. Adding just one more shaker brings the maximum required force from 180 pounds RMS to approximately 50 pounds RMS, and continuing to add shakers results in further reduction in force.

Even if large shakers are available so that force is not a limiting factor in the test setup, performing square control is not advisable. While the control points are forced to exactly match the targets, the rest of the test article will not match as well. This can be seen by examining the validation channels, shown in Fig. 18.18. The error in the validation channels, shown in

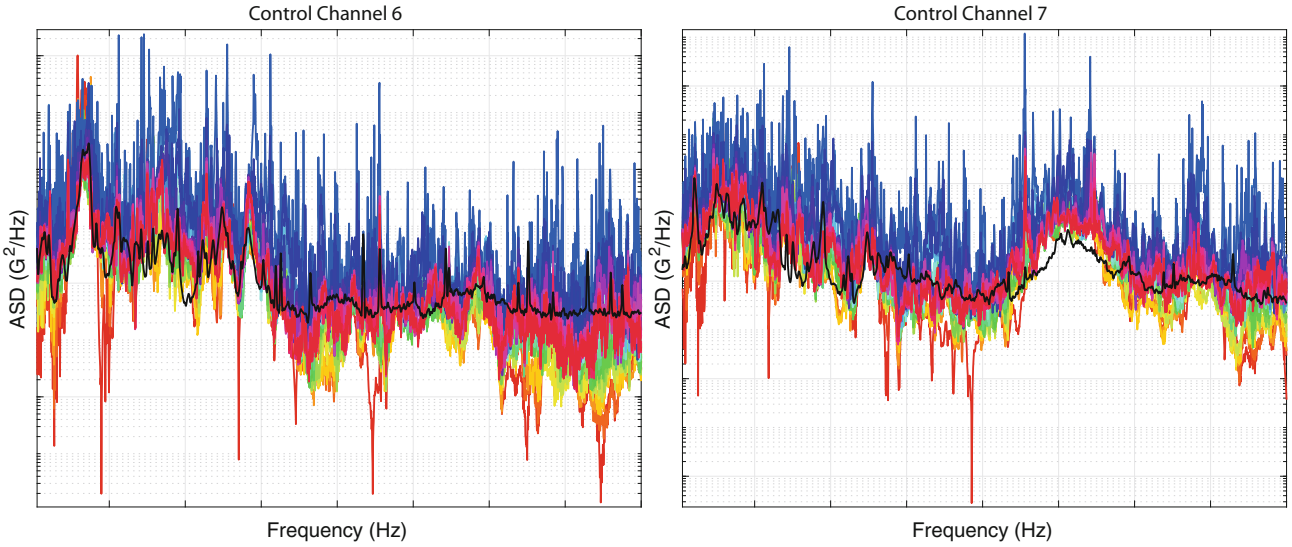

Fig. 18.18 Responses at the validation channels

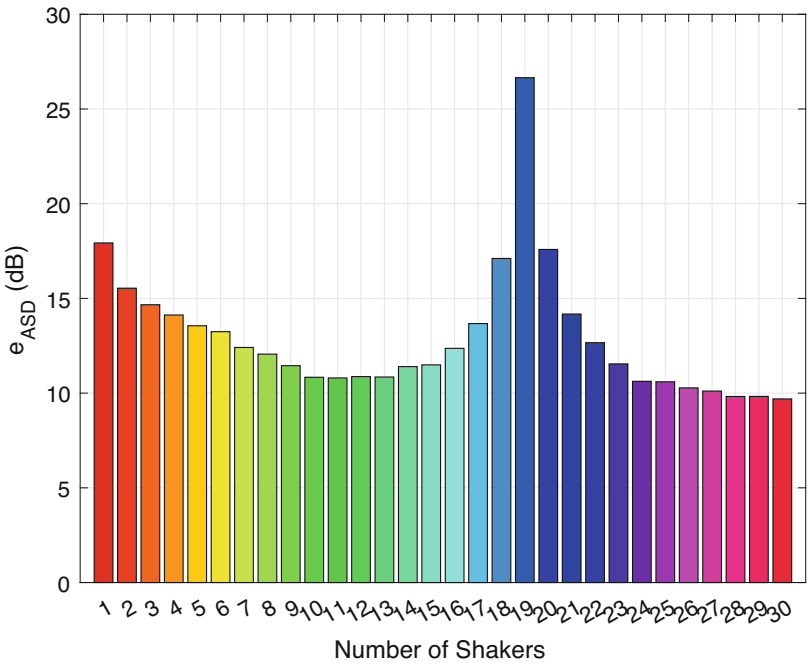

Fig. 18.19 RMS dB error (e_{ASD}) from only the validation channels (6 and 7)

Fig. 18.19, reaches a local minimum at 10 or 11 shakers, but then proceeds to grow to a very large value when the problem becomes square. The responses at the validation channels are much too high in the square problem. As more shakers are added the responses return to reasonable values and the error again decreases.

18.6 Conclusions

In order to perform comparisons between control strategies and shaker setups, a suitable metric to determine which test is "better" in some sense is required. In a single-axis shaker test with a single control accelerometer, it can be straightforward to determine how well a test met the specifications; with a single PSD to compare, metrics like dB error and number of frequency

lines outside of some tolerance are commonly used. However, for a MIMO control problem as is found in IMMAT, it can be more difficult to determine a metric that describes how good the test was. This work has characterized all testing performed in terms of two metrics, both focusing on the diagonal terms of the PSD matrix. The RMS dB error, e_{ASD}, seemed to be the better indicator of a good test in this work, though future work in this area would certainly be of value.

In terms of shaker positioning, engineering judgment seems to have selected reasonable shaker setups in the middle of the error distributions. The best shaker setup for a given test was found to be dependent on the control strategy used. As moving the shakers to different positions was a time-intensive task, shaker setups were instead examined computationally using transfer function matrices derived from impact tests using an instrumented modal hammer. These proved to be a good tool for examining candidate shaker setups, though in a more nonlinear test structure the hammer force to control response transfer functions may not match as well to the transfer functions that would be obtained in a high-level shaker test. For this test, however, many shaker setups could be quickly evaluated by populating a transfer function matrix from a combination of hammer test transfer functions. A finite element model could be another method to develop force to control gauge transfer functions. If large computational resources are available, the control problem could be solved for all combinations of input locations in a brute force way, selecting the true optimal shaker configuration from the candidate locations available. The computations are also easily parallelized by splitting the candidate shaker combinations over multiple processors. If brute forcing a solution is too computationally intensive, the Iterative Shaker Addition Algorithm technique provided a very good, though suboptimal, solution to shaker positioning for this test.

A smaller error on the control gauge responses does not necessarily indicate a better test, as was shown in the analysis of number of shakers. The key assumption of IMMAT is that the entire structure behaves as it does in an environment if the control gauges are behaving as they do in the environment. While nearly zero error can be obtained on the control gauges autopower spectral density functions if the number of shakers is equivalent to the number of control gauges, it was found that the rest of the structure was actually performing less like it was in the environment than when only one shaker was used (which might be similar to the results obtained in a uniaxial shaker test). Practically, one may not be able to use 19 shakers on a single test, so the problem with square control might not be very applicable in this case, but this is an important consideration when performing this technique on structures where a smaller number of control gauges are available.

The optimum number of shakers to best match the validation gauges in this test was found to be 11, which is a bit more than half the number of control gauges. Alternatively, if a very large number of shakers could be used (30+), it would seem from this analysis that the error could be similarly reduced. Again, using one and a half times the number of shakers as control gauges may not seem practical for 19 control channels, but it may be for tests where there are a smaller number of control channels. Also of interest is the fact that when using a number of shakers larger than the number of control gauges the required force drops off fairly rapidly, so smaller, less-expensive shakers could potentially be used.

References

1. Daborn, P., Ind, P., Ewins, D.: Enhanced ground-based vibration testing for aerodynamic environments. Mech. Syst. Sig. Process. **49**(1), 165–180 (2014)
2. Daborn, P.M.: Scaling up of the impedance-matched multi-axis test (IMMAT) technique. In: Harvie, J.M., Baqersad, J. (eds.) Shock & Vibration, Aircraft/Aerospace, Energy Harvesting, Acoustics & Optics, vol. 9, Conference Proceedings of the Society for Experimental Mechanics Series, pp. 1–10. Springer, Cham (2017)
3. Mayes, R.L., Rohe, D.P.: Physical vibration simulation of an acoustic environment with six shakers on an industrial structure. In: Brandt, A., Singhal, R. (eds.) Shock & Vibration, Aircraft/Aerospace, Energy Harvesting, Acoustics & Optics, vol. 9, Conference Proceedings of the Society for Experimental Mechanics Series, pp. 29–41. Springer, Cham (2016)
4. Lawson, C.L., Hanson, R.J.: Solving Least-Squares Problems, chap. 23, p. 161. Prentice Hall, Upper Saddle River (1974)

Chapter 19
Comparison of Vibration Comfort Criteria by Controlled Field Tests on an Existing Long-Span Floor

Lei Cao and Jun Chen

Abstract Problems such as few field tests evidence and irrationality or absence of vibration limits exists in criteria and researches. This experimental study investigated perception thresholds (at the frequency of 5.354 Hz) and the magnitudes of sensation to vibrations caused by an electrical shaker. Linear relationship between vibration magnitude and perception probability has been found. Similar linear relationship exists between mean value of vibration indexes and subject sensation magnitudes. A logarithmic normal distribution of vibration magnitudes causing equal vibration sensation have been found. Limits of criteria are checked, such as ISO 2631/ISO 10137/DIN 4150-2/VDI 2057-1/ATC DG1 et al.

Keywords Field test · Vibration perception · Comfort criteria · Relationship · Distribution

19.1 Introduction

Many researches about vibration comfort had been carried out and lots of criteria had been issued. Still problems exist, such as the irrationality or absence of vibration limits in researches and criteria and too few researches were carried out in real buildings other than simulators [1]. Hence this research is focused on ensuring feasibility of field tests and finding a new way to show the limits of vibration, which provide limits of a certain type of people's feeling on different percentage levels.

19.2 Method

The test was carried out on a 12 m × 12 m floor near Tongji University. A VRS2-M001 vibration generator was fixed on the middle of the next floor to provide vibration in the vertical direction. Vibration sensors were disposed on the middle or 1/4 span of the floor and several participants sat or stood around it (Fig. 19.1). The output frequency was settled on 5.354 Hz.

Frequency weighting (W_k ISO 2631 and W_b BS 6841) was used to assess the influence of different frequency components [2]. The vibration stimuli were all 30-s duration sinusoidal vibrations (with 10-s pause at the end) at 34 power levels. The orders of stimuli was random and all stimuli were repeated twice.

The test was composed with 2 sessions. In Session 1, subjects gave their judgements about the vibration they had been through: assessed sensation magnitudes by making a score from '0' to '10', representing 'No feeling at all' to 'unbearable'; subjects assessed sensation magnitudes by giving semantic labels ('not perceptible', 'weakly perceptible', 'easily perceptible', 'strongly perceptible', 'unpleasant', 'quite unpleasant'). In Session 2, subjects gave their judges on perceiving vibration or not by making marks of '√' or '×' in all stimuli.

L. Cao
College of Civil Engineering, Tongji University, Shanghai, People's Republic of China

J. Chen (✉)
College of Civil Engineering, Tongji University, Shanghai, People's Republic of China

State Key Laboratory of Disaster Reduction in Civil Engineering, Tongji University, Shanghai, People's Republic of China
e-mail: cejchen@tongji.edu.cn

C. Walber et al. (eds.), *Sensors and Instrumentation, Aircraft/Aerospace, Energy Harvesting & Dynamic Environments Testing, Volume 7*, Conference Proceedings of the Society for Experimental Mechanics Series,
https://doi.org/10.1007/978-3-030-12676-6_19

Fig. 19.1 Test site on the second floor of Wumei Laboratory

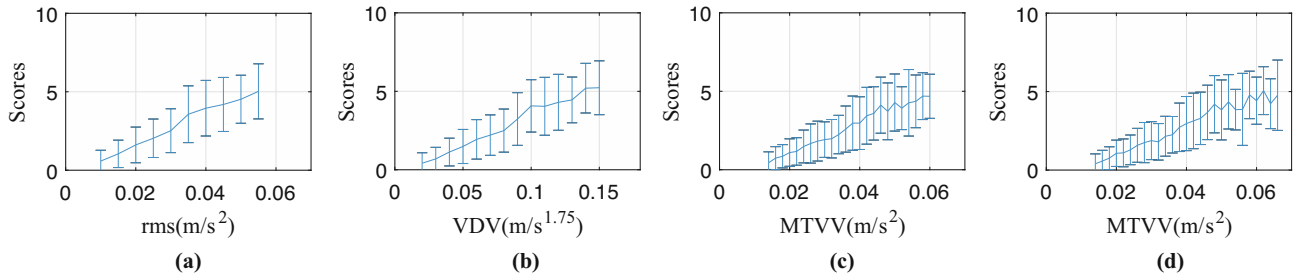

Fig. 19.2 Sitting position. μ and σ of scores corresponding to each group of vibration magnitudes weighted by W_k

Table 19.1 Coefficients of the standing situation (weighted by W_k, ISO 2631)

Index	a_1	b_1	adjrsquare	rmse
rms	76.1808	0.0259	0.9668	0.2133
VDV	28.3362	0.0894	0.9764	0.1842
1s MTVV	69.2729	−0.2378	0.9372	0.2532

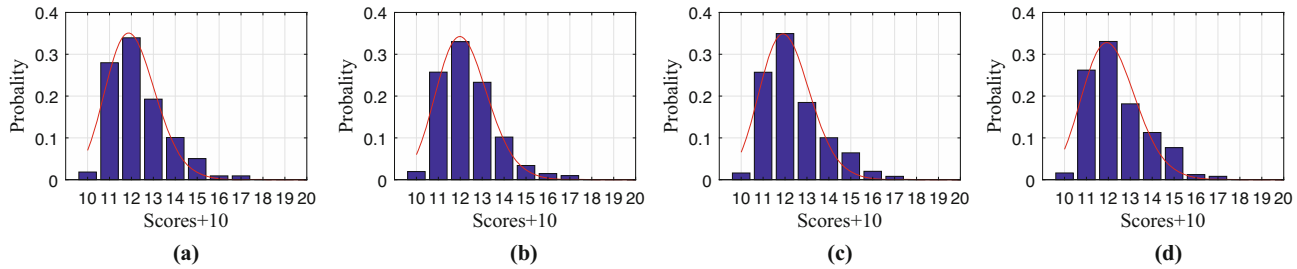

Fig. 19.3 Sitting position. Distribution of s (level 6). (**a**–**d**) represent for rms/VDV/1sMTVV/0.5sMTVV respectively

19.3 Results

Figure 19.2 shows the relationship between mean value of sensation magnitudes, E(s), and vibration magnitudes, v is a linear one.

$$v = a_1 \cdot E(s) + b_1 \tag{19.1}$$

v is the value of vibration magnitude (rms/VDV/MTVV); E(s) is the mean score; a_1/b_1 are fitting coefficients (Table 19.1).

The distribution of s on a certain v is showed in Fig. 19.3 and the range of v had been divided into 15 groups equally (Table 19.2).

$x = s + 10$, s is the score from $0 \sim 10$.

$$\ln x \sim N\left(\mu, \sigma^2\right) \tag{19.2}$$

Table 19.2 Coefficients of distribution on vibration magnitude of level 6 (0.0292 m/s^2 in rms weighted by ISO 2631-1)

Index	μ	σ	δ	rsquare	adjrsquare	KS test
rms	2.4829	0.0954	0.0384	0.9610	0.9567	0
VDV	2.4927	0.0968	0.0388	0.9810	0.9789	0
1s MTVV	2.4865	0.0956	0.0385	0.9506	0.9451	0

Table 19.3 Ranges of vibration magnitudes analyzed in the test

	rms	VDV	1s MTVV	0.5s MTVV
Vibration magnitude	0∼0.059 m/s^2	0∼0.164 m/s$^{1.75}$	0∼0.049 m/s^2	0∼0.051 m/s^2

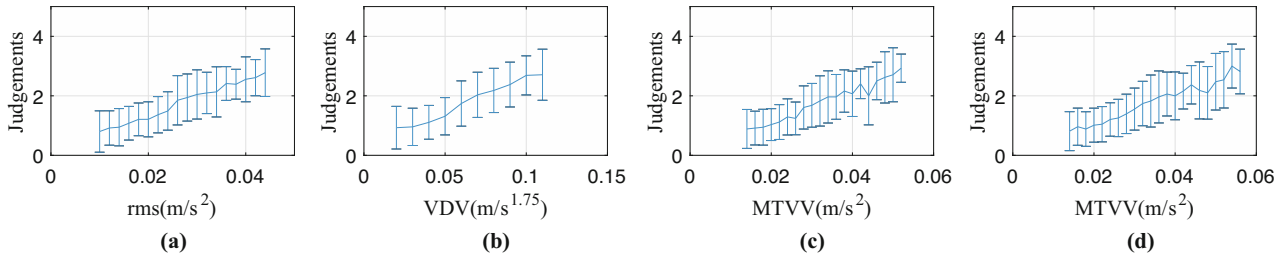

Fig. 19.4 Sitting position. μ and σ of judgements corresponding to each group of vibration magnitudes weighted by W_k

Table 19.4 Coefficients of the sitting situation (weighted by W_k, ISO 2631)

Index	a_2	b_2	adjrsquare	rmse
rms	60.4163	0.1374	0.9837	0.0830
VDV	22.6541	0.3311	0.9765	0.1128
1s MTVV	53.6722	0.0222	0.9618	0.1264

Table 19.5 Results of curve fitting (sitting gesture, weighted by W_b, BS 6841)

	a3	b3	adjrsquare	rmse
rms	51.7556	−0.1366	0.9290	0.0782
1s MTVV	37.3798	−0.1638	0.8857	0.0780
0.5s MTVV	37.5252	−0.2007	0.9207	0.0641

In this test, vibration magnitudes ranging from level 0 to level 10 (Table 19.3):
Figure 19.4 shows the relationship between semantic labels and vibration magnitudes:

$$E(j) = a_2 \cdot v + b_2 \tag{19.3}$$

j is the semantic label number given by subjects; a_2/b_2: coefficients. E(j) has a linear relationship with v. The data groups with high value of semantic judgements (>4) are very rare (Table 19.4).

It is found that there is a linear relationship between the perceptive percentages, p, and vibration magnitudes, v, if the capacity of sample in big enough:

$$p = a_3 \cdot v + b_3 \tag{19.4}$$

p: perceptive percentages; v: vibration magnitudes (Table 19.5).

The thresholds given by ISO 2631-1 [3] is lower than test, and the percentages of people perceiving vibration is set as 50% for perception threshold. In ISO 10137 [4], the thresholds is rational, but no percentages details are given. In ATC DG1 [5], the threshold is too high for the possibility to perceive is too high and no percentages details given. The threshold of perception (0.0036 m/s^2, rms) in DIN 4150-2 [6] fits well with the test since less than 2% of people will percept the vibration in the test. In VDI 2057-1 [7] the perception threshold (0.015 m/s^2 rms weighted by W_k) fits well with test but the limit of 0.01 m/s^2 for no one sensing vibration is too low. In BS 6472–1 [8], no detail of precise percentage is given, but 99.68% of people will tolerate vibration with v of 0.16 m/s$^{1.75}$ (VDV) by using the results of this test and it fits well with the criterion.

19.4 Conclusion

People have different s when they are in the same v. The parameters (μ and σ) of logarithmic normal distribution can be approached when the vibration magnitudes are known and interpolation is useful to get the σ if the value of v is not on the list. We can predict people's judgements about vibration and give the distribution of sensation magnitudes when the v is already known. The relationship between perception percentage and vibration magnitude is also linear and expressed in formula. Data from the sitting gesture fit better with the linear curve than standing. The perception threshold of sitting is lower than that in standing gesture. This conclusion match with previous studies [9]. But there is no clear relationship between peak values of vibration and percentages of perception. It is very difficult to compare results of different researches and criteria without knowing the percentage details of vibration comfort thresholds. But this problem can be fixed if the distribution of people's feeling about the same vibration is given.

Acknowledgments The authors would like to acknowledge the financial support provided by National Natural Science Foundation of China (51778465) and State Key Laboratory for Disaster Reduction of Civil Engineering (SLDRCE14-B-16). Moreover, the authors would like to thank all test subjects for participating in the project making possible the data collection.

References

1. Lamb, S., Kwok, K., Walton, D.: A longitudinal field study of the effects of wind-induced building motion on occupant wellbeing and work performance. J. Wind Eng. Ind. Aerodyn. **133**, 39–51 (2014)
2. Zhou, Z., Griffin, M.J.: Response of the seated human body to whole-body vertical vibration: discomfort caused by mechanical shocks. Ergonomics. **60**(3), 347–357 (2017)
3. International Organization for Standardization: Mechanical vibration and shock – evaluation of human exposure to whole-body vibration – Part 1: general requirements, ISO (1997)
4. International Organization for Standardization: Bases for design of structures – serviceability of buildings and walkways against vibrations, ISO (2007)
5. Applied Technology Council, Allen, D.E., Onysko, D.M., Murray, T.M.: ATC design guide . . . : Minimizing floor vibration. Applied Technology Council (1999)
6. Deutsches Institut für Normung: DIN 4150–2: structural vibrations–Part 2: human exposure to vibration in buildings (1999)
7. VDI: VDI 2057–1: human exposure to mechanical vibrations – Whole-body vibration (2002)
8. British Standard: Guide to evaluation of human exposure to vibration in buildings (2008)
9. Oborne, D.J., Clarke, M.J.: The determination of equal comfort zones for whole-body vibration. Ergonomics. **17**(6), 769–782 (1974)

Chapter 20
Flight Environments Demonstrator: Part III—Sensitivity of Expansion to Model Accuracy

Debby Fowler, Ryan A. Schultz, Brandon Zwink, and Brian C. Owens

Abstract The ability to extrapolate response data to unmeasured locations has obvious benefits for a range of lab and field experiments. This is typically done using an expansion process utilizing some type of transformation matrix, which typically comes from mode shapes of a finite element model. While methods exist to perform expansion, it is still not commonplace, perhaps due to a lack of experience using expansion tools or a lack of understanding of the sensitivities of the problem setup on results. To assess the applicability of expansion in a variety of real-world test scenarios, it is necessary to determine the level of perturbation or error the finite element model can sustain while maintaining accuracy in the expanded results. To this end, the structure model's boundary conditions, joint stiffness, and material properties were altered to determine the range of discrepancies allowable before the expanded results differed significantly from the measurements. The effect of improper implementations of the expansion procedure on accuracy is also explored. This study allows for better insights on prospective use cases and possible pitfalls when implementing the expansion procedure.

Keywords Expansion · Finite element model · Modal filter · Model calibration · Model updating

20.1 Introduction

The System Equivalent Reduction Expansion Process (SEREP) is a powerful, highly accurate technique allowing for the formulation of reduced order models and the expansion of test data to full field using a finite element (FE) model's mode shapes [1]. Past work has shown that SEREP allows for the accurate expansion of test data even when the FE model used for expansion has perturbed mass and stiffness, provided enough FE modes were included in the transformation matrix to span the space of the test modes [2]. Additionally, SEREP has been proven to accurately expand the time response of connected components using the individual component's mode shapes [3].

This paper aims to explore how perturbations of uncertain or tunable FE model properties and boundary conditions affect the expansion accuracy. Obviously, perturbations of properties and boundary conditions will affect the frequencies and mode shapes of the FE model, and therefore the accuracy of the expansion as the expansion transformation matrix is composed of a set of FE mode shapes. However, if the set of perturbed model shapes still spans the proper space, the expansion should be reliable. This paper considers both minor and significant changes to the FE model, including changes to the material properties as well as to the boundary conditions and joint stiffness. The expansion process is performed for these perturbed models to determine the sensitivity of the expansion process to the accuracy of the finite element model, and investigate methods to implement SEREP when confidence in the model is low. Additionally, common mistakes in the implementation of SEREP expansion are demonstrated and explained.

Sandia National Laboratories is a multimission laboratory managed and operated by National Technology and Engineering Solutions of Sandia, LLC., a wholly owned subsidiary of Honeywell International, Inc., for the U.S. Department of Energy's National Nuclear Security Administration under contract DE-NA0003525.

D. Fowler · R. A. Schultz (✉) · B. Zwink · B. C. Owens
Structural Dynamics and Environments Engineering Departments, Sandia National Laboratories, Albuquerque, NM, USA
e-mail: rschult@sandia.gov

C. Walber et al. (eds.), *Sensors and Instrumentation, Aircraft/Aerospace, Energy Harvesting & Dynamic Environments Testing, Volume 7*, Conference Proceedings of the Society for Experimental Mechanics Series,
https://doi.org/10.1007/978-3-030-12676-6_20

20.2 Theory

The SEREP expansion process utilizes a transformation matrix consisting of the mode shape values at the degrees of freedom (DOF) being expanded to ('n' DOF) and the points being expanded from ('a' DOF). The n-set DOF could be the entire set of FE DOF or a subset. The a-set are typically DOF in the model which match measurement locations from a test. The transformation matrix is calculated using:

$$[T] = [U_n]\,[U_a]^g, \tag{20.1}$$

where 'g' indicates a generalized inverse and the model mode shapes at a- and n-space are U_a and U_n, respectively. The transformation matrix can be used to expand test mode shapes from measured shapes, E_a, to full-field, expanded test shapes, E_n, with:

$$[E_n] = [T]\,[E_a]\,. \tag{20.2}$$

Similarly, time histories measured at a-DOF, x_a, can be expanded to all n-DOF via:

$$[x_n] = [T]\,[x_a]\,. \tag{20.3}$$

For this paper, the transformation matrix was calculated using the FE model's mode shape values at all model DOF so the test data could be expanded to full field.

The U_{12} matrix is a tool to project the mode shapes of a system at one state to the modal space of the system at another state. These states could be different perturbations of a model or a comparison of test mode shapes to model mode shapes. The U_{12} matrix will indicate how the modes of state 1 are used to combine to make the modes of state 2, and can be used to determine which model mode shapes need to be included in the SEREP transformation matrix when expanding test results. The U_{12} matrix is calculated using:

$$[U_{12}] = [U_1]^g\,[U_2]\,. \tag{20.4}$$

The Modal Assurance Criterion (MAC) is a vector correlation tool used to quantify the similarity between mode shape vectors [4]. The MAC is bounded between zero and one, with values near one indicating very similar modal vectors. The MAC is calculated using:

$$MAC_{ij} = \frac{\left[\{u_i\}^T\,\{e_j\}\right]^2}{\left[\{u_i\}^T\,\{u_i\}\right]\left[\{e_j\}^T\,\{e_j\}\right]}. \tag{20.5}$$

The Pseudo Orthogonality Check (POC) is a vector correlation tool that utilizes mass scaling in the correlation process. Similar to a MAC, values closer to 1 indicate high correlation. The POC is formulated as:

$$POC = [U_a]^T\,[M_a]\,[E_a] = [U_n]^T\,[M_n]\,[E_n] = [U_a]^g\,[E_a]\,. \tag{20.6}$$

Both MAC and POC will be used to compare the mode shapes of the finite element model to the test mode shapes and to compare the expanded shapes to the measured shapes. To compare time response, a time response assurance criterion, or TRAC, is used. A TRAC is simply a MAC except that the vectors are time histories rather than mode shapes. Similar to a MAC, a TRAC value near one indicates two time histories are very similar.

20.3 Test and Model Description

The Wedding Cake is a three-tiered structure consisting of three aluminum plates connected with columns made of ABS plastic, attached to a steel base plate. The Wedding Cake was instrumented with accelerometers at 37 DOFs and mounted to a seismic mass, shown in Fig. 20.1. An impact test was performed to retrieve mode shapes, which were later expanded to full field when studying mode shape expansion. Next, the Wedding Cake was excited using a 6DOF shaker to measure the

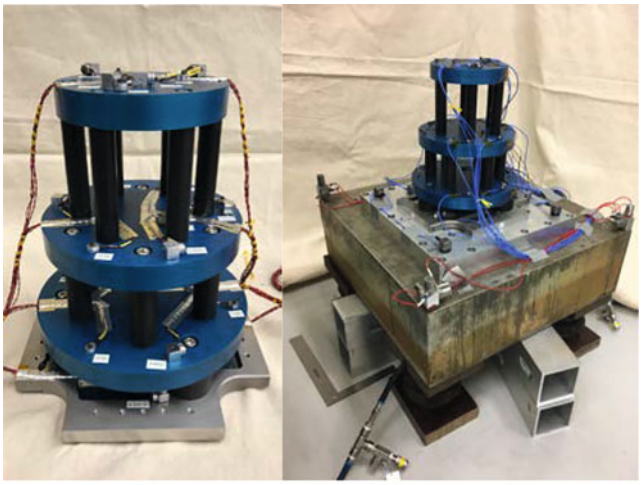

Fig. 20.1 Instrumentation (**a**) and impact test setup (**b**) for the Wedding Cake

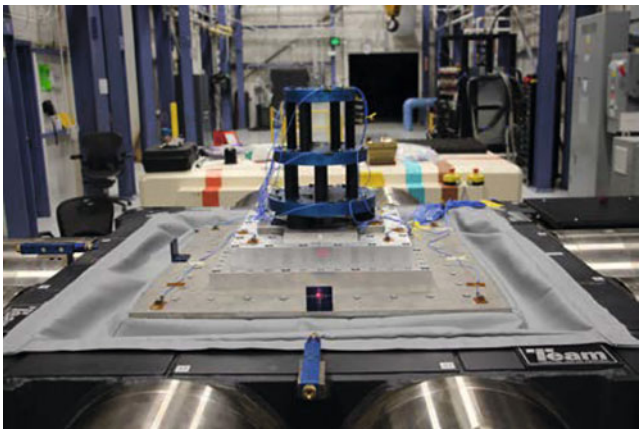

Fig. 20.2 6DOF shaker test setup for the Wedding Cake

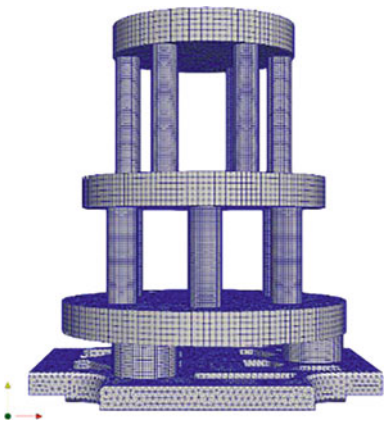

Fig. 20.3 Finite element mesh of the wedding cake

time response at the instrumented points, shown in Fig. 20.2. The time response was used when studying expansion of time response to full field.

A finite element model of the Wedding Cake was developed using the FE software Sierra/SD [5]. To simulate the fixed base boundary conditions, a point mass of 1e6 pounds was rigidly connected to the base plate. An eigen solution was performed to calculate mode shapes and frequencies, which were then used to form the SEREP transformation matrix in Eq. (20.1). The FE mesh is shown in Fig. 20.3.

20.4 Results of Expansion with Original Model

The mode shapes determined from the impact test described in Sect. 20.3 were expanded using the full-field mode shapes from the FE model. The MAC comparing the model's mode shapes to the test's mode shapes is shown in Fig. 20.4a, and indicates that a variety of the test modes retrieved did not correspond to a single FE mode. This could be due to several factors, including uncertainties in the mode shape extraction process resulting in shapes that were rotated incorrectly, or discrepancies between the model and the test structure. With a round symmetric structure like the Wedding Cake, mode shapes can be clocked arbitrarily which cannot be predicted by a model and this could be a contributing factor to the correlation results shown. Regardless of the reason for apparent poor correlation, the significance is that for many of the test mode shapes being expanded there is not a single FE mode that would perfectly describe the extracted behavior so a combination of FE mode shapes will be needed to expand the test mode shapes.

To understand which FE mode shapes will be used to expand each test mode shape, the U_{12} matrix shown in Fig. 20.4b can be used. The U_{12} details exactly which FE modes will be combined to describe each experimental mode shape and indicates that the shapes that appear in the MAC to be poorly correlated to the model can be approximated using multiple FE modes.

The expansion process was conducted using FE modes 1–24 and 34. Note that modes 25–33 represent local column modes which are not measured by the instrumentation used in the test. This set of modes was determined using the U_{12} matrix. The U_{12} matrix indicates this set of modes spans the space of the modes of interest and that the measured DOF sufficiently describe these modes. An optimization method was used to select 30 of the test DOF that optimized the independence between the mode shape vectors to be used in the expansion process. The first 25 test modes were expanded from the selection of measured points to full-field using the SEREP expansion process detailed in Eq. (20.2) and the results were compared to all 37 measured test points to determine the accuracy of the expansion. The MAC and POC comparing the expanded test mode shapes to the measured test mode shapes are shown in Fig. 20.5. They indicate excellent correlation between the expanded and measured behavior, which means that the finite element model modes used in the transformation matrix were able to span the space of the test modes and properly expand the test mode shapes.

The time response from the 6DOF shaker test was expanded to full-field using the same selection of measurement points and FE modes using Eq. (20.3). A low-pass filter was applied to the time response up to 1800 Hz to reduce the effect of high frequency response that cannot be described by the expansion process due to the modes in the transformation matrix. Figure 20.6a details the comparison between the measured time response and the expanded time response for a gage located on the second tier, and Fig. 20.6b shows the comparison of the power spectral densities (PSDs) of the measured and expanded accelerations at that gage. This gage, labeled 214X+, was not in the a-set. Figure 20.6 shows the TRAC values comparing the measured results to the expanded results for each test point, which indicate the expansion process successfully expanded the time response for most of the test points. In the TRAC plot in Fig. 20.6, bars in red indicate DOF used in the a-set and bars in blue represent expanded DOF (DOF not in the a-set).

While the expansion results shown were successful, it is important to consider the factors that go into successfully expanding test data. The two largest forms of error when utilizing the SEREP expansion process are not including enough

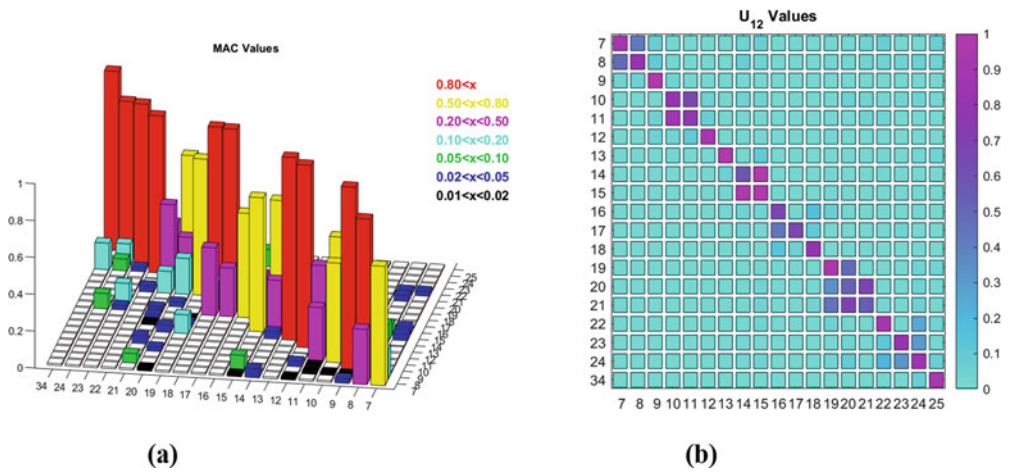

Fig. 20.4 MAC (**a**) and U_{12} matrix (**b**) comparing FE mode shapes to test mode shapes

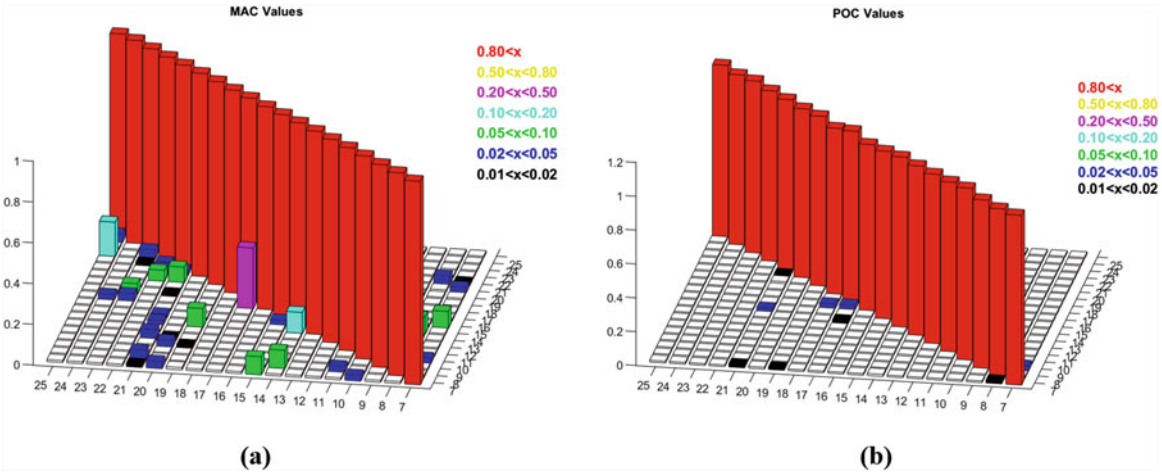

Fig. 20.5 MAC (**a**) and POC (**b**) comparing expanded mode shapes to measured mode shapes

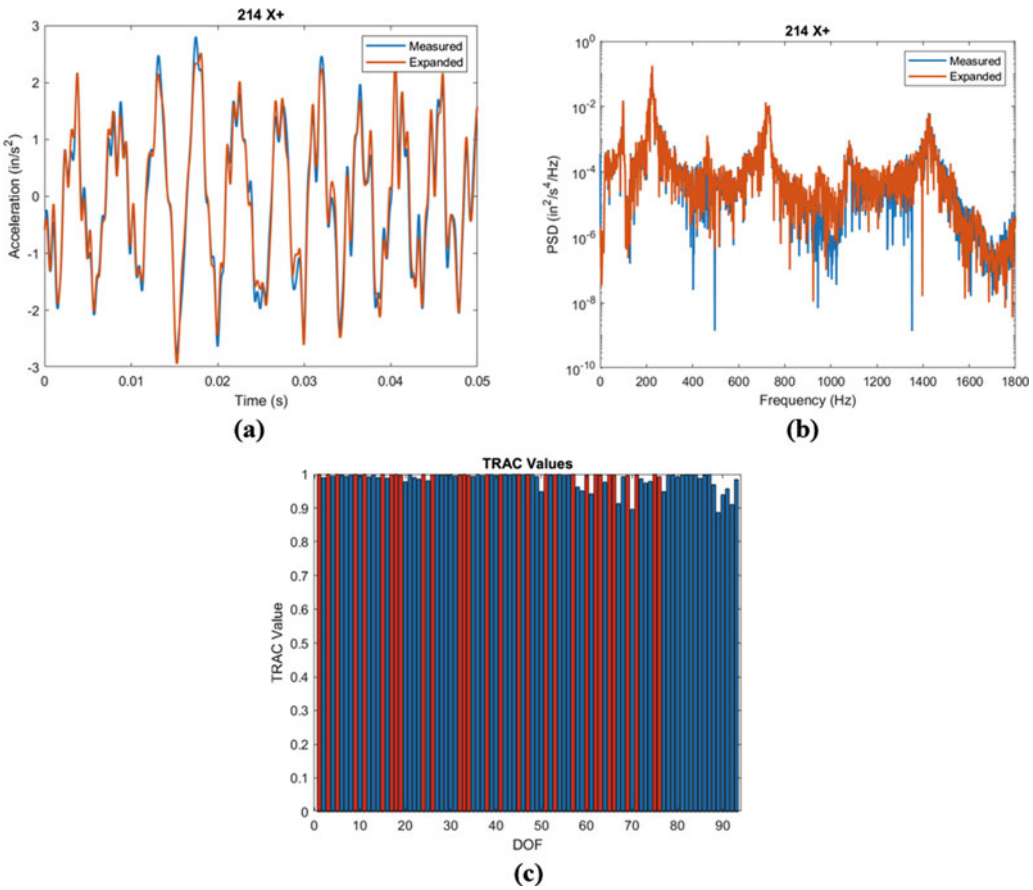

Fig. 20.6 Expanded response at a single gage, DOF 214X+ in terms of time history (**a**) and PSD (**b**), along with a TRAC (**c**) comparing expanded time response to measured time response at many DOF

DOF to fully describe the modes included in the transformation matrix, and not including enough modes to span the space of the test response or shape data. The following two examples show the consequences when these guidelines are not followed.

Modes 25–33 and modes 35–40 of the Wedding Cake were dominated by column motion and not adequately differentiated by the instrumentation because there was no instrumentation on the columns. For this reason these modes were originally excluded from the expansion process. Figure 20.7 shows the expansion results when modes 1–40 are all included in the expansion process. The MAC in Fig. 20.7a comparing the model to the test shows that the column modes were not

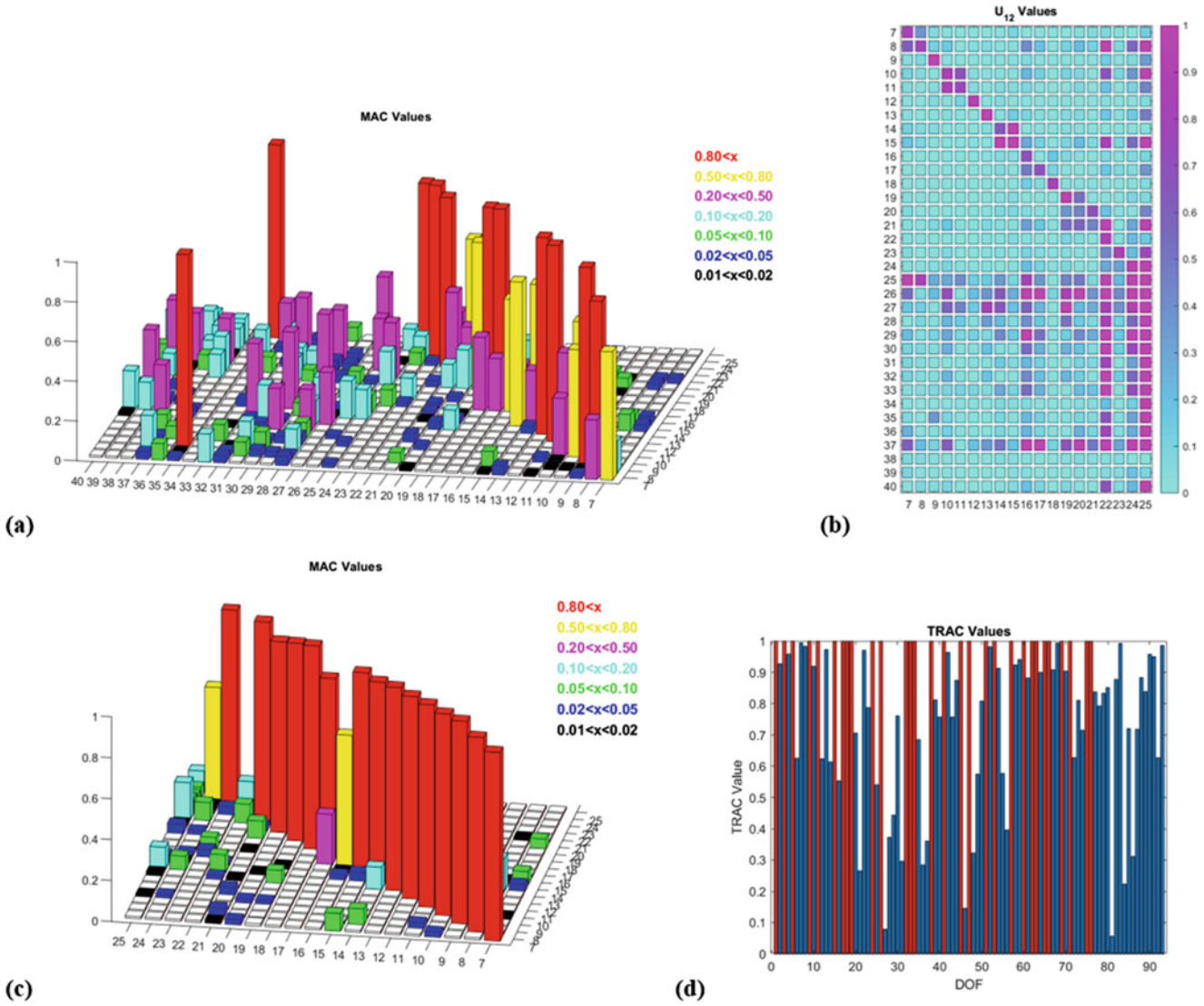

Fig. 20.7 Expansion when Modes 1 to 40 are included. MAC (**a**) and U_{12} (**b**) comparing model to test; MAC comparing expanded mode shapes to test mode shapes (**c**); TRAC comparing expanded time history to measured time history (**d**)

differentiated by the included DOF. The U_{12} matrix shows that because the modes can't be differentiated, the expansion process utilized many column modes to describe test modes inappropriately, resulting in the poor expansion results shown in the MAC comparing the expansion results to the test mode shapes, Fig. 20.7b. One item to note is that the four worst expanded test modes according to the MAC (modes 16, 22, 24, and 25) also were the modes that the U_{12} matrix indicated included the most column modes in the expansion process. The TRAC in Fig. 20.7d also indicates that the majority of test point's behavior was not expanded accurately. Overall, including mode shapes that the included DOF cannot differentiate between results in poor expansion results because the transformation into modal space is incorrect.

To demonstrate how the modes in the transformation matrix must span the space of the measured response, FE mode 11 was excluded from the expansion process. The U_{12} matrix from Fig. 20.4b shows that mode 11 was a strong contributor to the approximation of test modes 10 and 11, so the expectation would be that the excluding mode 11 would result in poor expansion results for test modes 10 and 11 but would not significantly affect the rest of the expanded modes. These results are detailed in Fig. 20.8. The U_{12} matrix shows that in the absence of FE mode 11, the behavior that was previously described by mode 11 is now being described by modes 7 and 17, both of which were not used in previous expansion processes and are not sufficient to approximate the behaviors of test modes 10 and 11. The MAC comparing the expansion results to the measured results show poor correlation for test modes 10 and 11, and the TRAC comparing the expanded time response to the measured time response show a significant degradation in expansion accuracy for many of the points. When there are

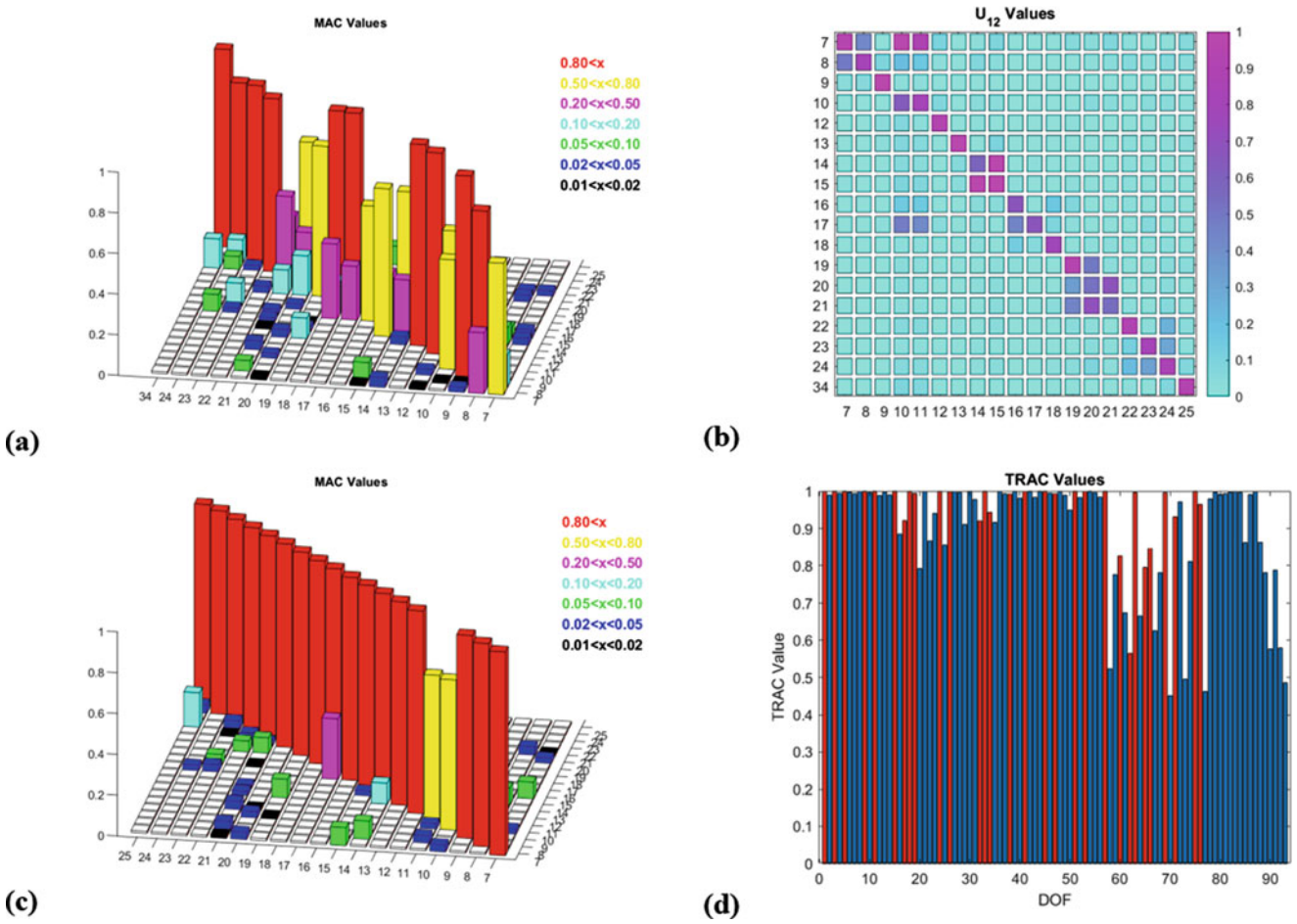

Fig. 20.8 Expansion when FE Mode 11 is excluded. MAC (**a**) and U_{12} (**b**) comparing model to test; MAC comparing expanded mode shapes to test mode shapes (**c**); TRAC comparing expanded time history to measured time history (**d**)

not enough modes included in the expansion process to span the space of the test data, only the modes shapes that need additional information to be described are significantly affected, whereas the time response is affected as a whole because it is the result of a superposition of modal responses.

20.5 Results of Expansion with Perturbed Model Modes

A series of perturbed models were used to generate new transformation matrices. These new transformation matrices were then used to expand test data in order to explore SEREP's sensitivity to typical model inaccuracies. These inaccuracies are commonly corrected by "tuning" the finite element model. The perturbed models described in this paper include: increasing the Young's Modulus of the abs plastic columns by 20%, increasing the density of the plastic columns by 10%, dividing the joint stiffness between the columns and each tier by 100, and using free-free rather than fixed boundary conditions. Table 20.1 shows each model's natural frequencies for the first five flexible modes included in the expansion process. The free-free model and the model with decreased joint stiffness had the largest difference in frequency compared to the original model, which also corresponded to a larger discrepancy in mode shapes. For each case, the perturbed model was compared to the original model and then the perturbed model mode shapes were used in the transformation matrix to expand both test mode shapes and time history data.

The first two perturbed models considered were alterations to the material properties of the ABS plastic columns: increasing the Young's Modulus of the ABS plastic columns by 20%, and increasing the density of the plastic columns by 10%. The results from using these perturbations to expand the test results are shown in Figs. 20.9 and 20.10, respectively.

Table 20.1 Comparison of frequencies of included modes across model perturbations

	Natural frequencies of perturbed models (Hz)				
Mode #	Original	Young's Modulus + 20%	Density + 10%	Joint stiffness*(1/100)	Free-Free
7	98.2	107.0	97.8	67.7	145.5
8	98.2	107.0	97.9	67.7	159.6
9	138.9	151.9	138.2	122.0	160.0
10	227.8	248.2	227.0	173.6	264.0
11	227.8	248.3	227.0	173.6	285.7

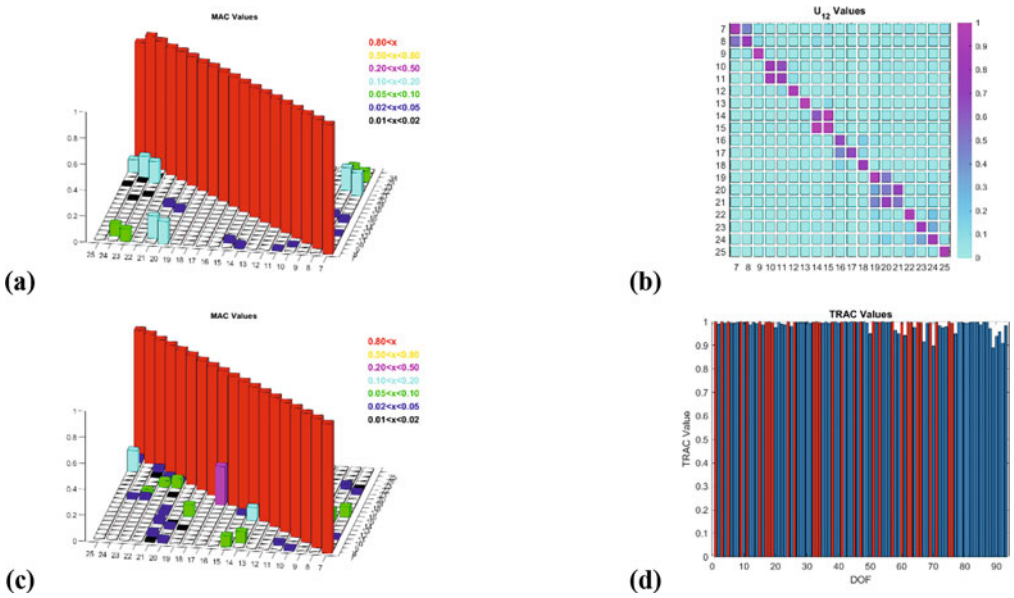

Fig. 20.9 Expansion using model perturbed by increasing the Young's Modulus of the Columns by 20%. MAC comparing perturbed model to original model (**a**); U_{12} comparing model to test (**b**); MAC comparing expanded mode shapes to test mode shapes (**c**); TRAC comparing expanded time history to measured time history (**d**)

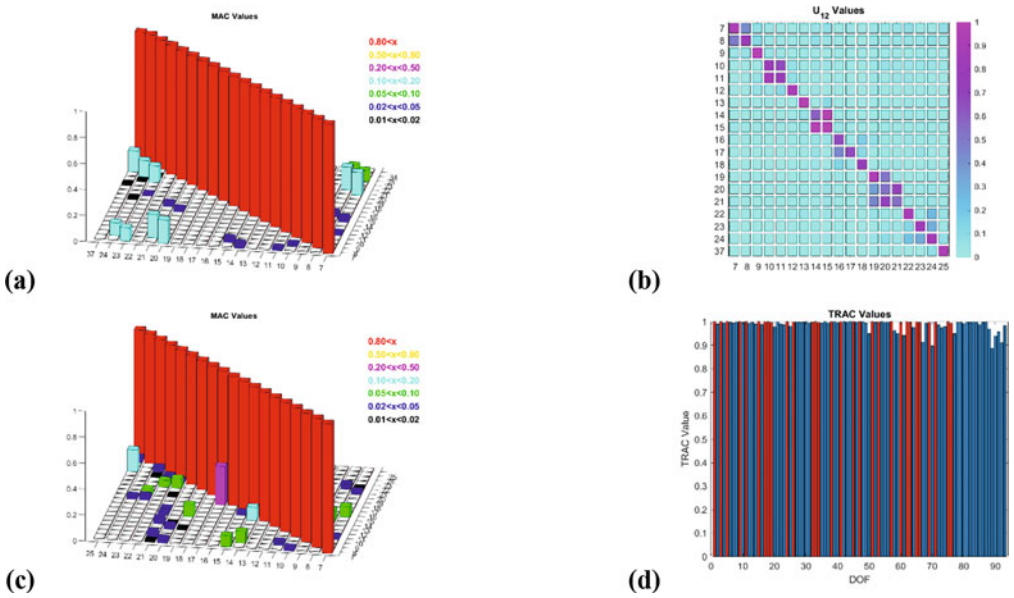

Fig. 20.10 Expansion using model perturbed by increasing the density of the columns by 10%. MAC comparing perturbed model to original model (**a**); U_{12} comparing model to test (**b**); MAC comparing expanded mode shapes to test mode shapes (**c**); TRAC comparing expanded time history to measured time history (**d**)

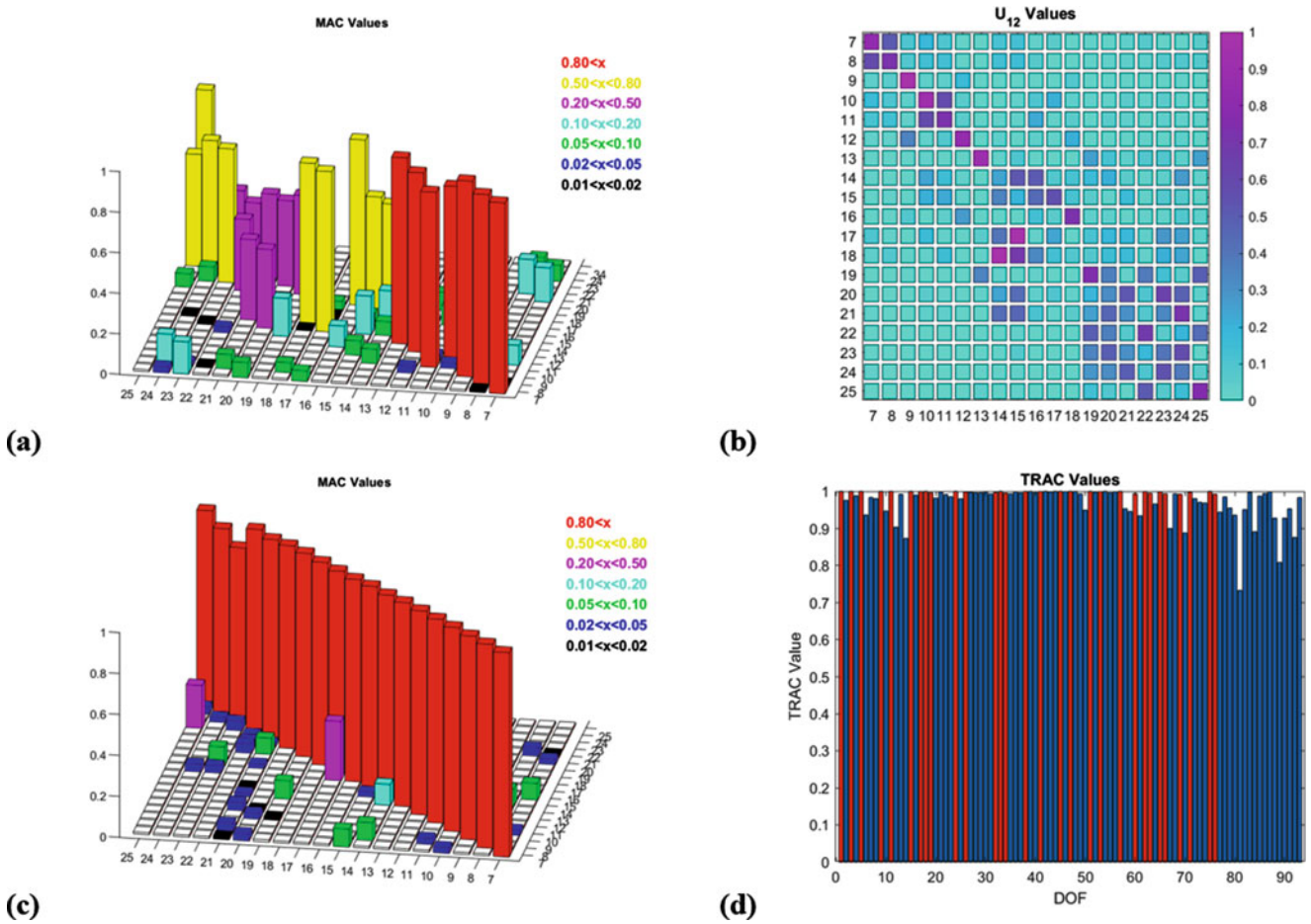

Fig. 20.11 Expansion using model perturbed by dividing tied joint stiffness by 100. MAC comparing perturbed model to original model (**a**); U_{12} comparing model to test (**b**); MAC comparing expanded mode shapes to test mode shapes (**c**); TRAC comparing expanded time history to measured time history (**d**)

When comparing the mode shapes of these perturbations to the original model, there appears to be larger discrepancies for the increased Young's Modulus case than the increased density case but overall both perturbed models have similar mode shapes to the original model. These minor changes to material properties did not have a large effect on the model mode shapes, so both model perturbations result in highly accurate expansion results, with no significant difference from the original model's expansion results. This indicates that the expansion process is not highly sensitive to the common range of error for material properties that results in slightly different mode shapes but still has the information needed to span the space of the test behavior.

A more drastically perturbed model was created by dividing the joint stiffness between the columns and tiers by 100. It is unlikely that this amount of error would exist in a model, but this perturbation is a good example of a model where the modes are significantly different from the test hardware. The results of using this model's mode shapes in the expansion process are shown in Fig. 20.11. A comparison of the perturbed model to the original model shows that the modes shapes are very different, Fig. 20.11a. The U_{12} matrix indicates that a much larger number of finite element model modes are needed to approximate each test mode. The expansion results are still excellent for the majority of the modes, with a decrease in accuracy for modes 23 and 24. This decrease in accuracy is due to not including enough FE modes to span the space of those test modes. Since more FE modes are needed to describe each test mode, if additional FE modes were included in the expansion process these higher order modes would be more fully described. However, the limiting factor in how many modes that can be included is the number of DOFs that are being expanded from – which leads to the conclusion that if there is less confidence in the FE model used for expansion, it would be advantageous to include more optimized DOF in the transformation matrix so that more modes can be included.

The final model perturbation was a significant change in the model boundary conditions from a fixed-free to a free-free condition. The free-free model was created by removing the point mass that was used to simulate a fixed condition. The

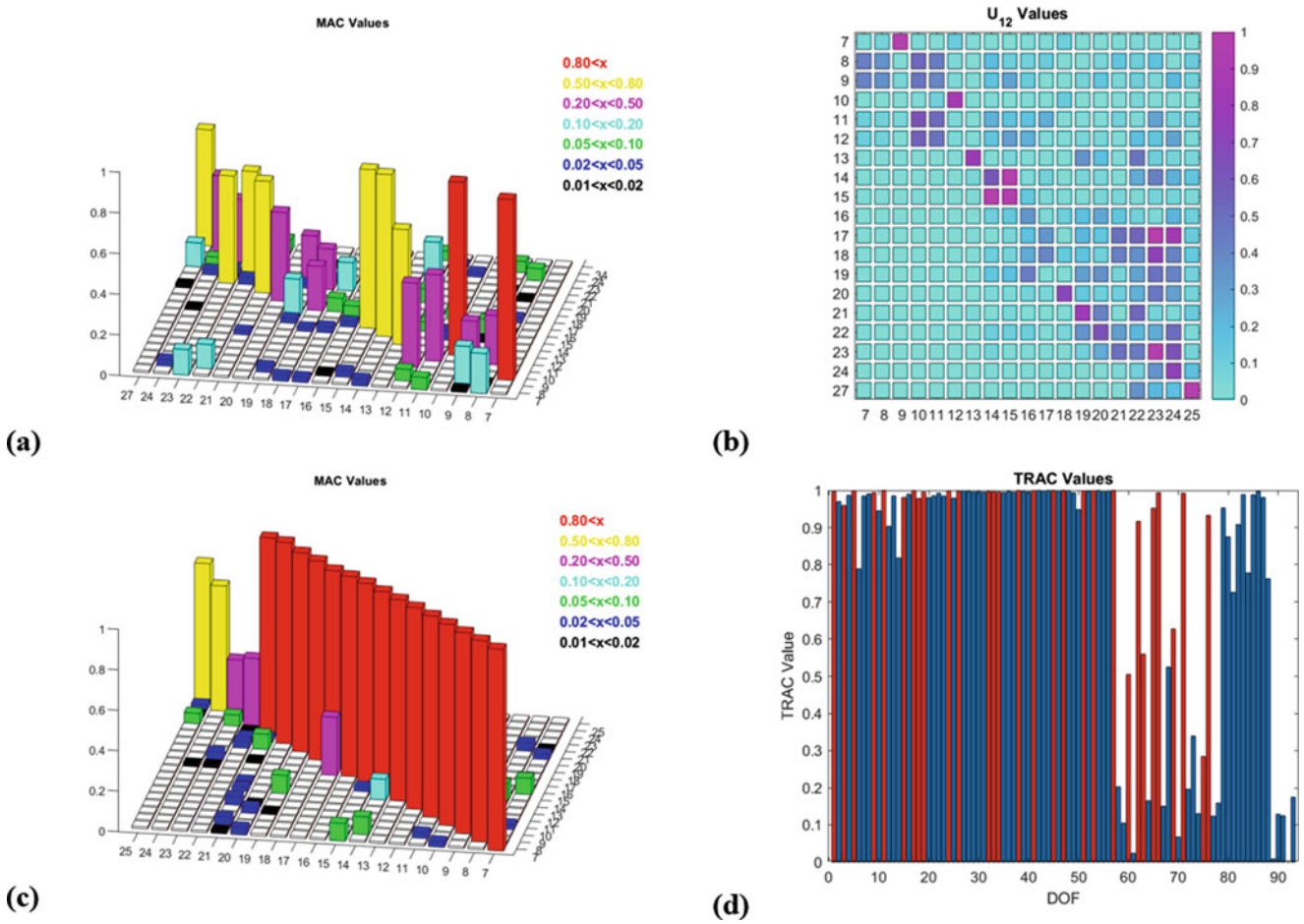

Fig. 20.12 Expansion using free-free Model. MAC comparing free-free model to original model (**a**); U_{12} comparing model to test (**b**); MAC comparing expanded mode shapes to test mode shapes (**c**); TRAC comparing expanded time history to measured time history (**d**)

test data was with the Wedding Cake attached to a seismic mass, so the fixed model was a much better representation of the boundary conditions during the test. The results for the expansion using the free-free model are shown in Fig. 20.12. The comparison of the free-free model to the original fixed model shows extremely different mode shapes, as would be expected. The U_{12} matrix indicates that many of the free-free model modes are needed to approximate any of the test modes. The comparison of the expanded test mode shapes to the measured test mode shapes show highly accurate expansion for the first 21 modes, but poor expansion for the last four modes. The poor expansion in higher order modes is due to not including enough free-free modes to span the space of the fixed base test modes. These results are similar to the findings from the joint stiffness case. The more perturbed the model is from the test setup and test structure, the more model modes are needed to span the space of the test setup. However, the more FE modes are included in the transformation matrix, the more DOF are needed in order to fully describe the included modes. This indicates if there is less certainty in the model used for expansion, it is advantageous to include more measurement points so that more model modes can be included.

20.6 Conclusions

A series of model perturbations were used to expand test mode shapes and time histories in order to explore the sensitivity of the SEREP expansion method to the common sources of inaccuracy in complex finite element models. The accuracy of the expansion was not affected by the common range of error in material properties which did not result in significant mode shape differences. For more extreme examples of modeling error that resulted in significant differences in mode shapes, the accuracy of higher order mode expansion was affected because not enough mode shapes were included to fully describe the

test's behavior. This error can be reduced by increasing the test DOF so that additional mode shapes can be included. The U_{12} matrix was used to understand how the model modes were combined to approximate the test mode's behavior, and is a useful tool to determine which modes need to be included in the expansion process. Additionally, examples where the DOF were insufficient to describe the modes included in the expansion process and where the included modes did not span the space of the test data were shown.

While the SEREP expansion process is not highly sensitive to small model inaccuracies causing small shape errors, the technique needs to be properly implemented in order to work well. The expansion will not be accurate if the modes included in the transformation matrix do not span the space of the test response. Additionally, the a-set DOF much be chosen to fully describe those modes in the transformation matrix. The more different the model is from the test the more modes will need to be included in order to achieve an accurate expansion, but the fundamental principles for implementing the technique do not change.

References

1. O'Callahan, J., Avitabile, P., Riemer, R.: System equivalent reduction expansion process (SEREP). In: Proceedings of the 7th International Modal Analysis Conference (IMAC VII), Las Vegas, NV (1989)
2. Thibault, L., Butland, A., Avitabile, P.: Variability improvement of key inaccurate node groups – VIKING. In: Conference Proceedings of the Society for Experimental Mechanics Series, Jacksonville, Florida (2012)
3. Harvie, J., Avitabile, P.: Computationally efficient nonlinear dynamic analysis for stress/strain applications. In: Special Topics in Structural Dynamics, Volume 6: Proceedings of the 32nd IMAC, A Conference and Exposition on Structural Dynamics, Orlando, FL (2014)
4. Avitabile, P.: Modal model correlation techniques. University of Massachusetts Lowell, Lowell, MA (1998)
5. Sierra Structural Dynamics Development Team: Sierra structural dynamics – user's notes, Sandia National Laboratories SAND Report (2015)

Chapter 21
A Demonstration of Force Estimation and Regularization Methods for Multi-Shaker Testing

Ryan A. Schultz

Abstract Design of multiple-input/multiple-output vibration experiments, such as impedance matched multi-axis testing and multi-shaker testing, rely on a force estimation calculation which is typically executed using a direct inverse approach. Force estimation can be performed multiple ways, each method providing some different tradeoff between response accuracy and input forces. Additionally, there are ways to improve the numerics of the problem with regularization techniques which can reduce errors incurred from poor conditioning of the system frequency response matrix. This paper explores several different force estimation methods and compares several regularization approaches using a simple multiple-input/multiple-output dynamic system, demonstrating the effects on the predicted inputs and responses.

Keywords Multiple-input/multiple-output · Force estimation · Regularization · Conditioning · Vibration testing

21.1 Introduction

Multiple-input/multiple output (MIMO) vibration testing is steadily increasing in usage and popularity among the dynamic testing community. Techniques such as the impedance-matched multi-axis test (IMMAT) method have shown great promise in using multiple shaker inputs to achieve good agreement to the response of dynamic systems in complicated environments, such as acoustic environments [1, 2]. These tests rely on MIMO control systems to determine the shaker inputs based on the system frequency response function (FRF) matrix and the target responses, typically in the form of a cross-power spectral density (CPSD) matrix. An input or force estimation method is used to invert that FRF matrix and provide an estimate of the inputs which matches the target responses [3, 4].

Inverting the FRF matrix introduces errors into the estimated inputs if the FRF matrix is poorly conditioned, which is typically the case for most dynamic systems. The condition number typically peaks at modes of the system, where the system response is dominated by a single mode. Numerical corrections, called regularization, can be used to change the FRF matrix to reduce the condition number and reduce the errors in the input estimation [5–7]. The objective of a good regularization scheme is to change the FRF matrix enough that errors will be small, while not changing it so much that it loses the important dynamics or changes the overall form of the matrix. The FRF matrix is inverted and regularization is applied on a frequency line by frequency line basis. Here, singular value and Tikhonov regularization methods are demonstrated on a simple MIMO dynamic system, a thin aluminum plate with multiple shaker inputs.

There are multiple force estimation methods, three of which are explored here: the standard direct method, the independent drives method, and the buzz test method [8, 9]. Each method is used to determine shaker inputs to replicate the response of the plate model to an acoustic, distributed pressure environment. The responses are compared at target (i.e. control) locations and reference (i.e. non-control) locations in terms of the auto-power spectral density (APSD) as well as coherence and phase between response points.

Sandia National Laboratories is a multimission laboratory managed and operated by National Technology and Engineering Solutions of Sandia, LLC., a wholly owned subsidiary of Honeywell International, Inc., for the U.S. Department of Energy's National Nuclear Security Administration under contract DE-NA0003525.

R. A. Schultz (✉)
Structural Dynamics Department, Sandia National Laboratories, Albuquerque, NM, USA
e-mail: rschult@sandia.gov

C. Walber et al. (eds.), *Sensors and Instrumentation, Aircraft/Aerospace, Energy Harvesting & Dynamic Environments Testing, Volume 7*, Conference Proceedings of the Society for Experimental Mechanics Series,
https://doi.org/10.1007/978-3-030-12676-6_21

21.2 Example Dynamic System and FRFs

For this study, a model-based approach is used because the system FRF can easily be modified to examine the effects of different input or output locations. Here, a free-free 12 inch by 24 inch by ¼ inch aluminum plate is the dynamic system. The finite element (FE) model of the plate uses only out-of-plane displacements, so there are three degrees of freedom (DOF) per node. Forty modes were computed which covers a frequency range up to 2800 Hz, sufficient for the 2000 Hz bandwidth of interest for this study. This bandwidth covers both low and high modal density regions. Modal damping is used with values between 0.2 and 1.0%, increasing with mode frequency and FRFs are computed from the modes using a modal FRF calculation.

21.3 Condition Number of the FRF Matrix

The first study examines how the system inputs, outputs, damping and noise affect the condition number of the FRF matrix. It is widely understood that a "bad" condition number causes errors when doing an inversion of the FRF matrix. The first step is to understand what causes the condition number of the matrix to change. The next step, discussed in Sect. 21.4, is to understand how a "bad" condition number translates to errors in the predictions when using an inverse of the FRF matrix in a force estimation process.

The condition number of a matrix is simply the ratio of the largest and smallest singular values. Large singular values indicate large, independent contributions to the overall matrix. For example, the singular values of a response matrix can identify the number of intendent sources which caused the response. For a FRF matrix, the singular values roughly indicate the number of contributing modes at a given frequency line. This is shown in the plots in Fig. 21.1, where an example FRF is shown as a sum of modal contributions. Take for example the region around 800 Hz, where the FRF is dominated by a single mode. Around 800 Hz, the condition number becomes large and there is one large singular value and several small singular values. Between peaks in the FRF, there are several modes which contribute at similar levels and also several singular values of similar levels.

21.3.1 Number and Location of Inputs or Outputs

As condition number is a measure of independence of the vectors in a matrix, the input and output locations of a FRF matrix will therefore affect the condition number. For example, if the input or output locations are very similar or tightly-packed, the FRFs for each location will be approximately similar and therefore less independent and the condition number will be large. Conversely, if the input or output locations are chosen to have good independence, then the condition number

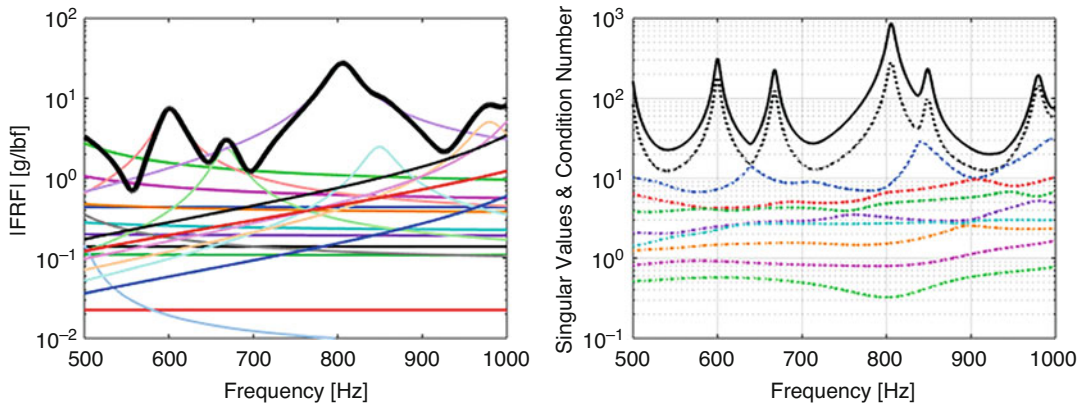

Fig. 21.1 Left: FRF (black, bold) shown as a sum of modal contributions (colors, thin). Right: Singular values (colors, dotted) and condition number (black, solid)

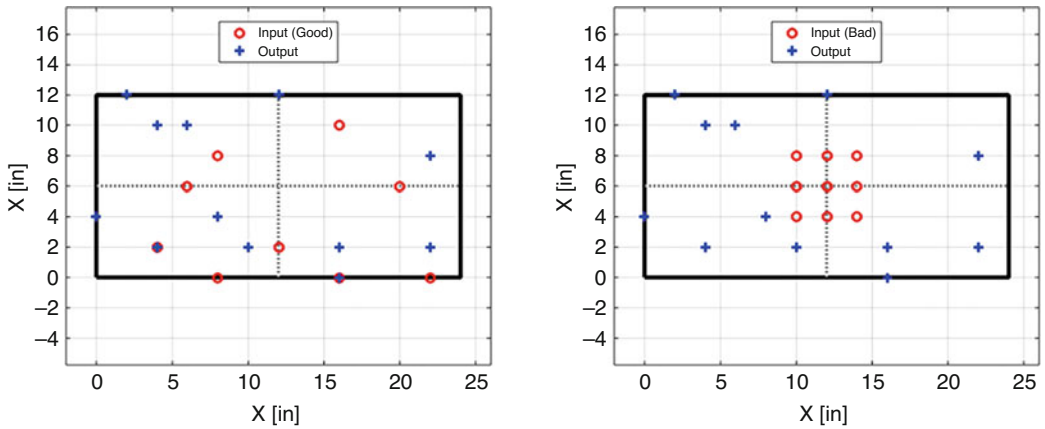

Fig. 21.2 Plate model with 12 outputs and 9 inputs. Left: 9 "good" input locations. Right: 9 "bad" input locations

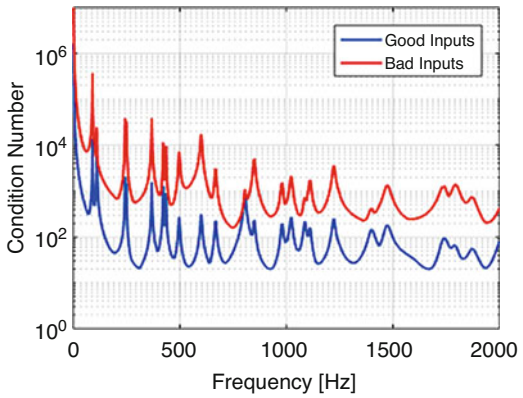

Fig. 21.3 Condition number of FRF matrix with "good" and "bad" input locations

will be smaller. There are various methods to choose gage locations to achieve good independence, such as methods based on effective independence, condition number minimization or minimizing the off-diagonal terms in the modal assurance criterion (MAC) matrix [10–12].

To demonstrate how input or output locations affect condition number, two systems were contrived, each with 12 outputs and nine inputs. The "good" system has nine input locations chosen with a condition number minimization method, resulting in a set of inputs that have good independence. The "bad" system has nine input locations chosen very close together, which should make the FRFs for those inputs very similar (i.e. not independent). Input and output locations for these systems are shown below in Fig. 21.2. The condition number computed from the FRF matrices of these two systems is shown in Fig. 21.3. Clearly, the "good" system has a much lower condition number than the "bad" system, by around an order of magnitude over the entire bandwidth.

Next, the number of inputs and outputs was changed for the "good" system to demonstrate how adding or removing an input or output affects condition number. The inputs and outputs to add or remove were not chosen using any method, they were simply chosen without analysis. The results, shown in Fig. 21.4, are interesting: removing a gage reduces the condition number, but adding an input or output may increase or decrease the condition number. It is not simply the number of inputs or outputs which determines the condition number. More important are the locations of the inputs and outputs—those locations, as a set, need to be independent.

21.3.2 Higher Damping

Next, the damping of the system was increased to observe how damping affects condition number. Here, the modal damping was increased by a factor of four for all modes. Figure 21.5 shows that increasing damping reduces the condition number at peaks in the FRF. Interestingly, the condition number is not affected between peaks, which is consistent with how damping affects the FRF amplitude.

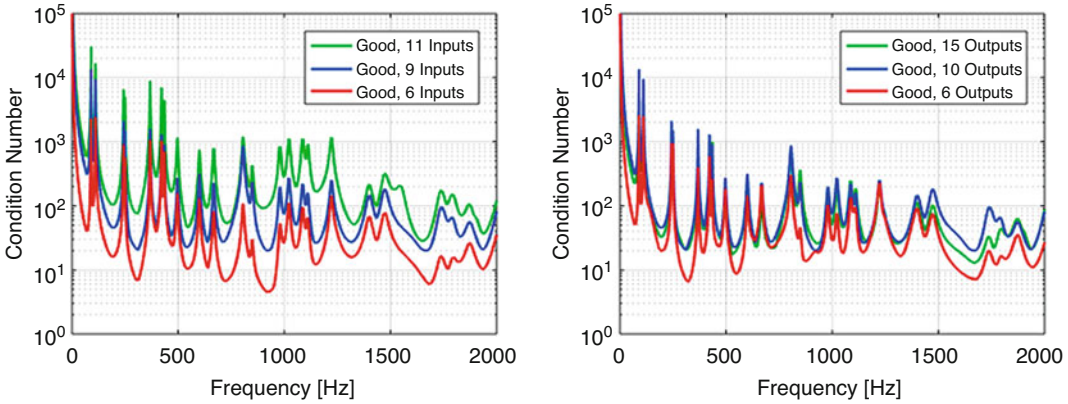

Fig. 21.4 Left: Condition number with different number of inputs (6 vs. 9 vs. 11). Right: Condition number with different number of outputs (6 vs. 10 vs. 15)

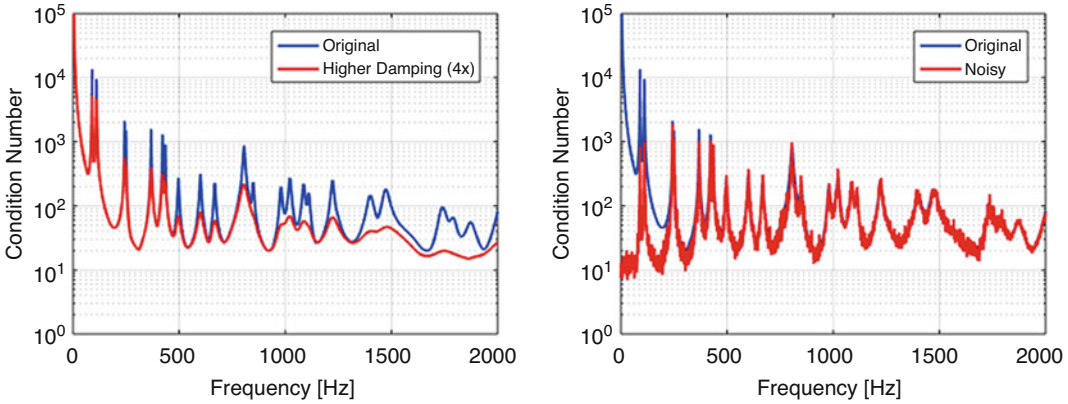

Fig. 21.5 Left: Condition number with higher damping. Right: Condition number with noise of the FRFs

21.3.3 Noise on the FRFs

To examine the effects of noise, the FRFs are transformed to impulse responses with an inverse Fourier transform. Then, independent Gaussian noise is added to each impulse response. Finally, the noisy impulse response is transformed back to an FRF with the Fourier transform. This provides noisy FRFs which look like typical test data, where the peaks are cleanly represented but the noise contaminates the valleys and anti-resonances.

Adding noise to the FRFs resulted in approximately the same condition number as the original system, except for the first couple of peaks. This indicates that simply having noise on the FRF estimates does not cause the condition number to increase. In this case, the noise is uncorrelated for each FRF in the matrix. One could imagine if the noise were correlated, as is the case with 60 Hz noise, then the condition number would be increased as the vectors would become less independent.

21.4 Errors Due to Poor Conditioning

Now that the condition number of the FRF matrix has been examined, the next step is to demonstrate how a poor condition number affects results. The general process is to use the measured FRF matrix in a force estimation calculation to estimate the inputs to achieve some desired response of the system. This force estimation generally uses an inverse (or pseudo-inverse) of the FRF matrix. Inverting poorly conditioned matrices causes problems in that noise is propagated or amplified through the poorly-estimated features in the FRF. This is typically shown using perturbation theory where the example system is [13]:

$$Ax = b. \tag{21.1}$$

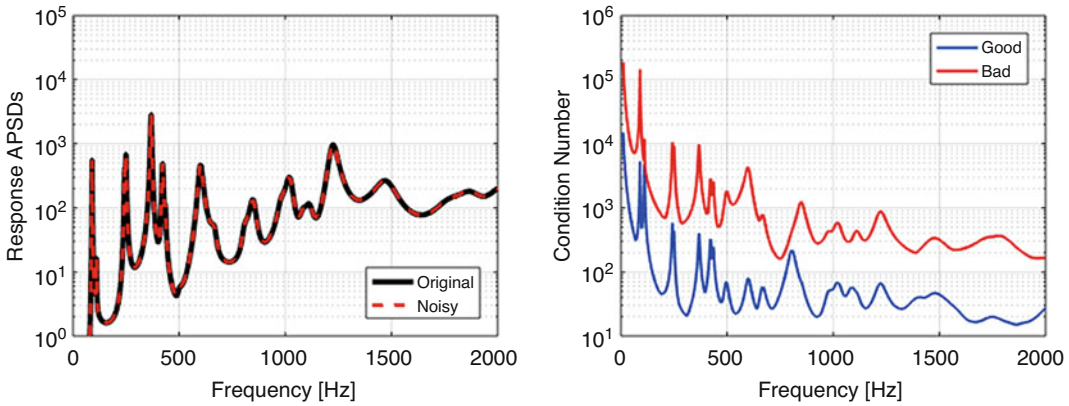

Fig. 21.6 Left: Sum of response APSDs from the original and perturbed (noisy) input. Right: Condition number of the "good" and "bad" inputs configuration for this system

Here, A would be the FRF matrix, x would be the input spectra, and b would be the response spectra. If there is noise or uncertainty, e, in the target response spectra, then the system is:

$$Ax = b + e. \tag{21.2}$$

Estimated inputs from this noisy target response would be:

$$x = A^{+}(b + e), \tag{21.3}$$

where A^{+} is the pseudo-inverse of the matrix A. If A is nicely conditioned, then the response error is not amplified through A^{+} and the effect on the estimated inputs, x, is small. If A is poorly conditioned, the response error is amplified in the estimated inputs. This is explained nicely in [13] and also in [6].

To demonstrate how condition number affects the estimated inputs, a simple example problem was developed using the "good" and "bad" systems described in the previous section, each with the higher damping levels (four times the original damping). A white noise input was generated to obtain some response, hereafter called the "truth" response:

$$S_{aa,0} = HS_{ff,0}H^{H} = HIH^{H}, \tag{21.4}$$

where the truth input cross-power spectral density (CPSD) matrix, $S_{ff,0}$, is simply the identity matrix for each frequency line. H^{H} is the Hermetian (conjugate transpose) of the FRF matrix. The resulting truth response CPSD matrix is $S_{aa,0}$. The objective is to see how slight perturbations (errors or noise) in the truth responses affect the inputs estimated with a direct force estimation calculation, given by:

$$S_{ff,1} = H^{+}S_{aa,e}H^{+H}, \tag{21.5}$$

where $S_{ff,1}$ is the estimated input CPSD and $S_{aa,e}$ is the truth response with some error. Error on the truth response was obtained by Equation 21.4 with $S_{ff,0}$ having 0.001% random change to the APSDs and 0.001 random change to the coherence and phase. This represents a nearly imperceptible change to the input and resulting response, shown in Fig. 21.6.

21.4.1 Example: Sensitivity to Errors in the Input

Figure 21.7 below shows the dB errors in the estimated responses for nine inputs for the "good" and "bad" systems, represented as an root-mean square (RMS) over the nine inputs. dB error here is computed as the dB error in the input and response APSDs, G_{ff}, G_{aa}:

$$dB_{input} = 10\log_{10}\left(\frac{G_{ff,1}}{G_{ff,0}}\right) \tag{21.6}$$

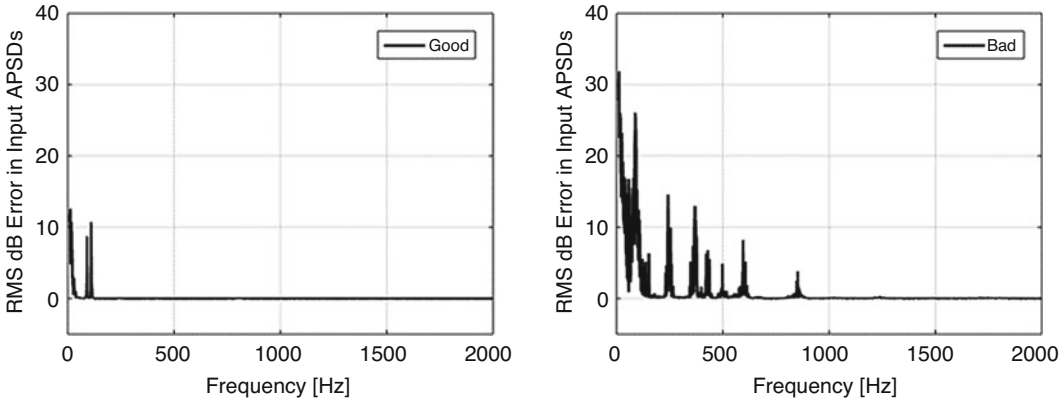

Fig. 21.7 RMS dB error in the estimated input APSDs for the "good" system (left) and "bad" system (right)

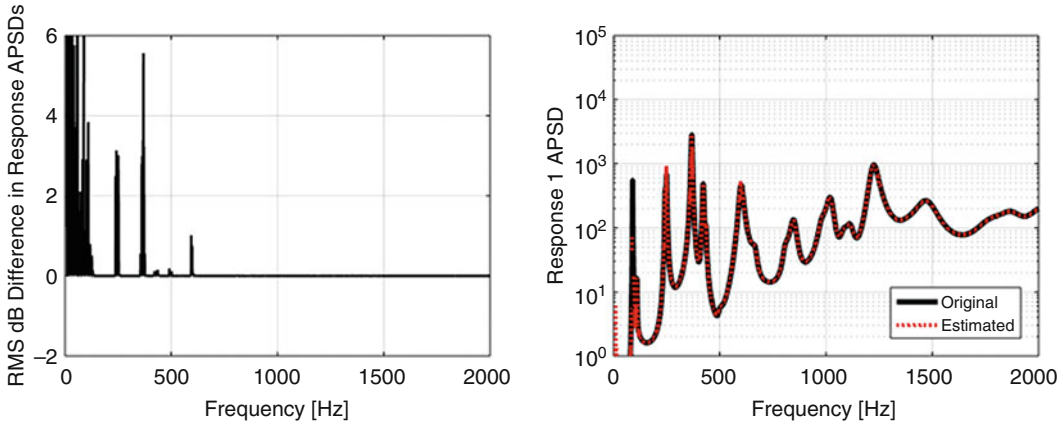

Fig. 21.8 Error in the estimated response due to errors in the estimated inputs. Left: RMS dB error relative to the truth response. Right: APSD at Accel. 1

$$dB_{response} = 10\log_{10}\left(\frac{G_{aa,1}}{G_{aa,0}}\right) \tag{21.7}$$

The "bad" system has high error up to approximately 1000 Hz and the "good" system only has errors below approximately 200 Hz. For each system, the errors occur where there are peaks in the condition number, shown in Fig. 21.6. Interestingly, the errors seem to correspond to frequencies with condition numbers above approximately 1000. These results agree with comments in [6] regarding condition number and significant error propagation in generic systems. For both the "good" and "bad" system, there is little error above 1000 Hz, where both systems have condition numbers below 1000.

The estimated response, $S_{aa,1}$, is computed from the forward equation:

$$S_{aa,1} = H S_{ff,1} H^H. \tag{21.8}$$

While it is possible that errors in the estimated inputs, $S_{ff,1}$, could cancel out and result in a response with little or no error, this is not generally true. For example, the estimated responses for the "bad" system with a noisy truth response matrix show large errors, Fig. 21.8. Similar to the estimated inputs, the estimated responses have errors only where the condition number is large.

21.5 Numerical Correction: Regularization

Typically, matrices with condition number issues are remedied using some type of regularization. Regularization methods attempt to fix small singular values, reducing the condition number and reducing the effects of errors on the estimated inputs. The objective of regularization is to change the FRF matrix enough to reduce the effects of those errors while not changing the overall form. Too much regularization can alter the important information in the matrix, such as the peak amplitudes or phase. The sections below examine different regularization methods and show how they can be used to reduce the error in the estimated inputs.

21.5.1 Singular Value Truncation and Perturbation

Regularization can be performed by simply modifying the singular values of the FRF matrix. As the condition number is directly tied to the singular values, changing the singular values changes the condition number. The objective is to modify the small singular values so they do not amplify errors. Changing the large singular values would drastically change the form of the matrix, so that is not desirable. Note that for very large matrices, computing the singular value decomposition (SVD) can be prohibitively expensive and it is more desirable to use some other regularization method, such as Tikhonov (discussed in the next section). However, for modal testing or multi-shaker testing the number of inputs and outputs is small and computing the SVD of the FRF matrix is trivial so using SVD-based regularization is tractable.

Two methods of changing the singular values are demonstrated here. Both compute the singular value decomposition of the FRF matrix at each frequency line. Regularization is obtained by modifying the singular values which are smaller than some threshold value. The FRF matrix is then re-formed with those new singular values, shown notionally in Equation 21.7, where S' is the matrix of modified singular values:

$$H = USV^H \rightarrow H' = US'V^H. \tag{21.9}$$

The threshold value can be determined by dividing the maximum singular value by some desired condition number. For example, the threshold value for a vector of singular values, s, and a desired condition number of 1000 would be:

$$s_{threshold} = \max(s)/1000. \tag{21.10}$$

The first method is singular value truncation, wherein the singular values below the threshold are simply set to zero, which has the effect of reducing the rank of the matrix. The second method perturbs the small singular values to larger, but still small values. Making the smallest singular values slightly larger improves the condition number and reduces the errors while still preserving the form of the matrix. Obviously, choosing too high a threshold would have a detrimental effect for either method. In the first method, a high threshold would result in zeroing out important information in the FRF matrix. In the second method, a high threshold would increase unimportant information to the same order of magnitude as important information, ruining the form of the matrix.

Figure 21.9 shows the effect of these singular value regularization methods. By truncating small values to zero or setting small values to larger values, the errors at peaks is greatly reduced. Either method works well in general, with the errors reduced at the peaks while not introducing significant errors elsewhere.

21.5.2 Tikhonov Regularization

Tikhonov regularization is a very popular regularization method. It has the benefit of not requiring a singular value decomposition. Rather, it simply perturbs the matrix directly in the Moore-Penrose pseudo-inverse. The Moore-Penrose pseudo-inverse of a matrix, A, is given by:

$$A^+ = \left(A^T A\right)^{-1} A^T \tag{21.11}$$

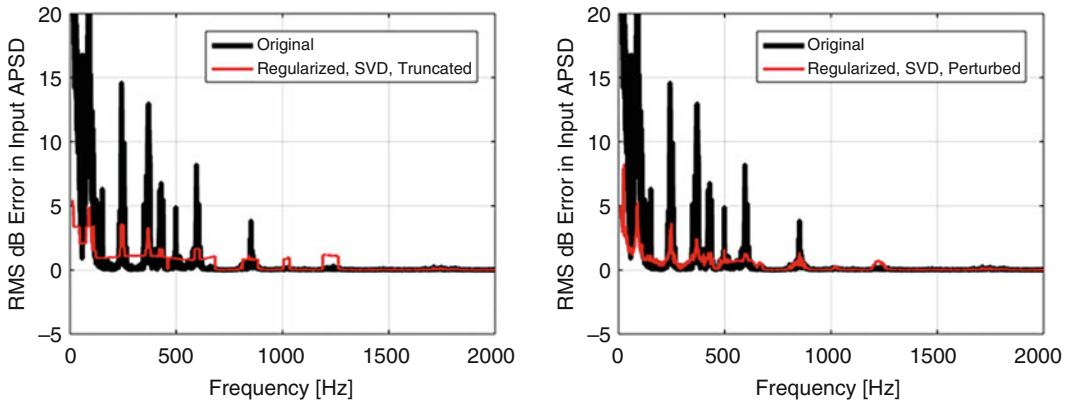

Fig. 21.9 RMS dB error in the input APSDs with and without singular value regularization. Left: Method using truncated singular values. Right: Method using perturbed singular values

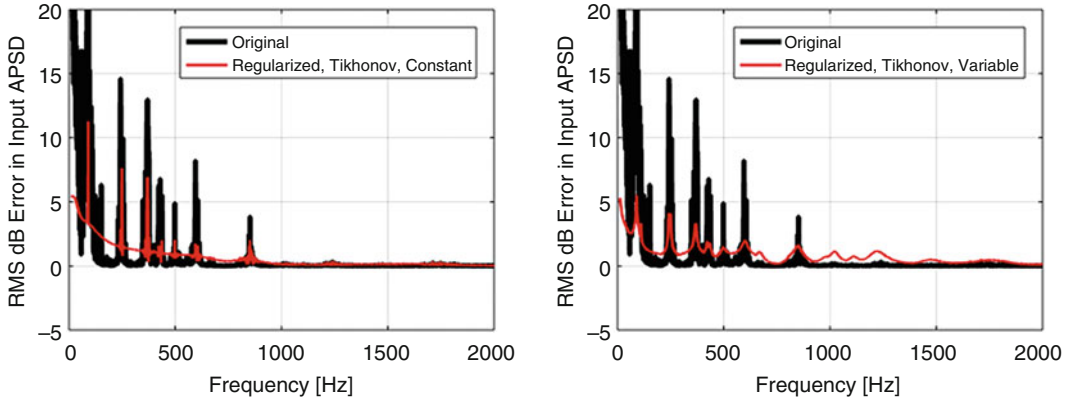

Fig. 21.10 RMS dB error in the input APSDs with and without Tikhonov regularization. Left: Constant regularization parameter value. Right: Variable regularization parameter value

Tikhonov regularization adds a diagonal matrix of regularization parameter values, λ, to the $A^T A$ argument in the inverse, which has the effect of improving the condition number [5]:

$$A^{+} = \left(A^T A + \lambda^2 I\right)^{-1} A^T \tag{21.12}$$

For the complex-valued FRF matrices here, this looks like:

$$H'^{+} = \left(H^H H + \lambda^2 I\right)^{-1} H^H \tag{21.13}$$

The regularization value can be a constant—the same value applied to the matrix at all frequency lines, or it can be variable, changing with each frequency line. For a variable value, the value at each frequency line is determined based on the Frobenius norm of the $H^H H$ matrix (Fig. 21.10):

$$\lambda_i^2 = \lambda_o^2 \left\| H^H H \right\|_2. \tag{21.14}$$

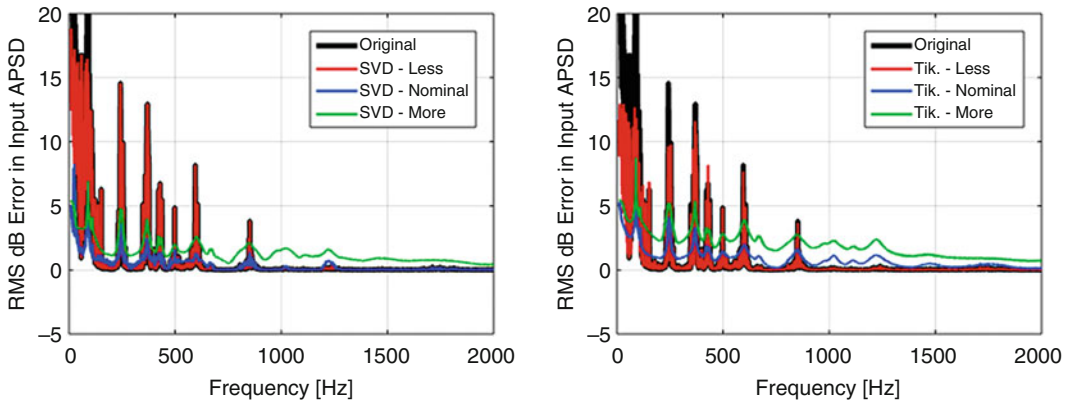

Fig. 21.11 RMS dB error in the inputs, showing the effect of regularization parameter value for SVD (left) and Tikhonov (right) regularization methods

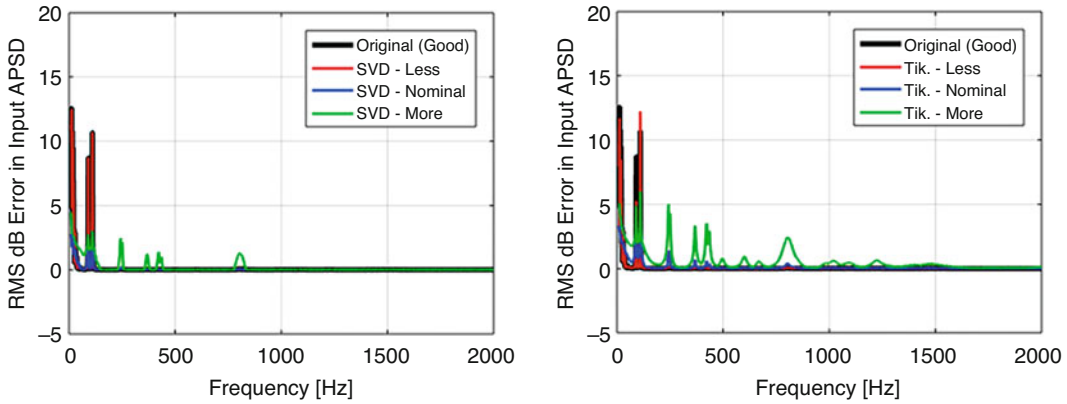

Fig. 21.12 Regularization applied to the "good" system with singular value (left) and Tikhonov regularization (right)

21.5.3 Choosing Regularization Parameter Values

It is evident that a regularization value (or singular value threshold) too large would result in a change in the overall form of the matrix. Similarly, too small a value would not sufficiently perturb the system FRF matrix and would not have a regularizing effect. Thus, there is an optimum value. Choosing optimum values is beyond the scope of this paper, but is discussed in the literature, for example in [5]. Instead, a simple demonstration is shown in Fig. 21.11 where the regularization value is changed to be larger or smaller than the nominal value by an order of magnitude. For both singular value and Tikhonov regularization, using too small a value does not result in much error reduction. Interestingly, using too much regularization, while reducing errors at the peaks, introduces new errors elsewhere. This is the result of changing the overall form of the matrix with too large a regularization value. Figure 21.12 shows the same input APSD error plots but for the "good" system. Again, errors are reduced with proper regularization, and new errors are introduced with too much regularization.

21.6 Force Estimation Methods

In this section, various force estimation methods are compared using the plate model and some acoustic pressure truth environment. The objective here is not to choose one single best method. Rather, it is to show that the force estimation method does matter and each method has specific benefits and faults. The key takeaway is simply that the force estimation method is another tool for the test engineer to use to tailor the test to achieve specific objectives.

The general process is as follows. First, a "truth test" is simulated wherein the plate model is subject to forces over the entire surface representing an acoustic environment. This generates target responses, captured at 12 points. Next, shakers are

applied to nine discrete input locations and the FRFs between those nine inputs and 12 outputs is computed. This FRF matrix is then used to estimate the inputs which can best match the target responses, using different force estimation methods. Finally, those estimated inputs are used in a "replica test", a forward calculation to estimate the replicated responses and compare those to the target, truth responses. Results for the different force estimation methods are then compared in terms of the inputs and outputs.

21.6.1 Responses from a Truth Test

Here, the "truth" environment is a set of forces over the entire surface of the plate, which represent acoustic pressures in a diffuse field. These distributed, correlated inputs of the diffuse acoustic field were chosen because it should generate response which cannot completely be replicated by a small number of shaker inputs. Additionally, this is a typical use case for multi-shaker testing—the truth environment is complicated, perhaps acoustic or aero-acoustic. Then, in the lab, the objective is to use a small number of shakers to best replicate that complicated environment. Daborn experimentally demonstrated this in [14].

The acoustic loads were synthesized using a typical aerospace test specification, from SMC-016 [15]. This specification provides the shape of the auto spectrum of the pressures. This was then arbitrarily scaled to 150 dB overall sound pressure level. The correlation between all the inputs is based on the spatial correlation of a diffuse field, which allows for the input CPSD to be formed [16]. Finally, the pressure CPSD matrix was scaled by area to obtain a force CPSD matrix which is then applied to the plate FRFs to get the truth response.

Figure 21.13 shows the nine input locations on the plate, along with the 12 output locations. The 12 outputs are divided into two groups. Accelerometers 1, 2, 3, 5, 6, 7, 8, 10, 11, and 12 are in the "target" set, which means those ten gages are used in the force estimation process. Accelerometers 4 and 9 are in the "reference" set, which means they are not used in the force estimation process. The responses from the replica test can then be compared at gages which are used in the estimation and gages which are not. This gives some indication as to how well the overall response of the structure is captured in a given replica test.

The nine inputs are from the "good" set of input locations, which should help reduce numerical errors in the force estimation process. In addition to a good set of input locations, regularization was applied to the FRF matrices to reduce numerical error, implemented with a singular value perturbation method and a condition number threshold of 1000. Note that these input locations were selected to have a low condition number of the FRF matrix, and were not selected to optimally replicate the truth environment or provide minimum inputs.

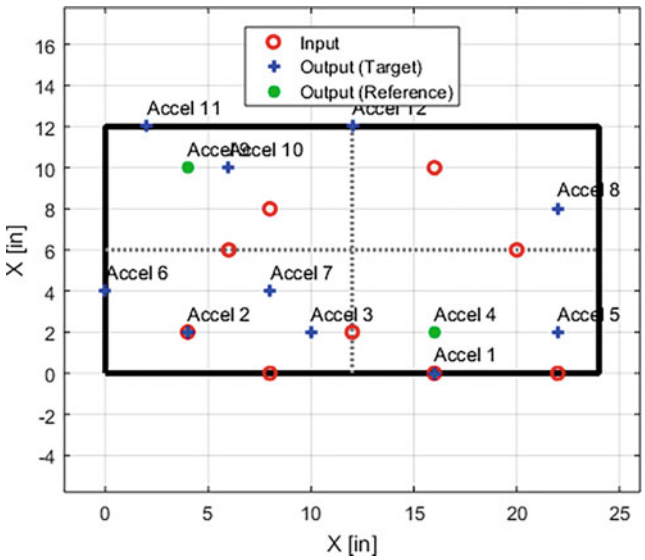

Fig. 21.13 Plate with input and output locations

21.6.2 Standard Method

The first method considered is just the standard, direct force estimation method which is shown in Equation 21.5. In this method, the truth response CPSD for the ten gages is used as the target data and the inputs are estimated using a Moore-Penrose pseudo-inverse of the regularized FRF matrix. This solution provides the set of inputs which provide the least squares fit to the response data, in terms of not only level (APSD), but also coherence and phase since the entire CPSD response matrix is given as the target data.

21.6.3 Uncorrelated Inputs (Independent Drives)

The second method is Independent Drives, a method explored by Smallwood [8], where the inputs are assumed to be uncorrelated (independent). This method requires a different form of the force estimation equation which uses the APSD of the target responses, $G_{aa,0}$, to estimate the APSD of the independent inputs, $G_{ff,1}$:

$$G_{ff,1} = \left(H \circ H^*\right)^+ G_{aa,0}, \tag{21.15}$$

where $H \circ H^*$ is a 10×9 real-valued matrix because H^* is the conjugate of the FRF matrix H and $\circ$ is the Hadamard product, which is an entry-by-entry matrix product. Clearly, this method makes no attempt to match the coherence or phase of the target responses.

Note that this can result in negative input APSDs, which is non-physical, so any negative values are set to zero. Also, as described by Smallwood, the inputs can be adjusted to better match the target response APSD with a simple scaling of the target responses based on the estimated responses and doing a second force estimation.

21.6.4 Modified Cross-Terms (Buzz Test)

The third method has been used by Daborn in recent years in a variety of multi-shaker tests [9]. This method, dubbed the buzz test method, replaces the cross terms in the target response CPSD matrix from the truth test with the coherence and phase from the system in the lab. These coherences and phases are obtained with a buzz test, wherein the shakers are attached to the structure in the lab and then uncorrelated, white noise inputs are used to excite the structure. This provides the coherence and phase of the target responses. Then, the new target response CPSD matrix can be formed using the APSDs from the truth test and the coherence and phase from the buzz test. Inputs are then estimated using the standard force estimation method.

21.6.5 Results

Figure 21.14 compares the three force estimation methods in terms of the sum of all 12 response APSDs and the sum of all nine input APSDs. Overall, the response is matched quite well by the standard and buzz test methods. Independent drives captures some of the response features, but has a fair amount of error at peaks and between peaks. The majority of the error in the standard method exists at frequencies between the peaks in the response. The buzz test method seems to work the best to match the overall response.

The required inputs are quite different, with the standard method requiring much more force than the other two methods. Independent drives requires the least input, with the buzz test method being only slightly higher at some frequencies. As the standard method is the only one which tries to achieve the truth test cross terms in the response, it may be assumed that matching the cross terms requires considerable force.

Figures 21.15 and 21.16 show the results in more detail, with a comparison of the APSDs at one target gage (Accel. 3) and one reference gage (Accel. 4), as well as the coherence and phase between those gages. As expected, the match to the truth response is better at the target gage than at the reference gage. Surprisingly, the standard method has quite a lot of error at the reference gage. The buzz test method and even the independent drives method do better to match the response at the reference gage. Only the independent drives method has a poor match at the target gage. Coherence and phase are notoriously

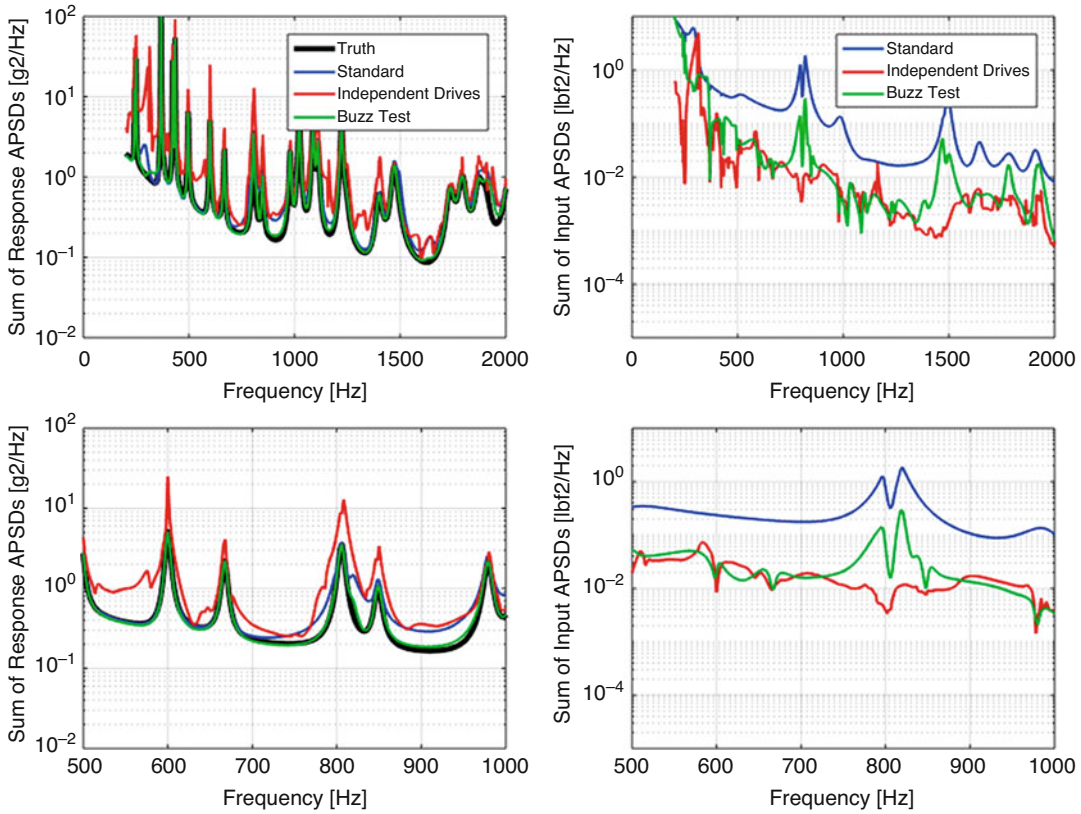

Fig. 21.14 Replica results for three different force estimation methods. Top Left: Sum of all 12 response APSDs. Top Right: Sum of all 9 input APSDs. Bottom Left: Sum of all 12 response APSDs, zoomed to 500–1000 Hz. Bottom Right: Sum of all 9 input APSDs, zoomed to 500–1000 Hz

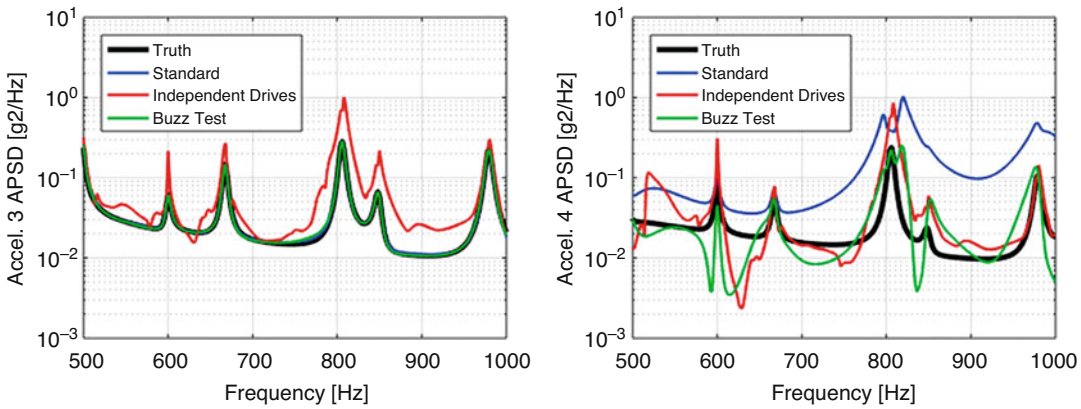

Fig. 21.15 Response APSD at a single gage. Left: Accel. 3, in the Target gage set. Right: Accel. 4, in the Reference gage set

difficult to assess for even simple systems. Here, it can be seen that the coherence is not well matched for the independent drives and buzz test methods, and is only approximately matched with the standard method. Phase is not captured well by any of the methods.

The results are aggregated in terms of RMS input and RMS response over the entire 200–2000 Hz band in Tables 21.1 and 21.2. The buzz test method has the best match to the RMS response over both target and reference gages. The independent drives method tends to over-test. The standard method is close at the target gages, but has large errors at the reference gages. In terms of inputs, the standard method requires the most input force and the independent drives method requires the least. The buzz test method is between the two for most input locations.

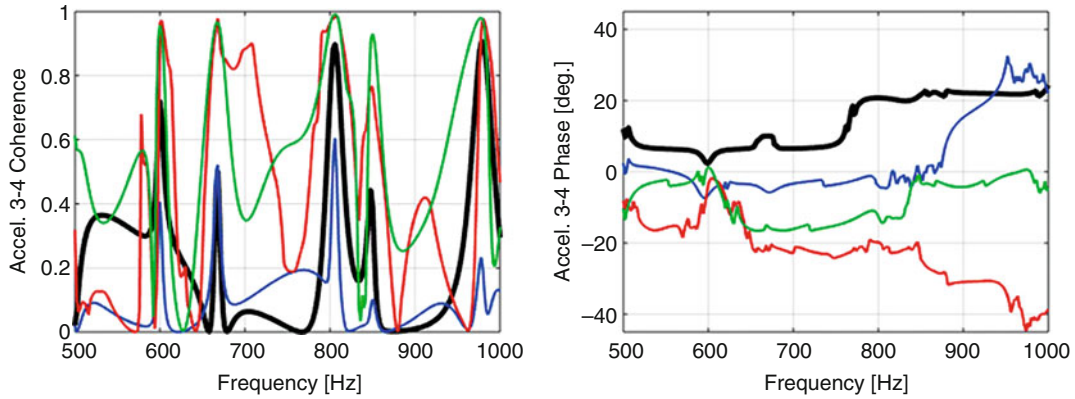

Fig. 21.16 Coherence (left) and phase (right) between accel. 3 and 4, compared with the truth coherence and phase

Table 21.1 RMS response over the 200–2000 Hz bandwidth. Reference gages highlighted in gray

g-RMS	Truth	Standard	Ind. Drives	Buzz Test
Output 1	19.1	19.1	29.0	19.1
Output 2	9.6	9.6	12.5	9.5
Output 3	8.7	9.2	13.9	8.9
Output 4	9.0	17.2	14.9	11.4
Output 5	9.2	9.1	14.3	9.2
Output 6	17.3	17.1	26.9	17.3
Output 7	10.5	10.2	14.4	10.2
Output 8	10.9	10.6	13.3	10.8
Output 9	9.2	10.3	11.9	8.5
Output 10	9.7	9.4	13.9	9.7
Output 11	22.4	22.2	32.1	22.4
Output 12	17.6	17.6	28.1	17.6

Table 21.2 RMS input over the 200–2000 Hz bandwidth

lbf-RMS	Standard	Ind. Drives	Buzz Test
Input 1	5.3	2.3	6.1
Input 2	5.6	3.4	4.5
Input 3	5.9	2.4	3.4
Input 4	8.6	2.9	6.5
Input 5	10.8	3.8	8.6
Input 6	16.8	3.4	8.9
Input 7	11.9	7.6	6.3
Input 8	9.2	3.5	6.5
Input 9	11.0	4.9	6.7

Singular value regularization was used to reduce the numerical error in these force estimation calculations, with a nominal condition number threshold of 1000. As previously discussed, the amount of regularization can have an effect on the regularized FRF matrix form and the amount of error in the estimated inputs. It was observed here that the amount of regularization affected the required input forces, as shown in.

Table 21.3 which shows the RMS input forces using condition number thresholds of 50, 100, 1000 and 10,000. A condition number threshold of 10,000 is nearly un-regularized and has significant errors in the inputs. These results indicate that increasing the amount of regularization can reduce the amount of input force required. A more detailed study would be needed to make general statements regarding the tradeoff between regularization, resulting input forces and response accuracy.

Table 21.3 RMS input using the standard force estimation method with different amounts of regularization applied, specified by the condition number threshold

lbf-RMS	C.N. 50	C.N. 100	C.N. 1000	C.N. 10,000
Input 1	4.3	4.8	5.3	5.3
Input 2	3.7	4.5	5.6	6.1
Input 3	5.0	5.5	5.9	6.0
Input 4	6.7	7.5	8.6	8.8
Input 5	9.4	10.1	10.8	10.9
Input 6	12.5	15.0	16.8	17.0
Input 7	9.9	11.0	11.9	12.0
Input 8	7.1	8.3	9.2	9.3
Input 9	7.2	8.4	11.0	12.2

21.7 Conclusions

Regularization and force estimation methods were demonstrated and compared using a simple multiple-input/multiple-output dynamic system, a plate with several shakers applied. The condition number of the FRF matrix provides a measure of the matrix and its invertibility. A poorly-conditioned matrix has a high condition number, which indicates that its vectors are non-independent. This was demonstrated by contriving two systems, one with very different input locations and one with very similar input locations. The system with the different input locations has an FRF matrix with independent vectors and the condition number was much lower than the system with very similar input locations. It was shown that changing the damping of the system does reduce the condition number because the peaks in the FRF are reduced. Random noise on each FRF in the matrix does not increase the condition number, however coherent noise (i.e. 60 Hz noise from a ground loop problem) would likely have a detrimental effect.

Regularization of the FRF matrix reduces the errors associated with performing the pseudo-inverse of a poorly-conditioned matrix. For this system, these errors were large for condition numbers greater than 1000. Both singular value and Tikhonov regularization methods proved effective at reducing errors. The amount of regularization is important; too little and the errors will not be reduced while too much will change the form of the FRF matrix, creating different errors.

Three force estimation methods were applied to determine nine shaker forces to replicate the response of the plate subject to an acoustic truth environment. None of the three methods was perfect, which is expected since the truth test here had forces at all locations on the plate and the replica test only had nine inputs. However, the standard and buzz test methods were the most effective at matching the overall response APSD. The independent drives method was less accurate for the response, but required the lowest force. The buzz test method, which replaces the truth response cross terms with new cross terms, had the best balance of response accuracy and low input forces in this case. Interestingly, while the replica response was accurate at the gages in the target set, there was some error at other, reference locations. Additionally, no method was effective at matching coherence or phase at the single gage pair of interest.

Overall, some comments can be made regarding MIMO testing and force estimation. First, regularization of the FRF matrix is likely necessary and useful to reduce numerical errors in the force estimation process, which can provide benefits to the accuracy of the replica responses and provide lower input forces. Second, each force estimation method has benefits and issues—there is a tradeoff between things like efficiency and accuracy. Pre-test predictions and modeling can be very useful to study the effects of these tradeoffs. Additionally, it was shown that simply comparing the APSDs at the control (target) locations is not a sufficient metric for assessing the response of the whole structure as the response at other locations can be inaccurate and the coherence and phase can be quite different even if the APSDs match very well. More work is needed to understand the objectives of multiple-input/multiple-output tests—should the focus be only on response levels at a small number of points, or should specifications and test objectives move toward a more full-field perspective, including more locations as well as metrics like phase, to better match not only the response acceleration but things like stress and strain as well.

References

1. Daborn, P.M., et. al.: Next-generation random vibration tests. In: IMAC XXXII, the 32nd International Modal Analysis Conference, Orlando, FL (2014)
2. Mayes, R.L., Rohe, D.P.: Physical vibration simulation of an acoustic environment with six shakers on an industrial structure. Sandia National Laboratories (2015)

3. Bernhard, R.: The characterization of vibration sources and measuremnt of forces using multiple operating conditions and matrix decomposition methods. In: Proceedings of Inter-Noise 2000, the 29th International Congress on Noise Control Engineering, Nice, France (2000)
4. O'Callahan, J., Piergentili, F.: Force estimation using operational data. In: Proceedings of IMAC XIV, the 14th International Modal Analysis Conference (1996)
5. Vogel, C.R.: Computational methods for inverse problems, SIAM, the Society for Industiral and Applied Mathematics (2002)
6. Yagle, A.E.: Application note: regularized matrix computations, Department of EECS, the University of Michigan. http://web.eecs.umich.edu/~aey/recent/regular.pdf. Accessed 2017
7. Choi, H.G., Thite, A.N., Thompson, D.J.: Comparison of methods for parameter selection in Tikhonov regularization with applicate to inverse force determination. J. Sound Vib. **304**, 894–917 (2007)
8. Smallwood, D.O.: A revised algorithm for minimum input trace to a multiple-input/multiple-output system (MIMO) to match the output autospectral densities. Sandia National Laboratories
9. Daborn, P.M.: Smarter dynamic testing of critical structures. PhD Thesis, University of Bristol (2014)
10. Kammer, D.C.: Sensor placement for on-orbit modal identification and correlation of large space structures. J. Guid. Control. Dyn. **14**(2), 251–259 (1991)
11. Carne, T.G., Dohrmann, C.R.: A modal test design strategy for model correlation. In: Proceedings of IMAC XII, the International Modal Analysis Conference (1994)
12. Thite, A.N., Thompson, D.J.: Selection of resposne measurement locations to improve inverse force determination. Appl. Acoust. **67**, 797–818 (2006)
13. Hansen, P.C.: Discrete inverse problems: insight and algorithms. SIAM: The Society for Industrial and Applied Mathematics (2010)
14. Daborn, P.M.: Scaling up of the impedance-matched multi-axis test (IMMAT) technique. In: IMAC XXXV, the 35th International Modal Analysis Conference, Garden Grove, CA (2017)
15. Test requirements for launch, upper-stage and space vehicles, SMC standard SMC-S-016, Air Force Space Command, Space and Missile Systems Center Standard (2014)
16. Smith, A.M., Davis, R.B., LaVerde, B.T., Fulcher, C.W., Jones, D.C., Hunt, R.A., Band, J.L.: Calculation of coupled vibroacoustics response estimates from a library of available uncoupled transfer function sets. In: Proceedings of the 53rd AIAA Structures, Structural Dynamics and Materials Conference, Honolulu, HI (2012)

Chapter 22
Input Signal Synthesis for Open-Loop Multiple-Input/Multiple-Output Testing

Ryan A. Schultz and Garrett D. Nelson

Abstract Many in the structural dynamics community are currently researching a range of multiple-input/multiple-output problems and largely rely on commercially-available closed-loop controllers to execute their experiments. Generally, these commercially-available control systems are robust and prove adequate for a wide variety of testing. However, with the development of new techniques in this field, researchers will want to exercise these new techniques in laboratory tests. For example, modifying the control or input estimation method can have benefits to the accuracy of control, or provide higher response for a given input. Modification of the control methods is not typically possible in commercially-available control systems, therefore it is desirable to have some methodology available which allows researchers to synthesize input signals for multiple-input/multiple-output experiments. Here, methods for synthesizing multiply-correlated time histories based on desired cross spectral densities are demonstrated and then explored to understand effects of various parameters on the resulting signals, their statistics, and their relation to the specified cross spectral densities. This paper aims to provide researchers with a simple, step-by-step process which can be implemented to generate input signals for open-loop multiple-input/multiple-output experiments.

Keywords MIMO · Signal synthesis · Random sampling · Open-loop testing · Signal processing

22.1 Introduction

Recent interest in multi-axis and multi-shaker vibration testing has many researchers looking into new force or input estimation algorithms to improve or customize their tests. There are many benefits of being able to customize the force estimation approach for a specific test article, test type, or vibration environment, including improved response accuracy, higher response levels, or improved control over the coherence and phase of the responses. Generally, the multiple-input/multiple-output (MIMO) tests are performed in the lab using an off-the-shelf closed-loop control system. These control systems have the benefits of being robust and friendly to the casual user, but generally do not allow the user to modify all aspects of the control problem, such as the force estimation equations.

The typical control system workflow is as follows: First, the system frequency response functions (FRFs) are estimated by measuring the response due to uncorrelated inputs. Second, the system inputs are estimated using those FRFs and the target response. Generally, the target response and estimated inputs are in the form of cross-power spectral density matrices (CPSDs). Next, input time histories are generated from that input CPSD matrix using some type of random sampling method. As shown in this paper, there are multiple ways to generate those time histories and the particular method employed can have an effect on the resulting signals' statistics and representation of the input CPSD matrix. Finally, these time histories are concatenated into long-duration signals using a constant overlap and add (COLA) process wherein the signals are windowed, overlapped, and added together to achieve a long-duration, smooth signal containing multiple realizations of the desired time histories [1, 2]. In a closed-loop control system, this process is continually performed, with the system FRFs and input signals

Sandia National Laboratories is a multimission laboratory managed and operated by National Technology and Engineering Solutions of Sandia, LLC., a wholly owned subsidiary of Honeywell International, Inc., for the U.S. Department of Energy's National Nuclear Security Administration under contract DE-NA0003525.

R. A. Schultz (✉) · G. D. Nelson
Structural Dynamics and Environments Engineering Departments, Sandia National Laboratories, Albuquerque, NM, USA
e-mail: rschult@sandia.gov

C. Walber et al. (eds.), *Sensors and Instrumentation, Aircraft/Aerospace, Energy Harvesting & Dynamic Environments Testing, Volume 7*, Conference Proceedings of the Society for Experimental Mechanics Series,
https://doi.org/10.1007/978-3-030-12676-6_22

continually updating to improve the control. In open-loop testing, the system FRFs are estimated once, then the input signals are simply played into the system.

It should be noted that this paper does not present new methods, rather it is presenting a collection of previous works and a comparison of methods. The general approaches used in this paper were developed years ago and studied by a number of researchers [3–5]. The objective is to make today's structural dynamics audience aware of the methods which are used to generate time signals for MIMO tests and allow them to implement these methods in their own laboratories. Results of the studies performed in this work show that using a singular value decomposition (SVD) for the matrix decomposition step, along with a Gaussian, two-part random process, provides the time histories with the best statistics. Also, a COLA windowing method is derived here which preserves the signal variance, important for vibration testing where the signals are random or pseudo-random. The hope is the processes described in this paper may open the door to more researchers implementing more creative and useful force estimation methods to improve MIMO test capabilities.

22.2 Multiple-Input/Multiple-Output Systems and Force Estimation

The typical input-output relationship of a linear dynamic system can be written as:

$$X = HF, \tag{22.1}$$

where H is the system frequency response function (FRF) matrix, F is the input force linear spectrum, and X is the output response linear spectrum. Note that each term is a function of frequency and this problem is evaluated on a frequency line by frequency line basis (frequencies are independent). Generally, measurements are made and processed into power spectral densities (PSDs) to take advantage of noise-reduction from averaging multiple time segments. Equation 22.1 can be written in terms of the input and output cross-power spectral density (CPSD) matrices as:

$$S_{xx} = HS_{ff}H^H, \tag{22.2}$$

where S_{ff}, S_{xx} are the input and output CPSDs, respectively, and H^H is the conjugate transpose, or Hermitian, of the FRF matrix. Generally, the control problem is solved in application where there is a target response CPSD matrix and a force or input estimation method is used to estimate the input CPSD matrix. For the basic direct force estimation method, this is most commonly solved as follows:

$$S_{ff} = H^+ S_{xx} \left(H^+\right)^H, \tag{22.3}$$

where H^+ is the Moore-Penrose pseudo-inverse of the FRF matrix [6, 7]. In a MIMO test, input signals are generated which represent that input CPSD matrix, S_{ff}, and should generate output response signals which represent the desired response CPSD matrix, S_{xx}. This work concerns how to turn that estimated input CPSD matrix into representative time histories. In the structural dynamics community, the input quantity of interest in a test is most often a voltage and the output an acceleration, so the input CPSD matrix will be written in terms of voltage, S_{vv}, and the output in terms of acceleration, S_{aa}.

22.3 Time History Synthesis

This section presents various methods for generating time histories based on the desired PSD, including methods for single and multiple, correlated signals. The basic process is the same in either case. First, a desired PSD is determined from a force estimation process. This PSD could be a single auto-power spectral density (APSD) in the case of a single signal, or it could be a full CPSD matrix in the case of multiple, correlated signals. Next, that PSD, which is a power-type quantity, is decomposed to linear space. Then, some random process is applied to generate realizations of linear spectra. Those linear spectra can then be transformed to the time domain using the inverse discrete Fourier transform (IDFT). The resultant time histories, on average, should have the desired PSD in terms of auto- and cross-terms (level, coherence and phase).

For single signals, the time histories can also be generated using a sum of cosine waves, one for each frequency line, for example:

$$x_k(t) = A_k \cos(\omega_k t + \psi_k), \tag{22.4}$$

where A_k, ψ_k are the amplitude and phase of the k-th frequency line at angular frequency ω_k. As shown in Grigoriu's paper, this can also be written as a summation of a sine and cosine, each with their own amplitude terms [5]:

$$x_k(t) = A_k \cos(\omega_k t) + B_k \sin(\omega_k t). \tag{22.5}$$

However, implementing signal generation in the time domain like this is not practical for broadband problems where there are many frequency lines as each frequency line must be generated and then added together, which is much more time consuming than using the IDFT method described above. For example, simulations were run using both time and frequency domain implementations and the time domain methods took approximately 60 times longer to run. Statistics of the generated signals were similar in the time and frequency domains. As such, all methods presented in this work will utilize the frequency domain implementation.

22.3.1 Single Signal

First, an amplitude is determined from the APSD, G_{vv}, at each frequency line, for example at the k-th frequency line:

$$\alpha_k = \sqrt{G_{vv,k}/df}, \tag{22.6}$$

where df is the frequency resolution. If the signal units are volts, then the APSD has units of [V^2/Hz], and the amplitude, α_k, has units of [V-s].

Two methods are shown for synthesizing time histories from a desired APSD, both using realizations of the linear spectra. The first method (Method 1) uses zero mean, unit variance Gaussian random variables for the real and imaginary parts, A_k, B_k, to generate the linear spectrum realizations at the k-th frequency line:

$$X_k = \alpha_k \frac{1}{\sqrt{2}} (A_k + j B_k). \tag{22.7}$$

The second method (Method 2) uses a constant amplitude with a random phase, ψ_k, which is uniformly distributed over the interval 0 to 2π:

$$X_k = \alpha_k e^{j\psi_k}. \tag{22.8}$$

Note that Method 1 is a linear combination of random processes whereas Method 2 is not. This has important implications in terms of the statistics of the resulting signals, shown in the next section.

22.3.1.1 Tonal Signal

As an example, time histories are synthesized using Method 1 and 2 for a single, 100 Hz tone. Here, the tone amplitude is chosen to provide unit variance. Realizations of 4096 point signals are generated with a sample rate of 8192 Hz. Then, these signals are simply stacked end to end to form a single, long signal. The distribution of signal values is very different between Method 1 and 2, as seen in the histograms in Fig. 22.1 below. Method 1 has a normal distribution where Method 2 has a distribution heavily weighted toward the high values; this is the distribution of a sine wave. Because Method 2 uses a constant amplitude and this is a pure sine tone, the maximum signal value never exceeds 1.41. Figure 22.2 shows how Method 1 produces signals with different amplitudes for each realization. Table 22.1 shows the variance and peak values from the different signals. Overall, if the objective of the test is to subject the device under test to a distribution of inputs (i.e. some spread about a mean level), then Method 1 is preferred as it provides a spread in the inputs, whereas Method 2 has exactly the same amplitude for each realization, which means there would be no distribution in the outputs. Both methods, on average, provide the correct level.

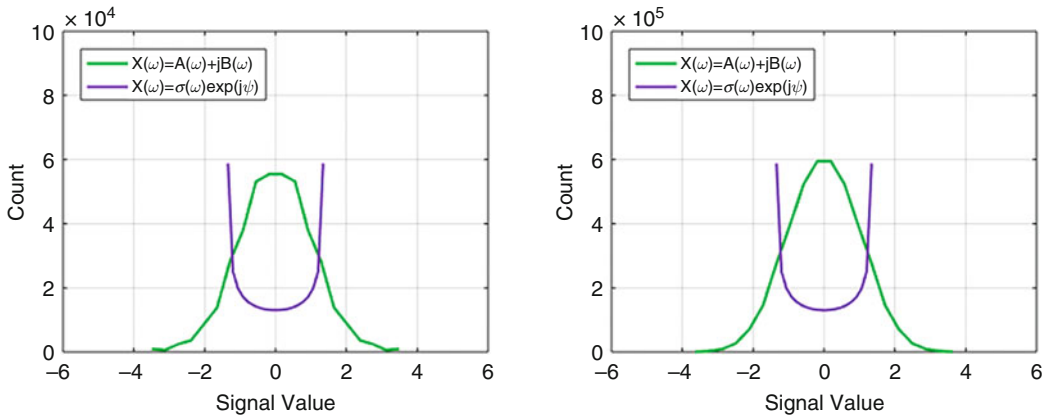

Fig. 22.1 Histogram of signal values for 100 realizations (left) and 1000 realizations (right)

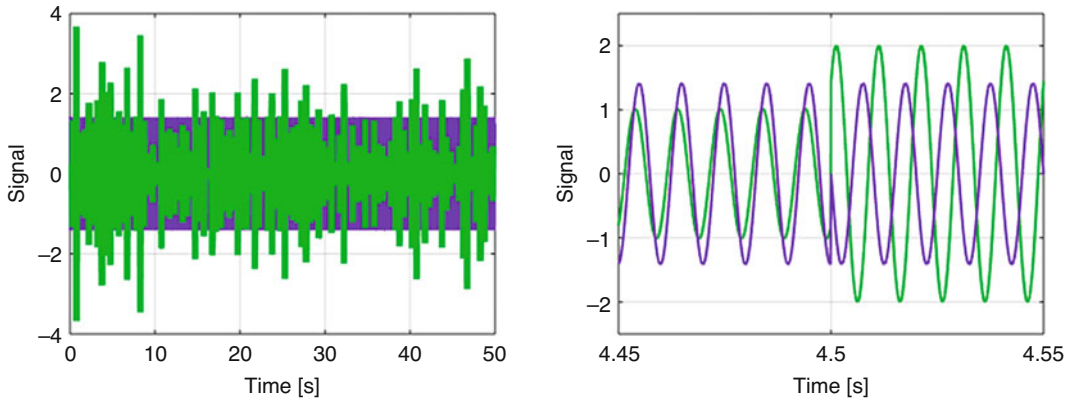

Fig. 22.2 100 signal realizations stacked end-to-end to form a single, long signal (left) and zoomed to the transition between two realizations (right)

Table 22.1 Variance and peak values for Method 1 and Method 2 tonal signals

Method	Variance	Peak
Method 1, 100 Realizations	1.100	3.67
Method 2, 100 Realizations	1.000	1.41
Method 1, 1000 Realizations	1.004	3.83
Method 2, 1000 Realizations	1.000	1.41

22.3.1.2 Broadband Signal

In this next example, the desired PSD is broadband with a specified shape, shown in the black dotted line of Fig. 22.3. Again, time histories are generated using Method 1 and Method 2 for multiple realizations. As seen in Fig. 22.3, Method 2 produces exactly the desired level at all frequency lines for all realizations whereas Method 1 produces levels that will approach the desired level after multiple realizations are averaged together. With multiple frequency lines, the statistics look very similar, Table 22.2. However, the underlying effects remain—for a given frequency line, Method 2 will have no distribution in the input amplitude. As such, it is recommended to use Method 1, where the real and imaginary components of the linear spectrum are Gaussian, zero mean, unit variance random processes, scaled by α_k. Method 1 will achieve, on average, the correct amplitude for each frequency line and provide some distribution in the amplitudes for the different realizations.

22.3.2 Multiple, Correlated Signals

For multiple, correlated signals the process is somewhat more complicated because in addition to matching some desired APSD, the coherence and phase between the signals must also be maintained. To accomplish this, the full CPSD matrix is used. First, the CPSD matrix, S_{vv}, is decomposed from power space to a linear space matrix, L. Cholesky decomposition

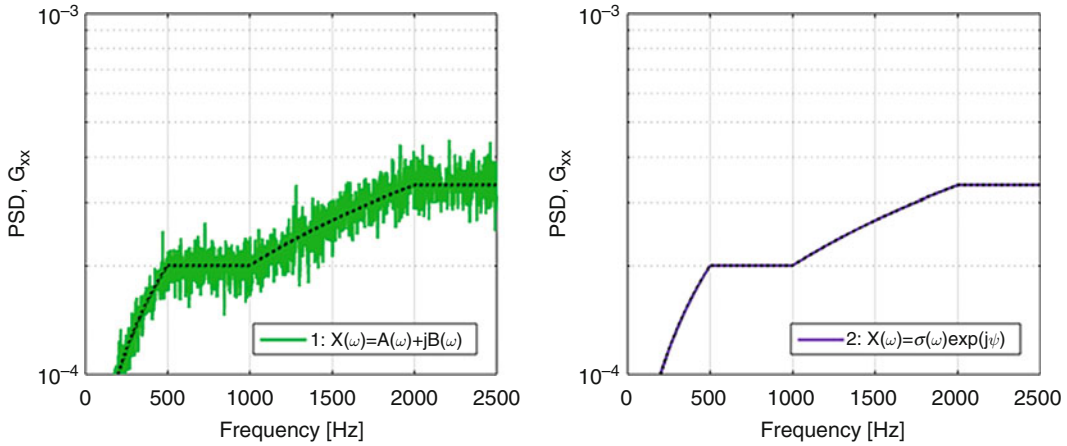

Fig. 22.3 PSD resulting from realizations of signals using Method 1 (left) and Method 2 (right) for a broadband, shaped APSD

Table 22.2 Variance and peak values for Method 1 and Method 2 broadband signals

Method	Variance	Peak
Method 1, 100 Realizations	0.998	4.88
Method 2, 100 Realizations	1.000	4.93

and singular value decomposition (SVD), among other methods, can be used for that decomposition, though they provide different results, discussed in detail below.

$$S_{vv} = LL^H \tag{22.9}$$

Note that the size of S_{vv} is number of signals by number of signals (square), for each frequency line. Next, realizations of the set of linear spectra are obtained by multiplying that linear space matrix by a vector random process, Ψ, which incorporates effects of both the auto- and cross-terms into the linear spectra:

$$X_v = L\Psi \tag{22.10}$$

Just like with the single signal synthesis methods shown above, the choice of the random process influences the resulting signal statistics. The remainder of the process is identical to that for single signals, where each of the linear spectra are transformed to the time domain using the IDFT. Note that the random process vector for Method 1 is:

$$\Psi = \frac{1}{df}\frac{1}{\sqrt{2}}\left(A_k + jB_k\right), \tag{22.11}$$

and for Method 2 is:

$$\Psi = \frac{1}{df}e^{j\psi_k}, \tag{22.12}$$

which is the same as for the single signal cases shown above. The difference is that now the amplitude scale is no longer a scalar value, but a matrix, L, and the random process vector is not a complex scalar value but a vector with a complex-valued entry for each signal.

Examples are shown below to compare the effects of the Cholesky and SVD decomposition methods and the random process methods. The same two random processes, Method 1 and Method 2, will be used, resulting in four cases: SVD Method 1, SVD Method 2, Cholesky Method 1 and Cholesky Method 2. For this example, a four signal CPSD matrix is generated using the same single tone and broadband APSD specifications as in the single signal examples above. A coherence of 0.25 and phase of $\pi/4$ is used for all cross terms and frequency lines. 100 realizations of signals were generated using all four combinations of methods.

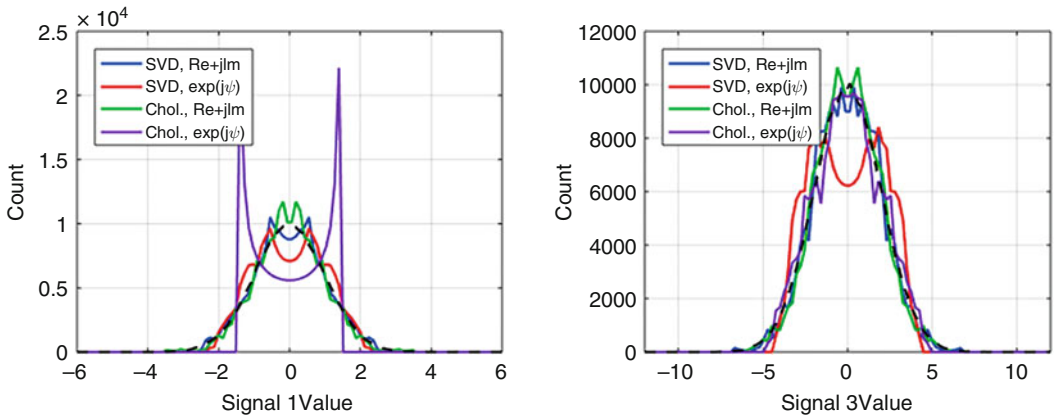

Fig. 22.4 Histograms of values of Signal 1 (left) and Signal 3 (right) generated with the four different methods

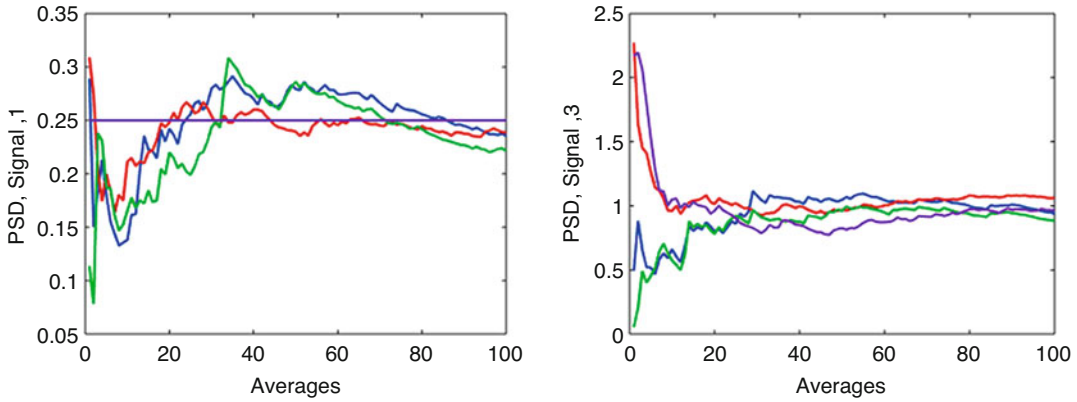

Fig. 22.5 Convergence of the APSD of Signal 1 (left) and Signal 3 (right) with increasing number of averages

22.3.2.1 Tonal Signals

With a 100 Hz tone, the effect on signal statistics is clear. Again, using a real and imaginary random process (Method 1) provides a Gaussian distribution of signal values, Fig. 22.4. The random phase process (Method 2) does not have that distribution of signal values, and the effect is most noticeable with a Cholesky decomposition. Although using a SVD decomposition along with Method 2 does perform well, Method 1 is still better in terms of achieving the Gaussian distribution of signal values irrespective of the decomposition approach.

To explore how the different methods approach the desired CPSD with increasing averages, the averaged APSD, coherence and phase at 100 Hz is plotted as a function of the number of averages in Figs. 22.5 and 22.6. With a sufficient number of averages, around 80 in this case, all four methods converge on the desired signal APSD, coherence and phase. Interestingly, using a Cholesky decomposition along with a Method 2 random process results in exactly the correct APSD for signal 1. This is because the Cholesky decomposition results in a lower triangular matrix, and signal 1 is the top of that triangle, so the value for signal 1 is not mixed with those of any other values and therefor the signal amplitude is perfectly maintained. Thus, the distribution of the resulting signals by this method is largely dependent on the order of the signals (i.e. the first signal is perfectly represented in amplitude where the others have a distribution). Using an SVD decomposition mixes all the signals together because the decomposed matrix remains full, and therefore no single signal is perfectly maintained. Overall, it seems that a SVD decomposition along with a Method 1 random process produces a set of signals that have the proper distributions, do not favor a single signal, and converge on the desired values.

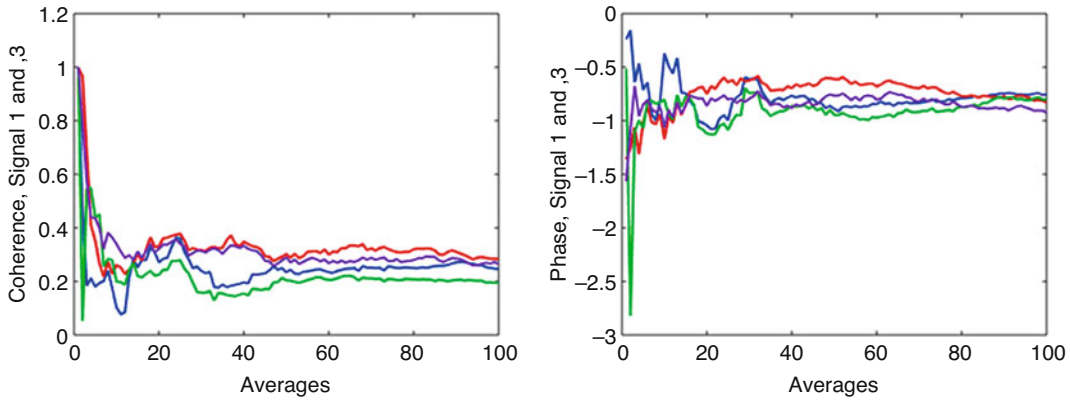

Fig. 22.6 Convergence of the Signal 1 to 3 coherence (left) and phase (right) with increasing number of averages

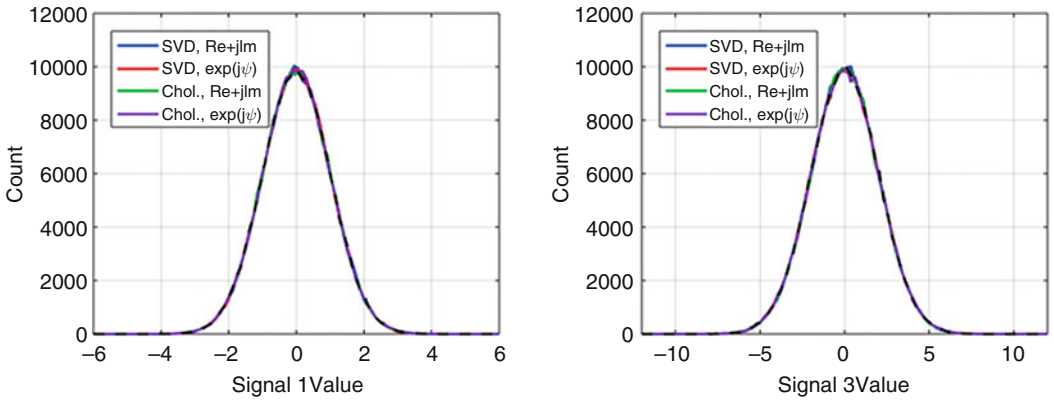

Fig. 22.7 Histograms of values of broadband Signal 1 (left) and Signal 3 (right) generated with the four different methods

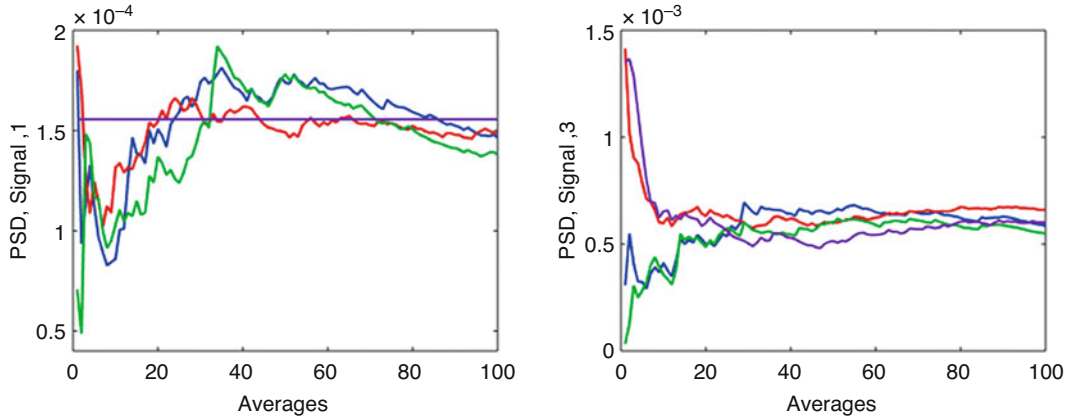

Fig. 22.8 Convergence of the APSD of Signal 1 (left) and Signal 3 (right) with increasing number of averages, shown at the 100 Hz frequency line

22.3.2.2 Broadband Signals

As was seen with the single signal, adding additional frequency content tends to obscure the effects of the signal generation methods. The histograms shown in Fig. 22.7 show that all four methods produce the Gaussian signal value distributions. Looking at the convergence of the signal APSD, coherence, and phase, there are no obvious winners, though again using a Cholesky decomposition along with a Method 2 random process results in a perfect signal 1 APSD, Figs. 22.8 and 22.9. Overall, with a sufficient number of averages, any of the four methods can achieve the desired specifications, as shown in the plots in Figs. 22.10 and 22.11.

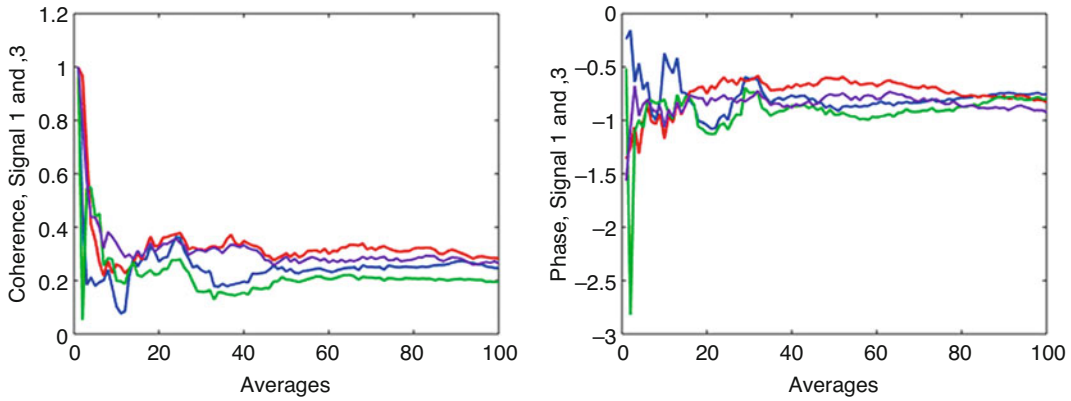

Fig. 22.9 Convergence of the Signal 1 to 3 coherence (left) and phase (right) with increasing number of averages, shown at the 100 Hz frequency line

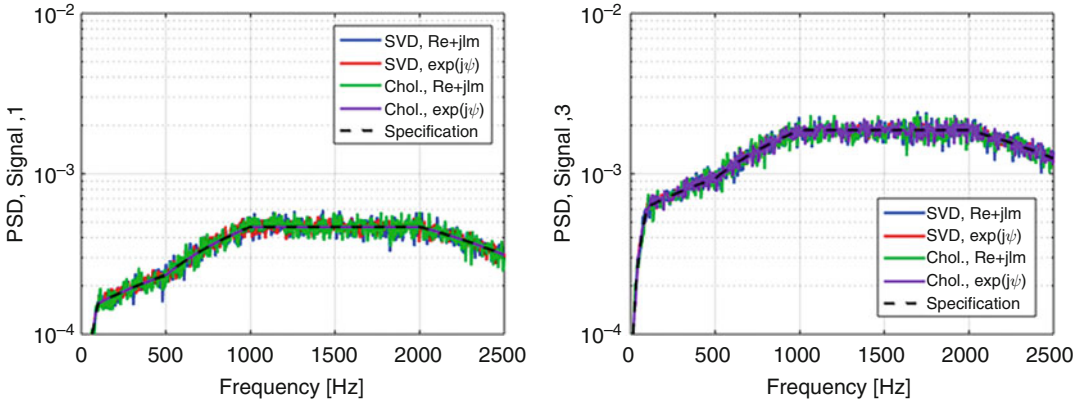

Fig. 22.10 APSD of Signal 1 (left) and Signal 3 (right) averaged over 100 realizations and compared to the specification

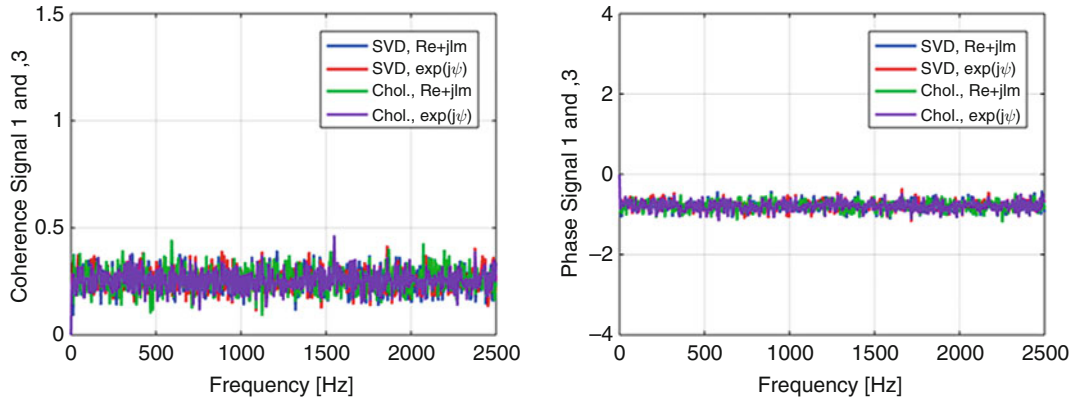

Fig. 22.11 Signal 1 to 3 coherence (left) and phase (right) with 100 averages

22.4 Long-Duration Signals Using Constant Overlap and Add

The signal generation methods described above result in fixed-length realizations of signals, the duration of which is determined by the frequency resolution. In general, longer duration signals are needed, so these realizations of signals are stacked end-to-end, resulting in a longer signal. However, simply stacking the signals end-to-end results in a discontinuity between one signal realization and the next since they result from independent processes. This discontinuity is a jump from one time point to the next, which would cause a shock-type input to the system, as shown in Fig. 22.12.

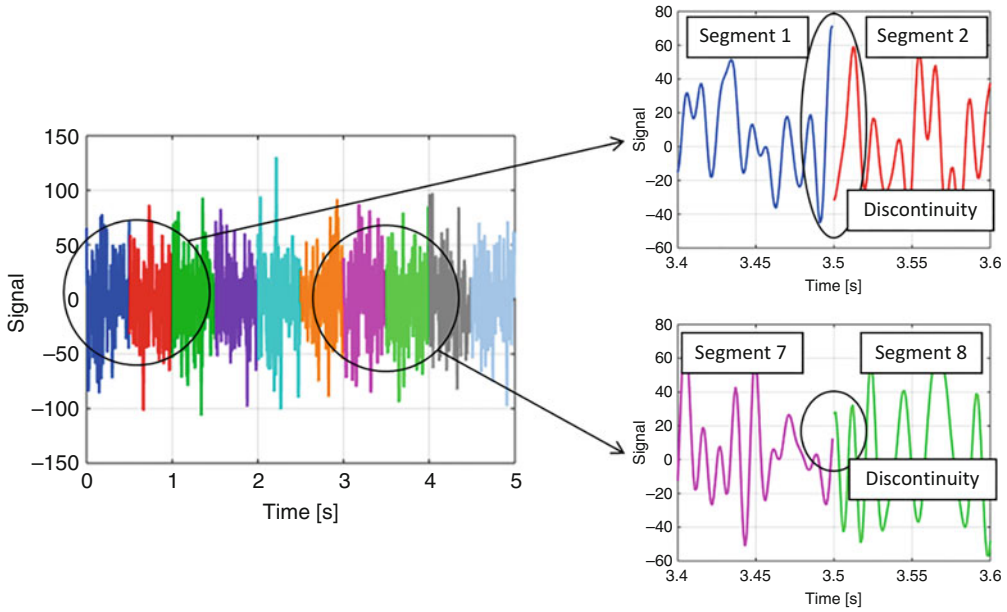

Fig. 22.12 Jump discontinuities between time history segments

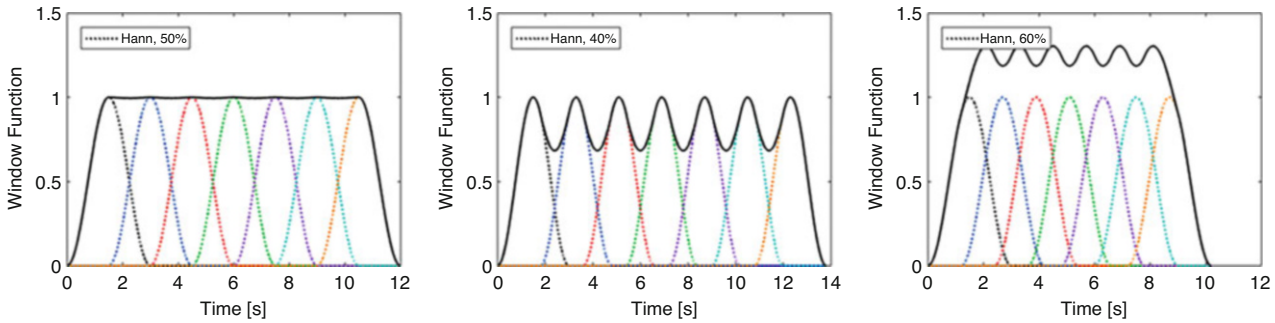

Fig. 22.13 Sum of overlapping Hann windows with the correct overlap (50%, left), too little overlap (40%, center), and too much overlap (60%, right)

Instead, it is best to apply some smoothing in the transition between segments, achieved by using the constant overlap and add (COLA) method. The first step in this method is to apply a smoothing window to each time history segment. This window can be anything—a simple trapezoid or a Hann window or a Tukey window, for example. Note that the amount of overlap between segments depends on the window type used. The objective is to set the overlap to achieve a sum of the windows equal to one. For a Hann window, unit amplitude is achieved with an overlap of 50% [1]. For Tukey or trapezoid windows, the overlap should be equal to the ramp portion of the window. Examples of overlapping Hann windows and the sum of the windows with different overlap is shown in Fig. 22.13. Less than 50% overlap results in a sum which is less than one and overlap greater than 50% results in a sum which is greater than one.

Once a window and overlap is chosen, the signal segments are overlapped, windowed, and then summed together to form a single, long-duration signal. This process is shown in Fig. 22.14 below where seven signal segments are generated, overlapped, then windowed with a trapezoid window, and finally summed together.

22.4.1 Variance Distortion Due to Windowing of Random Signals

Interestingly, while the window functions may sum to one, as desired, the resulting signal shows dips in the overlap region. These dips, highlighted by computing a running RMS of the signal, are shown in Fig. 22.15. These dips result from the fact that these are pseudo-random signals and applying the window skews the statistics in the overlap region. That is, in the

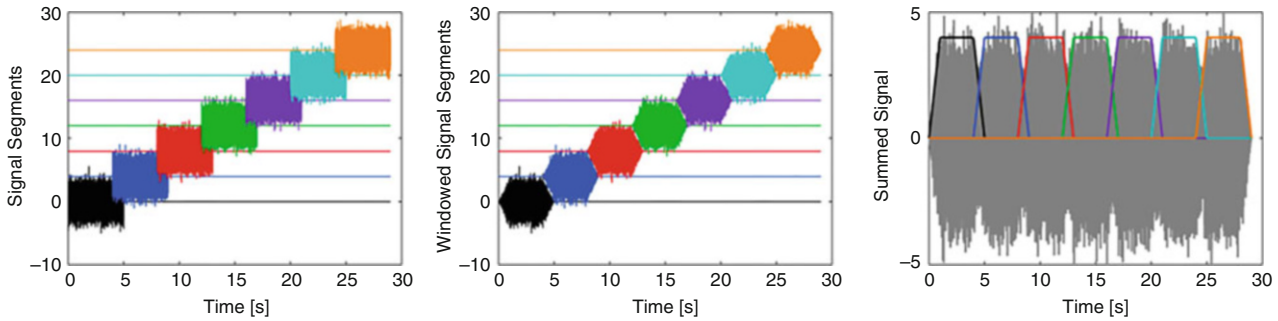

Fig. 22.14 Signal segments overlapped (left), windowed (center), then summed together (right)

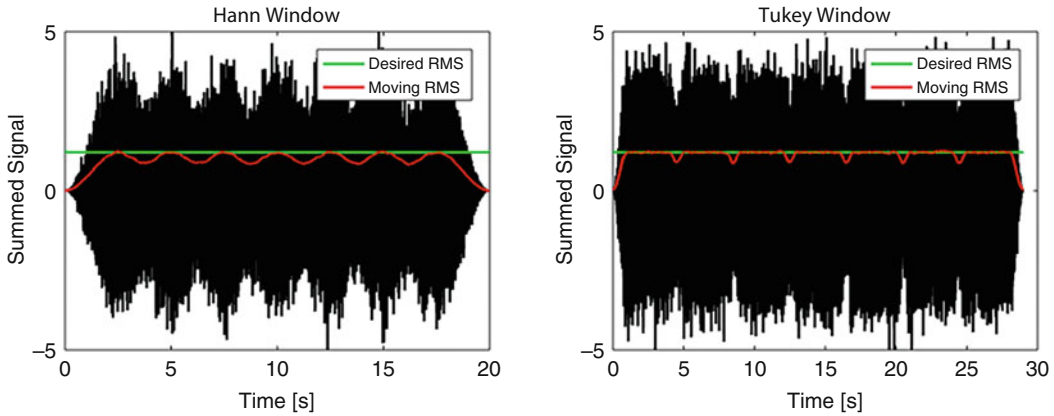

Fig. 22.15 Summed signal showing dips in the overlap regions, highlighted by the moving RMS of the signal, for a Hann window (left) and a Tukey window (right)

overlap region the total signal value is the sum of two windowed pseudo-random signals, w_1x_1 and w_2x_2, where the signals are x_1, x_2 and the window functions are w_1, w_2:

$$x_{total} = w_1x_1 + w_2x_2. \tag{22.13}$$

The variance, σ^2, of this composited signal is:

$$\sigma^2 = \frac{1}{N}\sum x_{total}^2 = \frac{1}{N}\sum (w_1x_1 + w_2x_2)^2 = \frac{1}{N}\sum \left(w_1^2x_1^2 + w_2^2x_2^2 + 2w_1w_2x_1x_2\right) . \tag{22.14}$$

The variance of an individual signal, σ_1^2 or σ_2^2 is equal to the desired signal variance (given by the desired APSD level), σ_0^2. Equation 22.14 can be re-written in terms of variance as:

$$\sigma^2 = w_1^2\sigma_0^2 + w_2^2\sigma_0^2 + 2w_1w_2\frac{1}{N}\sum x_1x_2 . \tag{22.15}$$

Note that the mean of the product of x_1, x_2 will be zero so the last term goes to zero, leaving the total signal variance as:

$$\sigma^2 = w_1^2\sigma_0^2 + w_2^2\sigma_0^2 . \tag{22.16}$$

For the total signal variance to equal the desired variance, the sum of the window functions squared must equal one:

$$\sigma^2 = w_1^2\sigma_0^2 + w_2^2\sigma_0^2 = \sigma_0^2\left(w_1^2 + w_2^2\right), \tag{22.17}$$

$$\left(w_1^2 + w_2^2\right) = 1 \rightarrow \sigma^2 = \sigma_0^2. \tag{22.18}$$

However, with the overlap set to obtain a sum of window amplitudes equal to one, (i.e. Hann window at 50% overlap), the sum of the window functions squared is less than one, which causes the error in the desired variance and summed signal in the overlap region.

22.4.2 Correcting Window Functions to Preserve Signal Variance

To obtain the proper total signal variance, the window functions squared must sum to one. This is simply obtained by leaving the overlap such that the sum of window functions equals one, then using the square root of the window function to window the signals:

$$w_1 + w_2 = 1, \tag{22.19}$$

$$\widehat{w}_1 = \sqrt{w_1}, \widehat{w}_2 = \sqrt{w_2}, \tag{22.20}$$

$$\widehat{w}_1^2 + \widehat{w}_2^2 = w_1 + w_2 = 1 \tag{22.21}$$

$$x_{total} = \widehat{w}_1 x_1 + \widehat{w}_2 x_2. \tag{22.22}$$

Using the square root of the window function provides the proper signal variance. This is demonstrated using two random signals and observing the distribution of signal values in the overlap region. Figure 22.16 shows the two signals windowed with a normal and square root trapezoid window. These windows are shown in Fig. 22.17. Signal values are extracted at a

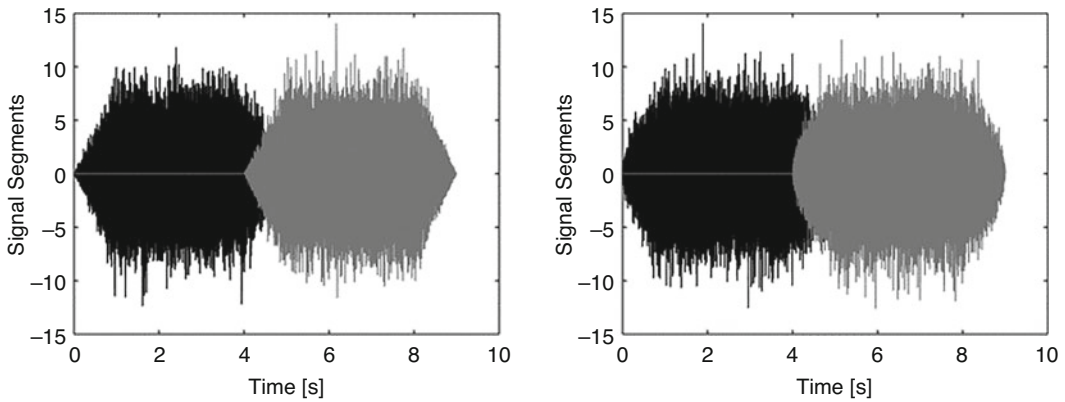

Fig. 22.16 Two overlapped random signals, windowed with a standard trapezoid window (left) and with a square root trapezoid window (right)

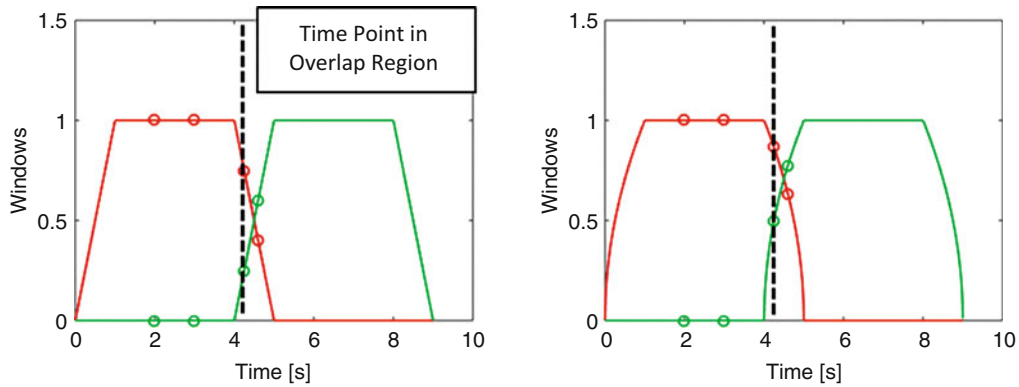

Fig. 22.17 Standard trapezoid window (left) and square root trapezoid window (right), with points shown for data extraction

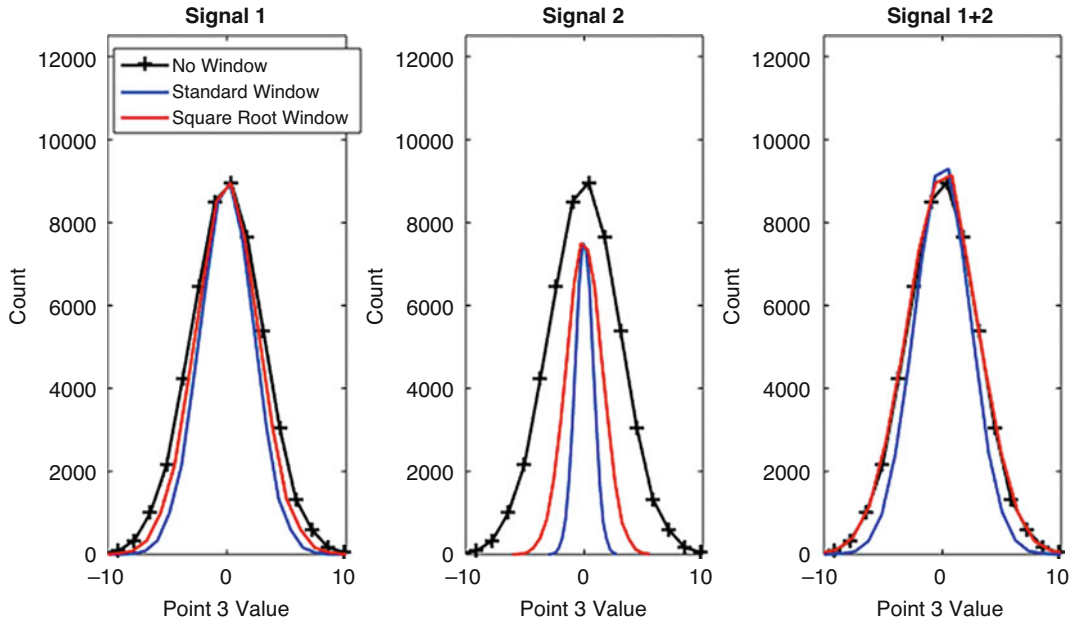

Fig. 22.18 Histograms of signal 1, signal 2, and signal 1 + signal 2 values at the third point (point in the overlap region)

time point in the overlap region for multiple realizations of the signals. The distribution of the signal values, for the standard and square root window, are shown in Fig. 22.18. It can be seen that using the standard window causes the variance of the sum to be too small. Changing to a square root window provides the proper signal variance.

22.5 Process Overview

This paper has discussed various methods for generating single and multiple random signals, and creating long duration signals from a series of signal realizations. Below is a step-by-step process which can be followed to generate multiple, correlated signal realizations:

1. Determine the specified CPSD matrix at all frequency lines from zero to the Nyquist frequency
2. Decompose from power (PSD) to linear (linear spectrum) space using a SVD-based matrix square root, giving the matrix L
3. Generate random process vectors, Ψ, using Method 1, the Gaussian real and imaginary components
4. Obtain a realization of linear spectra for each signal by: $X_x = L\Psi$, for each frequency line
5. Take the IDFT of the linear spectrums to get time histories for each signal
6. Repeat over multiple realizations, changing the random process vectors each time, resulting in time history segments for each signal
7. For each signal, generate a long-duration signal from the concatenation of multiple segments with the COLA method:
   (a) Window each time history segment with the square root of a window function
   (b) Overlap the segments such that the original window amplitudes sum to one
   (c) Sum the overlapped, windowed time history segments to obtain a long duration signal

22.6 Conclusions

With the current interest in multiple-input/multiple-output shaker testing for high-fidelity vibration testing, there is a need to develop and implement new control methods. Namely, new methods for estimating inputs with improved or specialized force estimation methods. These inputs are generally in the form of a CPSD matrix, which must be converted to representative

time histories to be useful in running a test. This paper presented and demonstrated multiple methods for generating time histories from a CPSD matrix. Interestingly, it was shown that the form of the random process vector has a significant effect on the statistics of the resulting signal. This was highlighted with studies at a single tone. Additionally, studies demonstrated how the method for decomposing the matrix from power to linear space affects results. In particular, it was shown that using a Cholesky decomposition results in one signal with no amplitude variation. Finally, the constant overlap and add method was demonstrated, which takes multiple signal segments and concatenates them to generate arbitrarily long signals, which is useful in performing vibration tests where multiple input realizations and multiple response averages are needed. In the overlap region between two signal segments, it was found that the total signal variance is reduced if standard window functions and overlap is used. Working through the variance equations, it was shown that simply taking the square root of the window function allows the variance of the total signal to be maintained, resulting in a signal with the correct variance and distribution of signal values at all times. These various methods were summarized into a step-by-step process which can be followed to generate multiple, correlated signals for performing multiple-input/multiple-output testing.

References

1. Heinzel, G., Rudiger, A., Schilling, R.: Spectrum and spectral density estimation by the discrete Fourier transform (DFT), including a comprehensive list of window functions and some new flat-top windows. Max-Planck-Institut fur Gravitationsphysik, Hannover (2002)
2. Trethewey, M.W.: Window and overlap processing effects on power estimates from spectra. Mech. Syst. Signal Process. **14**(2), 267–278 (2000)
3. Smallwood, D.O.: Multiple shaker random control with cross coupling. In: Proceedings of the Institue of Environmental Sciences (1978)
4. Smallwood, D., Paez, T.: A frequency domain method for the generation of partially coherent normal stationary time domain signals. Shock. Vib. **1**(1), 45–53 (1993)
5. Grigoriu, M.: On the spectral representation method in simulation. Probab. Eng. Mech. **8**, 75–90 (1993)
6. Bendat, J.S., Piersol, A.G.: Random data: analysis and measurement procedures. Wiley, New York (2010)
7. Bernhard, R.: The characterization of vibration sources and measuremnt of forces using multiple operating conditions and matrix decomposition methods. In: Proceedings of Inter-Noise 2000, the 29th International Congress on Noise Control Engineering, Nice, France (2000)

Chapter 23
Combining Test and Simulation to Tackle the Challenges Derived from Boundary Conditions Mismatches in Environmental Testing

Umberto Musella, Mariano Alvarez Blanco, Davide Mastrodicasa, Giovanni Monco, Di Lorenzo Emilio, Manzato Simone, Bart Peeters, Emiliano Mucchi, and Patrick Guillaume

Abstract Recent research stressed out the limitations of current practices on component level environmental vibration testing. These limitations are typically associated with non-realistic excitation mechanisms and the mechanical impedance mismatch due to differences between the operational and the test boundary conditions. General concern is that the real failure modes of the component are not correctly replicated, and more information might be needed to define a representative test practice. Does the current testing practice provide sufficient information? Is there a way to overcome the impedance mismatch between operational conditions and the test configuration by means of simulations and adequate control strategy for environmental tests? This work presents recent results from an intensive test campaign performed on the Box Assembly with Removable Component (BARC). Limitations of state-of-the-art random vibration testing techniques are investigated and Multiple-Input Multiple-Output Random control strategies are combined with simulation tools to find potential research directions to overcome the limitations. The final goal intends to tackle a rationale, rather than a single specific solution, to assess the design of a testing methodology leading to structural responses which are more representative of the operational environment in terms of potential failure mechanisms.

Keywords Environmental testing · Boundary condition challenge · MIMO control · Random vibration · Failure modes

23.1 Introduction

Random vibration control tests are performed to verify that a system and all its sub-components can withstand a random vibration environment during the operational life. These tests aim to accurately replicate via controlled shaker excitation the in-service structural response of a unit under test in the main axis of vibration and in all the possible axes where the levels exceed the acceptance thresholds [1]. The simplest way to expose a test article to an excitation in multiple axes is to

U. Musella (✉)
Siemens Industry Software NV, Leuven, Belgium

Test Division, Vrije Universiteit Brussel, Acoustic and Vibration Research Group, Elsene, Belgium
e-mail: umberto.musella.ext@siemens.com

M. Alvarez Blanco
Siemens Industry Software NV, Leuven, Belgium

D. Mastrodicasa
Department of Aeronautical Engineering, University of Rome La Sapienza, Rome, Italy

G. Monco
Department of Mechanical Engineering, University of Ferrara, Ferrara, Italy

D. L. Emilio · M. Simone
Test Division, Siemens Industry Software NV, Leuven, Belgium

B. Peeters
Siemens Industry Software NV, Leuven, Belgium

E. Mucchi
Department of Mechanical Engineering, University of Ferrara, Ferrara, Italy

P. Guillaume
Department of Mechanical Engineering, Vrije Universiteit Brussel, Elsene, Belgium

C. Walber et al. (eds.), *Sensors and Instrumentation, Aircraft/Aerospace, Energy Harvesting & Dynamic Environments Testing, Volume 7*, Conference Proceedings of the Society for Experimental Mechanics Series,
https://doi.org/10.1007/978-3-030-12676-6_23

perform a sequential Single-Input Single-Output (SISO) test: sequentially, the test article is rotated, the test set-up changed and a new test is performed with the required SISO profile as test specification. Practical aspects, linked for instance to the sizes of the article to be tested or to issues in changing multiple times the test set-up [2], can make the execution of these tests challenging or even impossible. However, the most critical aspect of sequential SISO test is that it poorly represents any real vibration environment and therefore can lead to an unacceptable time to failure estimation for the unit under test and different failure modes [3]. This has been shown in small-scale problems, such as printed wiring boards testing (where the inductors are critical components) [4] or thin plates [5], but also in large-scale tests, such as large spacecraft vibration testing as shown in [6]. The only alternative to overcome the sequential single-axis test limitations is to apply a simultaneous multi-axial excitation performing a Multi-Input Multi-Output (MIMO) vibration control test [7–9], that closely replicate the nature of the operational loads with advanced actuation systems.

Theoretically, a successful MIMO random control test can be performed in case the operational environment is fully replicated in the laboratory (within some tolerance margins), meaning that

1. operational measurements are available for all the control points.
2. the boundary conditions can be also exactly replicated with the available fixtures;

The works [10, 11] and more recently [12] describe in details advanced solutions to be adopted in case a full set of measurement at the control locations is not available, for example in case the PSD profiles come from enveloping, smoothing or averaging different operational conditions (or from standards). Since the solution of finding a full reference matrix with fixed PSD terms is not unique, these methods provide a meaningful solution to fill in the full reference Spectral Density Matrix (SDM) without the burden of considering the algebraic constraints deriving from its physical realizability [13].

In the recent years great visibility has been given to the problem of replicating in the laboratory the operational boundary conditions. The works of Daborn [14] and [15] on aerodynamically excited structures show how increasing the number of control channels and trying to match the operational mechanical impedance, on top of a successful random test, also allows to closely match the response in locations that are not controlled. These observations are at the basis of the so-called *IMMAT (Impedance-Matched Multi-Axial Test)*. Roberts in [16] shows that the (known) environmental replication further improves by increasing the number of shakers and adopting rectangular control strategies.

Even though the aforementioned limitations of the current testing practice are known to the environmental testing community (the first multi-input digital control algorithm was developed in 1978 by David Smallwood from Sandia National Laboratories and documented in the 1982's publication *A Random Vibration Control System for Testing a Single Test Item with Multiple Inputs* [17] and the influence of the vibration fixtures dynamic behavior was discussed by Avitabile in 1999 [18]), the high degree of expertise needed to upgrade the testing concepts and decades of single axis controlled excitation built meanwhile a legacy of rooted standards that currently represent the main reference for the environmental test engineers. Just recently, together with the increased complexity, sizes and cost of the article to be tested, also the concern increased of replicating as close as possible the in service vibration environments [2, 15, 16, 19–21]. In this frame, in 2016 a collaboration between Kansas City National Security Campus (managed by Honeywell Federal Manufacturing & Technology) and Sandia National Laboratories introduced the *Boundary Condition Challenge*. This project investigates the possibility of improving the in-service environment replication at a component level. Ultimately it is intended to propose a solution able to prove that the laboratory test will eventually lead to damage mechanisms closer to the one that the component would experience in service [22]. The challenge makes use of a simple hardware demonstrator that yet can introduce significant challenges in the environment replication at the component level. This structure is a Box Assembly (playing the role of a generic operational mounting) with Removable Component (playing the role of a unit under test). The BARC has been distributed to different research organizations, industries and universities and is currently extensively studied [23, 24].

Following the works of [12, 15] and [16], this paper aims to assess the influence of a specific random vibration control strategy on the responses at the component level. Specifically the aim of this work is to tackle the following research questions

1. What are the potential benefit to move to a MIMO random control strategy?
2. Can a specific control strategy improve the response at the component level?
3. Since the failure of the unit under test is directly related to the stresses and hence the strains, how well does the strain response correspond to operational conditions?

The long term goal intends to tackle a rationale, rather than a single solution, to assess the design of a testing methodology leading to structural responses which are more representative of the operational environment.

23.2 The BARC

The BARC provided to Siemens Industry Software is a specimen with a cut in the box (*cut* version), as illustrated in Fig. 23.1. Figure 23.1 shows the modification to the original design. Four M5 Holes have been drilled at the box base to directly connect

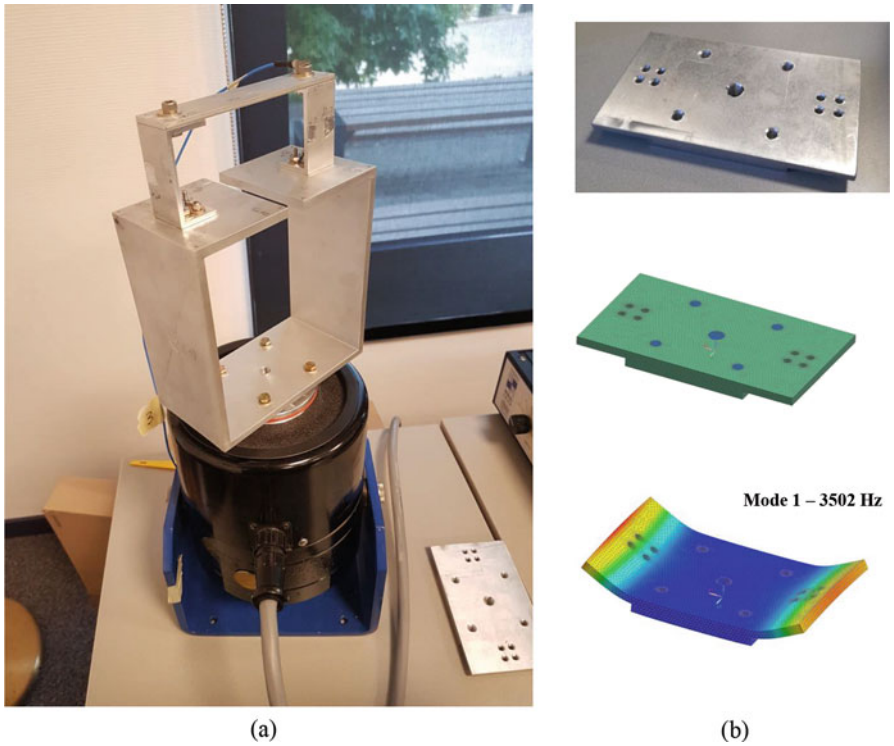

Fig. 23.1 The holes drilled on the base of the BARC allow the connection with a commonly used shaker of comparable size **(a)**. The fixture **(b)** has been designed to host the component on a vibration exciter, with a first numerical mode well above 2000 Hz (fixed conditions in correspondence of the holes)

Table 23.1 Comparison between the numerical and the experimental natural frequencies

Mode	Numerical nat. freq. in Hz	Experimental nat. freq. in Hz	Abs. % error
1	187.6	182.8	2.59
2	202	201.2	0.39
3	249.7	256.4	2.62
4	427.5	417.7	2.34
5	465.8	460.1	1.25
6	545.4	545.4	0.00
7	569.2	572.1	0.50
8	650.5	648.6	0.30
9	1023.1	1070	4.38
10	1087.7	1125.1	3.33

The absolute error is below the 5% for the first ten modes

the BARC to a commonly used 75 lbf shaker and an M8 hole in order to allow the connection with a larger shaker. In the figure the fixture specifically designed for component level testing (without the box) is also shown. The fixture is designed in order to consider the encumbrances with the aforementioned shaker when hosting first the full BARC and the component only and to have the first resonant mode (fixed in correspondence of the holes) well above the upper limit of the frequency range of interest (2000 Hz). The designed fixture proved to be also an attractive solution to connect the BARC to different next-level assemblies; for example in the current paper it has been used to mount the BARC on a commercial scooter to obtain operational data.

Before running an extensive environmental test campaign, the BARC has been modeled using Simcenter NX Nastran. The model was validated with test data coming from impact testing of the BARC in free-free conditions, processed with Simcenter Testlab. The details of this test campaign fall beyond the aim of this paper and will be discussed in the separate work [25]. Here only the correlation between the Test and the numerical model is shown. Table 23.1 shows that for the first ten modes the absolute error between the numerical and the experimental mode shapes is below 5%. The correlation between

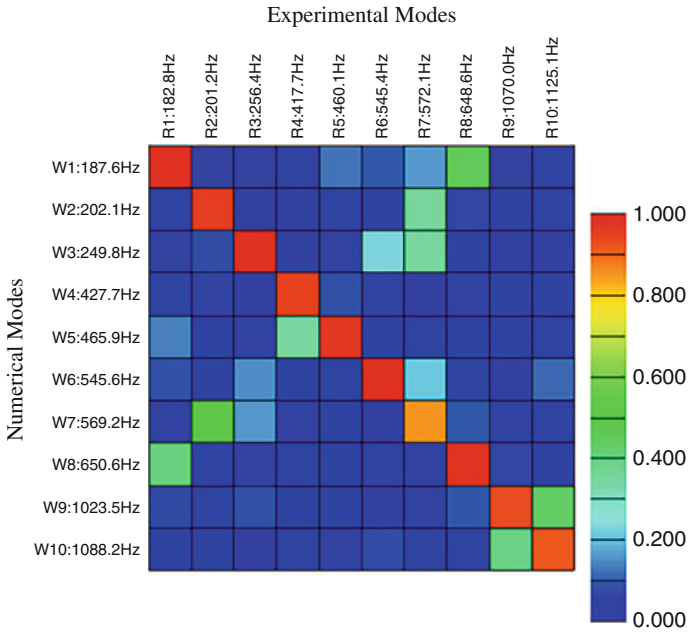

Fig. 23.2 The MAC between the numerical mode shapes and the experimental mode shapes is above 90% for the first ten modes

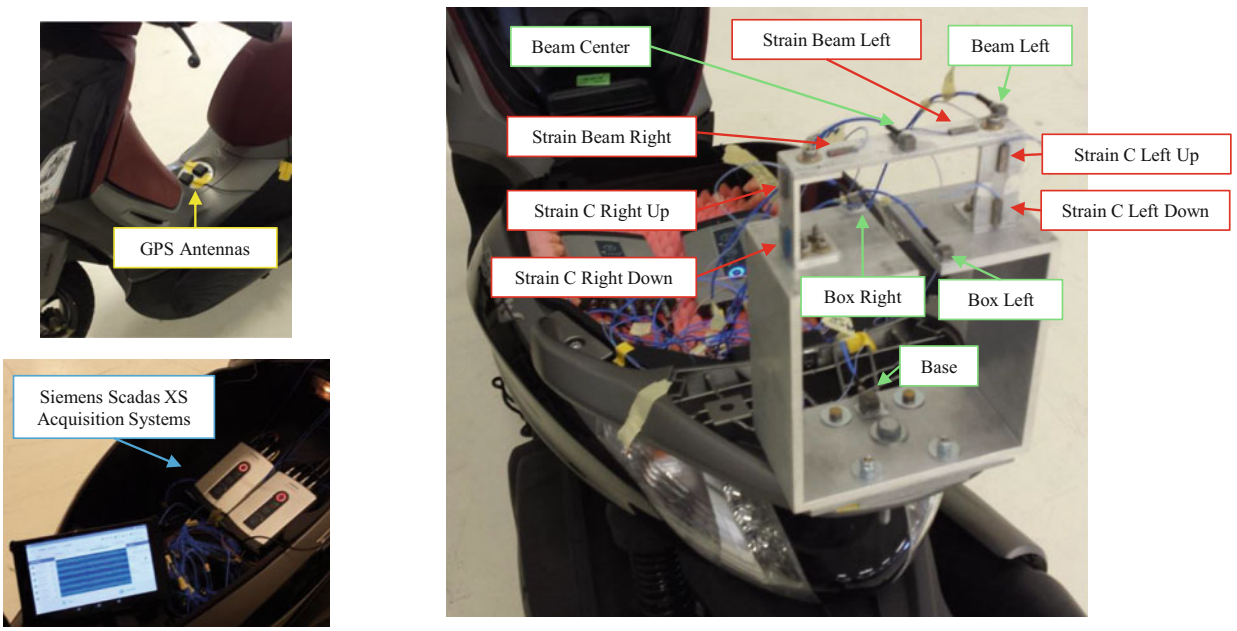

Fig. 23.3 Setup adopted to record the operational data on the BARC. 15 acceleration channels and 6 strain measurements were acquired with two Simcenter SCADAS XS units synchronized with GPS time

the numerical and experimental mode shapes is evaluated with the Modal Assurance Criterion (MAC) matrix, reported in Fig. 23.2. With MAC values above 90% for the considered modes, this correlation is very good.

23.3 Operational Environment

The BARC is instrumented with five ICP triaxial accelerometers (the same used for the modal model with an additional one at the box base) and six ICP strain sensors, in order to collect a set of operational data from a road excitation. Figure 23.3 illustrates the operational set-up. The BARC is mounted on the rear bar rack of a commercial scooter, fixed with an M8

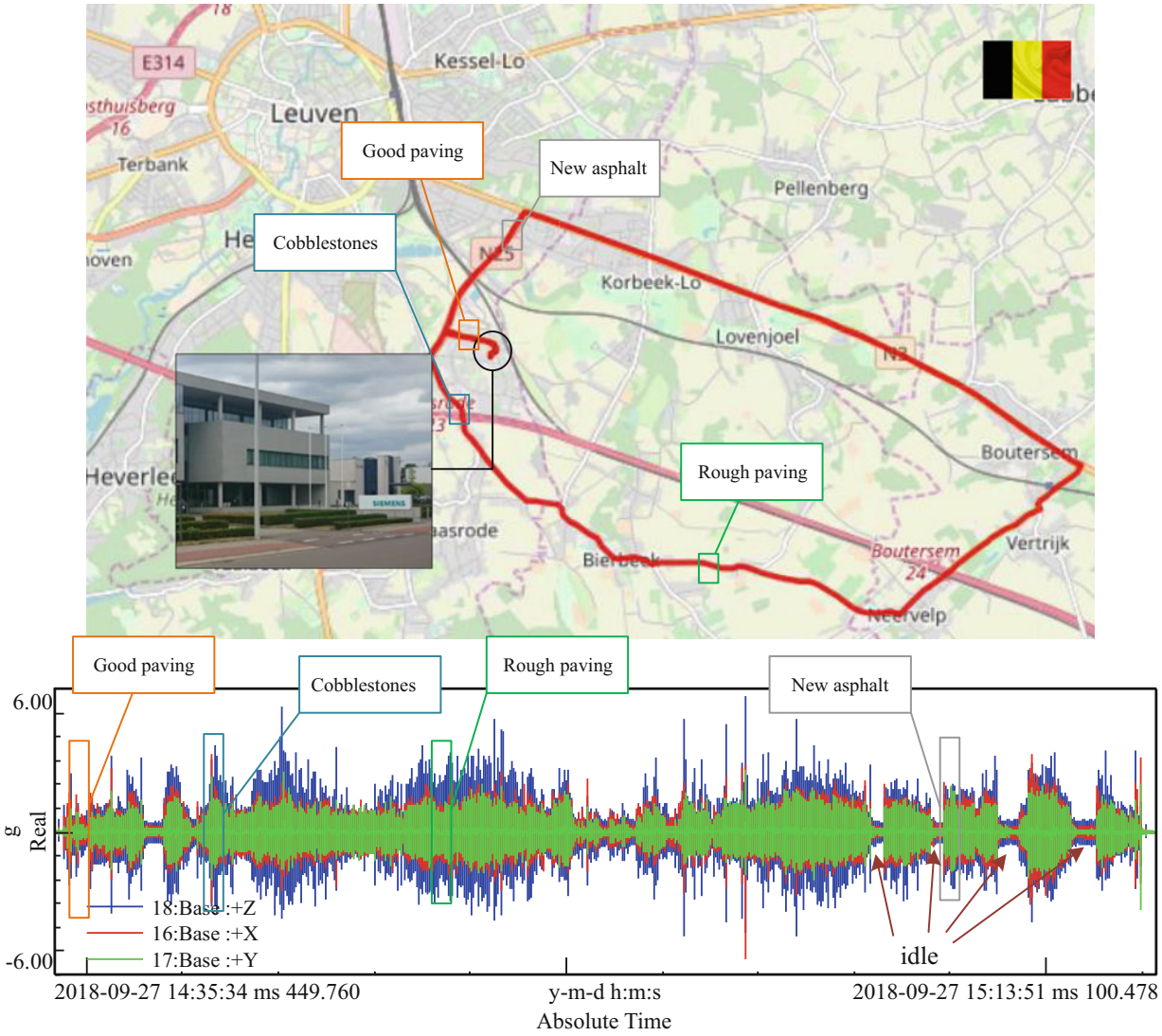

Fig. 23.4 GPS track of the 38 min driving on different pavings (top) and acceleration recordings at the base of the BARC (bottom). The processing in the paper refers to the data acquired driving on the rough paving

screw. The position of the BARC is adjusted in order to have the vertical axis (Z) perfectly vertical with the driver on the scooter. The data are acquired with two Simcenter SCADAS XS units, positioned under the seat storage compartment and synchronized with GPS time.

Figure 23.4 shows the track followed during the approximately 38 min drive in the neighborhoods of Leuven (Belgium), driving through different pavings. In the same figure, the segments corresponding to the different pavings are also highlighted. At this stage of the work only the segment corresponding to the rough paving is processed, obtaining a full Operational SDM (PSDs and CSDs) to be used as reference for the testing phase. The operational PSDs of the recordings are illustrated in Fig. 23.5. In the figure it is possible to see that the PSDs of the base accelerations roll-off at approximately 800 Hz, as also shown in the Table 23.2.

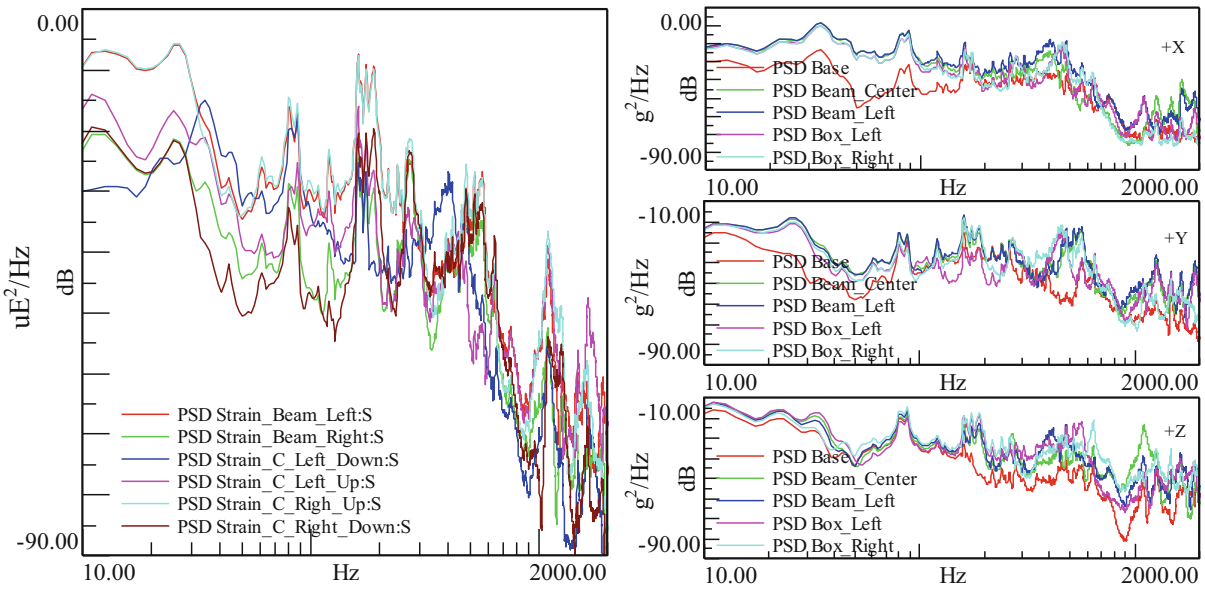

Fig. 23.5 Operational PSDs calculated from the time data recordings (rough paving)

Table 23.2 RMS from two different bandwidth

Channel	10–800 Hz	800–2000 Hz
Base +X	0.33 g_{RMS}	0.02 g_{RMS}
Base +Y	0.30 g_{RMS}	0.02 g_{RMS}
Base +Z	0.58 g_{RMS}	0.05 g_{RMS}

The PSD of the Base accelerometer channels drop at approximately 800 Hz

23.4 MIMO Random Vibration Testing

The operational data are used as reference for a series of multi-axis random tests carried out on the 10 kN 3-axis shaker of the MechLaV at the Tecnopolo of the University of Ferrara (Italy). The aim of the test campaign and generally of the current paper, is to investigate the behaviour at the component level addressing the research question formulated in Sect. 23.1. Specifically

1. The benefit of adopting simultaneous multi-axis excitation is supported by comparing the responses from MIMO Random Control tests with Random Control (SISO) tests, the latter on a shaker of similar sizes.
2. The acceleration PSDs at the component level are monitored during MIMO Random Control tests with different control strategies (square and rectangular).
3. Since the failure of the unit under test might be directly related to the dynamic stresses and hence the strains, also the strain PSDs at the component level are monitored during the tests.

The test setup is illustrated in Fig. 23.6 for the test with the full BARC and the component only. The BARC is attached to the shaker's head expander through a cast iron plate with an M8 screw at the base center. The plate is then fixed to the head expander with four M10 screws at the plate's corners. As data acquisition system and vibration controller, a Simcenter Scadas Mobile SCM205V is used with different input modules, driven by Testlab MIMO Random Control (and Random Control for the SISO case). For this test campaign, the target is the full spectral density matrix obtained after processing the data recorded during the rough paving segment of the operational acquisition. Different tests have been performed

1. Single axis tests using a single output with a shaker of comparable size. For the sake of brevity, as the X and Y direction provide results bringing the same conclusions, only the results related to the Z excitation are shown.
2. Simultaneous three-axial excitation, driving the three outputs of the shaker and controlling the responses at the Base in the three directions. In the environmental testing community this control strategy is often referred to as *square*, since the controlled system can be modeled with a square matrix of FRFs [7, 12] (number of controls equals the number of drives).

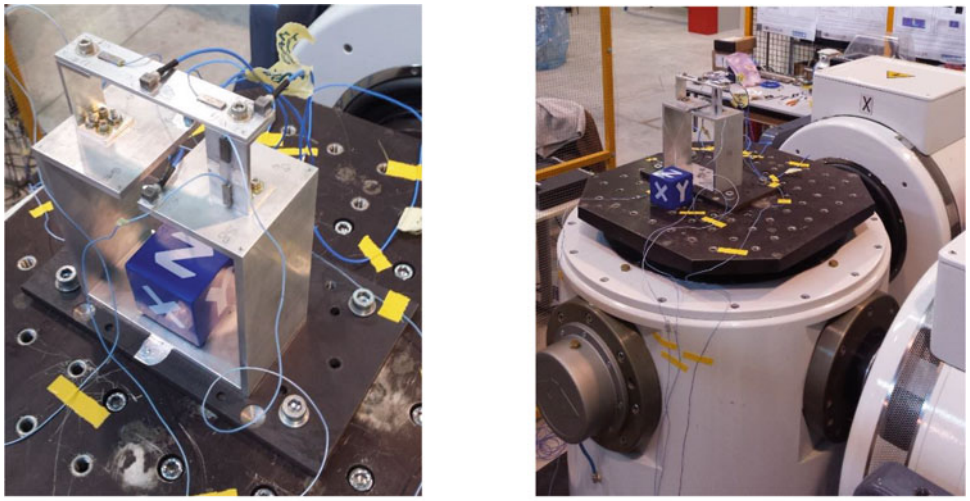

Fig. 23.6 Test set-up with BARC mounted on the Dongling three-axis shaker of the University of Ferrara **(a)**. The sensors on the unit under test are exactly at the same positions of the sensors used to acquire the operational data **(b)**

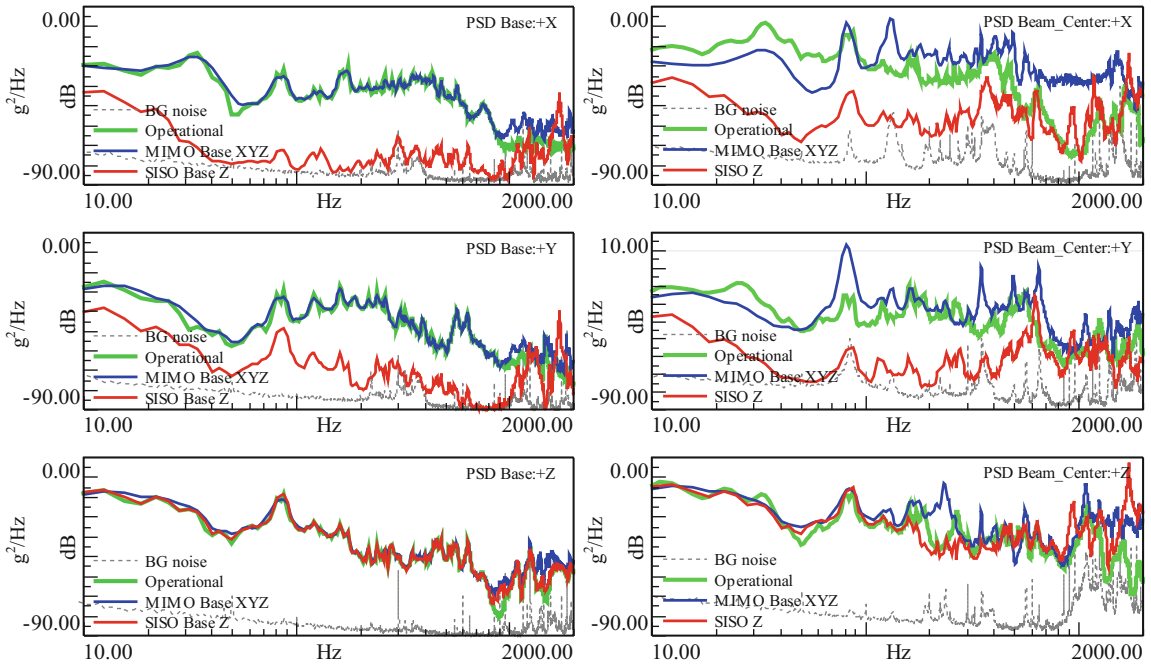

Fig. 23.7 PSDs of the controlled responses at the Base (left) and of the monitored component-level responses at the Beam center (right). Square control strategy (control channels: Base X, Y and Z)

3. Simultaneous three-axial excitation, driving the three outputs of the shaker and controlling the *Base* responses (X, Y and Z) and at the Box level (*Box Right* and *Box Left* X, Y and Z). The control system is in this case represented by a rectangular matrix of FRFs (9 controls × 3 drives), hence this control strategy is often referred to as *rectangular* [7, 12].

In the results shown in the Figs. 23.7, 23.9 and 23.10 the response PSDs corresponding to these tests are illustrated with red (1), blue (2) and magenta (3) solid lines. The reference PSDs profiles from the operational measurements are shown in solid green lines. For the sake of completeness a grey dotted line shows the PSDs of the background noise recordings for each measurement channel.

Figure 23.7 shows the comparison between the control results of the MIMO Random Control test (solid blue lines) controlling the three directions of the *Base* sensor while driving the three axis shaker and the SISO test run controlling the *Base:+Z* channel driving a shaker of comparable size (solid red line). In the figure (right column) are also reported the PSDs for the measurement sensor *Beam_Center*.

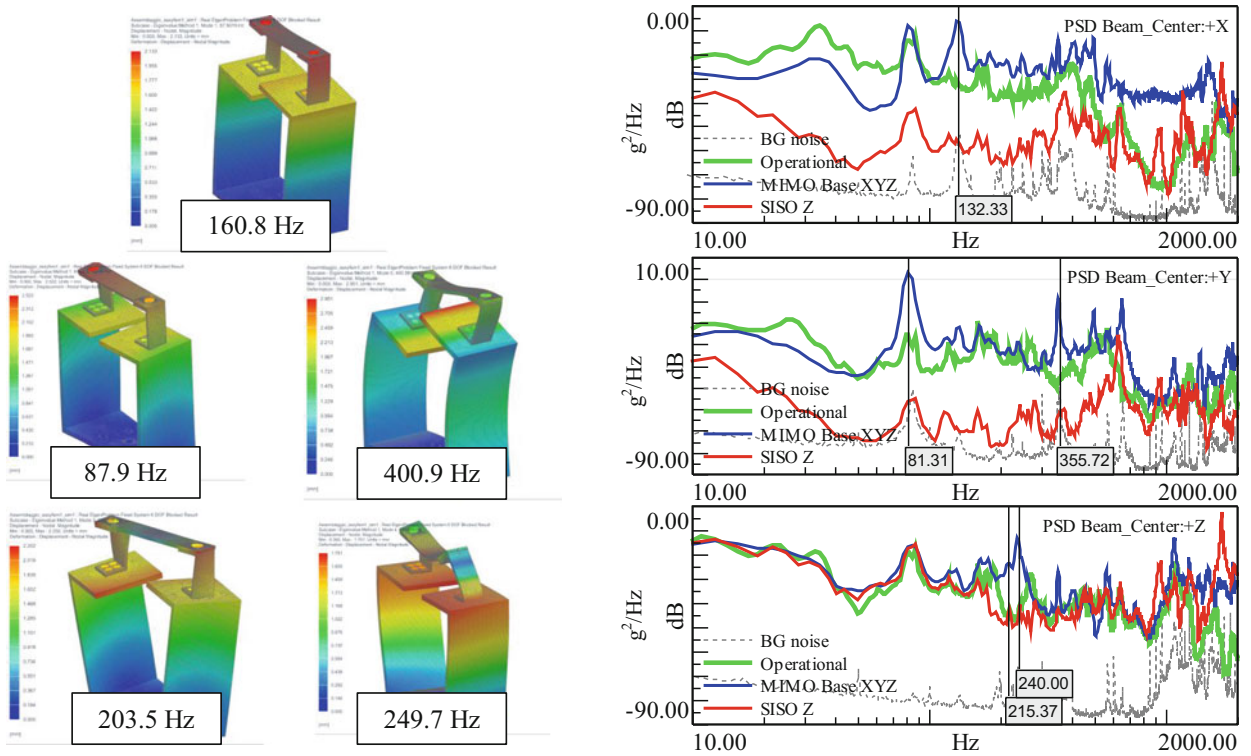

Fig. 23.8 PSDs of the monitored component-level responses at the Beam center (right). In the left, numerical real modes obtained with Simcenter NX fixing the holes at the base of the BARC

From the left side of the figure, it is possible to notice the advantage of adopting a simultaneous multi-axis excitation compared with a single axis excitation, as it is possible to simultaneously match the control PSDs (*Base* X, Y and Z). From the monitoring channels perspective, as shown on the right side of the figure, it is clear that for the single axis excitation the responses at the component level closely follows the reference in the controlled direction (Z, with some severe over-testing around 1700 Hz). On the contrary, the non controlled directions exhibit expected under-testing in almost the whole bandwidth, but also less expected over-testing at high frequencies (for example 1000, 1300 and 1700 Hz).

At the component level however, a closer look at the monitoring channels (*Beam_Center* X, Y and Z) shows that, even for the MIMO case, with the three control channels simultaneously matching the target at the base, the response PSDs significantly deviate from the operational ones. Even if a deeper analysis is sought, at this stage of the work it is remarkable to notice the correspondence of the peaks in the response PSDs with the numerical modal analysis results where the base of the BARC was fixed similarly as in the shaker test. In the numerical analysis it is clear how the box strongly participate to the specific mode shapes, as shown in Fig. 23.8. Therefore, the mismatches between targets and control responses in Fig. 23.7 can be preliminarily attributed to four reasons: (1) the presence of non controllable rotational degrees of freedom as input in the operational responses and (2) the non controlled dynamics of the box between the base and the component, (3) unavoidable mismatch between the operational mechanical impedance (the BARC was fixed on the scooter's rear bar rack) and the test one.

Following the results from the analysis and from the work [16], the proposed way to improve the response PSDs at the component level consists in adopting a rectangular control strategy, simultaneously controlling the three directions of *Base* and of the accelerometers on the Box (*Box_Right* and *Box_Left*). Figure 23.9 illustrates the comparison between the square control strategy and the rectangular control strategy, in terms of response PSDs at the base and at the beam center (monitoring channels at the component level). From the figure it is clear that controlling nine channels, distributed over the entire subassembly, greatly improves the responses at the component level. The PSDs for the monitored channels *Beam_Center* X, Y and Z, perfectly matching the operational ones. This result comes with a price: the PSDs at the control channels will unavoidably differ from the reference. This result was expected, as a perfect match of the responses at the Base was leading to a lack of replication at the component level of the operational environment.

Furthermore more aspects need to be considered when switching from a square to a rectangular control strategy (that go beyond the scope of the work at this stage). The achievable target will be unavoidably a *projection* of the defined target onto

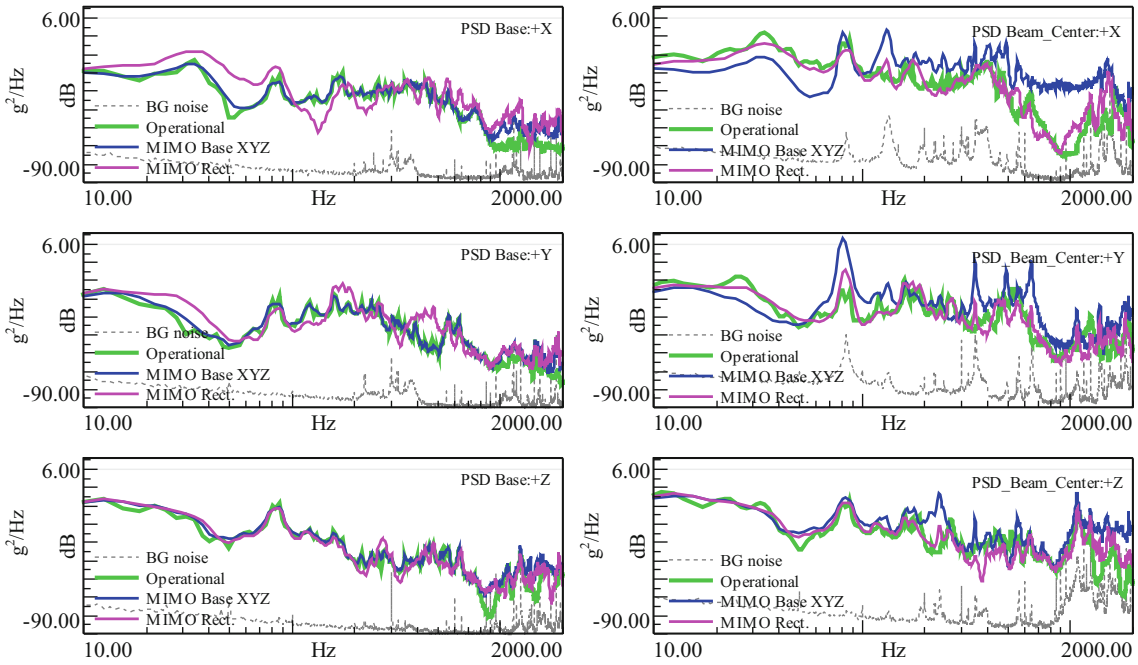

Fig. 23.9 PSDs of the controlled responses at the Base (left) and of the monitored component-level responses at the Beam center (right). Comparison between the rectangular control strategy (9 control channels: Base X, Y, Z, Box Left X, Y, Z and Box Right X, Y, Z)

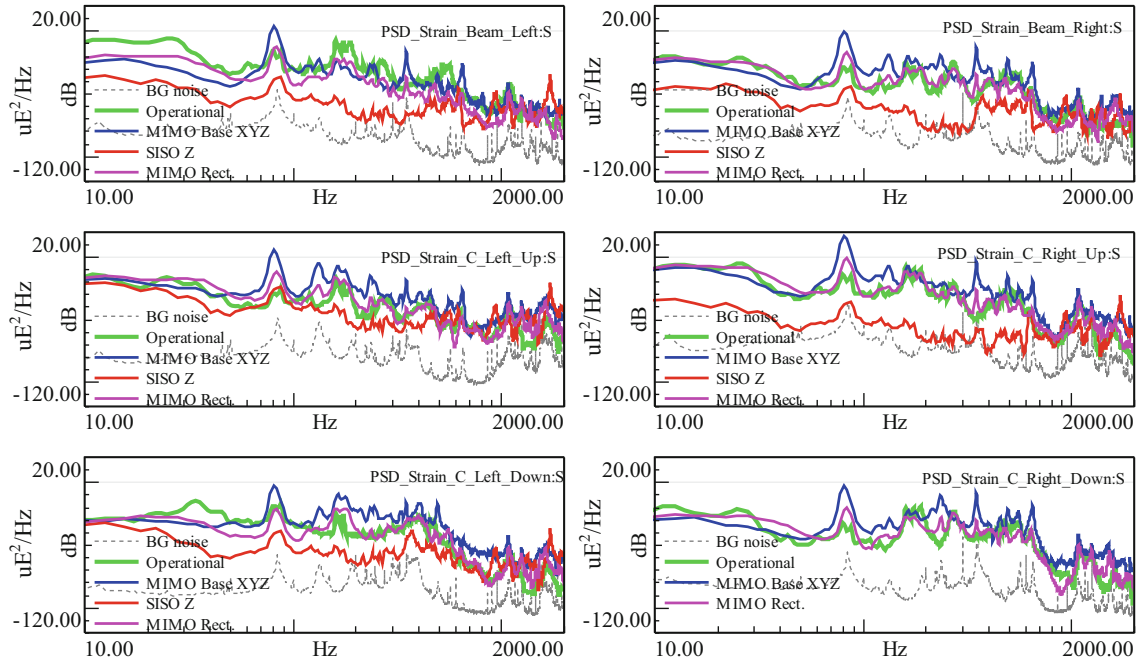

Fig. 23.10 PSDs of the monitored strain sensors measurements. Comparison between SISO, MIMO square and MIMO rectangular control strategy. The *Strain_C_Right_Down* sensor was not working correctly during the SISO measurements (was then replaced afterwards)

the reduced space defined by the number of drives (less than the number of controls), with potential *energy sinks* associated with the least square solution of the MIMO problem through pseudo-inversion [13].

Since the failure of the component might be directly related to the dynamic stresses and hence the strains, the measurements from the strain sensors were processed in order to analyze the validity of the results in terms of strain PSDs. Figure 23.10 shows the comparison between the different control strategies. The figure shows consistency with the

conclusions drawn by analyzing the test data from the accelerometers: even if a square MIMO control strategy brings to a strain field closer to the operational conditions, the rectangular MIMO control strategy, obtained by using also the channels on the box as controls, return a strain field that closely follows the strain field on the component during the real life operation.

23.5 Conclusions

In this paper the results of an intensive test campaign on the Box Assembly with Removable Component (BARC) are presented. First, a set of operational measurements has been collected fixing the BARC on a commercial scooter. Accelerations on the box and the component and strain measurements on the component have been processed to obtain operational PSDs and CSDs to be used as reference for the test campaign. Both single axis (Random Control) and simultaneous three-axis (MIMO Random Control) tests have been performed on the BARC (fixed on the head expander of the shaker through an iron plate). The acceleration PSDs at the center of the beam and the full set of strain PSDs have been used to compare the feature of the adopted control strategy to replicate the operational conditions. It is undoubtedly advantageous to get the responses controlled simultaneously in the three axes adopting a MIMO square control strategy as it will most probably return a failure mode close to the one that the BARC would experience in real-life. However, the test results with the MIMO square control show that, at the component level, there are still clear narrowband differences in the PSDs of the monitoring channels, due to the uncontrolled fixture dynamics (the Box in this case). These differences are almost completely overcome when using more control channels on the box itself and hence adopting a rectangular control strategy: the response PSDs are in this way matched in several points on the full BARC (in the least square sense). Even though a perfect replication is still not achieved, because of the aforementioned impedance mismatches and the fact that the real-life six-dof excitation is reduced to three axes only, adopting a rectangular control strategy provides accelerations and strain PSDs that closely follow the in-service PSDs at the component level. Even though the promising results obtained during this study are fruit of an early investigation and deeper analysis (and testing) are sought, matching the strain response PSDs obtained at the component level (without replicating the complete operational impedance), suggests that an appropriate choice of number and locations of multiple control channels could be considered in order to try to compensate for the impedance mismatch that is at the base of the boundary condition challenge.

Acknowledgements The authors gratefully acknowledge the MechLav Research Group of the University of Ferrara for providing access to their three-axis shaker, the eng. Giacomo D'Elia for assisting the test campaign. Sandia National Laboratories is gratefully acknowledged for motivating the Boundary Condition Challenge and providing the BARC.

References

1. United States Standard 810G *Method 514: vibrations* (2008)
2. United States Standard 810G *Method 527.1: multi-exciter tests* (2008)
3. Mršnik, M., Slavič, J., Boltežar, M.: Multi-axial vibration fatigue–a theoretical and experimental comparison. Mech. Syst. Signal Process. **76–77**, 409–23 (2016)
4. Ernst, M., Habtour, E., Abhijit, D., Polhand, M., Robeson, M., Paulus, M.: Comparison of electronic component durability under uniaxial and multiaxial random vibrations. J. Electron. Packag. **137** 165–80 (2015)
5. Gregory, D., Bitsie, F., Smallwood, D.O.: Comparison of the response of a simple structure to single axis and multiple axis random vibration inputs. In: Proceedings of the 79th Shock and Vibration Symposium (2008)
6. Soucy, Y., Côté, A.: Reduction of overtesting during vibration tests of space hardware. Can. Aeronaut. Space J. **48** 77–86 (2002)
7. Underwood, M.A.: Multi-exciter testing applications, theory and practice. In: Proceedings of Institute of Environmental Sciences and Technology (2002)
8. Smallwood, D.O.: Multiple shaker random vibration control–an update. In: Proceedings of the Institute of Environmental Sciences and Technology. Institute of Environmental Sciences and Technology, Illinois (1999)
9. Peeters, B., Debille, J.: Multiple-input-multiple-output random vibration control: theory and practice. Proc. Int. Conf. Noise Vibration Eng. **1**, 507–16 (2002)
10. Smallwood, D.O.: Multiple-input multiple-output (MIMO) linear systems extreme inputs/outputs. Shock. Vib. **14**, 107 (2007)
11. Smallwood, D.O.: Minimum input trace for multiple input multiple output linear systems. J. IEST **56**, 57–61 (2013)
12. Musella, U., D'Elia, G., Carrella, A., Peeters, B., Muchi, E., Marulo, F., Guillaume, P.: A minimum drives automatic target definition procedure for multi-axis random control testing. Mech. Syst. Signal Process. **107**, 452–68 (2018)
13. Alvarez Blanco, M.G., Janssens, K., Bianciardi, F.: Experimental verification of projection algorithms and optimization routines for acoustic field uniformity enhancement in MIMO direct field acoustic control. In: Proceedings of the International Conference on Noise and Vibration Engineering (2016)

14. Daborn, P.M., Ind, P.R., Ewins, D.J.: Enhanced ground vibration testing for aerodynamic environments. Mech. Syst. Signal Process. **49**, 165–80 (2014)
15. Daborn, P.M., Ind, P.R., Ewins, D.J.: Next-generation random vibration tests. Top. Modal Anal. II **8**, 397–410 (2014)
16. Roberts, C., Ewins, D.J.: Multi-axis vibration testing of an aerodynamically excited structure. J. Vib. Control. **24** (2016)
17. Smallwood, D.O.: A Random Vibration Control System for Testing a Single Test Item with Multiple Inputs. Technical Report, Sandia National Laboratories, Albuquerque (1982)
18. Avitabile, P.: Why you can't ignore those vibration fixture resonances. Sound Vib. **33**, 20–27 (1999)
19. Underwood, M.A., Keller, T.: Recent system developments for multi-actuator vibration control. Sound Vib. **35**, 16–23 (2001)
20. Underwood, M.A., Keller, T.: 8 Actuator system provides 1 DOF to 6 DOF controlled satellite qualification testing up to 100 Hz. In: Proceedings of the 28th Aerospace Testing Seminar (2014)
21. Appolloni, M., Dacal, R.B., Cozzani, A., Knockaert, R., Thoen, B.: Multi-degrees-of-freedom vibration platform with MIMO controller of future spacecraft testing: and application case for virtual shaker testing. In: Proceedings of the 29th Aerospace Testing Seminar (2015)
22. Harvie, J., Soine, D.E., Jones Jr, R.J., Skousen, T.J., Schoenherr, T.F., Starr, M.: Boundary conditions in environmental testing round robin. In: Proceedings of the IEST (2018)
23. Soine, D.E., Jones Jr, R.J., Harvie, J., Skousen, T.J., Schoenherr, T.F.: Designing hardware for the boundary condition round robin challenge. In: Proceedings of the XXXV IMAC Conference (2017)
24. Larsen, W., Blough, J.R., DeClerck, J.P., VanKarsen, C.D.: Initial modal results and operating data acquisition of shock/vibration fixture. In: Proceedings of the XXXV IMAC Conference (2017)
25. Rohe, D.P., Smith, S., Brake, M.R.W., DeClerck, J., Alvarez Blanco, M., Schoenherr, T.F., Skousen, T.: Testing summary for the box assembly with removable component structure. In: The Proceedings of the XXXVI IMAC Conference (2018)

Chapter 24
Defining Component Environments and Margin Through Zemblanic Consideration of Function Spaces

Michael J. Starr and Daniel J. Segalman

Abstract Historically the qualification process for vehicles carrying vulnerable components has centered around the Shock Response Spectrum (SRS) and qualification consisted of devising a collection of tests whose collective SRS enveloped the qualification SRS. This involves selecting whatever tests are convenient that will envelope the qualification SRS over at least part of its spectrum; this selection is without any consideration of the details of structural response or the nature of anticipated failure of its components. It is asserted that this approach often leads to over-testing, however, as has been pointed out several times in the literature, this approach may not even be conservative.

Given the advances in computational and experimental technology in the last several decades, it would be appropriate to seek some strategy of test selection that does account for structural response and failure mechanism and that pushes against the vulnerabilities of that specific structure. A strategy for such a zemblanic (zemblanity is the opposite of serendipity, the faculty of making unhappy, unlucky and expected discoveries by design) approach is presented.

Keywords Shock response spectra · Function spaces · Optimization · Component failure · Qualification testing · Zemblanity

24.1 Introduction

The qualification process is largely in thrall to its own history. A process that could be implemented in the 1960s (almost 60 years ago) is still largely in place for the usual reasons of technical and institutional inertia:

- It is a process with which practitioners have become very comfortable.
- The qualification documentation on a large number of currently deployed systems is heavily based on the legacy processes, which because of historical acceptance are rarely re-examined.
- Baseline environments data were collected and stored in a commensurate manner (SRS).
- Much of the current environmental procedures documents (such as MIL-STD-1540E and MIL-STD-810G) are built around the legacy process.
- Despite an acknowledgment of the limitations and non-rigorous character of the current system, no more physics-based approach has been proposed.

Given the restriction that almost all information on the excitation in the existing environments specification is in terms of SRS—original acceleration data has been lost or discarded—the challenge is to identify tests that more thoroughly interrogate the system at hand to gain confidence that it would survive any excitation consistent with the SRS. We refer to this search for the most severe test for the specific system at hand as zemblanic.

Sandia National Laboratories is a multimission laboratory managed and operated by National Technology and Engineering Solutions of Sandia, LLC., a wholly owned subsidiary of Honeywell International, Inc., for the U.S. Department of Energy's National Nuclear Security Administration under contract DE-NA-0003525.

M. J. Starr (✉)
Sandia National Laboratories, Albuquerque, NM, USA
e-mail: mjstarr@sandia.gov

D. J. Segalman
Michigan State University, East Lansing, MI, USA

C. Walber et al. (eds.), *Sensors and Instrumentation, Aircraft/Aerospace, Energy Harvesting & Dynamic Environments Testing, Volume 7*, Conference Proceedings of the Society for Experimental Mechanics Series,
https://doi.org/10.1007/978-3-030-12676-6_24

24.2 Problem Development

Let us consider the case where the environment is characterized by a one-dimensional SRS. We note that the shock response spectrum is a nonlinear operator on acceleration histories. Say that $S_1(\omega)$ is the SRS of acceleration history $f_1(t)$:

$$S_1(\omega) = N(f_1(t)) \tag{24.1}$$

A feature of this nonlinearity is that there is no unique inverse to the SRS, in particular, there may be two distinct acceleration histories f_1 and f_2 such that

$$\|N(f_1) - N(f_2)\| = 0 \text{ but } \|f_1 - f_2\| = \epsilon > 0 \tag{24.2}$$

where $||\bullet||$ is an L_2 norm. If our concern were just reproducing the SRS in the frequency range of interest, we might use any of a multitude of experiments to gain confidence that our structure could survive environments characterized by the specified SRS. It turns out that the choice of test is critical. Consider a structure having a vulnerability at some location. This could be a thin ceramic layer chemically attached to its substrate. Excessive bending would cause this ceramic to break.

Consider multiple tests that all are enveloped by an environments' SRS and that generate nearly identical SRS in some frequency range of interest. We note that experience shows that the potential for damage from each may be quite different. This suggests the wisdom of searching for the most damaging type of experiment when doing serious qualification. Though the acceleration histories contemplated have similar SRSs in the specified frequency range, the responses that they elicit in the structure and the consequent damage could be quite different. Of course, in the frequency ranges of interest we look to the type of experiment that most severely tests our structure and we select the parameters of the experiment along the same lines. It makes sense for qualification to include consideration of alternative experiments for each frequency range of interest, choosing the ones that best test the structure at hand. However, each experiment has some physical constraints on its parameters—for instance shakers have limitations on stroke and acceleration as well some resonant frequency bands that must be avoided.

24.3 Formulation as an Optimization Problem

Generally, acceleration data for structures are recorded in a unidirectional manner: accelerations are measured in each of three directions and each of those three signals are recorded as independent SRSs. Each SRS is used to guide specifications for tests in that direction. Starting modestly, we address the question of test selection on the basis of a single SRS. The SRS is defined in such a way that

$$N(\alpha f_1(t)) = \alpha N(f_1(t)) \tag{24.3}$$

but in general

$$N(f_1(t) + f_2(t)) \neq N(f_1(t)) + N(f_2(t)) \tag{24.4}$$

Because of Eq. (24.3), one anticipates that acceleration histories associated with larger SRSs will be the more severe tests of a structure. On the other hand, from Eq. (24.2) we anticipate that there might be two acceleration histories f_1 and f_2 for which $N(f_1) = N(f_2)$ but such that f_1 causes damage to the structure and f_2 does not. In fact, one might anticipate that there exist acceleration histories f_1 and f_2 for which $N(f_1) < N(f_2)$ but such that f_1 causes damage to the structure and f_2 does not. This possibility was proven by Smallwood [1]. Given the non-uniqueness of acceleration histories that map to a given SRS, it is not sufficient merely to find accelerations that map to that SRS. Instead we shall attempt to find the tests consistent with the given SRS that most severely challenge the structure.

Let us assume a mapping from acceleration history to some failure measure of the component. For instance, this mapping could derive from a finite element model of the structure coupled with some failure metric such as peak von Mises stress, max curvature, or high-load, low-cycle fatigue criterion. This failure measure can be expressed as:

$$m = \mathcal{F}(f) \tag{24.5}$$

Also, we have some sets of tests T_k and each test has a vector β_k of test parameters in a regime of physically realizable parameters B_k, obtaining the acceleration history:

$$f_k(t) = T_k\left(t, \beta_k \in B_k\right) \tag{24.6}$$

For the given test, we might look for the optimal set of parameters to probe the durability of the structure:

$$m_k^*(\omega) = \max_{N(T_k(t,\beta_k \in B_k)) \leq SRS} \mathcal{F}\left(T_k\left(t, \beta_k \in B_k\right)\right) \tag{24.7}$$

If we have multiple tests available to us, the maximum damage possible from among these tests is

$$m^*(\omega) = \max_k m_k^*(\omega) \tag{24.8}$$

It should also be mentioned that additional constraints could be added to this optimization problem. Temporal moments, for example, as discussed by Cap and Smallwood [2], are a class of constraints for consideration.

Let us further consider multi-dimensional cases where we are given SRS information in each of two directions, but the character of the corresponding accelerations is not given. We know neither the imposed acceleration histories or the phase relationship between the two signals. We pose this issue again as an optimization problem. We consider tests T_k that involve load in both the **i** and **j** directions

$$T_k\left(t, \beta_k\right) = f_{k,\beta_k}^x(t)\mathbf{i} + f_{k,\beta_k}^y(t)\mathbf{j} \tag{24.9}$$

The test to be specified is that experiment for which $N\left(f_{k,\beta_k}^x(t)\right) < SRS_1$ and $N\left(f_{k,\beta_k}^y(t)\right) < SRS_2$, but that most severely tests the vulnerabilities specific to that structure. We define

$$m_k^*(\omega) = \max_{N\left(f_{k,\beta_k}^x(t)\right) \leq SRS_1, N\left(f_{k,\beta_k}^y(t)\right) \leq SRS_2} \mathcal{F}\left(T_k\left(t, \beta_k \in B_k\right)\right) \tag{24.10}$$

The coupling between the x and y components of force is achieved through the physics and parameters of the experiment.

24.4 Discussion

Though the traditional methods of selecting and implementing qualification testing on the basis of reproducing SRS curves has been around for a very long time, so have its deficiencies. Because much if not most, of the environments information is stored as SRS, we are committed to employ it in our specification of qualification tests, but we are still free to look for the most intelligent and informed methods to select tests and test parameters. One approach is described conceptually here using an optimization formulation for selection and tailoring tests.

The approach outlined above will be demonstrated on the BARC structure introduced at IMAC XXXV. Means of expanding the method to consider multiple failure modes will be addressed, including the potential to devise failure mode-informed margin definition.

References

1. Smallwood, D.: Enveloping the shock response spectrum (SRS) does not always produce a conservative test. J. IEST. **49**(1), 48–52 (2006)
2. Cap, J.S., Smallwood, D.: A methodology for defining shock tests based on shock response spectra and temporal moments. In: Proceedings of the 68th Shock & Vibration Symposium, Baltimore, MD, Nov 3–7 (1997)

Chapter 25
European Service Module: Structural Test Article (E-STA) Building Block Test Approach and Model Correlation Observations

James P. Winkel, Samantha A. Bittinger, Vicente J. Suárez, and James C. Akers

Abstract The Orion European Service Module—Structural Test Article (E-STA) underwent sine vibration testing in 2016 using the Mechanical Vibration Facility (MVF) multi-axis shaker system at NASA Glenn Research Center's (GRC) Plum Brook Station (PBS) Space Power Facility (SPF). The main objective was to verify the structural integrity of the European Service Module (ESM) under sine sweep dynamic qualification vibration testing. A secondary objective was to perform a fixed-base modal survey, while E-STA was still mounted to MVF, in order to achieve a test correlate the finite element model (FEM). To facilitate the E-STA system level correlation effort, a building block test approach was implemented. Modal tests were performed on two major subassemblies, the crew module/launch abort structure (CM/LAS) and the crew module adapter (CMA) mass simulators. These subassembly FEMs were individually correlated and then integrated into the E-STA FEM prior to the start of the E-STA sine vibration test. This paper summarizes the modal testing and model correlation efforts of both of these subassemblies and how the building block approach assisted in the overall correlation of the E-STA FEM. This paper will also cover modeling practices that should be avoided, recommended instrumentation positioning on complex structures, and the importance of the FEM geometrically matching CAD in sufficient detail in order to adequately replicate internal load paths. The goal of this paper is to inform the reader of the hard earned lessons learned and pitfalls to avoid when applying a building block test approach.

Keywords Finite element correlation · Finite element modeling · Modal testing · Building block approach · Modal testing · Base-shake · Environmental testing

25.1 Introduction

The Orion Multi-Purpose Crew Vehicle (MPCV), shown in detail in Fig. 25.1, is the spacecraft that NASA is developing to send humans and cargo into space, beyond low earth orbit, and to return them safely to earth. The MPCV configuration can be broken down into the following major subassemblies which include (listed from top to bottom):

- Launch Abort System (LAS)
- Crew Module (CM) with its MPCV-ESM interface Crew Module Adapter (CMA)
- European Service Module (ESM)
- Spacecraft Adapter Jettisoned (SAJ or Fairing)
- Spacecraft Adapter (SA)

The ESM—Structural Test Article (E-STA) is the term used to designate the structural mock-up of the MPCV stack that underwent acoustic and sine vibration testing at the Space Power Facility (SPF) in the Reverberant Acoustic Test Facility (RATF) and the Mechanical Vibration Facility (MVF), respectively. Both RATF and MVF are located at the NASA Glenn Research Center, Plum Brook Station, in Sandusky, Ohio. The overall layout of SPF is shown in Fig. 25.2. The E-STA hardware was received in pieces into the Assembly Highbay, where it was assembled, and then transferred via rail cart to the RATF and MVF for environmental testing.

J. P. Winkel (✉) · S. A. Bittinger · V. J. Suárez · J. C. Akers
NASA Glenn Research Center, Cleveland, OH, USA
e-mail: james.winkel@nasa.gov

C. Walber et al. (eds.), *Sensors and Instrumentation, Aircraft/Aerospace, Energy Harvesting & Dynamic Environments Testing, Volume 7*, Conference Proceedings of the Society for Experimental Mechanics Series,
https://doi.org/10.1007/978-3-030-12676-6_25

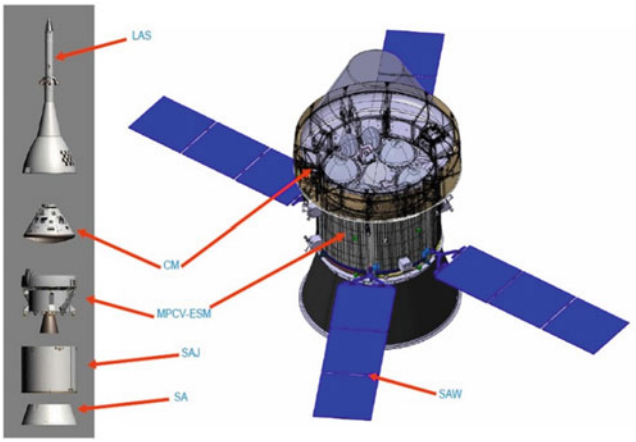

Fig. 25.1 Multi-purpose crew vehicle

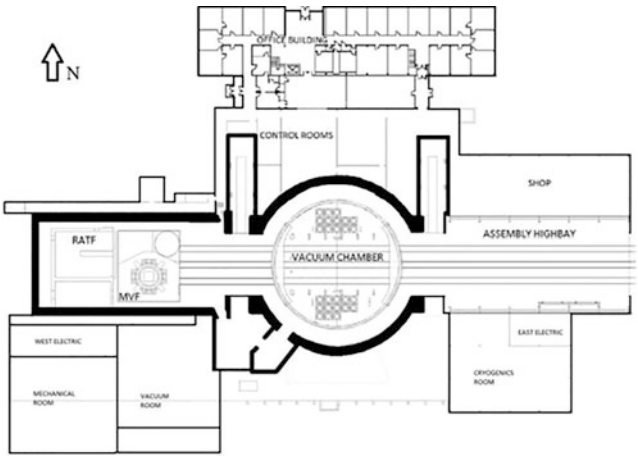

Fig. 25.2 Space power facility (SPF) overall layout

The E-STA has a near flight-specimen of the ESM hardware that is mass loaded by a mass simulator of the CMA subassembly and CM/LAS subassembly. It also utilized well characterized versions of the SA and SAJ subsystems from the Exploration Flight Test-1 (EFT-1). The E-STA subassemblies and the testing they underwent prior to integration into the overall assembly is shown in Fig. 25.3.

25.2 Building Block Modal Test Approach

In support of the following E-STA test objective: "Identify the modal parameters (frequency, mode shape and damping) for the primary modes of the E-STA and identify possible modal nonlinearities and resulting dynamic behavior", a "Building Block" modal testing approach was proposed to correlate the CM/LAS and CMA mass simulators prior to integration.

The "Building Block" Modal Test Approach consists of testing and model correlation of individual simulators allowing engineers the ability to more accurately predict the responses of E-STA to the sine vibration testing and to make E-STA correlation more manageable by allowing test engineers to focus primarily on updating the following:

- Interface stiffness between: CM/LAS—CMA, CMA—ESM, ESM—SA, and CMA—SAJ (NASA Major Focus)
- ESM internal components (ESA/Airbus Major Focus)

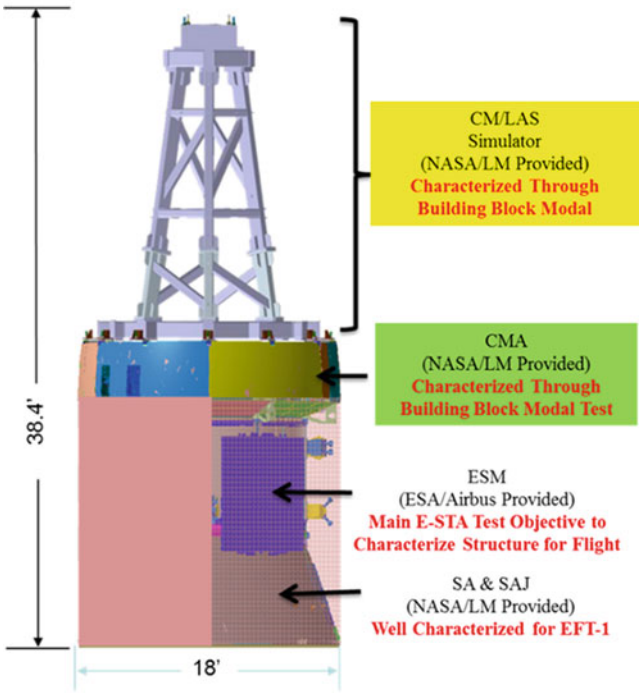

Fig. 25.3 ESM—structural test article (E-STA)

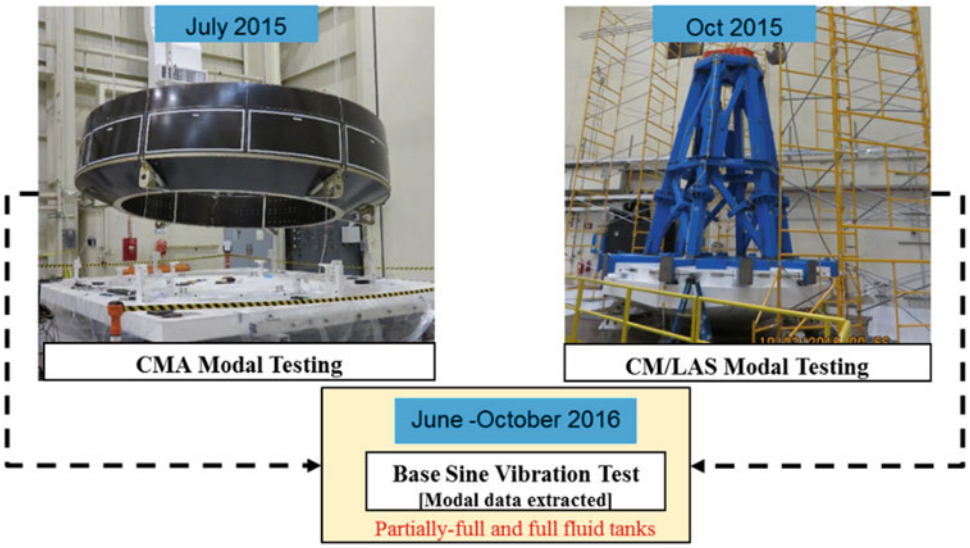

Fig. 25.4 CMA and CM/LAS building block modal tests

The E-STA FEM prior to the start of the sine vibration testing consisted of test correlated FEM's of the (Fig. 25.4):

- CM/LAS Simulator (Modal Test at SPF)
- CMA Simulator (Modal Test at SPF
- SA Simulators (EFT-1 Heritage)
- SAJ Simulators (EFT-1 Heritage)
- ESM (Static Stiffness Testing)

25.3 Crew Module Adapter (CMA) Mass Simulator Modal Test

The CMA connects the CM to the ESM. For the building block approach, the CMA mass simulator consisted of aluminum framing with composite panels attached. Large internal avionic mass simulators attached to the interior of the composite panels in several locations.

A fixed-base modal survey of the CMA mass simulator with its CM/CMA interfaces mass loaded would have been preferred due to its ability to better represent the dynamic characteristics of the load paths when integrated into E-STA. However, a fixed-base modal survey was not possible because there was no way of constraining the CMA/ESM interface due to this interface not being drilled until the CMA was integrated on top of the ESM, which had to be match drilled.

Instead, a free-free modal survey of the CMA mass simulator was performed where the free-free boundary condition was simulated by suspending CMA mass simulator on 1" thick bungee cords. The objective of this CMA mass simulator modal test was to identify the first five flexible (elastic) body modes, listed in Table 25.1. The highest frequency suspension mode was experimentally determined to be 1.0 Hz, which was sufficiently low that it did not couple with or impact the CMA simulator target modes. This free-free modal test was conducted in the SPF assembly highbay and is shown in Fig. 25.5.

Table 25.1 Target modes

	Mode #	Frequency	Mode Description (1005 Coordinate System)
	1	0.00	Rigid Body Mode 1
	2	0.00	Rigid Body Mode 2
	3	0.00	Rigid Body Mode 3
	4	0.61	Rigid Body Mode 4
	5	0.77	Rigid Body Mode 5
	6	0.81	Rigid Body Mode 6
Target Modes	7	22.52	Squeeze Mode aligned with to R and θ Axis
	8	25.14	Squeeze Mode aligned with 60 Degrees
	9	31.87	Potato Chip Mode aligned with to R and θ Axis
	10	35.20	Potato Chip Mode aligned with 60 Degrees
	11	41.04	Tri-Lobe Ovaling Mode

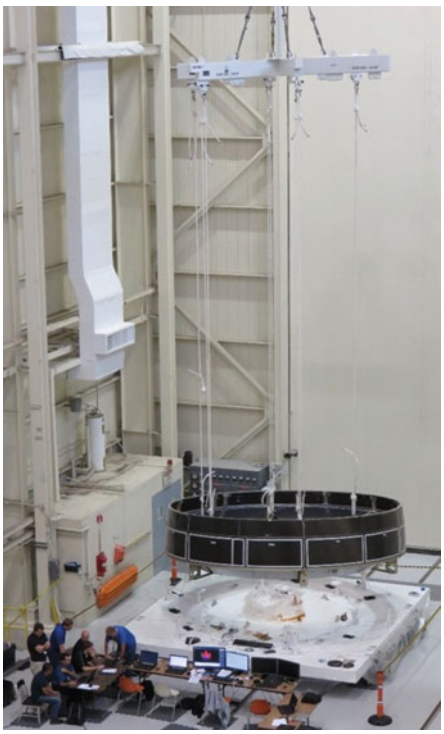

Fig. 25.5 CMA simulator modal test setup

Table 25.2 CMA TAM vs FEM cross orthogonality table

FEM/TAM Cross Orthogonality Table							
			FEM Shapes				
			1	2	3	4	5	6
		Oag	22.3	24.9	31.9	35.2	40.6	46.8
TAM Shapes	1	22.5	1.00					
	2	25.3		1.00				
	3	32.2			-1.00			
	4	35.6				-1.00		
	5	41.7					-1.00	0.07
	6	48.0						-0.99

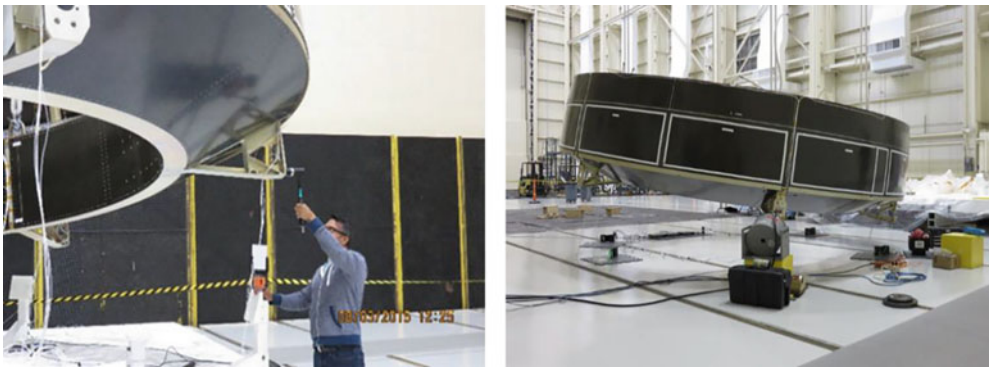

Fig. 25.6 CMA simulator test setups: impact hammer (left)—multi-shaker setup (right)

Table 25.3 CMA test modes

SHAPE REC	FREQUENCY (HERTZ)	DAMPING (%)	Shape Description
1	28.657	0.45	Squeeze Mode aligned with R and θ Axis
2	30.246	0.94	Squeeze Mode aligned with 60 degrees
3	44.857	0.54	Potato Chip Mode aligned with R and θ Axis
4	48.924	0.81	Potato Chip Mode aligned with 60 Degrees
5	50.311	0.81	Mass Simulators mode
6	54.647	0.73	Tri-Lobe Ovaling Mode
7	63.805	0.70	Mass Simulators mode

Table 25.2 shows the cross-orthogonality (x-ortho) comparison between the test TAM and the FEM. This table shows that the selected 52 DoF selected created a robust enough reduced mass matrix to capture the desired target mode shapes and will adequately support a model correlation effort.

Impact hammer testing along with multi-shaker testing was utilized to excite the CMA mass simulator. The multi-shaker testing was performed using both broadband random excitation and sine sweep excitation. In Fig. 25.6, one of the impact hammer drive point locations and multi-shaker layouts are shown.

Modes were extracted from all runs. The mode shapes were of high quality and were invariant from run to run. Based on the modal parameter data, it was decided to use the single point impact method as the final technique for modal extraction due to the simplicity of the test setup. Table 25.3 lists the extracted modes that most closely matched the FEM target mode set.

Table 25.4 Initial CMA correlation results

		Test Modes							
		28.57	30.27	44.84	48.86	50.33	54.65	63.61	Frequency %Diff
Analysis Modes	22.32	92.81	35.23				11.31	10.28	-21.88%
	24.93	29.77	92.36						-17.65%
	31.86			79.94	50.70	39.60	17.53	15.01	-28.95%
	35.18			40.32	76.95	79.43		22.43	-27.99%
	40.61					16.91	77.84	24.61	-25.69%
	46.85			15.11	16.25	18.29	24.84	71.85	-26.35%

Table 25.5 CMA mass simulator FEM model updating summary

Type of issue	Model Update
Modeling	FEM did not match as built hardware. Original FEM lumped masses did not include inertia properties, decided to model the mass simulators in greater detail. Updated the material coordinate orientation on the FWD and AFT composite panels to be rectangular instead of radial – this update did not have a large effect on the model behavior
Footprinting (heel-toe)	Increased the rotational stiffness of all the panel to frame springs. Merged nodes on the CMA frame to provide stiffer attachment between rings and frames and prevent heel-toe motion at the joints. Added additional row of CBUSH element between aft panels and lower inboard ring to stop heel-toe motion at the joints Added additional row of CBUSH element between aft panels and longeron/intermediate frames to stop heel-toe motion at the joints Added additional row of CBUSH element between inboard panels and frames and inboard panels and lower inboard ring to stop heel-toe motion at the joints.

Modes 4 and 5 showed to be identical, and it is believed that more instrumentation on the composite panels or accelerometers mounted internally might have helped to separate these modes. That is also why there are seven test modes extracted when there were only six FEM target modes.

The target correlation goals as defined by NASA were: cross-orthogonality >90% on the diagonal, <10% on the off diagonals, and a frequency difference between test and analytical <5%. An initial x-ortho was calculated to check the adequacy of the FEM. Table 25.4 shows frequencies errors as well as high cross-talk in several modes that exceeded the best practices guidelines mentioned above.

The next step was to update the FEM and rerun the x-ortho until the correlation goals were achieved. An overall summary of the types of updates that were made to the CMA FEM is presented in Table 25.5. The final x-ortho table presented in Table 25.6 does show some >10% off diagonal values and frequency differences >5%.

Table 25.6 CMA mass simulator FEM final correlation results

		Test Modes							
		28.66	30.25	44.86	48.92	50.31	54.65	63.80	Frequency %Diff
Analysis Modes	29.74	98.90						12.53	3.77%
	32.25		94.97						6.62%
	42.23			95.84	20.71				-5.86%
	47.21			12.32	94.42	94.70		10.07	-3.49%
	56.84					14.18	90.42	11.19	4.01%
	61.81			12.04		11.43		90.82	-3.13%

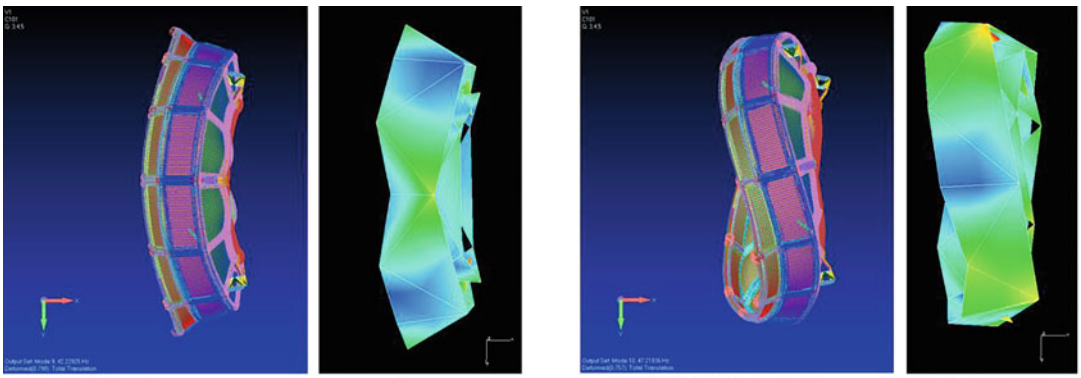

Analysis Mode 3: 42.23 Hz Potato Chip Mode aligned with R and θ Axis

Test Mode 3: 44.857 Hz Potato Chip Mode aligned with R and θ Axis

Analysis Mode 4: 47.22 Hz Potato Chip Mode aligned with 60 Degrees

Mode 4: 48.924 Hz Potato Chip Mode aligned with 60 Degrees

Fig. 25.7 CMA mass simulator mode shapes

At the time of performing the correlation, both mode shapes 3 and 4 (see Fig. 25.7) have large internal avionics mass simulators deforming in a similar manner. These internal avionics mass simulators make up over 30% of the total mass of the CMA mass simulator so the high off-diagonal values in the x-ortho comparisons between test and FEM were accepted. Test modes 4 and 5 were not able to be distinguished from each other even after further attempts of adding more accelerometers was utilized. Due to time constraints, these issues in meeting the correlation goals were accepted on the basis that the correlated modes encompassed the global behavior of the primary load path of the CMA. It turned out that later on in the E-STA correlation, the fact that the CMA mass simulator FEM was not matching the test data better in this free-free testing effort should have been a big "red flag" that something in the FEM was still incorrect. This is elaborated upon in later sections of the paper.

25.4 Crew Module/Launch Abort System (CM/LAS) Mass Simulator Modal Test

The CM/LAS mass simulator modal testing followed the CMA mass simulator modal test. The CM/LAS mass simulator modal test configuration included all hardware above its attachment to the CMA mass simulator. The CM/LAS mass simulator was fastened to the MVF modal floor creating a fixed-base boundary condition. Target modes were selected based on the best practice that greater than 90% of the modal effective mass should be captured in all 6 DOF in order to ensure all the significant modes are considered. Based on this guideline, six high effective mass modes were selected as the primary target modes (hi-lighted in green in Table 25.7) and 12 secondary target modes were selected to assist the overall model correlation effort (hi-lighted in yellow in Table 25.7).

A modal pretest analysis was performed on the CM/LAS mass simulator and a final ASET of 66 DOF was selected to independently capture the six primary target mode shapes, evidenced by Table 25.8. The secondary target modes were not within the pretest guidelines, as observed in Table 25.9, but it was considered acceptable. The primary target modes are outlined in green in Table 25.9 for clarification.

Table 25.7 CM/LAS modal effective mass table

	Mode #	Frequency	T1 %	T2 %	T3 %	R1 %	R2 %	R3 %	Mode Description (3100001 Coordinate System)
Target Modes	1	12.24	0.0%	0.0%	53.0%	0.0%	6.5%	0.0%	CMLAS Rotating about Y axis and the origin is the interface between the LAS tower and the heatshield. R&Rs flexing radially in and out
	2	18.73	0.0%	49.7%	0.1%	0.0%	0.2%	7.4%	CMLAS Rotating about Z axis and the origin is the interface between the LAS tower and the heatshield. LAS Tower Flexing in first bending along Y axis. R&Rs flexing radially in and out
	3	20.68	0.0%	0.0%	0.0%	93.4%	0.0%	0.0%	CMLAS Twisting mode about X axis
	4	26.17	0.0%	0.1%	44.3%	0.0%	86.0%	0.0%	CMLAS Pendulum Mode Translating Along Z Axis
Secondary Mode	5	29.75	0.0%	0.0%	0.0%	0.0%	0.1%	0.0%	-Y+Z Tangential Fitting Heat Shield First Bending Panel Mode
	6	31.78	0.0%	0.3%	0.0%	0.0%	0.0%	0.8%	+Y and -Y Tangential Fitting Heat Shield First Bending Panel Modes Out of Phase
	7	31.79	0.1%	0.0%	0.0%	0.0%	0.0%	0.0%	+Y and -Y Tangential Fitting Heat Shield First Bending Panel Modes In Phase
	8	31.82	0.1%	0.0%	0.0%	0.0%	0.0%	0.0%	+Y+Z and -Y-Z Tangential Fitting Heat Shield First Bending Panel Modes In Phase
	9	31.83	0.0%	0.1%	0.0%	0.0%	0.0%	0.1%	+Y+Z and -Y-Z Tangential Fitting Heat Shield First Bending Panel Modes Out of Phase
	10	31.86	0.0%	0.0%	0.0%	0.0%	0.0%	0.1%	+Y-Z Tangential Fitting Heat Shield First Bending Panel Mode
	11	32.55	0.0%	0.1%	0.0%	0.0%	0.0%	0.1%	+Y and -Y Tangential Fitting Heat Shield Second Bending Panel Modes In Phase
	12	32.55	0.0%	0.0%	0.0%	0.0%	0.0%	0.0%	+Y and -Y Tangential Fitting Heat Shield Second Bending Panel Modes Out of Phase
	13	32.56	0.0%	0.0%	0.0%	0.0%	0.0%	0.0%	+Y-Z Tangential Fitting Heat Shield Second Bending Panel Mode
	14	32.60	0.0%	0.0%	0.0%	0.0%	0.0%	0.0%	+Y+Z and -Y-Z Tangential Fitting Heat Shield Second Bending Panel Modes Out of Phase
	15	32.60	0.0%	0.0%	0.0%	0.0%	0.0%	0.0%	+Y+Z and -Y-Z Tangential Fitting Heat Shield Second Bending Panel Modes In Phase
Target Mode	16	34.28	0.0%	45.6%	0.0%	0.0%	0.0%	80.4%	CMLAS Pendulum Mode Translating Along Y Axis
Secondary Mode	17	38.49	0.0%	0.0%	0.0%	0.0%	0.0%	0.0%	-Y+Z Tangential Fitting Heat Shield Second Bending Panel Mode
	18	41.24	0.0%	0.0%	0.0%	0.0%	0.0%	0.0%	-Y+Z Tangential Fitting Heat Shield Third Bending Panel Mode
	19	46.97	0.0%	0.0%	0.0%	0.0%	0.0%	0.0%	+Y and -Y Tangential Fitting Heat Shield Third Bending Panel Modes Out of Phase
	20	46.97	0.0%	0.0%	0.0%	0.0%	0.0%	0.0%	+Y and -Y Tangential Fitting Heat Shield Third Bending Panel Modes In Phase
	21	47.02	0.1%	0.0%	0.0%	0.0%	0.0%	0.0%	+Y+Z and -Y-Z Tangential Fitting Heat Shield Third Bending Panel Modes In Phase
	22	47.02	0.0%	0.0%	0.0%	0.0%	0.0%	0.0%	+Y+Z and -Y-Z Tangential Fitting Heat Shield Third Bending Panel Modes Out of Phase
	23	47.44	0.2%	0.0%	0.0%	0.0%	0.0%	0.0%	+Y-Z Tangential Fitting Heat Shield Third Bending Panel Mode
	24	49.01	0.0%	0.0%	0.0%	0.0%	0.0%	0.0%	+Y and -Y Tangential Fitting Heat Shield Fourth Bending Panel Modes Out of Phase
	25	49.02	0.0%	0.0%	0.0%	0.0%	0.0%	0.0%	+Y and -Y Tangential Fitting Heat Shield Fourth Bending Panel Modes In Phase
	26	49.19	0.2%	0.0%	0.0%	0.0%	0.0%	0.0%	+Y-Z Tangential Fitting Heat Shield Fourth Bending Panel Mode
	27	49.49	1.2%	0.0%	0.0%	0.0%	0.0%	0.0%	+Z-Z Tangential Fitting Heat Shield Fourth Bending Panel Mode Out of Phase
	28	49.51	0.0%	0.0%	0.0%	0.0%	0.0%	0.0%	+Z-Z Tangential Fitting Heat Shield Fourth Bending Panel Mode In Phase
Target Mode	29	51.09	84.6%	0.0%	0.0%	0.0%	0.0%	0.0%	Dominate CMLAS vertical bounce and pushing R&Rs radially in and out. Tangential Fitting Heat Shield Complex panel bending

Table 25.8 CM/LAS mass simulator TAM vs FEM primary target modes cross-orthogonality table

FEM/TAM Cross Orthogonality Table								
FEM Shapes			1	2	3	4	5	6
		Oag	12.2	18.7	20.7	26.2	34.3	51.1
TAM Shapes	1	12.3	-1.00					
	2	18.8		1.00				
	3	20.8			1.00			
	4	26.4				-1.00		
	5	34.8					1.00	
	6	52.1						1.00

Nine impact locations were determined prior to testing using ATA Engineering's IMAT® software package, one of which can be seen in the left half of Fig. 25.8. Additionally, eleven shaker runs [single input multiple output (SIMO) and multiple input multiple output (MIMO)] were also performed. The shaker placement is better illustrated in the right images in Fig. 25.8.

Modal parameters were extracted for all runs and it was found that the modal parameters were very similar from test to test. Based on the modal parameter data, it was decided to use the single portable shaker method as the final technique for modal extraction because offered the cleanest data. Table 25.10 lists the six primary target modes in addition to one other higher frequency mode.

The same cross-orthogonality and frequencies goals used in the CMA modal testing were applied to the CMLAS correlation effort. To understand the effect of the model changes during the correlation process, the team started the correlation with the as-delivered FEM as shown Table 25.11. It can been seen that the as-delivered FEM did not provide a good starting point. The first target mode was the only mode that met the main diagonal goal; additionally, using the FEM as it was delivered to NASA GRC, the pretest would have not been accurate enough to provide proper instrumentation placement.

Table 25.9 CM/LAS pretest results—primary (outlined in green) and secondary target modes

FEM Mode	Freq (Hz)	TAM Mode	Freq (Hz)	%Difference	XORTHO
1	12.24	1	12.256	0.1	100.00
2	18.73	2	18.772	0.2	100.00
3	20.68	3	20.839	0.7	100.00
4	26.17	4	26.435	1.0	99.99
5	29.75	5	32.441	9.0	99.97
6	31.78	6	33.864	6.6	97.35
7	31.79	7	33.898	6.6	98.92
8	31.82	9	33.929	6.6	89.70
9	31.83	8	33.928	6.6	85.38
10	31.86	10	33.945	6.5	94.99
11	32.55	11	34.823	7.0	76.94
12	32.55	12	34.842	7.0	95.51
13	32.56	13	34.851	7.0	89.01
14	32.60	14	34.870	7.0	97.75
15	32.60	15	34.870	6.9	96.53
16	34.28	16	34.893	1.8	82.57
17	38.49	17	44.513	15.7	99.56
18	51.09	18	52.121	2.0	99.82

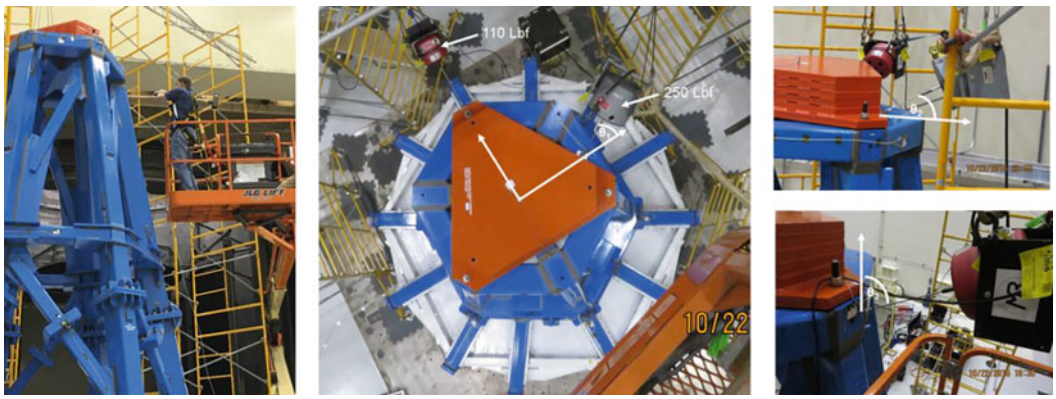

Fig. 25.8 CMLAS simulator test setups: impact hammer (left)—shaker setup (mid and right)

Table 25.10 CMLAS simulator modal test results

SHAPE REC	FREQUENCY (HERTZ)	DAMPING (%)	SHAPE DESCRIPTION
1	13.31	0.3	CMLAS Rotating about Y axis and the origin is the interface between the LAS tower and the heatshield.
2	20.87	0.37	CMLAS Twisting mode about X axis
3	21.18	0.34	CMLAS Rotating about Z axis and the origin is the interface between the LAS tower and the heatshield. Heat Shield is rotating about X Axis
4	25.74	0.61	CMLAS Pendulum Mode Translating Along Z Axis
5	32.42	0.71	CMLAS Pendulum Mode Translating Along Y Axis
6	49.05	0.94	CMLAS vertical bounce mode
7	57.2	0.25	CMLAS Out of phase torsion with Heat shield

Table 25.11 CM/LAS mass simulator as-delivered cross-orthogonality

As Delivered XORTHO (07/27/2015)									
	Test Extracted Mode Shapes								Diff.
Analytical Mode Shapes	Freq. (Hz)	13.29	20.87	21.16	25.70	32.32	49.24	57.19	(%)
	11.85	98.65	7.36	11.43	26.04	1.03	5.40	1.84	11%
	13.99	5.06	51.67	27.71	33.85	11.67	16.69	33.63	33%
	16.89	0.68	37.34	38.32	49.19	27.45	26.48	23.07	34%
	18.37	7.40	57.98	84.56	32.48	30.94	0.28	3.39	13%
	21.48	4.57	0.75	9.24	0.07	56.23	13.45	7.87	34%
	48.32	2.83	4.14	0.65	6.50	2.07	78.06	6.67	2%
	58.04	1.30	29.91	11.17	23.58	5.02	30.66	89.15	-1%

Table 25.12 CM/LAS mass simulator cross-orthogonality results using updated FEM

X-Ortho: 10/20/2015									
	Test Modes								
FEM Modes	Freq.	13.29	20.88	21.16	25.72	32.33	48.98	57.21	% Diff
	12.26	98.40	0.75	13.64	22.19	2.26	1.21	2.86	8%
	18.73	8.15	20.25	91.11	23.36	32.32	4.47	5.48	10%
	20.33	1.80	97.40	35.05	11.01	0.30	2.28	13.55	4%
	25.89	12.14	4.11	9.45	93.75	10.31	2.76	0.09	-1%
	33.95	6.74	6.11	11.82	5.42	94.01	1.09	2.09	-5%
	50.94	2.26	0.16	0.89	5.15	0.20	99.51	6.15	-4%
	58.48	0.02	5.29	1.60	0.62	0.94	0.09	98.89	-2%

Table 25.12 shows the correlation results using a FEM that was updated prior to the start of testing to better reflect the as-built hardware configuration. As previously mentioned, significant mismatches between the as-delivered FEM and the actual test hardware were noted prior to commencing testing activities. This data reaffirms what it is already known, but many times not applied: the FEM needs to accurately represent the as-built hardware. This not only provides more accurate pretest analysis and saves time during the model correlation effort, but is critical to ensuring the "test correlated" FEM accurately represents critical load paths.

The model updating of the FEM posttest still required an updating effort even with the inclusion of pretest FEM updates. The updates made after the test was completed is summarized in Table 25.13.

When including the model updates to the FEM, both pre and posttest, as well as modifying the boundary conditions at the base of the CMLAS, the correlation started to look much improved as seen in Table 25.14.

At this point, all the frequencies of the primary target modes were within acceptable ranges. However, Mode #3 still did not match the test shape as can be seen with the high off diagonal values in Table 25.14. There was rotation of the heat shield that was not being mimicked by the analytical model. Engineers first attributed this to the asymmetrical beam gussets that increased one side of the beam more than the other. In order to better capture this asymmetrical stiffness, the upper part of the FEM was recreated using 2D shell elements over the previously used 2D beam elements. This gave the engineers better ability to accurately model the gusset plates and joints. Figure 25.9 shows how engineers took advantage of the hardware symmetry and created only a mesh of 1/6 of the section and then duplicating it 5 additional times.

As shown in Table 25.15, the change to shell elements on the LAS tower did not address the primary issue of lowering the off diagonal values of Mode #3. However, it did correct the frequencies of secondary modes found in the test data in the 60 Hz range. These secondary modes had been incorrectly predicted in the FEM in the 50 Hz range.

Finally, it was determined that the only way to affect only Mode #3 without changing the others was to introduce a mass offset at the top of the tower along the Z axis. Because this 6500 lb mass simulator (orange part in Fig. 25.10) was over 18 feet above the base, engineers believed changing that mass offset just a small amount could have a large impact on the modes. The CG of the orange mass was moved along the axis of the black arrow in Fig. 25.10. To determine sensitivity to it, multiple iterations were done using offsets of 2 inches, 1 inch, 0.5 inches, and 1.125 inches. The offset of 1.125 inches was decided to be the final value.

Table 25.13 CM/LAS mass simulator model update summary

Issue	Fix
The test team first identified that the CMLAS tower had a very significant amount of non-structural mass all over it. The CG of the tower section was not accurate per the CMLAS mass and CG report	Update 1a – All overlapping beam elements were shortened and connected using RBE2 elements. Update 1b – Gusset Plates were extended through beam elements. Update 1c – Horizontal beams modified to include extra plate thickness on top and bottom surfaces Update 1d – Connection plates were included as extra thickness in the beam element properties at all welded joints on the LAS tower. Update 1e – Connection plates where the upper and lower LAS towers connect to each other were added into the model using shell elements Update 1f – Removed the previously added corner gussets.
The CMLAS FEM was still too heavy according to the mass and CG report supplied by LM	Engineers started to take measurements of the test hardware and compare to FEM. Several geometric issues with the model were uncovered. Update 2a – Top of the tower was modeled 14" wider than as-built hardware Update 2b – Entire CMLAS structure was positioned 2" higher above the D-Brackets than as-built hardware Update 2c – Support structure between the CMLAS base and the heat shield was modeled into the FEM, but was not present in the as-built hardware Update 2d – Mass Simulator at the top of the CMLAS tower was modeled with four connections when in the as-built hardware it only had three. Also added in mass moments of inertia. Update 2e – Mass properties of the super nut at each D-Bracket location was added into the FEM.
D-Bracket Stiffness	The base springs created before the test were greatly simplified to just having four on the corners and three along the middle support brace. Noticed that the boundary conditions at the base of the D-Brackets was not what was originally planned.

Table 25.14 CM/LAS mass simulator cross-orthogonality after first round of model updates

XORTHO (After Model Updates 3)									
		Test Extracted Mode Shapes							Freq.
		13.32	20.91	21.19	25.78	32.44	49.10	57.21	Diff.
Analytical Mode Shapes	13.55	98.71	2.11	11.45	7.24	6.07	1.30	0.08	-2%
	21.17	4.25	85.22	58.39	9.75	0.60	2.91	19.72	-1%
	21.20	10.18	50.97	79.93	8.76	4.84	1.83	4.35	0%
	25.42	1.75	0.68	8.41	98.24	12.16	2.78	0.98	1%
	31.81	6.32	3.86	1.22	10.39	98.66	1.62	0.67	2%
	50.52	1.85	0.25	1.04	0.75	3.12	98.99	3.25	-3%
	61.71	0.21	8.67	2.54	2.59	2.07	8.02	98.00	-8%

The final x-ortho results are shown in Table 25.16. At this point, it was determined that all target modes were successfully extracted. Additionally, the secondary target modes which had mostly local dynamics of the secondary support beams were able to be fully correlated in the FEM per the NASA guidelines.

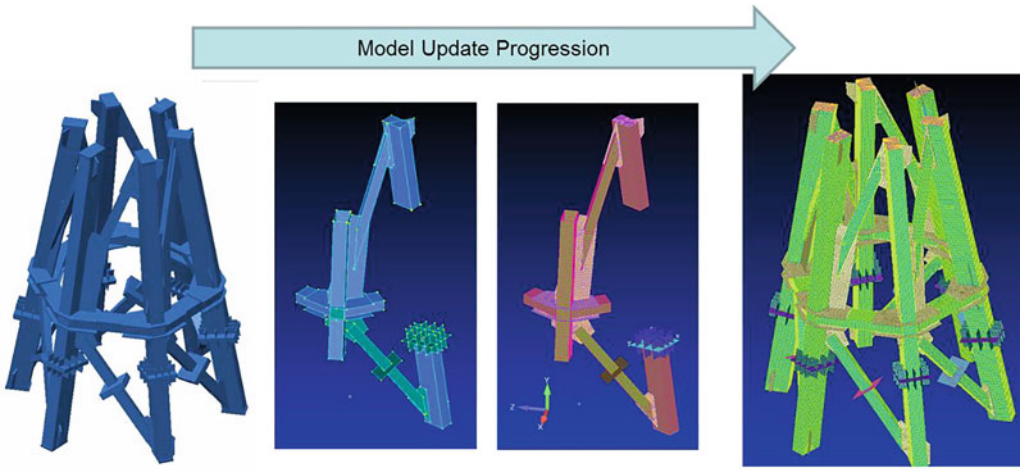

Fig. 25.9 LAS tower shell model

Table 25.15 Cross-orthogonality after LAS tower model updates

XORTHO (After Model Updates 4)									
		Test Extracted Mode Shapes							Freq.
		13.31	20.87	21.18	25.74	32.42	49.11	57.19	Diff.
Analytical Mode Shapes	13.41	98.88	1.16	10.84	4.04	4.87	1.11	0.49	-1%
	20.96	3.03	94.48	46.35	9.87	0.26	2.14	12.22	0%
	21.00	10.19	30.37	87.20	11.92	2.10	1.73	1.13	1%
	25.19	1.08	1.78	10.20	97.80	11.33	2.58	0.46	2%
	31.52	5.72	4.01	2.87	11.24	98.82	1.55	0.58	3%
	50.01	1.46	1.97	1.54	1.84	2.60	98.30	1.64	-2%
	59.46	0.03	2.70	0.36	1.91	2.03	3.28	95.86	-4%

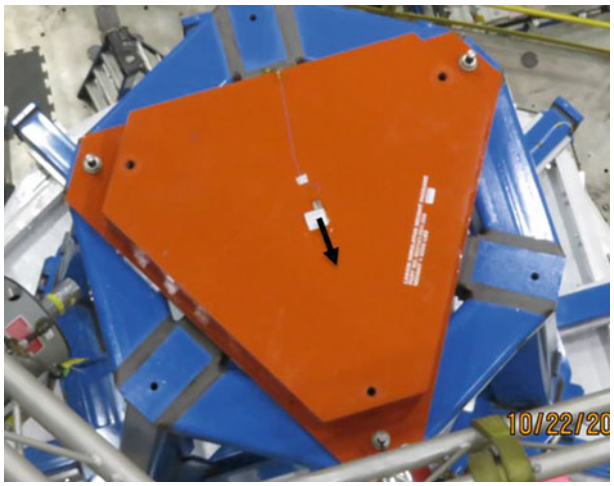

Fig. 25.10 6500 lbs mass simulator

25.5 E-STA Stack FEM Correlation

After all building block modal testing was completed, the subassemblies were assembled together. The full stack underwent both acoustic testing, low level random vibration testing, and finally full level sine vibration testing. After the conclusion of

Table 25.16 CMLAS final cross-orthogonality results

Final Correlated XORTHO (11/10/2015)									
	Test Extracted Mode Shapes								Freq. Diff.
Analytical Mode Shapes	Freq. (Hz)	13.31	20.87	21.18	25.74	32.42	49.11	57.19	(%)
	13.55	98.79	1.23	11.01	4.35	4.80	1.24	0.51	-2%
	20.93	1.17	98.82	7.98	4.19	1.88	2.76	12.35	0%
	21.19	10.78	8.44	98.39	14.77	2.70	0.70	1.63	0%
	25.38	1.40	1.79	10.06	97.79	11.24	2.33	0.25	1%
	31.88	5.80	4.31	2.05	11.04	98.80	1.60	0.36	2%
	50.31	1.22	2.00	1.43	1.80	2.50	98.28	1.88	-2%
	59.39	0.05	2.35	0.44	1.82	1.80	2.85	95.87	-4%

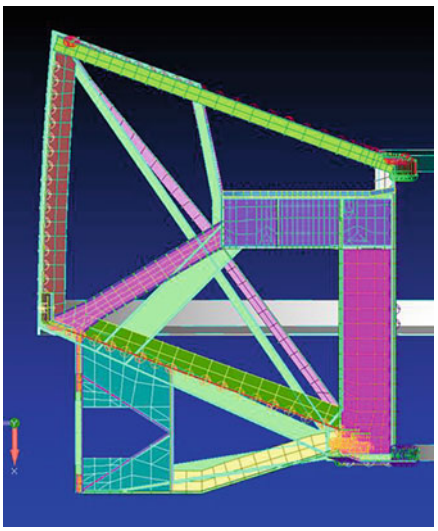

Fig. 25.11 CAD-FEM comparison of CMA cross-section

E-STA sine vibration testing, correlation work on the fully integrated stack FEM began. The correlation approach follows these five steps:

1. CAD-FEM Comparison
2. Measure Test Article Mass
3. Consider Nonlinearities
4. Hardware Interface Modeling Practices
5. Confirming the Load Path

25.6 CAD-FEM Comparison

Comparing as-built CAD to FEM is one of the most important steps in correlation. Ideally, this is done before testing even begins. Even when a FEM is received from a different group, the correlation group should still perform an independent CAD-FEM comparison. There are several steps to the comparison: check geometry placement mismatch, thickness comparisons, composite layup comparisons, and mass property comparisons. Test engineers should have full access to the as-built CAD or at the very least the drawings to enable these comparisons to be made.

The CMA model was thought to have been acceptably correlated by standard metrics during building block testing, thus a CAD-FEM review was not performed. It was discovered during the stack CAD-FEM review many months later that the CMA FEM was a design from an older mission. This is evident in Fig. 25.11 displaying a major load bearing section of the CMA. The light green is the CAD, the rest is from the FEM. The aft panel is placed at a different angle, and many of the cross-brace supports are in different positions and angles. Property thicknesses of different frame members were up to 100% different from the CAD. The CMA was fully remodeled from scratch by the correlation team. Looking back, the correlation

of the CMA during the free-free testing showed signs of modeling issues but were ignored due to schedule pressures. Had these CAD-FEM comparisons been done prior to the CMA free-free modal test even occurring, a significant amount of time could have been saved throughout the rest of the testing campaigns.

25.7 Measure Test Article Mass

Ideally, the subassemblies in a building block approach should be individually weighed, and the FEM should be updated to reflect the measured mass. In the E-STA FEM, several components' masses were updated to reflect as-measured mass. It was during the mass comparison effort that it was discovered that the FEM was missing 31% of the propellant mass from two of the tanks (approximately 3000 lbs). This may not have been otherwise discovered without the presence of as-measured masses. The smaller the subassemblies that the full stack can have the as-measured masses documented in the better. It allows the engineer performing the correlation to "zero" in on any issues that may be present. It is also very important to keep non-structural mass modeling to a minimum in the FEM. Some of the building block subassemblies relied on modeling significant structural members with non-structural mass or with concentrated masses without any inertia properties. These methods should be avoided if one hopes to have an accurate FEM.

25.8 Consider Nonlinearities

Especially for large, complex spacecraft, it is possible that the test article will exhibit nonlinear behavior. In E-STA, there was a large amount of nonlinearity in the stack especially located to the joints. The modal frequencies extracted from the low level random vibration tests were up to 40% higher than the modes extracted from the full flight level sine tests. At high levels, the joints began to behave differently than at low level. This should be taken into consideration when attempting to correlate a FEM. Usually, an engineer will first attempt to correlate the FEM to the low level test data where the joints are still behaving linearly. It is important that they understand from the test data though which joints are exhibiting significant non-linear behavior, and take steps in the low level correlation effort to implement modeling features that will be easily modified to capture the non-linear behavior at high excitation levels. This is generally done with CBUSH springs that can have their stiffness changed significantly without any remodeling effort. While it's a key part of the correlation process to match the lower level data, that really isn't the final goal. The final goal has to be matching the higher level excitation data due to it most closely resembling the flight loading conditions of the hardware. This entire process can be extremely time consuming.

25.9 Hardware Interface Modeling Practices

It is important to scan the entire FEM to check for good modeling practices, but because the building block approach was used in E-STA, the primary focus was only on the major interfaces. A great place to start is these checks is by reviewing the "footprinting" of the interface connections. "Footprinting" is the use of spider RBEs to spread the load of one CBUSH interface element to the area over which the physical joint acts. This modeling technique prevents heel-toe motion of bolted flanges in the FEM and properly capture the stiffness of the interface. Traditionally, only a single CBUSH is utilized to transfer load from one large structure to another at bolted interfaces. Even when footprints are utilized, they are often times still too small. Foot prints should be accurately placed and spaced at all interfaces if one hopes to capture the true stiffness of major joints. Sometimes, due to oversimplification of the loads FEM, foot printing cannot be implemented. It is at this point when engineers should take the time to go into the FEM and increase the fidelity.

While footprinting works great for large flange interfaces that are bolted together, it may not be the final answer for more complicated interfaces such as pyrotechnic separation joints, alignment bearings and pins, or other intricate mechanisms may be present. The engineer performing the correlation should be reviewing these major interfaces and inquiring about the following:

1. How much of the mechanism is supposed to be included in any simplified modeling (generally CBUSH elements)?
2. What are the reasonable ranges of stiffness for CBUSH elements at each interface?
3. Is there component level testing to back up these existing stiffness values?

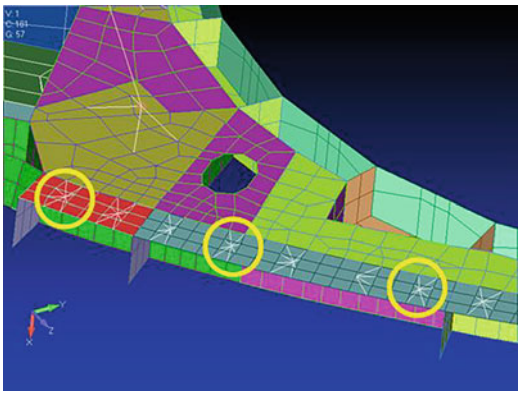

Fig. 25.12 Examples of footprinting to capture interface flange stiffness

E-STA has several complicated interfaces that utilize pyrotechnic joints because they need to separate at different stages during the launch. These complicated mechanisms should not be modeled with single CBUSH elements or even with small number of simple 2D elements. Oversimplification of the FEM, especially at the major interfaces, was one of the leading reasons why the E-STA stack did not match the test results (Fig. 25.12).

In addressing the second bullet above, there have been far too many instances where CBUSH elements at joints have been modeled either with too high or too low of stiffness values. Starting with the problem of too low of stiffness, one should take great care in avoiding using zeros as a stiffness value in any one of the six degrees of freedom. Even values below 100 lbf/inch can lead to unrealistic FEM behavior. If the primary stiffness direction of the interface is modeled with 1,000,000 lbf/inch or higher, then placing a value between 100 and 1000 lbf/inch in the non-primary directions is highly advised. On the other hand, if a CBUSH requires extremely large stiffness values to correlate an interface, one should look into seeing if more fidelity should be added in. There is a good chance that the CBUSH is trying to represent too much of the hardware and cannot accurately do so.

Finally, in some instances, there has been previous component level testing activities performed to help establish the mechanism stiffness values used in the FEM. It is a very wise practice to utilize this information during the correlation, but with a caveat. Do not blindly accept these component test results as the absolute truth. On some occasions, only simplified loading can be introduced at the component level that does not accurately reflect what occurred in the large scale testing. The engineer performing the correlation must first understand the loading applied during the fully assembled testing and then compare that with the load implemented during any simplified component testing.

25.10 Confirming the Load Path

The extracted modal parameters of natural frequencies and mode shapes are not the only metrics that should be utilized in model correlation, especially of large vehicles similar to E-STA. It has been observed that large vehicles such as E-STA rely on several different parallel paths to carry load throughout the vehicle. In E-STA, the one of these major parallel load paths consisted of an outer load path (SAJ Fairings & PSM) and an inner load path (ESM Longerons). There is a problem that can occur, and did with E-STA, when only the modal parameters of natural frequency and mode shapes are utilized for the correlation. The problem is that one of the two parallel load paths can be significantly incorrect, but the other load path is over compensating for it, albeit incorrectly, and thus the FEM will still predicts a matching natural frequency and mode shape. The cross-orthogonality matrices are not sensitive to showing inaccuracies of the parallel load paths because overall mode shapes and modal mass associated with the FEM shapes are still, as a whole, correctly mimicking the test results. Table 25.11 shows the x-ortho comparison of the E-STA stack, and indicates a very acceptable mode shape correlation between the test results and FEM predictions. However, looking at Fig. 25.13, it is obvious that this same FEM is predicting far more load going through the inner path (ESM Longerons) than the actual test results revealed. In E-STA, only the inner load path had full bridge strain gages to allow for this load comparison to take place between the FEM and test results. The team utilized a MSC Nastran SOL 111 frequency base drive simulation to calculate FRFs of these strain gauges at the longerons. Even after the correlation was complete, and the natural frequencies were brought into within the <5% frequency difference goal, there was still significant differences in the FEMs prediction of the inner load path results. The outer load path was not instrumented and measured during this test campaign thus it was not possible to confirm what engineers suspected the issue was. Engineers suspected and confirmed through sensitivity studies that a mechanism on the outer load path was most likely

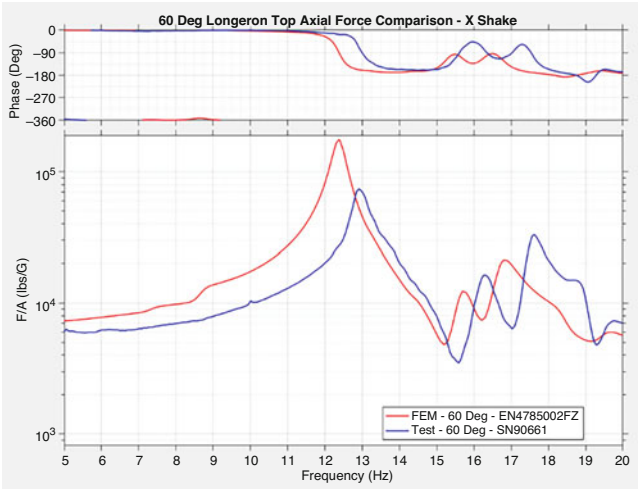

Fig. 25.13 Axial shake inner load path FRF

Table 25.17 Original cross-orthogonality matrix

FEM/Test Cross Orthogonality Table

			FEM shapes							
			1	2	3	4	5	6	7	8
		Otg	3.4	3.7	6.5	7.6	7.8	11.5	12.4	14.2
Test Shapes	1	4.7	0.97		0.23					
	2	6.1		0.97						
	3	9.7	0.23		0.96					
	4	10.5					0.97			
	5	11.6				0.91				
	6	13.8						0.98		
	7	14.2							0.21	0.96
	8	16.3						0.21	0.75	

modeled with too low of stiffness and thus the inner load path was overcompensating for it. Recommendations to future tests were made to ensure both load paths would be measured (Table 25.17).

Another point to keep in mind is that the load share can be different during dynamic loading and static loading. The ESM has went through static load testing and was partially correlated to this test data prior to the start of E-STA testing. This static testing was not able to cause joints to slip and move relative to each other in the same way they did during dynamic testing. Thus, even if a model is "correlated" to static testing, care should be taken to understand how the differences between the static and dynamic loading manifests itself in the hardware.

25.11 E-STA Correlation Progress

Immediately following the conclusion of the test, the FEM, comprised of individually correlated components based on building block testing, was compared to the modal test data. However, Table 25.18 illustrates the FEM to be up to 62% too soft when compared to the test data.

After struggling to correlate the model, the team looked into the nonlinear behavior of the E-STA during higher level sine testing. It was decided that the FEM was currently closer to being correlated to the high-level sine excitation test data. In an attempt to save time, it was decided to try to use the high-level sine data for the correlation because, as shown in Table 25.19,

Table 25.18 Low level random test frequency comparison

Mode	FEM	Test	Diff.
1BZ	3.37	4.73	40%
1BY	3.74	6.05	62%
2BZ	6.52	9.66	48%
2BY	7.57	11.58	53%
T	7.84	10.51	34%
A	11.47	13.84	21%
OZ	12.43	16.32	31%
OY	14.24	14.22	0%

Table 25.19 High level sine test frequency comparison

Mode	FEM	Test	Diff.
1BZ	3.37	3.77	12%
1BY	3.74	4.32	16%
2BZ	6.52	7.66	17%
2BY	7.57	9.27	22%
T*	7.84	11.06	41%
A	11.47	12.98	13%
OZ	12.43	13.31	7%
OY	14.24	13.46	-5%

Table 25.20 Post-correlation high level sine frequency comparison

Mode	FEM	Test	Diff.
1BZ	4.03	3.77	-6%
1BY	4.53	4.32	-5%
2BZ	7.7	7.66	-1%
2BY	9.22	9.27	1%
T*	9.54	11.06	16%
A	13.62	12.98	-5%
OZ	13.2	13.31	1%
OY	14.5	13.46	-7%

the max frequency difference when comparing to the same FEM was 22%. It is important to note that the torsion mode of the stack denoted with an * in Table 25.19 and in Table 25.20 was only able to be extracted from the low level random test results due to there not being significant sine excitation in a torsional direction.

After several months of correlating the FEM, the vehicle modes were able to be brought within 6% of the sine test data, as seen in Table 25.20 (exception of torsion mode). This was a large improvement over the original FEM, however, the correlation was never fully completed due to the inability to confirm why load share between the vehicles parallel load paths did not match the test results.

25.12 Lessons Learned from Correlation Campaign

In summary, four out of the five main subassemblies of the E-STA stack were correlated prior to the E-STA vibration tests. Two of those pieces were modally tested and successfully correlated by NASA GRC LMD branch. The building block modal test approach allowed engineers to do more accurate pretest analysis on the full ESTA stack, as well as make a very difficult correlation effort a much more manageable one. Those same engineers were then heavily involved with the correlation of the full E-STA stack. That experience gave them the opportunity to discover issues that they had not well understood during the building block testing as well as determine other lessons learned from the entire process. Those lessons are:

- Always perform CAD-FEM comparisons, even if there is good correlation to test, and ideally before test begins to save time for actual correlation.
- Carry out the building block modal tests with boundary conditions that closely resemble the configuration they will be in during the fully assembled testing. If a component is in the middle of the stack, attempt to mass load both sides of the interface.
- Measure the mass of each subassembly and compare to FEM.
- Check for nonlinear behavior in the test data and develop a basic understanding of how to implement it in the FEM. Always correlate to the lower level first, but ensure the correlation is ultimately carried out to the higher level excitation which more represents the flight.
- Check model for good modeling practices. Make sure major interfaces are "footprinted" appropriately, mechanisms are modeled with sufficient fidelity, and ensure all CBUSH values are within appropriate ranges.
- For vehicles with a dual load path, it is critical to instrument both load paths with strain gages and then verify that your correlated model is correctly simulating the load distribution.

After every test effort, there is always lessons learned that engineers hope to pass on so that the same mistakes are not duplicated. It is the hope that through this paper, some of these lessons will be utilized to make future large scale testing efforts even more successful than this.

Bibliography

1. Winkel, J.: CMLAS fixed base test pretest instrumentation plan overall effort summary, November 2015
2. NASA GRC/LMD modal test team "CM/LAS simulator modal test & model correlation results & summary", December 2015
3. Akers, J., Bittinger, S., Jones, T., Staab, L., Suárez, V., Winkel, J.: European service module structural test article (E-STA) "Building Block Approach" modal test results. Proceedings of the 87th Shock and Vibration Symposium, New Orleans, LA, October 2016
4. NASA GRC/LMD modal test team "CMA simulator modal test & model correlation results & summary", August 2015
5. Winkel, J.: CMA simulator free-free modal test pretest instrumentation, July 2015
6. NASA/GRC analysis team "E-STA sine vibration model update log", February 2017
7. Bittinger, S., Winkel, J.: Total correlation changes in 2017 ESTA, January 2017

Chapter 26
Control of Plate Vibrations with Artificial Neural Networks and Piezoelectricity

Onur Avci, Osama Abdeljaber, Serkan Kiranyaz, and Daniel Inman

Abstract This paper presents a method for active vibration control of smart thin cantilever plates. For model formulation needed for controller design and simulations, finite difference technique is used on the cantilever plate response calculations. Piezoelectric patches are used on the plate, for which a neural network based control algorithm is formed and a neurocontroller is produced to calculate the required voltage to be applied on the actuator patch. The neurocontroller is trained and run with a Kalman Filter for controlling the structural response. The neurocontroller performance is assessed by comparing the controlled and uncontrolled structural responses when the plate is subjected to various excitations. It is shown that the acceleration response of the cantilever plate is suppressed considerably validating the efficacy of the neurocontroller and the success of the proposed methodology.

Keywords Vibrations control · Artificial neural networks · Piezoelectricity · Plate vibrations · Smart plate

26.1 Introduction

With advancements in materials science and technology, engineering structures are getting more flexible and lighter [1–8]. Even though this can be considered as an advantage from economic stand point, the vibrations response becomes more critical for these structures [9–18]. Various engineering disciplines have been interested in controlling vibrations of engineering structures with active, semi-active, and passive methods [19–21]. Active control mechanisms use an array of sensor/actuator pairs to measure the vibration response of the structure and generate control forces for energy dissipation and response reduction.

For the vibration control of plates, the implementation of piezoelectric materials has been found efficient [22, 23] while Artificial Neural Networks have been started to be implemented with piezoelectricity. This study presented in this paper uses an updated version of the neural network based algorithm started by Ghaboussi and Joghataie [24] and upgraded by Bani-Hani [25]. In turn, a novel procedure is introduced for vibration control of flexible plates. The work presented in this paper involves the use of emulator neural networks (ENNs); design of a neurocontroller to calculate the required voltage for sensor/actuator units. In an attempt to formulate the model needed for running the simulations and designing the controller, finite difference technique is utilized on the cantilever plate response equations involving sensor/actuator piezoelectric patches for various excitations. The authors run numerical simulations for validating the model and verifying the efficacy of the active vibration control methodology.

26.2 Utilizing Finite Difference Method

For setting the boundary conditions in finite difference method, the nodes are generated outside the cantilever structure; also the nodes are divided into six set of nodes (Fig. 26.1).

O. Avci (✉) · O. Abdeljaber
Department of Civil Engineering, Qatar University, Doha, Qatar
e-mail: oavci@vt.edu

S. Kiranyaz
Department of Electrical Engineering, Qatar University, Doha, Qatar

D. Inman
Department of Aerospace Engineering, University of Michigan, Ann Arbor, MI, USA

C. Walber et al. (eds.), *Sensors and Instrumentation, Aircraft/Aerospace, Energy Harvesting & Dynamic Environments Testing, Volume 7*, Conference Proceedings of the Society for Experimental Mechanics Series,
https://doi.org/10.1007/978-3-030-12676-6_26

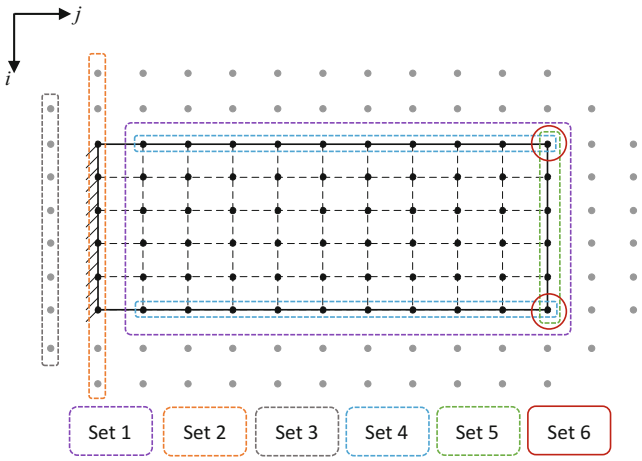

Fig. 26.1 Nodes and Node sets

26.2.1 Set 1 Nodes

Per the results of the study by Ugural [26], the equation of a rectangular thin plate subjected to time-varying dynamic excitation $P(x, y, t)$ is:

$$D\left[\frac{\partial^4 w\,(x,\,y,\,t)}{\partial x^4} + 2\frac{\partial^4 w\,(x,\,y,\,t)}{\partial x^2 \partial y^2} + \frac{\partial^4 w\,(x,\,y,\,t)}{\partial y^4}\right] + C_s \frac{\partial w\,(x,\,y,\,t)}{\partial t} + \rho h \frac{\partial^2 w\,(x,\,y,\,t)}{\partial t^2} = P\,(x,\,y,\,t) \tag{26.1}$$

where D is the flexural rigidity of the plate, $w(x, y, t)$ is for the deflection map of the structure at time t, C_s is the structural damping constant, ρ is the material density, and h is the thickness.

Equation (26.1) can be interpreted with the internal moments considering the fact that when N piezoelectric transducers are attached to the plate, there are external moments generated affecting the internal moments at various locations of the structure. Because the sensor/actuator units are predominantly lighter than the cantilever structure, they will have negligible effects on the dynamics of the plate. Introducing $m_x(x, y, t)$, $m_y(x, y, t)$, and $m_{xy}(x, y, t)$ for bending and twisting moments created by N piezoelectric patch units [27], the equation becomes:

$$\rho h \frac{\partial^2 w\,(x,\,y,\,t)}{\partial t^2} + C_s \frac{\partial w\,(x,\,y,\,t)}{\partial t} + D\nabla^4 w\,(x,\,y,\,t) = P\,(x,\,y,\,t) - \frac{\partial^2 m_x\,(x,\,y,\,t)}{\partial x^2} - 2\frac{\partial^2 m_{xy}\,(x,\,y,\,t)}{\partial x \partial y} - \frac{\partial^2 m_y\,(x,\,y,\,t)}{\partial y^2} \tag{26.2}$$

With that, each joint is matched by one equation per Eq. (26.2) and each joints' finite difference approximation, as shown below:

$$\begin{aligned}\nabla^4 w_{(i,j,t)} \cong & \left[\frac{6}{H^4} + \frac{6}{L^4} + \frac{8}{H^2 L^2}\right] w_{(i,j,t)} + \left[\frac{-4}{H^4} - \frac{-4}{H^2 L^2}\right]\left[\begin{array}{c} w_{(i,j-1,t)} + w_{(i,j+1,t)} \\ + w_{(i-1,j,t)} + w_{(i+1,j,t)} \end{array}\right] \\ & + \frac{2}{H^2 L^2}\left[\begin{array}{c} w_{(i-1,j-1,t)} + w_{(i-1,j+1,t)} \\ + w_{(i+1,j-1,t)} + w_{(i+1,j+1,t)} \end{array}\right] + \frac{1}{H^4}\left[\begin{array}{c} w_{(i,j+2,t)} + w_{(i,j-2,t)} \\ + w_{(i-2,j,t)} + w_{(i+2,j,t)} \end{array}\right]\end{aligned} \tag{26.3}$$

$$\frac{\partial^2 m_{x\,(i,j,t)}}{\partial x^2} \cong \frac{-C_0 d_{31}}{h_{PZT} H^2} V(t)\left[R_{(i,j-1)} - 2R_{(i,j)} + R_{(i,j+1)}\right] \tag{26.4}$$

$$\frac{\partial^2 m_y\,(i,\,j,\,t)}{\partial y^2} \cong \frac{-C_0 d_{32}}{h_{PZT} L^2} V(t)\left[R_{(i-1,\,j)} - 2R_{(i,\,j)} + R_{(i+1,\,j)}\right] \tag{26.5}$$

$$\frac{\partial^2 m_{xy}}{\partial x \partial y} = 0 \tag{26.6}$$

Inserting the Eqs. (26.3–26.6) into Eq. (26.2) results in:

$$\rho h \ddot{w}_{(i,j,t)} + C_s \dot{w}_{(i,j,t)} + D \left\{ \begin{array}{c} \left[\frac{6}{H^4} + \frac{6}{L^4} + \frac{8}{H^2 L^2}\right] w_{(i,j,t)} + \\ \left[\frac{-4}{H^4} - \frac{-4}{H^2 L^2}\right] \left[\begin{array}{c} w_{(i,j-1,t)} + w_{(i,j+1,t)} \\ + w_{(i-1,j,t)} + w_{(i+1,j,t)} \end{array}\right] + \\ \frac{2}{H^2 L^2} \left[\begin{array}{c} w_{(i-1,j-1,t)} + w_{(i-1,j+1,t)} \\ + w_{(i+1,j-1,t)} + w_{(i+1,j+1,t)} \end{array}\right] + \frac{1}{H^4} \left[\begin{array}{c} w_{(i,j+2,t)} + w_{(i,j-2,t)} \\ + w_{(i-2,j,t)} + w_{(i+2,j,t)} \end{array}\right] \end{array} \right\} = F(t) P_{(i,j)} - V(t) Z_{(i,j)} \tag{26.7}$$

$$Z_{(i,j)} = \frac{-C_0 d_{31}}{h_{PZT} H^2}\left[R_{(i,j-1)} - 2R_{(i,j)} + R_{(i,j+1)}\right] - \frac{C_0 d_{32}}{h_{PZT} L^2}\left[R_{(i-1,j)} - 2R_{(i,j)} + R_{(i+1,j)}\right] \tag{26.8}$$

26.2.2 Set 2–6 Nodes

Per [27], the equations are formed as the following:

$$\text{For Set 2}: w_{(i,j,t)} = 0 \tag{26.9}$$

$$\text{For Set 3}: w_{(i,j,t)} = w_{(i,j+2,t)} \tag{26.10}$$

$$\text{For Set 4}: (-2 - 2\upsilon)\, w_{(i,j,t)} + \upsilon\left[w_{(i,j-1,t)} + w_{(i,j+1,t)}\right] + w_{(i-1,j,t)} + w_{(i+1,j,t)} = 0 \tag{26.11}$$

$$(2\upsilon - 6)\left[w_{(i-1,j,t)} - w_{(i+1,j,t)}\right] + (2 - \upsilon)\left[w_{(i-1,j-1,t)} + w_{(i-1,j+1,t)} - w_{(i+1,j-1,t)} - w_{(i+1,j+1,t)}\right] + w_{(i-2,j,t)} - w_{(i+2,j,t)} = 0 \tag{26.12}$$

$$\text{For Set 5}: (-2 - 2\upsilon)\, w_{(i,j,t)} + \upsilon\left[w_{(i-1,j,t)} + w_{(i+1,j,t)}\right] + w_{(i,j-1,t)} + w_{(i,j+1,t)} = 0 \tag{26.13}$$

$$(2\upsilon - 6)\left[w_{(i,j+1,t)} - w_{(i,j-1,t)}\right] + (2 - \upsilon)\left[w_{(i-1,j+1,t)} + w_{(i+1,j+1,t)} - w_{(i-1,j-1,t)} - w_{(i+1,j-1,t)}\right] + w_{(i,j+2,t)} - w_{(i,j-2,t)} = 0 \tag{26.14}$$

$$\text{For Set 6}: w_{(i-1,j+1,t)} - w_{(i-1,j-1,t)} + w_{(i+1,j-1,t)} - w_{(i+1,j+1,t)} = 0 \tag{26.15}$$

26.3 State-Space Formulations

For Set 1, joints are assigned an index from 1 to n, where n is the total number of joints. With this, $R(x, y)$ can be calculated at a joint based on Eq. (26.16).

$$R\,(x,\,y) = \sum_{i=1}^{N}\left[H\left(x - x_1^i\right) - H\left(x - x_2^i\right)\right]\left[H\left(y - y_1^i\right) - H\left(y - y_2^i\right)\right] \tag{26.16}$$

For Sets 2-to-6 are the joints are matched by indices from $n + 1$ to n_t, where n_t is the sum of all joints. Forming a $2n$-dimensional state vector $\mathbf{x}(t) = [w_1, \ldots, w_n, \dot{w}_1, \ldots, \dot{w}_n]^{\mathrm{T}}$, the system per [27] becomes:

$$\dot{\mathbf{x}}(t) = \begin{bmatrix} \mathbf{0}_{\mathrm{n}} & \mathbf{I}_{\mathrm{n}} \\ -\mathbf{M}^{-1}\mathbf{K} & -\mathbf{M}^{-1}\mathbf{C} \end{bmatrix} \mathbf{x}(t) + \begin{bmatrix} \mathbf{0}_{\mathrm{n}} \\ \mathbf{M}^{-1} \end{bmatrix} \left\{ F(t) \begin{bmatrix} P_1 \\ P_2 \\ \vdots \\ P_n \end{bmatrix} - V(t) \begin{bmatrix} Z_1 \\ Z_2 \\ \vdots \\ Z_n \end{bmatrix} \right\} \tag{26.17}$$

$$\mathbf{y}(t) = \begin{bmatrix} \mathbf{0}_{\mathrm{n}} & \mathbf{I}_{\mathrm{n}} \end{bmatrix} \mathbf{x}(t) + [\mathbf{0}_n] \left\{ F(t) \begin{bmatrix} P_1 \\ P_2 \\ \vdots \\ P_n \end{bmatrix} - V(t) \begin{bmatrix} Z_1 \\ Z_2 \\ \vdots \\ Z_n \end{bmatrix} \right\} \tag{26.18}$$

where $\boldsymbol{y}(t)$ is the state-space output.

26.4 Piezoelectric Sensor Formulation

Based on previous work [28, 29], the voltage produced by a piezoelectric sensor is:

$$V_s(t) = R_p r \int_{y_1}^{y_2} \int_{x_1}^{x_2} \left(e_{31} \frac{\partial^2 \dot{w}}{\partial x^2} + e_{32} \frac{\partial^2 \dot{w}}{\partial y^2} + 2e_{36} \frac{\partial^2 \dot{w}}{\partial x \partial y} \right) dx dy \tag{26.19}$$

The state-space system for the unit output becomes:

$$\begin{aligned} \dot{\mathbf{x}}(t) &= \begin{bmatrix} \mathbf{0}_{\mathrm{n}} & \mathbf{I}_{\mathrm{n}} \\ -\mathbf{M}^{-1}\mathbf{K} & -\mathbf{M}^{-1}\mathbf{C} \end{bmatrix} \mathbf{x}(t) + \begin{bmatrix} \mathbf{0}_{\mathrm{n}} \\ \mathbf{M}^{-1} \end{bmatrix} \{F(t)\mathbf{P} - V(t)\mathbf{Z}\} \\ \mathbf{y}_{\mathbf{v}}(t) &= R_p r \mathbf{N}_{(1\times n)} \mathbf{S}_{(n\times n)} \begin{bmatrix} \mathbf{0}_{\mathrm{n}} & \mathbf{I}_{\mathrm{n}} \end{bmatrix} \mathbf{x}(t) + 0 \times \{F(t)\mathbf{P} - V(t)\mathbf{Z}\} \end{aligned} \tag{26.20}$$

In Eq. (26.20), $\mathbf{y}_{\mathbf{v}}(t)$ is the updated state-space output that is equal to $V_s(t)$. The final model will house a large number high-frequency dynamics; therefore, a model reduction is needed.

26.5 Model Reduction and Kalman Filter Design

The reduced model can be defined as the following:

$$\begin{aligned} \dot{\mathbf{x}}_{\mathbf{r}}(t) &= \mathbf{A}_r \mathbf{x}_{\mathbf{r}}(t) + \mathbf{B}_{\mathbf{r}} \{F(t)\mathbf{P} - V(t)\mathbf{Z}\} \\ \mathbf{y}_{\mathbf{v}_{\mathbf{r}}}(t) &= \mathbf{C}_r \mathbf{x}_{\mathbf{r}}(t) + \mathbf{D}_r \times \{F(t)\mathbf{P} - V(t)\mathbf{Z}\} \end{aligned} \tag{26.21}$$

The neurocontroller created for this work (Fig. 26.2) is based on the control of the lowest (first) natural frequency of the plate. For generating the data needed to train the ENNs, a regulated output vector $\boldsymbol{z}(t)$ is formed to calculate the response for the first state:

$$z(t) = \mathbf{C}_z \mathbf{x}_{\mathbf{r}}(t) + \mathbf{D}_z \times \{F(t)\mathbf{P} - V(t)\mathbf{Z}\} \tag{26.22}$$

The Kalman filter is defined as the following, per [27]:

$$\dot{\widehat{\mathbf{x}}}_{\mathbf{r}}(t) = \mathbf{A}_r \widehat{\mathbf{x}}_{\mathbf{r}}(t) + \mathbf{B}_{\mathbf{r}} \mathbf{u}(t) + \mathbf{L}\left[y_{v_r}(t) - \mathbf{C}_r \widehat{\mathbf{x}}_{\mathbf{r}}(t) - \mathbf{D}_r \mathbf{u}(t) \right] \tag{26.23}$$

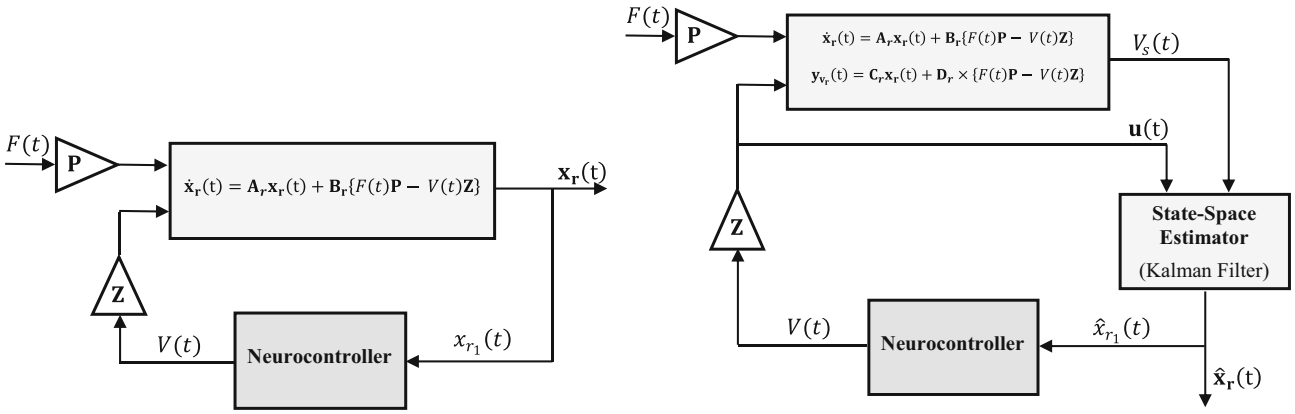

Fig. 26.2 Preliminary implementation of the Neurocontroller (left) and implementation of the Kalman Filter (right)

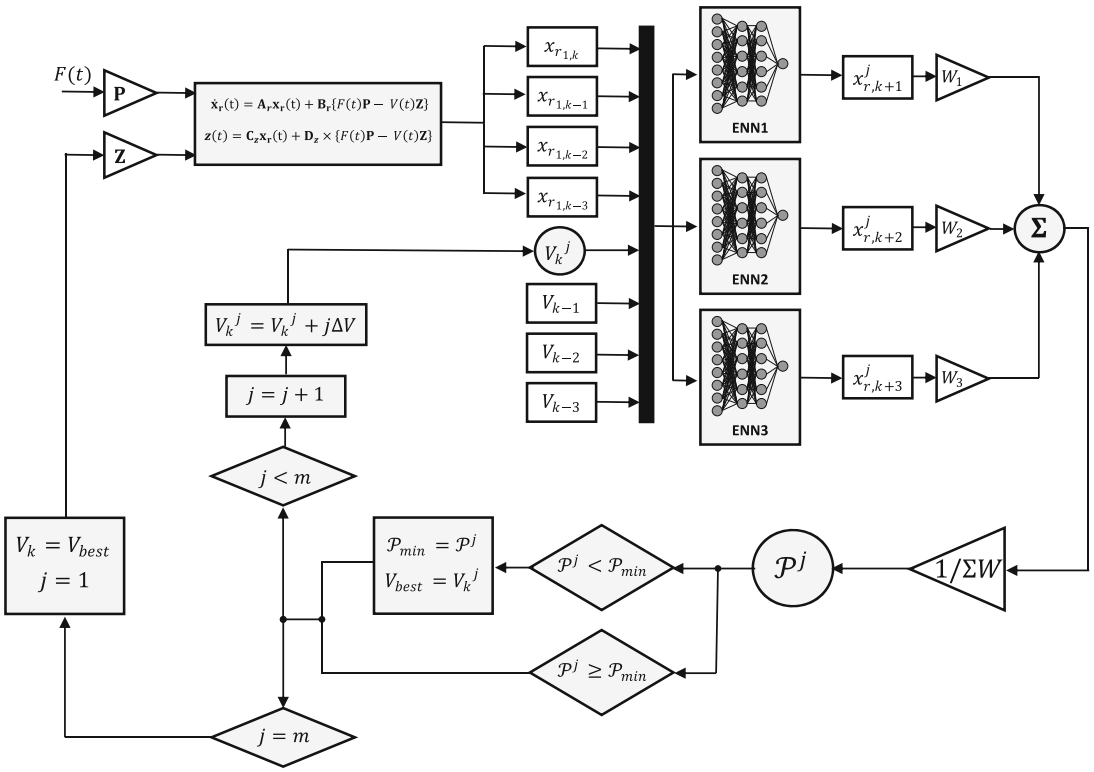

Fig. 26.3 The neurocontrol algorithm

As shown in Fig. 26.2, the initial scheme of the control algorithm is upgraded with the Kalman Filter.

26.6 The Neurocontroller

The neurocontroller training is performed on the multi-layer feedforward ENNs which are generated to compute the structural response. The neurocontrol algorithm is presented in Fig. 26.3. It is expected from the neurocontroller to generate the control voltage based on the immediate past values of the controlled state. In other words, the neurocontroller is trained to learn the transfer function from the controlled state for which the training data is produced by applying an excitation to the plate by white-noise signal and calculate the needed voltage based on the neurocontrol algorithm. With that, the data is classified in terms of input-output format, and an ANN learning algorithm is used for the training of the neurocontroller [27].

26.7 Numerical Example of a Plate with Sensor/Actuator Pair

For the numerical simulation of the thin cantilever structure with patches, the following information is used: plate dimensions $a = 0.5$ m, $b = 0.5$ m, and $h = 1.78$ mm; for material properties, the density is $\rho = 7800\text{kg/m}^3$, modulus of elasticity is $E = 200$ GPa, and Poisson's ratio is $\nu = 0.3$. The flexural rigidity is $D = 103.3$. Modal damping ratio for all modes is used as $\zeta = 0.006$. The dimensions of the patch are 6.67cm $\times$ 6.67cm with a thickness $h_{PZT} = 1$ mm. For the sensor/actuator pair, the material properties are $p_{pe} = 7650$ kg/m^3, $E_{PZ} = 63$ GPa, and $\nu_{PZT} = 0.30$. The strain constants are $d_{31} = d_{32} = 166 \times 10^{-12}$m/V, and the stress constants are $e_{31} = e_{32} = 10.46$m/V. The sensor and actuator patches are located at the same place, however, on the two opposite sides of the thin plate.

The authors wrote a MATLAB code to use finite difference technique to produce the Kalman Filter and the state-space system. The code uses Eq. (26.20) applying the MATLAB tools [30] eliminating the states with considerably small observability. As a next step, the Kalman Filter gain $\mathbf{L}$ is calculated. For the numerical simulation, the plate mesh size is $H \times L = 0.0167\text{m} \times 0.0167\text{m}$. The full state space model response and the reduced-order model response subjected to a white noise excitation are presented in Fig. 26.4. For verification purposes, the reduced-order state-space system frequencies are compared to the frequencies published by Plunkett [31] and the FE model predictions by Abaqus 6.12 [32]. All three methods frequencies are in perfect match as shown in [27].

26.7.1 Emulator Neural Network Training

A Simulink model is built to produce the training data for which the sampling period is $\Delta t = 0.001$ s and three excitations are used.

1. A uniformly distributed load is used to excite the structure for 10 seconds within a range of 0–60 Hz white noise signal.
2. A 0–5 Hz white noise signal is used to excite the piezoelectric patch for 10 seconds.
3. A uniformly distributed random load is used to excite the structure for 10 seconds while the actuator is subjected to a random voltage for 10 seconds.

Based on the above, the actual response is compared to the ENN predicted response in Fig. 26.5.

26.7.2 Evaluation of the Neurocontroller

The structural response controlled by the neurocontroller is simulated with three excitation cases:

1. A localized pulse force is applied at the point $x = 0.4$ m, $y = 0.25$ m (Fig. 26.6).
2. A distributed load is used to excite the within a range of 0–40 Hz white noise (Fig. 26.7).

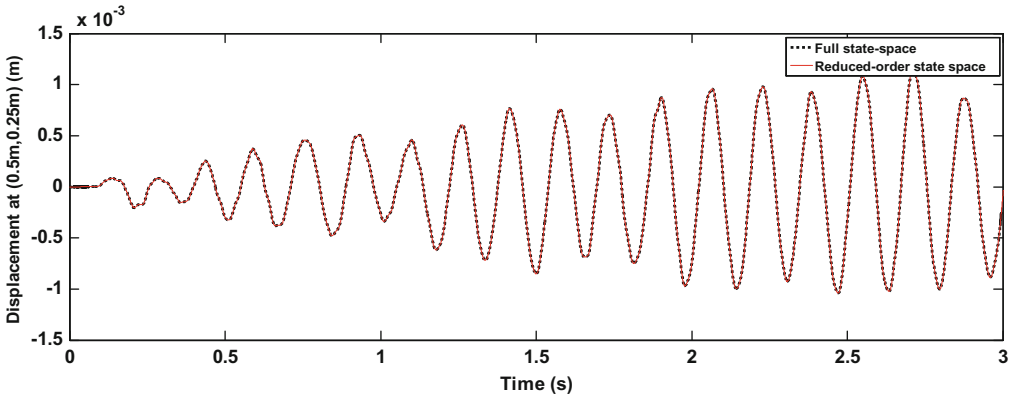

Fig. 26.4 The full state space response and the reduced-order state space response subjected to white noise

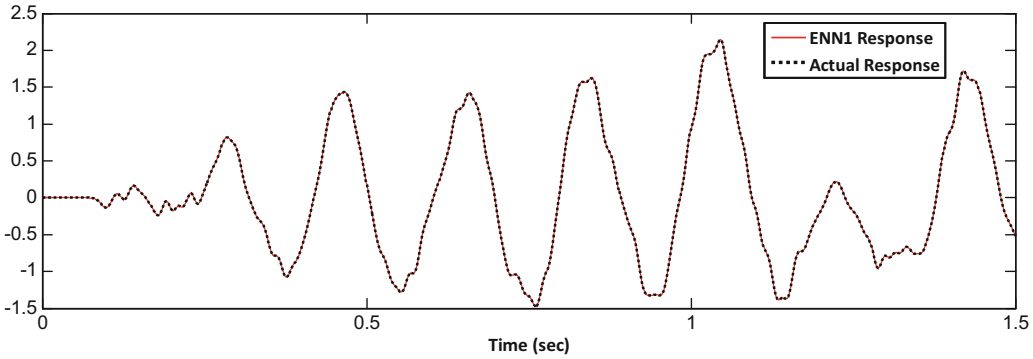

Fig. 26.5 The actual response and the emulator neural network predicted response

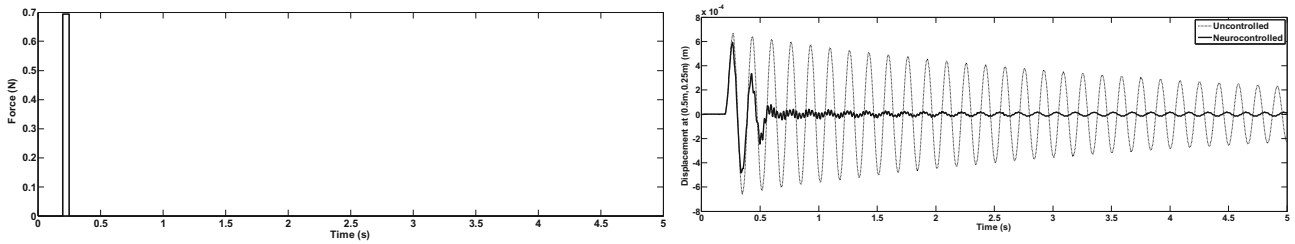

Fig. 26.6 Time histories: Load Case 1 signal (left); Uncontrolled and Neurocontrolled displacement response (right)

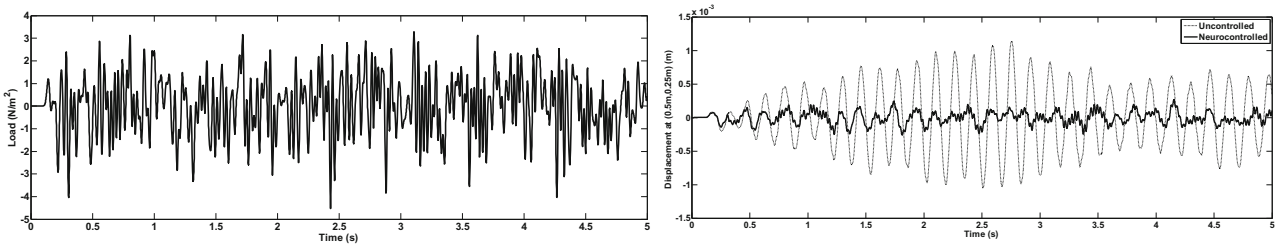

Fig. 26.7 Time histories: Load Case 2 signal (left); Uncontrolled and Neurocontrolled displacement response (right)

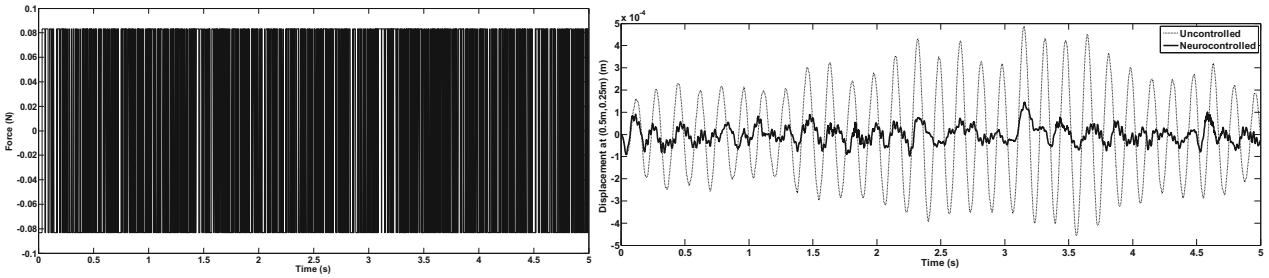

Fig. 26.8 Time histories: Load Case 3 signal (left); Uncontrolled and Neurocontrolled displacement response (right)

3. Two localized forces with varying magnitudes per pseudo random binary sequence is applied at the points $x = 0.4$ m, $y = 0.1$ m and $x = 0.4$ m, $y = 0.4$ m (Fig. 26.8).

For these excitations, the structural response is calculated at the point $x = 0.5$ m, $y = 0.25$ m (i.e. the center of the cantilever tip). Uncontrolled and neurocontrolled displacement responses are presented in Figs. 26.6, 26.7 and 26.8.

26.8 Conclusions

In this paper, the response of a thin cantilever plate structure with piezoelectric patches is studied. The first excitation was used to assess the performance of the neurocontroller in suppressing pulse loads. It is verified for this load that the response of the plate structure is reduced considerably; indicating that the proposed active control procedure is successful. The forced excitations of the second and the third load cases reveal that the proposed active control procedure is successful again. It can be concluded that the trained neurocontroller is efficient in active control of thin cantilever plates, for various kind of excitations.

References

1. Younis, A., Avci, O., Hussein, M., Davis, B., Reynolds, P.: Dynamic forces induced by a single pedestrian: a literature review. Appl. Mech. Rev. **69**, (2017). https://doi.org/10.1115/1.4036327
2. Celik, O., Do, N.T., Abdeljaber, O., Gul, M., Avci, O., Catbas, F.N.: Recent issues on stadium monitoring and serviceability: a review. In: Conference Proceedings of the Society for Experimental Mechanics Series (2016). https://doi.org/10.1007/978-3-319-29763-7_41
3. Barrett, A.R., Avci, O., Setareh, M., Murray, T.M.: Observations from vibration testing of in-situ structures. In: Proceedings of the Structures Congress Expo (2006). https://doi.org/10.1061/40889(201)65
4. Chaabane, M., Ben Hamida, A., Mansouri, M., Nounou, H.N., Avci, O.: Damage detection using enhanced multivariate statistical process control technique. In: 2016 17th International Conference on Sciences and Techniques of Automatic control & Computer Engineering STA 2016 – Proceedings (2017). https://doi.org/10.1109/STA.2016.7952052
5. Mansouri, M., Avci, O., Nounou, H., Nounou, M.: Iterated square root unscented Kalman Filter for nonlinear states and parameters estimation: three DOF damped system. J. Civ. Struct. Heal. Monit. **5**, (2015). https://doi.org/10.1007/s13349-015-0134-7
6. Mansouri, M., Avci, O., Nounou, H., Nounou, M.: A comparative assessment of nonlinear state estimation methods for structural health monitoring. In: Conference Proceedings of the Society for Experimental Mechanics Series (2015). https://doi.org/10.1007/978-3-319-15224-0_5
7. Mansouri, M., Avci, O., Nounou, H., Nounou, M.: Iterated square root unscented Kalman Filter for state estimation – CSTR model. In: 12th International Multi-Conference on Systems, Signals and Devices, SSD 2015 (2015). https://doi.org/10.1109/SSD.2015.7348243
8. Mansouri, M., Avci, O., Nounou, H., Nounou, M.: Parameter identification for nonlinear biological phenomena modeled by S-systems. In: 12th International Multi-Conference on Systems, Signals and Devices, SSD 2015 (2015). https://doi.org/10.1109/SSD.2015.7348187
9. Avci, O., Bhargava, A., Al-Smadi, Y., Isenberg, J.: Vibrations serviceability of a medical facility floor for sensitive equipment replacement: evaluation with sparse in-situ data. Pract. Period. Struct. Des. Constr. **24**, (2018)
10. Do, N.T., Gul, M., Abdeljaber, O., Avci, O.: Novel framework for vibration serviceability assessment of stadium grandstands considering durations of vibrations. J. Struct. Eng. (United States). **144**, (2018). https://doi.org/10.1061/(ASCE)ST.1943-541X.0001941
11. Avci, O., Abdeljaber, O., Kiranyaz, S., Hussein, M., Inman, D.J.: Wireless and real-time structural damage detection: a novel decentralized method for wireless sensor networks. J. Sound Vib. **424**, 158–172 (2018)
12. Avci, O., Abdeljaber, O., Kiranyaz, S., Inman, D.: Vibration suppression in metastructures using zigzag inserts optimized by genetic algorithms. In: Conference Proceedings of the Society for Experimental Mechanics Series (2017). https://doi.org/10.1007/978-3-319-54735-0_29
13. Abdeljaber, O., Avci, O., Kiranyaz, M.S., Boashash, B., Sodano, H., Inman, D.J.: 1-D CNNs for structural damage detection: verification on a structural health monitoring benchmark data. Neurocomputing. **275**, 1308–1317 (2018). https://doi.org/10.1016/j.neucom.2017.09.069
14. Abdeljaber, O., Younis, A., Avci, O., Catbas, N., Gul, M., Celik, O., Zhang, H.: Dynamic testing of a laboratory stadium structure. Geotech. Struct. Eng. Congr. **2016**, 1719–1728 (n.d.). https://doi.org/10.1061/9780784479742.147
15. Abdeljaber, O., Avci, O.: Nonparametric structural damage detection algorithm for ambient vibration response: utilizing artificial neural networks and self-organizing maps. J. Archit. Eng. (2016). https://doi.org/10.1061/(ASCE)AE.1943-5568.0000205
16. Abdeljaber, O., Avci, O., Kiranyaz, S., Gabbouj, M., Inman, D.J.: Real-time vibration-based structural damage detection using one-dimensional convolutional neural networks. J. Sound Vib. **388**, 154–170 (2017). https://doi.org/10.1016/j.jsv.2016.10.043
17. Abdeljaber, O., Avci, O., Do, N.T., Gul, M., Celik, O., Necati Catbas, F.: Quantification of structural damage with self-organizing maps. In: Conference Proceedings of the Society for Experimental Mechanics Series (2016). https://doi.org/10.1007/978-3-319-29956-3_5
18. Davis, B., Avci, O.: Simplified vibration response prediction for slender monumental stairs. In: Structures Congress 2014 – Proceedings of Structures Congress 2014 (2014). https://doi.org/10.1061/9780784413357.223
19. Inman, D.J.: Vibration with control, Wiley (2006). https://doi.org/10.1002/0470010533
20. Abdeljaber, O., Avci, O., Kiranyaz, S., Inman, D.J.: Optimization of linear zigzag insert metastructures for low-frequency vibration attenuation using genetic algorithms. Mech. Syst. Signal Process. **84**, (2017). https://doi.org/10.1016/j.ymssp.2016.07.011
21. Abdeljaber, O., Avci, O., Inman, D.J.: Optimization of chiral lattice based metastructures for broadband vibration suppression using genetic algorithms. J. Sound Vib. (2015). https://doi.org/10.1016/j.jsv.2015.11.048
22. Caruso, G., Galeani, S., Menini, L.: Active vibration control of an elastic plate using multiple piezoelectric sensors and actuators. Simul. Model. Pract. Theory. **11**, 403–419 (2003). https://doi.org/10.1016/S1569-190X(03)00056-X
23. Qiu, J., Haraguchi, M.: Vibration control of a plate using a self-sensing piezoelectric actuator and an adaptive control approach. J. Intell. Mater. Syst. Struct. **17**, 661–669 (2006). https://doi.org/10.1177/1045389X06055760
24. Ghaboussi, J., Joghataie, A.: Active control of structures using neural networks. J. Eng. Mech. **121**, 555–567 (1995). https://doi.org/10.1061/(ASCE)0733-9399(1995)121:4(555)
25. Bani-Hani, K., Ghaboussi, J.: Nonlinear structural control using neural networks. J. Eng. Mech. **124**, 319–327 (1998). https://doi.org/10.1061/(ASCE)0733-9399(1998)124:3(319)

26. Ugural, A.C.: Stresses in beams, plates, and shells (2010). https://doi.org/10.1007/s13398-014-0173-7.2
27. Abdeljaber, O., Avci, O., Inman, D.J.: Active vibration control of flexible cantilever plates using piezoelectric materials and artificial neural networks. J. Sound Vib. **363**, (2016). https://doi.org/10.1016/j.jsv.2015.10.029
28. Tavakolpour, A.R., Mailah, M., Mat Darus, I.Z., Tokhi, O.: Self-learning active vibration control of a flexible plate structure with piezoelectric actuator. Simul. Model. Pract. Theory. **18**, 516–532 (2010). https://doi.org/10.1016/j.simpat.2009.12.007
29. Quek, S.T., Wang, S.Y., Ang, K.K.: Vibration control of composite plates via optimal placement of piezoelectric patches. J. Intell. Mater. Syst. Struct. **14**, 229–245 (2003). https://doi.org/10.1177/1045389X03034686
30. The Mathworks Inc., MATLAB – MathWorks, www.Mathworks.Com/Products/Matlab (2016)
31. Plunkett, R.: Natural frequencies of uniform and non-uniform rectangular cantilever plates. J. Mech. Eng. Sci. **5**, 146–156 (1963). https://doi.org/10.1243/JMES_JOUR_1963_005_020_02
32. Dassault Systèmes Simulia, Fallis, A., Techniques, D.: ABAQUS documentation, Abaqus 6.12. (2013). https://doi.org/10.1017/CBO9781107415324.004

Chapter 27
Comparing Fixed-Base and Shaker Table Model Correlation Methods Using Jim Beam

James Ristow and Jessica Gray

Abstract The key to any dynamic model correlation is an understanding of how the boundary conditions of the test article interact with the test data. Due to budget and schedule constraints, some spacecraft programs opt to correlate the spacecraft dynamic model during the Environmental Qualification Test, conducted on a large shaker table. While this saves cost to the spacecraft program, the base-drive analysis of the dynamic model incorrectly assumes the boundary condition between the shaker and the spacecraft to be completely fixed, except for the prescribed force input.

This paper follows-up research published in IMAC 36, "Comparing Free-Free and Shaker Table Model Correlation Methods using Jim Beam." In that study a free-free impact modal test, a "fixed" base impact modal test on top of the shaker, and a base-drive vibration test were used to assess Finite Element Model (FEM) correlation using different boundary conditions. The NAVCON Jim Beam, a simple and well characterized structure featured in the round robin tests of IMAC 27, was chosen as the test article. Conclusions showed that due to the non-linear compliance of the shaker table, most time would be spent accounting for the boundary condition in the correlation, rather than correlating the test article itself.

Previous testing was conducted with the Jim Beam flush mounted to the shaker table, which restricted the motion of the bending and shear modes. To mitigate this constraint, this paper included the use of "donut" force gauges inserted between the shaker table and the Jim Beam. Not only was the direct force input of the vibration test measured, but the gauges acted as spacers which relieved the constraint on mode shapes caused by contact with the shaker table. This constraint was a source of error in the previous modal data.

The premise of this follow-on study is the same as before; to compare test data of the same structure with identical instrumentation across different boundary conditions. First, a fixed base modal impact test of the Jim Beam was conducted on a slip table to approximate a modal plate. During this test the Jim Beam was mounted on four disconnected force gauges to simulate the same bolted interface as the shaker table. Second, the Jim Beam was transferred to a large shaker table and a vibration test was conducted. Results of the two tests were compared to investigate the validity of using environmental test data alone to correlate a dynamic model.

Keywords Jim Beam · Modal test · Model correlation · Vibration test · Shaker table

27.1 Background and Motivation

By their very nature, dynamic systems interact with each other. Ideally, all spacecraft would be tested with their assigned launch vehicle to capture the coupled system dynamics. As it is impractical to fly a test spacecraft to measure the loads prior to launching the real one, it is equally impractical to ground test the spacecraft coupled with the launch vehicle, as spacecraft integration only occurs right before launch. A Coupled Loads Analysis, or CLA, is the only option to assess the spacecraft/launch vehicle coupled system dynamics for all phases of flight prior to launch. The accuracy of the CLA depends on using correlated Finite Element Models for the analysis. Launch vehicles have heritage testing and flight experience that give confidence in the pedigree and fidelity of their dynamic models, however, each new spacecraft has unique dynamic characteristics that must be captured correctly in the CLA.

J. Ristow (✉)
NASA, Merritt Island, FL, USA
e-mail: james.a.ristow@nasa.gov

J. Gray
University of Washington, Seattle, WA, USA

C. Walber et al. (eds.), *Sensors and Instrumentation, Aircraft/Aerospace, Energy Harvesting & Dynamic Environments Testing, Volume 7*, Conference Proceedings of the Society for Experimental Mechanics Series,
https://doi.org/10.1007/978-3-030-12676-6_27

NASA standards require the spacecraft dynamic model used in the Verification Load Cycle be correlated via modal test. Due to budget and schedule constraints, some spacecraft programs opt to correlate the dynamic model during the system level Environmental Qualification Test. This test is a contractual requirement to meet the launch vehicle sine vibration environment at the spacecraft interface. NASA's Launch Services Program (LSP) has developed minimum correlation criteria for spacecraft CLA models that are correlated using the environmental qualification test. A Frequency Response Function (FRF) derived from a base-drive analysis of the spacecraft stack Finite Element Model (FEM) must envelope the levels observed during test; primary modes should match test frequencies within 5%, and secondary modes should match within 10% [1]. Given the cost savings, some unmanned spacecraft choose to correlate the dynamic model during the environmental qualification test.

Classical base-drive analysis, an industry standard practice, analytically fixes the spacecraft model to a rigid seismic mass and drives the system by force input applied at the base of the spacecraft. Inherently, the base-drive analysis assumes no flexibility in the system other than the spacecraft. Several studies conducted by Aerospace Corporation and Sandia National Labs referenced in the previous paper [2] have illustrated challenges of correlating a spacecraft on a shaker table. Findings by Carne et al. reported "*modes attributable to the base-shake table, which violates the assumed theoretical boundary condition of zero motion at the attachment point, except for the prescribed input*" [3]. This finding essentially invalidates the fixed-base modeling assumption asserted in a base-drive analysis, the basis of correlation using a shaker table.

Dynamic Substructuring is a viable option, where instrumentation is placed on the table to generate a Hurty-Craig-Bampton model of the table and test article, and through dynamic condensation reduce out the modes of the table to be left with the modes of the test article [4, 5]. However, this would require the subcontractor conducting the spacecraft vibration test to allocate additional accelerometers, test channels, time and techs to install the extra instrumentation. Also, most spacecraft integration efforts are contracted out to various companies and test facilities, leaving very little repeatability in the shaker used for a given test.

The goal of this study is to identify potential pitfalls of using vibration testing for correlation, and account for them using existing instrumentation to keep vibration test time and cost as low as practicable.

27.2 Current Study

To improve upon the findings of the previous study, four force gauges were added to the base of the Jim Beam, one at each of the corners of the bolted interface between the bottom gold plate and the test fixture (Figs. 27.1 and 27.2). The

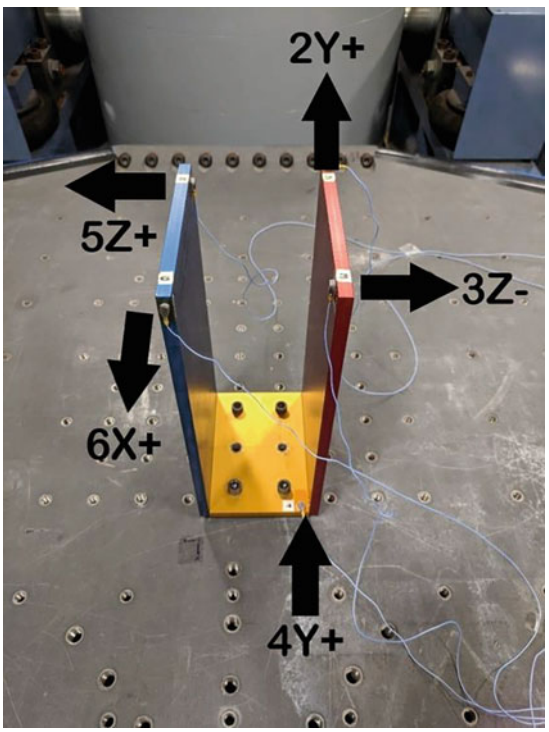

Fig. 27.1 Jim Beam on slip table with accelerometer locations and orientations

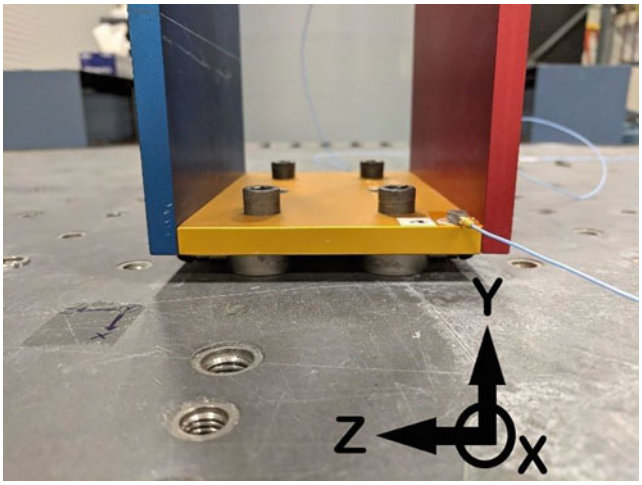

Fig. 27.2 Detail of force gauges at Jim Beam interface with coordinate system

advantage to using force gauges is threefold: First, the PCB "donut" force gauges acted as spacers between the test article and the test fixture. Previously, the Jim Beam was flush-mounted during the "fixed" modal test and the vibration test, which unintentionally added a friction constraint that restricted the motion of the blue and red plates. Second, the force gauges measured the force at the interface of the Jim Beam directly. This data provided important insight regarding the motion of the Jim Beam with respect to the shaker. Lastly, the use of force gauges between the shaker and the test article interface is more representative of instrumentation present during a full scale spacecraft environmental qualification test.

Another noteworthy improvement was the use of a non-operational slip table to act as a "modal plate" for the fixed base impact modal test. As noted in the previous paper, the "fixed base" testing conducted on the shaker table was not truly fixed. While the slip table was also not truly fixed, it did not contain the same compliance and non-linearities of the shaker mechanisms, and clean impact modal data was able to be collected.

27.3 The Fixed Base Impact Modal Test

The Jim Beam was mounted to the slip table on a disconnected Unholtz-Dickie T1000 22,000 lbf shaker, soon to be retired from the Kennedy Space Center vibration lab (Fig. 27.1). The slip table was never used in an operational sense for this study; it was used only as a makeshift modal plate. The slip table plate weighed 239 lbs and was constrained in two axes on a granite base. From a practical standpoint, the plate was constrained in all three axes, as it had not been used or lubricated for some time. While not an ideal modal plate, it was adequate for the purposes of this study. One force gauge was placed at each corner of the gold base plate, and the four interface bolts passed through the force gauges to connect the Jim Beam to the Slip Table. For the fixed base impact modal test, no force gauge data was collected, however these were kept in place to retain the same boundary condition as would be used for the shaker sine vibration test. Accelerometers were also kept at identical locations across all testing to keep data comparisons consistent.

A Bruel and Kjær LAN-XI six-channel data acquisition system was used to collect the modal impact data on the Jim Beam, and *BK Connect* software was used to curvefit the data using the RFP-Z algorithm. Drive point FRFs of reference channels 2, 3, 5 and 6 were plotted using Python software (Fig. 27.3). Note that channel 4 is very close to the bolted interface; this location was ideal for the shaker test, but not for capturing clean impact modal testing, therefore channel 4 is omitted from Fig. 27.3.

27.4 The Sine Vibration Test

Following the fixed base impact test on the slip table, the Jim Beam was mounted on the KSC Vibration Lab Unholtz-Dickie T2000 25,000 lbf shaker. The configuration was as follows: a 107 lb adaptor Cube was mounted to the shaker table, followed

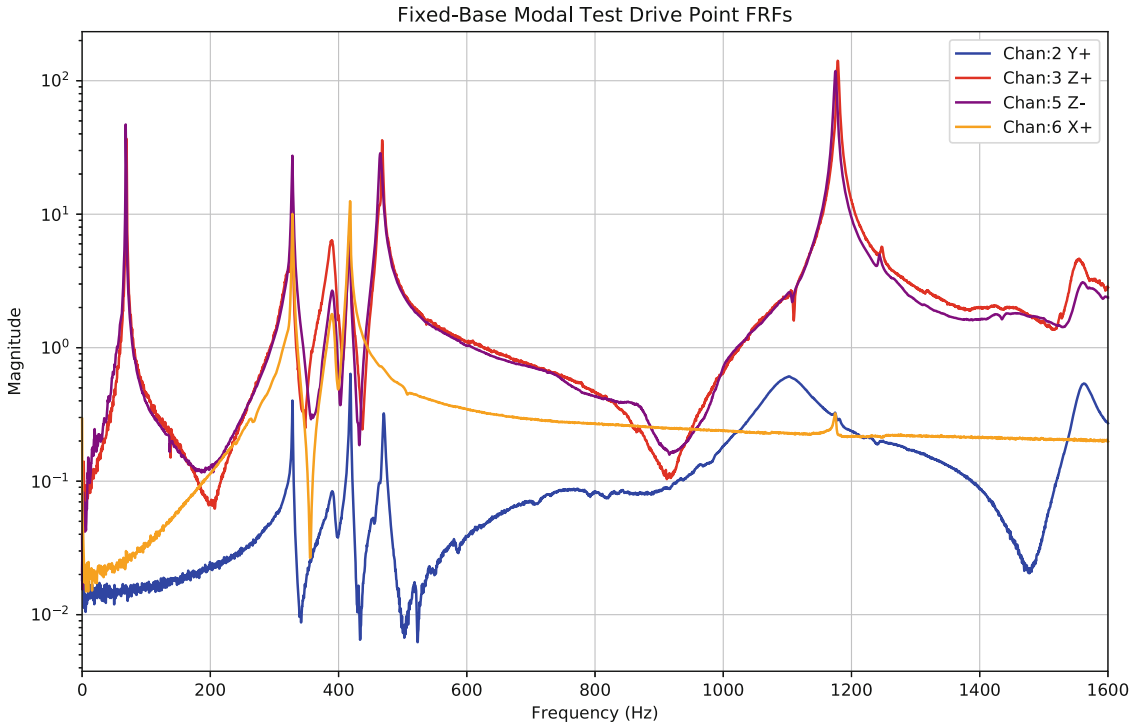

Fig. 27.3 Fixed base drive point FRFs of Jim Beam on Slip Table

by the four force gauges, the Jim Beam, and the 4 through bolts to hold the force gauges and Jim Beam in place. For the X, Y and Z directions the Jim Beam was rotated on the Cube, and the force gauges were kept at the interface between the Cube and the gold plate in each configuration. Four control channels were placed at each corner of the cube for the duration of the test to capture any rocking of the cube in tandem with the interface force gauges. These channels were averaged and used as the control channels for the shaker input. For the X and Z axis tests, only control channels 14 and 15 were averaged; the bending moment of the Jim Beam cantilevered on the side of the cube would otherwise cause the system to abort. Figure 27.4 shows the test configuration for the X, Y, and Z axes on the shaker table.

One of the improvements from the previous study was to take into consideration the sweep rate used during the sine vibe test to more accurately capture the frequency and damping. Research done by Aerospace Corporation [6] provided guidelines for selecting an appropriate sweep rate for a given damping value. The Jim Beam has very low damping, therefore a very slow sweep rate of 0.5 octaves per minute was estimated using Eq. 27.1, where η is a non-dimensional parameter (selected to be 1), f_n is the resonant frequency of a Single-Degree-Of-Freedom oscillator (Hz), Q is the amplitude ratio of the peak to steady state response, and Ke is the exponential sweep rate in octaves per minute.

$$K_e = \frac{\eta * 60 * f_n}{Q^2 * \ln 2} \tag{27.1}$$

An even slower sweep rate could have been derived from damping values obtained during fixed base testing, however, it was impractical to further reduce the sweep rate. At 0.5 octaves per minute, it took almost 17 min/axis to sweep from 5 to 1600 Hz.

27.5 Results

The results of each test axis are plotted in Figs. 27.5, 27.6, and 27.7. Each figure contains three sub-plots: The first plot contains traces from the four accelerometers placed at each corner of the cube, and the average response of the four channels. The middle plot contains the forces from the four force gauges at the Jim Beam/Cube interface. The bottom plot contains traces from the five accelerometers mounted to the Jim Beam. Notice that for each of the X, Y and Z directions, only select

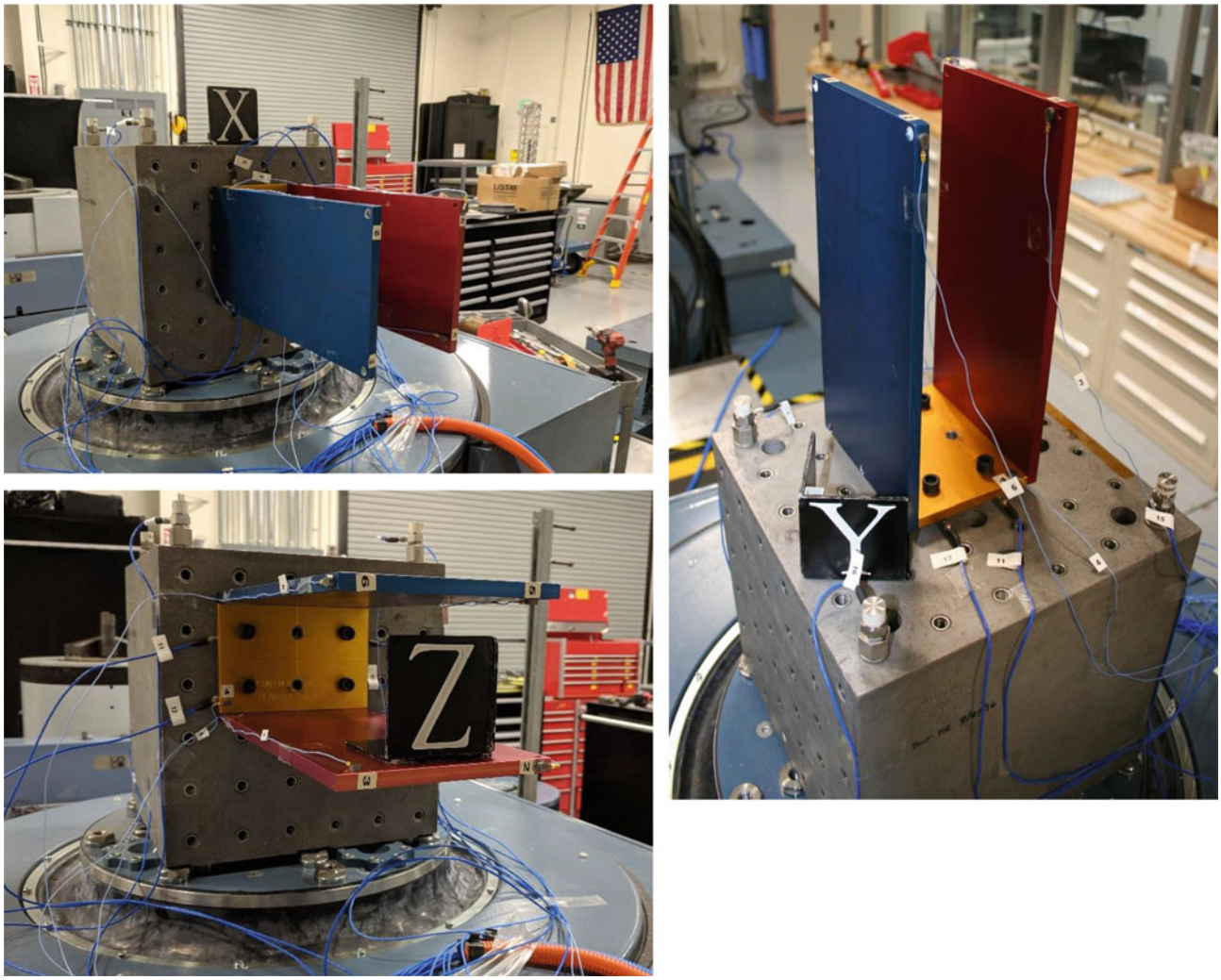

Fig. 27.4 Jim beam mounted to Cube on Shaker Table. Clockwise from top left: (**a**) X-Axis test, (**b**) Y-Axis test, and (**c**) Z-Axis test

accelerometers on the Jim Beam are in-axis with the test; therefore the off-axis accelerometers read much lower amplitudes than those that are in-axis.

27.5.1 X-Axis Observations (Fig. 27.5)

For the X-Axis, only channels 14 and 15 were averaged and used for controlling the shaker, and channel 6 on the Jim Beam is the only Jim Beam channel oriented in the X-Axis. Due to the cantilevered configuration, the shaker would have aborted when sweeping through the second mode of the Jim Beam at 400 Hz. This becomes clearer when observing channels 14 and 15, which show much lower magnitude than channels 1 and 16 opposite the Cube, indicating a bending moment of the cube at that frequency. Averaging control channels is desirable to ensure a constant input spectrum. Also, the Cube shows some active response between 600 and 800 Hz. Interestingly, the Jim Beam has no frequencies in this range, as indicated by the fixed base modal test results in Fig. 27.3.

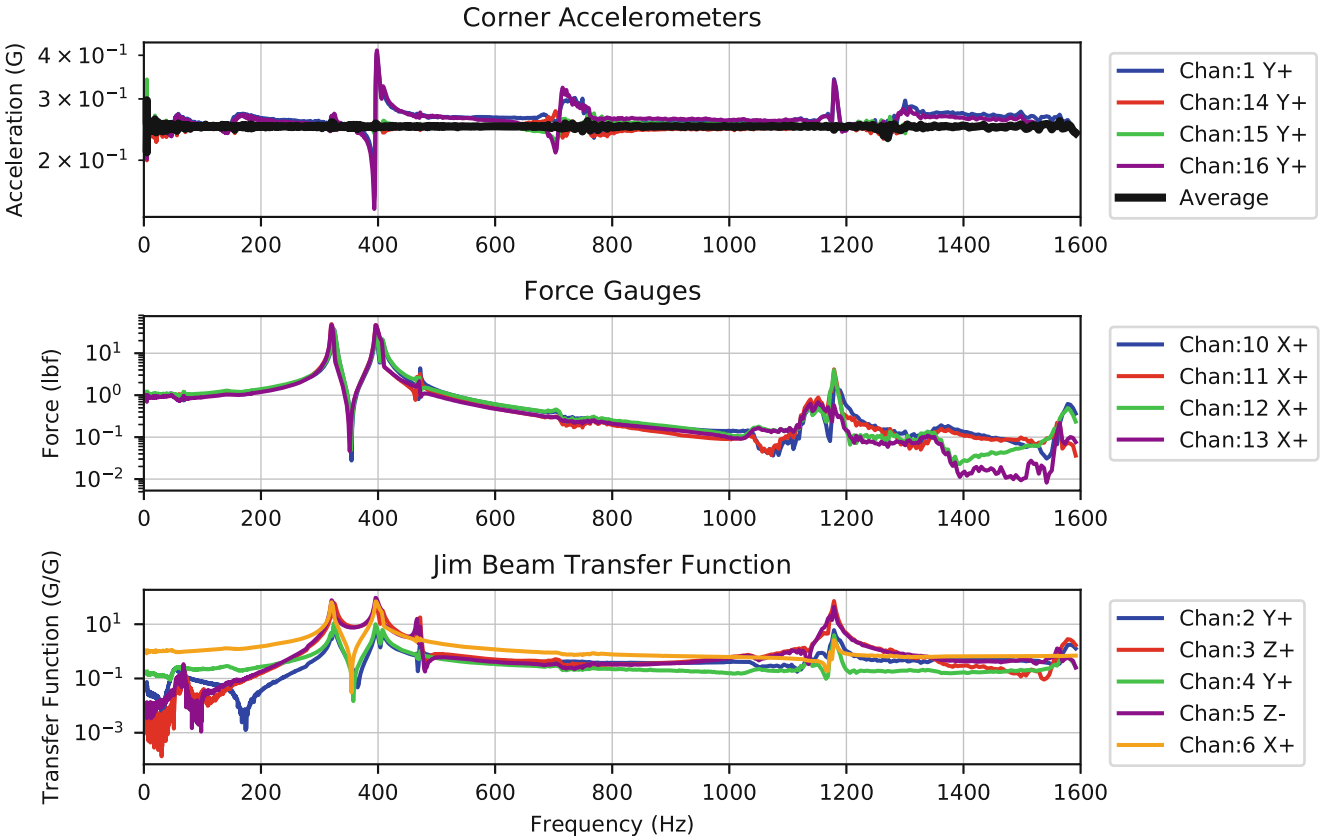

Fig. 27.5 X-Axis Sine Sweep

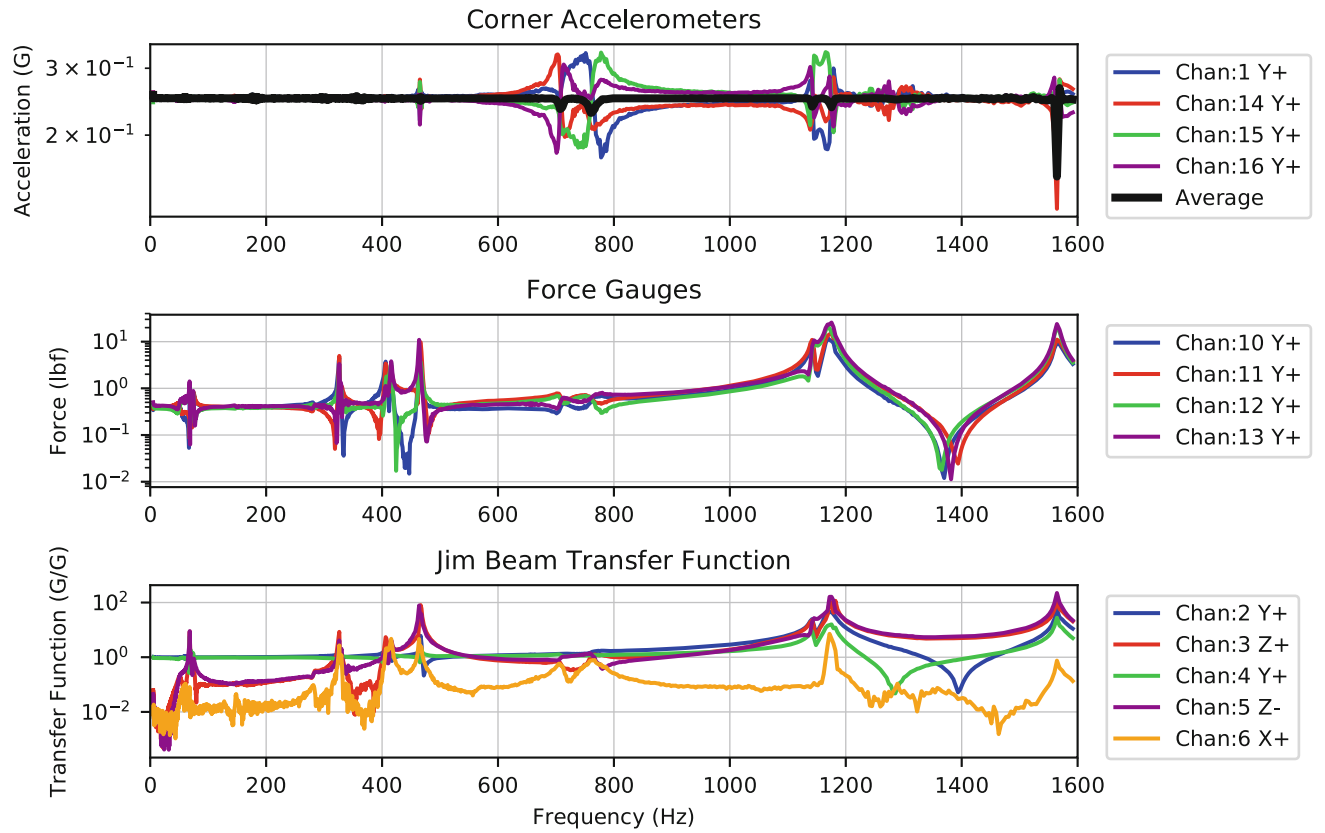

Fig. 27.6 Y-Axis Sine Sweep

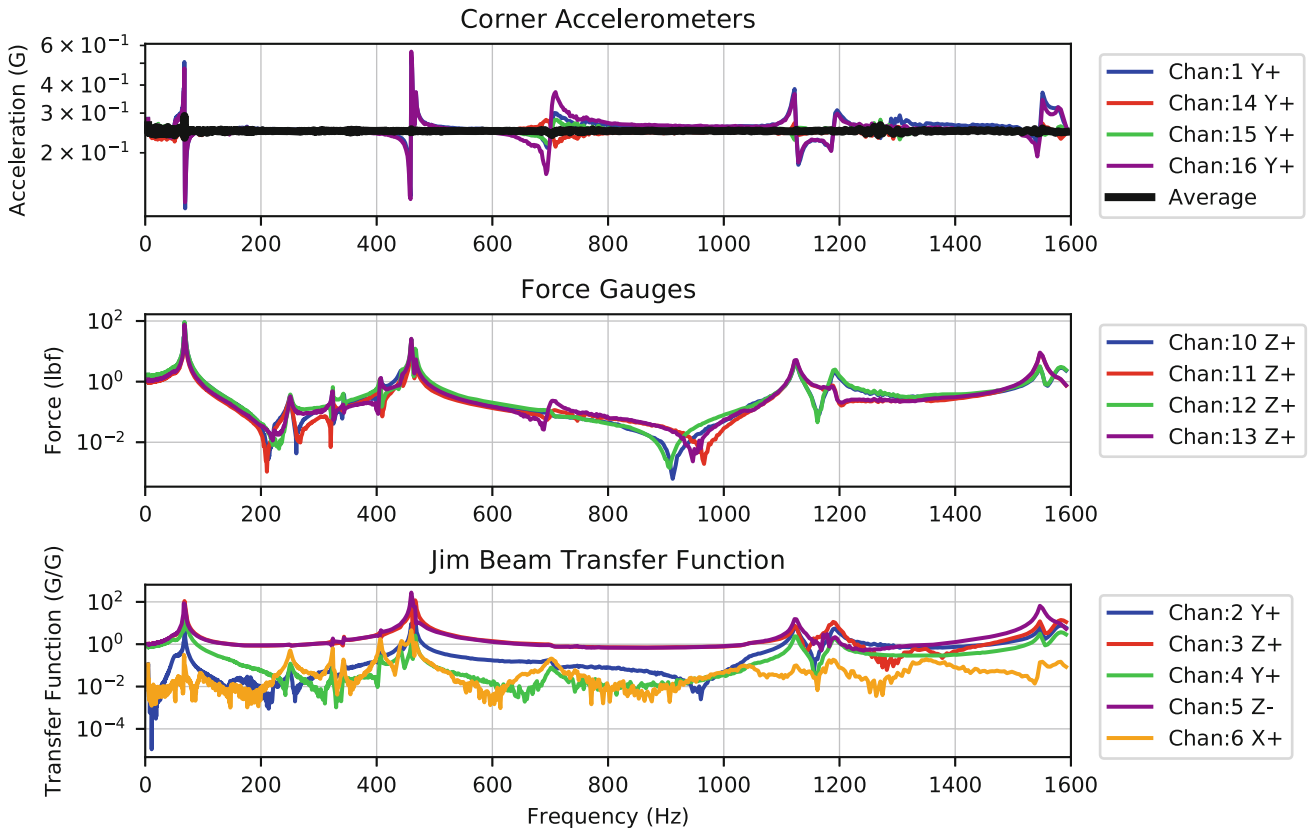

Fig. 27.7 Z-Axis Sine Sweep

27.5.2 Y-Axis Observations (Fig. 27.6)

For the Y-Axis, all four Cube channels were averaged for shaker control, and channels 2 and 4 on the Jim Beam are oriented in the Y-Axis. The spurious response of the control accelerometers between 600 and 800 Hz is most apparent in this axis. Following these accelerometer traces indicates a diagonal rocking moment of the Cube is occurring in this frequency range; as one corner dips, the diagonally opposite corner peaks, and vice-versa. There are no Jim Beam modes in this frequency range. As the sweep approaches 1200 Hz, the Cube again shows some rocking response, but this time it appears to correspond to the Jim Beam mode near 1200 Hz. Near 1600 Hz, the four averaged control channels couple with the corresponding Jim Beam mode and drop out, almost aborting the test. This phenomenon is also observed in the drive voltage plot in Fig. 27.9.

27.5.3 Z-Axis Observations (Fig. 27.7)

As with the X-Axis, only channels 14 and 15 were averaged and used for controlling the shaker in the Z-Axis. Channels 3 and 5 on the Jim Beam measure in the Z-Axis. Jim Beam resonant frequencies are again picked up by the corner control accelerometers, and Cube responses are again observed between 600 and 800 Hz.

27.5.4 Bare Cube Test Observations (Fig. 27.8)

Given the observations of the Cube responses, it was decided to test the Cube on the shaker by itself. Four tri-axial accelerometers were used, one at each corner, to better capture Cube motion. A single center Y-Axis channel was used to control the shaker, shown in the first subplot. All X-channels are plotted in the second subplot, all Y-channels are plotted

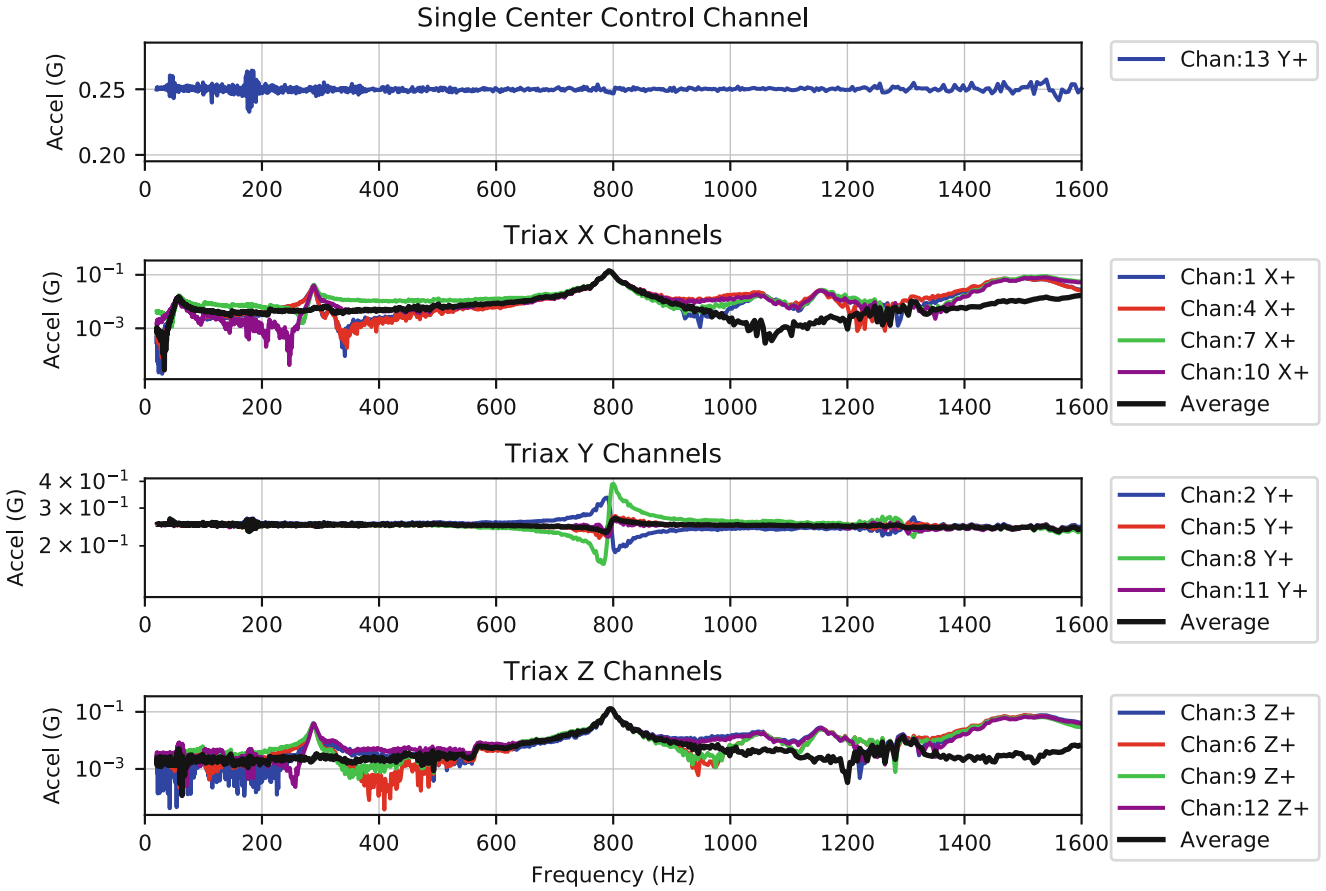

Fig. 27.8 Bare cube with Corner Triax Accels Sine Sweep

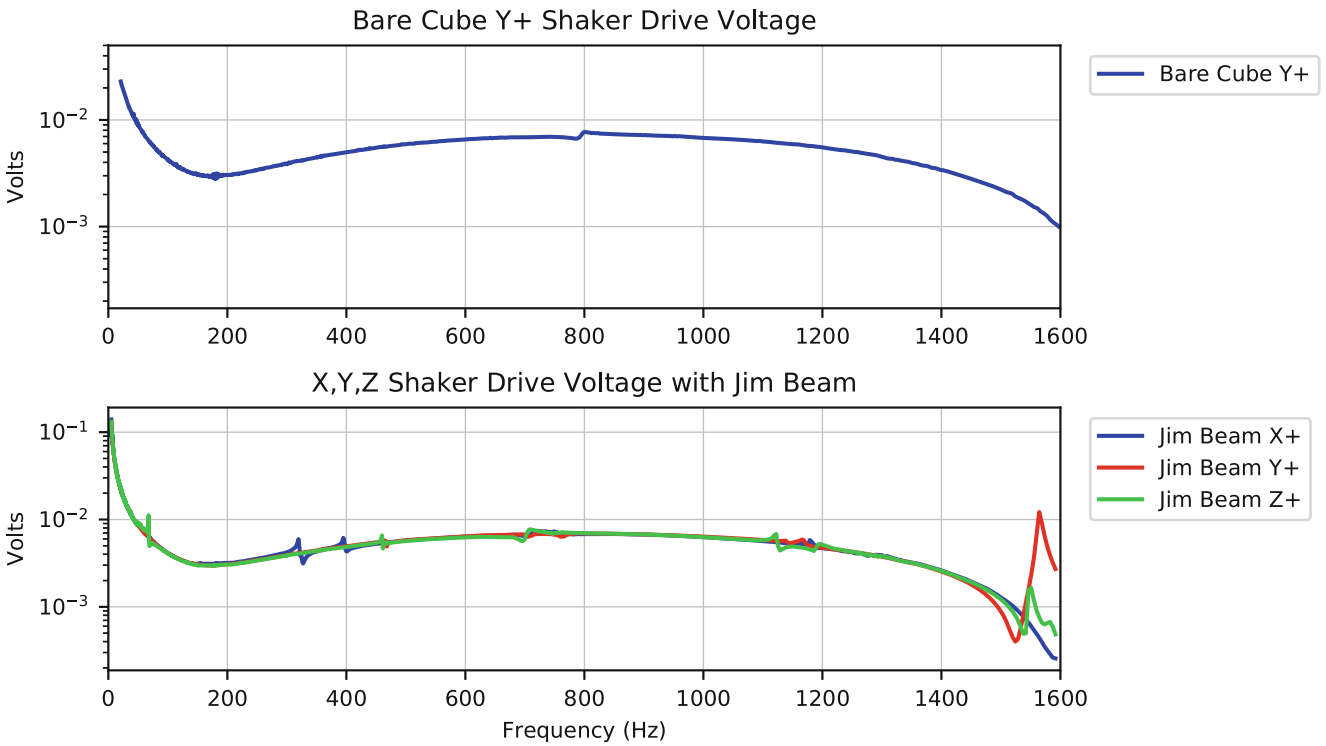

Fig. 27.9 Drive voltage vs frequency for bare cube and Jim Beam Tests

in the third subplot, and all Z-channels are plotted in the fourth subplot. The bare Cube appears to have a response around 800 Hz that never appears in the single control channel. Low-level movement of the Cube can be seen in all three axes.

As an additional check, the drive voltage of the shaker for all four tests was plotted in Fig. 27.9. Drive voltage is a useful indicator of the coupling frequency between the test article and the shaker. The shaker draws less power to drive the test article at its resonant frequency. The guidelines used by the vibration lab show the first mode of the Cube interface on the shaker table to be at 1642 Hz, well above the interactions observed between 600 and 800 Hz.

27.6 Conclusions

During sine vibration testing of the Jim Beam on the shaker table, unexpected responses were observed by the control channels on the mounting Cube. Comparing the control channels with the interface force gauges and Jim Beam instrumentation showed some unintended coupling between modes inherent to the shaker table and the Jim Beam, which are not present in the fixed base modal tests of the Jim Beam.

Interestingly, the interaction of the test article with the shaker would not have been captured through Finite Element Modeling changes to the Jim Beam alone. There are no "stiffness knobs" to be turned or connection springs to be tuned that would account for the dynamics of the shaker. Without a complete understanding of the boundary conditions, making changes to the model to correlate to test would still have fallen short of capturing the dynamics present in the test setup.

This study had the benefit of fixed base testing to inform the model leading up to the sine vibration test. In most cases, correlation on a shaker is only chosen because there are not additional tests from which to extract modal data. Without this a-priori knowledge, discerning Jim Beam modes from shaker modes could have been much more difficult, especially if the shaker modes appeared in the same frequency range as Jim Beam modes.

Shaker testing, while convenient and cost effective, may require additional care when used for correlating a dynamic model. A shaker table is a boundary condition with its own modes, and the assumption that only the prescribed input force is being applied to the test article is not entirely true.

27.7 Recommendations

While this paper has illustrated some of the difficulties in correlating a Finite Element Model on a shaker table, there are several observations that may help improve correlation on a shaker if that is the only available option.

1. Take advantage of Dynamic Substructuring techniques to reduce out the dynamics of the shaker table.
2. Use a detailed Finite Element Model of the shaker for pretest analysis and post-test correlation.
3. Use an average of the control channels. If only a single control channel was used to capture peak values during a qualification test, this may be impacted by a local mode or a shaker mode, therefore subjecting the test article to a different level than that being measured at the control location. A minimum of 3 accelerometers on the table would be required to capture table bending effects, but four or more are recommended to identify the direction of the bending moment.
4. Conduct a shaker dry run without the test article or with a mass simulator, and use that data to inform the correlation effort. Utilize as much additional instrumentation as practical to identify shaker responses.
5. Seismic mass base-drive analysis alone neglects the shaker boundary condition and must be used with judgement.

These recommendations alone may not inform model correlation efforts, however, they may help identify frequency bands where the table shows responses that are not present in the test article. Many spacecraft tests already implement multiple control channels and conduct shaker dry runs. Perhaps simply utilizing existing data for greater cognition of shaker modes would be enough to avoid wasting time correlating the boundary condition instead of the test article.

Acknowledgments The authors would like to thank Mark Hamilton and Justin Youney of the Kennedy Space Center Vibration Lab for all of their help and hard work in making this research possible.

References

1. Abdallah, A.: Verification of spacecraft dynamic models for coupled loads analysis. ELVL-2007-0038909. Kennedy Space Center, NASA, Florida, November 2007
2. Ristow, J.A., Smith Jr, K.W., Johnson, N.G., Kinney, J.R.: Comparing free-free and shaker table model correlation methods using Jim Beam. In: IMAC XXXVI. Orlando, FL, January 2018
3. Carne, T.G., Martinez, D.R., Nord, A.R.: A Comparison of Fixed-Base and Driven-Base Modal Testing of an Electronics Package. Sandia National Laboratories, Albuquerque, NM (1989)
4. Allen, M.S., Mayes, R.L.: Recent advances to estimation of fixed-interface modal models using dynamic substructuring. In: IMAC XXXVI. Orlando, FL, January 2018
5. Moldenhauer, B., Allen, M., DeLima, W.J., Dodgen, E.: Modeling an electrodynamic shaker using experimental substructuring. In: IMAC XXXVI. Orlando, FL, January 2018
6. Lollock, J.A.: The Effect of Swept Sinusoidal Excitation on the Response of a Single-Degree-of-Freedom Oscillator. The Aerospace Corporation, Los Angeles, CA (2002)

Chapter 28
Vibration Reduction for Camera Systems Onboard Small Unmanned Aircraft

William H. Semke

Abstract The performance of camera vibration isolation systems used on a popular small unmanned aircraft system (sUAS) is presented. The use of sUAS or drones for image collection is becoming ever more popular for hobbyists, as well as in commercial and military operations. Many types and methods for vibration isolation and absorption are used to create a more stable environment to acquire images or video. While many systems promise vibration reduction, few studies have been conducted to measure and evaluate their performance. Therefore, this review will provide data obtained by experimentally measuring the vibration levels of the camera and host aircraft. Using this data the transmissibility is determined and the effectiveness assessed. Along with the experimental data, analytic models of the systems will be generated to allow for the integration into future modeling efforts. The analysis utilized a common airframe used in the UAS community along with frequently used camera mounting systems. The data is obtained from aircraft fully powered and airborne in a hovering or level flight configuration. This study will provide sUAS operators the information required for choosing the most effective camera vibration reduction system and/or method for the system of interest.

Keywords Unmanned aircraft · Remote sensing · Camera stability · Vibration · Transmissibility

28.1 Introduction

In the exploding Unmanned Aircraft Systems (UAS) market due to the recent FAA certification process that allows much more access into the national airspace for Unmanned Aircraft Systems (UAS) under 55 lbs (25 kg) enhanced capacities for remote sensing systems is desired and expected. In the new markets and new applications that have capabilities and performance expectations that are ever growing, the ability to better isolate and control motion in remote sensing systems has a larger role. A summary of the vibration environment of several camera systems onboard multiple UAS platforms is presented.

The need to reduce or eliminate unwanted vibration in imaging systems is crucial in many applications of UAS. Researchers have carried out investigations into vibration isolation and active control for many years and numerous fundamental texts and articles are excellent resources into basic principles [1–4]. A basic underlying piece of information in effective vibration control is the knowledge of the vibration excitation levels and frequencies. Along with the excitation levels, the camera and attachment mechanism provide the key pieces of information such that an effective system is achievable.

In the military and civilian sectors, remote sensing capabilities are rapidly expanding as new sensors are developed that provide much more scientific and situational data. UAS are now delivering much of the data that are essential in modern applications, while in the past manned aircraft and satellites provided the remote sensing data. Extensive study to develop effective and efficient methods of reducing vibration have been implemented with both passive and active control schemes for manned aircraft and satellites [5–7]. However, systems for UAS have not reached the same maturity levels due to the pace of innovation and advances in the industry.

The development of vibration isolation systems for remote sensing systems onboard UAS is one of the many issues associated with proper UAS design and usage issues outlined in a text providing an introduction to UAS [8]. Potential solutions addressing processes to enhance remote sensing performance by reducing unwanted vibrations have been made by many researchers [9–17]. Previous and current efforts are supported and augmented with more and better data on current

W. H. Semke (✉)
Department of Mechanical Engineering, University of North Dakota, Grand Forks, ND, USA
e-mail: william.semke@engr.und.edu; william.semke@und.edu

C. Walber et al. (eds.), *Sensors and Instrumentation, Aircraft/Aerospace, Energy Harvesting & Dynamic Environments Testing, Volume 7*, Conference Proceedings of the Society for Experimental Mechanics Series,
https://doi.org/10.1007/978-3-030-12676-6_28

isolation systems in operation. To provide critical flight data information required by developers of vibration control systems for small UAS, several aircraft and camera mounting schemes were flown and the vibration environment measured.

28.2 Analytical Model

The camera aircraft system can be modeled as a single degree of freedom system with base excitation, as shown in Fig. 28.1. The mass, m, represents the camera and the base represents the host aircraft while the spring, k, and the damper, c, model the attachment mechanism of the camera to the host aircraft.

When the base of the system is subjected to a harmonic motion, Eq. (28.1), the equation of motion of the system is given in Eq. (28.2) where z = x – y.

$$y(t) = Y \sin(\omega t) \tag{28.1}$$

$$m\ddot{z} + c\dot{z} + kz = -m\ddot{y} \tag{28.2}$$

Letting the damping ratio be represented by Eq. (28.3), where c_c is the critical damping and the frequency ratio be represented by Eq. (28.4), where ω_n is the undamped natural frequency, the displacement transmissibility is given in Eq. (28.5).

$$\zeta = \frac{c}{c_c} \tag{28.3}$$

$$r = \frac{\omega}{\omega_n} \tag{28.4}$$

$$T_d = \frac{X}{Y} = \left\{ \frac{1 + (2\zeta r)^2}{\left(1 - r^2\right)^2 + (2\zeta r)^2} \right\}^{\frac{1}{2}} \tag{28.5}$$

In Eq. (28.5), the X and Y denote the displacement amplitude of the mass and base, respectively. By varying the damping ratio and the frequency ratio, a plot of the transmissibility of the system is shown in Fig. 28.2.

From Fig. 28.2, several observations are made. For low damped systems, the peak displacement transmissibility approaches infinity at resonance, which clearly requires that any undamped isolator must produce a natural frequency of the system far from the driving frequencies likely to be experienced. For frequency ratios close to 1, the motion of the mass is amplified from the base excitation level. For all damping values, the displacement transmissibly is exactly 1 when the frequency ratio is $\sqrt{2}$. The displacement transmissibility is greater than 1 for all frequency ratios less than $\sqrt{2}$ and less than 1 for all ratios greater than $\sqrt{2}$. Therefore, for more effective isolation a large frequency ratio is desired along with low damping. However, low damping can lead to large displacement amplification if the frequency ratio nears 1.

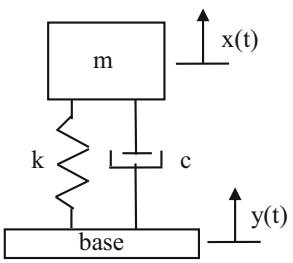

Fig. 28.1 Single degree of freedom system with base excitation

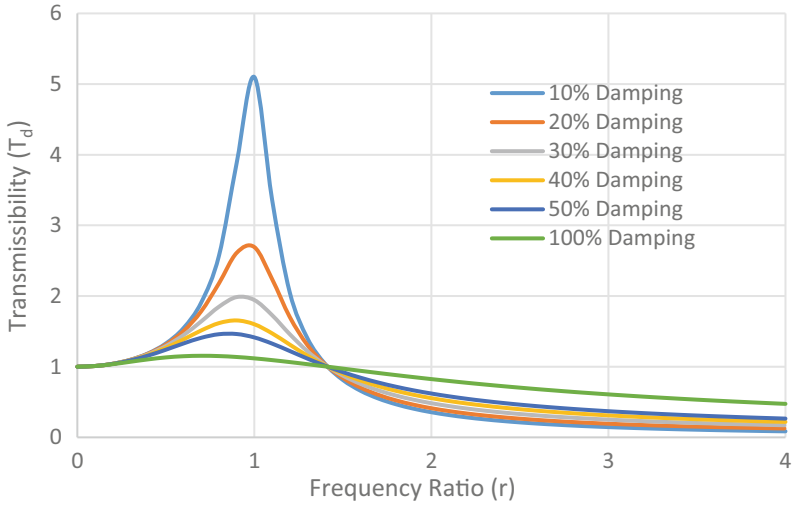

Fig. 28.2 Displacement transmissibility of the system as a function of damping ratio and frequency ratio

Fig. 28.3 DJI Phantom 4 UAS, one of the most common drones on the market

28.3 Experimental Testing

To assess common camera attachment mechanisms a DJI Phantom 4 aircraft was chosen for evaluation purposes. This is an extermely common UAS and serves a represeantive paltform for better understaading of the vibration enviroment. The aircraft used in the testing is shown in Fig. 28.3.

Several camera mounting schemes were evaluated in this study. The first, as shown in Fig. 28.4, was the Base Configuration where the camera utilizes the isolation mount that comes with the system. This recommended configuration is intended to provide high quality imagery with a commercial of the shelf (COTS) solution. In the second scheme, the camera is placed in the Stowed Configuration that typically is used when transporting the DJI Phantom system. This is not the intended imaging configuration, but this test was chosen to illustrate the impact the additional support on the vibration environment at the camera. In Fig. 28.5 the added support mechanism can be seen attaching the camera to the landing gear. An additional foam insert that is provided with the system was placed at the attachment point as well, which is not as clearly visible in

Fig. 28.4 Base configuration utilizing COTS mounting system

Fig. 28.5 Stowed configuration with support structure

Fig. 28.6 Standard hook and loop Velcro, double sided mounting tape, and 3M Dual Lock snap locking tape camera attachment mounting supplies

the image. The next three mounting schemes used attachment methods that are commonly used to attach cameras to drones, often for temporary installation or where specialty systems are utilized. They are shown in Fig. 28.6 and are standard hook and loop Velcro, double sided mounting tape, and 3M Dual Lock snap locking tape. In all cases, the mounting attachment is attached using a self-adhesive that comes pre-applied. The Velcro and Dual Lock allow for the attachment and removal of the cameras from the host aircraft repeatedly. The double sided tape only allows for a single attachment and cannot be

Table 28.1 Statistical metrics for drone and camera accelerometer data with the five mounting techniques

	Accel. (m/s^2)	Base Config.	Stowed	Velcro	Tape	Dual lock
Aircraft	Peak-to-peak	2.48	2.12	3.37	3.44	2.46
	Stand. dev.	0.42	0.36	0.44	0.47	0.32
Camera	Peak-to-peak	0.11	2.13	0.52	3.59	2.77
	Stand. dev.	0.02	0.40	0.09	0.54	0.37

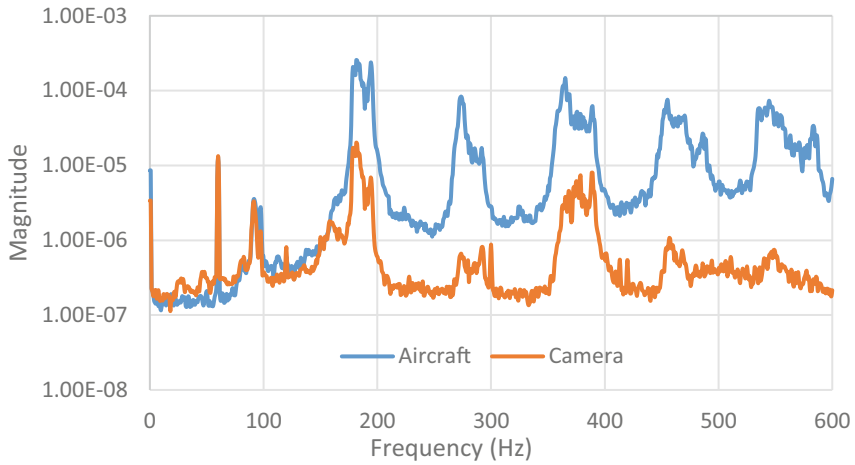

Fig. 28.7 Phantom 4 FFT data (Base Configuration)

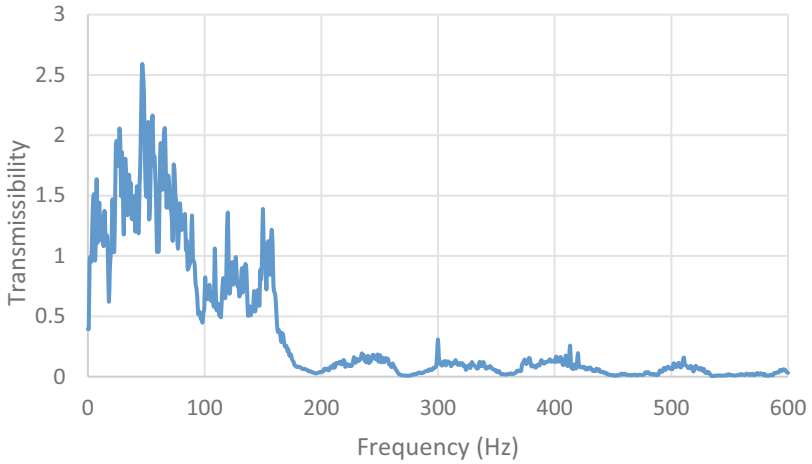

Fig. 28.8 Base configuration transmissibility

reused. In these cases, the camera was simulated by a 50-g mass with a 3 cm^2 flat mating surface covered with the mounting interface between it and the aircraft.

A PCB Model 352C18 single-axis accelerometer (1.0 $mV/m/s^2$) was attached to the base of each of the aircraft as well as the to the camera and the data was collected using a Data Physics Abacus 901 at a rate of 1536 Hz. The peak-to-peak amplitude and the standard deviation for the recorded accelerations are shown in Table 28.1. The data was collected while the aircraft was in a hovering configuration approximately 1–2 m above ground.

The Fast Fourier Transform (FFT) and transmissibility of each of the mounting configurations tests are shown in Figs. 28.7, 28.8, 28.9, 28.10, 28.11, 28.12, 28.13, 28.14, 28.15, and 28.16. The FFT plots show both the response of the aircraft and the camera over a wide frequency range and the transmissibility plots show the ratio of the vibration amplitude of the camera to the host aircraft as a function of the frequency.

The Base Configuration demonstrated reduction in vibration amplitudes very effectively at frequencies above 180 Hz. The transmissibility was much less than 1, indicating a great deal of isolation from the host aircraft. At frequencies below

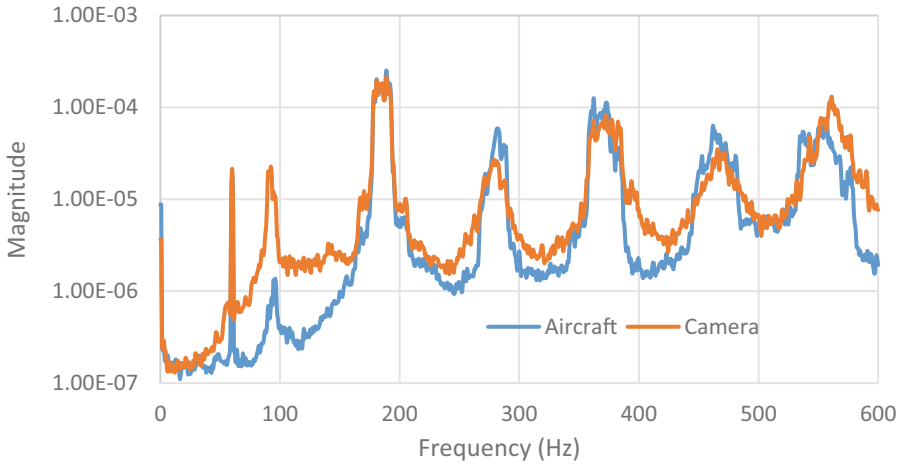

Fig. 28.9 Phantom 4 FFT data (Stowed Configuration)

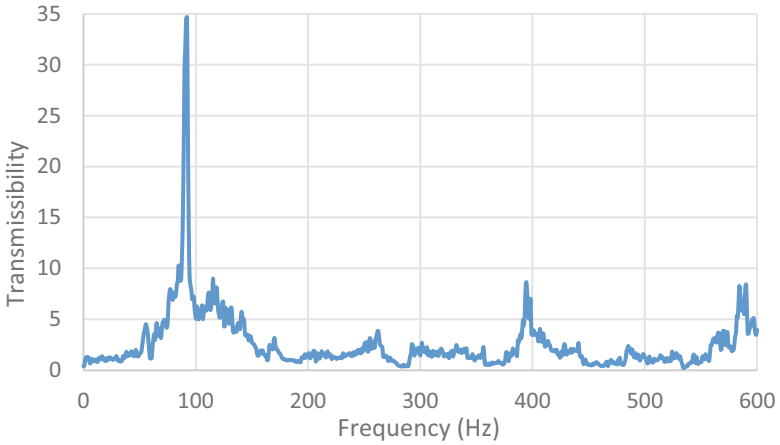

Fig. 28.10 Stowed configuration transmissibility

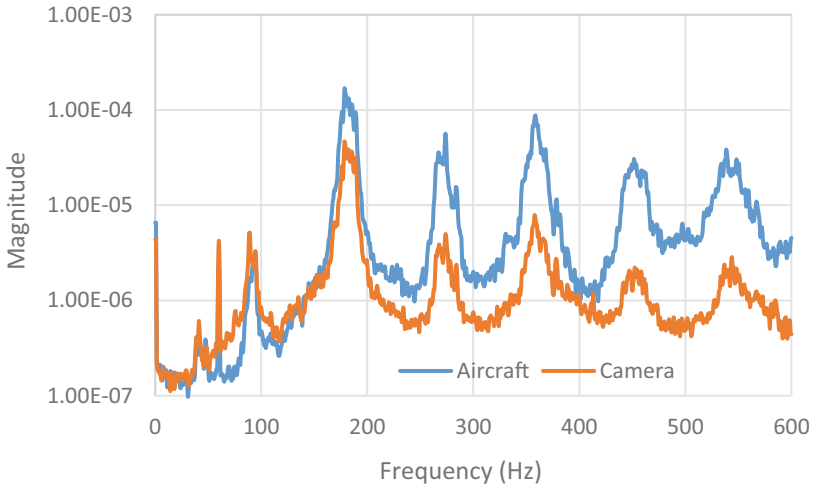

Fig. 28.11 Phantom 4 FFT data (Velcro Configuration)

180 Hz there is a moderate amplitude amplification. The COTS system is effective and performs well over a wide range of frequencies. When in the Stowed Configuration the systems is very ineffective in isolating the camera from the aircraft vibration. This configuration shows vibration amplification at nearly all frequencies tested with a very large amplitude

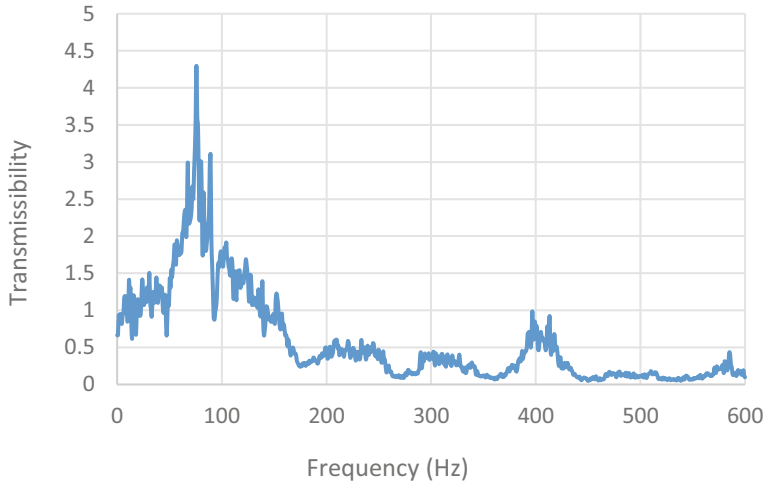

Fig. 28.12 Velcro configuration transmissibility

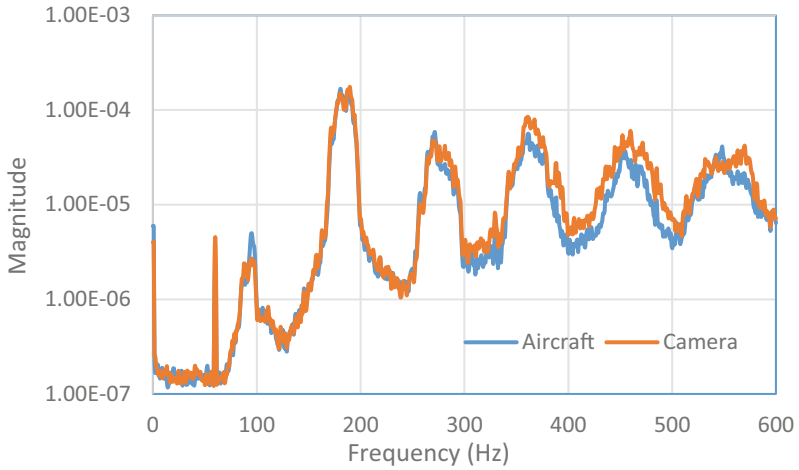

Fig. 28.13 Phantom 4 FFT data (Tape Configuration)

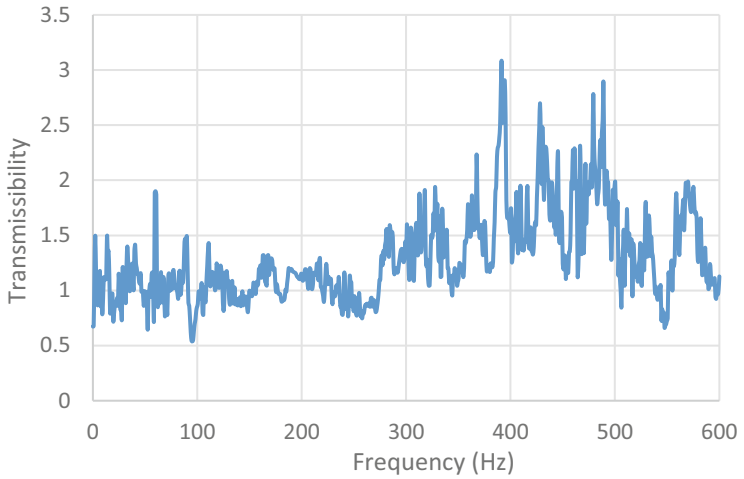

Fig. 28.14 Tape configuration transmissibility

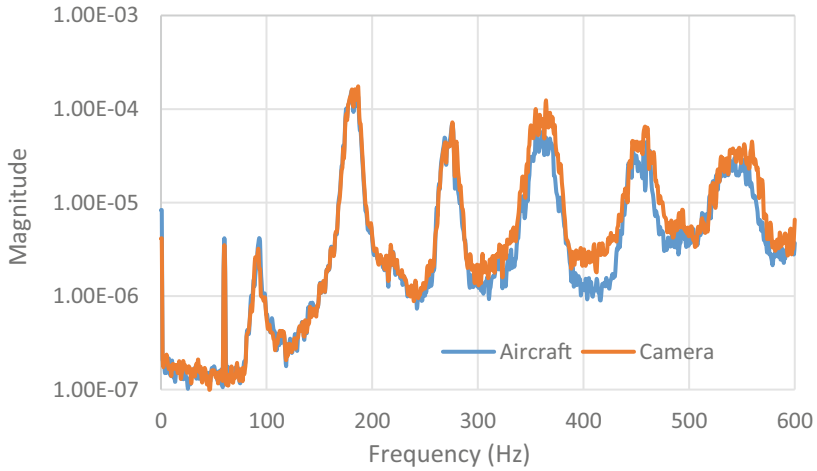

Fig. 28.15 Phantom 4 FFT data (Dual Lock Configuration)

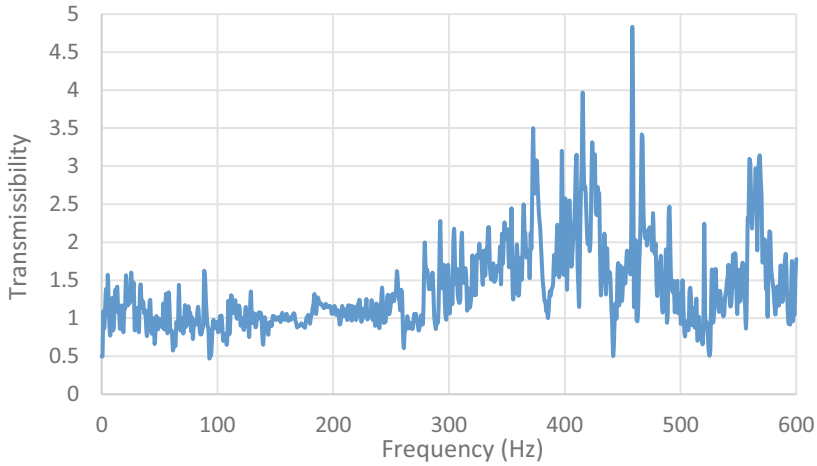

Fig. 28.16 Dual Lock Configuration transmissibility

amplification around 90 Hz. While this is not the recommend manner to operate, it clearly demonstrates the effectiveness of the COTS isolation system when properly used. In the Velcro Configuration, the testing shows fairly effective isolation at frequencies above 180 Hz, but moderate amplification at frequencies below 180 Hz. The results are somewhat similar to the COTS system, without an intricate mounting system. The Tape Configuration showed little to no isolation across all frequencies and actually had slight amplification consistently across the entire range investigated. There were no large spikes, but also no effective isolation provided. The results are similar to hard mounting the camera to the host aircraft. The Dual Lock Configuration had a similar outcome as the Tape Configuration. It also demonstrated ineffective isolation across all frequencies and actually had slight amplification consistently across the entire range investigated.

28.4 Conclusions

The performance of camera vibration isolation systems used on a popular sUAS was studied. Due to the increased usage of UAS by hobbyist, commercial, and military operators, camera isolation systems are of great interest. The DJI Phantom 4 was used in 5 configurations to evaluate isolation performance. The Base Configuration showed the best performance across a large range of frequencies. The Velcro Configuration also showed effective isolation, but the connection is not as secure and long-term use may result in camera separation. The hook and loop Velcro permitted a “soft” bond between the camera and aircraft resulting in the isolation observed. The Stowed Configuration was not effective and actually produced a

large amplitude amplification around 90 Hz. This is not the recommended flight configuration and this is supported by the findings presented. Therefore, as instructed, the camera support structure should be removed prior to flight. Both the Tape Configuration and Dual Bond Configuration resulted in a strong connection between the aircraft and the camera resulting in the acceleration amplitudes being the same or slightly higher than the host UAS in the camera systems. These attachment schemes are strong, but lead to little or negative isolation.

A study on advanced isolation schemes is planned to evaluate alternative mounting hardware with potential enhancements on a variety of sUAS. The study presented will serve as base examples of COTS and common camera isolation methods and provides useful representative data. It provides sUAS operators information to better choose the most effective camera vibration reduction system.

Acknowledgments The author would like to thank Joseph Schwalb and Charles Hoy for their piloting skills during data collection.

References

1. Crede, C.E.: Vibration and Shock Isolation. Wiley, New York (1951)
2. Rao, S.S.: Mechanical Vibrations. Prentice Hall, Upper Saddle River, NJ (2004)
3. Meirovitch, L.: Fundamentals of Vibrations. McGraw-Hill, New York (2001)
4. Ruzicka, J.E.: Active vibration and shock isolation, Paper no. 680747. SAE Trans. **77**, 2872–2886 (1969)
5. Wada, B., Rahman, Z., Kedikan, R., Kuo, C.: Vibration Isolation, Suppression and Steering (VISS). J. Intell. Mater. Syst. Struct. **7**, 241–245 (March 1996)
6. Maes, J., Binczak, S., Lhenry, V.: A passive stabilization solution for camera embedded onboard small planes. In: Proceedings of the 33rd Digital Avionics Systems Conference, October 2014
7. Deng, C., Mu, D., Guo, J., Xie, P.: Reducing the negative effects of flywheel disturbance on space camera image quality using the vibration isolation method. Front. Optoeectron. **10**(1), 80–88 (2017)
8. Marshal, D., Barnhart, R., Shappee, E., Most, M.: Introduction to Unmanned Aircraft Systems, 2nd edn, pp. 279–296. CRC Press, Taylor & Francis Group, Boca Raton, FL (2016)
9. Marichal, G., Tomas-Rodriguez, M., Hernandez, A., Castillo-Rivera, S., Campoy, P.: Vibration reduction for vision systems onboard unmanned aerial vehicles using a neuro-fuzzy controller. J. Vib. Control. **20**(15), 2243–2253 (2014)
10. Ranjan, P., Devendra, M., Khan, S.A., Goel, A.K.: Vibration measurement on mini helicopter for electro-optic payload integration. In: 2017 International Conference on Nascent Technologies in the Engineering Field (ICNTE-2017), IEEE, Navi Mumbai, India, 2017
11. Qadir, A., Semke, W., Neubert, J.: Vision based neuro-fuzzy controller for a two axes gimbal system with small UAV. J. Intell. Robot. Syst. (August 2013)
12. Qadir, A., Semke, W., Neubert, J.: Implementation of an onboard visual tracking system with small unmanned aerial vehicle (UAV). Int. J. Innov. Technol. Creat. Eng. **1**(10), 17–25. October 2011
13. Stuckel, K., Semke, W.: A piezoelectric actuated stabilization mount for payloads onboard small UAS. In: Proceedings of the International Modal Analysis Conference (IMAC) XXIX: A Conference and Exposition on Structural Dynamics (2011)
14. Locke, M., Czarnomski, M., Qadir, A., Setness, B., Baer, N., Meyer, J., Semke, W.: High-performance two-axis gimbal system for free space laser communications onboard unmanned aircraft systems. In: Proceedings of SPIE: Free-Space Laser Communication Technologies XXIII, Vol. 7923 (2011)
15. Stuckel, K., Semke, W., Baer, N., Schultz, R.: A high frequency stabilization system for UAS imaging payloads. In: Proceedings of the International Modal Analysis Conference (IMAC) XXVIII: A Conference and Exposition on Structural Dynamics (2010)
16. Semke, W., Dunlevy, M.: A review of the vibration environment onboard small unmanned aircraft. In: Proceedings of the International Modal Analysis Conference (IMAC) XXXVI: A Conference and Exposition on Structural Dynamics (2018)
17. Swetich, W., Semke, W.: Eliminating blur in small unmanned aircraft imaging systems. In: Proceedings of the International Modal Analysis Conference (IMAC) XXXV: A Conference and Exposition on Structural Dynamics (2017)

Chapter 29
Flight Environments Demonstrator: Part I—Experiment Design and Test Planning

Brian C. Owens, Randall L. Mayes, Moheimin Khan, D. Gregory Tipton, and Brandon Zwink

Abstract Flight testing provides an opportunity to characterize a system under realistic, combined environments. Unfortunately, the prospect of characterizing flight environments is often accompanied by restrictive instrumentation budgets, thereby limiting the information collected during flight testing. Instrumentation selection is often a result of bargaining to characterize environments at key locations/sub-systems, but may be inadequate to characterize the overall environments or performance of a system. This work seeks to provide an improved method for flight environment characterization through a hybrid experimental-analytical method, modal response extraction, and model expansion. Topics of discussion will include hardware design, assessment of hardware under flight environments, instrumentation planning, and data acquisition challenges. Ground testing and model updating to provide accurate models for expansion will also be presented.

Keywords Hybrid methods · Modal extraction · Model expansion · Test planning · Flight testing

29.1 Introduction

Flight testing of aerospace systems allows for qualification under the most realistic flight environments, including combined flight environments. While this is a great opportunity, characterization of environments and responses during these tests is prone to severe limitations on instrumentation. A system is often instrumented at a few locations of interest, without sufficient fidelity to characterize the response of the system in detail. As will be discussed, hybrid experimental-analytical methods using informed instrumentation sets and credible models allow flight data to be significantly augmented for a greater understanding of flight environments and system performance.

Part I of this work, presented in the current document, considers design of the flight experiment and associated test planning. Topics of discussion will include hardware design, assessment of hardware under flight environments, instrumentation planning, and data acquisition challenges. Ground testing and model updating to provide accurate models for expansion will also be presented. Part II of this work will discuss ground test trials of the demonstrator experiment and assessment of the method with flight data. Part III will examine full field expansion of flight environments and sensitivity of methods to model accuracy and acceptable model uncertainties/perturbations.

Modal response extraction techniques will employ a SEREP [1] based process as follows. Modal responses will be extracted from flight data using the theory shown in Eq. (29.1):

$$\vec{q}(t) = [\Phi_M]^g \vec{a}_M(t) \tag{29.1}$$

where $\vec{q}(t)$ is the modal degree of freedom vector, Φ_M is the mode shape matrix for the measurement degrees of freedom, g denotes the generalized inverse, and $\vec{a}_M(t)$ are measured physical accelerations. The mode shapes, Φ_M typically come from a model (i.e. a finite element model), and should have an appropriate model form to sufficiently capture the physics

Sandia National Laboratories is a multi-mission laboratory managed and operated by National Technology & Engineering Solutions of Sandia, LLC, a wholly owned subsidiary of Honeywell International Inc., for the U.S. Department of Energy's National Nuclear Security Administration under contract DE-NA0003525.

B. C. Owens (✉) · R. L. Mayes · M. Khan · D. G. Tipton · B. Zwink
Sandia National Laboratories, Engineering Sciences Center, Albuquerque, NM, USA
e-mail: bcowens@sandia.gov

C. Walber et al. (eds.), *Sensors and Instrumentation, Aircraft/Aerospace, Energy Harvesting & Dynamic Environments Testing, Volume 7*, Conference Proceedings of the Society for Experimental Mechanics Series,
https://doi.org/10.1007/978-3-030-12676-6_29

of the test article dynamics. Furthermore, the process will benefit from model updating procedures using test data. For a high-quality extraction, Φ_M must span the space of the modes for the physical responses of interest, and the measurement points must provide a discretization of mode shapes that are well-conditioned and invertible. Finally, and perhaps obviously, the quality of the extraction depends on the quality of the physical measurements. Although the process has been depicted for time domain applications, it is also suitable for frequency domain applications.

After extraction, the model mode shapes may be used to expand to un-instrumented degrees of freedom (DOFs) as shown in Eq. (29.2).

$$\vec{a}_A(t) = [\Phi_A]\,\vec{q}(t) \tag{29.2}$$

The physical acceleration vector $\vec{a}_A(t)$ and the modal matrix Φ_A for the un-instrumented degrees of freedom termed are the "A-set". The A-set may be discrete DOFs of interest or all DOFs in the finite element model. Although the expansion is shown for acceleration, it is also applicable for displacement, strain, or stress if the appropriate mode shapes are used.

To summarize, the following is required for a successful, high-quality modal extraction and model expansion:

- A model (likely a finite element model) with the appropriate model form to predict mode shapes of the article under test. Model updating to modal test data can further improve the mode shapes being used in this method.
- The instrumentation set should sufficiently characterize modes of interest (modes that span the frequency band of interest), and preferably result in a mode shape matrix that is easily invertible with a low condition number.
- Measurements and associated data acquisition should be of sufficient quality to provide meaningful data for this method. Noise contaminants should also be removed using signal processing techniques.

This paper describes experiment design and test planning activities to support a successful flight experiment. First, a relevant test article was designed with sufficient structural robustness against flight inertial, shock, and vibration environments. Next, model development and analytical studies were employed to identify an optimal instrumentation set for model development and extraction techniques. Modal testing of the hardware was then performed to provide test data for model updating procedures to improve the mode shapes used in the extraction and expansion process. Finally, potential data acquisition issues were addressed to mitigate risk and ensure a successful experiment. Part II of this work will discuss ground test trials of the demonstrator experiment and exercise the method with flight data. Part III will examine full field expansion of flight environments and sensitivity of methods to model accuracy and acceptable model uncertainties/perturbations.

29.2 Experiment Design

Mechanical experiment design typically focuses on selection of test hardware, instrumentation/measurements, environments, test specifications (inputs), and fixturing. For the flight test under consideration, environments and test specifications are dictated by the flight vehicle and are not a controllable test input. Therefore, experiment design will focus on the design of test hardware and instrumentation/measurements, and fixturing.

Test hardware design is dictated by the following criteria:

- Structural dynamic response of test article is representative of common aerospace vehicles and payloads (e.g. bending, axial, and torsional mode shapes in the frequency band of interest).
- Frequency band of interest is under 2 kHz. Hardware should have multiple modes under 2 kHz, and fundamental modes under 1 kHz.
- Hardware should be of moderate complexity to exercise modal techniques, but simple enough to develop an accurate finite element model.
- Hardware geometry and mass must comply with allotted mechanical envelope.
- Hardware must have sufficient structural robustness to survive the flight environment without significant changes to structural dynamics. Thus, the dynamic response of the test article should remain in the linear elastic regime.

Fixture design is dictated by the following criteria:

- Fixture design must have an appropriate interface between the test article and the next level assembly.
- Fixture geometry and mass must comply with allotted mechanical envelope.
- Fixture design must have sufficient structural robustness to survive the flight environment without significant changes to structural dynamics. The dynamic response of the fixture should remain in the linear elastic regime.
- Fixture should remain rigid at frequencies corresponding to the fundamental modes of the test article.

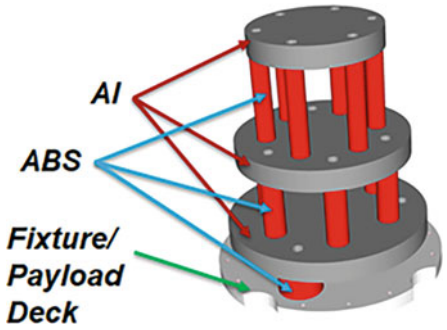

Fig. 29.1 "Wedding Cake" test hardware concept

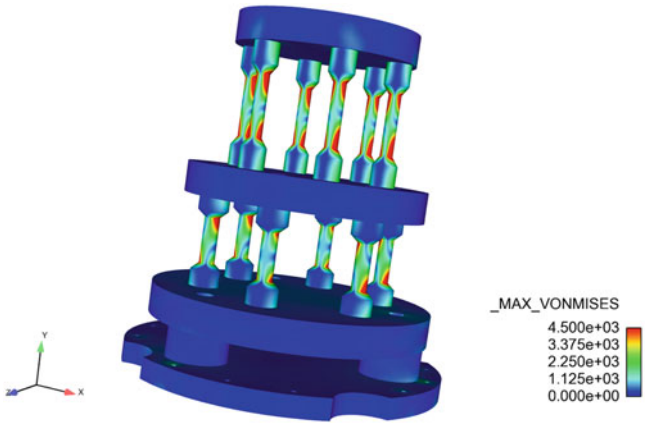

Fig. 29.2 Tapered column design with high column stresses under shock and vibration environments

Instrumentation design is dictated by the following criteria:

- Instrumentation set should uniquely identify the mode shapes of interest under 2 kHz.
- Mode shapes of interest should span the space of the true physical motion of the test article.
- The mode shape matrix comprised of the instrumentation set should be well-conditioned and invertible.
- Instrumentation set should have sufficient robustness to gauge loss.

29.2.1 Test Hardware Design

The hardware design has been nicknamed the "wedding cake" due to its multi-tiered structure of metal plates connected via bolted joints and ABS plastic columns (see Fig. 29.1). The tiers are connected via 6 ABS columns for a total of 12 ABS columns in the design. The lower tier is connected to a fixture plate via 3 ABS "pucks". This configuration will exhibit the desired structural dynamic modes (e.g. bending, axial, and torsional deformation). Dynamics of the test article will be dictated primarily by the mass of the plates and dimensions (length and cross-section) of the ABS columns. For simplicity in complying with mechanical envelope mass constraints, the dimensions of the plates are fixed, and plate material is designated as aluminum. As for the column design, the ABS plastic material will remain fixed as well as the column length. This simplifies meeting the requirements on the geometrical mechanical envelope and center of gravity. Therefore, the main design parameter will be the cross-sectional geometry of the ABS columns.

Various cross-sectional geometries were considered for the ABS columns to tailor modal frequencies. A tapered column design is shown in Fig. 29.2. Ultimately, uncertainties in the shock and vibration flight environments limited design options, and a conservative design with constant cross-sections was chosen as shown in Fig. 29.3. Pre-test predictions of modal response and structural assessments against conservative environments for similar flight vehicles suggests the final design will meet requirements. Predictions from pre-test modal analysis for a fixed-base boundary condition are shown in Fig. 29.4. The fixed-base condition is believed to be representative of that of the wedding cake in the next level assembly.

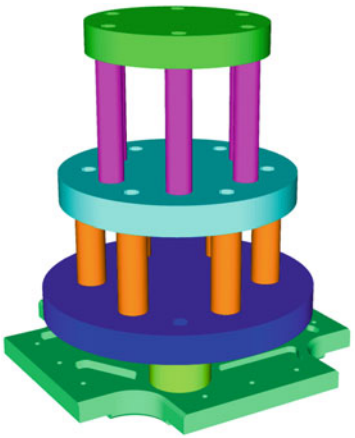

Fig. 29.3 Final wedding cake design

29.2.2 Fixture Design

The fixture design was mainly dictated by the need for interfacing with the next level assembly within the mechanical envelope requirements. Requirements on mass properties dictate that the fixture/payload deck was manufactured from stainless steel. As shown in the previous mode predictions, the fixture remains rigid at the lower frequency modes of the wedding cake, and becomes dynamic beyond 1 kHz. The final design of the fixture/payload deck is shown in Fig. 29.5. The fixture/payload deck was designed by the payload integration group to meet mechanical envelope requirements. This design was not expected to interact adversely with the flight experiment.

29.2.3 Instrumentation Set

The instrumentation set was dictated by the need to accurately characterize the mode shapes of the wedding cake with the minimum DOF set. There are 25 modes with modal frequencies up to 2 kHz (including rigid body modes, and excluding local column modes) that will be used for extraction and expansion of flight data. Therefore, the minimum set of measured DOFs is also 25. An additional five measurement DOFs were added to increase the robustness of the instrumentation set to gauge failure. Additional accelerometers were added to provide a basis for comparison/validation, or "truth" measurement to assess modal extraction/expansion techniques against.

A candidate set of 384 DOFs was considered at various locations on the wedding cake plates and payload deck as shown in Fig. 29.6. A custom software tool was employed to down-select an instrumentation set from the lager candidate set to those of the allotted budget. This method optimized on the condition number of the measured mode shape matrix (using an N-1 iterative approach), with the rationale that the instrumentation set with the lowest mode shape matrix condition number would provide the best inversion for modal extraction methods. After the optimized instrumentation set was determined, an additional utility was employed to add additional measurement DOFs and provide robustness against gauge loss. The proposed instrumentation set is shown in Fig. 29.7.

29.3 Modal Testing

The wedding cake hardware was modal tested to characterize the modes and provide data for model updating. Free-free (Fig. 29.8) and seismic mass (Fig. 29.9) boundary conditions were considered to provide a wealth of information to inform model credibility. The seismic mass boundary condition at the base exercised modes similar to those in a fixed base boundary condition without the associated complexities of simulating a true fixed-base condition or next level assembly boundary conditions. Modes extracted from the free-free and fixed-base testing are shown in Tables 29.1 and 29.2 respectively. Modes were extracted up to approximately 2 kHz. Further details of the modal testing are not discussed in this paper.

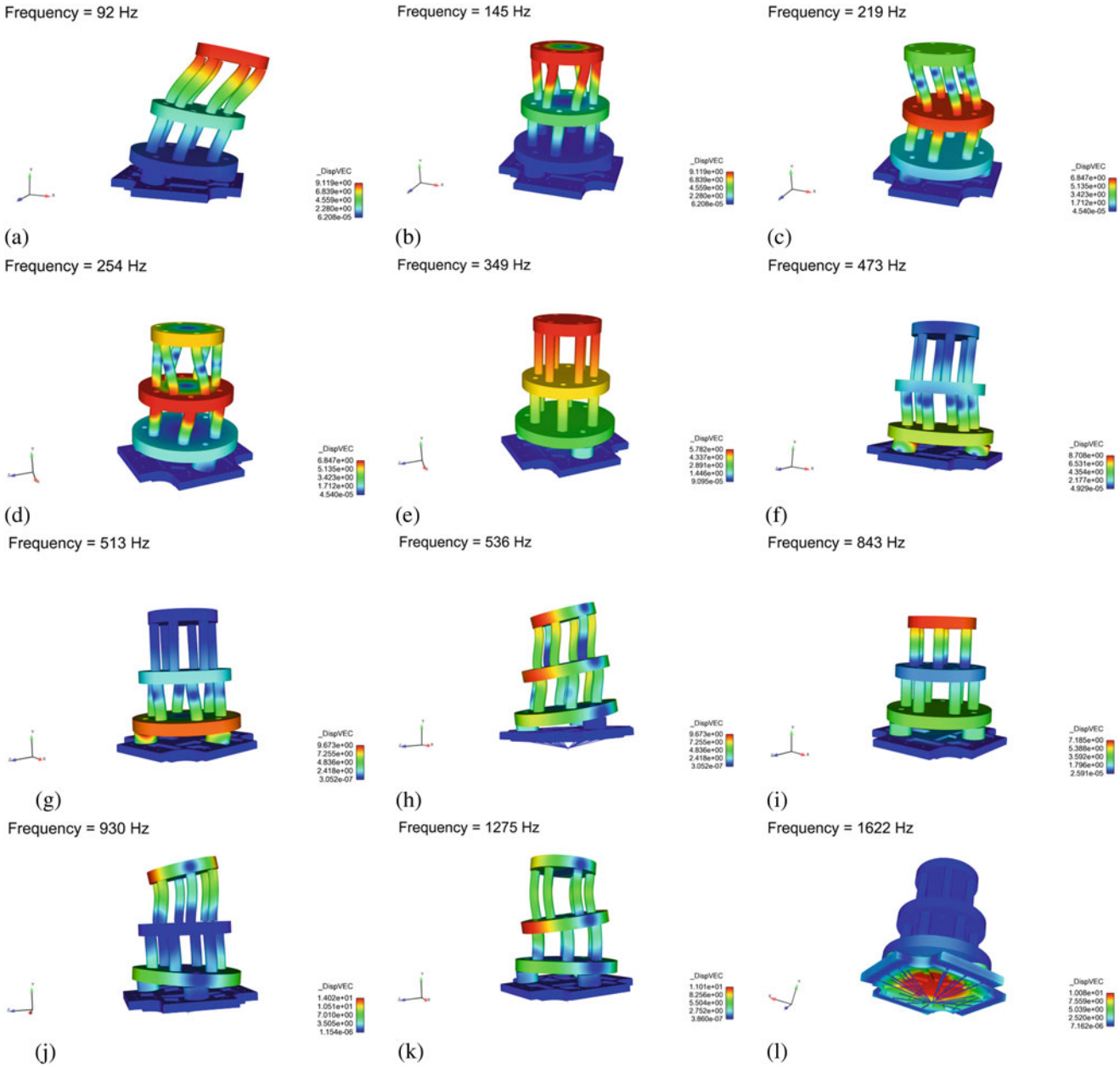

Fig. 29.4 Nominal pre-test modal predictions. (**a**) 1st bending mode (pair). (**b**) 1st torsional mode. (**c**) 2nd bending mode (pair). (**d**) 2nd torsional mode. (**e**) 1st axial mode. (**f**) Puck modes. (**g**) Lower deck torsional mode. (**h**) 3rd bending mode (pair). (**i**) 2nd axial mode. (**j**) 4th bending mode (pair). (**k**) Higher order bending mode (multiple). (**l**) Payload deck drumming mode

29.4 Model Updating

Model updating of the wedding cake model was performed using both free-free and fixed-base modal test data as depicted in Fig. 29.10. First, the model mass was calibrated on a part by part basis to the measured mass of the actual hardware on a part by part basis. This ensured the mass properties of the model were consistent with those of the test hardware. Next a baseline correlation of the model and test hardware modes were performed for the free-free modal test. Model updates were primarily in the form of minor modifications to the ABS modulus and bolted joint stiffness values. These were deemed appropriate

Fig. 29.5 Payload deck design

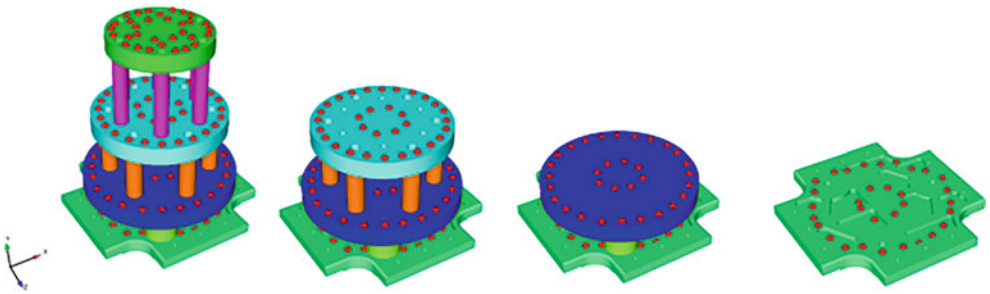

Fig. 29.6 Candidate instrumentation locations

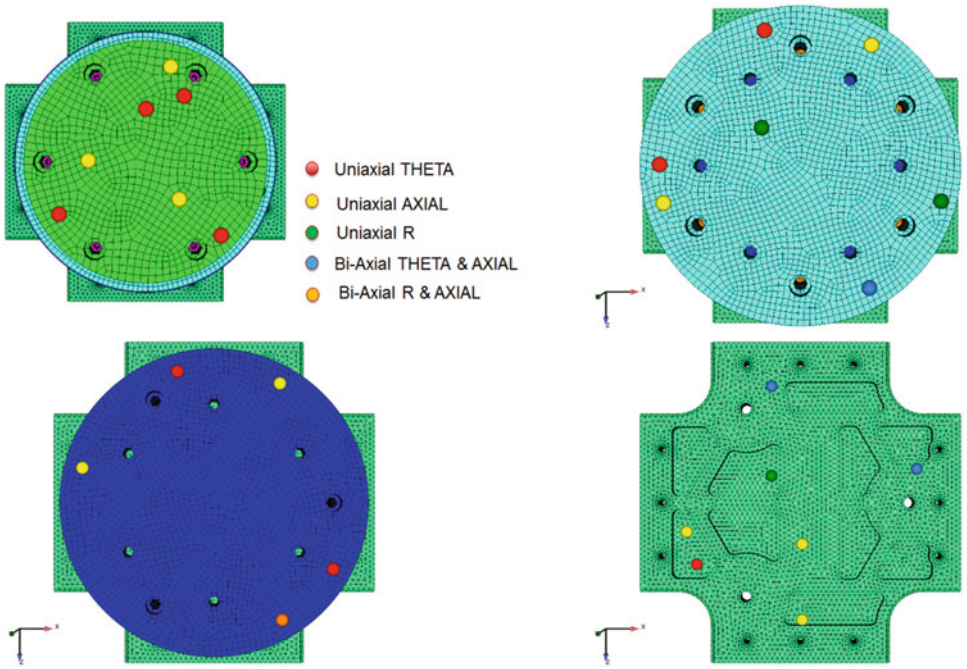

Fig. 29.7 Down selected instrumentation locations

modifications within the uncertainty of ABS modulus and joint properties. Finally, very small changes were made to the payload deck modulus for better agreement to modal data. This modification was deemed acceptable due to the coarseness of the payload deck mesh.

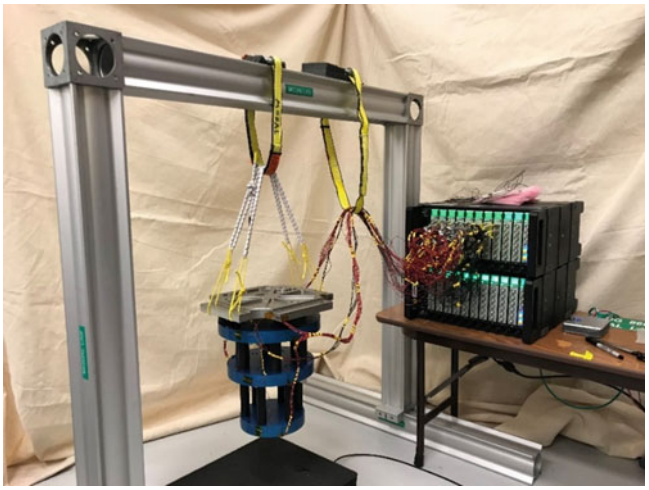

Fig. 29.8 Wedding cake free-free boundary condition test set-up

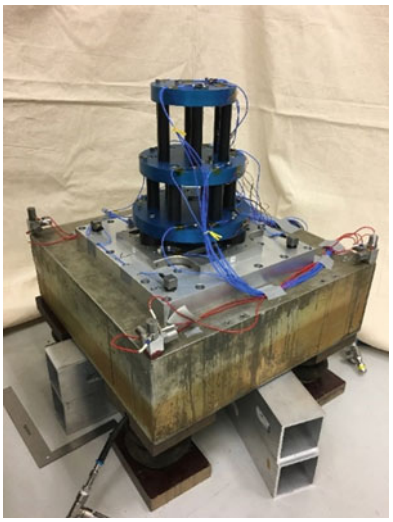

Fig. 29.9 Wedding cake fixed-base boundary condition test set-up

Next, the fixed-base modal test was considered to further inform model development. This boundary condition exercised the ABS puck joints at the base of the wedding cake more than the free-free boundary condition. Comparison of the updated model to the fixed base test motivated more modifications to the puck joints in the form of a fully tied connection instead of a compliant joint. Some other modifications included increasing ABS puck modulus and some increases in the joint stiffness parameters of the columns. Correlation results after model updating to the fixed-base test data are shown in Table 29.3 with good agreement. Note that due to the roughly symmetric nature of the design, bending modes often occur in pairs at the same frequency. Therefore, it is reasonable to allow these "repeated roots" of the system to be scaled and combined to allow for better agreement to a test mode. This combination is reflected in the "model modes" column. The highest frequency error for the fixed-base configuration is 3.8%, and the lowest diagonal MAC value is 0.65.

This final updated model was also correlated to the free-free modal test as shown in Table 29.4 with very good agreement. The highest frequency error for the free-free configuration is 5.6% and the lowest diagonal MAC is 0.89. The final updated model was also compared to a second wedding cake unit with similarly good agreement, indicating there is minimal variability in the as-built design. The updated wedding cake model is expected to serve as a sufficient basis for modal extraction and model expansion under operational environments. Overall, visual representations of mode shapes for the updated model are similar to those depicted in Fig. 29.5 and will not be repeated here. One could repeat the instrumentation optimization procedure with the updated finite element model. For the current application, however, the nominal predictions were believed to be a sufficient basis for the instrumentation set. It should be noted that modal extraction and expansion will employ the updated model.

Table 29.1 Wedding cake free-free boundary condition modes

Test mode	Test freq. (Hz)
Top plate torsion	144.3
Top plate translation	156.4
Top plate translation	160.1
Middle plate torsion	264.4
Middle plate translation	281.4
Middle plate translation	283.9
1st axial	573.0
Cake bending	655.4
Cake bending	660.4
Top plate rocking	902.5
Top plate rocking	928.2
Bottom plate torsion	986.6
Second cake bending	1002.6
Second cake bending	1007.2
2nd axial	1077.0
Middle plate rocking	1143.5
Middle plate rocking	1161.0
Base plate breathing	1573.9
Base plate bending	2078.4

Table 29.2 Wedding cake seismic mass/fixed base boundary condition modes

Test mode	Test freq. (Hz)
1st bending	98.1
1st bending	98.8
1st torsion	139.4
Middle plate translation	224.5
Middle plate translation	226.5
Middle plate torsion	252.7
1st axial	475.2
Rocking	627.4
Rocking	633
Bottom plate translation X	773.2
Bottom plate translation Z	784.5
Bottom plate torsion	887.5
2nd axial	983.6
2nd rocking X	1070.9
2nd rocking Z	1082
3rd axial	1360.2
Bottom plate “Potato Chip”	1438.7
Bottom plate “Potato Chip”	1472.8
Bottom and middle plate “Potato Chip”	2418.5
Bottom and middle plate “Potato Chip”	2490.5

29.5 Data Acquisition Considerations

During the process of test planning, it was determined that the accelerometers on the wedding cake would need to be split between two data acquisition/telemetry units on the flight hardware. This was problematic since it would be difficult to sync the various accelerometer channels exactly from the flight test data. Therefore, synthesized data from transient vibration analysis of the wedding cake was used to investigate the sensitivity of the SEREP expansion method to asynchronous accelerometer data.

A 6 DOF transient vibration input was applied to the base of the wedding cake model, with flat random vibration PSD profile from 10 to 2000 Hz. The responses at the accelerometer locations were arbitrarily split into two sets: “set 1” contained

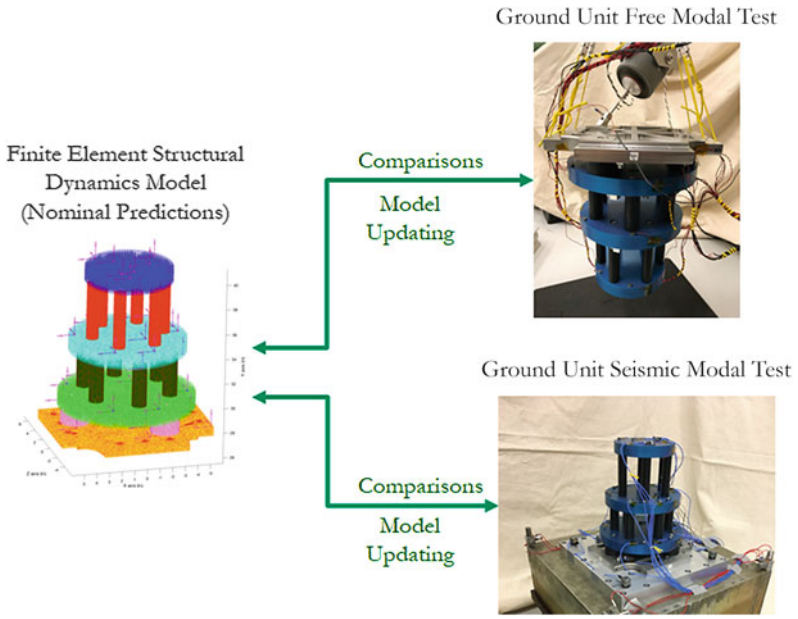

Fig. 29.10 Model updating process

Table 29.3 Model correlation to fixed base modal test

Test mode	Test freq. (Hz)	Model modes	Model freq. (Hz)	Freq err. (%)	MAC
1st bending	98.1	1 2	98.2	0.1	1
1st bending	98.8	1 2	98.2	−0.6	0.99
1st torsion	139.4	3	138.9	−0.4	0.99
Middle plate translation	224.5	4 5	227.8	1.4	1
Middle plate translation	226.5	4 5	227.8	0.6	0.98
Middle plate torsion	252.7	6	252.6	0	0.99
1st axial	475.2	7	485.4	2.1	0.99
Rocking	627.4	8 9	641.3	2.2	0.99
Rocking	633	8 9	641.3	1.3	0.99
Bottom plate translation X	773.2	10 11	803.6	3.8	0.97
Bottom plate translation Z	784.5	10 11	803.6	2.4	0.99
Bottom plate torsion	887.5	12	904.4	1.9	0.95
2nd axial	983.6	13	1020	3.6	0.7
2nd rocking X	1070.9	14 15	1050.8	−1.9	0.75
2nd rocking Z	1082	14 15	1079.8	−0.2	0.99
3rd axial	1360.2	16	1396.1	2.6	0.89
Bottom plate Potato Chip	1438.7	17 18	1451.1	0.9	1
Bottom plate Potato Chip	1472.8	17 18	1425.1	−3.3	0.95
Bottom and middle Plate Potato Chip	2418.5	19 20	2489.9	2.9	0.65
Bottom and middle Plate Potato Chip	2490.5	19 20	2489.9	0	0.97

the mid and top plate accelerometers and “set 2” contained the bottom and payload deck accelerometers. The two sets of channels were offset by 10 time steps and the modal extraction processed was performed with the “flawed”, offset data. After consulting with telemetry experts, an offset of 10 steps was deemed to be a conservative upper limit on the potential offset of data.

Figure 29.11 shows the FFT magnitude of extracted modal response for modes 7 through 24 using the theory in Eq. (29.1). Overall, the susceptibility of the method to asynchronous channel data appears to be minimal for lower modes, with the impact becoming more apparent for higher modes. Figure 29.12 shows expansion of asynchronous data to an un-

Table 29.4 Model correlation to free-free modal test

Test mode	Test freq. (Hz)	Model modes	Model freq. (Hz)	Freq err. (%)	MAC
Top plate torsion	144.3	1	145.5	0.8	0.89
Top plate translation	156.4	2 3	159.8	2.2	0.99
Top plate translation	160.1	2 3	159.8	−0.2	0.89
Middle plate torsion	264.4	4	264	−0.2	0.99
Middle plate translation	281.4	5 6	286.1	1.7	1
Middle plate translation	283.9	5 6	286.1	0.8	0.99
1st axial	573	7	593.4	3.6	0.98
Cake bending	655.4	8 9	667.4	1.8	0.97
Cake bending	660.4	8 9	667.4	1.1	0.98
Top plate rocking	902.5	10 11	952.7	5.6	0.93
Top plate rocking	928.2	10 11	952.7	2.6	0.98
Bottom plate torsion	986.6	12 13 14	999.8	1.3	0.94
Second cake bending	1002.6	12 13 14	999.8	−0.3	0.95
Second cake bending	1007.2	12 13 14	999.8	−0.7	0.94
2nd axial	1077	15	1098.7	2	0.9
Middle plate rocking	1143.5	16 17	1171.4	2.4	0.89
Middle plate rocking	1161	16 17	1171.4	0.9	0.99
Base plate breathing	1573.9	18 19 20	1579	−0.4	0.9
Base plate bending	2078.4	21	2082.1	0.2	0.99

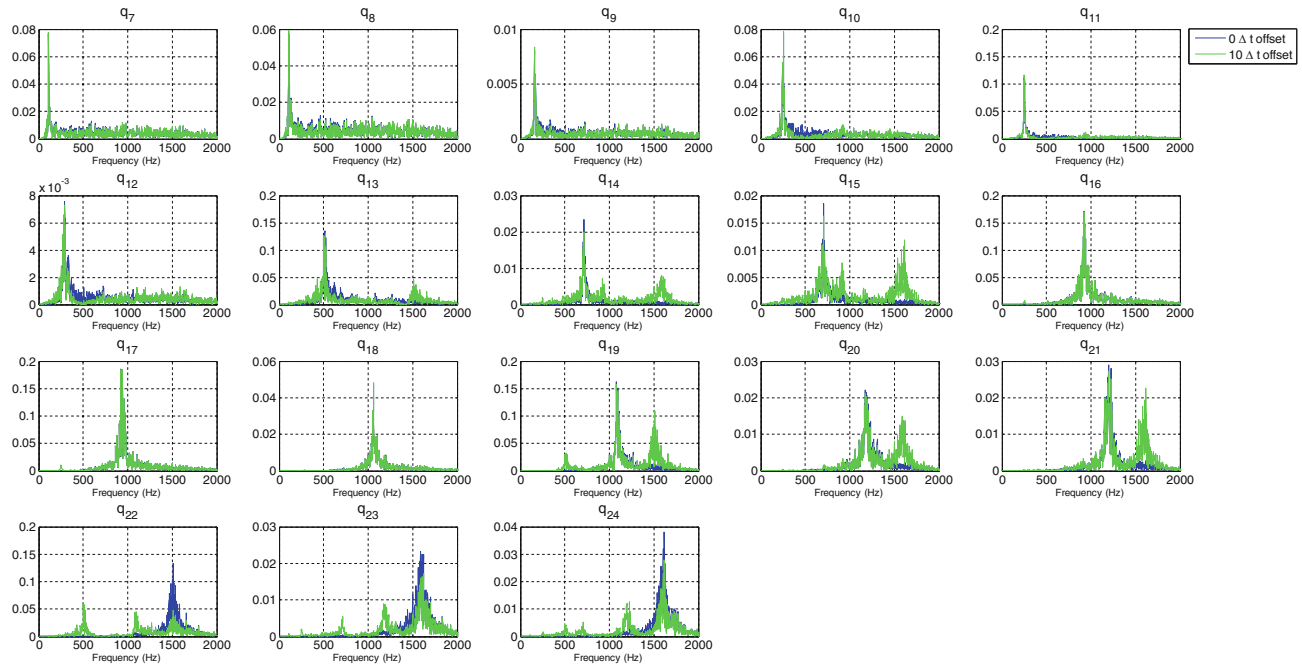

Fig. 29.11 Sensitivity of modal response extraction to asynchronous measurements

instrumented location. Overall, there appears to be minimal effect of asynchronous measurements for the offsets considered in this study. Ultimately, it was concluded that a slight offset in accelerometer data could be accommodated in post-test analysis. Also, it could be possible to synchronize the measurements by low-pass filtering the response data and using a cross-correlation or similar method to determine the delay times between the gauge sets.

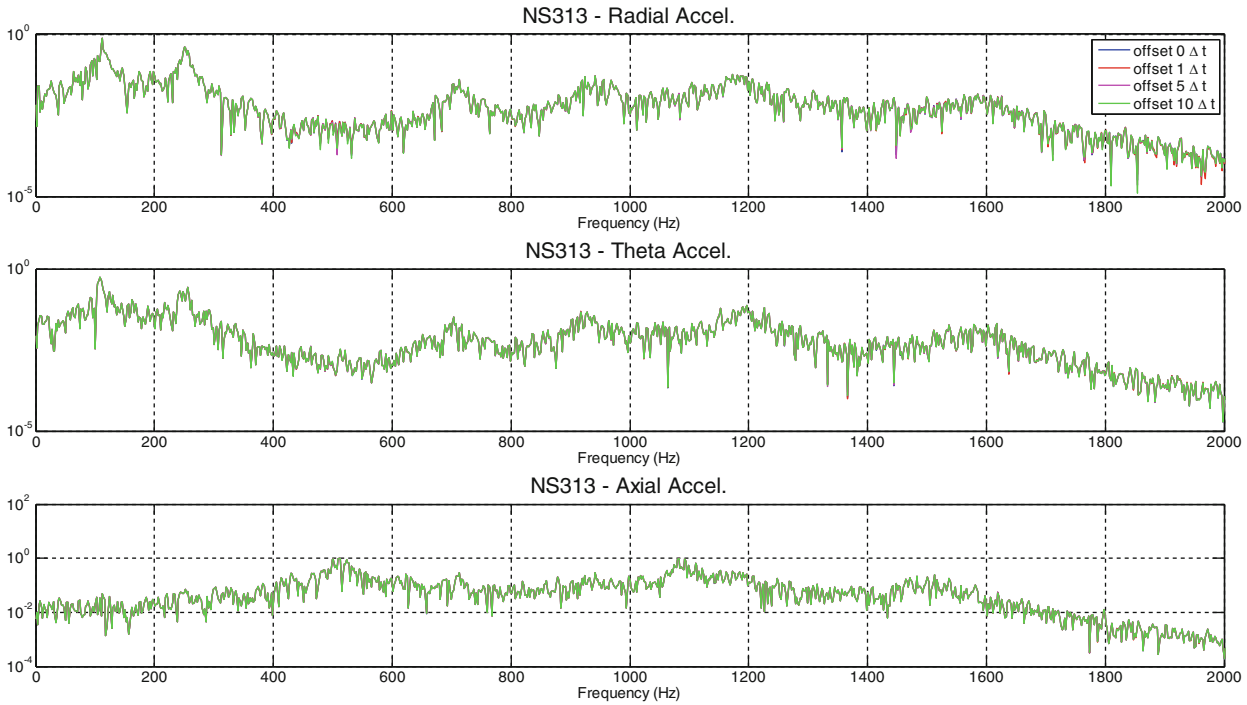

Fig. 29.12 Sensitivity of expansion to asynchronous measurements

29.6 Conclusion

This paper presented experiment design and test planning activities for a flight experiment to predict responses at uninstrumented locations via modal response extraction and model expansion methods. Structural dynamic modeling and simulation was effectively utilized to design experimental hardware and develop an optimized instrumentation set. Modal tests were performed to characterize modal response of hardware and support model updating for improved model credibility and a higher quality extraction and expansion. Model updating activities were discussed and a credible finite element model of flight test hardware was developed. Finally, "virtual testing" was employed through modeling and simulation to explore the effects of asynchronous data. Part II of this work will discuss ground test trials of the demonstrator experiment and assessment of the method with flight data. Part III will examine full field expansion of flight environments and sensitivity of methods to model accuracy and acceptable model uncertainties/perturbations.

Reference

1. O'Callahan, J., Avitabile, P., Riemer, R.: System Equivalent Reduction Expansion Process (SEREP). In Proceedings of the 7th International Modal Analysis Conference (IMAC VII), Las Vegas, NV (1989)

Chapter 30
Replicating Responses: A Virtual Environmental Test of Unknown Boundary Conditions

Timothy A. Devine, V. V. N. Sriram Malladi, and Pablo A. Tarazaga

Abstract Environmental testing focuses on producing more appropriate testing procedures in laboratory settings which result in more accurate verification and validation of high-performance and sensitive equipment. However, replicating operational conditions in a testing space is challenging due to the unknown nature of the excitations and boundary conditions the system is subject to in the field. If the boundaries can be formulated in a way such that the response can be replicated with different boundary conditions, this would allow for testing of these structures in laboratory settings of known and applicable boundary conditions.

The present work models a finite element beam under unknown boundary conditions and attempts to match its spectral response given a known boundary conditions (i.e., a fixed-fixed boundary condition). Forcing inputs are derived for cases of specified and unspecified cross spectral densities for a subset of the initial response locations. The response of the fixed-fixed beam at all initial response locations is compared to the unknown boundary condition target responses to determine how well the force recreation fits the unknown response. Future work aims to replicate these scenarios in an experimental setting.

Keywords MIMO · Virtual testing · Unknown boundary condition · Spectral density · Environmental testing

30.1 Introduction

Testing standards are often used for certifying that equipment can undergo a certain excitation profile without experiencing failure over a range of frequencies. These standards attempt to provide a realistic guide to the operational environments experienced by the test object. Attempting to recreate these profiles requires an excitation and knowledge of the boundary conditions, both of which often are unknown and very difficult to accurately replicate. Quite often as well, live systems have more than one input which requires more sophisticated testing procedures.

MIMO testing is rapidly being accepted as a more accurate approach to validating complex systems [1]. The traditional SISO techniques work well at measuring and reproducing single point responses but due to the intricacy of today's assemblies, using only a single point might not be enough to adequately capture and replicate the system's dynamics. MIMO testing allows for a more holistic approach, where matching more response locations on the structure with respect to field measurements will reduce overtesting or undertesting of the structure [2].

Quite often, the boundary conditions in operational environments are difficult to reproduce in laboratory settings. Whether the operational condition is aeroelastic excitation, ground vehicle transport, or another environmental excitation, the boundaries of the system are not as simple as free-free, fixed-fixed, or another common condition frequently used for testing. Being that these known configurations are more readily available in a laboratory environment, if they could potentially be manipulated to serve the purpose of matching responses of the system then there may be no need to struggle with the complex boundaries of the operational environment to produce a desired response.

T. A. Devine (✉) · V. V. N. S. Malladi · P. A. Tarazaga
Vibrations, Adaptive Structures and Testing (VAST) Laboratory, Department of Mechanical Engineering, Virginia Tech, Blacksburg, VA, USA
e-mail: timd@vt.edu

C. Walber et al. (eds.), *Sensors and Instrumentation, Aircraft/Aerospace, Energy Harvesting & Dynamic Environments Testing, Volume 7*, Conference Proceedings of the Society for Experimental Mechanics Series,
https://doi.org/10.1007/978-3-030-12676-6_30

30.2 Background

This work aims to replicate a structure's response given unknown boundary conditions with the same structure given a known boundary condition. In an actual system, the unknown boundary could be due to attachments to a frame or interactions between the structure and packaging. To do this the response of a finite element beam subject to virtual forces was studied and used to represent such a structure's scenario.

The beam was modeled as an aluminum beam in free-free boundary conditions, with a modification made to the stiffness matrix, where 4 of the 100 total nodes, 25, 26, 74, and 75, were increased by 1% of their nominal value. The modification is meant to serve as an unknown boundary conditions, where the first 5 modified mode shapes can be seen in Fig. 30.1. White noise was filtered to the Nyquist frequency and applied to the beam at all 100 nodes as an input excitation. The cross spectral densities (CSD) were calculated between five locations, which can be seen in Fig. 30.2a. Figure 30.2b also shows other key locations, such as input and output locations for the recreated response, on the beam. The target response spectrums can be seen in Fig. 30.3 with the magnitude of the cross terms shown as well.

The unknown boundaries case was then paired with a fixed-fixed virtual beam which served as the known boundary condition for this study. The first step in recreating the response was to determine optimal excitation and response locations. An LU decomposition [3] was performed on the first 5 fixed-fixed mode shapes to determine which nodes of the beam were the most responsive, seen in Fig. 30.4. The resulting top 3 locations from the decomposition were then used as excitation nodes. With the excitation nodes determined, the FRFs of the fixed-fixed beam were obtained between each of the 5 response locations and the 3 new input locations. The FRFs for the two chosen measurement points used to recreate the forcing spectrum are shown in Fig. 30.5. The remaining FRFs for the other 3 locations will be used in evaluating the accuracy of the approach. The output locations as well as the excitation locations can be seen in Fig. 30.2b.

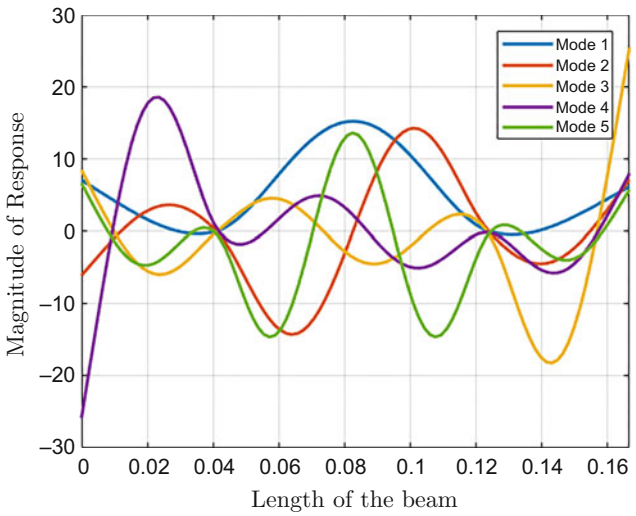

Fig. 30.1 Mode shapes of the unknown boundary condition beam

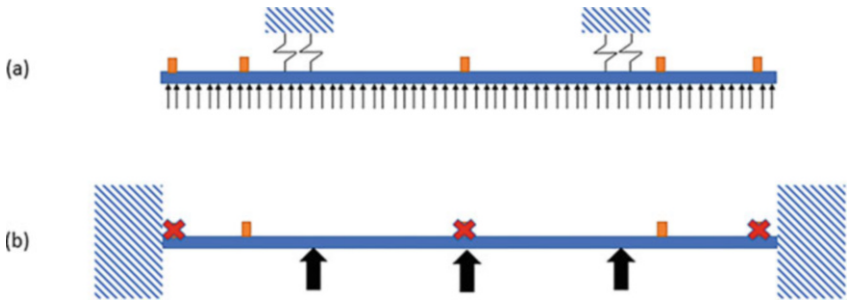

Fig. 30.2 Depiction of simulated cases: (**a**) shows the unknown boundary case, where a modification to the stiffness has occurred—shown by the added springs; (**b**) shows the known boundary conditions where 3 inputs are used and are shown by the black arrows. The number of outputs used has been reduced to 2 locations and are represented by the orange boxes in (**b**)

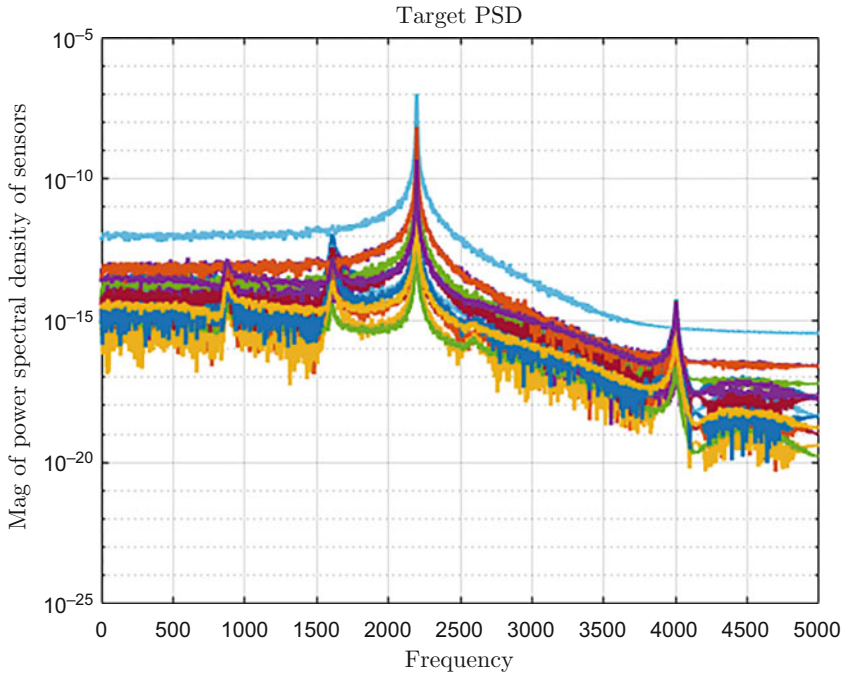

Fig. 30.3 The 25 spectral densities, both cross and auto, of the white noise application to the unknown boundary condition beam

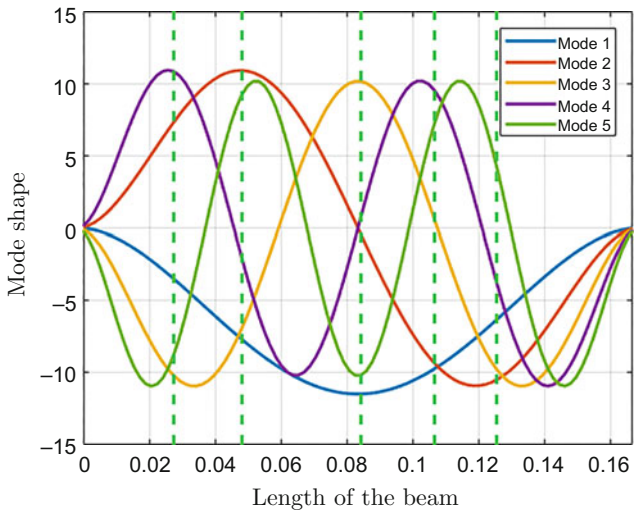

Fig. 30.4 LU decomposition of the first 5 fixed-fixed mode shapes. The second, third, and fourth locations, shown by the vertical bars, were used as input locations

With the CSDs known, it is possible, as shown by Smallwood [4], to invert the response spectrums (S_{yy}) and obtain the forcing spectrums (S_{xx}) using the FRFs (H) equation

$$\boldsymbol{S_{xx} = H^{+} S_{yy} H^{+\prime}},$$

where $^{+}$ represents the pseudo inverse. However, if the system is overdetermined, meaning there are more responses than inputs, then the inverse of the FRFs will not exist. To avoid this problem, a subset of 2 response locations were chosen to be matched. This made the number of inputs 3 and the number of outputs 2, creating an underdetermined scenario. The inverse was carried out for both the cases where response cross terms were provided as well as the scenario where the cross terms were unavailable. For the no-cross case, minimum and maximum trace forcing spectrums were calculated as well as compared to the inclusion of the response cross terms. The forcing spectrum was then applied to the system to determine the response of the 5 locations to the forcing spectrums and are compared to the target response auto spectra densities (ASD).

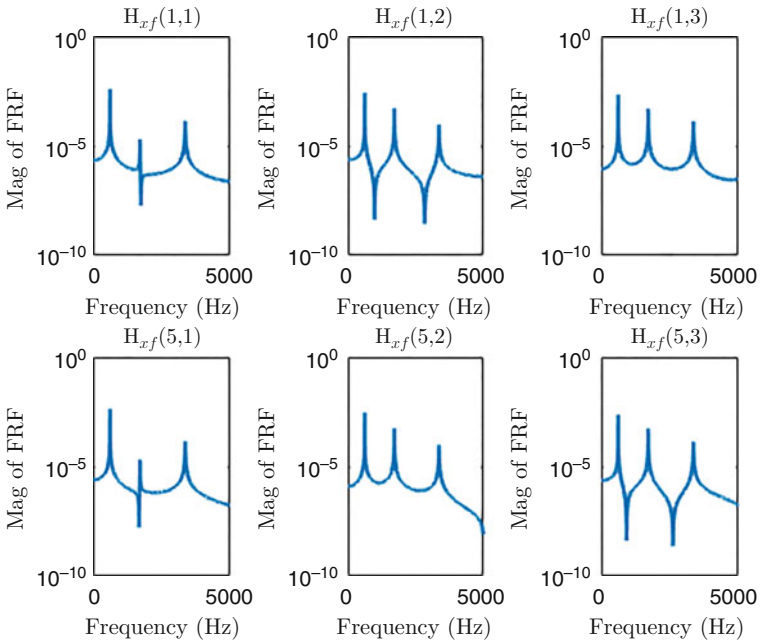

Fig. 30.5 FRFs of the response locations with inputs at the 3 excitation locations

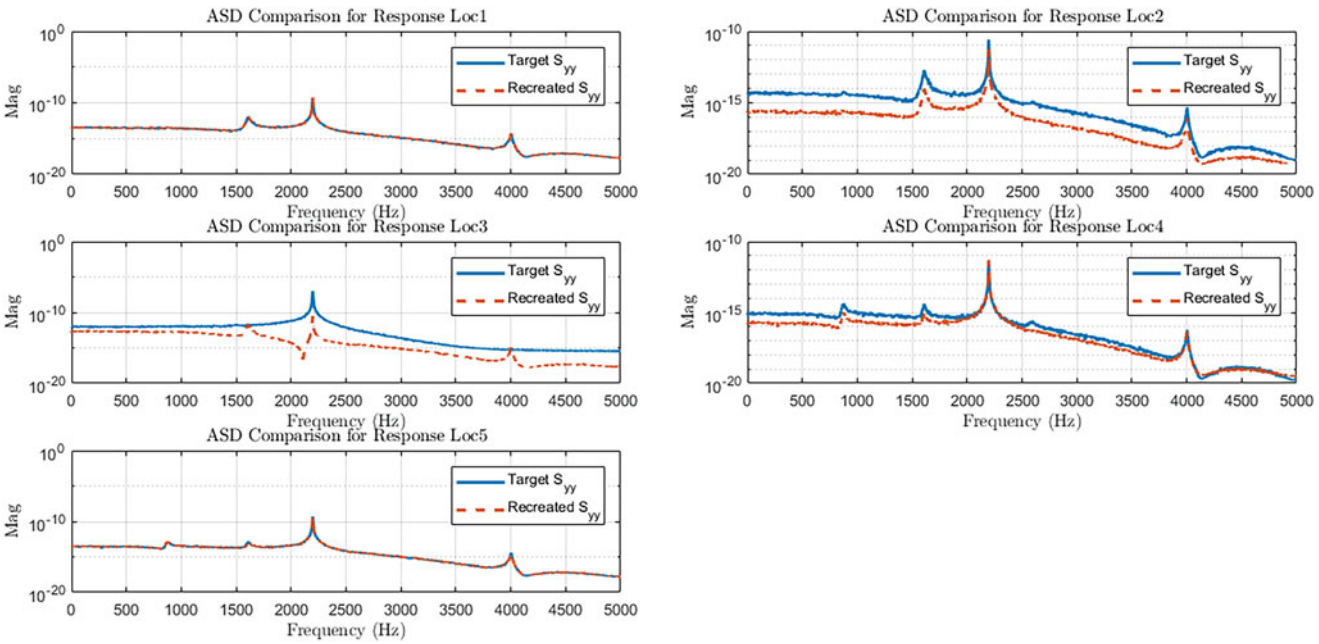

Fig. 30.6 Recreated ASDs of a fixed-fixed beam compared to target ASDs taken from a beam with unknown boundary conditions with cross terms included in the inversion process

30.3 Analysis

The results of the simulation for a known boundary beam are presented both with and without CSDs included in the process. Figure 30.6 shows the ASDs of the response of the fixed-fixed beam after being subjected to the recreated forces overlaid on the ASD of the response of the unknown boundary condition.

The location of the FRFs used for inverting were locations 1 and 5, which show close adherence to the target spectrum. Location 4 shows a somewhat accurate recreation, location 2 is near the target at the largest peak, however it is slightly less at other peaks as well as non-peak frequencies. Location 3 struggles to match any of the spectrum. This is most likely due

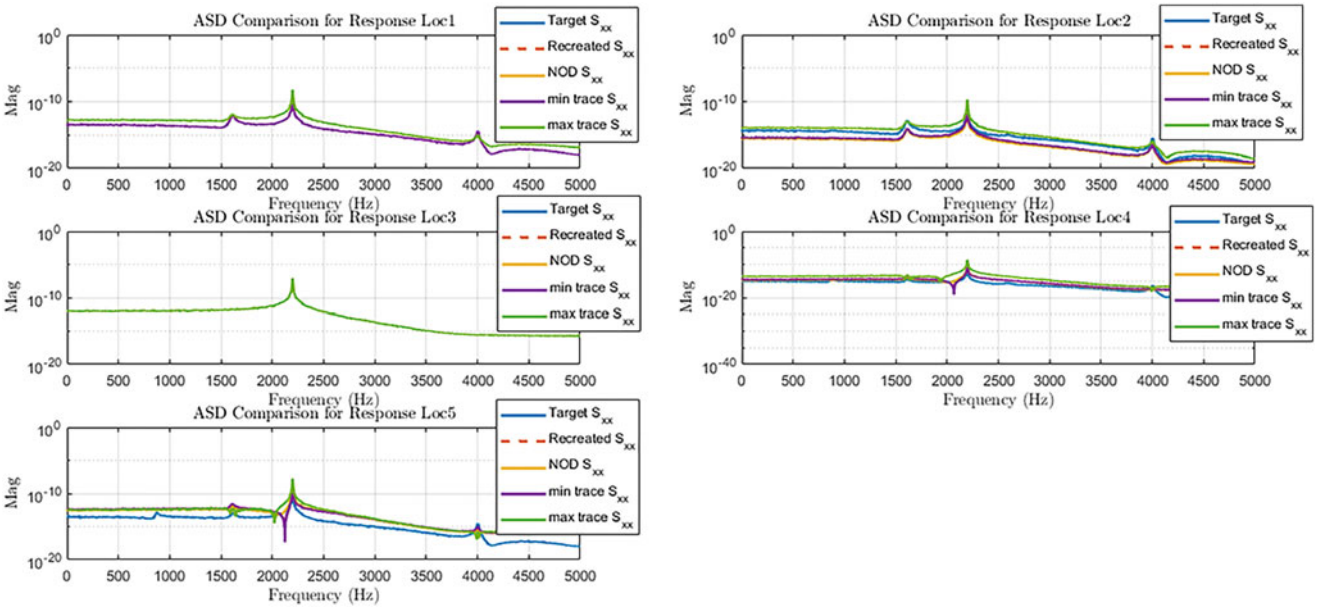

Fig. 30.7 Recreated ASDs of a fixed-fixed beam compared to target ASDs taken from a beam with unknown boundary conditions

Table 30.1 Description of the methods for generating resulting response curves when cross terms are removed

Curve name	Description	Effect on forcing spectrum
Target	Target response curve	–
Recreated	Calculates what the response spectrum will be if target response cross terms are included	Only possible response if cross terms are known
No Off Diagonal (NOD) cross terms	Calculates what the force spectrum will be if no target response cross terms are included	Provides a forcing spectrum to system that is somewhere between min and max
Min trace	Calculates what the response target spectrum will be that minimizes the trace of the force spectrum when no cross terms are included	Provide lowest possible forcing spectrum to system
Max trace	Calculates what the response target spectrum will be that maximizes the trace of the force spectrum when no cross terms are included	Provides highest possible forcing spectrum to system

to location 3 being at midspan of the beam, where an excitation location exists. As Smallwood describes, response locations near inputs tend to provide poor results [4].

When cross terms are removed, the ASDs shown in Fig. 30.7 result. A description of the different curves as well as their potential uses can be found in Table 30.1. Matching was done for this case at locations 1 and 3, where we see close matching for all ASDs, except in location 1, where the max trace input results in higher non-peak responses. At the non-matched locations, the recreated spectrums miss the target spectrum, with the minimum and no diagonal trace responses below the target for most of the spectrum and the maximum spectrum above the target for most of the spectrum. While it is overshooting the target spectrum at some locations, the maximum trace does match one of the two response locations and is close on the other. This could potentially lead to greater degrees of undertesting than testing the beam to an envelope profile.

30.4 Conclusion

This study was able to match the ASD response of points on a beam with unknown boundary conditions to a beam with known boundary conditions. The non-matched points' spectrums were matched in some testing configurations, however in others the recreated spectrums were widely different from the target by multiple orders of magnitude. Interestingly, the max trace scenario produced matched responses at the specified locations as well as responses that were higher than the target response at other locations. If this were applied to a real system, it could potentially tightly match a given point of concern in the system, while still ensuring all other points were below a specified envelop that was within an order of magnitude of the target response.

Future studies will aim to match the response of the unknown condition to different known conditions, such as a free-free beam or a cantilever beam. Additionally, future work will aim to experimentally test this method, by taking a beam's response in unknown condition and attempt to replicate the response in known conditions.

References

1. Robins, C., Ewins, D.: Multi-axis vibration testing of an aerodynamically excited structure. J. Vib. Control. 1–11 (2016)
2. Daborn, P., Ind, P., Ewins, D.: Replicating Aerodynamic Excitation in the Laboratory. In: International Modal Analysis Conference (2013)
3. Daborn, P.: Smarter dynamic testing of critical structures. PhD Thesis, University of Bristol (2014)
4. Smallwood, D.: Multiple-Input Multiple-Output (MIMO) linear systems extreme inputs/outputs. Shock Vib. **14**, 107–131 (2007)

Chapter 31
An Approach to Component Testing: An Analytical Study

Brandon J. Dilworth, Alexandra Karlicek, and Louis Thibault

Abstract Component testing is a standard process across many industries for multiple decades. A specification is typically derived from empirical data collected during a system-level test where input levels (usually in terms of acceleration) are prescribed at the mounting interface of the component. The component is then typically mounted to a rigid fixture for testing where fixture modes are designed to not interact with the structural modes of the component. An acknowledged shortcoming of a test of this type is that the rigid fixture does not represent the dynamics of the final integrated system. This shortcoming is typically referred to as the "impedance mis-match problem."

This paper introduces a possible approach to mitigate this shortcoming by designing a fixture assuming that knowledge of the system level dynamics are understood. For the purposes of the analytical study presented in this paper, the system level dynamics are understood well enough to characterize the boundary conditions of the component such that the modal parameters of the component are replicated from the system test in the component test. A fixture design is conceptualized based on the Box Assembly with Removable Component (BARC) hardware distributed by Sandia National Laboratories and Kansas City National Security Campus.

Keywords Model correlation · Component testing · Shock testing

Nomenclature

ELV	Expendable launch vehicle
FEA	Finite element analysis
FEM	Finite element model
GEVS-EV	General environmental verification specification for STS & ELV
MIT	Massachusetts Institute of Technology
STS	Space transportation system

31.1 Background and Motivation

For multiple decades, engineers have had to work the problem of testing components when full systems are not available. The fundamental question for testing components comes down to how to design a fixture for test. Historically, fixtures have been designed to be as stiff as possible as to not have structural modes within the test bandwidth of interest. At initial consideration, this general approach would seem to be simpler than having a fixture with multiple modes that potentially interact with the component of interest. In some regards, this can be true that developing an analysis that is representative of the test environment would be straightforward as the component design is likely mature, and the fixture would be simplistic to model. On the plus side, this approach does make predicting the loads in the component easier which provides insight to how the component will behave during testing, and ultimately help to determine if the component will survive the test or not. However, it is typical that a component is part of a larger system which likely has multiple modes within the test bandwidth of interest and these modes have a significant influence on the boundary conditions of the component.

B. J. Dilworth (✉) · A. Karlicek · L. Thibault
MIT Lincoln Laboratory, Lexington, MA, USA
e-mail: brandon.dilworth@ll.mit.edu

C. Walber et al. (eds.), *Sensors and Instrumentation, Aircraft/Aerospace, Energy Harvesting & Dynamic Environments Testing, Volume 7*, Conference Proceedings of the Society for Experimental Mechanics Series,
https://doi.org/10.1007/978-3-030-12676-6_31

Aerospace standards, such as NASA GEVS-SE [1], emphasize a philosophy to test or verify "under conditions that simulate the flight operations and flight environment as realistically as possible"—sometimes shortened to 'test like you fly' which infers that a component should be tested in a similar environment as it would experience in flight. Testing in conditions which alter the boundary conditions of the component (i.e. with a rigid fixture) fundamentally differs from this philosophy. Engineers are faced with the challenge of either conducting a test that is relatively easy to analyze or attempt to design a fixture which exhibits the dynamics of the larger system.

A couple of years ago, Sandia National Laboratories and the Kansas City National Security Campus initiated a volunteer collaboration within the modal analysis community with a goal to address this testing dilemma [2]. The community was effectively presented with two scenarios:

1. Consider a scenario where a component is designed to survive the test and then is analyzed for the larger system. The risk is that the model for the larger system is not as mature as the component due to its complexity. If the system model is not accurate, then it likely does not capture the proper boundary conditions and mode coupling dynamics between the system and the component. This scenario could result in a component that passes the test but fails in flight.
2. Another scenario is that the component has been surviving in flight tests, but a new component level test has to be developed to ensure new components are viable for flight. The risk here is that while the component may have history of surviving in flight with no issues, it may fail the component test due to differing boundary conditions. The different boundary conditions can result in the component having very different mode shapes as compared to when integrated with the system, which will alter the strain state observed. This scenario can result in unnecessary engineering effort to redesign the component to pass the test when the design was adequate to meet the needs of the system.

The community was faced with a basic question: how can we better test components such that they tested in a way that is more representative of the final system configuration assuming no physical aspect of the higher system is available. For this paper, we will assume that a mature model is available to represent the system.

31.2 Technical Approach

MIT Lincoln Laboratory received one of the BARC units for testing and analysis to support this round robin effort across the community. The approach summarized in this paper is to collect modal data on the BARC, update the system model of the BARC, then decouple the component from the larger system and attach compliant degrees of freedom at the mounting locations of the component. The compliant degrees of freedom at the mounting locations are intended to provide a similar boundary condition to the component as it would observe in the system. Several approaches described in a recent Practitioner's Guide [3] were used in the test setup, data collection, curve fitting, FEM analysis, model correlation, and model updating. A summary of the BARC hardware is shown in Fig. 31.1.

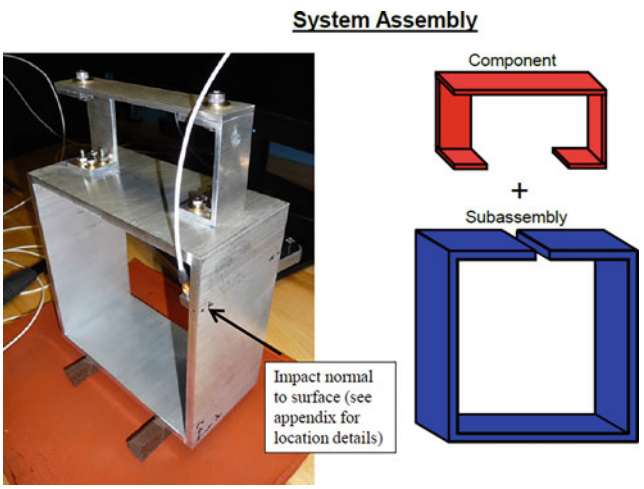

Fig. 31.1 Summary of BARC hardware

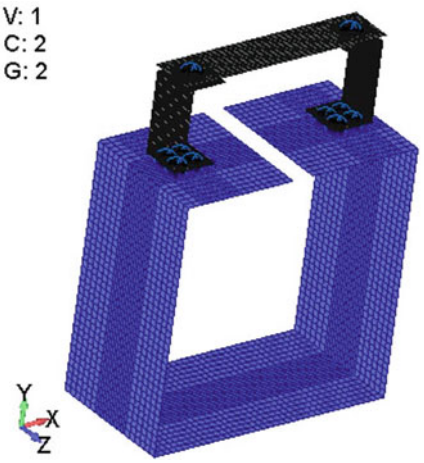

Fig. 31.2 FEM of BARC

Table 31.1 FEA–EMA correlation results

#	FEA	Hz	EMA	Hz	Diff. (%)	MAC (%)
1	7	188.33	1	186.36	1.06	98.8
2	8	205.28	2	205.95	−0.32	98.8
3	9	262.75	3	258.76	1.54	99.3
4	10	443.22	5	470.07	−5.71	26.2
5	11	491.31	4	428.05	14.78	65.9
6	12	563.85	7	578.96	−2.61	72.4
7	13	572.48	6	554.07	3.32	82.1
8	14	654.01	8	662.1	−1.22	98.7
9	15	1093.6	9	1100.3	−0.61	88.2
10	16	1158.2	10	1175	−1.43	94.5
11	17	1475.5	11	1493.2	−1.18	94.5

Fundamentally, the final iteration of the compliant boundary condition of the component could then be used to define design constraints for a fixture for the component test. This paper does not go into fixture design, but leaves it to the reader to speculate on many approaches to design which would mimic the stiffnesses described as a result of the model updating.

MIT Lincoln Laboratory developed a FEM to represent the BARC hardware. Mechanical measurements were made on the physical structure and those properties were included in the model. Getting these as-build properties accurate in the model helps reduce the model correlation and model updating time when comparing to measure modal data from the structure. The FEM is summarized in Fig. 31.2.

The FEM was run in both NASTRAN and FEMtools for a baseline comparison of the model, but FEMtools was used for all correlation analyses and model updating. To ground the model, an experimental modal analysis (EMA) was completed on the BARC with a Free-Free boundary condition. The results of this correlation study are summarized in Table 31.1 below for the first 11 flexible body modes. With the exception of only a couple of modes, the experimental modal and the analytical modal analysis are in good enough agreement to have confidence in the FEM to move forward.

With the model grounded with experimental results, the model was then modified to remove the base structure and estimate its dynamics with different compliant elements. Several approximations were studied to evaluate how this estimation compares with the full system model including fixed base, a single CBUSH, and 2 CBUSH elements at the feet of the component. A graphical representation of the component model with the constraint elements at the feet is shown in Fig. 31.3. For the fixed base, a RBE2 element joined the two feet and then was fixed in all 6 degrees of freedom. For the single CBUSH, a RBE2 element joined the two feet and then the RBE2 was connected to the single CBUSH. For the two CBUSH case, a RBE2 element connects each of the two feet of the component to an independent CBUSH element.

The component FEM with the different boundary condition elements was run through model updating to iterate on various stiffness values for the CBUSH elements using the component modes at the system level as the target modes for model updating.

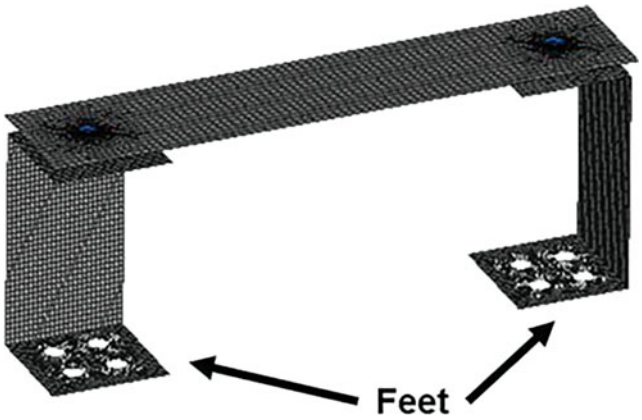

Fig. 31.3 Simplified component FEM

Table 31.2 Rigid base versus system modal results

Mode #	FEA (component)	Hz	EMA (system)	Hz	Diff. (%)	MAC (%)
1	1	471.6	5	491.3	−4.0	94.6
2	2	1087	10	1158	−6.1	95.6
3	3	1330	7	572.5	132.4	83.1
4	4	1868	16	1972	−5.3	83.7
5	5	2227	18	2227	0	88.6

Table 31.3 Single CBUSH versus system modal results

Mode #	FEA (component)	Hz	EMA (system)	Hz	Diff. (%)	MAC (%)
1	1	7.3	4	443.2	−98.4	58.2
2	4	189.4	1	188.3	0.6	50.9
3	5	204.6	2	205.3	−.31	74.3
4	9	2324	15	1870	24.32	41.2
5	10	2701	11	1476	83.23	40.8

31.3 Results

In the following results, the component model is labeled 'FEA' and the assembly system model is labeled 'EMA'. The first case that was studied is the fixed base constraint. This condition is representative of the 'typical' approach to component testing being mounted to a rigid fixture. Table 31.2 summarizes the mode pairing and shows that while there are modes that pair with a degree of success (i.e. high MAC values), the mode numbers of the system are all over the map to pair with the component model. The dynamics between these two models are dramatically different, which confirms the hypothesis stated earlier in this paper.

For the single CBUSH model, which effectively connects the two feet to a single compliant mount, the results show how poor this modeling assumption would be to represent the system. This matches engineering intuition in the sense that the system model effectively has the two feet of the component on independently (i.e. each foot mounted on the top of the base plate, but the plate is cut between the feet). The results are summarized in Table 31.3. Note that several of the rigid body modes from the component model are pulled into the mode pairing and map to what are flexible body modes of the base plate. Further study of the slope conditions of the feet would help to better understand if this behavior maps to physical expectations.

For the two CBUSH model, which intuitively is the most representative condition relative to the system model, the mode pairing is considerably more favorable as shown in Table 31.4. While the MAC values are not very high, the mode frequencies are in good family. Additional study is required to understand if other correlation metrics other than MAC would provide better insight to the comparison of the models. For the model updating in FEMtools, CCMAC was used with a maximum of 20 iterations. Note again that a couple of the rigid body modes from the component model were pulled in to mode pair with

Table 31.4 Two CBUSH versus system model

Mode #	FEA (component)	Hz	EMA (system)	Hz	Diff (%)	MAC (%)
1	4	198.9	2	205.3	−3.1	84.5
2	5	207.82	1	188.3	10.4	63.2
3	7	601.4	8	654.0	−8.0	44.0
4	9	1242	11	1476	−15.9	40.1
5	10	1602	12	1566	2.3	67.5
6	11	1966	16	1972	−0.3	41.2

some of the flexible body modes from the system model. Just like with the single CBUSH model, further study is required to better understand how the component rigid body modes compare to the modes observed at the system level.

31.4 Conclusion

An analytical approach was presented to consider component testing on a flexible mount to represent dynamics as if it was mounted in a system level assembly. These initial results show that there definite advantages to considering a compliant mount for the component to better represent behavior during system level testing compared to simply rigidly mounting the component at its base. However, further study is certainly required to refine these initial results in order to establish design guidelines for fixture designs.

Statement DISTRIBUTION STATEMENT A. Approved for Public Release. Distribution is unlimited.

This material is based upon work supported under Air Force Contract No. FA8702-15-D-0001. Any opinions, findings, conclusions or recommendations expressed in this material are those of the author(s) and do not necessarily reflect the views of the U.S. Air Force.

References

1. Baumann, R.: General environmental verification specification for STS & ELV payloads, subsystems, and components, NASA Goddard Space Flight Center (1996)
2. Soine, D., et al.: Designing hardware for the boundary condition round robin challenge, IMAC 36 Proceedings (2018)
3. Avitabile, P.: Modal Testing: A Practitioner's Guide. Wiley, Hoboken, NJ (2018)

Chapter 32
Issues in Laboratory Simulation of Field Vibration Data: Experimental Results on a Typical Structure

Paulo S. Varoto

Abstract Laboratory tests are required in order to qualify a given test item before it is exposed to its field vibration environment, a process that is frequently referred to as vibration or environmental testing. In a typical laboratory environment, a given test article is mounted on the vibration exciter through a test fixture thus forming a combined structure. The combined system is then driven according to prescribed testing conditions while the test item dynamic response is continuously monitored such that maximum dynamic strain are confined under safe and desired levels. The process of going from the field to the laboratory involves some key steps, that include but are not limited to: (1) knowledge of the dynamic characteristics of the systems involved; (2) design of test fixture in order to properly attach the test item to the vibration exciter table; (3) definition of suitable laboratory inputs that when applied to the test article are capable of predicting or at least simulate its field response. The article aims to discuss some of these important issues, particularly the important role of modal testing principles in obtaining accurate response models for the structures involved. Reasonably accurate and experimentally verified models certainly allow that further questions be addressed in the processing of simulating field vibration data.

Keywords Vibration testing · Environmental testing · Boundary conditions · Modal testing · Boundary conditions

32.1 Introduction

This article aims to present preliminary results from an experimental modal analysis study performed on the Box Assembly with Removable Component (BARC) structure that was specially designed [13] to motivate discussions and investigation on issues involved in simulating field vibration data. This topic is part of a more general theoretical framework, commonly referred to as *Vibration Testing*. Vibration testing can be suitably defined as [7–9] "*... the art and science of measuring a structure's response while exposed to its dynamic environment and simulating this environment in a satisfactory manner to ensure that the structure will either only survive or function properly while exposed to this dynamic environment*". Two main stages are involved in this definition. First, the structure's vibration signals from its dynamic environment must be available and this is usually the case of measuring these signals while the test item is exposed to some field vibration condition. Second, simulating the test item's dynamic response in the laboratory environment requires that suitable inputs be defined and applied to the test item in the laboratory. There are several reasons to conduct vibration tests on a given test item. They include, but are not restricted to: (1) Verify or validate a numerical model of the test item; (2) Qualify the test item to meet a set of specifications; (3) Develop taylored dynamic inputs using field data to use in either laboratory tests of finite element simulations or other simulation methods. From these, modal testing [3] clearly plays a key role in ensuring that reliable models can be formulated for the structures involved in the process of going from field to laboratory test environments.

In the field vibration environment, the test item is usually attached to a host structure as it is illustrated in Fig. 32.1a, forming a combined structure, with unique dynamic characteristics. The test item can be subjected to various forms of excitations [2, 7, 12] such as acoustic and aerodynamic, which is usually the case of flight hardware, contact loads, due to attachments to the host structure, and, in some cases internal loads, as it is the case of rotating unbalanced masses. The test item structural vibration response as measured in the field dynamic environment is due to all these loads, and hence, knowledge of the actual input forces, or at least a set of forces that can reproduce the observed motions of given test item in its field dynamic environment is very important issue in developing realistic vibration testing scenarios.

P. S. Varoto (✉)
Mechanical Engineering Department, Sao Carlos Engineering School, University of São Paulo, São Paulo, Brazil
e-mail: varoto@sc.usp.br

C. Walber et al. (eds.), *Sensors and Instrumentation, Aircraft/Aerospace, Energy Harvesting & Dynamic Environments Testing, Volume 7*, Conference Proceedings of the Society for Experimental Mechanics Series,
https://doi.org/10.1007/978-3-030-12676-6_32

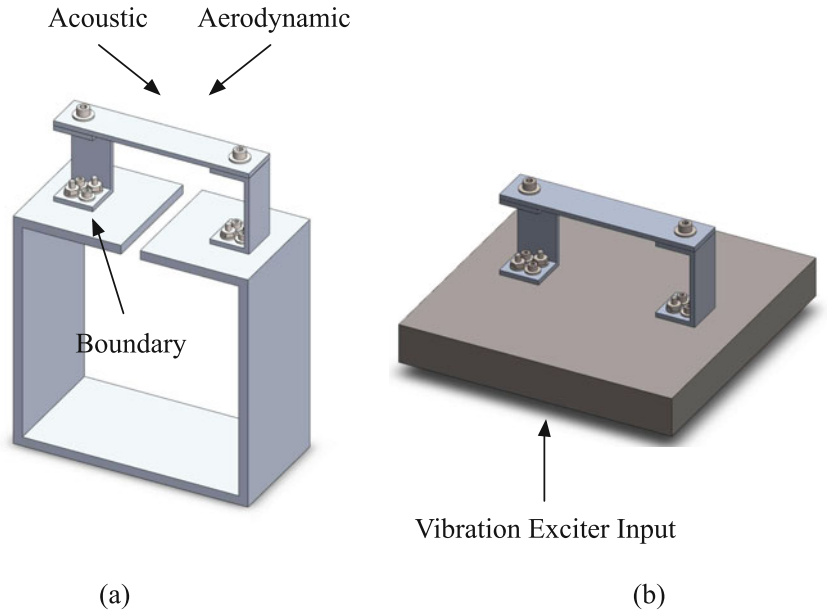

Fig. 32.1 Structural vibration environments: (**a**) Field; (**b**) Laboratory

In the laboratory environment, the test item is mounted on one or more vibration exciters [12] to create a laboratory structure. Usually, the mounting operation requires the use of a test fixture, as illustrated in Fig. 32.1b. The definition of appropriate inputs to the test item such that field vibration data can be properly simulated is crucial in laboratory testing. In this case, field interface forces and possibly motions are natural candidates as test item's input in laboratory simulations. However, interface properties, specially forces are difficult to obtain, since direct measurement of these forces usually requires that force transducers be placed in the forces paths, what naturally would change the test item's field boundary conditions [11]. Additionally, the test fixture has its own dynamic characteristics, that can influence on laboratory test results, and efforts have been endeavored in order to design optimized test fixtures as well as minimize its effects on test results [10, 14].

32.2 Theoretical Background

The purpose of this section is to review important theoretical concepts that directly affect both numerical and experimental aspects of the structures involved in the process of simulating field dynamics environments. The finite element equations of motion of a N degrees of freedom (DOF) viscously damped linear structure subjected to an external harmonic time varying load is written as [1, 3]

$$[M]\{\ddot{u}\} + [C]\{\dot{u}\} + [K]\{u\} = \{f_0\}e^{j\omega t} \tag{32.1}$$

where $[M]$, $[C]$ and $[K]$ are square and symmetric $N \times N$ matrices that account for the mass, damping and stiffness characteristics of the structure under investigation. The $N \times 1$ column vectors $\{f_0\}$ and $\{u\} = \{u(t)\}$ contain the amplitudes of the harmonic excitation at a given excitation frequency ω and the resulting absolute displacements, respectively. Equation (32.1) is the basis of modal analysis and testing when the structure under test is subjected to point applied single of multiple excitation loads.

Alternatively, if the structure is subjected to an external excitation given in terms of an input motion $u_b = u_b(t)$, Eq. (32.1) is re-written as

$$[M]\{\ddot{u}\} + [C]\{\dot{u^r}\} + [K]\{u^r\} = \{0\} \tag{32.2}$$

where the $N \times 1$ vector $\{u^r\} = \{u^r(t)\}$ corresponds to the structure *relative displacement* with respect to the input motion u_b. The absolute and relative displacements are related to each other by the following equation [1]

$$\{u\} = \{u^r\} + \{\delta\}u_b \tag{32.3}$$

where $\{\delta\}$ is a constant $N \times 1$ vector and is used to express the fact that a unit input static displacement in the direction of u_b produces a unit static displacement of all structure DOF in the same direction. In a sense, $\{\delta\}$ can be viewed as an influence coefficients vector that identifies all structure DOF that are in the direction of the input motion x_b. Thus, $\{\delta\}$ is composed of "ones" at the DOF coinciding with the direction of the input motion and "zeros" for the remaining orthogonal DOF. Equation (32.2) is the basis for modeling and conducting experimental texts in vibration testing, also referred to as *transmissibility testing* where the structure under test is usually mounted on the vibration exciter's table through a test fixture [9] and driven by taylored input motions. Under special circumstances, Eq. (32.2) can be also used to identify modal properties of the structure under test. Substitution of Eq. (32.3) in Eq. (32.2) leads to the equation of motion written in terms of the output relative displacement vector

$$[M]\{\ddot{u^r}\} + [C]\{\dot{u^r}\} + [K]\{u^r\} = -[M]\{\delta\}\ddot{u}_b \tag{32.4}$$

and it is seen from Eq. (32.4) that under base input motion the structure is actually driven by an inertia load, as seen from the right hand side of Eq. (32.4).

The structure's *Modal Model* [3], containing its undamped natural frequencies and mode shape vectors is obtained from the solution of the associated conservative and homogeneous problem from Eq. (32.1), under nonzero initial conditions

$$[M]\{\ddot{u}\} + [K]\{u\} = \{0\} \tag{32.5}$$

and solution of Eq. (32.5) is given as a summation of the linearly independent mode shape vectors

$$\{u\} = \sum_{p=1}^{N} \{\phi\}_p \; e^{\lambda_p t} \tag{32.6}$$

where $\{\phi\}_p$ and λ_p are the $N \times 1$ pth-mode shape vector and eigenvalue, respectively. The corresponding undamped natural frequency ω_n is obtained from $\omega_p = (\lambda_p)^{1/2}$. Once undamped natural properties are calculated, the modal model can be arranged in terms of two $N \times N$ matrices, the first being diagonal with the eigenvalues or undamped natural frequencies in the main diagonal entries and the second with the mode shape vectors as arranged in its columns

$$\left[\Omega_p\right] = \begin{bmatrix} \omega_1^2 & 0 & 0 & \dots & 0 \\ 0 & \ddots & \ddots & \ddots & \vdots \\ 0 & \ddots & \omega_p^2 & \ddots & 0 \\ \vdots & \ddots & \ddots & \ddots & 0 \\ 0 & \dots & 0 & 0 & \omega_N^2 \end{bmatrix} \tag{32.7}$$

$$[\Phi] = \left[\{\phi\}_1 \; \{\phi\}_2 \; \dots \; \{\phi\}_p \; \dots \; \{\phi\}_N \right] \tag{32.8}$$

Knowledge of the modal model is crucial in order to obtain the structure's *response model* that is composed of the force and/or transmissibility *frequency response functions* (*FRF*). In this case, the particular solution of Eq. (32.1) or (32.2) are sought for the case of a harmonic load. It is commonly assumed that the structures has a proportional damping spatial distribution and the general format of the resulting damping matrix is given as [1]

$$[C] = [M] \sum_b a_b \left[[M]^{-1} [K] \right]^b \tag{32.9}$$

and when $b = 0, \dots, 1$ the well known Rayleigh damping is obtained ($[C] = a_0[M] + a_1[K]$). Employing the simplest version of the proportional damping from Eq. (32.9) and using the orthogonality conditions [1], particular solutions for Eqs. (32.1) and (32.2) can be found by standard uncoupling modal analysis methods [3] and they are given as

$$\{u\} = \sum_{p=1}^{N} \frac{\{\phi\}_p \, \{\phi\}_p^T \{f_o\}}{m_p \left(\omega_p^2 - \omega^2 + j \; 2\zeta_p \omega_p \omega\right)} \; e^{j\omega t} \tag{32.10}$$

$$\{u^r\} = \omega^2 \sum_{p=1}^{N} \frac{\{\phi\}_p \{\phi\}_p^T [M] \{\delta\}}{m_p \left(\omega_p^2 - \omega^2 + j\, 2\zeta_p \omega_p \omega\right)} x_o\, e^{j\omega t} \tag{32.11}$$

From Eqs. (32.10) and (32.11) the structure's *receptance* and relative displacement transmissibility FRF matrix and vector can be obtained

$$[R(\omega)] = \sum_{p=1}^{N} \frac{\{\phi\}_p \{\phi\}_p^T}{m_p \left(\omega_p^2 - \omega^2 + j\, 2\zeta_p \omega_p \omega\right)} \tag{32.12}$$

$$\{\Gamma^r(\omega)\} = \omega^2 \sum_{p=1}^{N} \frac{\{\phi\}_p \{\phi\}_p^T [M] \{\delta\}}{m_p (\omega_p^2 - \omega^2 + j\, 2\zeta_p \omega_p \omega)} \tag{32.13}$$

where m_p is the *generalized* mass corresponding to the pth-mode shape. The importance of the results presented in the structure's response model, given by Eq. (32.12) or Eq. (32.13) relies on the fact that the entries of such matrices, i.e., the input force and relative input motion transmissibility FRFs are required for the identification of the modal properties of the test structure (damped natural frequencies, modal damping ratios and modal constants). Therefore, not only $[R(\omega)]$ and $\{\Gamma^r\ (\omega)\}$ can be calculated in numerical simulations but most importantly, they are measurable quantities in the general modal testing context.

32.3 Experimental Analysis

The goal of this section is to present some preliminary experimental results of a typical test structure. The structure under test is the previously mentioned Box Assembly with Removable Component (BARC) assembly, that has been subject of investigation among several institutions. Figure 32.2a shows the BARC structure in the laboratory environment where it is suspended by flexible cords in order to proper simulate the freely suspended boundary conditions. In this case, a combination of flexible and thin nylon and bungee cords is employed such that the natural frequencies associated with rigid body motion

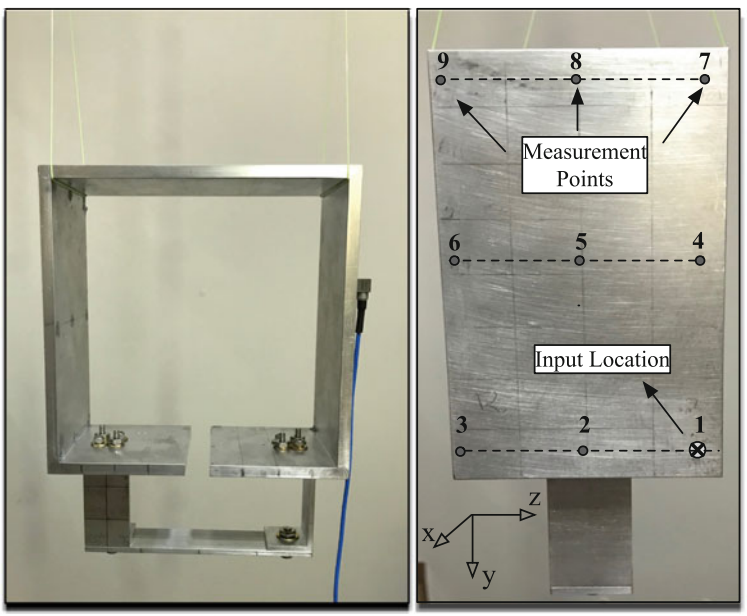

Fig. 32.2 BARC structure suspended by flexible cords: (**a**) front view; (**b**) side view

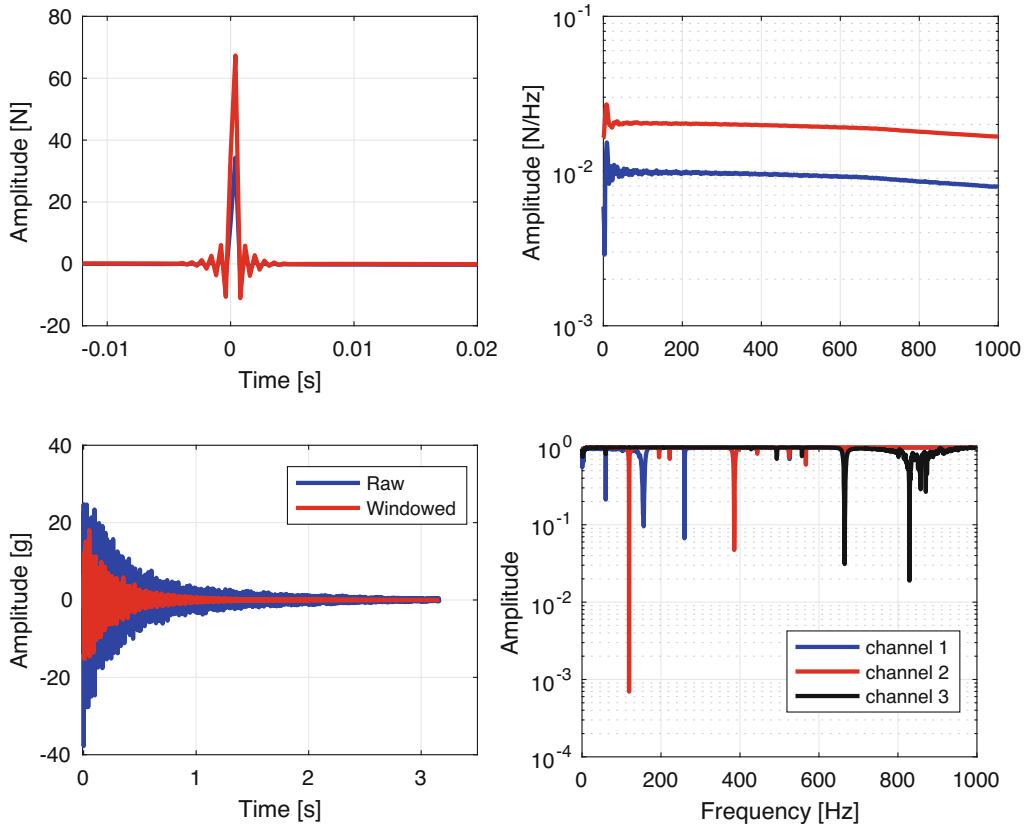

Fig. 32.3 Experimental results from BARC structure

are maintained at very low values. This combination of different materials for the suspension system also contributes for a better definition of the anti-resonance peaks on the measured FRFs since anti-resonances tend to be sensitive to effects of suspension systems in "freely" suspended test structures [9].

Impact modal tests are performed on the BARC structure in order to measure resulting accelerance FRFs. A PCB impact hammer (model 086C03, $S_f = 2.28$ mV/N) is used to provide the excitation signals to the structure under test. No extender mass was used with the impact hammer and two hammer tips were employed, plastic/vinyl and steel. The output acceleration response signals are measured with a PCB 356A01 miniature lightweight tri-axial ICP accelerometer ($S_a = 5$ mV/g, 1 g).

Signal acquisition was performed by using a four channels Data Physics Quattro spectrum analyzer. The analyzer's measuring parameters are set to a 0–1000 Hz frequency range and 3200 spectral lines, thus giving a frequency resolution of $\Delta f = 312.5$ mHz and analysis period of $T = 3.2$ s with time interval between consecutive samples of $\Delta t = 390.6\,\mu$s.

Figure 32.3 exhibits measured input and output signals on two different points shown in Fig. 32.2b. The signals on the upper left corner correspond to impact force signals on points 1 and 7, respectively and the results shown on the upper right corner are the corresponding spectral densities of the input signals. The results shown for the spectral densities of the input signal are reasonably constant along the test frequency range ensuring that all frequencies are properly excited along the 0–1000 Hz frequency range. Signals shown on the lower left and right corners of Fig. 32.3 correspond to the time domain output signals measured with the miniature accelerometer and coherence functions for all three output channels with respect to the reference force channel. In the case of the time domain output responses, the signals depicted on the lower left corner of Fig. 32.3 correspond to the raw and windowed signals, respectively. A force/response window combination was used in the data acquisition system and a 250 ms exponential window was used to filter the accelerometer output signal in order to reduce filter leakage problems during the FFT calculations.

Figure 32.4 shows accelerance FRF measurements obtained from the modal tests on six different points on the structure's side view shown in Fig. 32.2. These measurements are obtained by varying the location of the impact and maintaining the accelerometer at the reference location (point 1). The rational fraction polynomial multi-mode modal identification method using orthogonal polynomials [4] is then used in order to curve-fit the measured accelerance FRFs and identify the corresponding modal parameters. The regenerated FRFs from the identified modal parameters are shown along with the

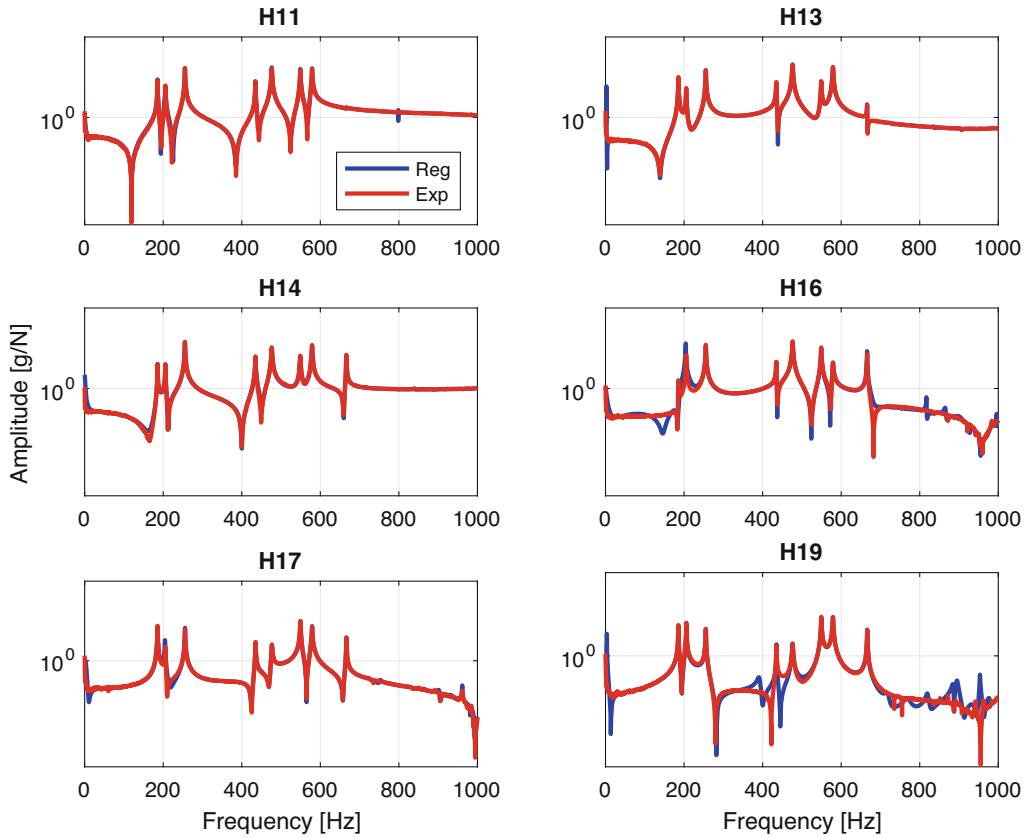

Fig. 32.4 Results from modal identification on BARC structure

Table 32.1 Modal parameters for BARC assembly

Mode No.	ω_p [Hz]	ω_{pref} [Hz]	$\zeta_p(\times 10^{-3})$
1	185.3	184.5	0.7983
2	204.8	205.3	5.1004
3	254.7	255.7	0.9320
4	417.4	428.5	0.9320
5	426.7	437.8	0.6106
6	475.1	470.1	1.2078
7	549.6	550.9	0.7902
8	578.9	576.7	0.6119
9	665.4	653.4	0.6119

corresponding measured FRF in Fig. 32.4. Very good curve fitting results are obtained for all measured FRFs along the entire frequency range. Minor discrepancies are observed in the results for FRFs $H_{16}(\omega)$ and $H_{19}(\omega)$.

The identified modal parameters for a preliminary measurement data set are shown in Table 32.1. A total of nine undamped natural frequencies were identified from the measured accelerance FRFs. Column 1 on Table 32.1 exhibits the values for these frequencies and they are compared to values previously identified on a previous work [6]. A reasonably good correlation is seen from these two results. Modal damping ratios identified from the experimental data is also shown in Table 32.1. Figure 32.5 shows a curve fitted driving point accelerance FRF that employed raw un-windowed data in order to assessment of modal damping ratios without the digital filter damping that is usually present on measured data when exponential windows are used in impact testing. Alternatively, the effects of such additional damping can be compensated from knowledge of the exponential window properties [9].

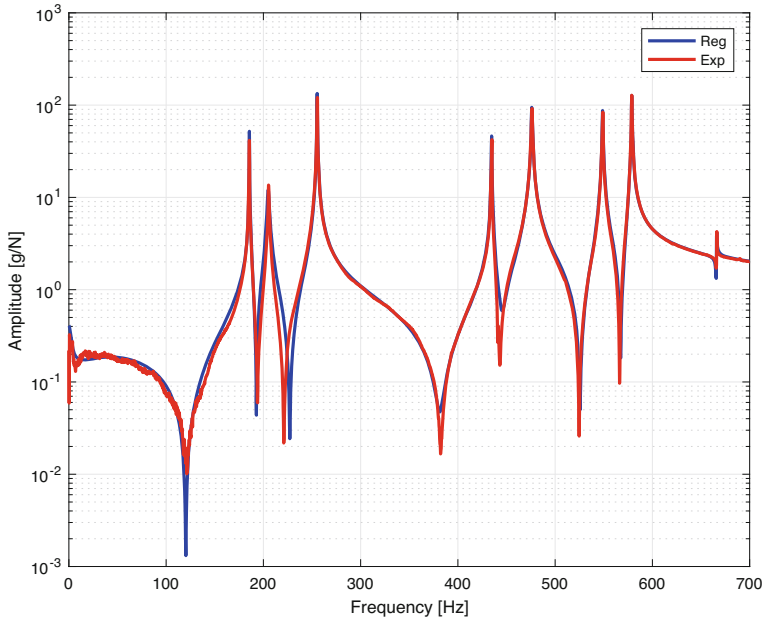

Fig. 32.5 Curve fitting result for rectangular windows

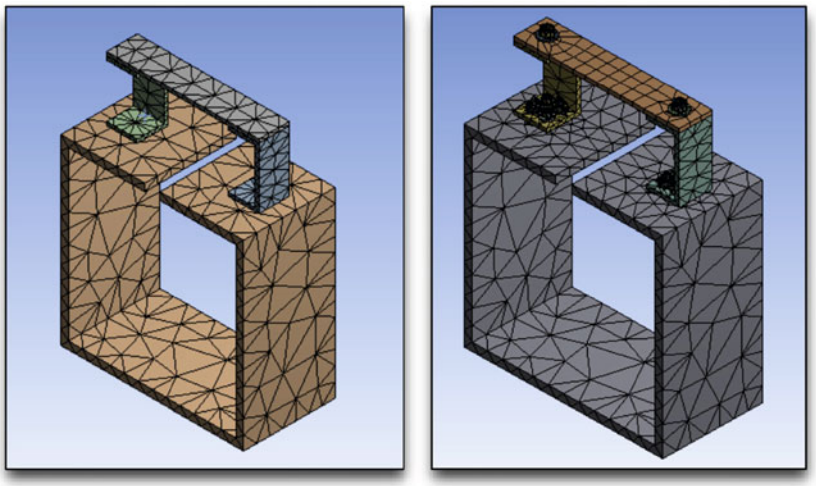

Fig. 32.6 Finite element model of BARC structure: (**a**) No screws; (**b**) with screws, nuts and washers

32.4 Final Remarks

In this article a preliminary modal testing was performed on the BARC assembly. Further measurements are needed in order to construct a reliable model for the test structure. Additionally, a numerical simulation study using the finite element method is currently being carried out. Two models are initially considered, as depicted in Fig. 32.6. The firs model considers the connection between the test item and the host structure neglecting the screws, nuts and washers, but some point masses are added to the model to compensate for the masses of the excluded accessories. The second model attempts to model the connections by adding the screws. Preliminary numerically simulated results point to: (1) The natural frequency corresponding to the fundamental mode shape in both models is at least 10% higher than the measured value when using the model shown in Fig. 32.6a. For the model shown in Fig. 32.6b larger differences are seen to occur. In addition, the natural frequencies associated to rigid body motions, that theoretically should be zero, result in values much higher than zero for the FE model shown in Fig. 32.6, probably due to local stiffness increase at the joints caused by particular meshing

characteristics of the FE software; (2) Results from FE simulations tend to be sensitive for small changes on the geometric parameters of the test structure, specially thickness of the members. This characteristic, already previously observed [6] deserves more attention in future model refinements. Sensitivity and uncertainty analysis are definitively on the road map towards constructing more reliable models for the BARC assembly.

Acknowledgements Author is grateful to SANDIA National Labs and Honeywell Federal Manufacturing & Technologies for the opportunity to be involved in this project. Special acknowledgments to Ms. Julie Harvie, David Soine and Tyler Shoenherr for the support in having one of the BARC assemblies being sent to Brazil. Laboratory support from the University of Sao Paulo and to FAPESP, the funding agency of the state of Sao Paulo, Brazil is very much appreciated.

References

1. Clough, R., Penzien, J.: Dynamics of Structures, 3rd edn. Computers & Structures, Berkeley (2003)
2. Daborn, P.M., Ind, P.R., Ewins, D.J.: Enhanced ground-based vibration testing for aerodynamic environments. Mech. Syst. Signal Process. **49**, 165–180 (2014)
3. Ewins, D.J.: Modal Testing: Theory, Practice and Applications. Research Studies Press, Baldock (2000)
4. Formenti, D., Richardson, M.: Parameter estimation from frequency response measurements using rational fractional polynomials. In: Proceedings of the 1st IMAC, pp. 1–10 (1982)
5. Harvie, J., Mayes, R.: Quantification of dynamic differences between boundary conditions for environment specification improvement. In: Proceedings of the 34th IMAC, pp. 117–131 (2016)
6. Larsen, W., Blough, J., DeClerck, J.P., VanKarsen, C.D.: Initial modal results and operating data acquisition of shock/vibration fixture. In: Proceedings of the 36th IMAC, pp. 1–7 (2018)
7. McConnell, K.G.: From field vibration to laboratory simulation. Exp. Mech. **34**, 181–193 (1994)
8. McConnell, K.G.: Vibration Testing: Theory and Practice, 1st edn. Wiley, New York (1995)
9. McConnell, K.G., Varoto, P.S.: Vibration Testing: Theory and Practice, 2nd edn. Wiley, New York (2008)
10. Reyes, J.M., Avitable, P.: Force customization to neutralize fixture-test article dynamic interaction. In: Proceedings of the 36th IMAC, pp. 1–18 (2018)
11. Scharton, T.: Motion and force controlled vibration testing. In: Proceedings of the IES, pp. 77–85 (1990)
12. Smallwood, D.O.: Multiple shaker random control with cross-coupling. In: Proceedings of the Institute of Environmental Sciences, pp. 341–347 (1978)
13. Soine, D.E., Jones Jr., R., Harvie, J.M., Skousen, T.J., Shoenherr, T.: Designing hardware for the boundary condition Round Robin challenge. In: Proceedings of the 36th IMAC, pp. 1–8 (2018)
14. Starr, M.J., Walsh, T.: Comparison of time-domain objective functions in dynamic fixture optimization. In: Proceedings of the 36th IMAC, pp. 1–3 (2018)

Chapter 33
Clamping Force Effects on the Performance of Mechanically Attached Piezoelectric Transducers for Impedance-Based NDE

Charles M. Tenney, Mohammad A. Albakri, Christopher B. Williams, and Pablo A. Tarazaga

Abstract Impedance-based non-destructive evaluation (NDE) constitutes a generalization of structural health monitoring (SHM), where comparisons between known-healthy reference structures and potentially-defective structures are used to identify damage. The quantity considered by impedance-based NDE is the electrical impedance of a piezoelectric element bonded to the part under test, which is linked to the dynamic vibrational response of the part under test through electromechanical coupling. In this work, the piezoelectric element is not bonded directly to the part under test, but rather to a c-shaped clamp, which is then mechanically attached to the part under test. Under this attachment condition, the effect of clamping force on the sensitivity of the impedance-based evaluation is investigated for machined steel blocks with varying levels of damage severity. The highest clamping force tested (600 lb, 2670 N) was the only condition exhibiting increasing damage metric values with increasing damage severity in the parts under test, suggesting that higher clamping force increases sensitivity to damage.

Keywords Electromechanical impedance · Non-destructive evaluation · Piezoelectrics · Manufacturing defects

33.1 Introduction

Impedance-based non-destructive evaluation (NDE) is rooted in the field of structural health monitoring (SHM). Speaking generally, SHM involves first evaluating a given structure as-built to obtain a 'baseline' state. Periodically thereafter, evaluations of the structure can be gathered and compared to the baseline. Deviations from the baseline indicate changes in the structure, usually interpreted as damage. In increasing order of difficulty, this information may also be used to estimate the severity of damage, estimate the type and location of damage, estimate the remaining useful life of the structure, and inform the decision to perform condition-based maintenance. The use of piezoelectric elements as actuators in SHM [1], combined with the development of electromechanical impedance measurement for structure characterization [2, 3], has led to the development of high-frequency interrogation for the detection of small, local defects [4].

Impedance-based NDE constitutes a generalization of the SHM process described above through introduction of inter-part comparisons. Instead of comparing a structure to itself over time, potentially-damaged structures are compared to known-healthy reference structures [5]. Here, the quantity being compared is the electrical impedance of a piezoelectric element bonded to the structure. Due to electromechanical coupling, the electrical impedance of the element is affected by the dynamic vibrational response of the structure. Impedance-based NDE assumes that two structures with the same measured state are equivalent, so that if one is undamaged, so must the other be undamaged.

C. M. Tenney (✉)
Vibrations, Adaptive Structures and Testing (VAST) Laboratory, Department of Mechanical Engineering, College of Engineering, Virginia Tech, Blacksburg, VA, USA

Design, Research, and Education for Additive Manufacturing Systems (DREAMS) Laboratory, Department of Mechanical Engineering, College of Engineering, Virginia Tech, Blacksburg, VA, USA
e-mail: charten@vt.edu

M. A. Albakri · P. A. Tarazaga
Vibrations, Adaptive Structures and Testing (VAST) Laboratory, Department of Mechanical Engineering, College of Engineering, Virginia Tech, Blacksburg, VA, USA

C. B. Williams
Design, Research, and Education for Additive Manufacturing Systems (DREAMS) Laboratory, Department of Mechanical Engineering, College of Engineering, Virginia Tech, Blacksburg, VA, USA

C. Walber et al. (eds.), *Sensors and Instrumentation, Aircraft/Aerospace, Energy Harvesting & Dynamic Environments Testing, Volume 7*, Conference Proceedings of the Society for Experimental Mechanics Series,
https://doi.org/10.1007/978-3-030-12676-6_33

Impedance-based NDE is of particular interest for structures with complex internal geometry, such as those achievable through additive manufacturing (AM). In previous studies by the authors, bonded piezoelectric elements have been used to detect voids in polymer-based AM specimens [6, 7] and conduct in-situ monitoring of polymer specimens during fabrication [8]. Additionally, previous efforts have shown that the piezoelectric element need not necessarily be directly bonded to the specimen, but instead the element can be bonded to a clamp which is then mechanically attached to a specimen [9].

In this work, impedance-based NDE performed using an instrumented clamp is studied in greater detail. In particular, the effect of clamping force on the effectiveness of damage detection through an instrumented clamp is investigated. In order to isolate the effect of clamping force from fabrication-related uncertainty, machined steel blocks are used as test specimens. This improves consistency between samples compared to additively manufactured specimens, and allows a wide range of clamping forces to be investigated without concern of specimen damage or deformation. Using impedance measurements for damaged and undamaged specimens over a range of clamping forces, a relationship between clamping force and sensitivity to defects is developed using common damage metrics.

33.2 Background

Impedance-based NDE examines the dynamic vibrational response of a test object and compares that response to some established baseline. The rationale for this comparison is that changes in mass, stiffness, and damping that result from manufacturing defects will manifest as changes in the object's dynamic response, affecting the frequency and magnitude of the object's resonances.

To make clear how the electrical impedance of the piezoelectric is related to the mechanical properties of the part under test, we will consider the case of a monolithic piezoelectric wafer excited in the 31 mode: electrical stimulus is applied across the thickness (3-direction), and strain is developed along the length (1-direction). For other configurations, a similar result can be derived. The basic concept relies only on the developed strain in the piezoelectric element sufficiently exciting the part under test.

First, the constitutive equations for linear piezoelectricity that capture the 31 mode are shown in Eq. (33.1) [10]

$$\begin{aligned} \varepsilon_{11} &= s_{11}^{E}\sigma_{11} + d_{13}E_3 \\ D_3 &= \left(d^T\right)_{31}\sigma_{11} + \epsilon_{33}^{\sigma}E_3 \end{aligned} \tag{33.1}$$

where ε_{11} is the normal strain in the 1-direction, s_{11}^{E} is the complex elastic compliance constant measured at constant electric field, σ_{11} is the normal stress in the 1-direction, d_{13} and $(d^T)_{31}$ are piezoelectric constants, E_3 is the electric field strength in the 3-direction, D_3 is the charge displacement in the 3-direction, and ϵ_{33}^{σ} is the complex permittivity in the 3-direction measured at constant stress.

For a test object, the dynamic response to excitation at any particular frequency can be approximated by a single degree of freedom system as shown in Fig. 33.1. The parameters of the system can be written as m_r, k_r, and ζ_r, denoting mass, stiffness, and damping, respectively.

Then, assuming the piezoelectric transducer is perfectly bonded to the test object, Eq. (33.2) shows the electrical impedance of the transducer written in terms of the properties of the piezoelectric and of the test object [2, 11].

$$Z(\omega) = \left[i\omega \frac{bl}{h} \left(\frac{d_{11}^2}{s_{11}^{E}} \left(\frac{\tan(kl)}{kl} \left(\frac{Z_{pzt}}{Z_{pzt} + Z_{st}} \right) - 1 \right) + \epsilon_{33}^{\sigma} \right) \right]^{-1} \tag{33.2}$$

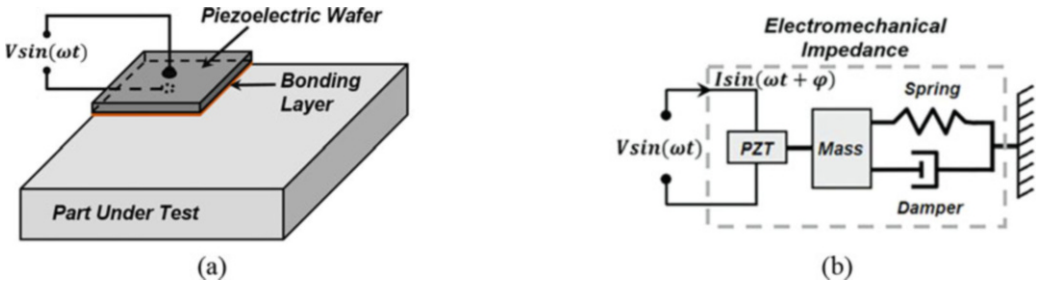

Fig. 33.1 (**a**) A piezoelectric transducer bonded to a test object and (**b**) an abstract system diagram for the arrangement in (**a**) when excited at a particular frequency [7]

where $Z_{pzt} = -i\,(bh/l)\left(s_{11}^{E}\omega\tan(kl)/kl\right)^{-1}$ is the piezoelectric transducer impedance under short-circuit conditions, $Z_{st} = 2\zeta_r(k_r m_r)^{1/2} + i(m_r\omega^2 - k_r)/\omega$ is the mechanical impedance of the test object, $k = \omega\left(\rho s_{11}^{E}\right)^{1/2}$ is the wavenumber, ρ, b, h, and $2l$ are the piezoelectric density, width, thickness, and length, respectively.

In order to quantitatively compare impedance signatures, Root-Mean-Square Deviation (RMSD) and a correlation metric (r) will be used as damage metrics. Increase in either damage metric value corresponds to divergence between the two signatures being compared, and this divergence will be interpreted as damage. This procedure has been carried out in many other studies, including the ones conducted by the authors of this paper [6, 7, 9]. These metrics can be calculated using Eqs. (33.3 and 33.4).

$$RMSD = \frac{1}{n}\sqrt{\sum \frac{(Z_D - Z_{BL})^2}{Z_{BL}^2}} \tag{33.3}$$

$$r = 1 - \left| \frac{n\sum Z_D Z_{BL} - \sum Z_D \sum Z_{BL}}{\sqrt{\left[n\sum Z_D^2 - \left(\sum Z_D\right)^2\right]\left[n\sum Z_{BL}^2 - \left(\sum Z_{BL}\right)^2\right]}} \right| \tag{33.4}$$

where Z_D is the impedance signature of the part being tested, Z_{BL} is the baseline impedance signature, and n is the number of data points in each impedance signature. As defined above, these metrics converge to zero when two signatures are identical, and increase as the signatures become less similar.

33.3 Test Specimen Design and Instrumentation

The test specimens considered in this study, shown in Fig. 33.2, are rectangular steel blocks 4 × 2 × 1 inches in size (101.6 × 50.8 × 25.4 mm). The control specimens weigh 2.28 lb (1.03 kg). Some of the specimens have had damage introduced in the form of a slot milled along one side. In all cases the slot length and width are identical, 4 and 0.5 inches (101.6 and 12.7 mm), while the slot depth is varied to represent various levels of damage severity. The slot depths are 0.1, 0.2, and 0.3 inches (2.5, 5, and 7.5 mm), which produce a mass reduction of 2.5, 5, and 7.5%, respectively, compared to the control specimens.

Additionally, each block specimen is instrumented with a circular piezoceramic element nominally 1 inch (25.4 mm) in diameter and 0.1 inch (2.5 mm) thick. In all cases, the piezoceramic is bonded to the face reverse of the slot in the lower right corner, labeled "4" on the undamaged control block shown in Fig. 33.2.

The instrumented clamp used here, shown in Fig. 33.3, is a small, metal, c-shaped clamp with a threaded rod that can be advanced to adjust the clamping force. On the bottom face, a macro-fiber composite (MFC) piezoelectric element is bonded to provide actuation/sensing capability. On the back face, a strain gauge is bonded to monitor the clamping force. The clamp fits within a volume of 4.1 × 2.5 × 2.4 inches (105 × 65 × 60 mm) when the threaded rod is retracted to minimize the height of the clamp. When fully extended, the clamp will accept an object with a height of approximately 2.9 inches (73 mm).

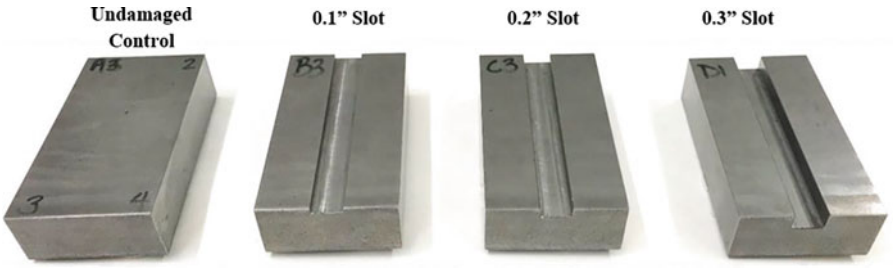

Fig. 33.2 Overview of specimen types. Control specimens are rectangular blocks, and damage is represented by slots milled along one face at several depths to represent damage severity

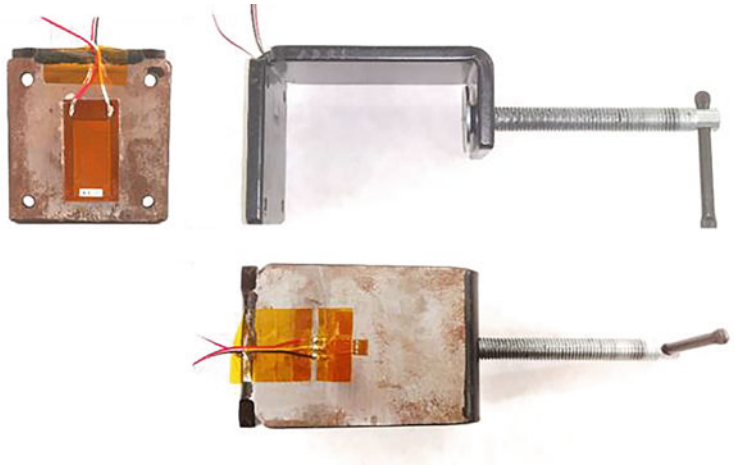

Fig. 33.3 The instrumented clamp. At upper left, the MFC can be seen bonded to the bottom side of the clamp, at lower right, a strain gauge can be seen that is used to monitor clamping force

For collection of impedance signatures using the instrumented clamp, the block specimens are clamped through their 2 inch dimension with the slot facing inwards, towards the strain gauge. To increase the repeatability of the boundary conditions, a mark was scribed on each block to mark where the threaded rod should contact the block. Additionally, a small ball bearing was placed between the block surface and the end of the threaded rod to simplify the boundary condition. The bearing both minimizes any torque applied to the specimen as the clamping force is adjusted and allows the contact point to be precisely positioned.

33.4 Test Procedure

The testing in this paper consists of two main sections: first, a standard impedance-evaluation of specimens using the directly-bonded piezoceramic elements is presented for reference, then an impedance-evaluation of specimens using the MFC patch bonded to the instrumented clamp is conducted at several clamping-force levels: 150, 300, and 600 lb (approximately 665, 1330, and 2670 N).

Prior to testing, the output of the strain gauge bonded to the clamp was calibrated using a force transducer gripped in the same manner as the specimens. The strain gauge output was produced by a Vishay 2110 strain gauge conditioner. A sensitivity of 200 lb/V was selected to make good use of the output voltage range of the conditioner.

During all tests, the impedance signature was collected using a Keysight E4490A impedance analyzer: a device built to precisely produce and measure sinusoidal voltage and current signals. A typical setup for impedance signature measurement is shown in Fig. 33.4. Evaluations of the impedance of the specimens were made over the range of 10–100 kHz at 20 Hz intervals. This resolution was chosen to minimize measurement time of the full spectrum while providing about 5–6 samples over the width of a typical resonant peak. Additionally, during all testing, the specimens were placed on a foam pad to reduce any effect of the surface during measurement.

33.5 Assessment of Specimen Uniformity

In this section, we will examine the impedance signatures of the blocks on their own, without the clamp attached, as measured by the piezoceramic elements bonded to each specimen. This is the typical procedure for impedance-based NDE, and will provide a basis for comparison when we examine the impedance signatures obtained from the clamped specimens in the following section.

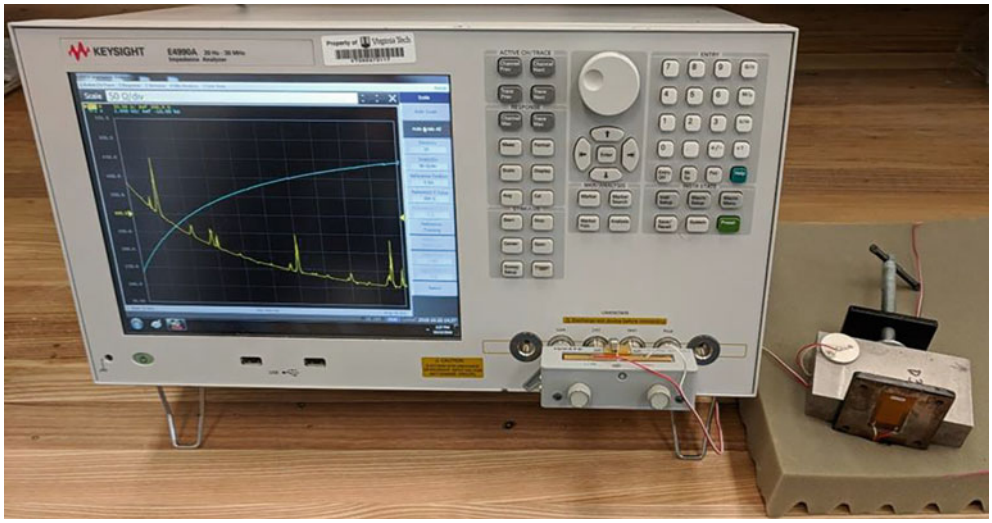

Fig. 33.4 Typical setup for impedance signature measurement. An impedance analyzer gathers data from the MFC patch bonded to the instrumented clamp while attached to a block specimen

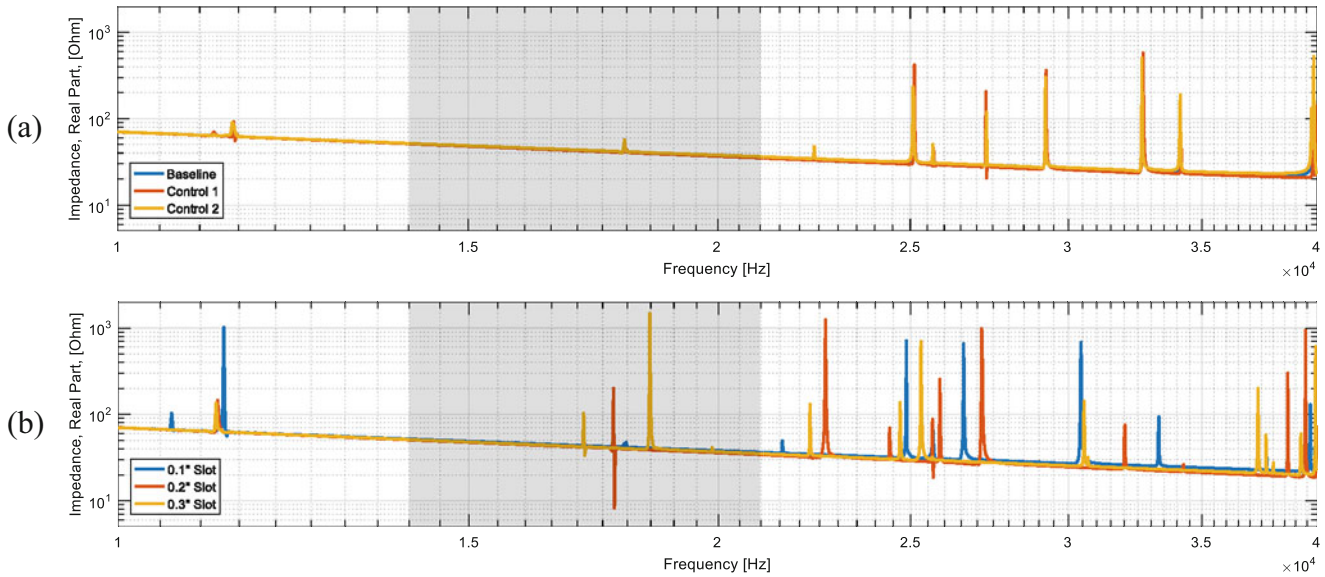

Fig. 33.5 Two signatures from undamaged control specimens are shown in (**a**), along with a calculated baseline: the arithmetic mean of the control specimen signatures. In (**b**), a signature from each of the three block specimens with varying levels of damage. The gray areas from 14 to 21 kHz will be examined in more detail below

In Fig. 33.5, the impedance signatures of five specimens are shown: two undamaged control specimens and three damaged specimens at three levels of severity. From the control specimen signatures, a baseline signature is calculated by taking their arithmetic mean. This baseline signature is intended to represent a typical signature for an undamaged specimen. The signature is limited to 40 kHz on the high end because the control signatures showed less agreement above that frequency, and 10 kHz on the low end because there were no resonant peaks observed below that value in initial testing.

It is evident from inspection of the impedance signatures that the control specimens are fairly consistent with one another, while the damaged specimens yield impedance signatures that are both different from the controls and from each other. The peaks around 18 kHz, indicated by the gray regions in Fig. 33.5, appear to be particularly sensitive to the depth of the slot.

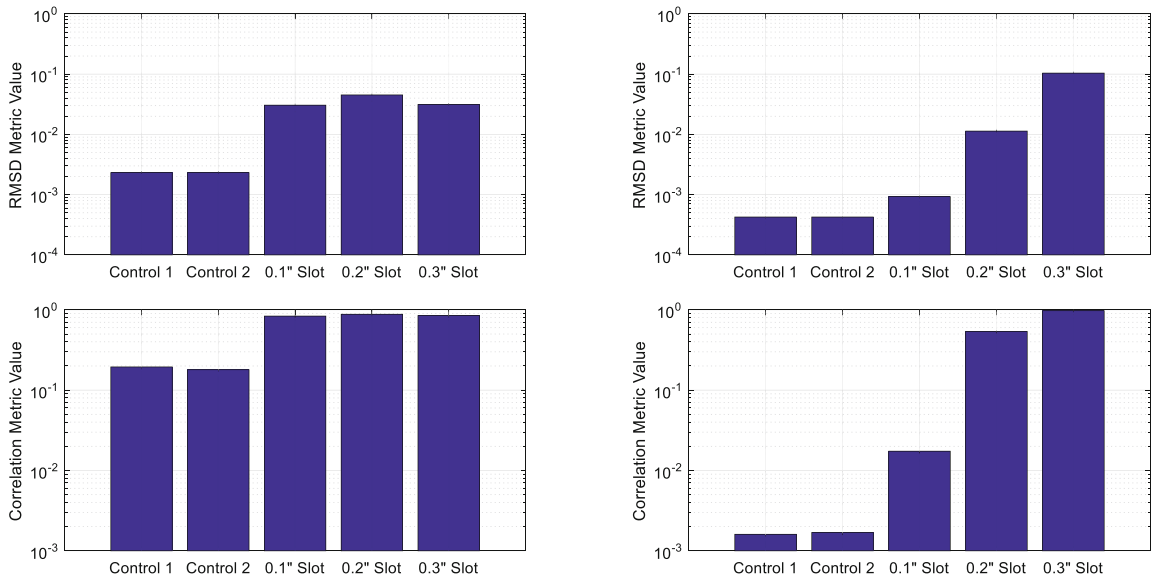

(a) 10 – 40 kHz (b) 14 - 21 kHz

Fig. 33.6 Damage metrics calculated between each block signature and the control group baseline over the intervals (**a**) 10–40 kHz and (**b**) 14–21 kHz. As expected, the damage metrics are small when the control specimens are compared to the baseline, and high when the damaged specimens are compared to the baseline

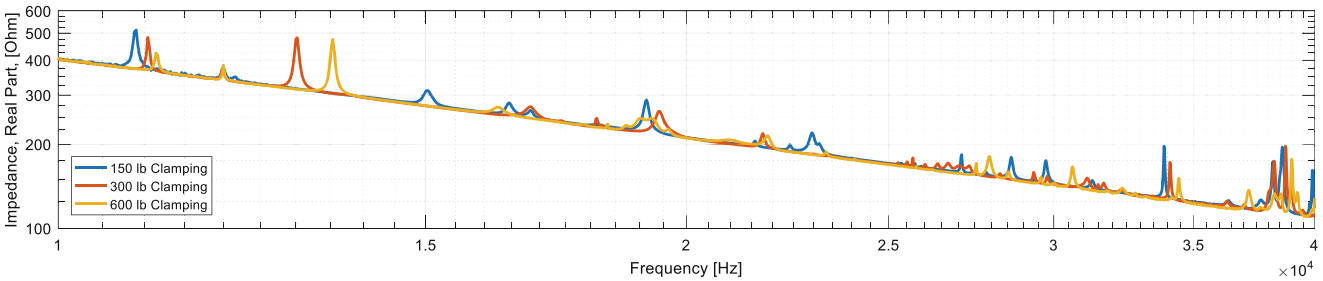

Fig. 33.7 Impedance signature for the undamaged control specimen measured by the clamp MFC over the interval 10–40 kHz as clamping force is varied. Peaks at 11 and 34 kHz show a clear increase with clamping force

To quantify the damage severity, damage metric values are presented in Fig. 33.6. The damage metrics, evaluated over the 10–40 kHz interval, show significantly better agreement between the controls and the baseline than between the damaged specimens and the baseline. However, the severity of damage is not apparent from metrics calculated over this wide range. Isolating a region where one resonant peak appears to shift in response to increasing damage severity, Fig. 33.6b, the damage metrics indicate a trend. In the following section, we will examine the same 14–21 kHz interval for the clamped measurement.

33.6 Assessment of the Influence of Clamping Force

In this section, the impedance evaluation will be conducted using the MFC bonded to the instrumented clamp at several levels of clamping force and for all levels of damage severity. The impedance signatures will be presented first, followed by the calculated damage metrics.

Before assessing the changes in the impedance signature due to damage severity, it should be noted that the changes in clamping force will also be expected to change the signature. In Fig. 33.7, the response of the undamaged control specimen is presented as measured by the instrumented clamp for the three clamping force levels.

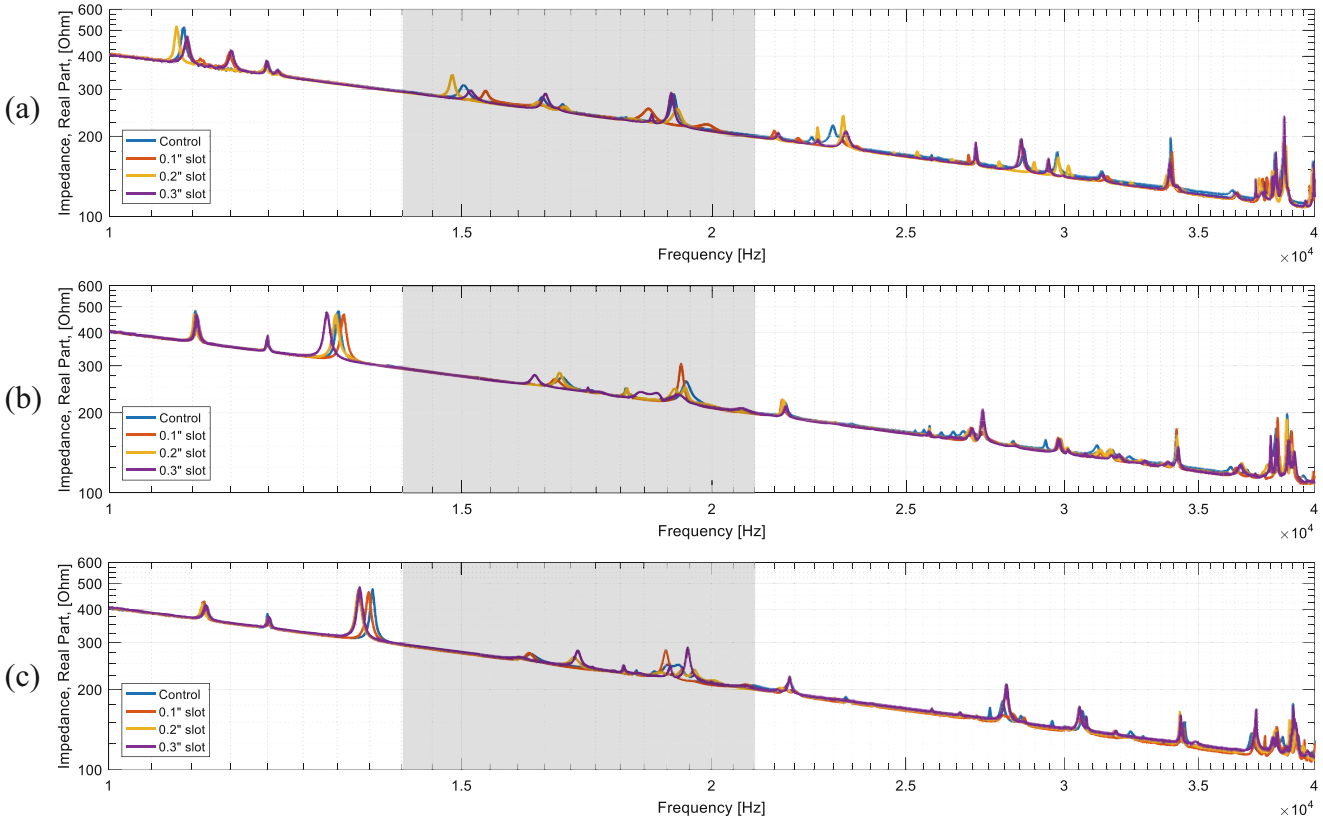

Fig. 33.8 Impedance signatures for each specimen as measured by the instrumented clamp over the interval 10–40 kHz for several clamping force levels: (**a**) 150 lb, (**b**) 300 lb, and (**c**) 600 lb. The regions in gray, 14–21 kHz, are the same frequency interval indicated in Fig. 33.5

At certain frequency ranges in the signature, such as 11 and 34 kHz, a clear trend of increasing peak frequency with clamping force is observed. For other resonant peaks, a clear relationship between clamping force and frequency shifts has not been observed.

Now, we will examine the change in impedance signature with damage severity at each tested clamping force level, shown in Fig. 33.8. In the clamped configuration, the impedance signature is less sensitive to damage severity as compared to measurements from a directly bonded element. Essentially, this is because the measurement is less direct: the damage in the test specimen is being inferred by its effect on the dynamics of the instrumented clamp.

As done in the previous section, we can evaluate damage metrics first over the entire interval then over a smaller interval where a limited number of peaks reside. The 14–21 kHz interval was chosen for comparison because it isolates a group of resonant peaks for both the directly-bonded impedance signatures in the previous section, and the impedance signatures measured by the instrumented clamp here.

In this case, the metric values (Fig. 33.9) are not as clearly influenced by the level of damage severity as they were in the directly bonded case. In fact, only in the 600 lb case is there an increase in the damage metric values with increasing damage severity. This would indicate that the sensitivity to damage severity increases with clamping force. This indication is also supported by the consistency of the trend in both frequency ranges. The 600 lb case shows an increasing trend with damage severity over both frequency ranges considered, while the 300 lb case shows a somewhat consistent trend, and the 150 lb case shows different trends.

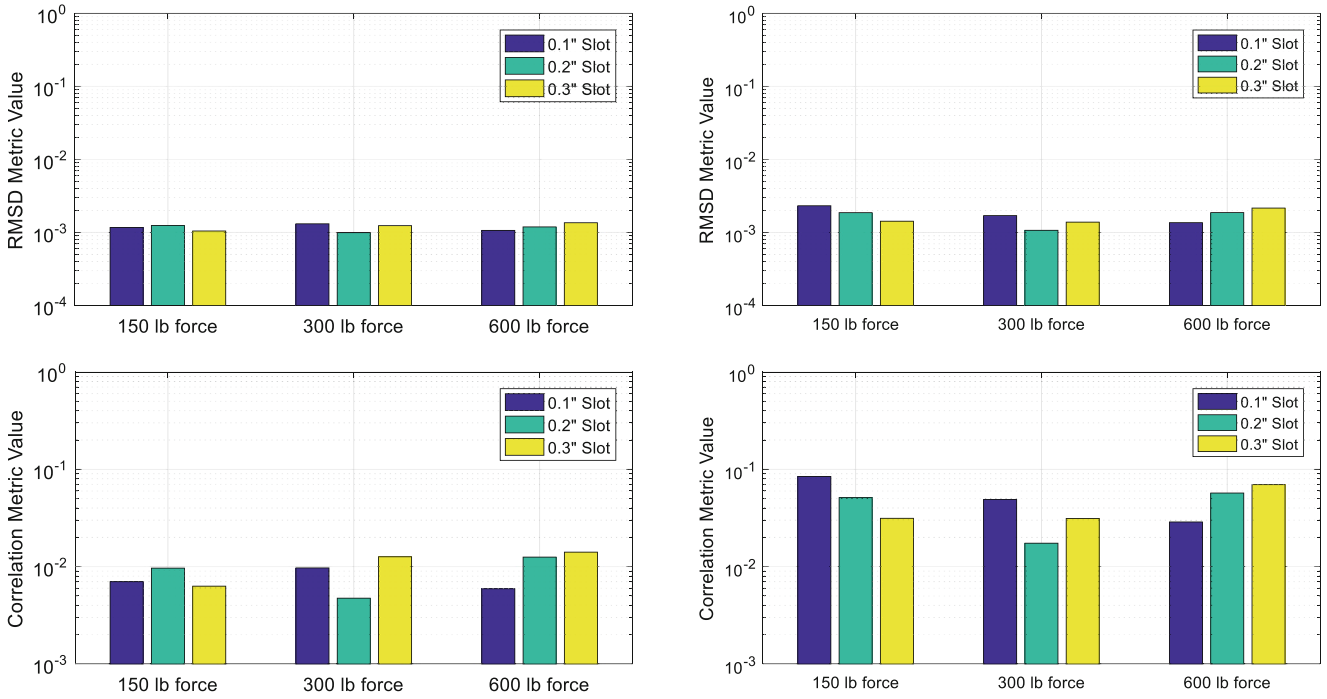

(a) 10 – 40 kHz (b) 14 - 21 kHz

Fig. 33.9 Damage metrics calculated between the damaged specimens and the undamaged control specimen over the intervals. (**a**) 10–40 kHz and (**b**) 14–21 kHz. At 150 and 300 lb, the severity of the damage is not apparent from the damage metrics. At 600 lb, the damage metrics increase with the level of damage in both cases

33.7 Conclusions

In this work, the effect of clamping force on the sensitivity of a mechanically-attached transducer for impedance-based NDE was investigated. The sensitivity was evaluated by first collecting the impedance signature for the test specimens over a wide range, selecting a smaller range where control specimens showed good agreement, selecting a region that isolated a group of resonant peaks for all damage severities, and finally calculating the values of common damage metrics over that range.

To provide reference values for the damage metrics, the test specimens were initially evaluated with directly-bonded piezoceramic elements. Then, the specimens were re-evaluated using an instrumented clamp to collect the impedance signature. It was found that the directly bonded piezoceramics showed high sensitivity to the damage in the test specimens, showing order-of-magnitude changes in the damage metric at different severity levels over the 14–21 kHz frequency range. For the data collected from the instrumented clamp, the damage metric showed much smaller changes between damage severity levels in the same interval, on the order of 50–200% changes in value. In the clamped case, only the highest-force case showed increases in damage metric values with increasing damage severity for the evaluated frequency ranges.

Going forward, further work needs to be done to quantify the uncertainty of the evaluations presented above. By repeating measurements for the same conditions, it would be possible to check whether the observed trends at the 600 lb clamping force are statistically significant. Additionally, considering more force levels and additional specimens would make the results more robust.

Acknowledgments The authors would like to thank Mr. T. Komolafe for providing the steel block specimens. Dr. Tarazaga would like to acknowledge the support provided by the John R. Jones III Faculty Fellowship. This material is based upon work supported by the National Science Foundation under Grant Number CMMI-1635356. Any opinions, findings, and conclusions or recommendations expressed in this material are those of the author(s) and do not necessarily reflect the views of the National Science Foundation.

References

1. Crawley, E.F., De Luis, J.: Use of piezoelectric actuators as elements of intelligent structures. AIAA J. **25**(10), 1373–1385 (1987)
2. Liang, C., Sun, F.P., Rogers, C.A.: Coupled electro-mechanical analysis of adaptive material systems-determination of the actuator power consumption and system energy transfer. J. Intell. Mater. Syst. Struct. **8**(4), 335–343 (1997)
3. Peairs, D.M., Tarazaga, P.A., Inman, D.J.: Frequency range selection for impedance-based structural health monitoring. J. Vib. Acoust. **129**(6), 701–709 (2007)
4. Naidu, A.S.K., Bhalla, S., Soh, C.K.: Incipient damage localization with smart piezoelectric transducers using high-frequency actuation. In: Proceedings of SPIE (2002)
5. Worden, K., Farrar, C.R., Manson, G., Park, G.: The fundamental axioms of structural health monitoring. Proc. R. Soc. A Math. Phys. Eng. Sci. **463**(2082), 1639–1664 (2007)
6. Albakri, M.I., Sturm, L.D., Williams, C.B., Tarazaga, P.A.: Impedance-based non-destructive evaluation of additively manufactured parts. Rapid Prototyp. J. **23**(3), 589–601 (2017)
7. Tenney, C., Albakri, M.I., Kubalak, J., Sturm, L.D., Williams, C.B., Tarazaga, P.A.: Internal porosity detection in additively manufactured parts via electromechanical impedance measurements. In: ASME 2017 Conference on Smart Materials, Adaptive Structures and Intelligent Systems, Snowbird, UT (2017)
8. Sturm, L., Albakri, M., Williams, C.B., Tarazaga, P.: In-situ detection of build defects in additive manufacturing via impedance-based monitoring. In: 27th Annual International Solid Freeform Fabrication Symposium – An Additive Manufacturing Conference (2016)
9. Tenney, C., Albakri, M.I., Williams, C.B., Tarazaga, P.A.: NDE of additively manufactured parts via directly bonded and mechanically attached electromechanical impedance sensors. In: International Modal Analysis Conference XXXVI, Orlando, FL (2018)
10. Meitzler, A.H., Tiersten, H.F., Warner, A.W.: An American National Standard IEEE Standard on Piezoelectricity (1987)
11. Park, G., Sohn, H., Farrar, C.R., Inman, D.J.: Overview of piezoelectric impedance-based health monitoring and path forward. Shock Vib. Dig. **35**(6), 451–463 (2003)

Chapter 34
Data Based Modeling of Aero Engine Vibration Responses

Manu Krishnan, Ran Jin, Ibrahim A. Sever, and Pablo A. Tarazaga

Abstract Data based modeling has garnered increased interests in the last decade in vibration response classification, particularly so if the relationships between the response variables and the forcing functions are complex and dependent on multiple factors. Aero engines are one of the most heavily instrumented parts of an aircraft, and the data from various types of instrumentation across these engines are continuously monitored both offline and online for potential anomalies. Measured aero engine responses vary widely in character and amplitude depending on the operating conditions and prevailing environmental conditions. The majority of the vibration assessment is done via monitoring engine vibration levels to fundamental shaft rotational orders. However, focus on shaft orders in isolation may not expose the full picture when a range of other factors are also known to be in effect during operation of a complex machine such as an aero engine. Various complex relationships exist between different parameters such as vibration, temperature, pressure, etc., which are all captured via different instrumentation and vary from engine to engine. A global model to establish the association among the sensitivities of various parameters via their existing instrumentation is highly desirable to establish accurate engine behavior.

In the present work, a data-driven approach towards modeling aero engine vibration responses will be presented. This will utilize instrumentation sensor data of various types, which has been generated from a series of test bed runs. Further, empirical relationships and correlation among different types of sensor measurements with the aero engine responses will also be presented.

Keywords Principal component analysis · Vibration · Lasso · Correlation

34.1 Introduction

One of the most sensitive parameters for continuous monitoring of the condition of aero-engines are engine vibrations. These vibrations are captured by one or more accelerometers mounted at carefully selected casing positions [1]. With these in-service gained signals and additional parameters from the various types of instrumentations across the engines, it is possible to reliably model the engine vibration using a data based approach. The data based methodology takes into account the data from different instrumentation such as temperature, pressure, velocity, etc. and utilize them to build a model. This is in contrary to conventional physics based methodologies which might be limited in scope and overlook the various complex relationships among the different parameters.

This work is divided into the following four main sections. First, some basic description of the data processing is shown. Second, a principal component analysis approach is used to reduce the data to its most basic and independent form. Third, a mapping approach is used to understand the interdependence of the variables with respect to each other. And Fourthly, a regression model is built and the most important variables describing the overall behavior are found.

M. Krishnan (✉)
Vibrations, Adaptive Structures, and Testing Lab, Department of Mechanical Engineering, Virginia Tech, Blacksburg, VA, USA
e-mail: manukris@vt.edu

R. Jin
Department of Industrial Systems and Engineering, Virginia Tech, Blacksburg, VA, USA

I. A. Sever
Rolls-Royce plc, Derby, UK

P. A. Tarazaga
Vibrations, Adaptive Structures and Testing (VAST) Laboratory, Department of Mechanical Engineering, College of Engineering, Virginia Tech, Blacksburg, VA, USA

C. Walber et al. (eds.), *Sensors and Instrumentation, Aircraft/Aerospace, Energy Harvesting & Dynamic Environments Testing, Volume 7*, Conference Proceedings of the Society for Experimental Mechanics Series,
https://doi.org/10.1007/978-3-030-12676-6_34

34.2 Data Preprocessing

The initial set of data contains a large number of variables out of which only a few of them are vibration variables. The objective of the present work is to model those vibration response variables using all the other relevant variables in the data set, hereafter referred to as the predictor variables. The data is generated from a test bed which is acquired over a span of several days. These data sets contain several cycles of the engine switching on and off. To have some uniformity in the data analysis procedure, the whole data has been divided into 10 zones, where each zone corresponds to one cycle of engine testing.

34.3 Data Reduction Using Principal Component Analysis

Principal Component Analysis (PCA), also known as Karhunen–Loève transform, is a multivariate statistical method that can be applied for dimensionality reduction, lossy data compression, feature extraction and data visualization. PCA is a linear orthogonal transformation that maps a set of physical variables to a new set of acquired virtual variables [2]. It also helps in reducing a complex data set to a lower dimension thereby revealing some hidden and simplified structures associated with the data set. In the present work, the dimensionality reduction capability of PCA is used to obtain a preliminary idea regarding the dimensionality of the data and to reveal outliers in the data.

It is important to remove the outliers from the analysis as it will lead to erroneous modeling as well as modeling of instances that might not represent any real conditions (i.e., sensor fallout, noise, etc.) (Fig. 34.1).

34.4 Correlation Mapping

Once the dimensionality of the data is known and outliers are removed, it is important to understand how the response variables are correlated with other predictor variables. The variables causing outliers in each of the zones are identified using PCA and removed from the further analysis. Figure 34.2 reveals insight into the most important variables from the vibration standpoint of view. The response variables are arranged from variable 72–77. A closer look on the rectangular portion of Fig. 34.2 reveals the correlation of different variables with the vibration variables. From the correlation "heat map" across different zones, it is observed that vibration variables are highly correlated with variables numbered 1–5, 21–28, and 31–38.

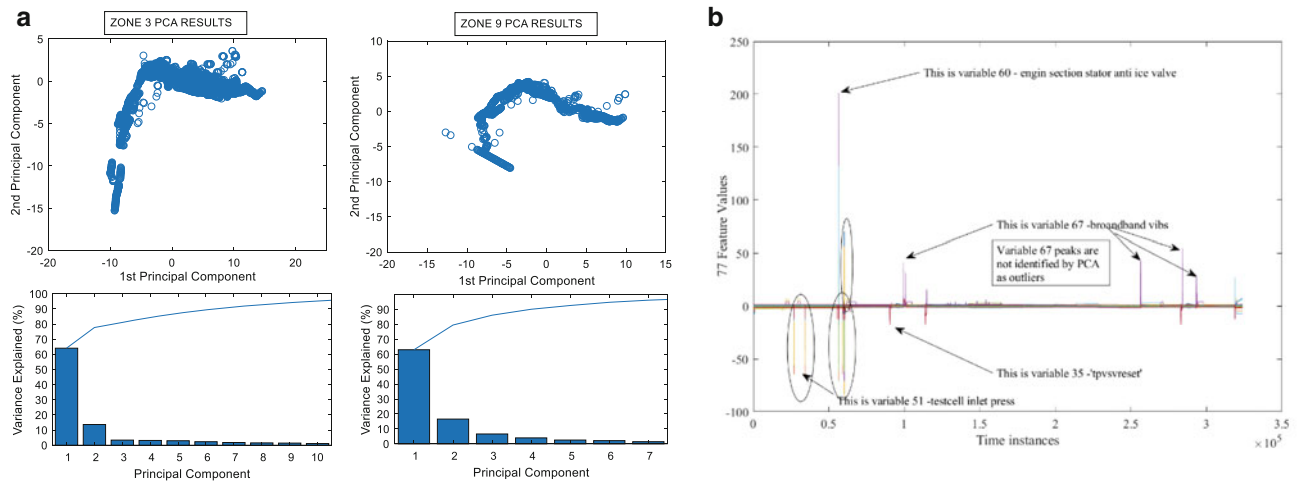

Fig. 34.1 A basic PCA analysis over certain zones is shown: (**a**) Zone 3 and Zone 9 PCA results demonstrating the low dimensionality of the data. (**b**) Outliers from the PCA clusters traced back in time axis

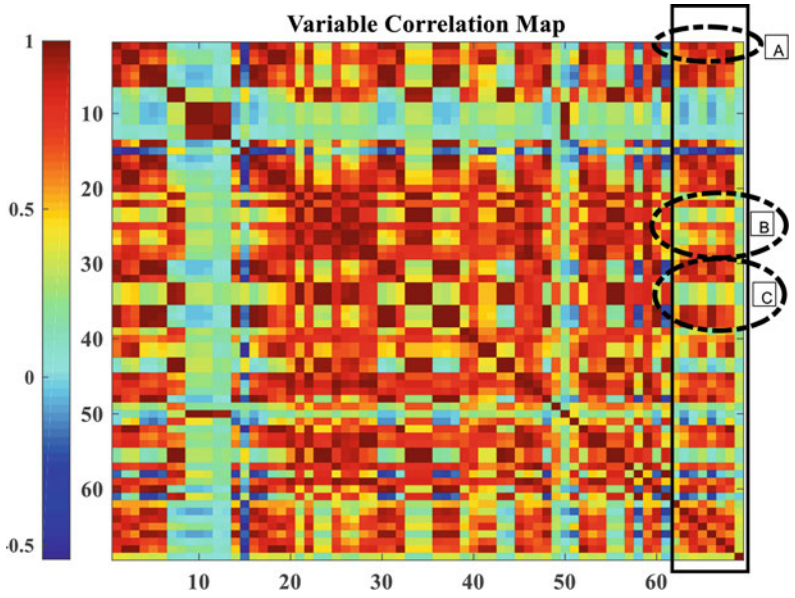

Fig. 34.2 Correlation "heat map" of Zone 4 between all the variables considered

It is also interesting to note that there are certain variables that do not indicate any correlation with the vibration variables. These variables are removed from the model building step to improve the efficiency of the analysis and reduce the model size requirements.

34.5 Regression Model Building and Variable Selection

The main objective of the present work is to model the vibration responses with the other predictor variables. The correlation "heat map" presented some insight about the variables which are highly correlated and also enabled the removal of redundant predictor variables from the analysis. In the present work, Lasso regression with automatic feature selection [3] is utilized to model the vibration response. For a given value of λ, a nonnegative parameter, Lasso solves the equation

$$\min_{\beta_0,\beta}\left(\frac{1}{2N}\sum_{i=1}^{N}\left(y_i-\beta_0-x_i^T\beta\right)^2+\lambda\sum_{j=1}^{p}|\beta_j|\right) \tag{34.1}$$

where N is the number of observations, y_i is the response at the observation which is the corresponding vibration response, x_i is data, a vector of length p at observation i. The parameters β, β_0 are a scalar and a vector of length p, respectively. λ is the most crucial tuning parameter and the performance of the model depends on the value of λ. The choice of λ depends on the data, hence cross validation is used to obtain the accurate estimation of λ. Once the parameters are obtained, different Lasso regression models are built which corresponds to the total number of vibration response variables.

Figure 34.3 shows the Lasso regression modeling result for one of the vibration variables of interest. It is evident from the figure that the proposed methodology captures the underlying trend in the response variable, but fails to map the variance in the data. This could be attributed to the absence of higher order terms and interaction terms in Eq. (34.1).

34.6 Conclusion

In the study,data based modeling of an aero engine vibration response is presented. The current work utilizes data generated from various onboard sensors to model its vibration response using different instrumentation sensor data as the predictor variables. Towards the same, standard data analysis steps are employed such as data preprocessing, data reduction, and

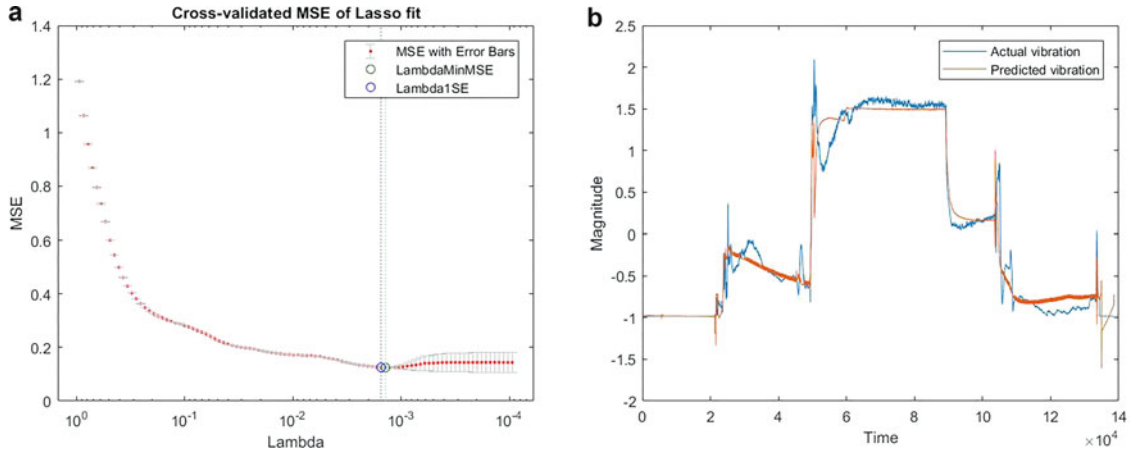

Fig. 34.3 Regression model for vibration response prediction: (**a**) Cross validation results for selecting optimal value of the tuning parameter λ and (**b**) Lasso modeling results for one of the vibration response variable

correlation analysis. Correlation analysis allowed the removal of redundant variables from the modeling step. The proposed methodology with Lasso regression provided an accurate estimation regarding the trend of the data, but higher order terms and interaction variables are required to capture the variance of the response. The work demostrated promise in being able to determine the crucial variables needed and then use such variables to develop a first stage model.

Acknowledgments Authors would like to acknowledge the generous support from Rolls Royce, UK. (TO#18-VT-20; PO 8000-00052929) that provided the funding for this project. Dr. Tarazaga would also like to acknowledge the support received through the John R. Jones III Faculty Fellowship.

References

1. Sever, I.A.: Nonlinear vibration phenomena in aero-engine measurements. In: Dynamics of Coupled Structures, vol. 4, 2016, pp. 241–252, Springer, Cham (2016)
2. Jolliffe, I.: Principal component analysis. In: International Encyclopedia of Statistical Science, pp. 1094–1096. Springer, Berlin (2011)
3. Tibshirani, R.: Regression shrinkage and selection via the Lasso. J. R. Stat. Soc. Ser. B (Methodological). **58**, 267–288 (1996)

Chapter 35
Experimental Mode Verification (EMV) Using Left-Hand Eigenvectors

Robert N. Coppolino

Abstract Estimation of structural dynamic modes associated with complicated spacecraft and launch vehicle assembly modal test articles is often a challenging endeavor. The mathematical process of modal parameter estimation, applied to measured FRF arrays, yields actual and artificial "noise" modes. Left-hand eigenvectors, estimated as part of the SFD modal identification technique, are used to compute SDOF modal FRFs from (a) the measured FRF array and (b) the estimated "effective" dynamic system. Both graphical displays of candidate SDOF modal FRFs and a modal "coherence" metric provide objective means of separating actual, credible system modes from artificial "noise" modes. Evaluation of modal test data for a Space Launch System component demonstrates the value of the new Experimental Mode Verification (EMV) technique.

Keywords Test · Mode · Verification · Left · Eigenvectors

35.1 Introduction

Verification and validation of modern aerospace systems, particularly NASA's Space Launch System (SLS), is a particularly challenging endeavor due to a variety of complicating factors including (1) high modal density in the important 0–50 Hz (primary structural loads) frequency band, (2) associated pronounced parametric uncertainty and sensitivity, and (3) the presence, in some components, of non-negligible nonlinearity. The first and second complicating factors are addressed by modern finite element analysis methods [1], systematic experimental modal analysis [2], and U.S. Government standards [3, 4]. Specific SLS challenges and solutions were documented in a recent NASA contractor report [5], which should be regarded as a "progress report". The present paper and its close companion [6] represent further progress on the subject of experimental mode verification (EMV).

Challenges encountered by NASA/MSFC on the Integrated Spacecraft Payload Element (ISPE) modal survey in the fall of 2016 bring an important challenge to the forefront. Specifically, which estimated test modes are "authentic", and which modes are associated with "noise" associated with measured frequency response functions (FRFs)? The present paper on EMV focuses on mathematical isolation of individual estimated test mode FRFs in a manner that is similar to the concept developed by Mayes and Klenke [7]. While the presently discussed EMV approach ought to be quite independent of the investigator's choice of experimental modal analysis algorithm, the results herein apply to methods that explicitly estimate the tested system's state-space plant matrix such as the Simultaneous Frequency Domain (SFD) method [8–10].

The present paper employs mathematical operations aimed at isolating individual candidate experimental modes without direct reliance on information associated with the subject system's mathematical model, specifically its "test-analysis model" (TAM) mass matrix. The key to mathematical and visual isolation of individual modes from measured data is the left-hand eigenvector. Virtually all modern experimental modal analysis techniques produce estimates of (right-hand) eigenvectors and eigenvalues (modal frequency and damping). While techniques for estimation of left-hand eigenvectors are well-known (e.g., the "real mode transpose times TAM mass matrix product" and the Moore-Penrose pseudo-inverse [11]), they have been judged inadequate during the course of the present EMV study. The purest approach to estimation of left-hand eigenvectors is a consequence specifically of those techniques that estimate the measured system's plant or effective dynamic system matrix. Since a complete set of raw experimental modes are identified consistent with the order of the estimated plant, the left-hand eigenvectors are calculated exactly from the inverse of the complete, raw right-hand eigenvector set.

R. N. Coppolino (✉)
Measurement Analysis Corporation, Torrance, CA, USA
e-mail: rcoppolino@macorp.net

C. Walber et al. (eds.), *Sensors and Instrumentation, Aircraft/Aerospace, Energy Harvesting & Dynamic Environments Testing, Volume 7*, Conference Proceedings of the Society for Experimental Mechanics Series,
https://doi.org/10.1007/978-3-030-12676-6_35

The following metrics provide a systematic basis for EMV:

1. The estimated Single-Degree-of-Freedom (SDOF) modal FRF, formed by the product of a single estimated left-hand eigenvector and measured FRF matrix, is plotted in terms of real and imaginary components vs. frequency, magnitude and phase components vs. frequency, and polar real vs. imaginary components. Authenticity of an estimated mode is then judged on the basis of quality of the plots.
2. The SDOF modal FRF is alternatively formed from exact mathematical solution of the estimated effective dynamic system. Graphical comparison of this result with the above left-handed product information offers further means of "authentic" vs. "noise" mode discrimination.
3. Finally, the coherence metric based on comparison of the results of "1" and "2" provides a 0-to-100% figure of merit for estimated experimental modes.

35.2 Nomenclature

Symbol	Definition		Symbol	Definition
[A]	State Variable Plant Matrix		$[\Phi]$	Modal Matrix
[B]	Viscous Damping Matrix		$[\Phi_L]$	Left-Hand Modal Matrix
COH	Modal Coherence		γ	Generalized Force Allocation Matrix
{F}	Excitation Force		η	State-Space Generalized Displacement
[H]	Frequency Response Function		ω	Frequency (rad/sec)
[K]	Stiffness Matrix		$\xi(f)$	SVD Generalized Displacement
[M]	Mass Matrix			
[R]	Residual Error Matrix		Subscript	Definition
[Γ]	Excitation Force Allocation Matrix		$(\,)_n$	Modal
[U]	Physical Displacement Matrix		$(\,)_\eta$	State-Space
[V]	SVD Trial Vector Matrix		$(\,)_A$	Analytical
			$(\,)_E$	Experimental
f	frequency (Hz)			
[h]	Generalized Frequency Response		Superscript	Definition
{q}	Modal Displacement		$[\tilde{\ }]$	Effective Dynamic System Matrix

35.3 Preliminary Thoughts

Consider a structural dynamic system subjected to applied excitation forces,

$$[M]\{\ddot{u}\} + [B]\{\dot{u}\} + [K]\{u\} = [\Gamma]\{F\}\,. \tag{35.1}$$

On the assumption that the real eigenvectors of the undamped system ($[B] = [0]$) represent a reasonable set of system modes,

$$\{u\} = [\Phi]\{q\}\,, \text{ where the diagonal modal matrices are,} \tag{35.2}$$

$$\left[\Phi^T M\right][\Phi] = [I]\,, \quad \left[\Phi^T K \Phi\right] = \left[\omega_n^2\right], \quad \left[\Phi^T B \Phi\right] \approx [2\zeta_n \omega_n]\,. \tag{35.3}$$

The uncoupled modal acceleration frequency responses are therefore (noting $\omega = 2\pi f$),

$$\ddot{q}_n(f)/F(f) = h_n(f) = \frac{-(f/f_n)^2}{1-(f/f_n)^2 + 2i\zeta_n(f/f_n)}\left(\Phi_n^T\Gamma\right) \tag{35.4}$$

Finally, the relationship between physical and modal frequency response functions is

$$[\ddot{u}(f)] = [H(f)] = [\Phi][h(f)], \text{ where } [h(f)] \text{ is the array of modal frequency responses.} \tag{35.5}$$

If the physical frequency responses, [H(f)], and modal vectors, [Φ], are "known" based on experimental modal analysis, then the uncoupled modal responses, [h(f)], may be estimated by manipulation of Eq. (35.5), specifically

$$[h(f)] = [\Phi]^{-1}[H(f)]. \tag{35.6}$$

Since a truncated set of modes are typically estimated in experimental modal analysis, there are two options for computation of the result in Eq. (35.6), namely, (a) exploitation of the mass-weighted modal orthogonality relationship in Eq. (35.3), and (b) estimation of $[\Phi]^{-1}$ as the Moor-Penrose pseudo-inverse of [Φ]. The first option is theoretically exact, i.e.,

$$[h(f)] = \left[\Phi^T M\right][H(f)]. \tag{35.7}$$

Accuracy of the above expression requires employment of the approximate theoretical TAM mass matrix. It is desired that the estimate for $[\Phi]^{-1}$ should not be contingent on mathematical model accuracy; evaluation of experimental modal analysis results should initially, at least, be independent of model predictions. While the second option, which employs the Moore-Penrose pseudo-inverse of [Φ] is independent of model predictions, it can be shown to substantially deviate from the theoretical inverse, $[\Phi^T M]$, in many situations. The continuing discussion presented below, addresses this issue for the cases of both real and complex experimental modal vectors.

35.4 The Simultaneous Frequency Domain (SFD) Method

The SFD method [8], introduced in 1981, has undergone substantial revision and refinement since that time [9, 10], primarily by this writer and principals at The Aerospace Corporation. SFD implicitly assumes that FRFs associated with a series of "N" excitations may be described in terms of a transformation described by,

$$\left[\ddot{U}_1(f)\ \ \ddot{U}_2(f)\ \ldots\ \ddot{U}_N(f)\right] = [V]\left[\ddot{\xi}_1(f)\ \ddot{\xi}_2(f)\ldots\ddot{\xi}_N(f)\right] \tag{35.8}$$

By performing SVD analysis of the FRF collection, a dominant set of real generalized trial vectors, [V], and complex generalized FRFs, $\left[\ddot{\xi}_1(f)\ \ddot{\xi}_2(f)\ldots\ddot{\xi}_N(f)\right]$, is obtained. Unit normalization of the SVD trial vectors is expressed as,

$$[V]^T[V] = [I] \tag{35.9}$$

Theoretically, the generalized FRF array describes the following dynamic system equations associated with the individual applied forces,

$$\left[\ddot{\xi}(f)\right] + \left[\tilde{B}\right]\left[\dot{\xi}(f)\right] + \left[\tilde{K}\right][\xi(f)] = \left[\tilde{\Gamma}\right][F(f)], \text{ where } \left[\tilde{B}\right] = \left[M^{-1}\right][B] \text{ and } \left[\tilde{K}\right] = \left[M^{-1}\right][K] \tag{35.10}$$

The real, effective dynamic system matrices, $\left[\tilde{B}\right]$, $\left[\tilde{K}\right]$, and $\left[\tilde{\Gamma}\right]$, are estimated by a linear least-squares analysis procedure. Estimation of experimental modal parameters is performed by complex eigenvalue analysis of the state variable form of the effective dynamic system,

$$\begin{Bmatrix}\ddot{\xi}\\ \dot{\xi}\end{Bmatrix} = \begin{bmatrix}-\tilde{B} & -\tilde{K}\\ I & 0\end{bmatrix}\begin{Bmatrix}\dot{\xi}\\ \xi\end{Bmatrix} + \begin{bmatrix}\tilde{\Gamma}\\ 0\end{bmatrix}\{F\}, \text{ which is of the general type, } \{\dot{\eta}\} = \left[A_\eta\right]\{\eta\} + \left[\Gamma_\eta\right]\{F\}. \tag{35.11}$$

Complex eigenvalue analysis of the effective dynamic system produces the following results:

$$\begin{aligned}
&\text{(a) } \{\eta\} = \left[\Phi_\eta\right]\{q\}\text{, where the "left-handed" eigenvectors are } \left[\Phi_{\eta L}\right] = \left[\Phi_\eta\right]^{-1} \\
&\text{(b) } \left[\Phi_{\eta L}\right]\cdot\left[\Phi_\eta\right] = [I]\,,\ \left[\Phi_{\eta L}\right]\cdot\left[A_\eta\right]\left[\Phi_\eta\right] = [\lambda] \text{ (complex eigenvalues)} \\
&\text{(c) } \left[\Phi_{\eta L}\right]\cdot\left[\Gamma_\eta\right] = [\gamma] \text{ (modal gains)} \\
&\text{(d) } \dot{q}_j - \lambda_j q_j = (\gamma)_j\,[F(f)] \text{ (frequency response of individual modes)}\,.
\end{aligned} \tag{35.12}$$

Recovery of experimental modes in terms of the physical DOFs involves back transformation employing the trial vector matrix, [V].

35.5 Selection of Valid Experimental Modal Data

Estimation of the effective dynamic system with the SFD method (and more generally any method that performs similar system "plant" estimation operations) will pick up spurious "noise" degrees of freedom and associated spurious modes. Over the years since 1981, the writer has employed a heuristic practice in versions of SFD algorithms that select "authentic" modes from the complete set, which is estimated in selected frequency bands. The heuristic criteria include, (1) elimination of modes having negative damping, (2) elimination of modes having very low modal gain, and (3) other modes that appear spurious from any number of physical/experience based considerations. The present discussion is a radical departure from past practice in that it replaces heuristic criteria with more rigorous criteria. The initial point of departure from past SFD practice is estimation of an effective dynamic system over the entire frequency band of interest (in the case of ISPE, the range is 15–65 Hz). In order to achieve a satisfactory estimation for the effective dynamic system, the "tolerance" factor employed in the SVD process described by Eqs. (35.8–35.9) is set to a sufficiently low value (10^{-5}); in previous "band-limited" SFD calculations, the SVD "tolerance" factor was set to a value of 10^{-2}. Computation of effective dynamic system modal parameters, from the first-order system described in Eq. (35.11), yields complex modes with eigenvalues having negative and positive imaginary parts. The first level of mode down-selection is to eliminate all modal eigenvalues and eigenvectors that are outside the positive frequency band of interest; for the ISPE modal test, there are 106 complex eigenvalues in the 15–65 Hz frequency band. A vital component of the mode down-selection process is selection of left-hand eigenvectors. $[\Phi_{\eta L}]$ that correspond to their $[\Phi_\eta]$ counterparts; this circumvents issues associated with more involved procedures for computation of a truncated left-hand eigenvector set.

Two computational procedures estimate uncoupled experimental modal FRFs. The first method computes the exact modal solution from the estimated modal parameters of Eq. (35.12d). Specifically,

$$\left(h_j\right)_A = \left(\dot{q}_j\right)_A = \left(\frac{i2\pi f}{i2\pi f - \lambda_j}\right)(\gamma_j)\,. \tag{35.13}$$

The second method estimates uncoupled experimental modal FRFs from linear combinations of the generalized FRFs (see Eqs. (35.12a) and (35.12b)) as follows:

$$\left(h_j\right)_E = \left(\dot{q}_j\right)_E = \left[\Phi_{\eta L}\right]_j \times (\dot{\eta}) \tag{35.14}$$

Verification and validation of any candidate estimated experimental mode is now to be judged on the basis of (a) graphical displays of the modal FRFs, and (b) a new modal coherence metric, which is defined as,

$$COH_j = \frac{\left|\left[h_j(f)\right]_A^* \times \left[h_j(f)\right]_E\right|^2}{\left|\left[h_j(f)\right]_A^* \times \left[h_j(f)\right]_A\right| \times \left|\left[h_j(f)\right]_E^* \times \left[h_j(f)\right]_E\right|} \tag{35.15}$$

35.5.1 ISPE Experimental Mode Verification (EMV)

The Integrated Spacecraft Payload Element (ISPE), depicted in Fig. 35.1, was the subject of modal testing at NASA/MSFC in the fall of 2016. Measured FRF data was quite extensive, and the NASA team had a great deal of difficulty in estimation of modal parameters in the 0–65 Hz frequency band. These challenges led to development of the present EMV methodology.

Uncoupled modal FRF estimates, computed using Eq. (35.13) (red) and Eq. (35.14) (blue) for several candidate modes illustrated in Figs. 35.2, 35.3 and 35.4, include FRF magnitude, magnitude and phase, polar, and real and imaginary parts.

It is clear in the above three figures that candidate modes 1 and 3 appear valid based on close agreement of the two types of uncoupled modal FRF estimates. In contrast, candidate mode 6 appears to be "spurious".

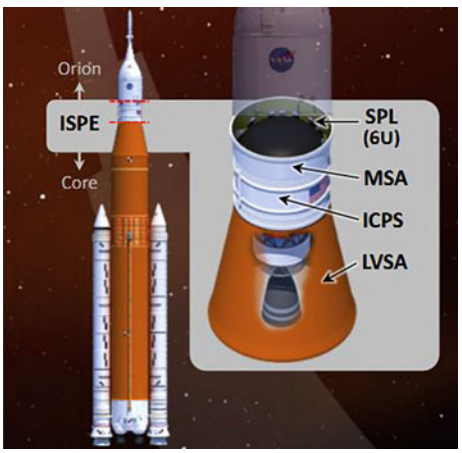

Fig. 35.1 ISPE pictorial (Courtesy of NASA)

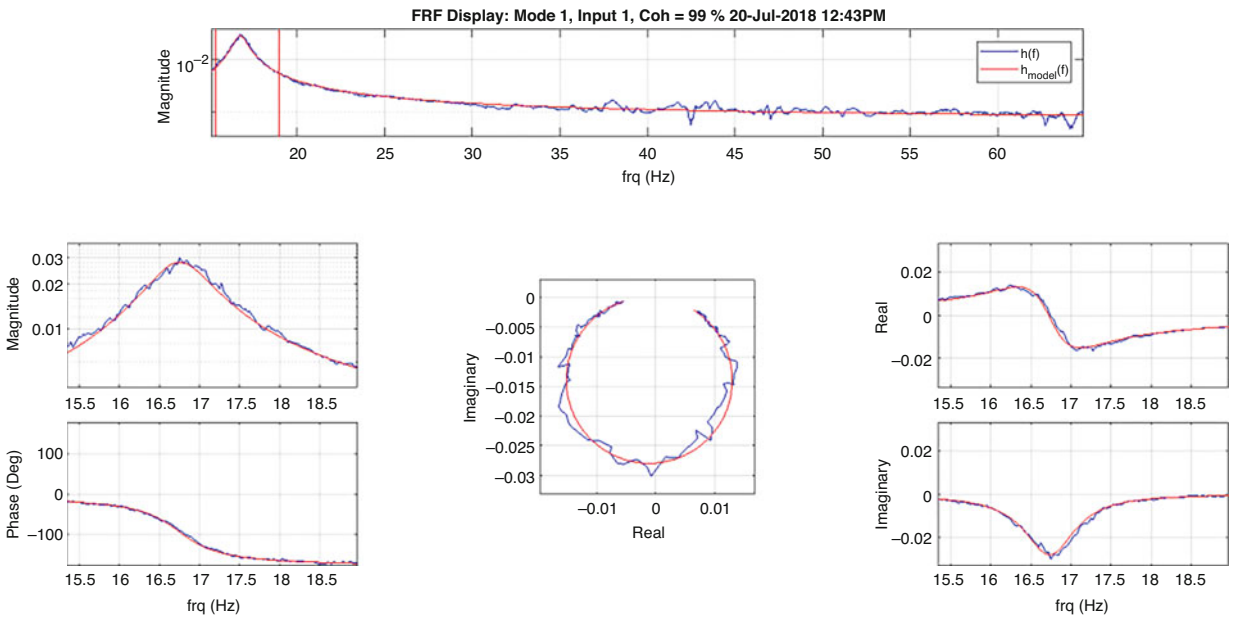

Fig. 35.2 EMV for SFD candidate mode 1, excitation 1 (99% coherence)

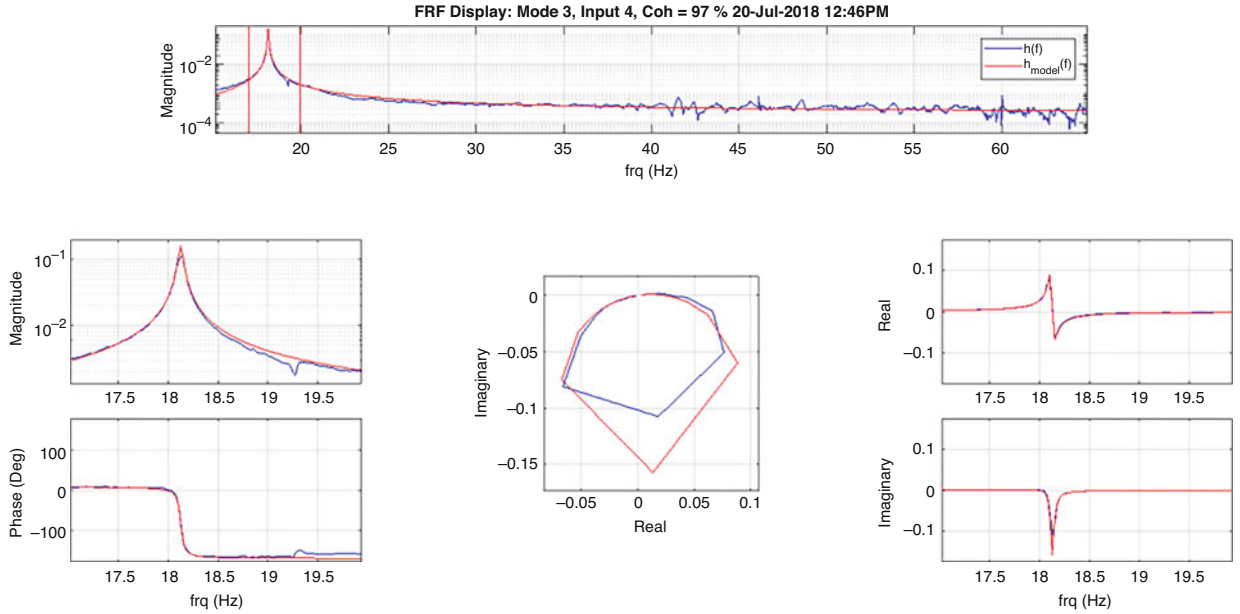

Fig. 35.3 EMV for SFD candidate mode 3, excitation 4 (97% coherence)

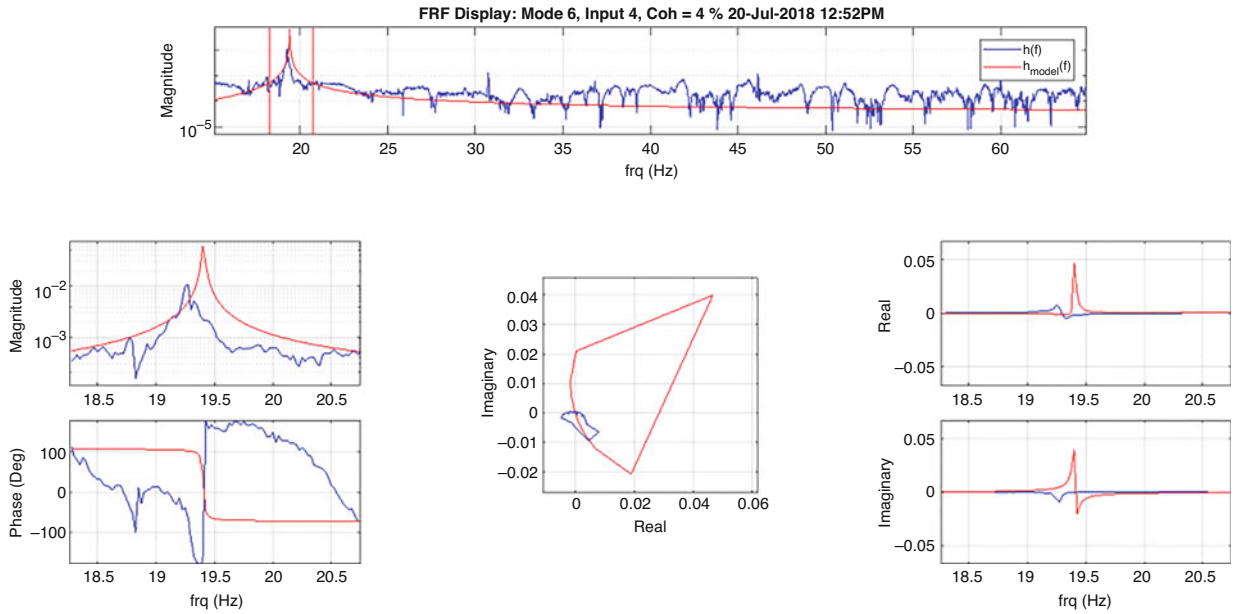

Fig. 35.4 EMV for SFD candidate mode 6, excitation 4 (4% coherence)

Table 35.1, shown below summarizes additional information related to the process of selection of 63 acceptable experimental modes from the 106 candidate modes (the first 30 candidate modes and associated modal coherences are illustrated).

The above table provides a clear demonstration of the utility of the newly introduced EMV metric. In particular, the modal coherence metric defined in Eq. (35.15) for which a value of 85% or greater is assumed to indicate a validly estimated mode.

Table 35.1 EMV modal selection criterion ($COH_j \geq 85\%$) for candidate modes 1–30

Candidate	Eigenvalue		Modal Coherences			
Mode	FREQ (Hz)	Zeta (%)	Excitation 1	Excitation 2	Excitation 3	Excitation 4
1	16.74	2.32	99.15	98.92	98.31	88.97
2	17.03	2.25	72.99	97.67	98.62	98.75
3	18.12	0.12	70.97	69.87	73.51	97.16
4	18.16	0.12	97.08	78.26	85.15	42.25
5	18.79	0.12	94.47	87.10	97.41	95.45
6	19.40	0.05	2.80	3.24	1.91	3.54
7	20.08	3.22	93.57	76.25	94.66	92.82
8	20.31	3.07	95.26	94.92	90.67	88.32
9	20.96	0.10	86.89	96.19	93.10	91.52
10	21.01	0.09	96.43	91.40	89.60	88.14
11	23.23	2.14	39.31	23.98	4.12	34.13
12	24.05	0.02	27.91	29.69	18.24	40.46
13	24.07	0.48	83.55	99.34	98.94	99.46
14	24.26	0.45	99.71	99.46	99.33	34.16
15	24.95	1.81	36.78	44.96	54.73	33.49
16	25.82	0.15	99.69	96.55	95.00	95.85
17	25.89	0.12	78.20	96.91	89.74	98.99
18	27.70	1.40	98.84	95.49	95.59	98.57
19	27.79	1.69	96.85	98.79	98.58	96.55
20	28.91	-1.44	0.76	0.36	1.09	2.55
21	30.15	0.07	87.03	88.28	69.70	86.86
22	32.52	0.95	8.29	81.46	91.37	97.65
23	32.52	0.11	28.00	27.15	3.47	25.12
24	33.42	0.16	87.29	95.81	95.64	91.84
25	33.65	1.56	66.09	96.78	93.51	15.07
26	34.61	2.28	90.14	79.40	65.22	93.04
27	35.53	1.17	83.46	80.42	64.20	88.29
28	35.76	0.86	72.07	72.16	62.79	22.99
29	36.24	0.15	95.91	96.93	80.51	93.78
30	36.46	0.26	99.76	99.38	99.68	99.75

35.6 Conclusions

Experimental modal analysis is a mature discipline in the structural dynamics community, which is as much an "art" as it is a "science". Modern procedures for estimation of modal parameters from measured data are highly automated; however, applications involving complicated structural systems and/or systems with closely-spaced, parametrically sensitive modes require the test engineer's experience and judgment ("art") to discern the difference between authentic and spurious ("junk" or "noise") system modes. A prevailing metric for experimental modal data validation is the orthogonality check, which relies on a model-based (TAM) mass matrix. In addition, reconstructive synthesis of measured frequency response function (FRF) data is another widely used strategy for experimental mode validation. The present EMV study employs mathematical operations aimed at isolating individual candidate experimental modes without reliance on a TAM mass matrix.

The key to mathematical and visual isolation of individual modes from measured data is the left-hand eigenvector. The most effective approach to determination of left-hand eigenvectors stems from employment of techniques that estimate the measured system's plant or effective dynamic system matrix. Since a complete set of (authentic and "noise") system modes are estimated for the plant, left-hand eigenvectors are determined from the inverse of the complete right-hand eigenvector set.

The following metrics provide a systematic basis for EMV:

1. The estimated Single-Degree-of-Freedom (SDOF) modal FRF, formed by the product of a single estimated left-hand eigenvector and FRF matrix, is plotted in terms of real and imaginary components vs. frequency, magnitude and phase components vs. frequency, and polar real vs. imaginary components. Authenticity of an estimated mode is then judged on the basis of quality of the plots.
2. The SDOF modal FRF is also formed from exact mathematical solution of the estimated effective dynamic system. Graphical comparison of this result with the above left-handed product information offers further means of authentic vs. "junk" mode discrimination.
3. Finally, a coherence metric based on comparison of the results of "1" and "2" provides a 0-to-100% figure of merit for estimated experimental modes.

References

1. Coppolino, R.: Chapter 23: finite element methods of analysis. In: Piersol, A., Paez, T. (eds.) Harris' Shock and Vibration Handbook, 6th edn. McGraw-Hill, New York (2010)
2. Allemang, R., Brown, D.: Chapter 21: experimental modal analysis. In: Piersol, A., Paez, T. (eds.) Harris' Shock and Vibration Handbook, 6th edn. McGraw-Hill, New York (2010)
3. Load analyses of spacecraft and payloads, NASA-STD-5002 (1996)
4. Independent structural loads analysis, Air Force Space Command, SMC-S-004 (2008)
5. Coppolino, R.: Methodologies for verification and validation of space launch system (SLS) structural dynamic models, NASA CR-2018-219800/Volume I (2018)
6. Coppolino, R.: Modal test-analysis correlation using left-hand eigenvectors, IMAC XXXVII (2019)
7. Mayes, R., Klenke, S.: The SMAC modal parameter extraction package, IMAC XVII (1999)
8. Coppolino, R.: A simultaneous frequency domain technique for estimation of modal parameters from measured data, SAE Paper 811046 (1981)
9. Coppolino, R., Stroud, R.: A global technique for estimation of modal parameters from measured data, SAE Paper 851926 (1985)
10. Coppolino, R.: Efficient and enhanced options for experimental mode identification, IMAC XXI (2003)
11. Penrose, R.: A generalized inverse for matrices. Proc. Camb. Philos. Soc. **51**, 406–413 (1955)

Chapter 36
Understanding Multi-Axis SRS Testing Results

William Larsen, Jason R. Blough, James DeClerck, Charles VanKarsen, David Soine, and Richard J. Jones

Abstract This paper presents a study done on a round resonant plate fixture used for Shock Response Spectrum (SRS) testing. The goal of this study was to understand the magnitude and character of both on axis and off-axis, with respect to shock input, response of the plate at various locations. The resonant plate was modeled using linear FEA as well as tested experimentally. Tools and approaches based on modal decomposition were developed to understand how the natural frequencies and mode shapes of the structure contribute to the SRS response at a given point and direction on the fixture and/or plate. It is seen that in some instances, the off-axis SRS response can have both a higher amplitude response as well as a different "knee" frequency which can make meeting a designated SRS target very difficult. It is shown that by understanding the modal properties of the plate/fixture assembly, the SRS results can be understood. These results will lead to the capability to predict both the on axis and off-axis SRS response for a given input/output set of locations and eventually the ability to choose the ideal locations to achieve a set of on and off-axis SRS responses to meet a given criteria.

Keywords Shock response · Modal decomposition · SRS · Multi-axis shock

36.1 Introduction

Shock Response Spectra (SRS) is a method that is used to characterize the acceleration response of a structure or system to a short duration (shock) transient event. In practice, testing facilities are required to replicate the acceleration response on specific 'fixtures'. Success is based on how well the SRS matches the SRS of the original event. In many cases this becomes a difficult task and many hours are spent in a trial and error effort to achieve the required response. Typically, this is accomplished by adjusting fixture characteristics such as size, geometry, and boundary conditions, as well as shaping the input excitation. Aizawa and Avitabile presented a methodology to modify the SRS of a system based on structural dynamics modification at IMAC 32 [1].

The goal of this effort is to understand how the modes of vibration of a system affect the characteristics of the SRS. Understanding this has the potential to reduce the time consuming trial and error effort that is currently experienced in many shock testing applications. In addition, it can provide insight into the 'off-axis' SRS.

36.2 Theory

The structures can be described in terms of mass, stiffness, and damping (energy dissipation). The traditional approach for understanding how these properties affect dynamic response begins with the single degree of freedom oscillator, Fig. 36.1.

The Department of Energy's Kansas City National Security Campus is operated and managed by Honeywell Federal Manufacturing & Technologies, LLC under contract number DE-NA0002839.

W. Larsen · J. R. Blough (✉) · J. DeClerck · C. VanKarsen
Department of Mechanical Engineering-Engineering Mechanics, Michigan Technological University, Houghton, MI, USA
e-mail: jrblough@mtu.edu; jdeclerck@mtu.edu

D. Soine · R. J. Jones
Honeywell Federal Manufacturing & Technologies, LLC, Kansas City, MO, USA

C. Walber et al. (eds.), *Sensors and Instrumentation, Aircraft/Aerospace, Energy Harvesting & Dynamic Environments Testing, Volume 7*, Conference Proceedings of the Society for Experimental Mechanics Series,
https://doi.org/10.1007/978-3-030-12676-6_36

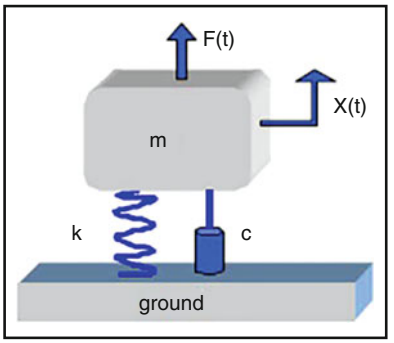

Fig. 36.1 Schematic of SDOF oscillator

The equation of motion for this system is:

$$m\ddot{x} + c\dot{x} + kx = f(t) \tag{36.1}$$

The solution to the equation of motion can be written in the frequency domain as:

$$x\,(j\omega) = H\,(j\omega)\,f\,(j\omega) \tag{36.2}$$

The equivalent time domain representation is:

$$x(t) = h(t) \otimes f(t) \tag{36.3}$$

where,

$$\begin{aligned} &H\,(j\omega) = \tfrac{1}{k-m\omega^2+jc\omega} = \tfrac{A}{j\omega-\lambda} + \tfrac{A^*}{j\omega-\lambda^*} \\ &h(t) = \tfrac{e^{-\sigma t}}{m\omega_d}\sin(\omega_d t) = Ae^{\lambda t} + A^* e^{\lambda^* t} \\ &\lambda = -\sigma \pm j\omega_d \quad \sigma = \zeta\omega_n \quad A = \tfrac{1}{2jm\omega_d} \end{aligned} \tag{36.4}$$

where: λ is the pole of the system
A is the residue
ω_d is the damped natural frequency
σ is the damping factor
ζ is the damping ratio

This concept can be applied to real structures that have an infinite number of degrees of freedom. In that case, the equation of motion can be written in matrix form as:

$$[m]\{\ddot{x}\} + [c]\{\dot{x}\} + [k]\{x\} = \{f(t)\} \tag{36.5}$$

The frequency and time domain solutions are:

$$\{x\,(j\omega)\} = [H\,(j\omega)]\,\{f\,(j\omega)\} \tag{36.6}$$

$$\{x(t)\} = [h(t)] \otimes \{f(t)\} \tag{36.7}$$

where:

$$
\begin{aligned}
H_{pq}(j\omega) &= \frac{b_{pq}(j\omega)}{a_{pq}(j\omega)} = \sum_{k=1}^{n} \frac{A_{pq_k}}{j\omega-\lambda_k} + \frac{{A_{pq_k}}^*}{j\omega-{\lambda_k}^*} \\
h_{pq}(t) &= \sum_{k=1}^{n} \frac{e^{-\sigma_k t}}{m_k \omega_{d_k}} \sin\left(\omega_{d_k} t\right) = \sum_{k=1}^{n} A_{pq_k} e^{\lambda_k t} + A^*_{pq_k} e^{{\lambda_k}^* t} \\
\lambda_k &= -\sigma_k \pm j\omega_{d_k} \quad \sigma_k = \zeta_k \omega_k \quad A_{pq_k} = Q_k \varphi_{p_k} \varphi_{q_k}
\end{aligned}
\tag{36.8}
$$

where: n is the number of modes.
k is the mode number

It is now obvious, that the response is a summation of the individual modes of the structure. In theory, $n = \infty$, in practice n is truncated to the number of modes that have a significant contribution to the overall solution. Therefore, the response at a location and direction on a structure p, due to a load applied at location and direction q, is given by:

$$
\begin{aligned}
& x_p(j\omega) = \sum_{k=1}^{n} \left(\frac{A_{pq_k}}{j\omega-\lambda_k} + \frac{{A_{pq_k}}^*}{j\omega-{\lambda_k}^*} \right) f_q(j\omega) \\
& \text{or} \\
& x_p(t) = \sum_{k=1}^{n} \left(A_{pq_k} e^{\lambda_k t} + A^*_{pq_k} e^{{\lambda_k}^* t} \right) f_q(t)
\end{aligned}
\tag{36.9}
$$

It should be noted this combination of modes which describes the response will also vary with the directions of both the input and the response, for this reason the response in direction x may be different than that in direction y at a given location. In terms of acceleration response, the time domain Eq. (36.9) becomes:

$$
\ddot{x}_p(t) = \sum_{k=1}^{n} \left(A_{pq_k} \lambda_k^2 e^{\lambda_k t} + A^*_{pq_k} {\lambda^*}_k^2 e^{{\lambda_k}^* t} \right) f_q(t) \tag{36.10}
$$

This result indicates that the response of a structure at any location p, is the weighted sum of the individual modal responses at that location. The amount of participation by any mode k, is a function of the pole $\lambda_k = -\sigma_k \pm j\omega_{d_k}$, and the scaled product of the mode shape values at the response and input locations $Q_k \varphi_{p_k} \varphi_{q_k}$. The SRS is calculated from the acceleration response, $\ddot{x}_p(t)$.

36.3 Modal Contribution to SRS

The effects of the modal participation in the acceleration response on the characteristics (shape) of the SRS can be studied by determining which modes participate and therefore shape the various regions (frequency range) of the SRS. To accomplish this, the acceleration response is computed for each individual mode of the structure. The SRS of each response is calculated and compared with the SRS of the total response. Based on this visual comparison, the acceleration response is computed from a subset of individual modal responses, using the minimum number of modes that account for all of the response. The SRS of this truncated set is computed and compared with the total response SRS. From this analysis, the modes which dominate the response and its SRS are determined and insight into why certain ranges of the SRS exhibit good or bad characteristics can be attributed to particular mode(s). This procedure is shown schematically in Fig. 36.2.

Note that due to the way in which the SRS is calculated, the SRS's from each mode cannot be summed to estimate the overall SRS of a structure. The acceleration responses from each mode must be summed in the time domain before the calculation of the SRS.

36.4 Application

The value of this analysis can be best illustrated by applying the method to an actual structure that could be used for a shock test with an SRS assessment of the structure's response. The circular shaped resonant plate fixture has been described in previous publications (ref). The structure consists of a 17 inch (432 mm) diameter circular aluminum plate, 1.125 inch (31.75 mm) thick. A 'device under test' (5 × 5 × 3 inch block of aluminum) is bolted on one side of the plate at the center

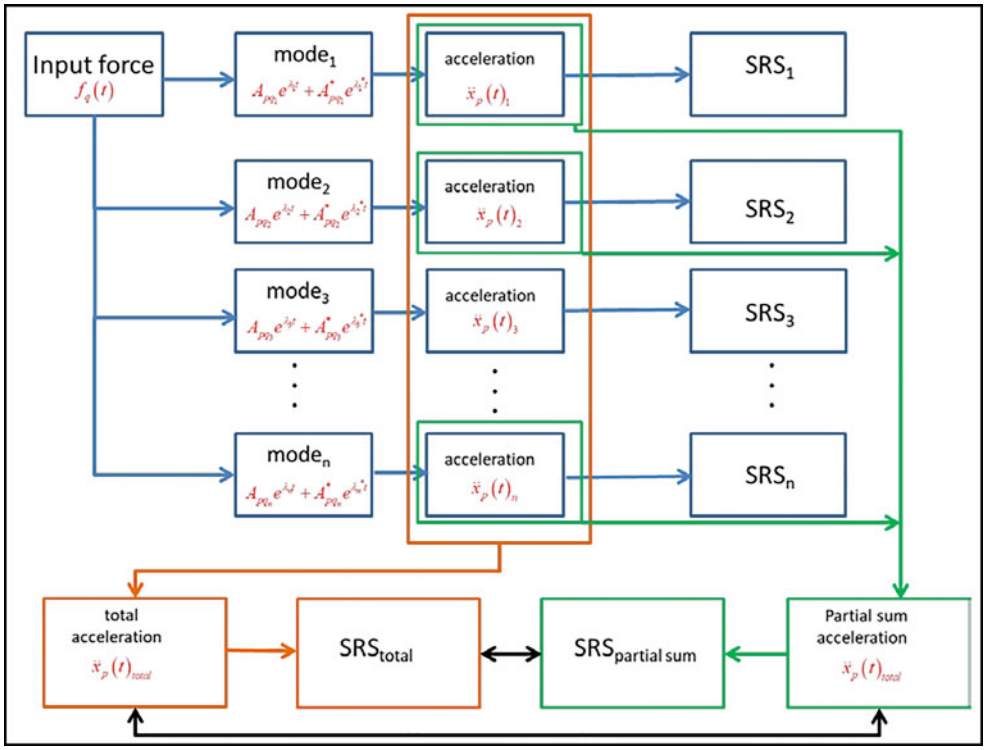

Fig. 36.2 Modal contribution to SRS

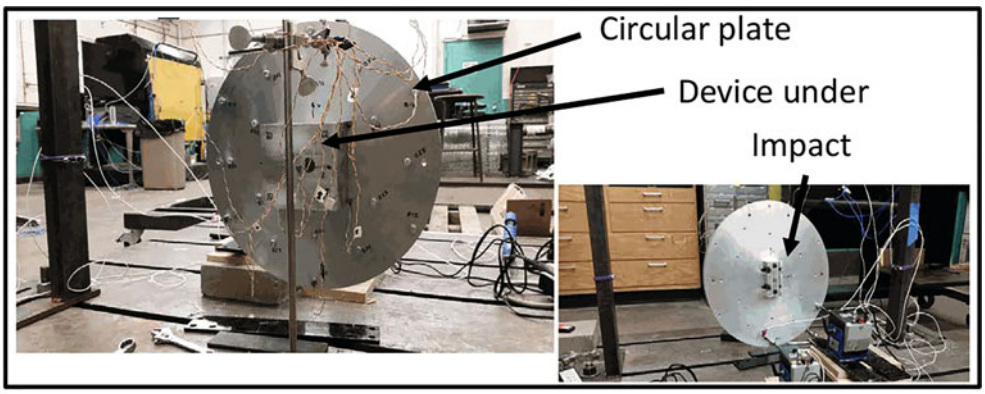

Fig. 36.3 Resonant shock plate fixture

of the plate. An impact block (4 × 2 × 1.50 inch block of aluminum) is bolted on the opposite side in the center of the plate. The resonant plate fixture is shown in Fig. 36.3.

An understanding of the modal contributions to the shape of the SRS requires the structure's natural frequencies, damping ratios, and associated mode shapes. Damping ratios were obtained from Frequency Response Function (FRF) measurements conducted on the actual structure. Natural frequency and mode shape information were obtained from a finite element model of the resonant plate structure. The finite element model is shown in Fig. 36.4. The plate was modeled with shell elements and the aluminum blocks with first order tetrahedral elements. Bushing elements simulated the attachment of the plate to ground (bunji cords in the lab test) and contact elements were used to connect the blocks to the plate. The eigen solution was computed using the Optistruct solver with 42 modes being found between 0 and 10,000 Hz. The rigid body modes (1–6) were assigned 1.5% critical damping and the flexure modes (7–42) were assigned 0.1% critical damping.

A subset of the modes found from the Eigen solution of the FEA model are shown in Fig. 36.5. The modes with red boxes around them are the dominant contributors the "knee mode."

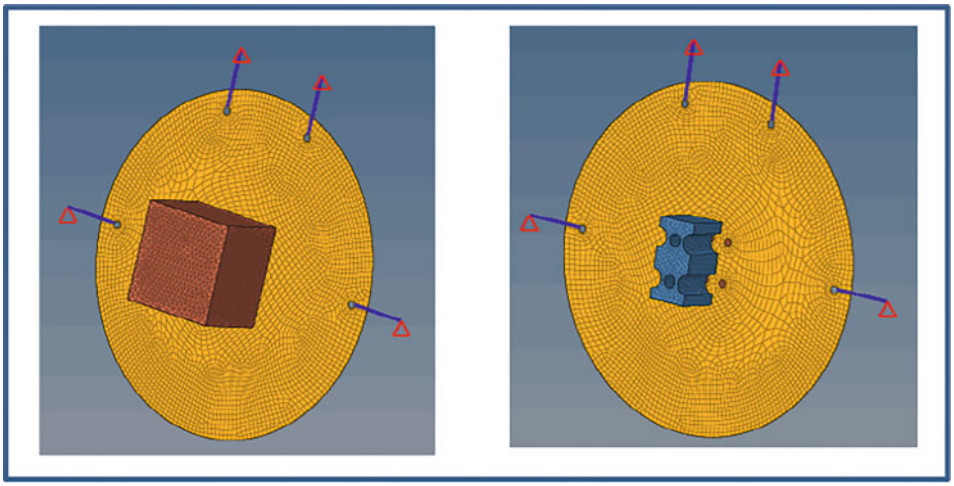

Fig. 36.4 FEA model of resonant plate

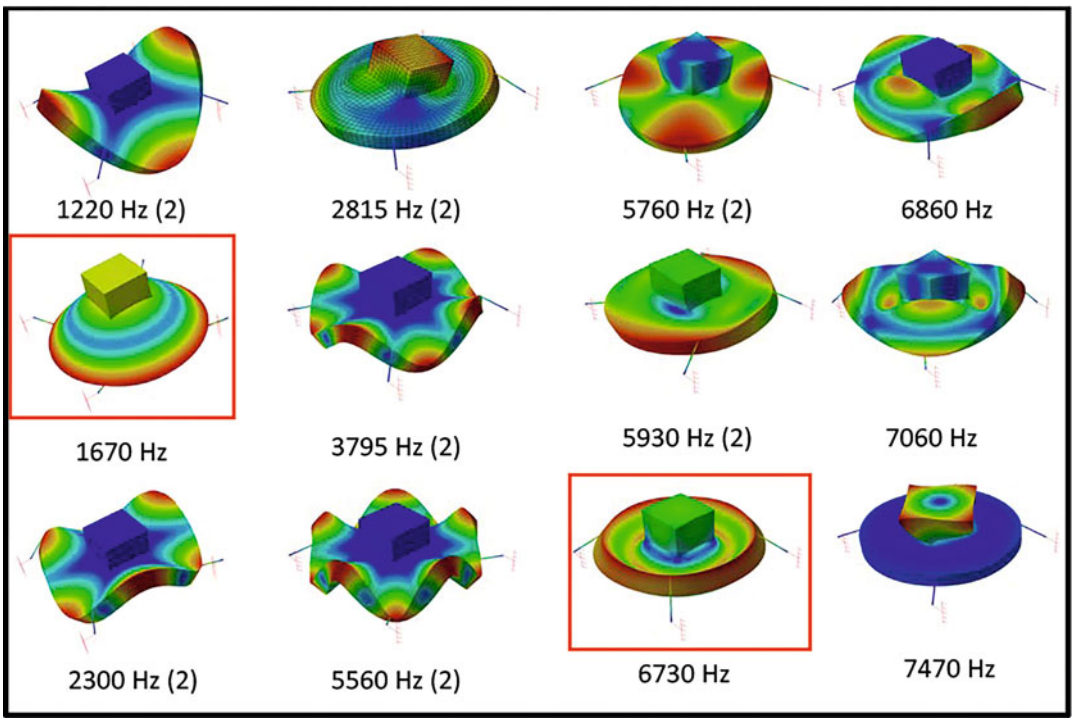

Fig. 36.5 Subset of FEA modes of shock response plate

The acceleration response of each mode was computed in Simcenter 1D (Amesim). Those results were transferred to Matlab for calculation of the SRS using Sherwood's code. The shock load was a haversine with a duration of 0.1 msec, Fig. 36.6. The SRS was computed using the maxi-max method with a damping ratio of 5%.

36.4.1 On Axis SRS Synthesis

For the first test case the input (Fig. 36.7) was applied at the center of the impact block, normal to the surface (Z-direction) and the response was computed at the center of the device under test block in the same direction, see Fig. 36.7.

The SRS obtained from the total acceleration response (all 42 modes, black) along with the SRS from the response of each individual mode is shown in Fig. 36.8.

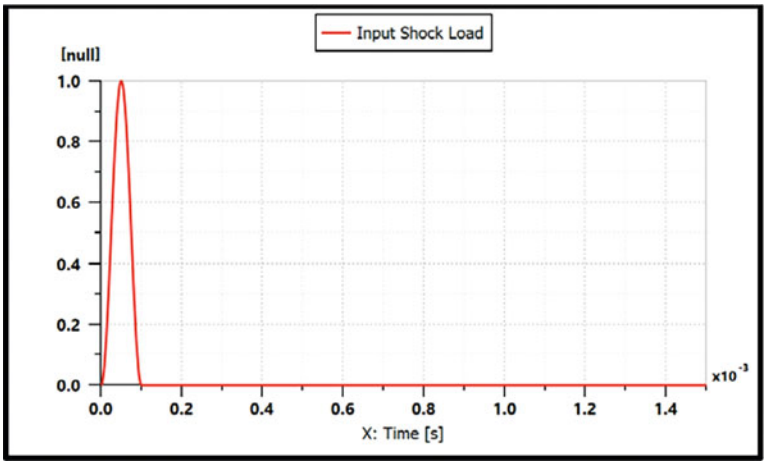

Fig. 36.6 Shock load

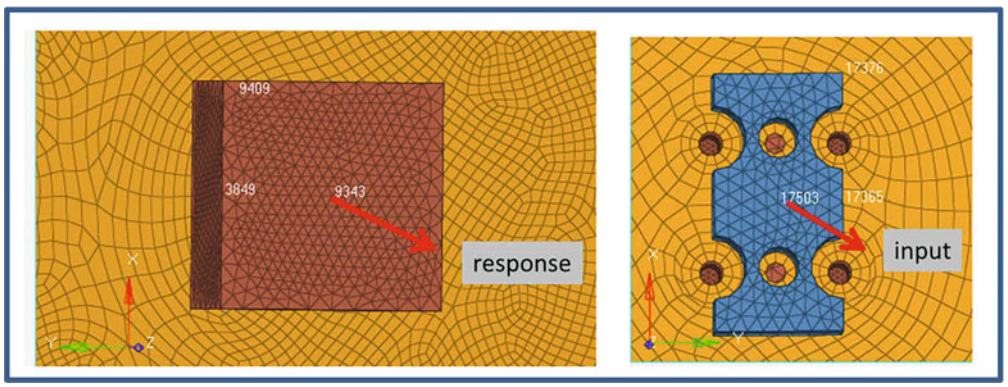

Fig. 36.7 Case 1 Input-output locations

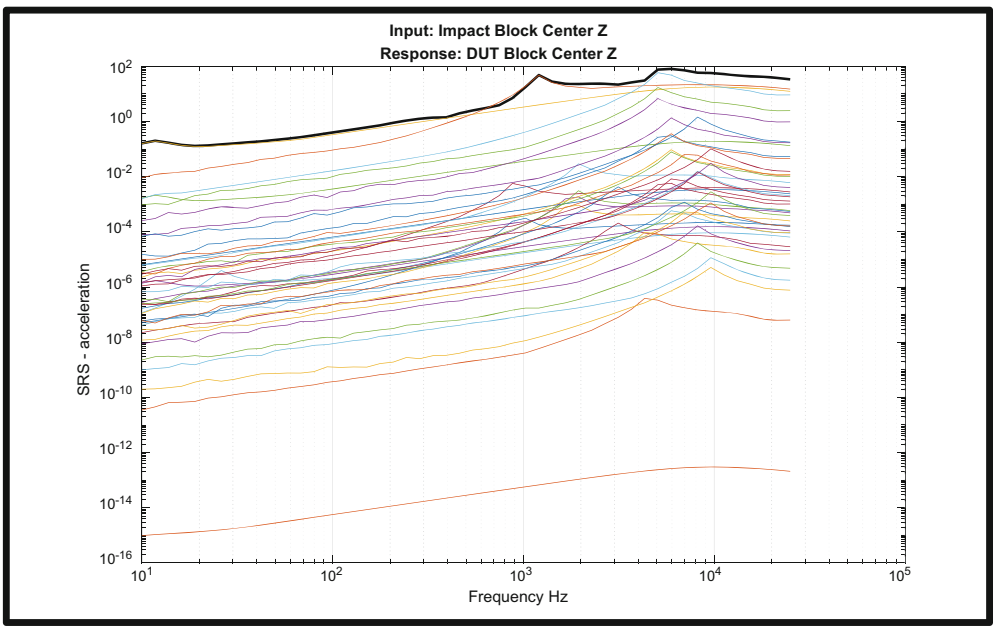

Fig. 36.8 Modal contribution to SRS

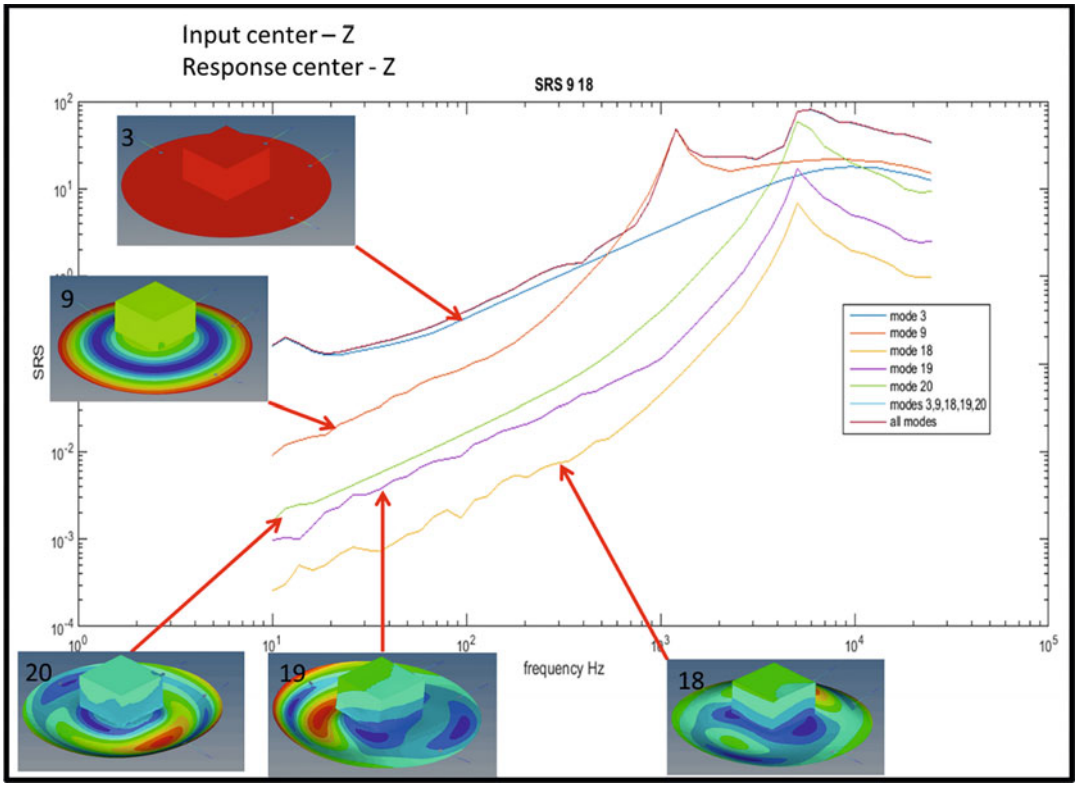

Fig. 36.9 SRS from a subset of modes

The data in Fig. 36.8 indicates that only a small subset of the structure's modes contribute to the overall shape of the SRS for this input-response condition. The modes with significant contribution to the SRS are shown in Fig. 36.9. The total SRS is based on the response of 5 of the 42 modes of the structure. The low frequency range is controlled by the rigid body response. The mode at 1100 Hz controls the knee range and three modes participate in the high frequency, 'plateau', range of the SRS.

Another way to show the contribution of modes to the SRS is to observe how the SRS evolves as modes are added to the acceleration response. In Fig. 36.10 the SRS using all 42 modes is compared with mode 3, upper left, modes 3 and 9, upper right, etc. It is clearly seen in the bottom left plot that only 5 dominant modes are required to estimate the total SRS of this system.

36.4.2 Off Axis SRS Synthesis

A pair of excitation/response locations was investigated to understand the modes involved with the synthesis of the SRS where the response and excitation are in different axes. In this case, the excitation was in the Z direction, where the response was in the Y direction. It can be seen in Fig. 36.11 that this combination of excitation and response locations/directions requires both a different and larger set of modes to synthesize the SRS even though it is on the same structure.

36.5 Conclusions

A method to synthesize an SRS function from a set of mode shapes and poles of a system was presented to better understand which modes contribute to the SRS of a system. The information required can come from either an FEA model, with some estimates for damping for each mode, or from an experimental modal analysis. The method presented was in the form of a

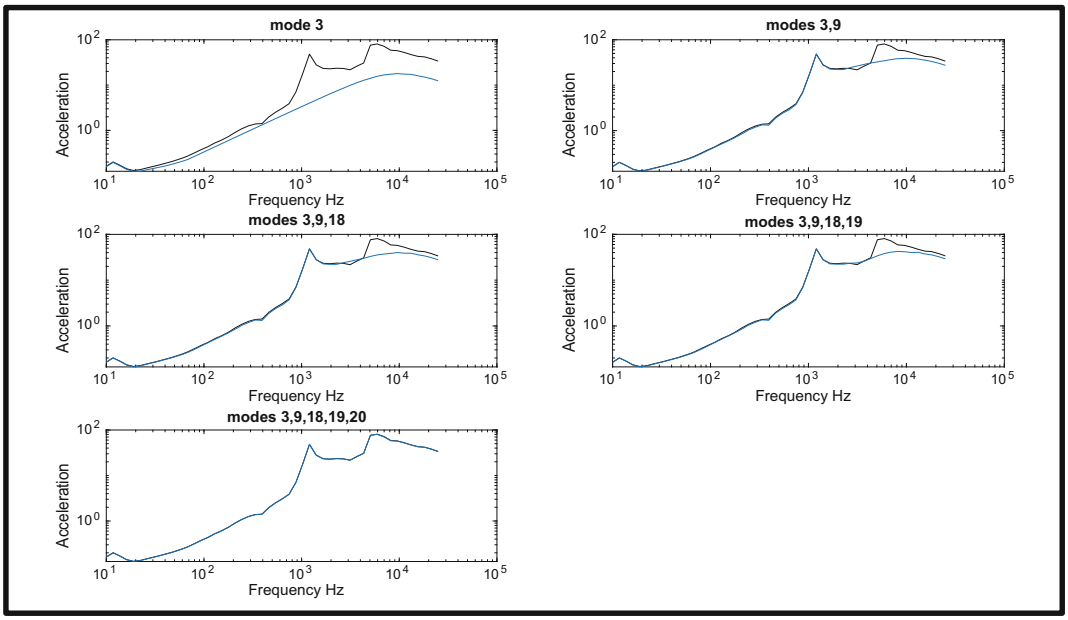

Fig. 36.10 Evolution of SRS as modes are added

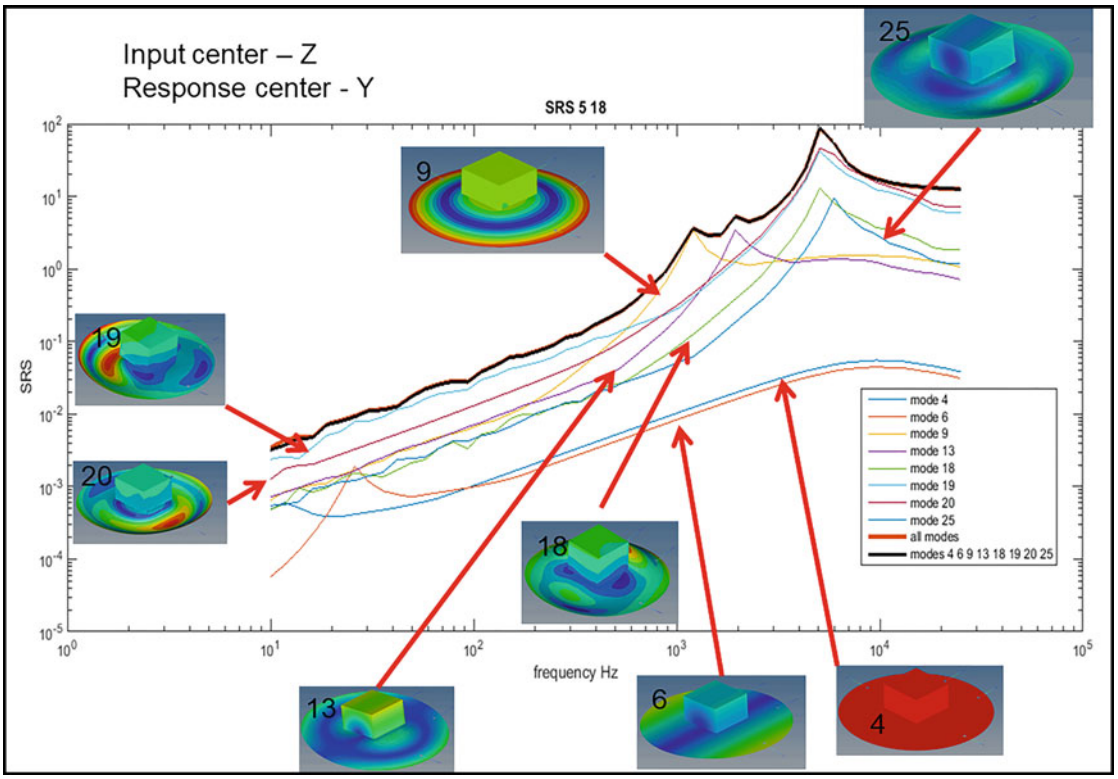

Fig. 36.11 Off axis SRS synthesis summary

co-simulation model using Amesim and Matlab to generate the time domain responses from each mode and then computing SRS functions for each mode or subset of modes.

The final conclusions from the analysis, which included two different examples from a shock response plate, were that the modes active in a SRS function depend on both the direction and location of the measured response as well as the location of excitation. It is clearly shown that off-axis SRS functions can have a different "knee frequency" as well as different

amplitudes as the on-axis SRS for the same structure, and even the same excitation location and direction when the response direction changes.

To fully predict and optimize the multi-axis SRS testing process an understanding of the participating modes for a given input/output location/direction pair can prove to be very informative. Further, this work will be expanded to include the ability to predict a multi-axis SRS function or group of functions for a given input/output location so as to expedite the future testing process. It is also apparent that there may be situations where it is very difficult to achieve a set of SRS functions on the X, Y, and Z axes simultaneously that all meet a given set of SRS targets if a significant understanding of the modes of the system is not used when the targets are set.

Reference

1. Kai Aizawa, K., Avitabile, P.: Shock response fixture developed from analytical and experimental data and customized using structural dynamics modification techniques, IMAC 32 Orlando, FL (2014)

Chapter 37
Generating Anechoic Traveling Wave in Beams with Various Boundary Conditions

Seyedmostafa Motaharibidgoli, V. V. N. Sriram Malladi, and Pablo A. Tarazaga

Abstract The basilar membrane (BM) is one of the prominent structural members of the inner ear which transports acoustic signals, received by the tympanic membrane in the middle ear, as structural waves to the hair cells. Another characteristic of the BM is its ability to absorb the energy of the structural waves at the apex end of the cochlea. As a result of this biological mechanism, the acoustic energy does not reflect at its boundary and as a result does not resonate back into the BM. This is a key feature of the BM, in particular effects by the helicotrema, that enables humans to hear and comprehend a string of continuous acoustic signals without any overlap. The present work is the result of the inspiration to develop waves propagating in engineering structures with such anechoic characteristics.

In a previous study, the authors have established the feasibility of generating such anechoic waves in one-dimensional beams through numerical simulations. This is carried out by augmenting a uniform beam with a spring-damper system. As a continuation to this study, the present work investigates the basis for choosing the spring-damper parameters to absorb structural wave energy. Furthermore, the relationship between various parameters such as location, spring stiffness, and damping coefficient and how they affect the quality of the anechoic waves generated is investigated. The results of this study will lead to a better understanding of anechoic wave generation in finite structures.

Keywords Travelling waves · Standing waves · Passive absorber · Anechoic waves · One-point excitation

37.1 Introduction

Travelling waves are mechanical waves transferring energy in a medium. Travelling waves have multiple applications such as, mimicking function of biological organisms, mimicking swimming behaviours, inducing drag reduction [1], transportation, etc. Work in this field has looked at generated travelling waves in finite structures such as strings, beams, and plates, to name a few [2–8]. Malladi et al. generated travelling waves in piezoelectric augmented beams with different boundary conditions by applying the two point excitation method [2]. The structure was excited at both ends with the same frequency and a phase difference of 90°. In another study by Bergman et al., travelling waves were simulated in a string with fixed boundary conditions using base excitation and a spring-damper attached to the string [3]. They showed in their work that by changing the spring and damper coefficients and exciting the string, pure travelling and standing waves can be generated in different portions of the string. Furthermore, the authors' previous work, simulated the travelling and standing waves generation in different portions of a cantilever beam [9]. In that study, one point excitation was used at the free end of the beam and a passive absorber (spring-damper) system was attached to the beam at various locations of the cantilever. Also, a parameter study has been done to observe and analyze the effect of absorber's damping coefficient and its location on the quality of the generated travelling wave.

In this study, one-point excitation and a passive absorber is used to generate travelling waves in beam structures with different boundary conditions. The absorber parameters are optimized to obtain high quality travelling waves for various configurations using the cost function introduced in [2]. The results of this work can be used to generate high quality travelling waves using passive elements in structures with reduced number of external excitations.

S. Motaharibidgoli (✉) · V. V. N. S. Malladi · P. A. Tarazaga
Department of Mechanical Engineering, Virginia Tech, Blacksburg, VA, USA
e-mail: mostafa4@vt.edu

C. Walber et al. (eds.), *Sensors and Instrumentation, Aircraft/Aerospace, Energy Harvesting & Dynamic Environments Testing, Volume 7*, Conference Proceedings of the Society for Experimental Mechanics Series,
https://doi.org/10.1007/978-3-030-12676-6_37

37.2 Generating Travelling Waves in a Beam

In this study, a passive absorber system consisting of a spring and a damper attached to a beam is developed to produce travelling waves. The beam modeled in the present work is an Aluminum beam. The beam parameters are listed in Table 37.1.

To study the quality of a travelling wave, a cost function is calculated based on the wave envelope introduced by Malladi et al., in [2] as,

$$CF = \frac{MaxAmp - MinAmp}{MaxAmp + MinAmp}, \tag{37.1}$$

where, Max Amp and Min Amp stand for the maximum amplitude and minimum amplitude of the wave envelope over a prescribed period of time as shown in Fig. 37.1, respectively. By definition, the cost function (CF) takes on a value between 0 and 1, where for a pure travelling wave CF is zero and for a pure standing wave CF is one. These two extreme examples are shown on the right hand side of Fig. 37.1. It should be noted that $CF = 0$ are not necessarily possible in finite mediums. A real-world unrealizable example, that could theoretically have a $CF = 0$ is a free-free string with forces at both ends. Thus, by getting closer to a CF of zero, a hybrid wave, that is a wave which is a combination of both travelling and standing waves, looks more like a travelling wave than a standing wave.

In the next section, different boundary conditions of a beam, including Free-free and clamped-clamped boundary conditions, are considered. Then, the passive absorber coefficients are optimized using the CF definition to achieve high quality travelling waves with one-point excitation of the beam.

37.3 Simulation Results

The first boundary condition (BC) studied is a free-free condition. There are two different approaches to generate travelling waves in the beam with this BC. The first approach is to apply a harmonic force at one end and attach a spring damper to the other end. The second approach is to replace the force by a spring and apply a harmonic base excitation.

In the first case, a harmonic force with a frequency between the sixth (1486 Hz) and the seventh (1978 Hz) natural frequency of the system is applied to one end and a spring-damper is attached to the other end. Then, the stiffness and damping coefficients are optimized using the CF of the generated waves to get a high quality travelling wave. Figure 37.2 shows a schematic of the beam as well as an optimal condition for travelling wave after a parameter search. It is shown in

Table 37.1 Beam parameters

Length	Width	Thickness	Density	Elasticity
460 mm	24.46 mm	3.2 mm	2700 kg/m^3	71 GPa

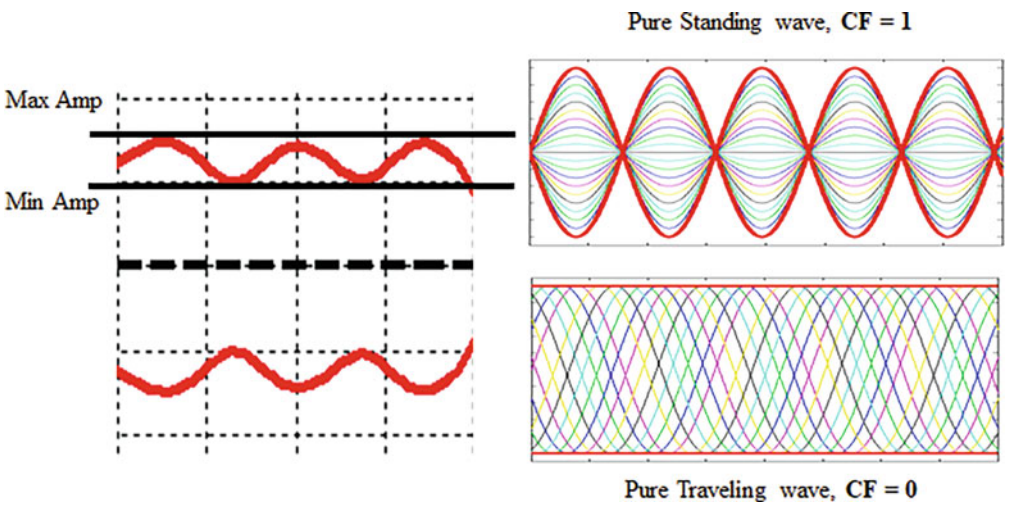

Fig. 37.1 Cost function definition

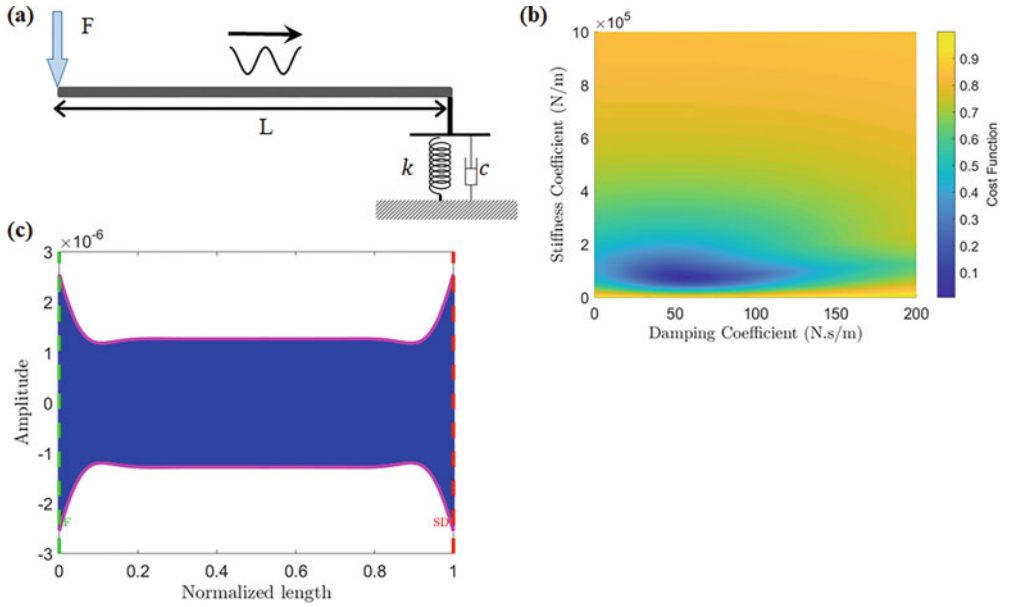

Fig. 37.2 Free-free beam with a harmonic excitation and attached spring-damper at the right boundary, (**a**) System schematic, (**b**) cost function of the simulated waves for a parameter sweep of damping and spring stiffness, and (**c**) optimal wave envelope

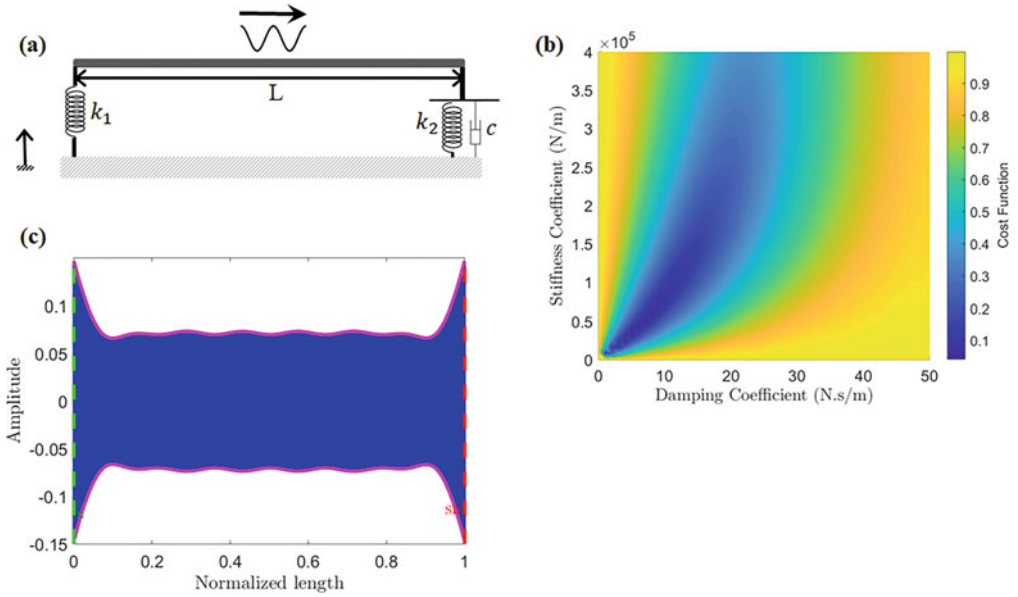

Fig. 37.3 Free-free beam with base excitation, (**a**) System schematic, (**b**) cost function of the simulated waves for a parameter sweep of damping and spring stiffness, and (**c**) optimal wave envelope

Fig. 37.2c that the stiffness and damping coefficients can be defined so that CF gets close to zero (getting closer to a pure travelling wave). The optimized parameters and the resulting CF are $k = 1.2 \times 10^5$ N/m, $c = 51$ N s/m, and $CF = 0.002$, respectively.

The next configuration consists of a spring ($k_1 = 5 \times 10^6$ N/m) connected to one end and a spring-damper attached to the other end, with a base excitation input to the system. The resultant optimal travelling wave is shown in Fig. 37.3. In this case the optimized travelling wave with $CF = 0.025$ is obtained by $k_2 = 4.9 \times 10^4$ N/m and $c = 5.5$ N s/m.

In the third case, a clamped-clamped beam is excited by a harmonic force, with a driving frequency between the eighth (2541 Hz) and the ninth (3174 Hz) natural frequency of the system, at one end is studied. An absorber system is attached near the opposite boundary as compared to the force. As shown in Fig. 37.4, a high quality travelling wave ($CF = 0.005$) is also generated in this case. The optimized coefficients are $k = 1.44 \times 10^6$ N/m and $c = 23$ N s/m.

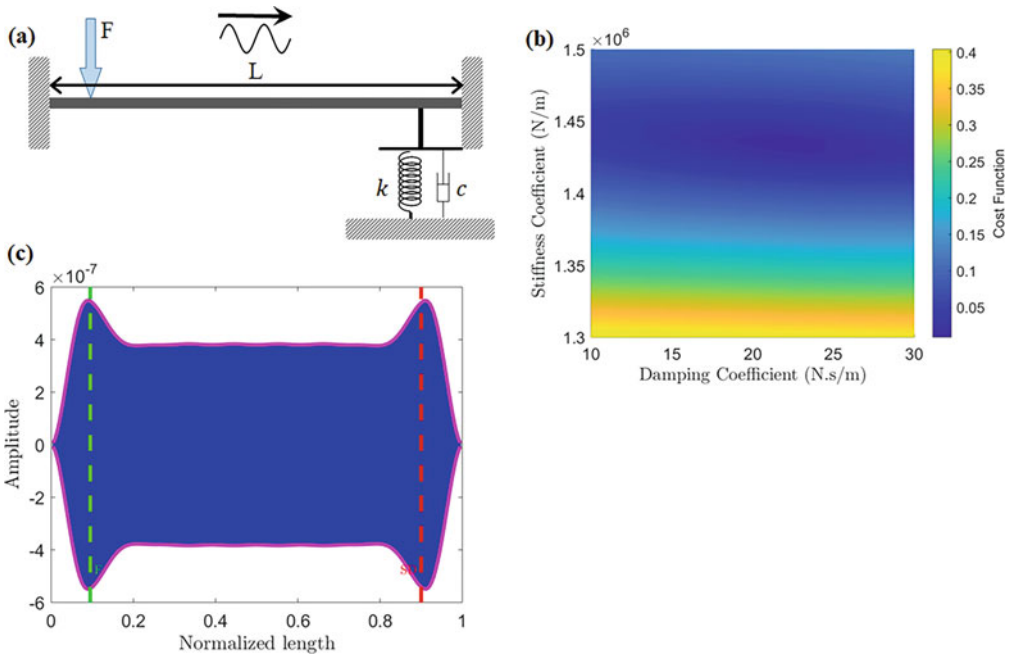

Fig. 37.4 Clamped-clamped beam with a harmonic excitation and attached spring-damper near right boundary, (**a**) system schematic, (**b**) cost function of the simulated waves for a parameter sweep of damping and spring stiffness, and (**c**) optimal wave envelope

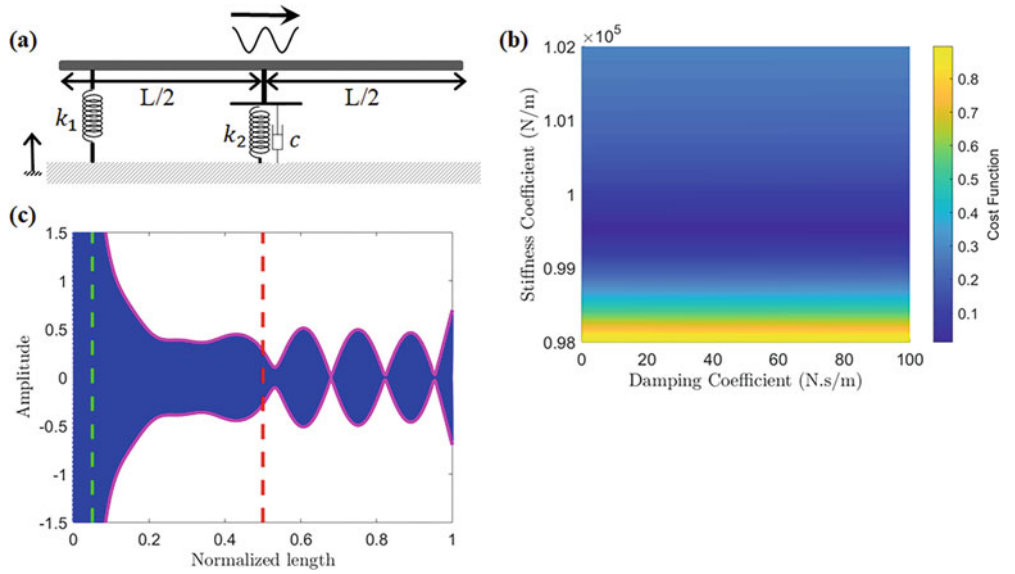

Fig. 37.5 Free-free beam with base excitation and attached spring-damper in the middle, (**a**) System schematic, (**b**) cost function of the simulated waves for a parameter sweep of damping and spring stiffness, and (**c**) optimal wave envelope

To study the effect of the spring-damper location on the generated waves in the beam, the absorber is attached to the middle and one quarter of the beam's length. The simulation is done for a free-free beam with base excitation and clamped-clamped beam with harmonic excitation.

The first two cases have a free-free beam with the absorber attached to the middle of the beam and at one quarter of the beam's length, respectively. The results are shown in Figs. 37.5 and 37.6.

It can be observed that the travelling waves coexist with standing waves in the beam. The optimized parameters and CF for each case are summarized in Table 37.2. The cost function is calculated for the travelling wave portion. Although not discussed in this paper, it is clear that the requirements of the damper and stiffness component, in order to maintain a low CF traveling wave, drops drastically and has a relation with respect to beam location that remains to be studied.

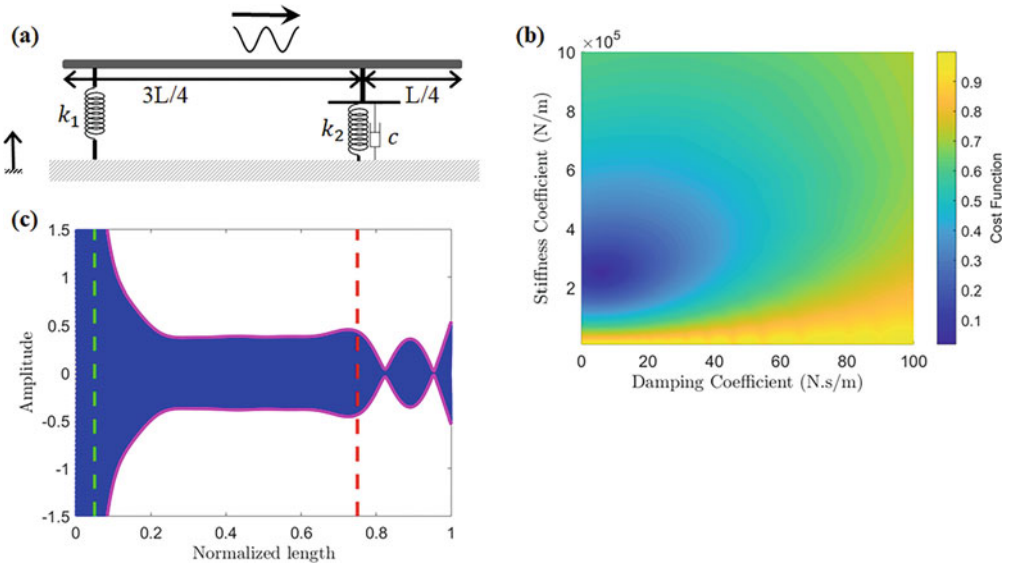

Fig. 37.6 Free-free beam with base excitation and attached spring-damper to the one quarter, (**a**) system schematic, (**b**) cost function of the simulated waves for a parameter sweep of damping and spring stiffness, and (**c**) optimal wave envelope

Table 37.2 Optimized parameters for free-free beam

Absorber location	Stiffness coeff.	Damping coeff.	Cost function
L/2	7×10^4 (N/m)	38.5 (N s/m)	0.01
L/4	2.5×10^4 (N/m)	9.5 (N s/m)	0.02

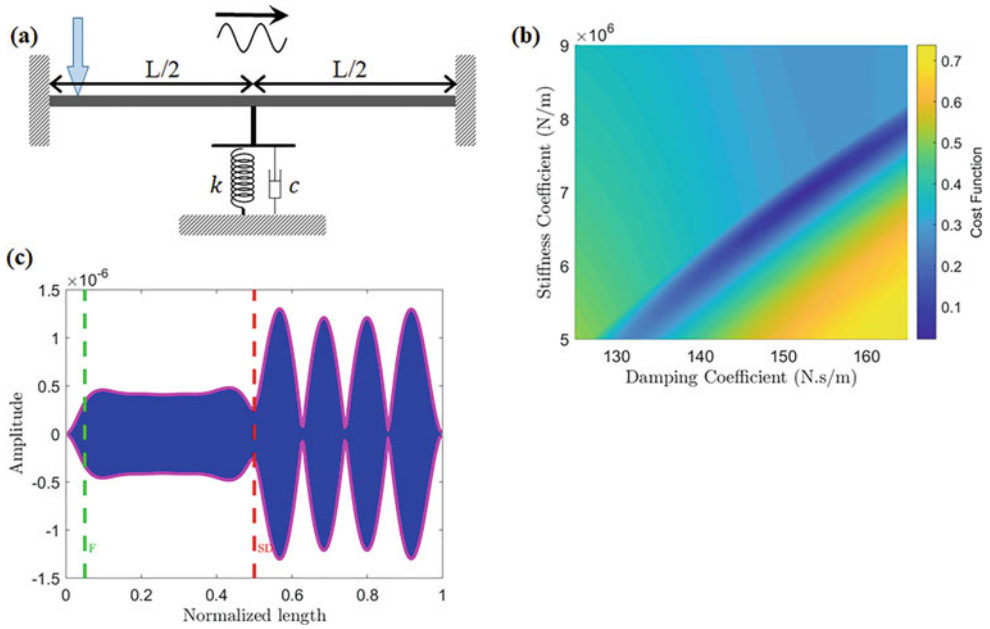

Fig. 37.7 Clamped-clamped beam with a harmonic excitation and attached spring-damper at the middle, (**a**) System schematic, (**b**) cost function of the simulated waves for a parameter sweep of damping and spring stiffness, and (**c**) optimal wave envelope

The next cases are of clamped-clamped beams with attached spring-dampers to the middle and one quarter of the beam's length. Figures 37.7 and 37.8 show the results of these two cases.

Travelling and standing waves can be generated locally in the beam using the presented configurations. Table 37.3 shows the optimized parameters for these cases. The cost function is tabulated for the optimal travelling wave.

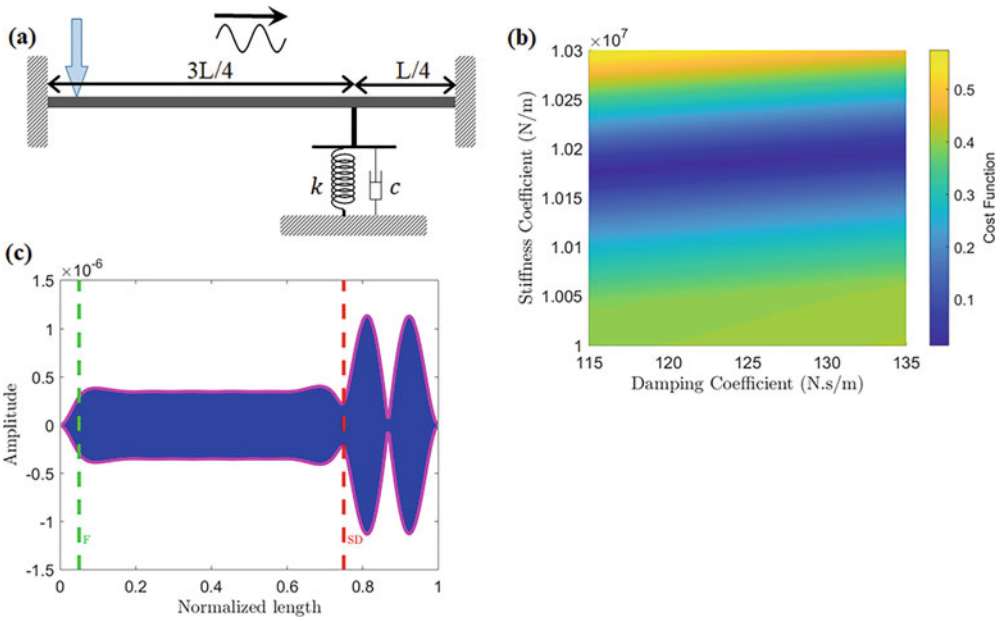

Fig. 37.8 Clamped-clamped beam with a harmonic excitation and attached spring-damper at one quarter of the beam's length, (**a**) system schematic, (**b**) cost function of the simulated waves for a parameter sweep of damping and spring stiffness, and (**c**) optimal wave envelope

Table 37.3 Optimized parameters for the clamped-clamped beam

Absorber location	Stiffness coeff.	Damping coeff.	Cost function
L/2	7.3×10^6 (N/m)	157 (N s/m)	0.02
L/4	10.1×10^6 (N/m)	127 (N s/m)	0.01

37.4 Conclusion

In this work, a beam with different boundary conditions, spring-damper configurations, and harmonic excitation is studied to generate travelling waves. This study has shown that travelling waves can be generated in a beam with boundary conditions using harmonic force and an attached spring-damper as a passive absorber. In the configurations which the spring-damper was not attached somewhere close to the ends, travelling waves and standing waves were generated proportionally along the beam. The results showed that the stiffness and damping coefficients affect the quality of travelling wave. The cost function was defined to optimize the values of stiffness and damping coefficients to get a higher quality of travelling wave for each case.

Future work will focus on validating the models experimentally, so that we can predict the system's responses. Moreover, we will analytically investigate the theoretical basis for choosing the spring-damper system to absorb structural wave energy.

Acknowledgements The authors would like to acknowledge the support of the Air Force Office of Scientific Research through the Young Investigator Program (FA9550- 15-1-0198). Dr. Tarazaga would also like to acknowledge the support provided by the John R. Jones III Faculty Fellowship.

References

1. Musgrave, P.F., Malladi, V.V.N.S., Tarazaga, P.A.: Generation of traveling waves in a 2d plate for future drag reduction manipulation. In: Special Topics in Structural Dynamics, vol. 6, pp. 129–138. Springer, Cham (2016)
2. Malladi, V.V.N.S., Avirovik, D., Priya, S., Tarazaga, P.: Characterization and representation of mechanical waves generated in piezo-electric augmented beams. Smart Mater. Struct. **24**(10), 105026 (2015)
3. Blanchard, A., McFarland, D.M., Bergman, L.A., Vakakis, A.F.: Damping-induced interplay between vibrations and waves in a forced non-dispersive elastic continuum with asymmetrically placed local attachments. Proc. R. Soc. A **471**(2176), 20140402 (2015)

4. Bucher, I.: Estimating the ratio between travelling and standing vibration waves under non-stationary conditions. J. Sound Vib. **270**(1–2), 341–359 (2004)
5. Malladi, V.V.N.S., Albakri, M., Tarazaga, P.A.: An experimental and theoretical study of two-dimensional traveling waves in plates. J. Intell. Mater. Syst. Struct. **28**(13), 1803–1815 (2017)
6. Loh, B.-G., Ro, P.I.: An object transport system using flexural ultrasonic progressive waves generated by two-mode excitation. IEEE Trans. Ultrason. Ferroelectr. Freq. Control **47**(4), 994–999 (2000)
7. Anakok, I., Malladi, V.V.N.S., Tarazaga, P.A.: A study on the generation and propagation of traveling waves in strings. In: Topics in Modal Analysis & Testing, vol. 9, pp. 257–261. Springer, Cham (2019)
8. Avirovik, D., Malladi, V.V.N.S., Priya, S., Tarazaga, P.A.: Theoretical and experimental correlation of mechanical wave formation on beams. J. Intell. Mater. Syst. Struct. **27**(14), 1939–1948 (2016)
9. Motaharibidgoli, S., Malladi, V.V.N.S., Tarazaga, P.A.: Developing a passive vibration absorber to generate traveling waves in a beam. In: Special Topics in Structural Dynamics, vol. 5, pp. 245–248. Springer, Cham (2019)

Chapter 38
Flexible and Multipurpose Data Acquisition System Design and Architecture for a Multi-force Testing Facility

Matthew S. Stefanski and Tristan A. Linck

Abstract Testing facilities that combine simultaneous forces on test articles, such as the Air Force Research Laboratory's Combined Environment Acoustic Chamber (CEAC), require a data acquisition system that is both robust, flexible, and able to record data at different acquisition rates and store the data separately and simultaneously. This paper will provide an overview of how the Air Force Research Laboratory, Structural Dynamics Lab designed their data acquisition architecture using National Instruments PXIe model hardware and LabVIEW software interface to meet the current and future technical requirements for a flexible combined environment data acquisition system.

Keywords Sensors · Instrumentation · AFRL · DAQ · LabVIEW

38.1 Introduction

Structural testing to investigate the combined effects of multiple forces on test articles is a demanding process for a data acquisition system. Such a system must be capable of storing data from multiple sources in a way that allows the data to be understood in the context of the input conditions and the other data collected. Different types of data often require different types of analysis, so the system must be capable of processing and storing data simultaneously in different ways. A data system capable of this data collection must be able to handle tests with widely varying numbers of sensors, of multiple types, and at multiple acquisition rates. This paper will discuss the data acquisition system used by the Air Force Research Laboratory Structural Dynamics Laboratory for the Combined Environment Acoustic Chamber (CEAC). The system uses National Instruments PXIe hardware with LabVIEW software to provide a powerful and flexible data acquisition system.

38.2 Background

In order to accomplish structural dynamics testing, the CEAC facility applies combinations of thermal, acoustic, and mechanical loads to test articles, individually or simultaneously. Measuring the responses of a test article to these conditions, as well as monitoring of the test facility, requires a wide variety of sensors. Temperature, sound pressure, acceleration, strain, heat flux, mechanical force, velocity, displacement, and air velocity measurements may all be collected through the data system, along with electrical monitoring of the thermal control system. In some cases, notably temperature and strain, there may be multiple types of sensors measuring that data as appropriate for different conditions.

In broad terms, the data collected can be divided into two parts: high-speed (sample rate) and low-speed data. High-speed data encompasses dynamic measurements which vary relatively quickly over time. As such, these measurements are handled in such a way as to facilitate frequency-domain analysis and monitoring. High-speed measurements include dynamic strain, acceleration, dynamic pressure, and dynamic mechanical force. Quantities that vary more slowly are considered low-speed data. These can be acquired at lower rates to improve performance in storage, visualization, and processing. Low-speed measurements include static strain, thermal response, heat flux, and mechanical loading.

M. S. Stefanski (✉) · T. A. Linck
U.S. Air Force Research Laboratory, Aerospace Systems Directorate, Aerospace Vehicles Division, Structural Validation Branch (AFRL/RQVV), Wright-Patterson AFB, OH, USA
e-mail: matthew.stefanski@us.af.mil

C. Walber et al. (eds.), *Sensors and Instrumentation, Aircraft/Aerospace, Energy Harvesting & Dynamic Environments Testing, Volume 7*, Conference Proceedings of the Society for Experimental Mechanics Series,
https://doi.org/10.1007/978-3-030-12676-6_38

As different types of sensors produce different output signals, the system has a wide variety of settings available to accept these signals through the National Instruments PXIe hardware. The system also includes the option to accept an arbitrary voltage input and apply user-defined scaling to handle any sensors not explicitly available in the system.

38.2.1 Dynamic Facility DAQ System

Three main components comprise the data system for the facility: the Master DAQ system, the low-speed viewer, and the high-speed viewer. This modular structure allows for the flexibility and robustness required for the facility. The Master DAQ system receives data from the National Instruments PXIe based hardware and streams the data to the low-speed and high-speed viewers. This system also interacts with the thermal control Programmable Logic Controller (PLC), passing thermal or heat flux data for feedback and reading electrical control data from the PLC for monitoring and analysis (Fig. 38.1).

The Master DAQ system runs on a rack based controller connected by a MXI network for high speed and throughput to the National Instruments PXIe hardware. The PXIe hardware is selected for each test based on the sensors used in that test, and the channels are configured through the Master DAQ. In this system, data channels are designated low-speed or high-speed, assigned descriptive names, and configured with appropriate parameters for the corresponding sensors.

38.2.2 MasterDAQ

The MasterDAQ program is the "traffic controller" for the data system. In the MasterDAQ system all the hardware channels are set up with the options necessary to provide excitation and correct signal processing for each individual channel. Each PXIe card can then be assigned to either the high-speed or low-speed system for data acquisition. Each channel on the card is then assigned a given data type based upon the type of card and instrumentation supported. The system uses native DAQmx drivers to configure the type of the channel. Using DAQmx drivers, only supported instruments for each card can be selected, eliminating mistakes from selecting an unsupported device. Each channel in the system can then be individually named, and enabled or disabled by clicking on a toggle button. This allows for easy addition or removal of data channels based upon the current test and if loss of instrumentation occurs during testing. Data channels don't have to be removed, rewired, or reconfigured using this method. With each channel type selected and named the channels can then be configured for sensitivity and excitation. The DAQmx drivers contain all the information for each channel so that all the correct sensitivity options, excitation, and engineering units are seamlessly integrated between the LabVIEW software and the PXIe data acquisition cards.

The MasterDAQ also communicates over Modbus with the PLC system that provides thermal control in the facility. For closed-loop control, the system sends real-time temperature or heat flux data to the PLC for feedback. This function supports primary and backup sensors for multiple independent control channels. The system can also read and stream selected data values from the PLC for storage. This is used to monitor and record the control signals and the electrical measurements from the thermal control system. These are added as additional channels to the data system and may be displayed and stored alongside the sensor data from the test.

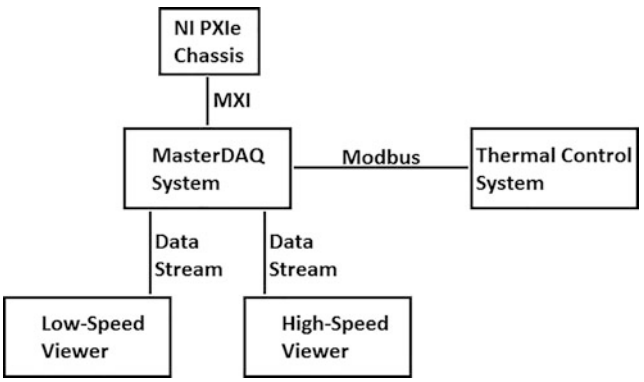

Fig. 38.1 Block diagram of DAQ system

38.2.3 Low-Speed Viewer

The Low-Speed Viewer program is the interface by which the user monitors and stores the low-speed data streamed from the MasterDAQ. The program can display data in multiple independent windows, each with a user-selected set of channels. There are three modes of visualization available. Data may be displayed in a tabular format, showing channel names, numerical values, and optionally unit information for each selected channel. Text color and size are configurable to facilitate legibility of the data and to readily differentiate between sets of channels. Data may also be displayed graphically as a time history. In this format, multiple data channels are plotted simultaneously with reference to the time on the system clock, allowing observed events to be compared with events on other systems. Multiple plot windows can be created with multiple channels to maximize and centralize data to be shown together. Each plot has two vertical axes available, each configurable to allow the user to optimize the utility of the display. The other mode of graphical display available in the Low-Speed Viewer is an X-Y Scatter Plot, allowing one or more data channels to be displayed with reference to another selected channel. The data storage interface for the Low-Speed Viewer allows the user to manually begin and end data collection, storing data at a selectable rate up to the sampling rate set in the MasterDAQ. For size and backup purposes the data can be streamed and stored directly to a Network Access Storage (NAS) in a redundant array of independent disks (RAID) configuration to prevent and protect against hard drive failure and data loss.

38.2.4 High-Speed Viewer

The High-Speed Viewer program is the interface by which the user monitors and stores the high-speed data streamed from the MasterDAQ. Like the Low-Speed viewer, the program can display data in multiple independent windows, each with a user-selected set of channels. Data may be displayed in a tabular format, showing channel names, RMS values, and optionally unit information for each selected channel. Text color and size are likewise configurable. Data may also be displayed graphically. Each graph window displays data for a specific channel, showing both a short-term time history (time domain) and a frequency response (frequency domain) plot. Streaming near real-time time and frequency domain data the test operators can watch for events and trends that may signal a change occurring in the test article. This information is useful to make decisions during test runs by not having to wait for a test to conclude and post-processing the data. The data storage interface for the High-Speed Viewer stores data for a user-defined time duration. The user has the option of storing a single data file, useful for short test runs, or to repeatedly store files of a set duration, allowing the data from long test runs to be stored and processed in manageable segments as opposed to the large files that would be produced by recording a long test run at a high sample rate. The data is stored in a binary format where metadata can be embedded so that the files can be easily searched and sorted for post-processing. The High-Speed Viewer can also stream and store data directly to a local NAS in RAID configuration to prevent data loss and protect against hard drive failure.

38.3 Conclusion

The data acquisition system in AFRL's Structural Dynamics Laboratory built upon National Instrument's PXIe based hardware and LabVIEW software provide necessary signal processing options, flexible channel count, and multiple acquisition rates. The Low-Speed and High-Speed remote viewer programs are able to deliver the data to the test operators in real time in multiple formats to allow decisions to be made quickly and to watch trends in data during the test. The data acquisition system's flexibility, robustness, and multiple data viewing options provide the Structural Dynamics Laboratory the necessary information and data storage options needed for operating aerospace tests in a combined environment R&D facility.

Acknowledgment Distribution A cleared by 88th ABW PA Case Number: 88ABW-2018-5180.

Chapter 39
Monitoring of Environmental and Sound-Induced Vibrations on Artistic Stained Glasses

Alberto Lavatelli, Emanuele Zappa, Alfredo Cigada, and Francesco Canali

Abstract Stained glasses are a key component of the artistic heritage of most European Christian cathedrals. During the last thousand years they grew in complexity and extension until they reached the size of several square meters. Therefore, artistic stained glasses are one of the elements of cultural heritage that are most exposed to environmental hazard though seldom considered until recent days. One of the modern danger sources for stained glasses are environmental vibrations and sound pressure induced vibrations. Considering the lack of modern literature on this topic, the authors carried out an experimental investigation on the Duomo di Milano stained glasses vibrations. The experimental campaign focused on the dynamic response of glasses due to both environmental vibration and to sound-induced excitation during some events which took place in the big square facing the church. As a result, a preliminary vibration analysis has been computed, thus enabling the characterization of vibrations and their effects under operating conditions. Data show that the response for this type of glass under operating conditions is limited to the 30–200 Hz band, with a concentration of energy in the 40–80 Hz band. Furthermore, considering a 30–200 Hz band, the RMS vibration level due to pop/rock concerts is about 10 times higher than that due to environmental excitation.

Keywords Artistic glasses · Environmental vibration · Sound vibration · Heritage conservation

39.1 Introduction

Old cathedrals are a landmark of most European cities. Usually placed in big town squares, they are an active part of the social life of the cities. In recent years many cities pushed towards the organization of musical events (concerts, shows events and demonstrations) in town central areas, thus exposing ancient buildings to environmental hazards due to noise and vibration. In this sense, the case of Milan is peculiar, since the square facing the Duomo (the old cathedral) has been continuously hosting musical events in the last two decades. The nature of the events is similar every year: from May to June the square hosts a series of 3–4 concerts composed by two rock/pop events and one or two classical music concerts.

The Duomo cathedral has been maintained through the centuries by the Veneranda Fabbrica del Duomo di Milano that is a 600-year-old organization established to supervise the construction of the Cathedral of Milan (the "Duomo") and then its conservation. The organization is still active and involved with the maintenance, preservation, and restoration of the cathedral in an everyday complex activity. The technicians and engineers of the Veneranda Fabbrica raised several concerns about the exposure of the cathedral to the mentioned music events. Among others, the integrity of stained artistic glasses is a major concern.

The Duomo hosts a cycle of 55 artistic stained glasses manufactured between the fourteenth and the twentieth century [1]. Those glasses are exposed to the noise and the vibration of the external environment. Consequently, heavy sound pressure loading may be considered a realistic threat to the preservation of these artworks.

Despite the stained glasses of cathedrals are exposed to noise/sound vibrations almost ubiquitously in all European cities, there is still a lack of knowledge on how to deal with this preservation problem. The analysis of literature highlights that the only documented research on the vibration effects of on cathedral artistic stained glasses has been carried out by F. L. Hunt

A. Lavatelli (✉) · E. Zappa · A. Cigada
Department of Mechanical Engineering, Politecnico di Milano, Milan, Italy
e-mail: alberto.lavatelli@polimi.it

F. Canali
Veneranda Fabbrica del Duomo di Milano, Milan, Italy

C. Walber et al. (eds.), *Sensors and Instrumentation, Aircraft/Aerospace, Energy Harvesting & Dynamic Environments Testing, Volume 7*, Conference Proceedings of the Society for Experimental Mechanics Series,
https://doi.org/10.1007/978-3-030-12676-6_39

[2, 3], when the English government commissioned a study on the effects of Concorde airplane sonic booms on cultural heritage.

In Ref. [2] the author proposed a test setup to assess the possibility that a sonic boom shock wave could damage artistic stained glasses. Its findings are summarized in the conclusion of the paper where he writes "The windows, one of which was in poor condition before the tests, were in no way damaged by the bangs. Tests showed that bangs caused lower strains in the glass of a leaded window than in a plain glass window of the same size" and "It is suspected that the vulnerability of a leaded window to sonic bang damage can increase if the condition of the saddle bars and attachment wires is neglected". In Ref. [3] the same author provided a long and extensive monitoring of vibrations on the artistic glasses of St. David's Cathedral, Pembrokeshire (which was close to the sonic-boom point of a Concorde typical flight plan on the West Coast Route). The findings of the author were interesting: music, especially low tones when organ was playing loudly, provided a vibration base level on stained glasses that was much higher than that of sonic boom. Moreover, he showed a table comparing the vibration amplitude due to sonic bangs for 4 different glasses (of the same window), but with different ages. Data suggests that the older the window, the bigger the vibration level. The author then concludes by saying that "There is little doubt therefore that the organ is likely to cause more window damage than would be caused by sonic bangs".

To sum up, the work of Hunt suggests that music can be a dangerous vibration source for artistic stained glasses, however only little is known on this phenomenon. Therefore, in this study, we propose an extensive monitoring study on the effects of concert music on the artistic glasses of the Duomo di Milano. The work will concentrate on the first the analysis of the problem and a characterization of the vibrations produced by noise in a confined space, that is the rectangular shaped square in front of the cathedral. For what concerns the assessment of a "dangerous" level of vibration (or more generally a safe sound level), the authors couldn't find a wide literature on stained glass vibration resistance, since, generally, the problem is solved for common building glasses as in Refs. [4–7].

39.2 Monitoring Program and Measurement Setup

The layout of the square and the stage position during concerts is highlighted in Fig. 39.1b. For Pop/Rock events the stage is positioned laterally with respect to the cathedral façade, with sound propagating from the left nave to the right nave: sound propagates from the loudspeakers in a direction roughly parallel to the cathedral façade. Classic/symphonic music concerts, instead, are usually held on a stage positioned in front of the façade, thus using the Duomo churchyard as backstage in this case the sound propagation line is normal to the church façade. The summer concert program of 2016 had a total of four concerts:

1. June 8th, 2016: Pop/rock festival with various Italian artists—First night
2. June 9th, 2016: Pop/rock festival with various Italian artists—Second night
3. June 12th, 2016: Symphonic music concert with *Teatro alla Scala* Chorus and Orchestra
4. June 18th, 2016: Marching band concert with the National Marching Band of *Carabinieri, a corp of the Italian army*

The first two concerts (Pop/Rock events) had the stage aside the church, the third and fourth (the Symphonic and the Marching Band concert respectively) have performed with the stage on the churchyard as shown in Fig. 39.1b.

Fig. 39.1 The square of Duomo (**a**) and the layout of the stages (**b**) for the concert season (Pop/Rock concert in red, symphonic music in blue) with sound propagation directions

Table 39.1 Monitoring program for the concert events

Event	Start acquisition (dd/mm/yy hh:mm)	End acquisition (dd/mm/yy hh:mm)
Pop/rock festival—First night	08/06/2016 17:30	09/06/2016 1:00
Pop/rock festival—Second night	09/06/2016 17:30	10/06/2016 1:00
Symphonic music concert	12/06/2016 18:30	13/06/2016 1:00
Marching band concert	18/06/2016 18:30	19/06/2016 1:00

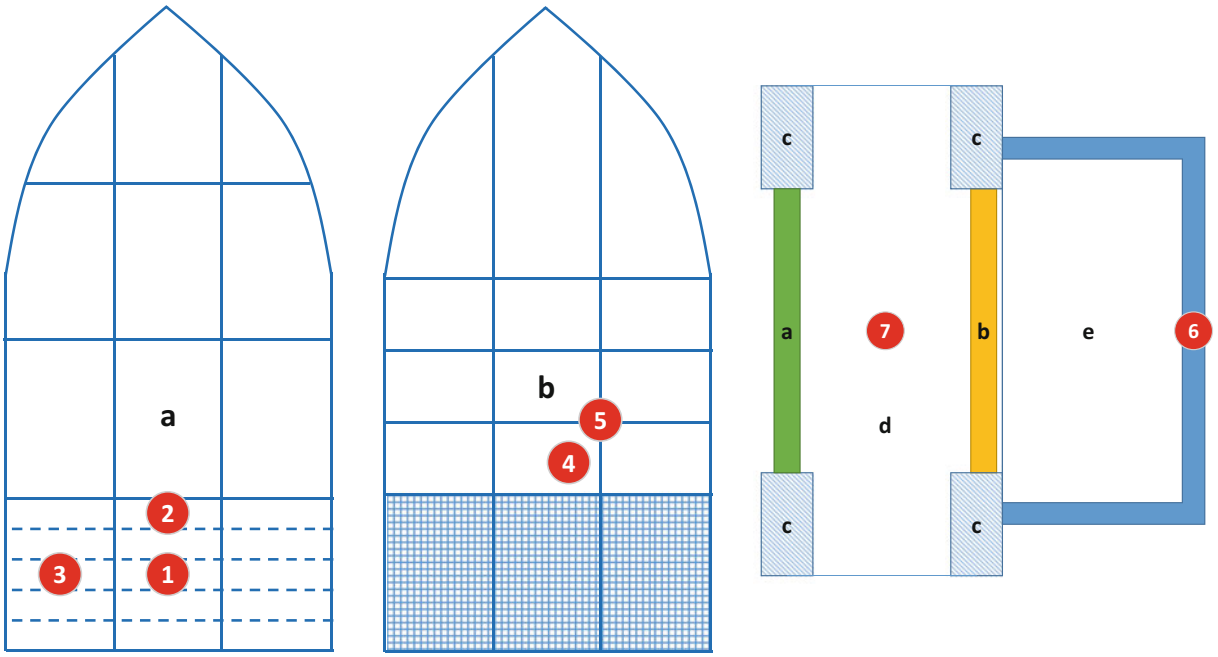

a)Artistic stained glass b)External cover window c)Plan view of the measurement area

Fig. 39.2 Position of the instrumentation on the main artistic glass of the façade. Measurement points are labelled with red dots and channel number. Channel 1–5 are ICP accelerometers. Channel 6 and 7 are ICP microphones

The concerts were very different from the musical point of view: music style, loudness and the total attendance were expected to vary sensibly from one event to another. In any case, for all the events it was expected that the façade of the cathedral could be the most solicited points: windows are wider and more directly exposed to the sound action, even if, worried by the possibility of stationary waves in confined and fixed spaces at the cathedral sides, measurements have been repeated in different positions: on the biggest artistic glass of the façade and also on two lateral glasses (North and South), with the same monitoring scheme. The monitoring program is described in Table 39.1. The monitoring system has been switched on roughly one hour before the concert start and switched off at 1 am, which is exactly 1 h after the concert time limits as for Milano regulations: also some reference periods have been acquired both without the action of loudspeakers and during the sound checks.

The main façade glass was equipped with the most complex setup, though being conscious that, at a preliminary step, it was necessary to get in touch with the problem without risking any failure of ancient glass: a preliminary requirement was to fix any sensor in a safe and reversible way, without any risk for the windows. As described in Fig. 39.2c, the structure of the cathedral is made by an outer and an inner wall, separated by an internal interspace (highlighted with letter "d"). In front of the window, towards the main square, In front of the stained glass there is a balcony (letter "e") leaning over the churchyard. Measurements have tried to correlate vibrations and sound, by the use of accelerometers fixed to the windows and microphones to get the sound pressure (though not according the standard requested for sound measurements—the aim was to have a reference pressure in critical points. Sound signals have been recorded with a pair of ICP microphones, one positioned outside, on the balcony and one positioned in the crawl space. Then ICP accelerometers have been used to monitor glass vibrations. The artistic glass "a" has been equipped with 3 accelerometers, roughly aligned in a L shape, while the external glass (the cover window) has been equipped with a pair of accelerometers: one directly on the glass, one on the window frame. The accelerometers employed in this activity were PCB ceramic shear ICP® model 333B30,

with the main aim to limit weights and therefore the related load effect. The principal characteristics of these sensors are:

- Sensitivity: (±10%) 100 mV/g (10.2 mV/(m/s^2))
- Measurement Range: ±50 g pk (±490 m/s^2 pk)
- Broadband Resolution: 0.00015 g rms (0.0015 m/s^2 rms)
- Frequency Range: (±5%) 0.5 to 3000 Hz
- Weight: 0.14 oz. (4.0 gm)

Sound pressure, has been measured with ICP microphones Bruel&Kjaer model 4188 (class 1 microphones according to the standard IEC 61672). The product specification is the following:

- Sensitivity: 31.6 mV/Pa
- Frequency: 8 Hz – 12.5 kHz
- Dynamic Range: 15.8–146 dB
- Temperature: −30 to +125 °C (− 22 to +257 °F)
- Prepolarized

Data have been acquired by means of a permanent monitoring system made with National Instruments hardware. The data acquisition boards were NI 9234, equipped with a 24 bit sigma-delta converter. Data were acquired at 2560 Hz, then decimated to 1280 Hz for the analysis in a 640 Hz bandwidth. All the same a preliminary screening carried out with a sampling frequency of 10 kHz confirmed the correct choice for the vibration bandwidth: the main worries were about the possibilities that impacts of the main frame against the church wall, due to the putty aging, could require a higher bandwidth to properly reconstruct these peaks.

39.3 Characterization of Vibrations on Artistic Stained Glasses due to Concerts

As a first operation, we looked at the distribution of the vibration energy in the various regions of the frequency domain for the artistic glass. Figure 39.3 (left) shows the power spectral density of the acceleration signal for channel 1, during the first Pop/Rock concert. A first evidence is that during the night, the vibration level is at least 2 orders of magnitude lower than during the concert, therefore the effect of the sound pressure plays a fundamental role in the excitation of the glass vibration level. The cumulative power distribution shown in Fig. 39.3 (right) represents the power distribution, normalized with respect to the overall signal power. This representation highlights the frequency bands where the vibration power is higher. It is interesting to see that 90% of the vibration energy is concentrated in the 30–200 Hz band, both during the concert and during the night. This piece of information suggests that the response of the glass is strongly related to the incoming sound pressure level in terms of overall vibration level, while the frequency band where the vibration power is

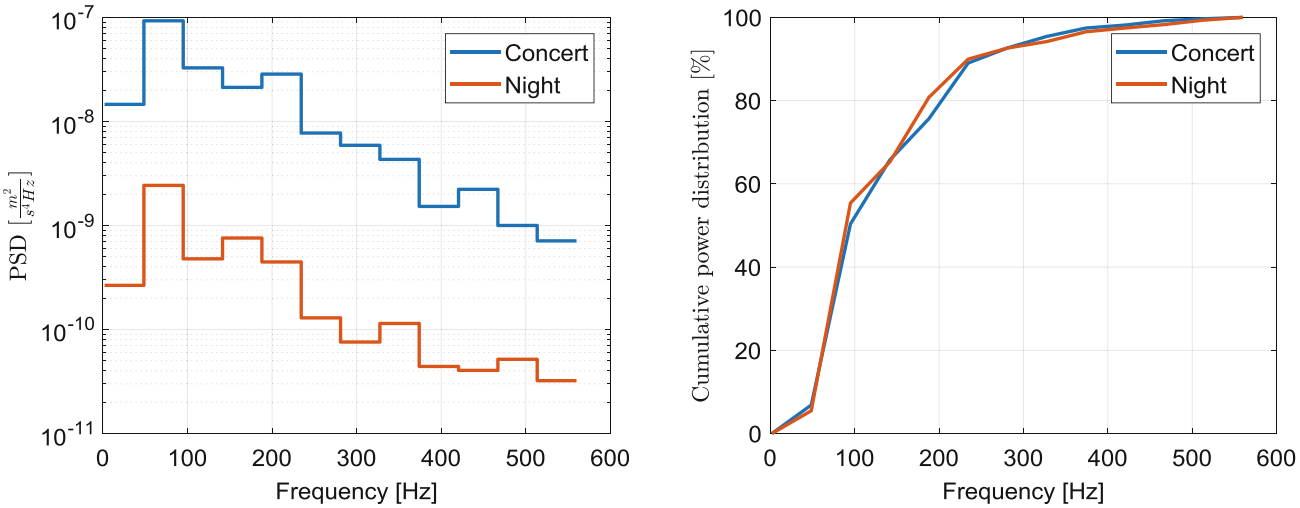

Fig. 39.3 Power spectral distribution of the acceleration signal (Channel 1) during the first Pop/Rock concert

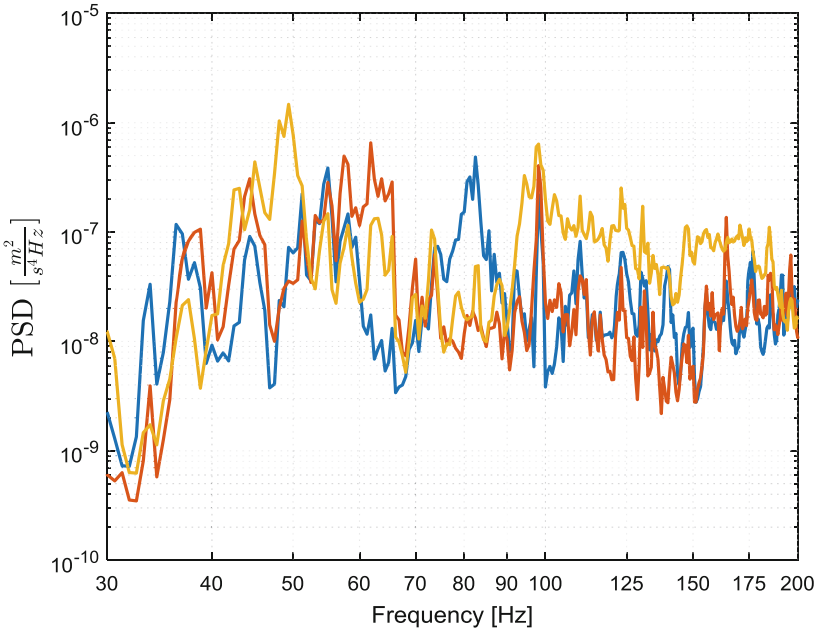

Fig. 39.4 PSD of the three accelerometers mounted on the artistic glasses (Channel 1 in blue, Channel 2 in red, Channel 3 in orange)

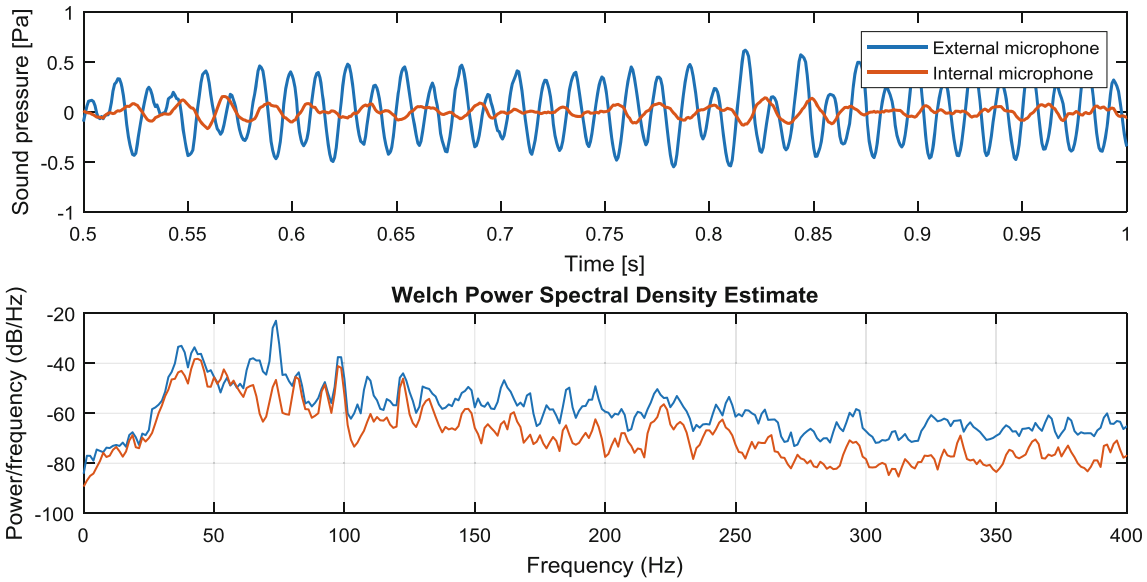

Fig. 39.5 Microphones sound pressure levels and PSD in the case of a bass tone burst (acquired during the first Pop/Rock concert)

concentrated, mainly depends on the characteristics of the glass. This consideration will be confirmed by the analysis shown in the next section.

It was observed that also for the other considered measurement points, the vibration energy is concentrated in the frequency between 30 and 200 Hz, therefore in Fig. 39.4 the comparison of the PSD of the 3 accelerometers on the artistic glass is shown in this band. Although the average vibration levels are similar for the 3 sensors, there is no evident trend of the power distribution, rather the local response of the glass is quite different, even for measurement points a few hundreds of millimeters apart. This is due to the characteristic of the glass: it is made of glass pieces inserted into a lead frame, with different shapes and with non-uniform characteristics of the connecting media.

Figure 39.5 shows the microphone sound pressure levels and the corresponding PSDs in the case of a bass tone burst, acquired during the first Pop/Rock concert: one microphone is outside, the second is in the crawl space. It is possible to see that the pressure transfer from the external to the internal microphone is suspected to be affected by complex transformations: the external input is the almost pure tone visible in the data (a D2 note), while the internal microphone displays a very

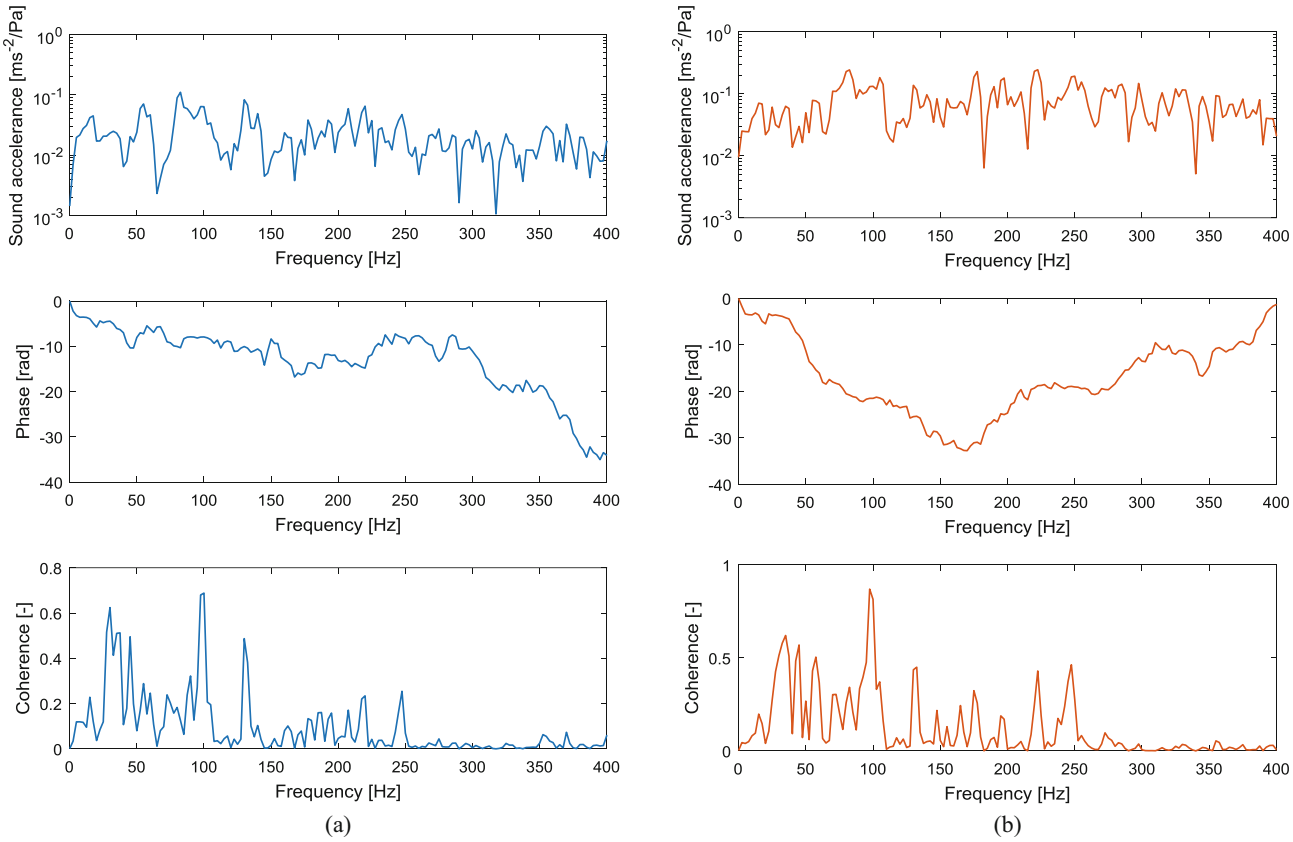

Fig. 39.6 Transfer function estimation (from sound pressure to acceleration) for the accelerometer Channel 1. (**a**) Input external microphone. (**b**) Input internal microphone

harmonically distorted signal. The effect of the external glass is therefore relevant, not only for the overall reduction of the Sound Pressure Level but also for the distortion of the spectral distribution of the sound.

Figure 39.6 shows the transfer function between the pressure levels acquired by the two microphones and the vibration on the glass measured by accelerometer 1. As demonstrated by the very low values of the coherence function, the spectral distribution of the acceleration data is weakly correlated with the spectra of the sound pressure level: the acceleration data mainly depend on the local response of the artistic glass.

39.4 Analysis of the Vibration Level for Different Music Events

Now that the vibration patterns are characterized, it is possible to proceed in analyzing the vibration levels. The level of vibration is evaluated as the RMS value of acceleration. This choice is justified by the essential randomness of the vibration response, so that the average energy metric is more meaningful than frequency domain evaluations. The first operation is to compute the RMS of the signal in a moving window of 1 s of length. The length of 1 s has been selected as a suitable solution to achieve the above-mentioned goal: it is not sensitive to a single signal voltage peak that can be induced by instantaneous spikes in the power supply, at the same time gives a fine representation of the physical phenomenon. The result of the computation is shown in Fig. 39.7, where the RMS of Accelerometer 1 is displayed (full scales of the plots are automatically adapted to the peak levels). As a first comment, it is possible to see that Pop/Rock concerts generate a much higher power of vibration in the 200 Hz band. The third graph (black one, Symphonic music) demonstrates the high correlation between the loudness of music and the vibration level of artistic stained glasses: at minute 225 of the acquired data the orchestra started to play Ravel's Bolero. The dynamics of the music sheet is designed with a continuous crescendo where more and more elements of the orchestra join the play. The loudness of music is expected to grow with a sort of power law. As one can see from vibration data, also the vibration of the artistic stain glasses follows the orchestra dynamics. So this is a further confirmation that the glasses are very sensitive to the type of concerts.

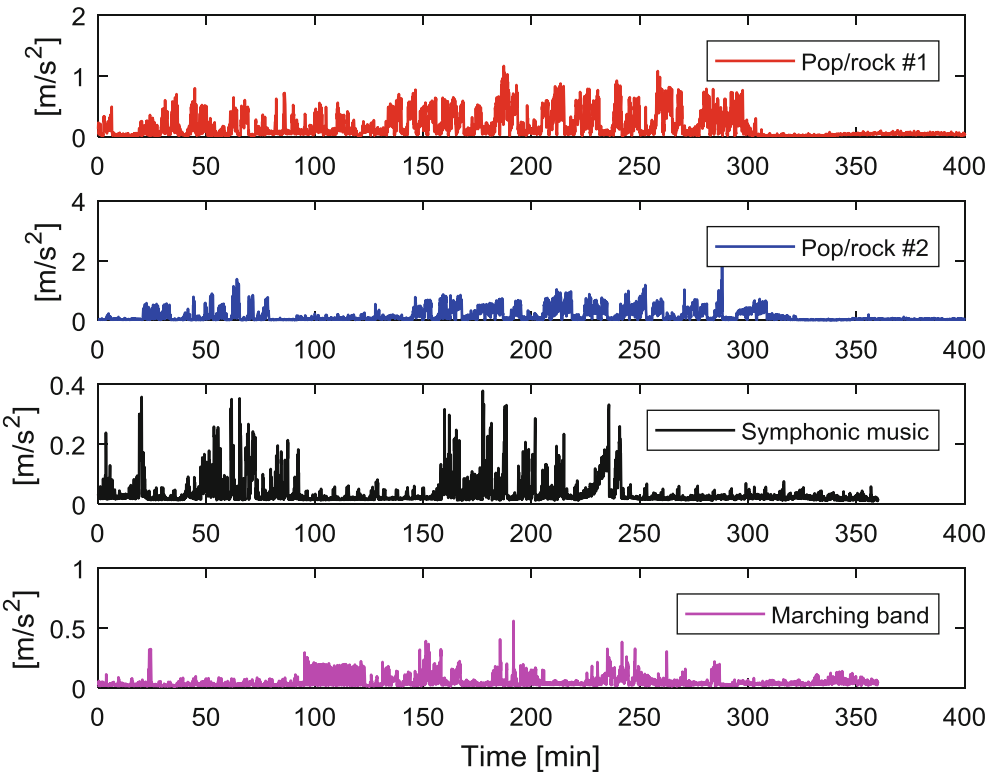

Fig. 39.7 Time history of signal RMS on a time window of 1 s for accelerometer Channel 1

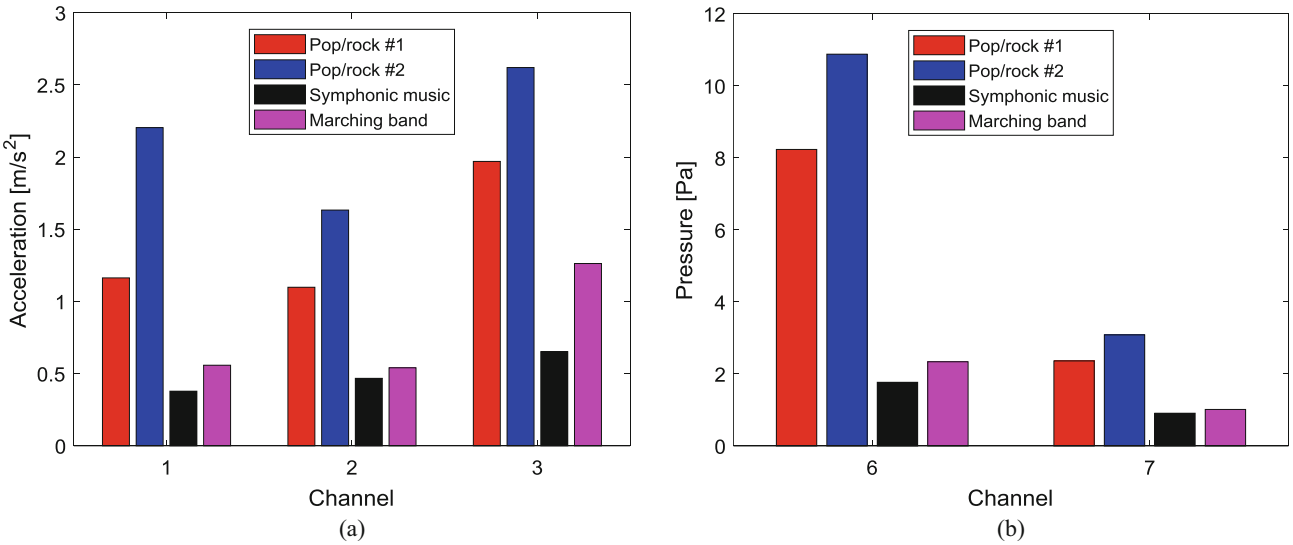

Fig. 39.8 Peak of RMS level of signals for the main artistic glass on the facade. (**a**) Artistic glass accelerometers. (**b**) Microphones

Another interesting viewpoint is offered by the comparison given in Fig. 39.8: the peaks of the recorded RMS (always evaluated every 1 s, according to what already discussed) for the artistic glass and for the microphones are shown, as recorded in the same point during various events. We can see that the peak vibration levels are completely different, with the pop/rock concerts providing twice the maximum solicitation to the stained glasses with respect to those produced by classic music. In addition, the graphs of Fig. 39.9 suggest that for Pop/Rock concerts the RMS vibration level is sustained at values close to the maxima peaks for several minutes. Instead symphonic music has a more variegate dynamic, so peaks are sustained for shorter times. It is also important to note that the peaks of Symphonic music are about the average value of the Pop/Rock events.

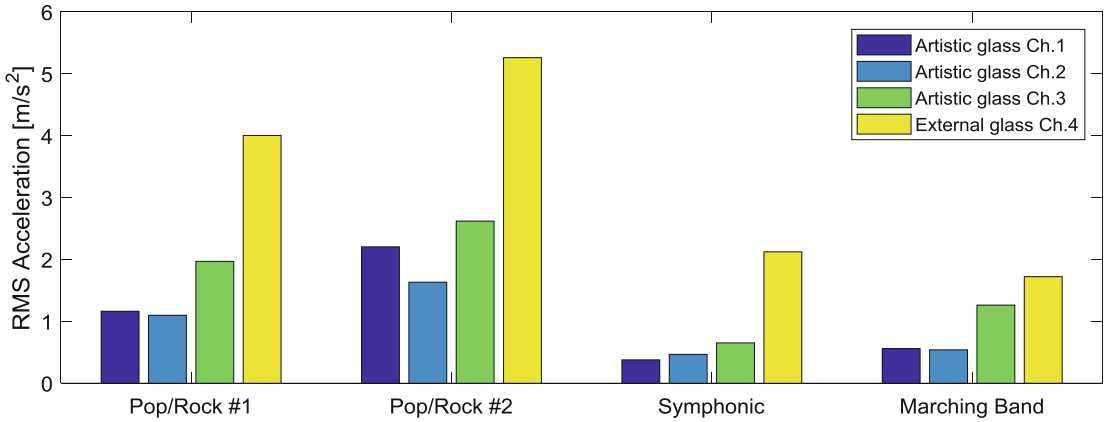

Fig. 39.9 Comparison among the vibration levels of the outer window and the ones of the artistic stained glasses

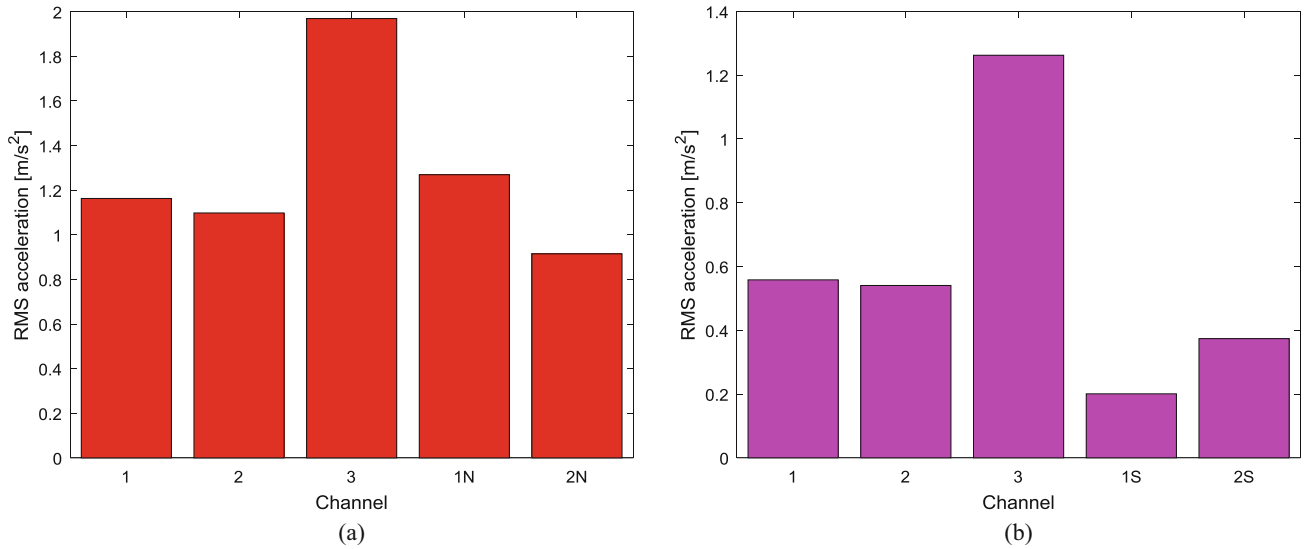

Fig. 39.10 Comparison of vibration levels among different artistic glasses. Channels tagged with N and S letters refer to north and south wall glasses respectively. (**a**) Pop/rock concert #1. (**b**) Marching band concert

It is also interesting to analyze the reduction in the sound pressure level produced by the outer glass: in fact, the pressure level decreases by 70% from the outside microphone to that localized in the crawl space. This demonstrates that the outer window plays a major role in reducing the input to the artistic glasses. The comparison among the RMS acceleration levels of the external glasses against those of the internal artistic glasses throughout the different musical events demonstrates that the noise reduction effect of the outer window is complex to describe. This behavior accords with the complex transformation received by the sound in the external/internal transfer as demonstrated previously in Fig. 39.5. This kind of behavior makes it impossible to specify a vibration attenuation factor for the protection given by the external glass. In any case the vibration attenuation is detectable in all musical environments monitored in this work.

One last comparison will be among the RMS levels of the façade with the lateral ones: in fact until now data have been considered about the main window, facing the main square: in this case different windows under different conditions have been considered. In Fig. 39.10 the bar graphs display the RMS vibration peaks for the 3 sensors mounted on the artistic glass of the façade and for a pair of sensors mounted on the lateral glasses. Lateral glasses are not directly exposed to the loud sound pressure of the concert stage of the, since they receive reflected sound waves. In this sense, it is expected that they should vibrate much less than front glasses. However, they are not equipped with a shielding window as the ones on the façade and they are in more confined and reverberating volumes, also having different mounting frames. For this reason, it is possible to see that the vibration level is about the same range as for the glasses in front of the cathedral. This is a clear indicator that shielding glasses should be considered could play a fundamental role for the preservation of artistic stained glasses.

39.5 Conclusion

The motivation of this study is found in the great concerns of the Veneranda Fabbrica del Duomo for the possible damages to the invaluable artistic stained glasses caused by environmental vibrations generated by concerts held in the front of the cathedral. Literature review was not helpful to determine the risks of sound induced vibrations. Also, it was not possible to find a standard or a preservation practice that states a safe level of vibration.

For this reason, a monitoring campaign on the vibration of the artistic glasses has been run for the whole concert season of Summer 2016. The first operation has been to characterize vibrations on stained glasses. It is possible to observe that about the totality of the vibratory energy is concentrated in the 30–200 Hz band. At the same time, it has been documented that the transfer phenomenon (from sound pressure to stained glasses vibration) cannot be described with a simple linear model. Consequently, it was not possible to proceed with the identification of a frequency response function.

The analysis of RMS levels of vibrations indicates clearly that different musical events expose the stained glasses to very different levels of vibration, ranging from 0.5 m/s^2 for classic music to 2.5 m/s^2 for pop/rock concerts. Data also suggest that shielding the glasses with outer protective windows is a very effective way to reduce vibration levels, since the façade glasses (equipped with shielding windows and exposed directly to the blast of the loudspeakers) vibrated with almost the same energy as the lateral ones (which received sound reflections but were not shielded at all).

The future development of this investigation will see the development of experimental procedures to understand the damaging mechanisms of stained glasses exposed to vibration. In this way, the authors wish to identify a safe threshold of vibrations to help the preservation of this part of the heritage.

References

1. Pirina, C.: Le vetrate del Duomo di Milano dai Visconti agli Sforza. Corpus vitrearum Medii Aevi, Provincia di Milano, Italia (1986.) (in Italian)
2. Hunt, F.L.: An experimental assessment of the possibility of damage to leaded windows by Sonic Bangs. Royal Aircraft Establishment (1969)
3. Hunt, F. L.: Vibration amplitudes produced in St. David's Cathedral by Concorde Sonic Bangs. HM Stationery Office (1971)
4. Pretlove, A.J.: Acousto-elastic effects in the response of large windows to sonic bangs. J. Sound Vib. **9**(3), 487–500 (1969)
5. Carden, H.D.: Vibration characteristics of walls and a plate glass window representative of those of a wood-frame house, NASA Technical Paper 1447 Nasa Technical Reports (1979)
6. Doi, T., Iwanaga, K., Jimbo, M.: Experimental approach on natural frequency of window vibration induced by low frequency sounds. In: Proceedings of the INTER-NOISE 2016 – 45th International Congress and Exposition on Noise Control Engineering: Towards a Quieter Future, pp. 116–124 (2016)
7. Doi, T., Iwanaga, K., Naka, Y.: Experimental approach on transmission of low-frequency sound into a building. In: INTERNOISE 2014 – 43rd International Congress on Noise Control Engineering: Improving the World Through Noise Control (2014)

Chapter 40
Sensitivity Study of BARC Assembly

William Larsen, Jason R. Blough, James DeClerck, Charles VanKarsen, David Soine, and Richard J. Jones

Abstract This paper will present modal analysis results from a systematic study of the assembly of the Box Assembly with Removable Component (BARC). The paper will present results from testing done with both the cut and un-cut version of the BARC and with the different pieces of the BARC both bolted together and attached with a structural adhesive. The boundary condition will be a fixed base excitation. The results will be presented in terms of both Frequency Response Functions (FRFs) and mode shapes and natural frequencies with a goal of showing how the BARC fixture changes with each assembly modification. Upon completion of this testing it is anticipated that a thorough understanding of how assembly methods change the dynamic response of the fixture. This may lead to a suggested assembly method for anyone testing a BARC fixture.

Keywords Box assembly with removable component · BARC · Assembly sensitivity · Boundary conditions · Modal test

40.1 Introduction

The Box Assembly with Removable Component (BARC) [1] fixture was designed to be a surrogate baseline structure representing an object exposed to a shock event. The purpose is to design, build, and validate shock test fixtures that would enable a similar shock experience to a surrogate component. The BARC design and hardware provide "truth data" as a basis of comparison and assessment for fixture designs. Several BARC samples were fabricated, assembled, and shipped to members of the shock and vibration community.

Initial modal tests of BARC showed variation in results. These inconsistencies were claimed to be the results on non-linearity in the bolted joints and inconsistent boundary conditions. This study will focus on trends and variation of the first 9–10 modes of the BARC in the free-free boundary condition.

The BARC assembly [1] is shown in Fig. 40.1. For this document, the BARC assembly consists of two parts: the component and subassembly. The component has three parts: one beam and two brackets. For simplicity, the term box means subassembly.

For the baseline configuration, the beam is attached to each bracket by a single bolt/nut. Each bracket is connected to the box by 4 bolt/nut sets. The BARC has a free-free boundary conditions in this study as shown in Fig. 40.2. Assembly conditions for this study are:

1. Baseline—dry bolted and torqued joints
2. Epoxy the joints between the beam and each bracket (dry bolted between each bracket and the box)
3. Epoxy the joints between each bracket and the box (dry bolted between the beam and each bracket)
4. Epoxy all joints.

The Department of Energy's Kansas City National Security Campus is operated and managed by Honeywell Federal Manufacturing & Technologies, LLC under contract number DE-NA0002839.

W. Larsen · J. R. Blough · J. DeClerck (✉) · C. VanKarsen
Department of Mechanical Engineering-Engineering Mechanics, Michigan Technological University, Houghton, MI, USA
e-mail: jrblough@mtu.edu; jdeclerck@mtu.edu

D. Soine · R. J. Jones
Honeywell Federal Manufacturing & Technologies, LLC, Kansas City, MO, USA

C. Walber et al. (eds.), *Sensors and Instrumentation, Aircraft/Aerospace, Energy Harvesting & Dynamic Environments Testing, Volume 7*, Conference Proceedings of the Society for Experimental Mechanics Series,
https://doi.org/10.1007/978-3-030-12676-6_40

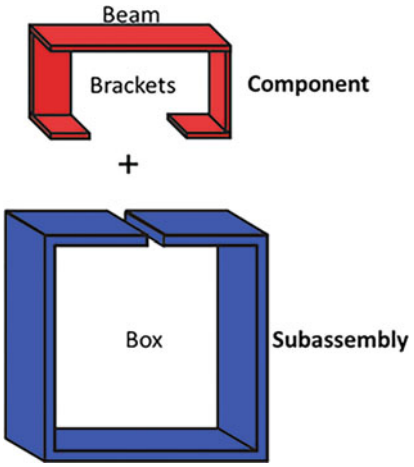

Fig. 40.1 BARC assembly sketch [1]

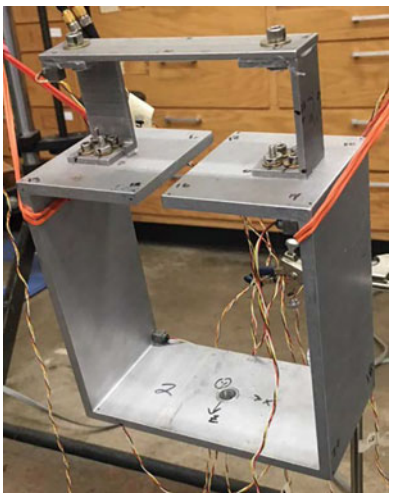

Fig. 40.2 BARC assembly in free boundary condition

40.2 Test Setup and Instrumentation

For all modal tests, the BARC was suspended from a steel frame using rubber bands (Fig. 40.3) to simulate a free-free boundary condition.

The BARC geometry was represented by 24 measurement locations shown in Fig. 40.4. These points were selected for the purpose of visualizing: (1) the geometry of the test article and (2) animated mode shapes. Five triaxial accelerometers were placed near points: 3, 8, 14, 17 and 18. These sensors provided 15 reference degrees of freedom. Roving impact force was applied at 44 degrees of freedom. The remaining response degrees of freedom were constrained to a corresponding measured degree of freedom (e.g. Base: 20 moves the same in the Y-direction as Base: 14).

The triaxial accelerometers were PBC model 356A31. Due to the size of the BARC, a miniature modal hammer (PCB 086E80 [2]) was used. With the white, plastic handle shown in Fig. 40.5, the hammer was 5.2 inches long.

Frequency response functions (FRF) were averaged from five samples. Each sample was 2 seconds in duration, resulting in 0.5 Hz FRF resolution. Sample rate was 8192 samples per second resulting in 4096 Hz bandwidth. A force-exponential window reduced the amplitude by 50% at the end of the 2 second sample.

40.3 Test Plan

Two different BARC samples were used during this study, #2 and #5. Sample numbers were assigned at the very beginning of the overall project prior to distribution to participating facilities. Sample #2 was bare aluminum, as delivered. Sample #5 had been speckle painted for a prior test. The mass of each sample was 0.81 kg.

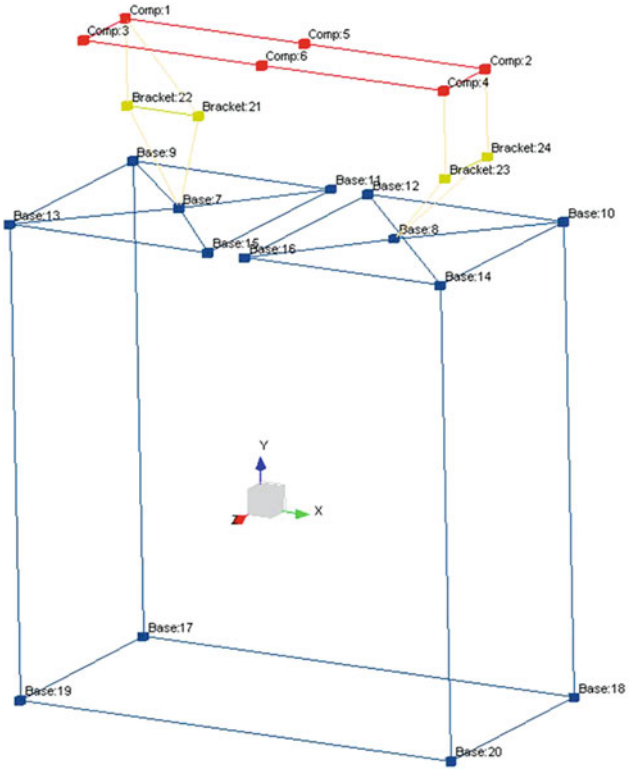

Fig. 40.3 Measurement locations and labels for BARC modal tests

Fig. 40.4 Miniature impulse hammer model 086E80 [2]

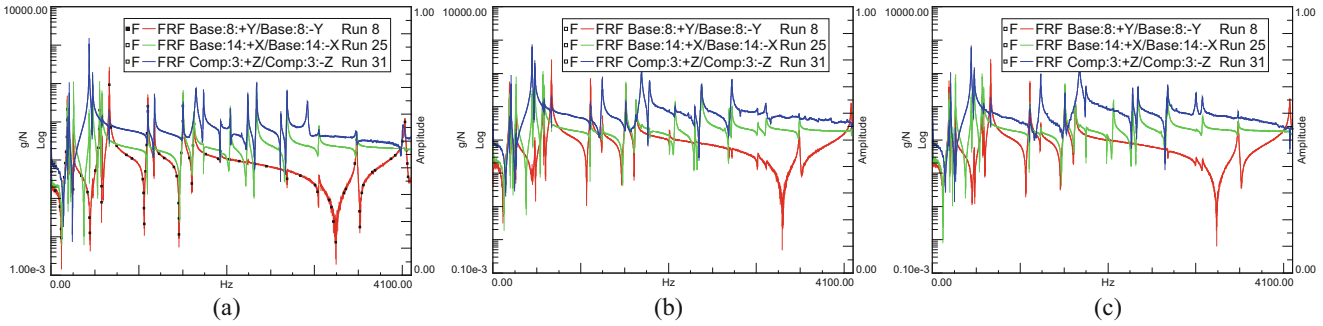

Fig. 40.5 Comparison of sample drive point measurements for the BARC baseline test condition. (**a**) BARC #2. (**b**) BARC #5. (**c**) #2 subassembly with #5 brackets and component

Table 40.1 Test plan to measure effects of different BARC boundary and assembly conditions

Test condition	Boundary condition	Assembly condition	A	B	C
1	Free	Baseline	BARC #2	BARC #5	#2 Subassembly with #5 Brackets and Component
3	Free	Epoxy component to bracket	BARC #2	#5 Subassembly with #2 Brackets and Component	
5	Free	Epoxy bracket to subassembly	BARC #5		
7	Free	Epoxy all joints	BARC #5		

The test plan is shown in Table 40.1. Having two samples allowed for replicate testing for the first two assembly conditions. This enabled assessment of test and dry assembly variation. A fixed-base boundary condition was used for the even numbered test iterations. The iteration numbers are not shown because the fixed-base results are not presented in this paper.

40.4 Test Condition 1: Baseline Assembly

Three modal tests were performed for Test Condition 1. Sample drive point measurements are shown in Fig. 40.5. The Y-axis ranges from 0.001 to 10,000 g/N and the X-axis ranges is 0–4100 Hz. These FRFs show similarity in overall level. The resonant and anti-resonance frequencies are also similar over the measurement frequency band. These measurements indicate that BARC has approximately 25 modes over this frequency band.

The BARC has 10 modes below 1400 Hz. A comparison of the measurement sum over this band is shown in Fig. 40.6. The measurement sums show the same number of resonant peaks with less than 3% frequency variation, with the notable exception of the peak near 1200 Hz for BARC sample #2. BARC #2 was tested in "as received" condition where it was already assembled and torqued. Residual stress was released when this sample was disassembled for subsequent tests. This could be the reason for the observed inconsistency.

FRFs from five references (8x, 8y, 8z, 3x, and 3z) were used to estimate modal parameters. Mode shapes were matched and shown in Table 40.2. The first nine natural frequency sets agree within 3%. The predicted natural frequency for mode 10 is more than 50 Hz lower than the other samples. This is consistent with observations in the measurement sum (Fig. 40.7).

40.5 Test Condition 3: Epoxy Component to Bracket Assembly Condition

Two modal tests were performed for Test Condition 3. Sample drive point measurements are shown in Fig. 40.8. The Y-axis ranges from 0.001 to 10,000 g/N and the X-axis ranges is 0–4100 Hz. These FRFs also show similar overall level. The resonant and anti-resonance frequencies are also similar over the measurement frequency band. These measurements indicate that BARC has approximately 25 modes over this frequency band.

The BARC has 10 modes below 1400 Hz. A comparison of the measurement sum over this band is shown in Fig. 40.9. FRFs from five references (8x, 8y, 8z, 3x, and 3z) were used to estimate modal parameters. Mode shapes were matched and shown in Table 40.3. All natural frequency sets agree within 1%.

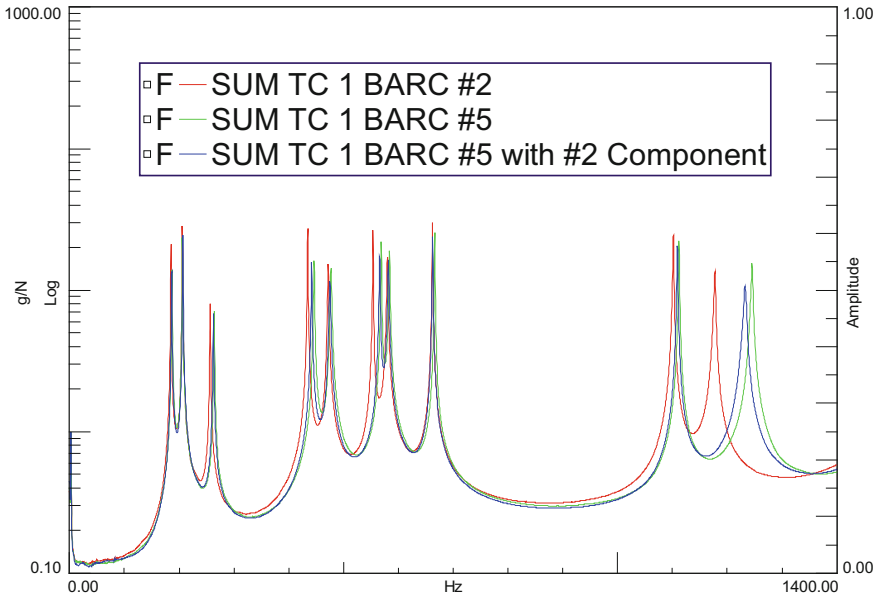

Fig. 40.6 Comparison of amplitude sum of all FRF measurements for each sample for the BARC baseline test condition

Table 40.2 Natural frequency estimates for each sample for the BARC baseline test condition

Mode	BARC #2 (Hz)	BARC #5 (Hz)	#2 Subassembly with #5 brackets and component (Hz)
1	185.0	186.8	186.3
2	205.6	205.6	206.6
3	256.5	263.8	262.3
4	434.3	446.1	441.6
5	471.8	476.9	474.9
6	553.3	568.8	566.0
7	579.9	583.7	581.8
8	662.0	666.1	662.2
9	1101.3	1111.8	1109.0
10	1175.7	1244.2	1230.4

40.6 Test Conditions 5 and 7

Due to limited test samples and observed consistency of the previous tests, only one sample was tested for Test Conditions 5 and 7. Sample drive point measurements are shown in Figs. 40.10 and 40.11. The Y-axis ranges from 0.001 to 10,000 g/N and the X-axis ranges is 0–4100 Hz. These FRFs show similar levels over the measurement frequency band. Many of the resonant and anti-resonance frequencies are also similar with the notable exception being two peaks near 2000 Hz in the (blue) 3Z drive point FRF. These measurements indicate that BARC has approximately 25 modes over this frequency band.

40.7 Comparison of Results for Free Boundary Test Conditions

Modal results from all Free Boundary Condition test are compared to identify and quantify consistency. BARC #5 was chosen for this comparison because it was the sample used for the last two test cases. A comparison of the measurement sum for the four Free Boundary Contrition Test Cases shown in Fig. 40.12.

Mode shapes for each test condition were matched and corresponding natural frequencies are shown in Table 40.4. The first nine natural frequency sets agree within 2%. Mode 10 shows sensitivity when the component is epoxied to the bracket. Mode shapes six and seven swap order when all joints are glued. This is not uncommon when modes are close in natural frequency.

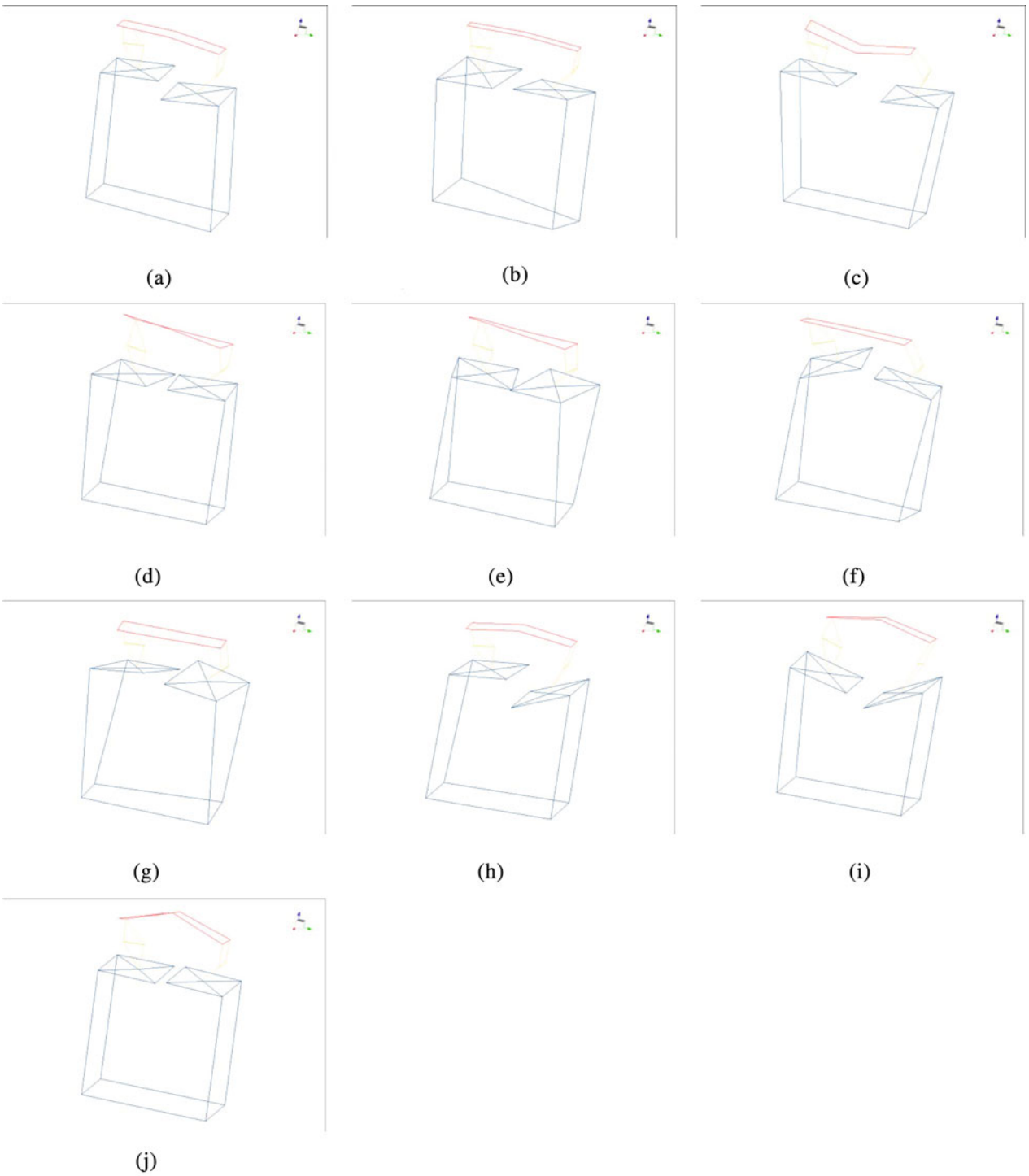

Fig. 40.7 BARC mode shapes for free boundary and baseline assembly. (**a**) Mode 1. (**b**) Mode 2. (**c**) Mode 3. (**d**) Mode 4. (**e**) Mode 5. (**f**) Mode 6. (**g**) Mode 7. (**h**) Mode 8. (**i**) Mode 9. (**j**) Mode 10

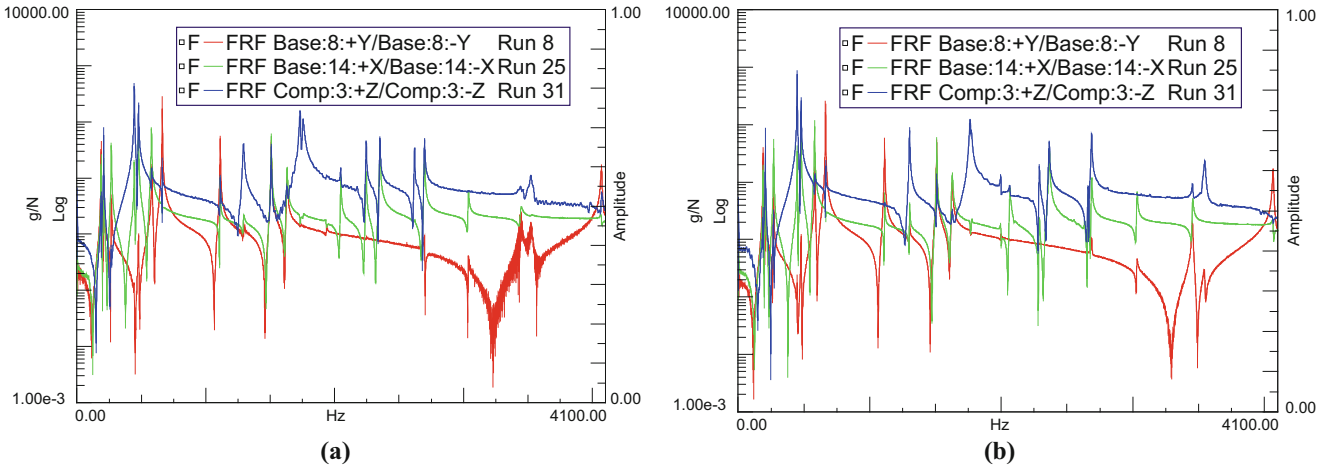

Fig. 40.8 Sample drive point measurements for test condition 3—epoxy component to bracket. (**a**) BARC #2. (**b**) BARC #5 with BARC #2 component and bracket

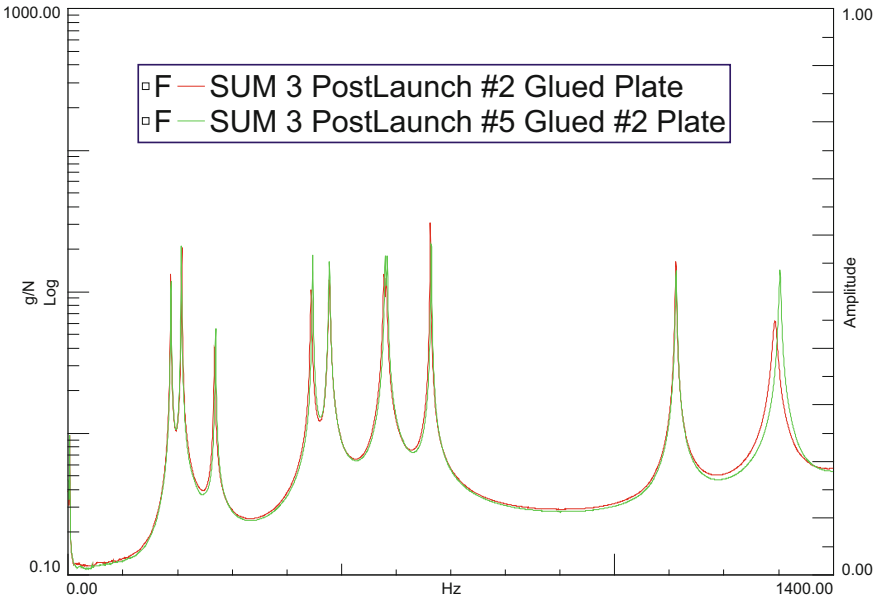

Fig. 40.9 Comparison of amplitude sum of all FRF measurements for each sample for test condition 3—epoxy component to bracket

40.8 Conclusions

- The results of this study show that the natural frequencies of the BARC are sensitive to stiffness changes to the bolted joints.
- Stiffening the interface at the single bolt joint between the component and the brackets has the greatest effect and increases the natural frequency of eight of the first 10 modes.
- Stiffening the 4-bolt joints between the brackets and subassembly affects only a few of the first 10 modes.
- Stiffening all bolted joints has the greatest effect, increasing all natural frequencies compared to baseline and caused the 6th and 7th mode shapes to swap order.
- Natural frequencies of the BARC are also sensitive to residual stress in the assembly.

Table 40.3 Natural frequency estimates for each sample for test condition 3—epoxy component to bracket

Mode	BARC #2 (Hz)	#5 Subassembly with #2 brackets and component (Hz)
1	187.6	187.9
2	207.5	206.6
3	267.7	269.6
4	444.7	447.4
5	477.8	477.7
6	577.9	580.2
7	582.0	583.6
8	662.4	664.1
9	1111.9	1112.4
10	1293.2	1302.1

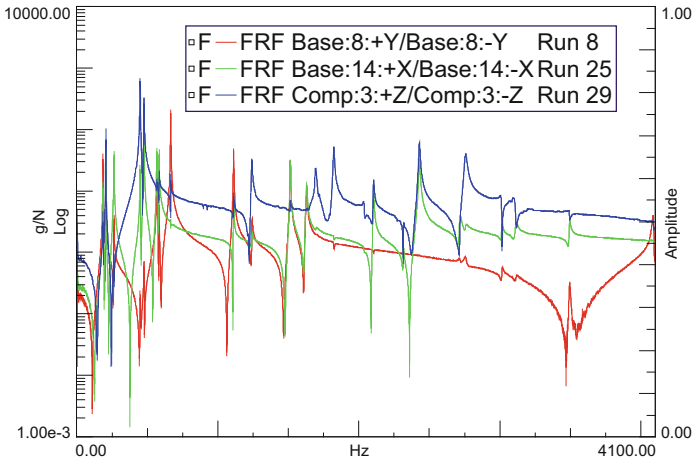

Fig. 40.10 Sample drive point measurements for test condition 5—epoxy bracket to subassembly

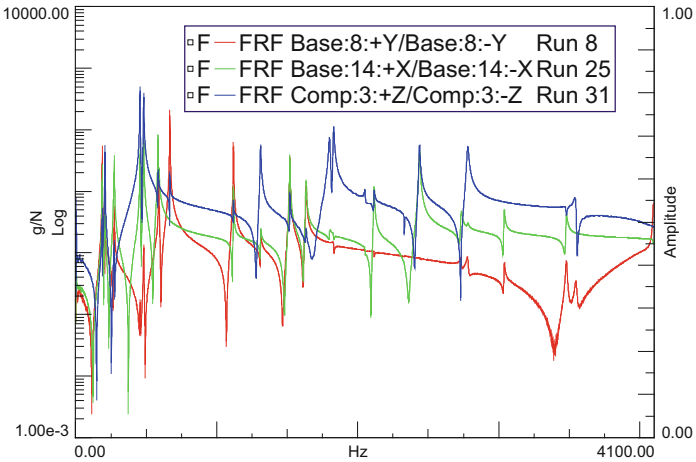

Fig. 40.11 Sample drive point measurements for test condition 7—epoxy all joints

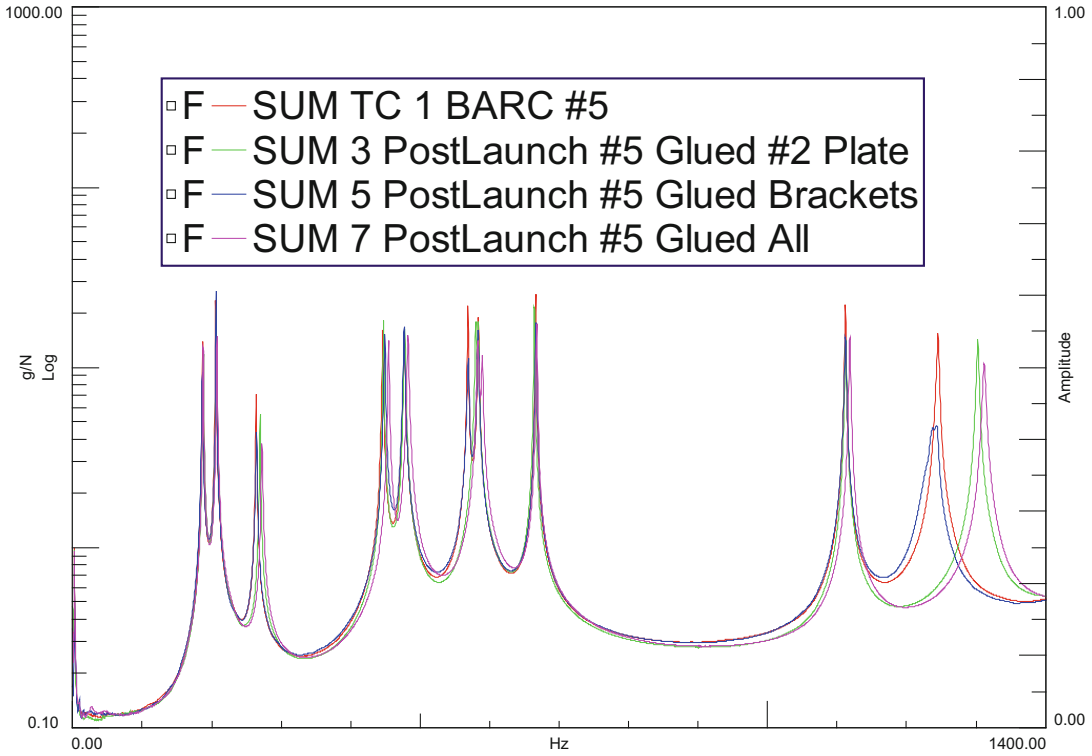

Fig. 40.12 Comparison of amplitude sum of all FRF measurements for each sample across all free boundary condition tests

Table 40.4 Natural frequency estimates across all free boundary condition tests

Mode	TC 1—Baseline (Hz)	TC 3—Epoxy component to bracket (Hz)	TC 5—Epoxy bracket to subassembly (Hz)	TC 7—Epoxy all joints (Hz)
1	186.8	187.9	186.4	187.7
2	205.6	206.6	206.0	207.4
3	263.8	269.6	264.2	272.5
4	446.1	447.4	449.0	454.8
5	476.9	477.7	476.7	482.4
6	568.8	580.2	569.1	589.5
7	583.7	583.6	583.5	583.2
8	666.1	664.1	666.4	667.7
9	1111.8	1112.4	1111.8	1118.4
10	1244.2	1302.1	1232.7	1312.1

References

1. Harvie, J.: Boundary conditions in environmental testing challenge problem
2. PCB Model 086E80 Product Manual. http://www.pcb.com/Products/model/086e80